IFMBE Proceedings

Teodiano Freire Bastos-Filho · Eliete Maria de Oliveira Caldeira · Anselmo Frizera-Neto Editors

Volume 83

XXVII Brazilian Congress on Biomedical Engineering

Proceedings of CBEB 2020, October 26–30, 2020, Vitória, Brazil

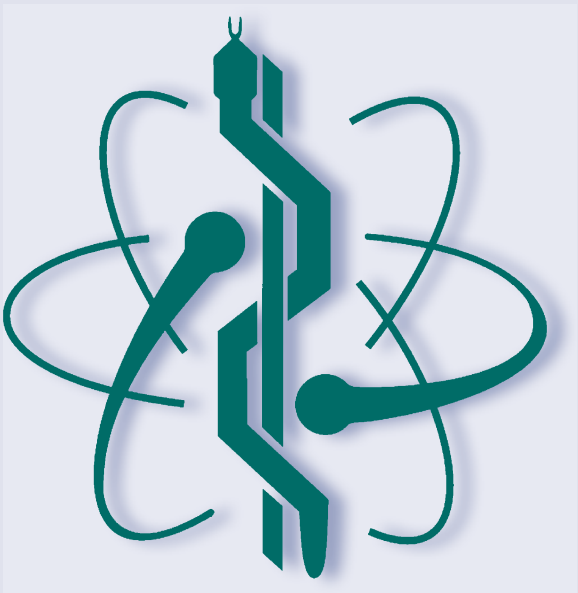

Springer

IFMBE Proceedings

Volume 83

The IFMBE Proceedings Book Series is an official publication of *the International Federation for Medical and Biological Engineering* (IFMBE). The series gathers the proceedings of various international conferences, which are either organized or endorsed by the Federation. Books published in this series report on cutting-edge findings and provide an informative survey on the most challenging topics and advances in the fields of medicine, biology, clinical engineering, and biophysics.

The series aims at disseminating high quality scientific information, encouraging both basic and applied research, and promoting world-wide collaboration between researchers and practitioners in the field of Medical and Biological Engineering.

Topics include, but are not limited to:

- Diagnostic Imaging, Image Processing, Biomedical Signal Processing
- Modeling and Simulation, Biomechanics
- Biomaterials, Cellular and Tissue Engineering
- Information and Communication in Medicine, Telemedicine and e-Health
- Instrumentation and Clinical Engineering
- Surgery, Minimal Invasive Interventions, Endoscopy and Image Guided Therapy
- Audiology, Ophthalmology, Emergency and Dental Medicine Applications
- Radiology, Radiation Oncology and Biological Effects of Radiation

IFMBE proceedings are indexed by SCOPUS, EI Compendex, Japanese Science and Technology Agency (JST), SCImago.

Proposals can be submitted by contacting the Springer responsible editor shown on the series webpage (see "Contacts"), or by getting in touch with the series editor Ratko Magjarevic.

More information about this series at https://link.springer.com/bookseries/7403

Teodiano Freire Bastos-Filho ·
Eliete Maria de Oliveira Caldeira ·
Anselmo Frizera-Neto
Editors

XXVII Brazilian Congress on Biomedical Engineering

Proceedings of CBEB 2020, October 26–30, 2020, Vitória, Brazil

Springer

Editors
Teodiano Freire Bastos-Filho
Department of Electrical Engineering
Universidade Federal do Espírito Santo
Vitória, Brazil

Eliete Maria de Oliveira Caldeira
Department of Electrical Engineering
Universidade Federal do Espírito Santo
Vitória, Brazil

Anselmo Frizera-Neto
Department of Electrical Engineering
Universidade Federal do Espírito Santo
Vitória, Brazil

ISSN 1680-0737 ISSN 1433-9277 (electronic)
IFMBE Proceedings
ISBN 978-3-030-70600-5 ISBN 978-3-030-70601-2 (eBook)
https://doi.org/10.1007/978-3-030-70601-2

This Springer imprint is published by the registered company Springer Nature Switzerland AG
The registered company address is: Gewerbestrasse 11, 6330 Cham, Switzerland

Organization

Steering Committee

General Chair

Teodiano Bastos-Filho, Federal University of Espirito Santo, Brazil

Members

Eliete Maria Caldeira, Federal University of Espirito Santo, Brazil
Anselmo Frizera-Neto, Federal University of Espirito Santo, Brazil
Francisco Santos, Federal University of Espirito Santo, Brazil

Program Committee

Adriano Andrade, Universidade Federal de Uberlândia (Brazil)
Adson Ferreira, Universidade de Brasília (Brazil)
Alcimar Soares, Universidade Federal de Uberlândia (Brazil)
Ana Maria Marques da Silva, Pontifícia Universidade Católica—RS (Brazil)
Ana Carolina de Oliveira, Universidade Federal do Triângulo Mineiro (Brazil)
Ana Cecilia Villa Parra, Universidad Politécnica Salesiana—Cuenca (Ecuador)
André Fábio Kohn, Universidade de São Paulo (Brazil)
Anibal Cotrina, Universidade Federal do Espírito Santo (Brazil)
Antônio Padilha Bó, University of Queensland (Australia)
Antonio Carlos Almeida, Universidade de São Paulo (Brazil)
Aparecido Augusto Carvalho, Universidade Estadual Paulista (Brazil)
Daniel Cavalieri, Instituto Federal de Ensino Superior—Vitória-ES (Brazil)
Denis Delisle, Universidade Federal do Espírito Santo (Brazil)
Elisa Berenguer, Universidad Nacional de San Juan (Argentina)
Frederico Tavares, Universidade Federal do Rio de Janeiro (Brazil)
Henrique Takachi Moriya, Universidade de São Paulo (Brazil)
Idagene Cestari, Instituto do Coração—USP (Brazil)
Jes Cerqueira, Universidade Federal da Bahia (Brazil)
João Salinet, Universidade Federal do ABC (Brazil)
John Jairo Villarejo Mayor, Universidade Federal do Paraná (Brazil)
José Wilson Bassani, Universidade Estadual de Campinas (Brazil)
Karin Komati, Instituto Federal de Ensino Superior—Serra-ES (Brazil)
Leandro Bueno, Instituto Federal de Ensino Superior—Vitória-ES (Brazil)
Leonardo Felix, Universidade Federal de Viçosa (Brazil)

Liliam Oliveira, Universidade Federal do Rio de Janeiro (Brazil)
Marcus Vieira, Universidade Federal de Goiás (Brazil)
Mauro Callejas Cuervo, Universidad Pedagógica y Tecnológica de Colombia (Colombia)
Mario R. Gongora-Rubio, Instituto de Pesquisas Tecnológicas (Brazil)
Pablo Diez, Universidad Nacional de San Juan (Argentina)
Percy Nohama, Pontifícia Universidade Católica—PR (Brazil)
Renato Zangaro, Universidade Anhembi Morumbi (Brazil)
Richard Tello, Instituto Federal de Ensino Superior—Serra-ES (Brazil)
Rodrigo Andreao, Instituto Federal de Ensino Superior—Vitória-ES (Brazil)
Rosana Bassani, Universidade Estadual de Campinas (Brazil)
Sandra Muller, Instituto Federal de Ensino Superior—Vitória-ES (Brazil)
Sônia Maria Malmonge, Universidade Federal do ABC (Brazil)
Sridhar Krishnan, Ryerson University (Canada)
Pablo Diez, Universidad Nacional de San Juan (Argentina)
Roberto Sagaro Zamora, Universidad de Oriente (Cuba)
Vicente Lucena, Universidade Federal do Amazonas (Brazil)

Preface

This volume contains selected papers presented at the XXVII Brazilian Congress on Biomedical Engineering (Congresso Brasileiro de Engenharia Biomédica—CBEB), held virtually in Vitoria, Brazil, on October 26–30, 2020. The conference was organized by the Federal University of Espirito Santo (Universidade Federal do Espírito Santo—UFES) (Brazil).

CBEB 2020 is 27th edition of this conference organized by the Brazilian Society on Biomedical Engineering (Sociedade Brasileira de Engenharia Biomédica—SBEB), with biannual periodicity, organized by researchers of a local research institution, with the collaboration of the entire scientific community linked to the area of Biomedical Engineering in Brazil. The conference has a tradition of bringing together academic communities, researchers, scientists from various fields, undergraduate and postgraduate students, as well as representatives from industry, commerce and governments, so that everyone can discuss and present their ideas about the main Biomedical Engineering problems in the country. This conference addresses the following areas: Biomedical Signal and Image Processing; Bioengineering; Biomaterials, Tissue Engineering and Artificial Organs; Biomechanics and Rehabilitation; Biomedical Devices and Instrumentation; Clinical Engineering and Evaluation of Technology in Health; Neuroengineering; Medical Robotic, Assistive Technology and Informatics in Health; Biomedical Optics and Systems and Technologies for Therapy and Diagnosis; Basic Industrial Technology in Health; and Special Topics in Biomedical Engineering.

The book was organized in eleven parts, according to the main conference topics of the conference. Each part is devoted to research in different fields of biomedical engineering, in the areas of (1) Biomedical Signal and Image Processing, (2) Bioengineering, (3) Biomaterials, Tissue Engineering and Artificial Organs, (4) Biomechanics and Rehabilitation, (5) Biomedical Devices and Instrumentation, (6) Clinical Engineering and Evaluation of Technology in Health, (7) Neuroengineering, (8) Medical Robotic, Assistive Technology and Informatics in Health, (9) Biomedical Optics and Systems and Technologies for Therapy and Diagnosis, (10) Basic Industrial Technology in Health and (11) Special Topics in Biomedical Engineering.

CBEB 2020 received 665 contributions from authors of 19 countries around the world. After a thorough peer-review process, the Program Committee accepted 358 papers to be published in this book. We appreciate all authors for their contribution. These papers are published in the present book, achieving an acceptance rate of about 53%.

We would like to take this opportunity to thank members of Program Committee and invited external reviewers for their efforts and expertise in contribution to reviewing, without which it would be impossible to maintain the high standards of peer-reviewed papers. 32 Program Committee members and 547 invited external reviewers devoted their time and energy for peer-reviewing manuscripts. Our reviewers come from all over the world and represent 19 countries.

We also would like to thank the following keynote speakers of CBEB 2020: Nitish Thakor (USA), Sridhar Krishnan (Canada), André Fabio Kohn (Brazil), Vanderlei Salvador Bagnato (Brazil), Edgard Morya (Brazil), João Machado (Brazil) and Idagene Cestari (Brazil) for sharing their knowledge and experience.

We appreciate the partnership with Springer, EasyChair, SBEB, FEST and Softaliza as well as our sponsors (CNPq, FAPES and Prolife) for their essential support during the preparation of CBEB 2020.

Thank you very much to CBEB 2020 Team. Their involvement and hard work were crucial to the success of the CBEB 2020 conference.

Vitória, Brazil
February 2021

Teodiano Freire Bastos-Filho
Anselmo Frizera-Neto
Eliete Maria de Oliveira Caldeira

Contents

Basic Industrial Technology in Health

Analysis of the Acoustic Power Emitted by a Physiotherapeutic Ultrasound Equipment Used at the Brazilian Air Force Academy 3
J. G. S. N. Cavalcanti, W. C. A. Pereira, and J. F. S. Costa-Júnior

Synthesis and Antibacterial Activity of Maleimides 11
E. Conrado, C. J. Francisco, R. H. Piccoli, and A. F. Uchoa

Bioengineering

Study of the Effect of Bioceramic Compressive Socks on Leg Edema 19
A. A. S. Sakugawa, L. A. L. Conrado, A. Balbin Villaverde, and E. Munin

Analysis of the Electric Field Behavior on a Stimulation Chamber Applying the Superposition Principle 25
L. A. Sá, E. M. S. Bortolazzo, J. A. Costa JR, and P. X. de Oliveira

Development of a Non-rigid Model Representing the Venous System of a Specific Patient 31
M. C. B. Costa, S. D. F. Gonçalves, T. C. Lucas, M. L. F. Silva, C. M. P. Junior, J. Haniel, and R. Huebner

Comparative Study of Rheological Models for Pulsatile Blood Flow in Realistic Aortic Arch Aneurysm Geometry by Numerical Computer Simulation 37
M. L. F. Silva, S. D. F. Gonçalves, M. C. B. Costa, and R. Huebner

Total Lung Capacity Maneuver as a Tool Screen the Relative Lung Volume in Balb/c Mice 43
A. E. Lino-Alvarado, J. L. Santana, R. L. Vitorasso, M. A. Oliveira, W. Tavares-Lima, and H. T. Moriya

The Influence of Cardiac Ablation on the Electrophysiological Characterization of Rat Isolated Atrium: Preliminary Analysis 49
J. G. S. Paredes, S. Pollnow, I. Uzelac, O. Dössel, and J. Salinet

Evaluation of the Surface of Dental Implants After the Use of Instruments Used in Biofilm Removal: A Comparative Study of Several Protocols 55
D. P. V. Leite, G. E. Pires, F. V. Bastos, A. L. Sant'ana, L. Frigo, A. Martins e Silva, J. E. P. Nunes, M. H. B. Machado, A. Baptista, R. S. Navarro, and A. T. Araki

Comparison of Hemodynamic Effects During Alveolar Recruitment Maneuvers in Spontaneously Hypertensive Rats Treated and Non-treated with Hydralazine 59
L. C. Ferreira, R. L. Vitorasso, M. H. G. Lopes, R. S. Augusto, F. G. Aoki, M. A. Oliveira, W. Tavares-Lima, and H. T. Moriya

Experimental Study of Bileaflet Mechanical Heart Valves 65
Eraldo Sales, M. Mazzetto, S. Bacht, and I. A. Cestari

Preliminary Results of Structural Optimization of Dental Prosthesis Using Finite Element Method 71
M. M. Togashi, M. P. Andrade, F. J. dos Santos, B. A. Hernandez, and E. A. Capello Sousa

Biomaterials, Tissue Engineering and Artificial Organs

Tribological Characterization of the ASTM F138 Austenitic Stainless-Steel Treated with Nanosecond Optical Fiber Ytterbium Laser for Biomedical Applications 79
Marcelo de Matos Macedo, Giovanna Vitória Rodrigues Bernardes, Jorge Humberto Luna-Domínguez, Vikas Verma, and Ronaldo Câmara Cozza

Computational Modeling of Electroporation of Biological Tissues Using the Finite Element Method 85
M. A. Knabben, R. L. Weinert, and A. Ramos

The Heterologous Fibrin Sealant and Aquatic Exercise Treatment of Tendon Injury in Rats 91
S. M. C. M. Hidd, E. F. Dutra Jr, C. R. Tim, A. L. M. M. Filho, L. Assis, R. S. Ferreira Jr, B. Barraviera, and M. M. Amaral

Myxomatous Mitral Valve Mechanical Characterization 97
A. G. Santiago, S. M. Malmonge, P. M. A. Pomerantzeff, J. I. Figueiredo, and M. A. Gutierrez

Qualitative Aspects of Three-Dimensional Printing of Biomaterials Containing Devitalized Cartilage and Polycaprolactone 101
I. M. Poley, R. Silveira, J. A. Dernowsek, and E. B. Las Casas

Chemical Synthesis Using the B-Complex to Obtain a Similar Polymer to the Polypyrrole to Application in Biomaterials 107
Lavínia Maria Domingos Pinto, Mariane de Cássia Rodrigues dos Santos, Mirela Eduarda Custódio, F. E. C. Costa, Larissa Mayra Silva Ribeiro, and Filipe Loyola Lopes

Evaluation of the Effect of Hydrocortisone in 2D and 3D HEp-2 Cell Culture 113
M. O. Fonseca, B. H. Godoi, N. S. Da Silva, and C. Pacheco-Soares

Surface Topography Obtained with High Throughput Technology for hiPSC-Derived Cardiomyocyte Conditioning 119
Lucas R. X. Cortella, I. A. Cestari, M. S., M. Mazzetto, A. F. Lasagni, and Ismar N. Cestari

The Effect of Nitrided Layer on Antibacterial Properties of Biomedical 316L Stainless Steel 127
M. Benegra, G. H. Couto, and E. A. Bernardelli

Biomechanical Analysis of Tissue Engineering Construct for Articular Cartilage Restoration—A Pre-clinical Study 133
R. R. de Faria, M. J. S. Maizato, I. A. Cestari, A. J. Hernandez, D. F. Bueno, R. Bortolussi, C. Albuquerque, and T. L. Fernandes

Cytotoxicity Evaluation of Polymeric Biomaterials Containing Nitric Oxide Donors Using the Kidney Epithelial Cell Line (Vero) 139
V. C. P. Luz, F. N. Ambrosio, C. B. Lombello, A. B. Seabra, and M. H. M. Nascimento

Cellular Interaction with PLA Biomaterial: Scanning Electron Microscopy Analysis 145
L. H. S. Mazzaron and C. B. Lombello

Development of a Gelatin-Based Hydrogel to be Used as a Fibrous Scaffold in Myocardial Tissue Engineering 153
C. Parente and S. M. Malmonge

Experimental and Clinical Performance of Long-Term Cannulas for Mechanical Circulatory Assistance 161
H. T. T. Oyama, S. Bacht, M. Mazzetto, L. F. Caneo, M. B. Jatene, F. B. Jatene, and I. A. Cestari

Evaluation of *Lantana Trifolia* Total Extract in Cell Culture: Perspective for Tissue Engineering 167
C. F. L. Silva, L. R. Rezende, F. N. Ambrosio, J. Badanai, R. A. Lombello, and C. B. Lombello

Study on the Disinfection Stability of Bullfrog Skin 173
D. N. de Moraes, D. IKozusny-Andreani, C. R. Tim, L. Assis, A. P. Da Costa, and M. M. Amaral

Corrosion Analysis of a Marked Biomaterial 179
Eurico Felix Pieretti, Maurício David Martins das Neves, and Renato Altobelli Antunes

Mechanical and Morphological Analysis of Electrospun Poly(ε-Caprolactone) and Reduced Graphene Oxide Scaffolds for Tissue Engineering 185
M. J. S. Maizato, H. T. T. Oyama, A. A. Y. Kakoi, and I. A. Cestari

Experimental Apparatus for Evaluation of Calcium Fluctuations in Cardiomyocytes Derived from Human-Induced Pluripotent Stem Cells 191
M. C. Araña, R. D. Lahuerta, L. R. X. Cortella, M. Mazzetto, M. Soldera, A. F. Lasagni, I. N. Cestari, and I. A. Cestari

Cytotoxicity of Alumina and Calcium Hexaluminate: Test Conditions 197
R. Arbex, L. R. Rezende, F. N. Ambrosio, L. M. M. Costa, and C. B. Lombello

Tendon Phantom Mechanical Properties Assessment by Supersonic Shear Imaging with Three-Dimensional Transducer 207
V. C. Martins, G. B. G. Rolando, L. L. De Matheo, W. C. A. Pereira, and L. F. Oliveira

Physiological Control of Pulsatile and Rotary Pediatric Ventricular Assist Devices 213
T. R. Melo, T. D. Cordeiro, I. A. Cestari, J. S. da Rocha Neto, and A. M. N. Lima

Evaluation of Calcium Phosphate-Collagen Bone Cement: A Preliminary Study 221
C. Ribeiro, V. A. D. Lima, and L. F. G. Setz

Qualitative Hemolysis Analyses in VAD by Stress Distribution Using Computational Hemodynamics 227
G. B. Lopes Jr, E. G. P. Bock, and L. Cabezas-Gómez

Biomechanics and Rehabilitation

Development and Comparison of Different Implementations of Fuzzy Logic for Physical Capability Assessment in Knee Rehabilitation 235
Thiago B. Susin, R. R. Baptista, Henrique S. Dias, and Fabian L. Vargas

Serious Games and Virtual Reality in the Treatment of Chronic Stroke: Both Sides Rehabilitation 239
C. M. Alves, A. R. Rezende, I. A. Marques, D. C. Silva, T. S. Paiva, and E. L. M. Naves

Technologies Applied for Elbow Joint Angle Measurements: A Systematic Review 245
A. R. Rezende, C. M. Alves, I. A. Marques, D. C. Silva, T. S. Paiva, and E. L. M. Naves

The Importance of Prior Training for Effective Use of the Motorized Wheelchair 251
D. C. Silva, C. M. Alves, A. R. Rezende, I. A. Marques, T. S. Paiva, E. L. M. Naves, and E. A. Lamounier Junior

Kinematic Approach for 4 DoF Upper Limb Robotic Exoskeleton in Complex Rehabilitation Tasks 257
Daily Milanés-Hermosilla, Roberto Sagaró-Zamora, Rafael Trujillo-Codorniú, Mauricio Torres-Quezada, D. Delisle-Rodriguez, and T. Bastos-Filho

An Integrated Method to Analyze Degenerative Bone Conditions on Transfemoral Amputees 267
Leonardo Broche Vázquez, Claudia Ochoa-Diaz, Roberto Sagaró Zamora, and Antônio Padilha L. Bó

Forced Oscillations and Functional Analysis in Patients with Idiopathic Scoliosis 277
Cíntia Moraes de Sá Sousa, Luis Eduardo Carelli, André L. C. Pessoa, Agnaldo José Lopes, and P. L. Melo

Differences in Respiratory Mechanics in Emphysema and Chronic Bronchitis Evaluated by Forced Oscillations 285
E. M. Teixeira, A. J. Lopes, and P. L. Melo

Automated 3D Scanning Device for the Production of Forearm Prostheses and Orthoses 293
M. C. de Oliveira, M. C. de Araújo, and M. G. N. M. da Silva

Low Amplitude Hand Rest Tremor Assessment in Parkinson's Disease Based on Linear and Nonlinear Methods 301
Amanda Rabelo, João Paulo Folador, Ana Paula Bittar, Luiza Maire, Samila Costa, Alice Rueda, S. Krishnan, Viviane Lima, Rodrigo M. A. Almeida, and Adriano O. Andrade

Adaptation of Automatic Postural Responses in the Dominant and Non-dominant Lower Limbs 307
C. D. P. Rinaldin, J. A. De Oliveira, C. Ribeiro de Souza, E. M. Scheeren, E. F. Manffra, D. B. Coelho, and L. A. Teixeira

Influence of the Layout of the Ludic Tables on the Amplitude and Concentration of Upper Limb Movements 313
E. J. Alberti, A. Brawerman, and S. F. Pichorim

Photobiomodulation Reduces Musculoskeletal Marker Related to Atrophy 319
S. R. Gonçalves, C. R. Tim, C. Martignago, A. Renno, R. B. Silva, and L. Assis

Effectiveness of Different Protocols in Platelet-Rich Plasma Recovery 325
C. Dall'Orto, R. Ramsdorf, L. Assis, and C. Tim

Evaluation of the Motor Performance of People with Parkinson's Disease Through the Autocorrelation Function Estimated from Sinusoidal Drawings . . . 329
V. C. Lima, M. F. Vieira, A. A. Pereira, and A. O. Andrade

Shear Modulus of Triceps Surae After Acute Stretching 337
M. C. A. Brandão, G. C. Teixeira, and L. F. Oliveira

Estimation of the Coordination Variability Between Pelvis-Thigh Segments During Gait at Different Walking Speeds in Sedentary Young People and Practitioners of Physical Activities 343
G. A. G. De Villa, A. Abbasi, A. O. Andrade, and M. F. Vieira

Gait Coordination Quantification of Thigh-Leg Segments in Sedentary and Active Youngs at Different Speeds Using the Modified Vector Coding Technique 349
G. A. G. De Villa, F. B. Rodrigues, A. Abbasi, A. O. Andrade, and M. F. Vieira

Demands at the Knee Joint During Jumps in Classically Trained Ballet Dancers 353
T. S. Lemes, G. A. G. De Villa, A. P. Rodrigues, J. M. A. Galvão, R. M. Magnani, R. S. Gomide, M. B. Millan, E. M. Mesquita, L. C. C. Borges, and M. F. Vieira

Modeling and Analysis of Human Jump Dynamics for Future Application in Exoskeletons 357
Mouhamed Zorkot, Wander Gustavo Rocha Vieira, and Fabricio Lima Brasil

Functional Electrical Stimulation Closed-Loop Strategy Using Agonist-Antagonist Muscles for Controlling Lower Limb Movements 365
D. C. Souza, J. C. Palma, R. A. Starke, G. N. Nogueira-Neto, and P. Nohama

Control System Viability Analysis on Electrical Stimulation Platform 373
D. G. S. Ribeiro and R. F. Kozan

Influence of the Use of Upper Limbs in the Vertical Jump on the Ground Reaction Force of Female Athletes from the Development Basketball Categories 381
A. P. Xavier, S. C. Corrêa, E. R. S. Viana, C. S. Oliveira, and C. P. Guimarães

Wearable System for Postural Adaptation 387
B. C. Bispo, N. A. Cunha, E. L. Cavalcante, G. R. P. Esteves, K. R. C. Ferreira, A. C. Chaves, and M. A. B. Rodrigues

On the Use of Wrist Flexion and Extension for the Evaluation of Motor Signs in Parkinson's Disease 395
N. R. Lígia, A. O. Adriano, and P. A. Adriano

Motor Performance Improvement in a Technological Age: A Literature Review 401
J. F. Vilela, L. Basso, D. S. F. Magalhães, and A. F. Frade-Barros

Modulation of EMG Parameters During Ankle Plantarflexor Fatigue in Trained Gymnasts and Healthy Untrained Controls 405
M. C. da Silva, C. R. da Silva, F. F. de Lima, J. R. Lara, J. P. Gustavson, and F. H. Magalhães

Amputation Rates in Southeastern Brazil 413
A. R. F. Jorge, A. M. de Freitas, and A. B. Soares

Design and Manufacturing of Flexible Finger Prosthesis Using 3D Printing 419
V. V. P. Pinto, J. E. Alvarez-Jácobo, and A. E. F. Da Gama

Characterization of Sensory Perception Associated with Transcutaneous Electrostimulation Protocols for Tactile Feedback Restoration 425
A. C. P. R. Costa, F. A. C. Oliveira, S. R. J. Oliveira, and A. B. Soares

Differences in Shear Modulus Among Hamstring Muscles After an Acute Stretching 433
G. C. Teixeira, M. C. A. Brandão, and L. F. Oliveira

Adapted Children's Serious Game Using Dennis Brown Orthotics During the Preparatory Phase for the Gait 439
A. T. D. Silva, B. C. Bispo, A. M. Conceição, M. B. C. Silva, G. R. P. Esteves, and M. A. B. Rodrigues

A Serious Game that Can Aid Physiotherapy Treatment in Children Using Dennis Brown Orthotics 445
A. T. D. Silva, B. C. Bispo, G. R. P. Esteves, M. B. C. Silva, and M. A. B. Rodrigues

A Neuromodulation Decision Support System: A User-Centered Development Study 451
G. B. A. Maranhão, T. M. De Santana, D. M. De Oliveira, and A. E. F. Da Gama

Mechanisms of Shoulder Injury in Wheelchair Users 459
H. O. Rodrigues and O. L. Silva

Development and Customization of a Dennis Brown Orthosis Prototype Produced from Anthropometric Measurements by Additive Manufacturing 465
A. T. D. Silva, A. S. Lages, J. V. B. D. Silveira, G. R. P. Esteves, B. C. Bispo, N. A. Santos, M. E. Kunkel, and M. A. B. Rodrigues

Comparison of Kinematic Data Obtained by Inertial Sensors and Video Analysis 471
J. C. Silva, J. S. Oliveira, A. B. F. Luz, J. L. Pinheiro, and I. M. Miziara

NNMF Analysis to Individual Identification of Fingers Movements Using Force Feedback and HD-EMG 477
V. C. Ecard, L. L. Menegaldo, and L. F. Oliveira

Nonlinear Closed-Loop Control of an OpenSim Wrist Model: Tuning Using Genetic Algorithm 485
W. C. Pinheiro, P. B. Furlan, and L. L. Menegaldo

Quantification of Gait Coordination Variability of Pelvis-Thigh Segments in Young Sedentary and Practitioners People Walking in Different Slopes Using the Vector Coding Technique 491
G. A. G. De Villa, L. Mochizuki, A. Abbasi, A. O. Andrade, and M. F. Vieira

Prediction of the Heel Displacement During the Gait Using Kalman Filter in 2D Image . . . 497
E. M. Mesquita, R. S. Gomide, R. P. Lemos, and M. F. Vieira

Achilles Tendon Tangent Moduls of Runners . . . 505
M. S. Pinto, C. A. R. Sánchez, M. C. A. Brandão, L. L. Menegaldo, and L. F. Oliveira

Modeling and Simulation of Lower Limbs Exoskeleton for Children with Locomotion Difficulties . . . 511
N. R. Wahbe, V. N. O. Louro, R. C. Martins, J. P. H. Lima, and R. R. de Faria

Remote Control Architecture for Virtual Reality Application for Ankle Therapy . . . 517
J. Y. M. Villamizar, I. Ostan, D. A. E. Ortega, and A. A. G. Siqueira

Callus Stiffness Evolution During the Healing Process—A Mechanical Approach . . . 523
J. R. O. S. Neto, R. R. P. Rodarte, and P. P. Kenedi

An Analytical Model for Knee Ligaments . . . 531
J. E. Silva, R. R. P. Rodarte, L. S. P. P. Segmiller, S. A. S. Barros, and P. P. Kenedi

Anterior–Posterior Ground Reaction Forces During Gait in Children and Elderly Women . . . 537
V. L. Vargas, A. G. Aires, G. S. Heidner, M. F. Vieira, and R. R. Baptista

Gait Speed, Cadence and Vertical Ground Reaction Forces in Children . . . 541
A. M. B. S. das Neves, A. G. Aires, V. L. Vargas, L. D. de Souza, T. B. de Souza, T. B. Villar, M. F. Vieira, and R. R. Baptista

May Angular Variation Be a Parameter for Muscular Condition Classification in SCI People Elicited by Neuromuscular Electrical Stimulation? . . . 547
C. D. P. Rinaldin, C. Papcke, E. Krueger, G. N. Nogueira-Neto, P. Nohama, and E. M. Scheeren

Kinematics and Synergies Differences Between Horizontal and Vertical Jump Test . . . 553
H. L. C. Oliveira, P. V. S. Moreira, and L. L. Menegaldo

Modeling, Control Strategies and Design of a Neonatal Respiratory Simulator . . . 563
A. B. A. Campos and A. T. Fleury

Application of Recurrence Quantifiers to Kinetic and Kinematic Biomechanical Data . . . 573
A. O. Assis, A. O. Andrade, and M. F. Vieira

Virtual Environment for Motor and Cognitive Rehabilitation: Towards a Joint Angle and Trajectory Estimation . . . 579
D. Soprani, T. Botelho, C. Tavares, G. Cruz, R. Zanoni, J. Lagass, S. Bino, and P. Garcez

Kinematic Model and Position Control of an Active Transtibial Prosthesis . . . 587
V. Biazi Neto, G. D. Peroni, A. Bento Filho, A. G. Leal Junior, and R. M. Andrade

Development of a Parallel Robotic Body Weight Support for Human Gait Rehabilitation . . . 593
L. A. O. Rodrigues and R. S. Gonçalves

Comparison Between the *Passé* and *Coupé* Positions in the Single Leg Turn Movement in a Brazilian Zouk Practitioner: A Pilot Study 599
A. C. Navarro, A. P. Xavier, J. C. Albarello, C. P. Guimarães, and L. L. Menegaldo

Automatic Rowing Kinematic Analysis Using OpenPose and Dynamic Time Warping 605
V. Macedo, J. Santos, and R. S. Baptista

Analysis of Seat-to-Hand Vibration Transmissibility in Seated Smartphone Users 613
R. M. A. Dutra, G. C. Melo, and M. L. M. Duarte

Analysis of Matrix Factorization Techniques for Extraction of Motion Motor Primitives 621
P. F. Nunes, I. Ostan, W. M. dos Santos, and A. A. G. Siqueira

Control Design Inspired by Motors Primitives to Coordinate the Functioning of an Active Knee Orthosis for Robotic Rehabilitation 629
P. F. Nunes, D. Mosconi, I. Ostan, and A. A. G. Siqueira

Mechanical Design of an Active Hip and Knee Orthosis for Rehabilitation Applications 637
J. P. C. D. Freire, N. A. Marafa, R. C. Sampaio, Y. L. Sumihara, J. B. de Barros, W. B. Vidal Filho, and C. H. Llanos

A Bibliometric Analysis of Lower Limb Exoskeletons for Rehabilitation Applications 645
N. A. Marafa, C. H. Llanos, and P. W. G. Taco

Biomechatronic Analysis of Lower Limb Exoskeletons for Augmentation and Rehabilitation Applications 653
N. A. Marafa, R. C. Sampaio, and C. H. Llanos

Numerical Methods Applied to the Kinematic Analysis of Planar Mechanisms and Biomechanisms 661
H. N. Rosa, M. A. Bazani, and F. R. Chavarette

Project of a Low-Cost Mobile Weight Part Suspension System 667
L. C. L. Dias, C. B. S. Vimieiro, R. L. L. Dias, and D. M. C. F. Camargos

Design of a Robotic Device Based on Human Gait for Dynamical Tests in Orthopedic Prosthesis 673
D. Rosa, T. M. Barroso, L. M. Lessa, J. P. Gouvêa, and L. H. Duque

Analysis of an Application for Fall Risk Screening in the Elderly for Clinical Practice: A Pilot Study 681
P. V. S. Moreira, L. H. C. Shinoda, A. Benedetti, M. A. M. R. Staroste, E. V. N. Martins, J. P. P. Beolchi, and F. M. Almeida

Development of Prosthesis and Evaluation of the Use in Short Term in a Left Pelvic Limb in a Dog 689
G. C. Silveira, A. E. M. Pertence, A. R. Lamounier, E. B. Las Casas, M. H. H. Lage, M. X. Santos, and S. V. D. M. El-Awar

Estimation of Muscle Activations in Black Belt Taekwondo Athletes During the *Bandal Chagui* Kick Through Inverse Dynamics 695
P. V. S. Moreira, K. A. Godoy Jaimes, and L. L. Menegaldo

Biomedical Devices and Instrumentation

Study of a Sonothrombolysis Equipment Based on Phased Ultrasound Technique 705
A. T. Andrade and S. S. Furuie

Development and Characterization of a Transceiver Solenoid RF Coil for MRI Acquisition of Ex Situ Brain Samples at 7 Teslas 711
L. G. C. Santos, K. T. Chaim, and D. Papoti

Analysis of Breast Cancer Detection Based on Software-Defined Radio Technology 717
D. Carvalho, A. J. Aragão, F. A. Brito-Filho, H. D. Hernandez, and W. A. M. V. Noije

Prototype of a Peristaltic Pump for Applications in Biological Phantoms 725
I. Sánchez-Domínguez, I. E. Pérez-Ruiz, J. Chan Pérez, and E. Perez-Rueda

Performance Evaluation of an OOK-Based Visible Light Communication System for Transmission of Patient Monitoring Data 731
K. vd Zwaag, R. Lazaro, M. Marinho, G. Acioli, A. Santos, L. Rimolo, W. Costa, F. Santos, T. Bastos, M. Segatto, H. Rocha, and J. Silva

Equipment for the Detection of Acid Residues in Hemodialysis Line 737
Angélica Aparecida Braga, F. B. Vilela, Elisa Rennó Carneiro Déster, and F. E. C. Costa

Using of Fibrin Sealant on Treatment for Tendon Lesion: Study in Vivo 741
Enéas de Freitas Dutra Junior, S. M. C. M. Hidd, M. M. Amaral, A. L. M. Maia Filho, L. Assis, R. S. Ferreira, B. Barraviera, and C. R. Tim

Analysis of Respiratory EMG Signals for Cough Prediction 745
T. D. Costa, T. Z. Zanella, C. S. Cristino, C. Druzgalski, Guilherme Nunes Nogueira-Neto, and P. Nohama

Integrating Power Line and Visible Light Communication Technologies for Data Transmission in Hospital Environments 751
R. Lazaro, Klaas Minne Van Der Zwaag, Wesley Costa, G. Acioli, M. Marinho, Mariana Khouri, G. C. Vivas, F. Santos, T. Bastos-Filho, Marcelo Vieira Segatto, H. Rocha, and Jair Adriano Lima Silva

Design of an Alternating Current Field Controller for Electrodes Exposed to Saline Solutions 757
J. L. dos Santos, S. A. Mendanha, and Sílvio Leão Vieira

Electrooculography: A Proposed Methodology for Sensing Human Eye Movement 763
G. de Melo and Sílvio Leão Vieira

Analysis of Inductance in Flexible Square Coil Applied to Biotelemetry 771
S. F. Pichorim

A Method for Illumination of Chorioallantoic Membrane (CAM) of Chicken Embryo in Microscope 777
M. K. Silva, I. R. Stoltz, L. T. Rocha, L. F. Pereira, M. A. de Souza, and G. B. Borba

Development and Experimentation of a rTMS Device for Rats 785
P. R. S. Sanches, D. P. Silva, A. F. Müller, P. R. O. Thomé, A. C. Rossi, B. R. Tondin, R. Ströher, L. Santos, and I. L. S. Torres

Diagnostic and Monitoring of Atrial Fibrillation Using Wearable Devices: A Scoping Review 791
Renata S. Santos, M. D. C. McInnis, and J. Salinet

The Effects of Printing Parameters on Mechanical Properties of a Rapidly Manufactures Mechanical Ventilator 799
T. R. Santos, M. A. Pastrana, W. Britto, D. M. Muñoz, and M. N. D. Barcelos

Fully Configurable Real-Time Ultrasound Platform for Medical Imaging Research 807
S. Rodriguez, A. F. Osorio, R. O. Silva, L. R. Domingues, H. J. Onisto, G. C. Fonseca, J. E. Bertuzzo, A. A. Assef, J. M. Maixa, A. A. O. Carneiro, and E. T. Costa

Proposal of a Low Profile Piezoelectric Based Insole to Measure the Perpendicular Force Applied by a Cyclist 813
M. O. Araújo and A. Balbinot

Soft Sensor for Hand-Grasping Force by Regression of an sEMG Signal 821
E. E. Neumann and A. Balbinot

Development of a Low-Cost, Open-Source Transcranial Direct-Current Stimulation Device (tDCS) for Clinical Trials 827
N. C. Teixeira-Neto, R. T. Azevedo-Cavalcanti, M. G. N. Monte-da-Silva, and A. E. F. Da-Gama

Velostat-Based Pressure Sensor Matrix for a Low-Cost Monitoring System Applied to Prevent Decubitus Ulcers 835
T. P. De A. Barros, J. M. X. N. Teixeira, W. F. M. Correia, and A. E. F. Da Gama

Analysis and Classification of EEG Signals from Passive Mobilization in ICU Sedated Patients and Non-sedated Volunteers 843
G. C. Florisbal, J. Machado, L. B. Bagesteiro, and A. Balbinot

Use of Fluorescence in the Diagnosis of Oral Health in Adult Patients Admitted to the Intensive Care Unit of a Public Emergency Hospital 849
M. D. L. P. Matos, E. N. Santos, M. D. C. R. M. Silva, A. Pavinatto, and M. M. Costa

A Non-invasive Photoemitter for Healing Skin Wounds 857
F. J. Santos, D. G. Gomes, J. P. V. Madeiro, A. C. Magalhães, and M. Sousa

Intermittent Suctioning for Patients Under Artificial Ventilation: A Digital Model Study 865
F. V. O. C. Médice, M. C. B. Pereira, H. R. Martins, and A. C. Jardim-Neto

Prototype for Testing Frames of Sunglasses 873
Larissa Vieira Musetti and Liliane Ventura

Evaluation of Hyperelastic Constitutive Models Applied to Airway Stents Made by a 3D Printer 881
A. F. Müller, Danton Pereira da Silva Junior, P. R. S. Sanches, P. R. O. Thomé, B. R. Tondin, A. C. Rossi, Alessandro Nakoneczny Schildt, and Luís Alberto Loureiro dos Santos

Are PSoC Noise Levels Low Enough for Single-Chip Active EMG Electrodes? 891
W. S. Araujo, I. Q. Moura, and A. Siqueira-Junior

Implementation of an Ultrasound Data Transfer System via Ethernet with FPGA-Based Embedded Processing 897
J. de Oliveira, A. A. Assef, R. A. C. Medeiros, J. M. Maia, and E. T. Costa

Software for Physiotherapeutic Rehabilitation: A Study with Accelerometry . . . 905
A. M. Conceição, M. C. P. Souza, L. P. G. Macedo, R. J. R. S. Lucena, A. V. M. Inocêncio, G. S. Marques, P. H. O. Silva, and M. A. B. Rodrigues

B-Mode Ultrasound Imaging System Using Raspberry Pi 909
R. A. C. Medeiros, A. A. Assef, J. de Oliveira, J. M. Maia, and E. T. Costa

Access Control in Hospitals with RFID and BLE Technologies 917
B. C. Bispo, E. L. Cavalcante, G. R. P. Esteves, M. B. C. Silva, G. J. Alves, and M. A. B. Rodrigues

Piezoelectric Heart Monitor 925
A. de S. Morangueira Filho, G. V. B. Magalhães, and F. L. Lopes

Transducer for the Strengthening of the Pelvic Floor Through Electromyographic Biofeedback 935
C. M. Silva, B. C. Bispo, G. R. P. Esteves, E. L. Cavalcante, A. L. B. Oliveira, M. B. C. Silva, N. A. Cunha, and M. A. B. Rodrigues

Monitoring Hemodynamic Parameters in the Terrestrial and Aquatic Environment: An Application in a 6-min Walk Test 941
K. R. C. Ferreira, A. V. M. Inocêncio, A. C. Chaves Filho, R. P. N. Lira, P. S. Lessa, and M. A. B. Rodrigues

***Scinax tymbamirim* Amphibian Advertisement Sound Emulator Based on Arduino** 947
K. C. Grande, V. H. H. Bezerra, J. G. V. Crespim, R. V. N. da Silva, and B. Schneider Jr.

Microphone and Receiver Calibration System for Otoacoustic Emission Probes 953
M. C. Tavares, A. B. Pizzetta, and M. H. Costa

Pneumotachograph Calibration: Influence of Regularization Methods on Parameter Estimation and the Use of Alternative Calibration Models 961
A. D. Quelhas, G. C. Motta-Ribeiro, A. V. Pino, A. Giannella-Neto, and F. C. Jandre

Geriatric Physiotherapy: A Telerehabilitation System for Identifying Therapeutic Exercises 969
A. C. Chaves Filho, A. V. M. Inocêncio, K. R. C. Ferreira, E. L. Cavalcante, B. C. Bispo, C. M. B. Rodrigues, P. S. Lessa, and M. A. B. Rodrigues

UV Equipament for Food Safety 975
F. B. Menechelli, V. B. Santana, R. S. Navarro, D. I. Kozusny-Andreani, A. Baptista, and S. C. Nunez

Method to Estimate Doses in Real-Time for the Eyes 981
J. C. de C. Lourenco, S. A. Paschuk, and H. R. Schelin

An IoT-Cloud Enabled Real Time and Energy Efficient ECG Reader Architecture 989
M. C. B. Pereira, J. P. V. Madeiro, Adriel O. Freitas, and D. G. Gomes

Development of a Hydraulic Model of the Microcontrolled Human Circulatory System 997
Andrew Guimarães Silva, B. S. Santos, M. N. Oliveira, L. J. Oliveira, D. G. Goroso, J. Nagai, and R. R. Silva

A Design Strategy to Control an Electrosurgery Unit Output 1003
Paulo Henrique Duarte Camilo and I. A. Cestari

Near Field Radar System Modeling for Microwave Imaging and Breast Cancer Detection Applications 1009
F. A. Brito-Filho, D. Carvalho, and W. A. M. V. Noije

Biomedical Optics and Systems and Technologies for Therapy and Diagnosis

Development and Validation of a New Hardware for a Somatosensorial Electrical Stimulator Based on Howland Current-Source Topology 1019
L. V. Almeida, W. A. de Paula, R. Zanetti, A. Beda, and H. R. Martins

Autism Spectrum Disorder: Smart Child Stimulation Center for Integrating Therapies 1027
R. O. B. Ana Letícia, C. M. Lívia, A. P. Phellype, B. V. Filipe, L. F. A. Anahid, and S. A. Rani

Fuzzy System for Identifying Pregnancy with a Risk of Maternal Death 1035
C. M. D. Xesquevixos and E. Araujo

Evaluation of Temperature Changes Promoted in Dental Enamel, Dentin and Pulp During the Tooth Whitening with Different Light Sources 1041
Fabrizio Manoel Rodrigues, Larissa Azevedo de Moura, and P. A. Ana

Effects of a Low-Cost LED Photobiomodulation Therapy Equipment on the Tissue Repair Process 1047
F. E. D. de Alexandria, N. C. Silva, A. L. M. M. Filho, D. C. L. Ferreira, K. dos S. Silva, L. R. da Silva, L. Assis, N. A. Parizotto, and C. R. Tim

Occupational Dose in Pediatric Barium Meal Examinations 1051
G. S. Nunes, R. B. Doro, R. R. Jakubiak, J. A. P. Setti, F. S. Barros, and V. Denyak

Synthesis of N-substituted Maleimides Potential Bactericide 1057
A. C. Trindade and A. F. Uchoa

A Review About the Main Technologies to Fight COVID-19 1063
P. A. Cardoso, D. L. Tótola, E. V. S. Freitas, M. A. P. Arteaga, D. Delisle-Rodríguez, F. A. Santos, and T. F. Bastos-Filho

Evaluation of Cortisol Levels in Artificial Saliva by Paper Spray Mass Spectrometry 1067
A. R. E. Dias, B. L. S. Porto, B. V. M. Rodrigues, and T. O. Mendes

Tinnitus Relief Using Fractal Sound Without Sound Amplification 1073
A. G. Tosin and F. S. Barros

Analysis of the Heat Propagation During Cardiac Ablation with Cooling of the Esophageal Wall: A Bidimensional Computational Modeling 1079
S. de S. Faria, P. C. de Souza, C. F. da Justa, S. de S. R. F. Rosa, and A. F. da Rocha

Development of a Rapid Test for Determining the ABO and Rh-Blood Typing Systems 1087
E. B. Santiago and R. J. Ferreira

In Silico Study on Electric Current Density in the Brain During Electrochemotherapy Treatment Planning of a Dog's Head Osteosarcoma 1095
R. Guedert, M. M. Taques, I. B. Paro, M. M. M. Rangel, and D. O. H. Suzuki

Evaluation of Engorged Puerperal Breast by Thermographic Imaging: A Pilot Study 1101
L. B. da Silva, A. C. G. Lima, J. L. Soares, L. dos Santos, and M. M. Amaral

Study of the Photo Oxidative Action of *Brosimum gaudichaudii* Extract 1105
V. M. de S. Antunes, C. L. de L. Sena, and A. F. Uchoa

Electrochemotherapy Effectiveness Loss Due to Electrode Bending: An In Silico and In Vitro Study 1109
D. L. L. S. Andrade, J. R. da Silva, R. Guedert, G. B. Pintarelli, J. A. Berkenbrock, S. Achenbach, and D. O. H. Suzuki

Conductive Gels as a Tool for Electric Field Homogenization and Electroporation in Discontinuous Regions: In Vitro and In Silico Study . . . 1115
L. B. Lopes, G. B. Pintarelli, and D. O. H. Suzuki

Line Shape Analysis of Cortisol Infrared Spectra for Salivary Sensors: Theoretical and Experimental Observations 1121
C. M. A. Carvalho, B. L. S. Porto, B. V. M. Rodrigues, and T. O. Mendes

Differential Diagnosis of Glycosuria Using Raman Spectroscopy 1129
E. E. Sousa Vieira, L. Silveira Junior, and A. Barrinha Fernandes

Development of a Moderate Therapeutic Hypothermia Induction and Maintenance System for the Treatment of Traumatic Brain Injury 1135
Reynaldo Tronco Gasparini, Antonio Luis Eiras Falcão, and José Antonio Siqueira Dias

Temperature Generation and Transmission in Root Dentin During Nd:YAG Laser Irradiation for Preventive Purposes 1141
Claudio Ricardo Hehl Forjaz, Denise Maria Zezell, and P. A. Ana

Photobleaching of Methylene Blue in Biological Tissue Model (Hydrolyzed Collagen) Using Red (635 nm) Radiation 1147
G. Lepore, P. S. Souza, P. A. Ana, and N. A. Daghastanli

Effect of Photodynamic Inactivation of Propionibacterium Acnes Biofilms by Hypericin (*Hypericum perforatum*) 1153
R. A. Barroso, R. Navarro, C. R. Tim, L. P. Ramos, L. D. de Oliveira, A. T. Araki, D. B. Macedo, K. G. Camara Fernandes, and L. Assis

Evaluating Acupuncture in Vascular Disorders of the Lower Limb Through Infrared Thermography 1157
Wally auf der Strasse, A. Pinto, M. F. F. Vara, E. L. Santos, M. Ranciaro, P. Nohama, and J. Mendes

Photodynamic Inactivation in Vitro of the Pathogenic Fungus *Paracoccidioides brasiliensis* 1165
José Alexandre da Silva Júnior, R. S. Navarro, A. U. Fernandes, D. I. Kozusny-Andreani, and L. S. Feitosa

In Vitro Study of the Microstructural Effects of Photodynamic Therapy in Medical Supplies When Used for Disinfection 1173
A. F. Namba, M. Del-Valle, N. A. Daghastanli, and P. A. Ana

Technological Development of a Multipurpose Molecular Point-of-Care Device for Sars-Cov-2 Detection 1183
L. R. Nascimento, V. K. Oliveira, B. D. Camargo, G. T. Mendonça, M. C. Stracke, M. N. Aoki, L. Blanes, L. G. Morello, and S. L. Stebel

Chemical Effects of Nanosecond High-Intensity IR and UV Lasers on Biosilicate® When Used for Treating Dentin Incipient Caries Lesions 1189
M. Rodrigues, J. M. F. B. Daguano, and P. A. Ana

Antioxidant Activity of the Ethanol Extract of *Salpichlaena Volubilis* and Its Correlation with Alopecia Areata 1197
A. B. Souza, T. K. S. Medeiros, D. Severino, C. J. Francisco, and A. F. Uchoa

Evaluation of the Heart Rate Variability with Laser Speckle Imaging 1205
C. M. S. Carvalho, A. G. F. Marineli, L. dos Santos, A. Z. de Freitas, and M. M. Amaral

Photobiomodulation and Laserpuncture Evaluation for Knee Osteoarthritis Treatment: A Literature Review 1211
L. G. C. Corrêa, D. S. F. Magalhães, A. Baptista, and A. F. Frade-Barros

Methodology for the Classification of an Intraocular Lens with an Orthogonal Bidimensional Refractive Sinusoidal Profile 1217
Diogo Ferraz Costa and D. W. d. L. Monteiro

Discrimination Between Artisanal and Industrial Cassava by Raman Spectroscopy 1225
Estela Doria, S. C. Nunez, R. S. Navarro, J. C. Cogo, T. O. Mendes, and A. F. Frade-Barros

Effect of Light Emitted by Diode as Treatment of Radiodermatitis 1231
Cristina Pires Camargo, H. A. Carvalho, R. Gemperli, Cindy Lie Tabuse, Pedro Henrique Gianjoppe dos Santos, Lara Andressa Ordonhe Gonçales, Carolina Lopo Rego, B. M. Silva, M. H. A. S. Teixeira, Y. O. Feitosa, F. H. P. Videira, and G. A. Campello

Effect of Photobiomodulation on Osteoblast-like Cells Cultured on Lithium Disilicate Glass-Ceramic 1237
L. T. Fabretti, A. C. D. Rodas, V. P. Ribas, J. K. M. B. Daguano, and I. T. Kato

Reference Values of Current Perception Threshold in Adult Brazilian Cohort 1243
Diogo Correia e Silva, A. P. Fontana, M. K. Gomes, and C. J. Tierra-Criollo

Analysis of the Quality of Sunglasses in the Brazilian Market in Terms of Ultraviolet Protection 1249
L. M. Gomes, A. D. Loureiro, M. Masili, and Liliane Ventura

Do Sunglasses on Brazilian Market Have Blue-Light Protection? 1253
A. D. Loureiro, L. M. Gomes, and Liliane Ventura

Thermography and Semmes-Weinstein Monofilaments in the Sensitivity Evaluation of Diabetes Mellitus Type 2 Patients 1259
G. C. Mendes, F. S. Barros, and P. Nohama

Biomedical Robotics, Assistive Technologies and Health Informatics

Design and Performance Evaluation of a Custom 3D Printed Thumb Orthosis to Reduce Occupational Risk in an Automotive Assembly Line 1269
H. Toso, D. P. Campos, H. V. P. Martins, R. Wenke, M. Salatiel, J. A. P. Setti, and G. Balbinotti

Handy Orthotics: Considerations on User-Centered Methodology During Development Stages of Myoelectric Hand Orthosis for Daily Assistance 1277
H. V. P. Martins, J. A. P. Setti, and C. Guimarães

Human Activity Recognition System Using Artificial Neural Networks 1285
Vinícius Ferreira De Almeida and Rodrigo Varejão Andreão

Modeling and Simulation of a Fuzzy-Based Human Control Using an Interaction Model Between Human and Active Knee Orthosis 1293
D. Mosconi, P. F. Nunes, and Siqueira

Wearable Devices in Healthcare: Challenges, Current Trends and a Proposition of Affordable Low Cost and Scalable Computational Environment of Internet of Things 1301
Fabrício Martins Mendonça, Mário A. R. Dantas, Wallace T. Fortunato, Juan F. S. Oliveira, Breno C. Souza, and Marcelo Q. Filgueiras

Use of RGB-D Camera for Analysis of Compensatory Trunk Movements in Upper Limbs Rehabilitation 1309
Alice Tissot Garcia, L. L. da C. Guimarães, S. A. V. e Silva, and V. M. de Oliveira

Repetitive Control Applied to a Social Robot for Interaction with Autistic Children 1319
R. P. A. Pereira, C. T. Valadao, E. M. O. Caldeira, J. L. F. Salles, and T. F. Bastos-Filho

Analysis of Sensors in the Classification of the Brazilian Sign Language 1325
Thiago Simões Dias, J. J. A. Mendes Júnior, and S. F. Pichorim

A Smart Wearable System for Firefighters for Monitoring Gas Sensors and Vital Signals 1333
Letica Teixeira Nascimento, M. E. M. Araujo, M. W. A. Santos, P. D. Boina, J. V. F. Gomes, M. K. Rosa, T. F. Bastos-Filho, K. S. Komati, and R. J. M. G. Tello

Importance of Sequencing the SARS-CoV-2 Genome Using the Nanopore Technique to Understand Its Origin, Evolution and Development of Possible Cures 1341
A. M. Corredor-Vargas, R. Torezani, G. Paneto, and T. F. Bastos-Filho

Vidi: Artificial Intelligence and Vision Device for the Visually Impaired 1345
R. L. A. Pinheiro and F. B. Vilela

Mobile Application for Aid in Identifying Fall Risk in Elderly: App Fisioberg 1355
D. C. Gonçalves, F. P. Pinto, and D. S. F. Magalhães

Real-Time Slip Detection and Control Using Machine Learning 1363
Alexandre Henrique Pereira Tavares and S. R. J. Oliveira

Programmable Multichannel Neuromuscular Electrostimulation System: A Universal Platform for Functional Electrical Stimulation 1371
T. Coelho-Magalhães, A. F. Vilaça-Martins, P. A. Araújo, and H. Resende-Martins

Absence from Work in Pregnancy Related to Racial Factors: A Bayesian Analysis in the State of Bahia—Brazil 1379
A. A. A. R. Monteiro, M. S. Guimarães, E. F. Cruz, and D. S. F. Magalhães

Perspectives on EMG-Controlled Prosthetic Robotic Hands: Trends and Challenges 1387
C. E. Pontim, Arturo Vaine, H. V. P. Martins, Kevin Christlieb Deessuy, Eduardo Felipe Ardigo Braga, José Jair Alves Mendes Júnior, and D. P. Campos

Use of Workspaces and Proxemics to Control Interaction Between Robot and Children with ASD 1393
Giancarlo Pedroni Del Piero, E. M. O. Caldeira, and T. F. Bastos-Filho

Proposal of a New Socially Assistive Robot with Embedded Serious Games for Therapy with Children with Autistic Spectrum Disorder and down Syndrome 1399
João. Antonio Campos Panceri, E. V. S. Freitas, S. L. Schreider, E. Caldeira, and T. F. Bastos-Filho

Performance Assessment of Wheelchair Driving in a Virtual Environment Using Head Movements 1407
E. F. dos Santos Junior, J. T. de Souza, F. R. Martins, D. de Cassia Silva, and E. L. M. Naves

Use of Artificial Intelligence in Brazil Mortality Data Analysis 1415
Sérgio de Vasconcelos Filho and Cristine Martins Gomes de Gusmão

Dual Neural Network Approach for Virtual Sensor at Indoor Positioning System 1423
Guilherme Rodrigues Pedrollo and A. Balbinot

Development of Simulation Platform for Human-Robot-Environment Interface in the UFES CloudWalker 1431
J. C. Rocha-Júnior, R. C. Mello, T. F. Bastos-Filho, and A. Frizera-Neto

Assisted Navigation System for the Visually Impaired 1439
Malki-çedheq Benjamim C. Silva, B. C. Bispo, C. M. Silva, N. A. Cunha, E. A. B. Santos, and M. A. B. Rodrigues

Development of Bionic Hand Using Myoelectric Control for Transradial Amputees 1445
C. E. Pontim, M. G. Alves, J. J. A. Mendes Júnior, D. P. Campos, and J. A. P. Setti

Communication in Hospital Environment Using Power Line Communications 1451
N. A. Cunha, B. C. Bispo, K. R. C. Ferreira, G. J. Alves, G. R. P. Esteves, E. A. B. Santos, and M. A. B. Rodrigues

Influence of Visual Clue in the Motor Adaptation Process 1457
V. T. Costa, S. R. J. Oliveira, and A. B. Soares

Application of MQTT Network for Communication in Healthcare Establishment 1465
N. A. Cunha, B. C. Bispo, E. L. Cavalcante, A. V. M. Inocêncio, G. J. Alves, and M. A. B. Rodrigues

Artificial Neural Network-Based Shared Control for Smart Wheelchairs: A Fully-Manual Driving for the User 1471
J. V. A. e Souza, L. R. Olivi, and E. Rohmer

Identifying Deficient Cognitive Functions Using Computer Games: A Pilot Study 1479
Luciana Rita Guedes, Larissa Schueda, Marcelo da Silva Hounsell, and A. S. Paterno

A State of the Art About Instrumentation and Control Systems from Body Motion for Electric-Powered Wheelchairs 1487
A. X. González-Cely, M. Callejas-Cuervo, and T. Bastos-Filho

Socket Material and Coefficient of Friction Influence on Residuum-Prosthesis Interface Stresses for a Transfemoral Amputee: A Finite Element Analysis 1495
Alina de Souza Leão Rodrigues and A. E. F. Da Gama

Subject Specific Lower Limb Joint Mechanical Assessment for Indicative Range Operation of Active Aid Device on Abnormal Gait 1503
Carlos Rodrigues, M. Correia, J. Abrantes, M. A. B. Rodrigues, and J. Nadal

Web/Mobile Technology as a Facilitator in the Cardiac Rehabilitation Process: Review Study 1511
Hildete de Almeida Galvão and F. S. Barros

Biomedical Signal and Image Processing

Regression Approach for Cranioplasty Modeling 1519
M. G. M. Garcia and S. S. Furuie

Principal Component Analysis in Digital Image Processing for Automated Glaucoma Diagnosis 1527
C. N. Neves, D. S. da Encarnação, Y. C. Souza, A. O. R. da Silva, F. B. S. Oliveira, and P. E. Ambrósio

Pupillometric System for Cognitive Load Estimation in Noisy-Speech Intelligibility Psychoacoustic Experiments: Preliminary Results 1533
A. L. Furlani, M. H. Costa, and M. C. Tavares

VGG FACE Fine-Tuning for Classification of Facial Expression Images of Emotion 1539
P. F. Jaquetti, Valfredo Pilla Jr, G. B. Borba, and H. R. Gamba

Estimation of Magnitude-Squared Coherence Using Least Square Method and Phase Compensation: A New Objective Response Detector 1547
F. Antunes and L. B. Felix

Image Processing as an Auxiliary Methodology for Analysis of Thermograms . . . 1553
C. A. Schadeck, F. Ganacim, L. Ulbricht, and Cezar Schadeck

Performance Comparison of Different Classifiers Applied to Gesture Recognition from sEMG Signals 1561
B. G. Sgambato and G. Castellano

Modelling of Inverse Problem Applied to Image Reconstruction in Tomography Systems 1569
J. G. B. Wolff, G. Gueler Dalvi, and P. Bertemes-Filho

Towards a Remote Vital Sign Monitoring in Accidents 1575
A. Floriano, R. S. Rosa, L. C. Lampier, E. Caldeira, and T. F. Bastos-Filho

Analysis About SSVEP Response to 5.5–86.0 Hz Flicker Stimulation 1581
G. S. Ferreira, P. F. Diez, and S. M. T. Müller

Correlations Between Anthropometric Measurements and Skin Temperature, at Rest and After a CrossFit® Training Workout 1589
E. B. Neves, A. C. C. Salamunes, F. De Meneck, E. C. Martinez, and V. M. Reis

Channel Influence in Armband Approach for Gesture Recognition by sEMG Signals 1597
J. J. A. Mendes Jr., M. L. B. Freitas, D. P. Campos, C. E. Pontim, S. L. Stevan Jr., and S. F. Pichorim

Human Activity Recognition from Accelerometer Data with Convolutional Neural Networks 1603
Gustavo de Aquino e Aquino, M. K. Serrão, M. G. F. Costa, and C. F. F. Costa-Filho

Multimodal Biometric System Based on Autoencoders and Learning Vector Quantization 1611
C. F. F. Costa-Filho, J. V. Negreiro, and M. G. F. Costa

Evaluating the Performance of Convolutional Neural Networks with Direct and Sequential Acyclic Graph Architectures in Automatic Segmentation of Breast Lesions in Ultrasound Images 1619
Gustavo de Aquino e Aquino, M. K. Serrão, M. G. F. Costa, and C. F. F. Costa-Filho

Evaluation and Systematization of the Transfer Function Method for Cerebral Autoregulation Assessment 1627
A. M. Duarte, R. R. Costa, F. S. Moura, A. S. M. Salinet, and J. Salinet

Anomaly Detection Using Autoencoders for Movement Prediction 1635
L. J. L. Barbosa, A. L. Delis, P. V. P Cotta, V. O. Silva, M. D. C. Araujo, and A. Rocha

A Classifier Ensemble Method for Breast Tumor Classification Based on the BI-RADS Lexicon for Masses in Mammography 1641
Juanita Hernández-López and Wilfrido Gómez-Flores

A Comparative Study of Neural Computing Approaches for Semantic Segmentation of Breast Tumors on Ultrasound Images 1649
Luis Eduardo Aguilar-Camacho, Wilfrido Gómez-Flores, and Juan Humberto Sossa-Azuela

A Preliminary Approach to Identify Arousal and Valence Using Remote Photoplethysmography 1659
L. C. Lampier, E. Caldeira, D. Delisle-Rodriguez, A. Floriano, and T. F. Bastos-Filho

Multi-label EMG Classification of Isotonic Hand Movements: A Suitable Method for Robotic Prosthesis Control 1665
José Jair Alves Mendes Junior, C. E. Pontim, and D. P. Campos

Evaluation of Vectorcardiography Parameters Matrixed Synthesized 1673
Amanda Nunes Barros, V. B. S. Luz, F. M. C. Bezerra, R. M. Tavares, F. Albrecht, A. C. Murta, R. Viana, M. C. Lambauer, E. B. Correia, R. Hortegal, and H. T. Moriya

Microstate Graphs: A Node-Link Approach to Identify Patients with Schizophrenia 1679
Lorraine Marques Alves, Klaus Fabian Côco, Mariane Lima de Souza, and Patrick Marques Ciarelli

Eigenspace Beamformer Combined with Generalized Sidelobe Canceler and Filters for Generating Plane Wave Ultrasound Images 1687
L. C. Neves, J. M. Maia, A. J. Zimbico, D. F. Gomes, A. A. Assef, and E. T. Costa

Anatomical Atlas of the Human Head for Electrical Impedance Tomography 1693
L. A. Ferreira, R. G. Beraldo, E. D. L. B. Camargo, and F. S. Moura

Sparse Arrays Method with Generalized Sidelobe Canceler Beamformer for Improved Contrast and Resolution in Ultrasound Ultrafast Imaging 1701
D. F. Gomes, J. M. Maia, A. J. Zimbico, A. A. Assef, L. C. Neves, F. K. Schneider, and E. T. Costa

Center of Mass Estimation Using Kinect and Postural Sway 1707
G. S. Oliveira, Marcos R. P. Menuchi, and P. E. Ambrósio

Estimation of Directed Functional Connectivity in Neurofeedback Training Focusing on the State of Attention 1713
W. D. Casagrande, E. M. Nakamura-Palacios, and A. Frizera-Neto

Characterization of Electroencephalogram Obtained During the Resolution of Mathematical Operations Using Recurrence Quantification Analysis 1719
A. P. Mendes, G. M. Jarola, L. M. A. Oliveira, G. J. L. Gerhardt, J. L. Rybarczyk-Filho, and L. dos Santos

Performance Evaluation of Machine Learning Techniques Applied to Magnetic Resonance Imaging of Individuals with Autism Spectrum Disorder 1727
V. F. Carvalho, G. F Valadão, S. T. Faceroli, F. S Amaral, and M. Rodrigues

Biomedical Signal Data Features Dimension Reduction Using Linear Discriminant Analysis and Threshold Classifier in Case of Two Multidimensional Classes 1733
E. R. Pacola and V. I. Quandt

Facial Thermal Behavior Pre, Post and 24 h Post-Crossfit® Training Workout: A Pilot Study 1739
D. B. Castillo, V. A. A. Bento, E. B. Neves, E. C. Martinez, F. De Merneck, V. M. Reis, M. L. Brioschi, and D. S. Haddad

Implementation of One and Two Dimensional Analytical Solution of the Wave Equation: Dirichlet Boundary Conditions 1747
S. G. Mello, C. Benetti, and A. G. Santiago

Application of the Neumann Boundary Conditions to One and Two Dimensional Analytical Solution of Wave Equation 1755
S. G. Mello, C. Benetti, and A. G. Santiago

Comparative Analysis of Parameters of Magnetic Resonance Examinations for the Accreditation Process of a Diagnostic Image Center in Curitiba/Brazil 1761
M. V. C. Souza, R. Z. V. Costa, and K. E. P. Pinho

Information Theory Applied to Classifying Skin Lesions in Supporting the Medical Diagnosis of Melanomas 1767
L. G. de Q. Silveira-Júnior, B. Beserra, and Y. K. R. de Freitas

Alpha Development of Software for 3D Segmentation and Reconstruction of Medical Images for Use in Pre-treatment Simulations for Electrochemotherapy: Implementation and Case Study 1773
J. F. Rodrigues, Daniella L. L. S. Andrade, R. Guedert, and D. O. H. Suzuki

A Systematic Review on Image Registration in Interventionist Procedures: Ultrasound and Magnetic Resonance 1781
G. F. Carniel, A. C. D. Rodas, and A. G. Santiago

Application of Autoencoders for Feature Extraction in BCI-SSVEP 1787
R. Granzotti, G. V. Vargas, and L. Boccato

An LPC-Based Approach to Heart Rhythm Estimation 1795
J. S. Lima, F. G. S. Silva, and J. M. Araujo

Spectral Variation Based Method for Electrocardiographic Signals Compression 1801
V. V. de Morais, P. X. de Oliveira, E. B. Kapisch, and A. J. Ferreira

Centre of Pressure Displacements in Transtibial Amputees 1809
D. C. Toloza and L. A. Luengas

Lower Limb Frequency Response Function on Standard Maximum Vertical Jump 1815
C. Rodrigues, M. Correia, J. Abrantes, M. A. B. Rodrigues, and J. Nadal

Time-Difference Electrical Impedance Tomography with a Blood Flow Model as Prior Information for Stroke Monitoring 1823
R. G. Beraldo and F. S. Moura

Development of a Matlab-Based Graphical User Interface for Analysis of High-Density Surface Electromyography Signals 1829
I. S. Oliveira, M. A. Favretto, S. Cossul, and J. L. B. Marques

Development of an Automatic Antibiogram Reader System Using Circular Hough Transform and Radial Profile Analysis 1837
B. R. Tondin, A. L. Barth, P. R. S. Sanches, D. P. S. Júnior, A. F. Müller, P. R. O. Thomé, P. L. Wink, A. S. Martins, and A. A. Susin

Gene Expression Analyses of Ketogenic Diet 1843
A. A. Ferreira and A. C. Q. Simões

Comparison Between J48 and MLP on QRS Classification Through Complexity Measures 1851
L. G. Hübner and A. T. Kauati

Low Processing Power Algorithm to Segment Tumors in Mammograms 1857
R. E. Q. Vieira, C. M. G. de Godoy, and R. C. Coelho

Electromyography Classification Techniques Analysis for Upper Limb Prostheses Control 1865
F. A. Boris, R. T. Xavier, J. P. Codinhoto, J. E. Blanco, M. A. A. Sanches, C. A. Alves, and A. A. Carvalho

EEG-Based Motor Imagery Classification Using Multilayer Perceptron Neural Network 1873
S. K. S. Ferreira, A. S. Silveira, and A. Pereira

Real-Time Detection of Myoelectric Hand Patterns for an Incomplete Spinal Cord Injured Subject 1879
W. A. Rodriguez, J. A. Morales, L. A. Bermeo, D. M. Quiguanas, E. F. Arcos, A. F. Rodacki, and J. J. Villarejo-Mayor

Single-Trial Functional Connectivity Dynamics of Event-Related Desynchronization for Motor Imagery EEG-Based Brain-Computer Interfaces 1887
P. G. Rodrigues, A. Fim-Neto, J. R. Sato, D. C. Soriano, and S. J. Nasuto

A Lightweight Model for Human Activity Recognition Based on Two-Level Classifier and Compact CNN Model 1895
Y. L. Coelho, B. Nguyen, F. A. Santos, S. Krishnan, and T. F. Bastos-Filho

Applicability of Neurometry in Assessing Anxiety Levels in Students 1903
Aline M. D. Meneses, Marcello M. Amaral, and Laurita dos Santos

Using PPG and Machine Learning to Measure Blood Pressure 1909
G. S. Cardoso, M. G. Lucas, S. S. Cardoso, J. C. M. Ruzicki, and A. A. S. Junior

Resting-State Brain in Cognitive Decline: Analysis of Brain Network Architecture Using Graph Theory 1917
C. M. Maulaz, D. B. A. Mantovani, and A. M. Marques da Silva

Exploring Different Convolutional Neural Networks Architectures to Identify Cells in Spheroids 1925
A. G. Santiago, C. C. Santos, M. M. G. Macedo, J. K. M. B. Daguano, J. A. Dernowsek, and A. C. D. Rodas

A Dynamic Artificial Neural Network for EEG Patterns Recognition 1931
G. J. Alves, Diogo R. Freitas, A. V. M. Inocêncio, E. L. Cavalcante, M. A. B. Rodrigues, and Renato Evangelista de Araujo

Pelvic Region Panoramic Ultrasonography 1937
J. S. Oliveira, G. S. Almeida, J. E. C. Magno, V. R. da Luz, M. C. P. Fonseca, and I. M. Miziara

Functional Connectivity During Hand Tasks 1943
T. S. Nunes, G. A. Limeira, I. B. Souto, A. P. Fontana, and C. J. Tierra-Criollo

Estimation of Alveolar Recruitment Potential Using Electrical Impedance Tomography Based on an Exponential Model of the Pressure-Volume Curve 1949
G. E. Turco, F. S. Moura, and E. D. L. B. Camargo

Assessment of Respiratory Mechanics in Mice Using Estimated Input Impedance Without Redundancy 1953
V. A. Takeuchi, V. Mori, R. Vitorasso, A. E. Lino-Alvarado, M. A. Oliveira, W. T. Lima, and H. T. Moriya

Dispersive Raman Spectroscopy of Peanut Oil—Ozone and Ultrasound Effects 1961
P. A. L. I. Marrafa, H. C. Carvalho, C. J. Lima, A. B. F. Moretti, and L. Silveira Jr.

Comparison Between Linear and Nonlinear Haar Wavelet for the Detection of the R-peak in the Electrocardiogram of Small Animals 1967
P. Y. Yamada and E. V. Garcia

Data Extraction Method Combined with Machine Learning Techniques for the Detection of Premature Ventricular Contractions in Real-Time 1973
L. C. Sodré, B. G. Dutra, A. S. Silveira, and I. M. Mizara

Extraction of Pendelluft Features from Electrical Impedance Tomography Images 1979
V. J. Fidelis, E. D. L. B. Camargo, M. B. P. Amato, and J. A. Sims

Classification of Raw Electroencephalogram Signals for Diagnosis of Epilepsy Using Functional Connectivity 1985
T. T. Ribeiro, J. S. Fiel, E. M. Melo, R. E. S. Navegantes, F. Gomes, and A. Pereira Junior

On Convolutional Neural Networks and Transfer Learning for Classifying Breast Cancer on Histopathological Images Using GPU 1993
D. C. S. e Silva and O. A. C. Cortes

Acquisition and Comparison of Classification Algorithms in Electrooculogram Signals 1999
A. R. Borchardt, L. S. Schiavon, L. G. L. Silva, A. A. Souza Junior, and M. G. Lucas

Muscle Synergies Estimation with PCA from Lower Limb sEMG at Different Stretch-Shortening Cycle 2005
C. Rodrigues, M. Correia, J. Abrantes, M. A. B. Rodrigues, and J. Nadal

Measurement Techniques of Hounsfield Unit Values for Assessment of Bone Quality Following Decompressive Craniectomy (DC): A Preliminary Report . . . 2013
Silvio Tacara, Rubens Alexandre de Faria, J. C. Coninck, H. R. Schelin, and Irene T. Nakano

Method for Improved Image Reconstruction in Computed Tomography and Positron Emission Tomography, Based on Compressive Sensing with Prefiltering in the Frequency Domain 2019
Y. Garcia, C. Franco, and C. J. Miosso

Non-invasive Arterial Pressure Signal Estimation from Electrocardiographic Signals 2027
J. C. Silva, J. S. de Oliveira, S. E. Silva, M. H. de Carvalho, and A. S. Silveira

Comparison Among Microvolt T-wave Alternans Detection Methods and the Effect of T-wave Delimitation Approaches 2033
T. Winkert and J. Nadal

Detection of Schizophrenia Based on Brain Structural Analysis, Using Machine Learning over Different Combinations of Multi-slice Magnetic Resonance Images 2039
J. S. Avelar Filho, N. Silva, and C. J. Miosso

Simulation of Lung Ultrasonography Phantom for Acquisition of A-lines and B-lines Artifacts 2045
F. A. M. Silva, M. Pastrana-Chalco, C. A. Teixeira, and W. C. A. Pereira

Recognition of Facial Patterns Using Surface Electromyography—A Preliminary Study 2051
M. R. Lima, J. J. A. Mendes Júnior, and D. P. Campos

Classification of Red Blood Cell Shapes Using a Sequential Learning Algorithm 2059
W. D. Font, S. H. Garcia, M. E. Nicot, M. G. Hidalgo, A. Jaume-i-Capó, A. Mir, and L. F. Gomes

Possible Caveats of Ultra-short Heart Rate Variability Reliability: Insights from Recurrence Quantification Analysis 2067
Hiago Murilo Melo, Mariana Cardoso Melo, Roger Walz, Emílio Takase, and Jean Faber

Clinical Engineering and Health Technology Assessment

Unidose Process Automation: Financial Feasibility Analysis for a Public Hospital 2079
L. H. V. de Santana and M. G. N. M. da Silva

Identifying Monitoring Parameters Using HFMEA Data in Primary Health Care Ubiquitous Technology Management 2085
J. Martins, R. D. Soares Filho, and R. Garcia

Rapid Review of the Application of Usability Techniques in Medical Equipment 2091
M. R. Brandão and R. Garcia

Changes in Respiratory Mechanics Associated with Different Degrees of Parkinson's Disease 2099
B. T. Caldas, F. C. V. Ribeiro, J. S. Pereira, W. C. Souza, A. J. Lopes, and P. L. Melo

Machine Learning Platform for Remote Analysis of Primary Health Care Technology to Support Ubiquitous Management in Clinical Engineering 2105
Rafael Peixoto, R. Soares Filho, J. Martins, and R. Garcia

Evaluation of the Efficacy of Chloroquine and Hydroxychloroquine in the Treatment of Individuals with COVID-19: A Systematic Review 2111
L. C. Mendes, J. Ávila, and A. A. Pereira

Embracement with Risk Classification: Lead Time Assessment of the Patient in a Tocogynecology Emergency Service 2117
G. R. da Costa, R. C. G. Berardi, E. S. de Oliveira, and A. M. W. Stadnik

Health Technology Management Using GETS in Times of Health Crisis 2123
Jose W. M. Bassani, Rosana A. Bassani, and Ana C. B. Eboli

Life-Sustaining Equipment: A Demographic Geospace Analysis in National Territory 2131
E. Cruz, I. H. Y. Noma, A. C. Dultra, and M. Negri

Geospatial Analysis of Diagnostic Imaging Equipment in Brazil 2137
I. H. Y. Noma, E. Cruz, A. C. Dultra, and M. Negri

A Review About Equipment for Mechanical Ventilation in Intensive Care to Combat COVID-19 and the Role of Clinical Engineers 2143
E. V. S. Freitas, M. A. P. Arteaga, P. A. Cardoso, D. L. Tótola, Y. L. Coelho, G. C. Vivas, D. Delisle-Rodríguez, F. A. Santos, and T. F. Bastos-Filho

Evaluation of Adverse Events Recorded in FDA/USA and ANVISA/Brazil Databases for the Medical Equipment: Pulmonary Ventilators, Defibrillators, Infusion Pumps, Physiological Monitors and Ultrasonic Scalpels 2149
Josiany Carlos de Souza, Sheida Mehrpour, Matheus Modolo Ferreira, Y. L. Coelho, G. C. Vivas, D. Delisle-Rodriguez, Francisco de Assis Santos, and T. F. Bastos-Filho

Quality Assessment of Emergency Corrective Maintenance of Critical Care Ventilators Within the Context of COVID-19 in São Paulo, Brazil 2157
A. E. Lino-Alvarado, S. G. Mello, D. A. O. Rosa, M. S. Dias, M. F. Barbosa, K. N. Barros, E. Silva Filho, B. A. Lemos, J. C. T. B. Moraes, A. F. G. Ferreira Junior, and H. T. Moriya

Comparison of the Sensitivity and Specificity Between Mammography and Thermography in Breast Cancer Detection 2163
T. G. R. Da Luz, J. C. Coninck, and L. Ulbricht

COVID-19: Analysis of Personal Protective Equipment Costs in the First Quarter of 2020 at a Philanthropic Hospital in Southern Bahia- Brazil 2169
L. O. de Brito, S. C. Nunez, R. S. Navarro, and J. C. Cogo

Evaluation of the Power Generated by Ultrasonic Shears Used in Laparoscopic Surgeries 2173
I. P. H. Rosario and J. M. Maia

Neuroengineering

Influence of Visual Feedback Removal on the Neural Control Strategies During Isometric Force Production 2183
C. M. Germer, E. P. Zambalde, and L. A. Elias

Neurofeedback Training for Regulation of Sensorimotor Rhythm in Individuals with Refractory Epilepsy 2189
S. C. Souza, R. E. S. Navegantes, D. S. Miranda, J. S. Fiel, and A. Pereira

Gelotophobia in the Academic Environment: A Preliminary Study 2193
T. S. Rêgo, D. E. S. Pires, T. T. Ribeiro, R. E. S. Navegantes, D. S. Miranda, E. M. Melo, and A. Pereira-Junior

A Single Administration of GBR 12909 Alters Basal Mesocorticolimbic Activity 2199
L. Galdino, A. C. Kunicki, L. C. N. Filho, R. C. Moioli, and M. F. P. Araújo

Fuzzy Assessment for Autism Spectrum Disorders 2205
M. M. Costa and E. Araujo

Subthalamic Field Potentials in Parkinson's Disease Encodes Motor Symptoms Severity and Asymmetry 2211
J. B. de Luccas, B. L. Bianqueti, A. Fim Neto, M. S. Rocha, A. K. Takahata, D. C. Soriano, and F. Godinho

Subthalamic Beta Burst Dynamics Differs for Parkinson's Disease Phenotypes 2219
A. Fim Neto, J. B. de Luccas, B. L. Bianqueti, M. S. Rocha, S. J. Nasuto, F. Godinho, and D. C. Soriano

Development of a Low-Cost Software to Obtain Quantitative Parameters in the Open Field Test for Application in Neuroscience Research 2225
T. R. M. Costalat, I. P. R. Negrão, and W. Gomes-Leal

Depolarizing Effect of Chloride Influx Through KCC and NKCC During Nonsynaptic Epileptiform Activity 2233
D. M. Soares, S. G. Cecílio, L. E. C. Santos, A. M. Rodrigues, and A. C. G. Almeida

Increase of Lactate Concentration During Spreading Depression 2239
Silas Moreira de Lima, B. C. Rodrigues, J. N. Lara, G. S. Nogueira, A. C. G. Almeida, and A. M. Rodrigues

Microglial Response After Chronic Implantation of Epidural Spinal Cord Electrode 2245
A. O. B. Suassuna, J. R. Oliveira, V. S. Costa, C. C. M. Castro, M. S. L. Nascimento, and M. F. P. Araújo

Immediate Cortical and Spinal C-Fos Immunoreactivity After ICMS of the Primary Somatosensory Cortex in Rats 2251
V. S. Costa, A. O. B Suassuna, L. Galdino, and A. C. Kunicki

Identical Auditory Stimuli Render Distinct Cortical Responses Across Subjects —An Issue for Auditory Oddball-Based BMIs 2257
J. N. Mello, A. F. Spirandeli, H. C. Neto, C. B Amorim, and A. B. Soares

Proposal of a Novel Neuromorphic Optical Tactile Sensor for Applications in Prosthetic Hands 2265
M. G. Pereira, A. Nakagawa-Silva, and A. B. Soares

An Object Tracking Using a Neuromorphic System Based on Standard RGB Cameras 2271
E. B. Gouveia, L. M. Vasconcelos, E. L. S. Gouveia, V. T. Costa, A. Nakagawa-Silva, and A. B. Soares

Classification of Objects Using Neuromorphic Camera and Convolutional Neural Networks 2277
E. B. Gouveia, E. L. S. Gouveia, V. T. Costa, A. Nakagawa-Silva, and A. B. Soares

Acoustic and Volume Rate Deposition Simulation for the Focused Ultrasound Neuromodulation Technique 2283
Patrícia Cardoso de Andrade and E. T. Costa

Neuromorphic Vision-aided Semi-autonomous System for Prosthesis Control 2289
E. L. Gouveia, E. B. Gouveia, A. N. Silva, and A. B. Soares

Finding Discriminant Lower-Limb Motor Imagery Features Highly Linked to Real Movements for a BCI Based on Riemannian Geometry and CSP 2295
L. A. Silva, D. Delisle-Rodriguez, and T. Bastos-Filho

Computational Model of the Effects of Transcranial Magnetic Stimulation on Cortical Networks with Subject-Specific Neuroanatomy 2301
V. V. Cuziol and L. O. Murta Jr.

Special Topics in Biomedical Engineering

Strategy to Computationally Model and Resolve Radioactive Decay Chain in Engineering Education by Using the Runge-Kutta Numerical Method 2311
F. T. C. S. Balbina, F. J. H. Moraes, E. Munin, and L. P. Alves

Effects of LED Photobiomodulation Therapy on the Proliferation of Chondrocytes 2319
Soraia Salman, Cintia Cristina Santi Martignago, L. Assis, Eduardo Santos Trevisan, Ana Laura Andrade, Julia Parisi, Genoveva Luna, Richard Liebano, and C. R. Tim

Characterization of Cultured Cardiomyocytes Derived from Human Induced Pluripotent Stem Cell for Quantitative Studies of Ca^{2+} Transport 2325
Fernanda B. de Gouveia, Talita M. Marin, José W. M. Bassani, and Rosana A. Bassani

Electrochemical Characterization of Redox Electrocatalytic Film for Application in Biosensors 2331
R. M. Gomes, R. A. Lima, and R. A. F. Dutra

DXA and Bioelectrical Impedance: Evaluative Comparison in Obese Patients in City of Cáceres 2337
Cassiano A. G. Dalbem, C. M. M. G. Dalbem, J. E. P. Nunes, T. C. Macedo, B. O. Alves, and Laurita dos Santos

On the COVID-19 Temporal Evolution in Brazil 2341
J. A. Costa Jr., A. C. Martinez, and J. C. Geromel

Use of Apicectomy in the Treatment of Refractory Injury 2347
L. C. T. Moreti, K. G. C. Fernandes, L. Assis, and C. R. Tim

Electronics Laboratory Practices: A Didactic ECG Signal Generator 2353
A. C. Martinez, M. S. Costa, L. T. Manera, and E. T. Costa

Feature Analysis for Speech Emotion Classification 2359
R. Kingeski, L. A. P. Schueda, and A. S. Paterno

Muscle Evaluation by Ultrasonography in the Diagnosis of Muscular Weakness Acquired in the Intensive Care Unit 2367
Thayse Zerger Gonçalves Dias, A. M. W. Stadnik, F. S. Barros, and L. Ulbricht

Development of an Application to Assess Quality of Life 2373
D. S. Oliveira, W. S. Santos, L. M. Ribeiro, G. S. Oliveira, D. S. F. Magalhães, and A. F. Frade-Barros

Tetra-Nucleotide Histogram-Based Analysis of Metagenomic Data for Investigating Antibiotic-Resistant Bacteria 2379
S. P. Klautau, S. L. Pinheiro, A. M. Nascimento, P. A. Castro, R. Ramos, and A. Klautau

Use of Ultrasound in the Emergency and Initial Growth of *Copaifera Reticulata* Ducke (Fabaceae) 2385
I. O. Santos, I. F. N. Ribeiro, N. L. Silva, J. R. Rocha, L. B. Andrade, A. F. R. Rodriguez, W. C. A. Pereira, and L. E. Maggi

Proposal for a Low-Cost Personal Protective Equipment (PPE) to Protect Health Care Professionals in the Fight Against Coronavirus 2391
J. A. F. M. Serra, D. A. C. Filho, J. S. Oliveira, M. C. Teixeira, and I. M. Miziara

Cutaneous Manifestations Related to COVID-19: Caused by SARS-CoV2 and Use of Personal Protective Equipment 2397
A. Almeida, R. S. Navarro, S. Campos, R. D. B. Soares, B. C. Hubbard, A. Baptista, and S. C. Nunez

Low-Cost Modified Swab Graphite Electrode Development as a Point-of-Care Biosensor 2405
A. K. A. Lucas, V. M. Bezerra, R. A. Lima, P. D. Mendonça, and R. A. F. Dutra

Thermographic Evaluation Before and After the Use of Therapeutic Ultrasound in Breast Engorgement 2409
L. E. Maggi, M. P. F. Pereira, S. O. Moura, and W. C. A. Pereira

Thermal Effect of Therapeutic Ultrasound on Muscle-Bone Interface of Swine Tissue (*Sus Scrofa Domesticus*) with Metallic Implant 2413
L. E. Maggi, V. L. Souza, S. O. Moura, C. K. B. F. Nogueira, F. S. C. Esteves, D. C. C. Barros, F. G. A. Santos, K. A. Coelho, and W. C. A. Pereira

Evaluation of Dynamic Thermograms Using Semiautomatic Segmentation Software: Applied to the Diagnosis of Thyroid Cancer 2417
H. Salles, V. Magas, F. Ganacim, H. R. Gamba, and L. Ulbricht

Assessment of Dose with CaF_2 OSL Detectors for Individual Monitoring in Radiodiagnostic Services Using a Developed Algorithm Based on OSL Decay Curve 2425
I. Pagotto, R. Lazzari, D. Filipov, L. Mariano, and A. L. M. C. Malthez

Author Index 2431

Basic Industrial Technology in Health

Analysis of the Acoustic Power Emitted by a Physiotherapeutic Ultrasound Equipment Used at the Brazilian Air Force Academy

J. G. S. N. Cavalcanti, W. C. A. Pereira, and J. F. S. Costa-Júnior

Abstract

Therapeutic ultrasound (TUS) is one of the most widely used methods for treating musculoskeletal injuries, in view of the benefits that this treatment provides: it speeds up the tissue repair process, for example. However, when TUS devices operate outside the range recommended by International Standard IEC 61689:2013, they can cause ineffective treatments or even aggravate the injury. This study aims to analyze the acoustic power emitted by a TUS device from Esquadrão de Saúde de Pirassununga and observe whether the values obtained are within the range established by the IEC 61689:2013. An acoustic radiation force balance was used to measure the power emitted by the equipment. The results showed that on all test days there was a divergence between the nominal and the emitted powers, which exceeded the value recommended by the IEC.

Keywords

Therapeutic ultrasound • Injuries • IEC 61689:2013 • Acoustic power • Repeatability

1 Introduction

The use of therapeutic ultrasound devices (TUSD) is among the most used options for the treatment by diathermy of musculoskeletal injuries. Acoustic energy absorption by the treated tissue promotes repair, accelerating the phases of inflammation and reducing the healing time [1]. Thermal effects include increased blood flow in the treated region, reduced muscle spasm, increased extensibility of collagen fibers and reduced inflammatory process [2]. For these effects to be achieved, it is necessary to maintain the temperature of the treated region between 40 and 45 °C for at least five minutes [1]. If the tissue temperature is below the recommended temperature range, the treatment may be ineffective. On the other hand, if the tissue temperature exceeds 45 °C, the lesion may worsen and may occur protein denaturation, resulting in cell death [3].

It is possible to observe in the literature that since 1972, researchers have been concerned with the output parameters of TUSD, such as the rated output power (ROP) [4]. Despite these concerns, many users of TUSD lack the skills, competences and adequate instruments to analyze the functioning (acoustic parameters) of these devices, so they merely perform a test known as "cavitation method", when they believe that a device is malfunctioning [5]. This test subjectively indicates whether ultrasound is being emitted. In general, physiotherapists are unaware of the importance of testing and preventive maintenance of this equipment or do not request the performance check of these services due to the cost. Some professionals send their equipments to companies to carry out these services, but do not receive pre and post-maintenance and/or testing reports to monitor the proper functioning of the TUSD. Shaw and Hodnett [6] mentioned that the difference between the output (real) and nominal (shown on the equipment display) values of power, intensity and ERA (Effective Radiation Area) can interfere with the treatment, and may even compromise the safety of the patient, which can occur when the value of the acoustic output power is very high or the ERA is much lower than the nominal value. Some studies have shown that many of the analyzed devices had ROP, ERA and/or intensity values above the values recommended by the International Standard IEC 61689:2013 [5, 7, 8 and 9].

IEC 61689:2013 establishes the safety requirements for TUSD [10]. It determines that the ROP, ERA and intensity

J. G. S. N. Cavalcanti · J. F. S. Costa-Júnior (✉)
Brazilian Air Force Academy, Estrada de Aguaí, s/nº, Pirassununga, SP, Brazil
e-mail: francisco@sbeb.org.br

W. C. A. Pereira · J. F. S. Costa-Júnior
Biomedical Engineering Program, Federal University of Rio de Janeiro, Rio de Janeiro, RJ, Brazil

T. F. Bastos-Filho et al. (eds.), *XXVII Brazilian Congress on Biomedical Engineering*, IFMBE Proceedings 83, https://doi.org/10.1007/978-3-030-70601-2_1

can have a maximum variation of ±20%, ±20% and ±30%, respectively, in relation to the nominal values. In this way, the temperature in the treated region is likely to be within the desired temperature range (40 and 45 °C).

According to the Physiotherapy Section of the Esquadrão de Saúde de Pirassununga (ES-YS), in 2018, 6437 ultrasound treatments were performed on military personnel and their dependents. In addition, many cadets (students) were treated with therapy ultrasound (TUS) after joining the Brazilian Air Force Academy (AFA), due to their participation in the Military Adaptation Stage (MAS) and the cadets' routine after the MAS. In the same year, 2,912 ultrasound treatments were performed on Cadets, representing 45.2% of the treatments with TUS performed in the Physiotherapy Section.

The objective of this study was to perform accuracy tests of the acoustic power emitted by a physiotherapy equipment manufactured in Brazil and used by the Physiotherapy Section of ES-YS over 5 consecutive Sundays and to analyze if the device had acoustic power values within the range determined by the International Standard. In addition, the repeatability of the measurements was evaluated. It is worth mentioning that this TUSD was tested in May 2019, and its next testing in May 2020. Additionally, preventive maintenance and electrical safety inspection were carried out in September 2019.

2 Materials and Methods

The materials used in this study were a TUSD model Sonopulse (Amparo, SP, Brazil) configured to operate in continuous mode, an acoustic radiation force balance (ARFB) (UPMDT 1; Ohmic Instruments, Easton, MD, USA) to directly measure the rated power output in 5 days of testing, and a digital thermometer (MT-455A; Minipa do Brasil Ltda, São Paulo, SP, Brazil), which was used to measure the ambient and water of the balance reservoir temperatures. The TUSD has an ergonomic soundhead applicator with dual function, which allows the user to select a transducer with nominal ERA of 3.5 cm^2 (T_1) or 1.0 cm^2 (T_2). When T_1 is used, the TUSD can operate at the nominal frequency of 1 MHz or 3 MHz and with a maximum output nominal power of 7 W. On the other hand, T_2 allows the use of a nominal frequency of 1 MHz and maximum output nominal power of 2 W.

Soundhead applicator was fixed on a support of the ARFB itself, so that the radiation-emitting surface was approximately 0.5 cm below the reservoir water level of the balance, which contained 950 ml of a commercial mineral water without gas "Qualitá". The central axis of the transducer was visually aligned with the center of the metal cone of the balance and the submerged face of the soundhead

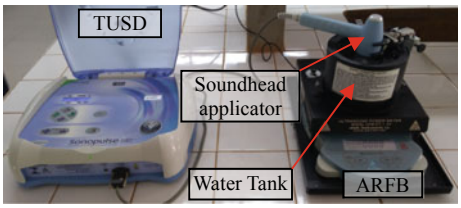

Fig. 1 Illustration of the experimental arrangement used to measure the values of the acoustic power emitted by the TUSD

applicator was positioned parallel to the cone. The system was assembled at the same location in the Physics and Chemistry Laboratory of the AFA, on a stable surface, isolated from airflow and with an ambient temperature of 24.5 ± 1.3 °C over the 5 days, in compliance with that established by the manufacturer of the TUSD for the operation of the device (between 5 and 45 °C). During the experiments, the absence of bubbles between the balance cone and the transducer was observed.

After the assembly of the experimental apparatus shown in the Fig. 1, the balance was activated and 5 min later, the test to verify the calibration and programming of the equipment began, which was performed using an object with a mass of 1 g, equivalent to the rated output power of 14.650 W, but can vary by as much as ±1% (furnished by the manufacturer). The method used to measure the ROP by the TUSD is described in subsections A and B. In these subsections, the test used to assess whether the ROP values were within the range recommended by IEC 61689:2013 and the evaluation of the repeatability of the measurement of ROP values obtained on 5 consecutive Sundays are described.

2.1 Evaluation of the Relative Error of the ROP

The acoustic power emitted by the TUSD was measured over the entire nominal range of the equipment. When T_1 was used at the frequency of 1.0 MHz or 3.0 MHz, 10 ROP measurements were made for each nominal power value, *NP* (0.3, 0.7, 1.0, 1.4, 1.7, 2.1, 2.4, 2.8, 3.1, 3.5, 3.8, 4.2, 4.5, 4.9, 5.2, 5.6, 5.9, 6.3, 6.6 e 7.0 W). In addition, 10 ROP measurements were performed for each *NP* value (0.1, 0.2, 0.3, 0.4, 0.5, 0.6, 0.7, 0.8, 0.9, 1.0, 1.1, 1.2, 1.3, 1.4, 1.5, 1.6, 1.7, 1.8, 1.9 and 2.0 W) with a frequency of 1.0 MHz and ERA of 1.0 cm^2, on 5 consecutive Sundays from the first Sunday in November 2019.

The accuracy test was used in order to calculate the relative error, *RE*, (%) between the nominal power and the ROP obtained with the radiation force balance, for this, Eq. 1 was utilized:

$$RE = [(NP - ROP)/NP] \cdot 100 \quad (1)$$

According to the IEC 61689:2013 [10], the acoustic powers emitted by TUSD with a *RE* above ±20% must be considered outside the tolerance limit and the equipment must be sent for maintenance and/or testing.

2.2 Repeatability Analysis of ROP Measurement

According to JCGM 200:2012 [11], repeatability consists of making measurements using the same measurement system, the same experimental protocol, the same operator, the same location and a repetition over a short period of time. In this study, measurement repeatability was performed using statistical tests to compare measurements made on 5 consecutive Sundays by the same operator, using the same measurement system, at the same location in the Physics and Chemistry Laboratory and using the same experimental protocol.

Initially, the Shapiro–Wilk test was used to assess the normality of the distribution of each subgroup (10 measurements on 5 consecutive Sundays, for each *NP* value, total of 300 subgroups) considering the use of T_1 (1 and 3 MHz) and T_2 (1 MHz). This test was chosen as it is the most powerful test, when compared to the Kolmogorov–Smirnov, Lilliefors and Anderson–Darling tests [12]. Then, the Bartllet test was applied to the data that showed normal distribution as it presents better performance than the others [13]. The aim was to evaluate the homogeneity of the variances of the data that presented a normal distribution, as these are the necessary conditions for the use of the one-way analysis of variance (ANOVA) for repeated measures. When ANOVA was not possible, the Kruskal–Wallis test was employed. Statistical analyzes were performed with the Action Stat 3.7 software (ESTATCAMP, Campinas, SP, Brazil) and the significance level of 5% was adopted.

2.3 Estimation of the ROP Variation Coefficient

The coefficient of variation (*CV*) was utilized to indicate the precision in estimating the rated output power values for each nominal power, using the equation below:

$$CV(\%) = [STD_{ROP}/M_{ROP}] \cdot 100 \qquad (2)$$

where STD_{ROP} and M_{ROP} represent the standard deviation and the mean of ROP values obtained in the experiments.

3 Results

3.1 Evaluation of Rated Output Power (ROP)

The mean (column) and standard deviation (vertical bar) of the ROP values obtained on 5 consecutive Sundays (A, B, C, D and E) using T_1 and T_2 can be seen in Figs. 2 and 3, respectively. Figures 2aa and ab show the ROP values obtained with the frequency of 3 MHz, and Figs. 2ba and bb present the results obtained with 1 MHz.

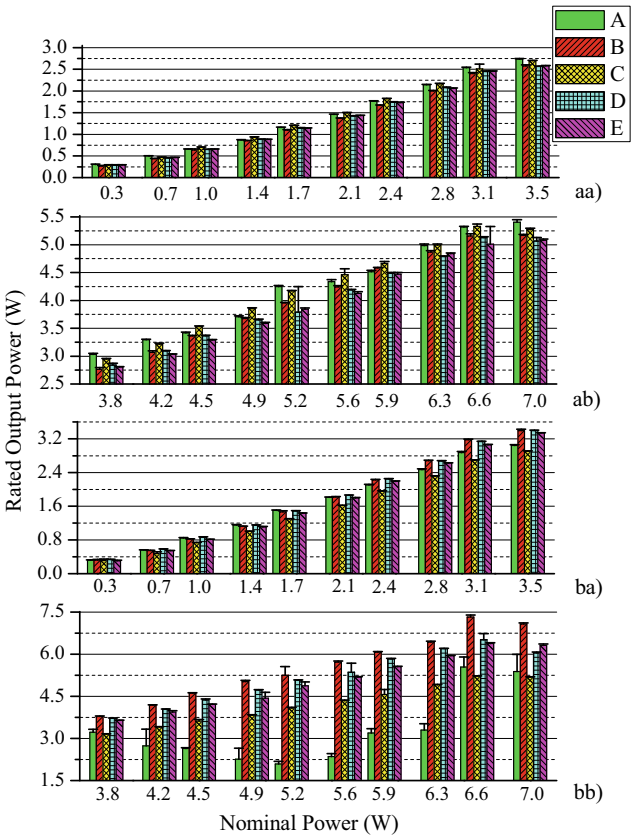

Fig. 2 Mean (column) and standard deviation (vertical bar) of the ROP obtained with T_1 at the frequencies of 3 MHz (**aa** and **ab**) and 1 MHz (**ba** and **bb**)

Table 1 shows the mean and standard deviation of the *RE* values obtained over the five test days (A, B, C, D and E), using T_2 and the entire *NP* range. The mean and standard deviation of the relative error obtained with T_1 in the frequencies of 1.0 W and 3.0 MHz can be seen in Table 2. The highlighted data (bold) represents the day and the nominal power value in which the relative error (%) measured is outside the range established by the International Standard IEC 61689:2013 (± 20 %). The values of the relative error with a negative sign indicate that the acoustic power emitted is higher than the value of the nominal power, which may represent a risk of tissue damage.

3.2 Repeatability Analysis of ROP Measurement

The Shapiro–Wilk test indicated that 33.0% and 31.0% of the 100 T_1 subgroups at frequencies of 1 and 3 MHz,

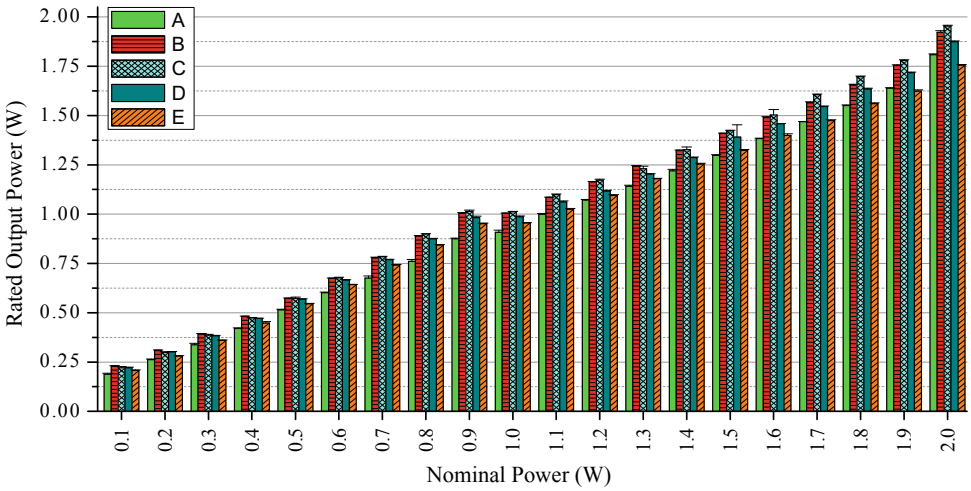

Fig. 3 Mean (column) and standard deviation (vertical bar) of the ROP obtained with T_2 at the frequencies of 1 MHz

Table 1 Mean and standard deviation of the *RE* (%) values obtained over the five test days (A, B, C, D and E) using T_2 and the entire range of *NP*

Nominal power (W)	A	B	C	D	E
0.1	**−87.80 ± 5.61**	**−130.20 ± 1.48**	**−120.60 ± 6.47**	**−120.80 ± 3.68**	**−107.60 ± 3.24**
0.2	**−31.20 ± 1.81**	**−54.90 ± 0.74**	**−49.30 ± 1.95**	**−50.70 ± 1.16**	**−40.20 ± 1.40**
0.3	−12.53 ± 2.39	**−31.00 ± 0.57**	**−28.93 ± 1.18**	**−27.93 ± 0.58**	**−20.07 ± 0.58**
0.4	−5.05 ± 0.93	**−20.55 ± 0.37**	−18.65 ± 0.24	−17.80 ± 0.42	−12.15 ± 1.58
0.5	−2.80 ± 0.82	−14.72 ± 0.41	−14.60 ± 1.28	−13.80 ± 0.34	−9.20 ± 0.33
0.6	−0.37 ± 0.43	−12.50 ± 0.18	−12.90 ± 0.50	−11.00 ± 0.22	−7.17 ± 0.18
0.7	3.40 ± 1.55	−11.37 ± 0.30	−11.94 ± 0.38	−9.89 ± 0.24	−5.89 ± 0.54
0.8	4.85 ± 1.12	−11.20 ± 0.26	−12.38 ± 0.18	−9.45 ± 0.23	−5.42 ± 0.21
0.9	2.73 ± 0.32	−11.69 ± 0.28	−12.71 ± 0.65	−9.18 ± 0.74	−5.80 ± 0.27
1.0	9.16 ± 1.07	−0.42 ± 0.15	−1.18 ± 0.18	1.38 ± 0.45	4.40 ± 0.16
1.1	9.20 ± 0.38	1.36 ± 0.10	0.05 ± 0.32	3.44 ± 0.42	6.84 ± 0.39
1.2	10.68 ± 0.18	2.98 ± 0.12	2.32 ± 0.45	6.90 ± 0.36	8.82 ± 0.38
1.3	12.17 ± 0.38	4.32 ± 0.23	5.32 ± 0.90	7.42 ± 0.14	9.29 ± 0.19
1.4	12.90 ± 0.58	5.47 ± 0.12	5.20 ± 0.96	8.10 ± 0.25	10.47 ± 0.34
1.5	13.48 ± 0.25	6.01 ± 0.10	5.16 ± 0.18	7.31 ± 4.21	11.77 ± 0.33
1.6	13.59 ± 0.19	6.84 ± 0.28	6.10 ± 1.73	8.85 ± 0.10	12.59 ± 0.57
1.7	13.61 ± 0.10	7.92 ± 0.25	5.51 ± 0.16	9.09 ± 0.16	13.28 ± 0.24
1.8	13.81 ± 0.15	7.99 ± 0.15	5.73 ± 0.20	9.18 ± 0.22	13.34 ± 0.26
1.9	13.76 ± 0.15	7.67 ± 0.16	6.32 ± 0.16	9.63 ± 0.17	14.56 ± 0.38
2.0	9.59 ± 0.20	3.90 ± 0.45	2.31 ± 0.20	6.28 ± 0.17	12.22 ± 0.13

respectively, did not present a normal distribution. In addition, 42% of the 100 T_2 subgroups did not have a normal distribution. In view of these results, it was only possible to apply the Bartllet test to assess the homogeneity of the variances of the ROP values obtained in the 5 days for *NP*: 2.8 W, 3.1 W and 6.3 W with T_1 at the frequency of 1 MHz (p-value < 0.05 in all cases), 0.3 W, 0.7 W and 2.8 W with T_1 at the frequency of 3 MHz (p-value = 0.24, 0.96 and 0.31, respectively), and 0.7 W with T_2 (p value < 0.05). This test indicated that only the data obtained with T_1 at the frequency of 3 MHz (0.3, 0.7 and 2.8 W) were not significantly different.

Table 2 Mean and standard deviation of the *RE* values obtained over the five test days (A, B, C, D and E) using T_1 and the entire range of *NP*

Frequência MHz	NP W	A	B	C	D	E
1 MHz	0.3	−5.73 ± 3.00	−7.67 ± 4.02	−4.33 ± 11.36	−13.27 ± 1.11	−2.13 ± 4.72
	0.7	19.80 ± 0.62	**21.14 ± 0.54**	**31.49 ± 5.46**	16.17 ± 0.41	**21.94 ± 0.76**
	1.0	15.30 ± 1.08	17.54 ± 0.37	**26.16 ± 0.62**	13.34 ± 0.58	18.96 ± 0.71
	1.4	17.47 ± 0.79	19.70 ± 0.30	**28.13 ± 0.33**	17.84 ± 0.42	**20.60 ± 0.51**
	1.7	11.61 ± 0.54	13.87 ± 1.59	**23.46 ± 0.28**	12.2 ± 0.19	15.44 ± 0.17
	2.1	13.70 ± 0.26	13.19 ± 0.27	**22.92 ± 0.22**	11.23 ± 0.17	14.41 ± 0.50
	2.4	12.23 ± 0.51	7.21 ± 0.42	18.53 ± 0.39	6.09 ± 0.13	8.76 ± 0.38
	2.8	11.84 ± 0.81	4.20 ± 0.44	17.27 ± 0.29	4.36 ± 0.11	6.14 ± 0.18
	3.1	7.21 ± 0.77	−2.61 ± 0.39	13.15 ± 0.23	−1.33 ± 0.05	1.35 ± 0.35
	3.5	13.11 ± 0.52	2.90 ± 0.97	17.01 ± 0.29	2.82 ± 0.12	4.49 ± 0.07
	3.8	15.15 ± 2.62	0.46 ± 0.51	16.93 ± 0.31	2.07 ± 0.19	4.07 ± 0.16
	4.2	**34.80 ± 14.18**	0.29 ± 0.29	18.88 ± 0.35	3.60 ± 0.11	6.13 ± 1.01
	4.5	**41.22 ± 0.60**	−2.55 ± 0.36	19.63 ± 1.26	2.78 ± 0.71	6.37 ± 0.34
	4.9	**53.87 ± 8.01**	−2.51 ± 0.93	**21.84 ± 0.26**	3.44 ± 0.20	9.51 ± 4.27
	5.2	**59.82 ± 1.82**	−0.95 ± 6.01	**21.43 ± 0.43**	2.35 ± 0.18	6.28 ± 2.76
	5.6	**57.93 ± 1.80**	−2.15 ± 0.69	**22.37 ± 0.30**	4.24 ± 5.72	7.35 ± 0.20
	5.9	**45.87 ± 2.63**	−3.07 ± 0.26	**22.59 ± 3.03**	1.05 ± 0.26	5.71 ± 0.10
	6.3	**47.63 ± 3.55**	−2.12 ± 0.48	**21.94 ± 0.14**	1.54 ± 0.18	5.52 ± 0.11
	6.6	16.03 ± 5.47	−10.96 ± 1.12	**20.89 ± 0.19**	1.23 ± 3.32	3.30 ± 0.45
	7.0	**23.08 ± 8.76**	−1.05 ± 0.61	**25.92 ± 0.12**	13.54 ± 0.38	9.75 ± 0.72
3 MHz	0.3	−1.67 ± 2.23	9.53 ± 2.09	2.80 ± 1.50	2.53 ± 1.12	1.07 ± 1.38
	0.7	**28.23 ± 0.57**	**36.97 ± 0.51**	**32.26 ± 0.46**	**34.49 ± 0.57**	**33.40 ± 0.51**
	1.0	**34.10 ± 0.38**	**36.20 ± 2.57**	**29.74 ± 0.53**	**34.32 ± 0.14**	**34.04 ± 0.23**
	1.4	**37.89 ± 0.44**	**39.00 ± 0.21**	**33.10 ± 0.35**	**36.49 ± 0.12**	**36.71 ± 0.10**
	1.7	**31.99 ± 0.57**	**35.40 ± 0.61**	**28.98 ± 0.08**	**32.53 ± 0.41**	**33.00 ± 0.58**
	2.1	**30.41 ± 0.26**	**34.70 ± 0.19**	**28.91 ± 0.54**	**32.02 ± 0.19**	**31.70 ± 0.41**
	2.4	**26.56 ± 0.35**	**30.42 ± 0.29**	**24.05 ± 0.44**	**27.29 ± 0.22**	**27.88 ± 0.47**
	2.8	**23.42 ± 0.28**	**28.41 ± 0.24**	**22.56 ± 0.32**	**25.64 ± 0.35**	**26.43 ± 0.48**
	3.1	18.03 ± 0.31	**22.49 ± 0.64**	19.03 ± 3.56	**20.90 ± 0.33**	**20.88 ± 0.31**
	3.5	**21.82 ± 0.38**	**26.29 ± 0.67**	**22.75 ± 0.16**	**26.55 ± 0.18**	**26.26 ± 0.20**
	3.8	**20.25 ± 0.53**	**27.18 ± 0.79**	**22.41 ± 0.32**	**25.21 ± 0.79**	**26.19 ± 0.18**
	4.2	**21.53 ± 0.23**	**26.91 ± 0.58**	**23.46 ± 0.47**	**26.27 ± 0.10**	**27.74 ± 0.17**
	4.5	**24.01 ± 0.24**	**25.22 ± 0.23**	**21.52 ± 0.24**	**25.19 ± 0.20**	**26.90 ± 0.17**
	4.9	**24.31 ± 0.33**	**24.98 ± 0.33**	**21.32 ± 0.22**	**25.42 ± 0.22**	**26.79 ± 0.40**
	5.2	18.29 ± 0.37	**23.90 ± 0.16**	19.74 ± 0.10	**27.09 ± 8.78**	**26.10 ± 0.41**
	5.6	**22.53 ± 0.63**	**24.26 ± 0.43**	**20.34 ± 1.90**	**25.11 ± 0.05**	**26.33 ± 0.52**
	5.9	**23.49 ± 0.43**	**22.29 ± 0.17**	**20.89 ± 0.52**	**23.88 ± 0.17**	**24.22 ± 0.51**
	6.3	**20.87 ± 0.42**	**22.76 ± 0.41**	**20.73 ± 0.28**	**23.98 ± 0.15**	**23.19 ± 0.18**
	6.6	19.41 ± 0.15	**21.86 ± 0.57**	19.25 ± 0.61	**22.31 ± 0.27**	**24.12 ± 4.81**
	7.0	**22.77 ± 0.61**	**26.16 ± 0.22**	**24.69 ± 0.35**	**27.60 ± 0.86**	**27.43 ± 0.33**

The Kruskal–Wallis test indicated that there was a significant difference between the power values measured on 5 consecutive Sundays, regardless of the nominal power and the equipment configuration. ANOVA also showed that there was a significant difference between the measurements made in the 5 days when T_1 with a frequency of 3 MHz was used with *NP* of 0.3 W, 0.7 W or 2.8 W.

3.3 Estimation of the ROP Variation Coefficient

Considering the data obtained in the 5 days of experiments, the use of 3.5 cm^2-ERA with a frequency of 1 MHz resulted in a CV in the range from 5.09% to 7.66% for ROP values related to the NP in the range of 0.3 W to 3.8 W, except for 1.4 and 2.1 W. Accuracy was worse in the range of 4.2 to 7.0 W, as the CV varied from 12.23 to 27.72%. When only the transducer frequency was changed to 3 MHz, the CV variation was from 1.67% to 4.41% for the NP from 0.3 W to 7.0 W, except for the nominal power of 5.2 W (6.68%).

The highest precision obtained with the use of the other face of the soundhead applicator, with ERA of 1.0 cm^2 and frequency of 1 MHz, was from 3.12% to 4.35% for the *NP* range from 0.5 W to 2.0 W, except for *NP* of 0.7 W, 0.8 W and 0.9 W (5.26% to 5.93%). There was a change in the *CV* from 5.01% to 7.23% for a NP variation from 0.1 to 0.4 W.

4 Discussion

The testing and programming test of the radiation balance carried out in the 5 days of experiments resulted in the average of the PAE of 14.651 ± 0.001 W (5 measurements per day), so it was observed that the balance was working properly, because the power equivalent to mass of the 1 g disk is 14.650 W and the acceptable range recommended by the manufacturer is 14.504 to 14.796 W.

The mass calibration of a radiation force balance can just assure that the balance is working to measure mass, so it is important that the user choose the "custom mode" (Watts) option on the front panel to check the calibration and programming of the ARFB. If the reading on the ARFB display is not stable, the user can employ the "grams" mode and multiply the readings by 14.650 to obtain Watts.

The ultrasonic energy emitted by the transducer is reflected in the conic-shaped metallic target and is then absorbed by the reservoir rubber lining (thus avoiding reflections and reverberations inside the reservoir).

The radiant power is directly proportional to the total down-ward force (weight) on the target. The weight on the target is transferred to an electromechanical load cell inside the balance. This cell is part of a dedicated electronic system to perform a digital reading in watts of power (custom units) or grams of force.

Although the device had preventive maintenance, electrical safety inspection and testing up to date, there were discrepancies between the ROP values obtained on 5 consecutive Sundays, regardless of the nominal power used. It can be seen in Table 1 that 93% of the *RE* values of the ROP in the 5 days showed values higher than the established by IEC 61689:2013, for nominal powers of 0.1, 0.2 and 0.3 W. In addition, the *RE* values obtained are negative, which implies that the rated output power is greater than the nominal power, which could potentially damage the biological tissue. Despite of that, the Physiotherapy Section mentioned that these values are not used in the treatment of musculoskeletal injuries.

The use of T_1 with a frequency of 3 MHz showed that this equipment must be tested, since 89% of the *ROP* values are above that established by IEC 61689:2013, regardless of the *NP* values used. When T_1 was used with a frequency of 1 MHz, only 23% of the 100 values of the *RE* were above the limit of ±20% (See Table 1).

In general, the equipment showed good accuracy, as the variation coefficient was less than 7.7%, except when T_1 with a frequency of 1 MHz and the following *NP* values were used: 4.2, 4.5, 4.9, 5.2, 5.6, 5.9, 6.3, 6.6 and 7.0 W.

The results obtained in this study are not surprising, since several studies found in the literature show that many therapy ultrasound devices operate outside the range recommended by the International Standard [5, 8, 14]. Pye and Milford [14], for example, analyzed 85 TUSD, of which 59 devices (about 69.4%) had at least one acoustic power value exceeding the ±30% margin, and the IEC 61689:2013 recommends that this variation is a maximum of ±20%. The difference between the paper of these researchers and the present study is the quality of the services provided by the company that carried out the preventive and corrective maintenance and the testing of the equipments, as they observed that after the repair and testing, all measurements performed with 76 devices were less than ±30% of the nominal power, and 95% of the measurements were within the ±20% range. The results showed that 42.6% of the 3000 measurements were outside the previously mentioned range and 13.5% of the ROP measurements were outside the ±30% range. It is also worth mentioning that 88.9% of the 1000 measurements made with T_1 at the frequency of 3 MHz were outside the range recommended by IEC 61689:2013.

Martins et al. [7] evaluated the *ROP* of two nationally manufactured devices that had just left the corrective maintenance and calibration and observed that some *ROP* values (16.3% of 80 measurements) were higher than that recommended by IEC 61689.

Guirro e Santos [15] analyzed 8 TUSD produced in Brazil and found that 5 models (Sonamed I, Sonacel, Sonacel Plus, Sonacel III and Avatar I) had relative errors above ±30% of the intensity selected on the device panel in more than one measured intensity. It is worth mentioning that this result was surprising, since the devices with a testing and/or maintenance problem were new. The acoustic intensity (I) is related to the rated output power through the equation $I = ROP/ERA$.

The cited authors observed that the majority of the TUSD analyzed had some discrepancy between the nominal and measured powers, even when using new devices or after returning from maintenance and/or testing.

5 Conclusion

The accuracy test of the acoustic power emitted by a physiotherapy equipment manufactured in Brazil and used by the Physiotherapy Section of ES-YS over 5 consecutive Sundays showed that the device requires corrective maintenance and/or testing, especially when the ERA of 3.5 cm^2 is used with a frequency of 3 MHz, as many measured values are outside the range recommended by IEC 61689:2013, even if the device is within the maintenance deadlines. The rated output power values obtained showed good precision, because, in general, the coefficient of variation was less than 7.7%, but the devices analyzed showed deficiency in the question of repeatability.

This fact demonstrates a deficiency in relation to the TUSD manufactured in Brazil and/or the maintenance of the device, considering that the equipment was analyzed under temperature circumstances consistent with that required by the manufacturer (between 5 and 45 °C) and in accordance with the established by the IEC 61689:2013.

As a future study, it is intended to evaluate other therapeutic ultrasound devices of the Physiotherapy Section, to observe a possible failure in the company that performs the maintenance of the equipments.

Acknowledgements The authors would like to thank the LUS-PEB-COPPE-UFRJ and the Physiotherapy Section of ES-YS for having provided the equipments used in this study.

Conflict of Interest The authors declare that they have no conflict of interest.

References

1. Prentice WE (2011) Therapeutic modalities in rehabilitation. McGraw-Hill, New York
2. Kumar V, Abbas AK, Aster JC (2013) Patologia Básica. Elsevier, Rio de Janeiro
3. Habash RWY, Bansal R, Krewski D et al (2006) Thermal therapy, part 1: an introduction to thermal therapy. Crit Rev Biomed Eng 34:459–489
4. Stewart HF, Harris GR, Herman BA et al (1974) Survey of the use and performance of ultrasonic therapy equipment in Pinellas County. Phys Ther 54:707–715
5. Lima LS, Costa Júnior JFS, Costa RM et al (2012) Exatidão da potência acústica de equipamentos comerciais de ultrassom fisioterapêutico. CBEB 2012. XXIII Congresso Brasileiro De Engenharia Biomédica, Porto De Galinhas, Brazil 2012:2443–2447
6. Shaw A, Hodnett M (2008) Calibration and measurement issues for therapeutic ultrasound. Ultrasonics 48:234–252
7. Martins ARA, AAS, Omena TP et al (2016) Aferição da intensidade de dois aparelhos de ultrassom fisioterapêutico pós-manutenção. CBEB 2016, XXV Congresso Brasileiro de Engenharia Biomédica, Foz do Iguaçu, Brazil, pp 1989–1992
8. Ferrari CB, Andrade MAB, Adamowski JC et al (2010) Evaluation of therapeutic ultrasound equipments performance. Ultrasonics 50:704–709
9. Johns LD, Straub SJ, Howard SM (2007) Variability in effective radiating area and output power of new ultrasound transducers at 3 MHz. J Athl Train 42:22–28
10. IEC 61689:2013. Ultrasonics—Physiotherapy systems—Field specifications and methods of measurement in the frequency range 0.5 MHz to 5 MHz, 3rd ed. 2013.
11. International vocabulary of metrology: basic and general concepts and associated terms, 3rd. ed. JCGM 200:2012 (2012)
12. Razali NM, Wah YB (2011) Power comparisons of Shapiro-Wilk, Kolmogorov-Smirnov, Lilliefors and Anderson-Darling tests. J Stat Model 2:21–33
13. Riboldi J, Barbian MH, Kolowski ABS et al (2014) Accuracy and power of parametric and non-parametric homoscedasticity tests assessed for simulation. Rev Bras Biom 32:334–344
14. Pye SD, Milford C (1992) The performance of ultrasound physiotherapy machines in Lothian Region. Ultrasound Med Biol 20:347–359
15. Guirro R, Santos SCB (2002) Evaluation of the acoustic intensity of new ultrasound therapy. Ultrasonics 39:553–557

Synthesis and Antibacterial Activity of Maleimides

E. Conrado, C. J. Francisco, R. H. Piccoli, and A. F. Uchoa

Abstract

Previous studies have shown that cyclic imides and their subclasses have obtained positive results in biological activities, showing antimicrobial, analgesic and antifungal therapeutic potential. Arousing the interest of the scientific community and the pharmaceutical industry, surpassing expectations in relation to certain drugs used in the market. In this work we specifically perform the synthesis of one of the subclasses of cyclic imides, called maleimides, as they are easy to obtain and with good yields, in addition to being versatile for conjugation with other molecules. The synthesized compounds were identified by 1H and 13C nuclear magnetic resonance, mass spectroscopy and antibacterial activity was analyzed. In this work, a maleimide platform was obtained with different functional groups. These molecules showed synthesis yields (90%) and the activity was superior to the antibiotic streptomycin.

Keywords

Maleimides • Drugs • Antibacterial activity

1 Introduction

With the development of humanity, new diseases have emerged, which may be of a bacteriological, fungal or viral nature. Generally, of a complex nature such as AIDS and Covid-19. The emergence of new diseases requires ingenious studies in the sense of designing, synthesizing and determining the biological activity of new molecules. In this sense, organic synthesis has been a great ally with the scientific community, favoring the significant growth of new drugs. Which can show promising results in biological effects and in advancing pre-clinical and clinical studies. Among these compounds, cyclic imides stand out [1]. In order to enhance the biological activity, chemical processes are used that imply molecular changes, this depends on the pharmacological and pharmacophobic groups present in the molecule. In this way, we seek to insert groups that can alter the physico chemical properties, such as: hydrophobicity of the substance; alteration of the potential of pharmacological groups. This change occurs through the insertion of groups of donors and/or electron acceptors. This allows the application of qualitative and quantitative methods and can be correlated with chemical structure and biological activity [2].

These methods make it possible to verify the interaction between the chemical structure and biological activity, or the chemical structure and some physical chemical properties. Additionally, it is possible to verify its effects caused in a substance (ligand) during the interaction with the biological receptor, justifying the main factors of this interaction [3]. The introduction of substituents produces changes in the physicochemical properties of the molecule (hydrophobicity, electronic density and structural conformation) and may lead to new syntheses [4]. Several methods have been developed to obtain a better understanding of the different physical chemical parameters, in a small series of substances or test group, which we mention the methods of Hansch [5], Craig [6], Topliss [7]., and the modified Topliss method [7].

In this sense, cyclic imides are compounds that have great therapeutic potential. This family of compounds has the functional group characteristic of imides –CO-N (R) (Fig. 1), where R can be a hydrogen atom, an alkyl or aryl group linked to a carbon chain. Among the cyclic imides we can highlight: Maleimides, Succinimides, Glutarimides,

E. Conrado · A. F. Uchoa
Universidade Anhembi Morumbi, Instituto de Engenharia Biomédica, São José dos Campos, SP, Brazil

C. J. Francisco (✉)
Universidade Nilton Lins, Parque das Laranjeiras, Av. Prof. Nilton Lins, 3259 - Flores, Manaus, AM 69058-030, Brazil

R. H. Piccoli
Universidade Federal de Lavra, Lavras, MG, Brazil

T. F. Bastos-Filho et al. (eds.), *XXVII Brazilian Congress on Biomedical Engineering*, IFMBE Proceedings 83, https://doi.org/10.1007/978-3-030-70601-2_2

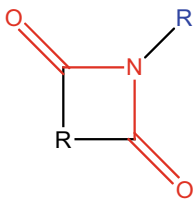

Fig. 1 General structure of cyclic Imides

Phthalimides, Naphtha-limides and their derivatives [1]. With relevance to Maleimides, for being inhibitors of Prostaglandin Endoperoxide Synthase (PGHS). This process occurs by enzymatic attack on olefinic and carbonyl carbons [8]. Proving the importance of studying the biological activity of maleimides, as they are closely related to antimicrobial processes.

Cyclic imides and their subclasses have biological effects of great importance which we cite as maleimide as the main representative in antifungal, antibacterial and insecticidal activities [1]. The main objective of this work was to obtain a maleimide platform with different functional groups (R) and to determine the antibacterial activity of the compounds obtained against *Escherichia coli* ATCC 055, *Pseudomonas aureginosas* ATCC 27853, *Staphylococcus aureus* ATCC 25923 and *Listeria monocytogenes* ATCC 15313.

2 Material and Methods

2.1 Syntesis

Anilines and anhydride came from Sigma Aldrich; high purity analytical reagents. The solvents ethyl ether, acetic anhydride, chloroform, methanol and sodium acetate from Sinthya. Maleimides were synthesized in two stages: 1) the addition of anilines to maleic anhydride for the formation of the corresponding acid and 2) reflux in acetic anhydride for the cyclization of the imide ring. This procedure was performed according to the process described in the literature [8], with a yield between 32 and 78%. The characterization was performed by nuclear magnetic resonance at 500 MHz, using deuterated chloroform (CDCl3) as a solvent and TMS as a reference.

2.2 Antimicrobial Activity

The radial diffusion method on nutrient agar was used, where the bacteria were grown in Brain Heart Infusion. After activation, the turbidity was corrected using the McFarland 0.5 scale. The sterile paper discs were immersed in a solution of the compounds dissolved in DMSO, at a concentration of 250 mMol/mL. These plates were incubated at 37 °C for 24 hours and the inhibition halos (mm) were read. Controls were performed with solvent (DMSO) and antibiotic (Streptomycin). The tests were carried out with the following bacteria: *Pseudomonas aureginosas* ATCC 27853 (gram negative), *Escherichia coli Enteropatogênica* ATCC 055 (gram negative), *Staphylococcus aureus* ATCC 25923 (gram positive) e *Listeria monocytogenes* ATCC 15313 (gram positive).

3 Results

3.1 Synthesis and Structural Characterization

In this research, 11 compounds were obtained, compound 1 has recognized antibacterial activity. Compounds 2, 3 and 4, have already been synthesized, but never had their biological activities determined. The remaining compounds (5–11) are new. Figure 2 shows the synthetic scheme for obtaining these compounds.

The 11 compounds were perfectly purified on a column with silica gel and characterized by high resolution mass spectrometry, and nuclear magnetic resonance of Hydrogen (NMR1H) and carbon 13 (NMR13C). Only the spectra referring to methyl 4-(2,5-dioxo-2,5-dihydro-1H-pyrrol-1-yl) benzoate (compound 9), are presented in Figs. 3, 4 and 5, respectively.

3.2 Biological Activity

Antibacterial activity was determined in four strains of bacteria. Two gram positive (*Staphylococcus aureus* ATCC 25923 e *Listeria monocytogenes* ATCC two gram negative (*Pseudomonas aureginosas* ATCC 27853 e *Escherichia coli* ATCC 055 (Table 1).

Since it is known that the biological activity of maleimides is related to structural factors and their physiochemical properties, in this work a platform of maleimides with different functional groups was synthesized, which provided a study of the chemical structure related to biological activity. In *P. aureginosas* bacteria ATCC 27853, *E. coli* ATCC 055, *S. aureus* ATCC 25923 and *L. monocytogenes* ATCC 15313. The Fig. 1 presents a scheme of the synthesis strategy of the compounds that were used to study biological activity.

Within the concentrations used, no activity was observed for *experiments*. DMSO. The antibiotic Streptomycin did not show selectivity between gram positive and gram negative bacteria. For gram negative bacteria, compounds 11 and 1 showed a potential close to Streptomycin. The same was observed for compounds 10, 5, 1 and 3 in *P. aureginosas*. On the other hand, the gram positive results showed an inhibitory potential of the compounds in the following order

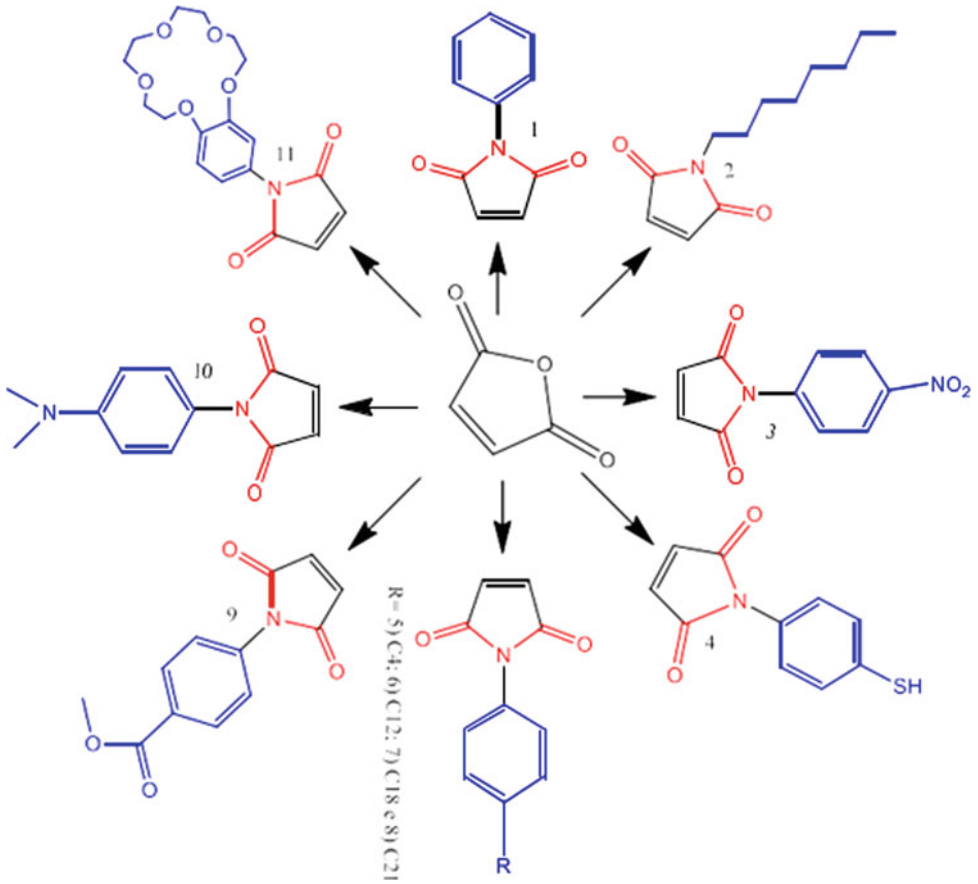

Fig. 2 Compound platform structure: (1) 1-phenyl-1H-pyrrole-2,5-dione; (2) 1-octyl-1H-pyrrole-2,5-dione, (3) 1-(4-nitrophenyl)-1H-pyrrole-2,5-dione; (4) 1-(4-mercaptophenyl)-1H-pyrrole-2,5-dione; (5) 1-(4-butylphenyl)-1H-pyrrole-2,5-dione; (6)1-(4-dodecylphenyl)-1H-pyrrole-2,5-dione; (7) 1-(4-octadecylphenyl)-1H-pyrrole-2,5-dione; (8) 1-(4-henicosylphenyl)-1H-pyrrole-2,5-dione

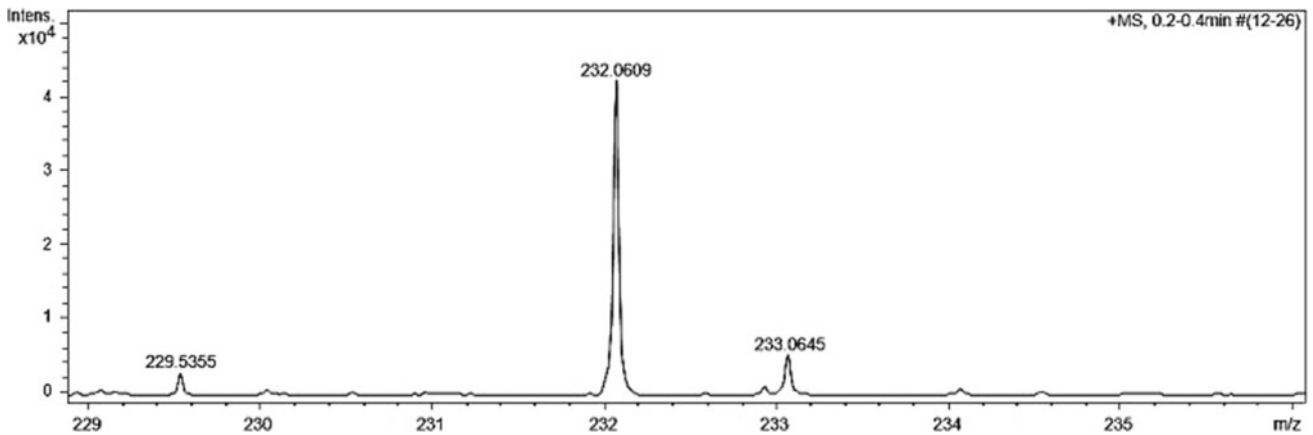

Fig. 3 Mass spectrum of methyl 4-(2,5-dioxo-2,5-dihydro-1H-pyrrol-1-yl) benzoate

1, 11, and 5, higher than Streptomycin when applied to S. aureus. For L. monocytogenes, compounds 1, 5, and 10 also showed an inhibitory potential greater than Streptomycin.

Considering that these compounds have the maleimide ring as a pharmacological group, and that the mechanism of action occurs by enzymatic attack on the vinyl group conjugated to carbonyls and / or carbonyl group, and that they are present in all compounds; In this work, that the differences between the activities seem to be related to the hydro/lipophilic balance.

The solvent (DMSO) had no inhibitory effect. Streptomycin (control) showed a regular inhibition pattern within

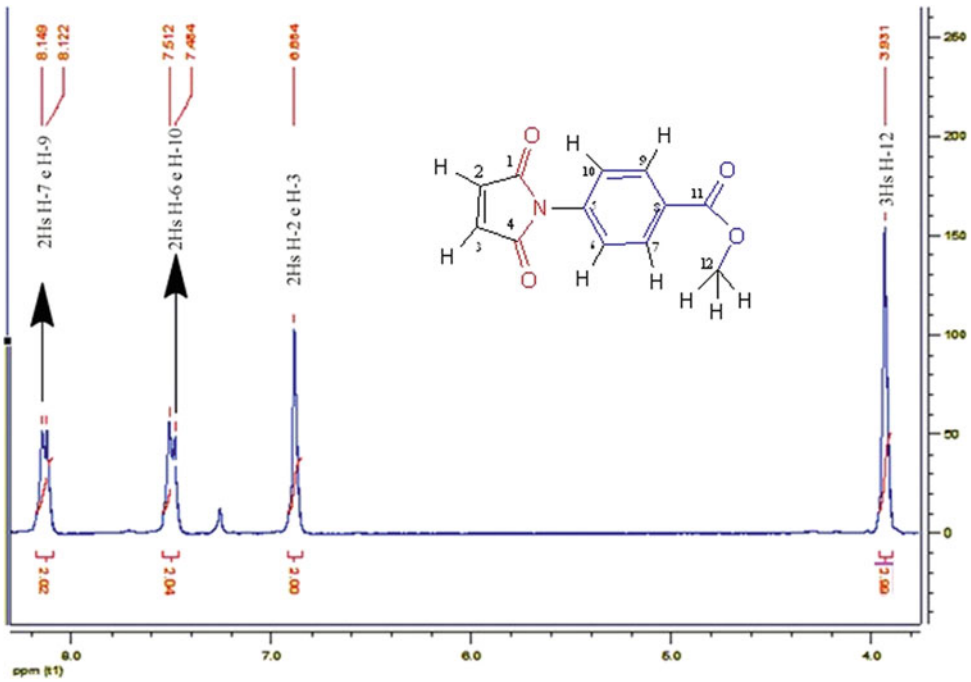

Fig. 4 Spectrum of RMN 1H, in CDCl3 a 500 MHz 4-(2,5-dioxo-2,5-dihydro-1H-pyrrol-1-yl) benzoate

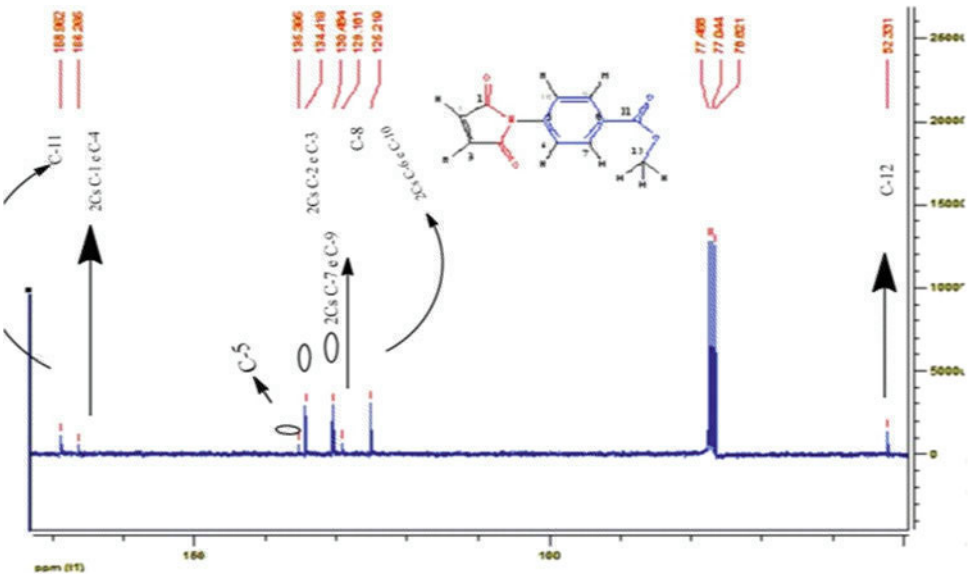

Fig. 5 Spectrum of RMN 13C, in CDCl3 a 125 MHz 4-(2,5-dioxo-2,5-dihydro-1H-pyrrol-1-yl) benzoate

the group of bacteria analyzed. With zone of inhibition of 15.2–16.4 mm for gram negative and 13.5–13.2 mm for gram positive. For gram negative bacteria, *E. coli* was most affected by compounds 1 and 11 (15.0–15.8 mm) and 5 (13.0 mm). *P. aureginosas* was more affected by compounds 1, 3, 5 and 10 (13.47–13.98 mm). For gram positive *S. aureus* was more affected by 5, 11 and 1 (16.7–18.4 mm). *L. monocytogenes* was more affected by 10, 5 and 1 (17.0–20.3 mm).

4 Discussion

The 1-octyl-1H-pyrrole-2,5-dione (compound 2) was obtained from octan-1-amine, with 38% yield. On the other hand, those obtained by anilines, showed much higher yields, between 78 and 92%. This reaction yield is related to the nucleophilicity of the amines. The higher yields were obtained for the alkylated anilines of compounds 4, 5, 6, 7

Table 1 Antibacterial activity of maleimides by the agar diffusion method; Data are presented as mean and standard error of three independent

Compound		Inhibition zone (mm)		
	Escherichia coli 250 mMol/mL	*Pseudomonas aeruginosa* 250 mMol/mL	*Staphylococcus aureus* 250 mMol/mL	*Listeria monocytogenes* 250 mMol/mL
Streptomycin	16.4 ± 0.00	15.23 ± 0.00	13.51 ± 0.00	13.6 ± 0.00
DMSO	0 ± 0.00	0 ± 0.00	0 ± 0.00	0 ± 0.00
1	15.8 ± 0.24	13.73 ± 0.84	18.4 ± 1.09	20.3 ± 0.57
2	8.43 ± 2.27	4.60 ± 1.88	0 ± 0.00	6.6 ± 0.13
3	8.4 ± 0.28	13.93 ± 0.67	10.5 ± 1.03	14.0 ± 0.75
4	9.0 ± 1.24	10.05 ± 1.44	8.1 ± 0.69	7.8 ± 0.60
5	13.3 ± 0.38	13.98 ± 1.05	16.7 ± 0.17	17.8 ± 0.09
6	4.2 ± 1.70	0 ± 0.00	2.1 ± 1.74	8.1 ± 0.36
7	5.4 ± 2.31	7.25 ± 0.18	0 ± 0.00	7.5 ± 0.14
8	8.8 ± 0.61	12.44 ± 0.95	11.2 ± 0.16	9.6 ± 1.01
9	4.7 ± 1.94	0 ± 0.00	6.4 ± 0.14	0.0 ± 0.00
10	9.6 ± 0.46	13.47 ± 0.82	13.6 ± 0.31	17.0 ± 0.46
11	15.0 ± 0.71	12.04 ± 0.59	16.8 ± 0.54	12.5 ± 1.25

and 8, all with yields greater than 85%. The higher yield of these compounds is related to the greater reactivity of these anilines, which was increased by the inductive effect of the alkyl chain donor. These compounds were perfectly purified by chromatography on silica gel, since the polarity of the products differs significantly from the reaction reagents and by-products. The characterization was performed unequivocally by mass spectrometry and nuclear magnetic resonance (^{1}H NMR) and ^{13}CNMR at 500 MHz and 125 MHz, respectively. The NMR1H spectra show a characteristic singlet in chemical displacement (σ) of 6.8 ppm for the 2H vinyls, characteristic of the maleimide ring. In the ^{13}CNMR the carbons of carbonyls 1 and 4 appear in $\sigma \approx 170$ ppm. This relationship seems to be maximalized for compound 1, 5, 10 and 11 in gram positive.

5 Conclusions

For the synthetic process, it was found that the compounds obtained from anilines present a much higher yield than those obtained by aliphatic amines. Compounds 1, 5, 10 and 11 were the ones with the greatest potential. Since, the pharmacological group is the maleimide ring, and the mechanism of enzymatic attack on this ring is dependent on an internalization in microorganisms and specific structures, it is concluded that this biological activity is dependent on the functionalization group, because allows adequate permeability, which is dependent on the hydro/lipophilic balance.

Acknowledgements The authors wish to thank Fapesp, Process 2013 / 07937-8, CEPID REDOXOMA - Research Center on Redox Processes in Biomedicine

Conflict of Interest The author(s) declared no potential conflicts of interest with respect to the research, authorship, and/or publication of this article.

References

1. Cechinel Filho V, Corrêa R, Yunes RA, Nunes RJ (2003) Aspectos químicos e potencial terapêutico de imidas cíclicas: uma revisão da literatura. Química Nova 26:230–241
2. Kalgutkar A S, Crews B C. Marnett L J (1996) J. Med.Chem. 39, 8
3. Hansch C, Fujita T (1964) ρ-σ-π Analysis. A method for the correlation of biological activity and chemical structure. J Am Chem Assoc 86:1616–1626
4. Craig PN (1971) Interdependence between physical parameters and selection of substituent groups for correlation studies. J Med Chem 14(8):680–684
5. Topliss JG (1972) Utilization of operational schemes for analog synthesis in drug design. J Med Chem 15:1006
6. Ferreira RS, Oliva G, Andricopulo A (2011) Integração das técnicas de triagem virtual e triagem biológica automatizada em alta escala: oportunidades e desafios em P&D de fármacos. Química Nova 34 (10):1770–1778
7. Huisgen R, Granskey R, Saver J (1964) The chemistry of alkenes. In: S Patai (ed) Interscience Publishers, London, p 739
8. Cava MP, Deana AA, Muth K et al (1973) *N*-phenylmaleimide. In: Baumgarten HE (ed) Org. Synth. Collective, vol 5. Wiley, New York, pp 944–946

Bioengineering

Study of the Effect of Bioceramic Compressive Socks on Leg Edema

A. A. S. Sakugawa, L. A. L. Conrado, A. Balbin Villaverde, and E. Munin

Abstract

The aim of the present study is to investigate the therapeutic effect of wearing compressive socks composed of synthetic fibers with IR- emitting ceramic particulates on patients with edema of inferior member extremities. Thirty patients of both genders and age ranging from 30 to 70 years old (54.9 ± 13.3 years) were enrolled in the study and separated into two groups: C^+ and placebo. The C^+ group wore the compressive socks with embedded ceramic powder for at least 8 h a day for four weeks. The placebo group wore compressive socks made with fabrics of same material but without the ceramic particulate. The evolution of the treatment was assessed through plethysmographic measurements. The statistical analysis was done using the Kolmogorov–Smirnov normality test and a parametric two-tailed t-test with Welch correction at the significant level of $\alpha = 0.05$. The Prism 8.0 software (GraphPad Software Inc., La Jolla, CA, USA) was used for the analysis. The experimental data showed a statistically significant reduction in edema volume for the ceramic-active group C+ , as compared to the placebo group. The treatment of leg edema using compressive socks containing ceramic particulate in its fabrics seemed to be more effective when compared with placebo socks.

Keywords

Leg edema • Bioestimulation • Infrared therapy • Black body emission • Bioceramic socks

1 Introduction

Biological effects resulting from the occlusion of body parts by pieces of clothes and devices containing ceramic particulates have been reported [1–7]. Those published results indicate that the presence of inorganic particulates in the composition of occluding devices and fabrics modulates the radiation exchange between the human body and the surrounding medium. Increment in the local tissue temperature and vasodilatation seems to be the primary effects attributed to creams and garments containing inorganic particulates and other ceramic devices as well.

In the last decades, the interest for studying IR ceramic garment therapies has been increased and reports of successful treatments for a variety of diseases are numerous. Among the diseases treated with garments embedded with ceramic particulates it can be mentioned Raynaud's syndrome (thermo flow gloves) [5]; chronic foot pain (polyethylene terephthalate fiber socks) [6]; primary dysmenorrhea (far infrared-emitting sericite belt) [8, 9]; cellulite reduction (bioceramic-coated neoprene shorts) [1, 2]; impairment of limb movements in post-polio syndrome (Infrared MIG3 bioceramic fabrics) [7]; postoperative effusion after total knee arthroplasty (knee pad of Nexus-ES fiber) [10]. Likewise, studies on the reduction of body measurements of individuals wearing bioceramic high-waist undershorts were reported [3, 4]. It was also found that some bioceramic appliances improve athlete's performance, such as reduction in time recovery of futsal players by using bioceramic pants [11], control bacterial load in runners by wearing socks embedded with ceramic particulates [12], and performance improvement of gymnast when wearing

A. A. S. Sakugawa · A. Balbin Villaverde · E. Munin (✉)
Anhembi Morumbi University (UAM), Biomedical Engineering Center, Estrada Dr. Altino Bondensan, 500 Distrito de Eugênio de Melo, CEP: 12.247-016, São José dos Campos, SP, Brazil
e-mail: emmunin@anhembi.br

L. A. L. Conrado · A. Balbin Villaverde · E. Munin
Center for Innovation, Technology and Education (CITE), Estrada Dr. Altino Bondensan, 500, Distrito de Eugênio de Melo, CEP: 12.247-016, São José dos Campos, SP, Brazil

T. F. Bastos-Filho et al. (eds.), *XXVII Brazilian Congress on Biomedical Engineering*, IFMBE Proceedings 83, https://doi.org/10.1007/978-3-030-70601-2_3

modified suits with ceramic materials [13]. The effects of bioceramic textiles used in sports activities are disclosed in a recently published review [14].

All materials in the nature emit electromagnetic radiation that depends on the temperature and composition of the material. If the material were perfectly absorbing (black body) the spectrum of the emitted radiation presents a maximum wavelength (λ_{max}) given by Wien's law and a total power per unit area (P/A) that satisfy the Stefan-Boltzmann Law:

$$l_{max} = [2.897/T)] \times 10^{-3}m$$

$$P/A = sT^4$$

where T is the absolute temperature in degrees Kelvin (K) (273 + °C) and $\sigma = 5.67040 \times 10^{-8}$ W/m^{2}K^4 is the Stefan' constant. For real materials in the nature (not black body), the λ_{max} does not depend on the material properties, being only a function of its temperature. On the other hand, the total power per unit area depends also on the material properties.

$$P/A = \varepsilon\sigma T^4$$

where ε is the emissivity of the material and ranges from zero (non-absorbing material) to 1 (black body). For bioceramic particulates the emissivity is 0.9 or even higher. At room temperature that emission falls into the infrared range (IR) of the spectrum. Figure 1 displays the value of λ_{max} as a function of the temperature T. It can be observed that for a human skin temperature of 33 °C the ceramic particulates emit radiation with a maximum at 9,47 μm and receives from the environment, at an average temperature of 23 °C, radiation with a maximum wavelength around 9.8 μm.

The aim of the present study is to elucidate if wearing socks with embedded ceramic particulates is effective for reducing edema of the legs in persons with chronic inflammation of vascular origin. The edema reduction will be assessed using a plethysmographic method.

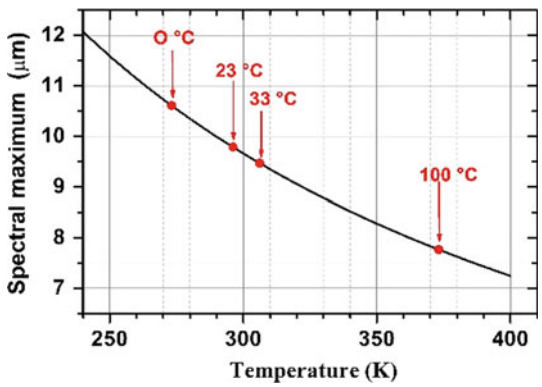

Fig. 1 Maximum wavelength of the black body radiation as a function of the body temperature (Wien's Law)

2 Materials and Methods

The study protocol was in accordance with the Declaration of Helsinki, and it was approved by the University Ethics Committee (Universidade do Vale do Paraiba - Ethics Committee approval number H42/CEP2010). All subjects provided written informed consent before data collection.

The subjects of this research were 30 patients of both sexes, who ranged from 30 to 70 years old, suffering from edema of vascular or lymphatic origin in the extremities of the inferior members, presenting symptoms diagnosed for more than one year. The 30 patients were equally distributed in two groups. The group C+ wore socks with particulate ceramic embedded in the fabrics and the placebo group wore socks of the same fabrics without ceramic material. Since some patients presented edema in both legs, a total of 48 inferior members were diagnosed with edema, in such a way that each group contained 24 edematous members. The patients were advised not to apply cosmetics on the edematous site, and neither to perform massage nor lymphatic drainage.

Exclusion criteria: pregnant or lactating women, endocrine disease, disorders of diabetic origin, venous ulcers and arterial disorders, being under treatment with anti-inflammatory drugs.

Each of the volunteers of both groups received a set of two socks with compression factor of 20 mmHg, containing or not the ceramic particulates. The socks were manufactured with Emana™ polyamide yarns with embedded ceramic particulates containing oxides of Al, Si, Zn e Ca, and were provided by BIOS (São José dos Campos, Brazil). The volunteers were requested to wear the socks daily for eight consecutive daytime hours, during four weeks, and were evaluated weekly.

The edema reduction from before to after treatment was assessed by a homemade plethysmograph, which consisted of a rigid boot made with fiberglass containing 2.5 L of water. The edema volume was determined by measuring the volume of water displaced when the patients inserted their leg into the boot with water. The research subjects did not move or shake their legs, to reduce measurement errors.

The edema size evolution over the time of treatment was assessed by plethysmographic measurements of the leg volume weekly for four weeks. A quantitative evaluation parameter was defined by $\Delta V = V - Vo$, where V is the leg volume at each week and V_o is the leg volume before treatment. The negative value of ΔV indicates that there was a reduction of the edema.

2.1 Statistical Analysis

The statistical analysis of the data was done using the Kolmogorov–Smirnov test for normality of the data and a parametric two-tailed t-test with Welch correction for analyzing the difference between the means of C^+ and placebo groups, at the significant level of $\alpha = 0.05$. The Prism 8.0 software (GraphPad Software Inc., La Jolla, CA, USA) was used for the analysis. Data is expressed as mean ±SEM.

3 Results

The mean age of the thirty volunteers that participated in the study was 54.9 ± 13.3 years (mean ± SD). The age dispersion of the patients in both groups showed to be statistically homogenous (mean ± SD): 50.7 ± 12.0 years (placebo group) versus 59.1 ± 13.7 years (C^+ group), p = 0.831.

Figure 2 depicted the results of the edema volumetric change (ΔV) obtained by plethysmographic measurements from before to after treatment. The initial volume Vo covers the range: placebo from 838 to 1388 mL and C^+ from 898 to 1520 mL The statistical box plot of Fig. 2 gives a perception of data dispersion and shows that the mean volumetric reduction for the group that wore socks containing ceramic particulates in the fabrics composition was (−78.9 ± 10.7) mL, while for the placebo group the mean volumetric reduction was only (−41.3 ± 5.6) mL.

Intragroup analysis of both groups using the Kolmogorov–Smirnov normality test indicates that data of each group pass the normality test. A statistical comparison among the experimental data for the two study groups with parametric unpaired t test returned a two-tailed p value of 0.003, pointing out that the difference among the group means is very significant.

Figure 3 displays the frequency as a function of edema volumetric change at the end of the treatment for the two groups. The histograms of Fig. 3 show that, for the group

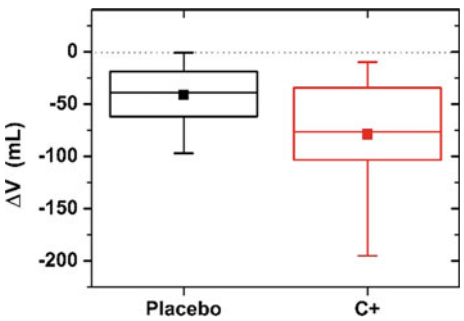

Fig. 2 Edema reduction from before to after treatment as quantified by Plethysmographic measurements disclosed in statistical box plot

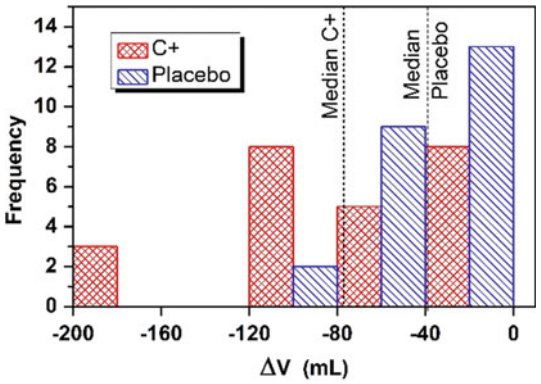

Fig. 3 Frequency histogram chart for C^+ and placebo groups

that wore socks containing ceramic particulate, the distribution of measured values for edema volumetric change is clearly shifted toward higher volume reductions, as compared to the distribution achieved for the placebo group.

The time evolution of the edema volumetric change (ΔV) over the treatment is an important information, since it indicates if the reduction is consistent. It is displayed in Table 1 the data about the edema change for the placebo and the C^+ groups at each week of treatment and the corresponding p-value obtained from the intergroup statistical analysis. It is possible to see that the edema volume undergoes a systematic reduction along the treatment for the two groups, although the reduction is larger for the group that wore socks with ceramic particles. It can be observed that the values of p consistently decrease from the 1st to the 4th week reaching a statistically significant difference at the 3rd and 4th weeks. The results indicate that treatment by wearing socks containing ceramic particulates becomes more efficient with continued use when compared to wearing socks without ceramics.

4 Discussion

The better clinical results observed in the present study that are promoted using ceramic-containing socks may be attributed to a stimulation of blood perfusion and lymphatic drainage, as a consequence of an increment in the local tissue temperature produced by the topical occluding garment containing ceramic particulates. This hypothesis is strengthened by the work reported by Ko and Berbrayer [5], who treated Raynaud's syndrome patients with ceramic-containing gloves. A mean temperature increases of 1 °C in the finger dorsum of the patients who wore the ceramic gloves was reported, suggesting that the gloves, active by the incorporated ceramic, were beneficial in the management of Raynaud's symptoms. Other study on the thermal effects of wearable ceramic materials was reported

Table 1 Edema volumetric change for each week of treatment expressed as mean ± SEM for placebo and C+ groups

	Edema volumetric change (ΔV)		p value
	Placebo	C^+	
1st week	−20.2 ± 5.8	−34.6 ± 11.4	0.260
2nd week	−30.2 ± 6.7	−52.5 ± 11.2	0.080
3rd week	−38.3 ± 7.1	−66.1 ± 11.5	0.040[a]
4th week	−41.3 ± 5.6	−78.9 ± 10,7	0.003[a]

The value of p corresponds to the weekly intergroup statistical analysis of group means
[a]Mean difference statistically significant

recently by Papacharalambous et al. [15]. They introduced the hands of healthy voluntaries first in cold water and then in pouches, being one pouch bioceramic-active and the other one a placebo. It was found a percentage temperature increase of 6.34% (dorsal side) and 4.74% (palm side) when the use of an active pouch is compared to a placebo one [15].

The data presented in this work show that compressive socks are beneficial in the treatment of edema of the lower member extremities and that the addition of particulate ceramics in the fabrics from which the socks are manufactured enhances the clinical results even further. The experimental data for the time evolution of edema volume reduction over the four weeks of treatment reveal an increase of edema reduction capacity of the socks containing bioceramic particulates, as compared with the placebo ones: 1st week 14.4 mL, 2nd week 22.3 mL, 3rd week 27.8 mL, and at the 4th week 37.6 mL. The difference between mean values of both groups increases in a monotonic way over time, and at 3rd and 4th weeks that difference becomes statistically significant, $p = 0.04$ and $p = 0.003$, respectively.

The frequency histograms of Fig. 3 show that, for the group that wore socks containing ceramic particulate, the distribution of measured values for edema volumetric change is clearly shifted toward higher absolute volumes, as compared to the distribution achieved for the placebo group.

Anderson et al. [16] disclosed a thorough study about the radiative interactions between the body, garments and ambient, and the energy flux formed by the reflected, transmitted and emitted IR radiation. They discussed the way how the IR energy is transferred back and forth between the three elements: body, fabric and surrounding medium.

More recently, Washington et al. [17] presented a carefully investigation about the possible mechanism for the phototherapy using IR radiation produced by Bioceramic materials embedded in fabrics, which are used for wearable garments such as the compressive socks of the present study. Ceramic particulates embedded in the garments absorb energy that comes from the body by radiative process and by conductive/convective heat transfer, and then re emit back to the body. The radiation emitted by the body is centered at about 9 μm, assuming a skin temperature of 33 °C (Fig. 1), however the ceramic particles emit with a slightly longer wavelength, because the garment temperature is lower than that of the skin.

Other point to be considered is whether the clothing change the body's boundary conditions and interfere with the radiant heat exchange between the body and the surrounding medium [3]. They considered that the garments might be working as a radiation trap that sends reflected IR radiation back to the body [3].

An interest question was raised by the work of Vatansever and Hamblin [18] about the correlation between non-heating IR phototherapy and the visible-NIR low power phototherapy. They asserted that the effect of both therapies may be due to vasodilation by NO release from cytochrome c oxidase or NO bound to hemoglobin, among other possible mechanisms.

Further studies will be necessary for a better understanding of the IR phototherapy processes responsible for the results presented herein.

5 Conclusion

The present study seems to indicate the effectiveness of wearing compressive socks with embedded ceramic material for edema volumetric reduction in individuals suffering from edema of vascular or lymphatic origin in the extremities of the inferior members.

Conflict of Interest The authors declare that they have no conflict of interest.

References

1. Rao J, Paabo KE, Goldman MP (2004) A double-blinded randomized trial testing the tolerability and efficacy of a novel topical agent with and without occlusion for the treatment of cellulite: a study and review of the literature. J Drugs Dermatol 3:417–425
2. Rao J, Gold MH, Goldman MP (2005) A two-center, double-blinded, randomized trial testing the tolerability and efficacy of a novel therapeutic agent for cellulite reduction.

J Cosmet Dermatol 4:93–102. https://doi.org/10.1111/j.1473-2165.2005.40208.x
3. Conrado LAL, Munin E (2011) Reduction in body measurements after use of a garment made with synthetic fibers embedded with ceramic nanoparticles. J Cosmet Dermatol 10:30–35. https://doi.org/10.1111/j.1473-2165.2010.00537.x
4. Conrado LAL, Munin E (2013) Reductions in body measurements promoted by a garment containing ceramic nanoparticles: a 4-month follow-up study. J Cosmet Dermatol 12:18–24. https://doi.org/10.1111/jocd.12027
5. Ko GD, Berbrayer D (2002) Effect of ceramic-impregnated thermo flow gloves on patients with Raynoud´s Sindrome: randomized, placebo-controlled study. Alter Med Rev 7:328–334
6. York RMB, Gordon IL (2009) Effect of optically modified polyethylene terephthalate fiber socks on chronic foot pain. BMC Complement Alter Med 9:10. https://doi.org/10.1186/1472-6882-9-10)
7. Silva TM, Moreira GA, Quadros AAJ et al (2009) Effects of the use of MIG3 bioceramics fabrics use—long infrared emitter—in pain, intolerance to cold and periodic limb movements in post-polio syndrome. Arq Neuropsiquiatr 67:1049–1053. https://doi.org/10.1590/s0004-282x2009000600016
8. Lee CH, Roh JW, Lim CY et al (2011) A multicenter, randomized, double-blind, placebo-controlled trial evaluating the efficacy and safety of a far infrared-emitting sericite belt in patients with primary dysmenorrhea. Complement Ther Med 19:187–193. https://doi.org/10.1016/j.ctim.2011.06.004
9. Liau BY, Leung TK, Ou MC et al (2012) Infrared ray-emitting belts on primary dysmenorrhea. Int J Photoener ID 238468. https://doi.org/10.1155/2012/238468
10. Innocenti M, Mancini M, Faccio M et al (2017) The use of a high-tech knee pad for reduction of the postoperative effusion after total knee arthroplasty. Joints 5:7–11. https://doi.org/10.1055/s-0037-1601406
11. Nunes RFH, Cidral-Filho FJ, Flores LJF et al (2020) Effects of Far-infrared emitting ceramic materials on recovery during 2-week preseason of elite futsal players. J Strength Cond Res 34:235–248. https://doi.org/10.1519/JSC.0000000000002733
12. Nova AM, Marcos-Tejedor F, Martín BG et al (2018) Bioceramic-fiber socks have more benefits than cotton-made socks in controlling bacterial load and the increase of sweat in runners. Text Res J 88:696–703. https://doi.org/10.1177/0040517516688631
13. Cian C, Gianocca V, Barraud PA et al (2015) Bioceramic fabrics improve quiet standing posture and handstand stability in expert gymnasts. Gait & Posture 42:419–423. https://doi.org/10.1016/j.gaitpost.2015.07.008
14. Pérez-Soriano P, Sanchis-Sanchis R, Aparicio I (2012) Effects of bioceramic textiles used in physical activity or sport: a systematic review. Int J Cloth Sci Tech 30:854–863. https://doi.org/10.1108/IJCST-05-2018-0066
15. Papacharalambous M, Karvounis G, Kenanakis G et al (2019) The effect of textiles impregnated with particles with high emissivity in the Far Infrared, on the temperature of the cold hand. J Biomech Eng 141:034502. https://doi.org/10.1115/1.4042044
16. Anderson DM, Fessler JR, Pooley MA et al (2017) Infrared radiative properties and thermal modeling of ceramic-embedded textile fabrics. Biomed Opt Express 8(3):1698–1711. https://doi.org/10.1364/BOE.8.001698
17. Washington K, Wason J, Thein MS et al (2018) Randomized controlled trial comparing the effects of far-infrared emitting ceramic fabric shirts and control polyester shirts on transcutaneous PO_2. J Textile Sci Eng 8 pii:349 https://doi.org/10.4172/2165-8064.1000349
18. Vatansever F, Hamblin MR (2012) Far infrared radiation (FIR): Its biological effects and medical applications. Photon Lasers Med 1:255–266. https://doi.org/10.1515/plm-2012-0034

Analysis of the Electric Field Behavior on a Stimulation Chamber Applying the Superposition Principle

L. A. Sá, E. M. S. Bortolazzo, J. A. Costa JR and P. X. de Oliveira

Abstract

This paper investigates the possibility of applying electric fields in different directions in a circular chamber using two insulated electrical pairs of electrodes positioned in orthogonal directions. Controlling the current on each axis—with two independent stimulator channels—we would be able to stimulate the central area in different direction according to superposition principle. This physical hypothesis is reasonable, and the work was focused on investigating if the resulting electric fields would be homogeneous in a small work area in a circular chamber. The electric field magnitude and orientation was determined with the measured electric potential data, and then the homogeneity tested with monofactorial ANOVA. A computational model was developed, based on the experimental setup, using finite element method to solve the electric field distribution within the chamber, in order to compare the experimental results. We tested the resulting electric field for theoretical orientations of 0° and 31.7°, and our results shows a electric field magnitude of 6.31 ± 0.11 V/m with p = 0.07 and 6.74 ± 0.40 V/m with p = 0.7032, and orientation of 0° with p = 0.9997 and 31.7° with p = 0.9999, respectively. Comparing the results with the analytical solution and the computational model, we observed that there was no statistical difference between them, which allows future biological experiment.

Keywords

Multidirectional stimulation • Electric field • Superposition principle

1 Introduction

Among the cardiac arrhythmias, the ventricular arrhythmias represent a higher risk of life, because they interfere directly in the ejection of blood into the systemic circulation [1]. The only existing therapy for ventricular fibrillation (VF) is defibrillation, that stimulates a critical mass—between 75 and 90%—of the heart tissue, applying electric fields (E) on the patient's chest, in order to stop fibrillation [2]. However, high levels of intensity of defibrillatory shocks can injure, or even be lethal [3], to heart cells, which makes it necessary to research ways to stimulate the heart using a lower E.

One way to minimize the intensity of the applied E in the heart would be varying the direction of the electric field vector (**E**)[1] with sequential application of stimuli within the refractory period, through several pairs of electrodes in different orientations—known as multidirectional stimulation [4]. A previous study allowed to observe that, in a cell population, 80% of cardiomyocytes were recruited using multidirectional stimuli with three pairs of electrodes [4]. Also, there was a 30% decrease in the required energy to reverse 50% of induced VF protocols in a pig population through multidirectional stimuli, using three pairs of electrodes [5], when comparing with unidirectional protocols.

However, it is reasonable that the use of three, or more, pairs of electrodes is not always clinically viable, since time and space allocation are critical on an emergency protocol. We hypothesize that is possible to stimulate and defibrillate a heart using multidirectional stimuli with only two pairs of electrically isolated electrodes, using the superposition principle.

The superposition principle is illustrated in Fig. 1 for the case of a cylindrical chamber with two orthogonal pairs of electrodes. Stimuli are applied concomitantly in both pairs. The resulting electric field vector ($\mathbf{E_R}$) is equal to the vector

L. A. Sá (✉) · E. M. S. Bortolazzo · J. A. Costa JR · P. X. de Oliveira
School of Electrical and Computer Engineering, University of Campinas, Av. Albert Einstein, No. 400, Campinas, Brazil

[1]The bold font notation denotes a vector element.

T. F. Bastos-Filho et al. (eds.), *XXVII Brazilian Congress on Biomedical Engineering*, IFMBE Proceedings 83, https://doi.org/10.1007/978-3-030-70601-2_4

sum of the two **E** that would be separately generated by each pair of electrodes.

Previous studies had employed a cylindrical chamber to analyse electrical stimulation on isolated cells with a single pair of electrodes at a x-axis, and **E** at any point of the chamber can be calculated by [6]. In that study, a concentric work area with a 10% radius was determined and was verified that **E** varied less than 1% in magnitude and 1° in phase. Let x_{WA} and y_{WA} be all the coordinates inside the work area, **E** can be considered constant and given by

$$\mathbf{E}(\mathbf{x_{WA}}, \mathbf{y_{WA}}) = \mathbf{E}(\mathbf{0}, \mathbf{0}) = \frac{2 \cdot I}{b \cdot \pi \cdot \sigma \cdot h} \hat{\mathbf{a}}_\mathbf{x} \tag{1}$$

where $\mathbf{E}(\mathbf{0}, \mathbf{0})$ is the electric field given by [6] for a single pair of stimulation electrode, I is the stimulation current, b is the chamber inner radius, h is the height of solution, σ is the aqueous solution conductivity in chamber and $\hat{\mathbf{a}}_\mathbf{x}$ is the versor that indicates the stimulation axis. $\mathbf{E}(\mathbf{0}, \mathbf{0})$ has the same direction as the stimulation axis defined by the electrodes line.

We propose that, when two electrically insulated pair of electrodes are used, as can be seen on Fig. 1, $\mathbf{E_1}$ can be given exactly by the same solution determined by [6] and $\mathbf{E_2}$ determined using the same equation but orthogonally to the first. Assuming that the uniformity of **E** within the work area is not affected by the second electrode pair, and that the system is linear [6], the superposition principle says that $\mathbf{E_R}$ within the work area can be determined by Eqs. (2) and (3), given by

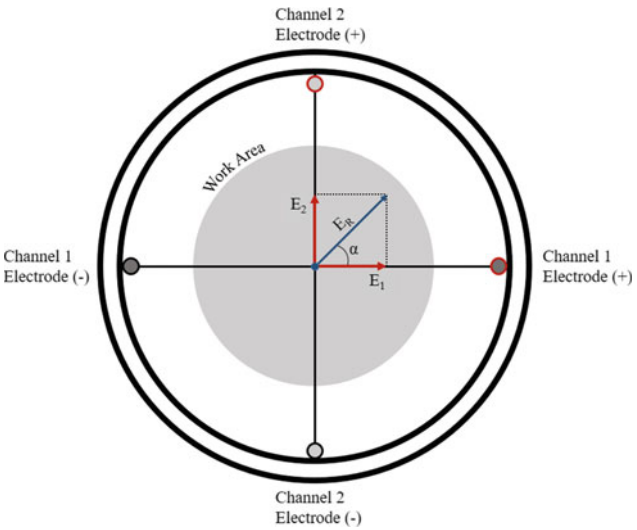

Fig. 1 Top view of a cylindrical chamber. $\mathbf{E_1}$ and $\mathbf{E_2}$ (red) are the electric fields generated considering just one pair of electrode (small filled circles) are active. When stimuli are applied concomitantly in both pairs, E_R (blue) is the resultant electric field and equals the vector sum of $\mathbf{E_1}$ and $\mathbf{E_2}$. α is the angle of E_R to channel 1 axis. The work area, where E_R is considered uniform, is represented (out of scale) as the shaded area

$$|\mathbf{E_R}|(x_{WA}, y_{WA}) = \sqrt{(E_1(x_{WA}, y_{WA})^2 + E_2(x_{WA}, y_{WA})^2)} \tag{2}$$

$$\alpha(x_{WA}, y_{WA}) = \arctan\left(\frac{E_2(x_{WA}, y_{WA})}{E_1(x_{WA}, y_{WA})}\right) \tag{3}$$

where $|\mathbf{E_R}|(x_{WA}, y_{WA})$ is the $|\mathbf{E_R}|$ magnitude within the work area, $\mathbf{E_1}(\mathbf{x_{WA}}, \mathbf{y_{WA}})$ and $\mathbf{E_2}(\mathbf{x_{WA}}, \mathbf{y_{WA}})$ are the linear contribution of electric field intensity of channel 1 and channel 2 at the work area, respectively, and $\alpha(x_{WA}, y_{WA})$ is the angle that $\mathbf{E_R}$ is positioned in reference to the channel 1 axis, within the work area.

By varying the amplitude of current stimulus in the two insulated electrical pairs of electrode positioned in orthogonal directions, we hypothesised that is possible to apply a multidirectional stimulus with any amount of stimulus, intensity and in any direction.

Our aim in this work was focused on investigating if the resulting electric fields would be homogeneous in a small work area in a circular chamber, and compare with a computational model developed at this work and the analytical solution determined by [6].

2 Materials and Methods

This section was divided in two complementary parts to test the superposition principle of **E** in a cylindrical chamber with two orthogonal electrode pairs. First, a experimental study is presented to test our hypothesis and homogeneity of **E** inside a delimited area of the chamber. A special case with a single electrode pair being stimulated is also analysed. Second, a computational model is developed and simulated to validate the study with the same conditions of the experimental study. In both studies we took advantage of the relationship given by:

$$\mathbf{E} = -\nabla\Phi \tag{4}$$

where **E** is the electric field in V/m, ∇ is the gradient operator, and Φ is the electric potential in Volts.

2.1 Experimental Study

The experimental setup is presented as a block diagram in Fig. 2. A cylindrical chamber made of polylactic acid, 9 cm radius and 1 cm height was built in a 3D printer. The first pair of stainless steel electrodes, with 1 mm in diameter and 2 cm long, was positioned at diametrically opposite points of the chamber and reaching perpendicularly the bottom of the chamber. A second pair of identical electrodes was also positioned at diametrically opposite points but perpendicularly to the line determined by the first pair. Next, the chamber was

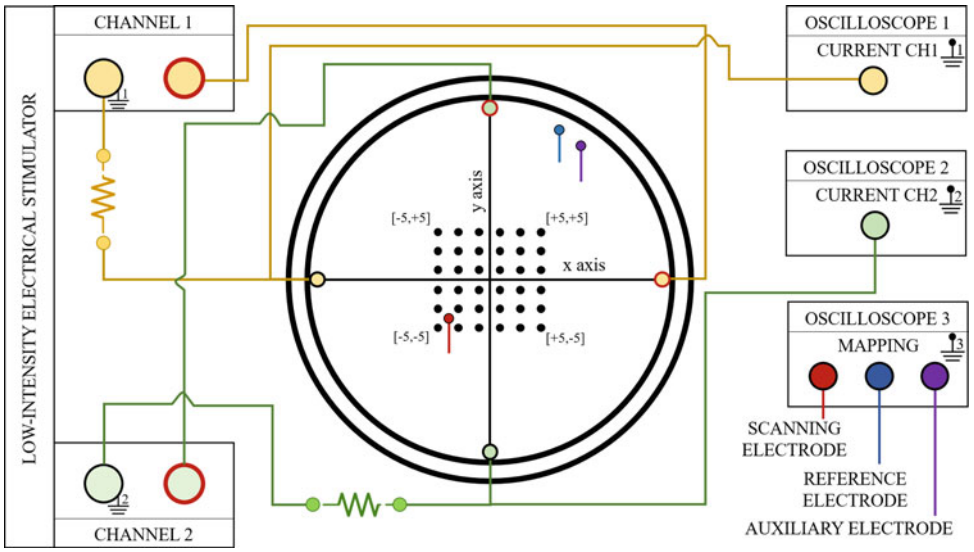

Fig. 2 Experimental setup for validation of the superposition principle. Two insulated voltage stimulators are connected to two pairs of orthogonally displaced electrodes. Oscilloscopes 1 and 2 used for current sensing through series resistor, and oscilloscope 3 used for electric field mapping. The scanning points presented as black bullets on the chamber center (out of scale) were scanned with the scanning electrode (red). A reference electrode (blue) and a auxiliary electrode for differential acquisition (purple) are also represented

partially filled with Tyrode's solution [6] at 23°C, and the height was measured since it is a parameter of the chamber conductivity and $\mathbf{E_R}$.

A low-intensity electrical voltage stimulator—developed for this work—with two insulated channels, was connected to the pairs of electrodes. The stimulator channels were adjusted to provide symmetrical rectangular bipolar pulses with 25 ms duration in each phase and frequency 0.3 Hz, in order to avoid electrode polarization. Simultaneously, the current in each channel was continuously measured with electrically isolated oscilloscopes through 22.2 Ω series resistors.

We delimited a 10 mm edge square-shape concentric work area for experimental mapping of $\mathbf{E_R}$, and we assume that $\mathbf{E_R}$ is constant inside this area and determined by the set of Eqs. (1), (2) and (3). For the first experiment set, the current in the second pair of electrodes was adjusted to zero so the theoretical phase $\alpha(\mathbf{x_{WA}}, \mathbf{y_{WA}})$ had a value of 0° according to Eq. (3), reducing to a one single channel stimulation case. At the second experiment set, the voltage amplitude was adjusted to obtain a measured current at each channel so the phase $\alpha(\mathbf{x_{WA}}, \mathbf{y_{WA}})$ had a theoretical value approximately 33°, according to Eqs. (1) and (3). Next, we started to perform the actual **E** mapping. This can be achieved indirectly by mapping the electric potential (Φ) as indicated by Eq. (4).

Hence, a third electrically insulated oscilloscope and three Ag-AgCl electrodes, with 0.2 mm diameter, were used to measure Φ in a 36-point matrix (black bullet points in Fig. 2). The edge of the collection data was coincident with the 10 mm edge square-shape concentric work area and the measurement points were spaced with 2 mm on each direction. Next, the points were sequentially scanned by the first Ag-AgCl electrode, a scanning electrode coupled to a microscope chariot (Zeiss, Jena, Germany) with resolution of 0.05 mm. The second electrode was used as a reference for the oscilloscope and positioned close to the chamber edge, at a point where we observed a maximum amplitude of the signal. A third electrode was used to obtain a differential signal and reduce noise, and it was positioned close to the reference electrode.

After completing the data collection for Φ, we derived $\mathbf{E_R}$. Since our data are not continuous, we did not directly apply Equation (4), but we derived $\mathbf{E_R}$ within a smallest square-shape scanning points with the edge potential measurements. First, we calculated **E** at the main diagonal by taking the negative difference of that two main diagonal points and divided by the distance. Next, we do the same approach for the **E** in the secondary diagonal. This operation was applied for the 36-point matrix, and results on a 25-point vector matrix that can be decomposed in intensity $|\mathbf{E_R}|(x,y)$ and phase $\alpha(x, y)$.

The scanning process was repeated 10 times (N = 10) and each of the 25 points was considered a single group for statistical analysis. Since we expected $|\mathbf{E_R}|(x,y)$ and $\alpha(x, y)$ to be uniform within the measured area, each group was analyzed using three normality tests: Kolmogorov-Smirnov, D'Agostino & Pearson and Shapiro-Wilk. The distribution of a group was considered normal if at least two tests had $p > 0.05$. Under the null hypothesis test, the samples of each group were compared with the expected value, given by Eqs. (1), (2) and (3), using monofactorial ANOVA. A p-value lower than 0.05 was indicative of statistical difference. The absence of any statistical difference between the groups was indicative of uniformity of the $\mathbf{E_R}(x,y)$.

2.2 Computational Study

The computational model was built using COMSOL Multiphysics 5.3 (COMSOL, Burlington, MA, USA), a software for solving partial differential equations (PDE) based on finite elements method (FEM).

As it can be seen in our experimental setup, it can be divided in two different electrical systems: an electrical circuit—used for electrodes stimulation and current sensing—and electric field distribution in the chamber. The major concern in modeling the proposed system is to assure that both stimulation channels are isolated from each other.

The electrical circuit was built using 0D space dimension geometry. Two physics of *Electrical Circuit* were added—one per channel—to solve circuits using Kirchhoff's Laws, including a voltage source V_s, a sensing resistor R_{sens} and an external I vs. U block—-used for connect the electrical circuit to a circuit terminal in other space dimension. Each circuit has its own ground signal, due to channels isolation, and the external block is connected to the electrodes.

We assume that our conductive solution is isotropic and that only the inner chamber geometry influences the electric field. Thus, we used a 2D space dimension geometry to represent the inner stimulation chamber just like in our experimental method.

Electric field was calculated by Equation (4) using two *Electric Currents* physics—one per channel—of the *AC/DC module* in a stationary study.

Besides that, the outer circle, that represents the chamber boundaries, is modeled as an electric insulator, and the electrodes as terminals—connected to external I vs. U block from *Electrical Circuit*.

The mesh was generated automatically using the physics-controlled mesh builder (available on COMSOL), for extra fine element size, which resulted in approximately 6800 finite triangular elements.

The parameters values used on simulation are chamber radius $R = 9\,\text{cm}$, Tyrode's electrical conductivity $\sigma_{tyrode} = 1.46\,\text{S/m}$ [6], height of solution and current in each channel are obtained from the experimental results.

3 Results

3.1 Experimental Results

We performed the mapping first for 0° and, sequentially, for 33°. Due to the low precision on the electric stimulator, we were unable to fine adjust the phase to 33°, resulting in a phase of 31.7°. For each case, the values of measured and adjusted current at each channel, the measured height of the solution, the p-value from the statistical analysis derived for the $|\mathbf{E_R}|$(x,y), and $\alpha(x, y)$ ($\mathbf{E}$) distributions, as well the value of the theoretical $|\mathbf{E_R}|$ and α are presented in Table 1. The values of mean ± standard error of the mean (SEM) of electric field magnitude and phase for each point in our mesh, derived from the mapping explained in the section *Experimental Study* are presented in Fig. 3.

3.2 Computational Results

We measured the sensing current I_{sens} on each channel sensing resistor, in order to determine the voltage sources V_{s1} and V_{s2}. The voltage sources were calculated by:

$$V_s = (R_{sol} + R_{sens})\, I_{sens} \tag{5}$$

where R_{sol} is the solution resistance, and R_{sens} is the sensing resistor. The current measurement was done by adding a very small resistor value, $R_{sens} = 100\mu\Omega$, so that the voltage drop on R_{sens} is negligible and Eq. 5 can be approximated to $V_s = I_{sens} R_{sol}$. Thus, a first simulation for each case was run to determine R_{sol} to the measured height of solution, and then R_{sol} and I_{sens} were used to estimate the voltage source.

As mentioned on section *Computational Study*, two electric currents were added to isolate channels, and the resulting electric field $|E_R|$ and measured phase α was calculated as in Eqs. 2 and 3, respectively, where $\mathbf{E_1}$ and $\mathbf{E_2}$ are the electric fields due to channel 1 and channel 2, respectively.

The computational results are summarized on Table 2.

Table 1 Experimental results

Parameter (Unit)	$\alpha = 0[^\circ]^2$	$\alpha = 31.7[^\circ]^2$
Height of solution h (mm)[a]	6.0 ± 0.1	8.0 ± 0.1
Current in x-axis I_{sens_x} (mA)	7.82	9.46
Current in y-axis I_{sens_y} (mA)	0	5.86
ANOVA p-value for magnitude	0.069335	0.9997
ANOVA p-value for phase	0.7032	0.9999
Electric field $\|E_R\|$ (V/m)[a,b]	6.31 ± 0.11	6.74 ± 0.40

[a]Measured value ± accuracy from charriot
[b]Theorically values given by Eqs. (1) and (3) ± accuracy given the height accuracy

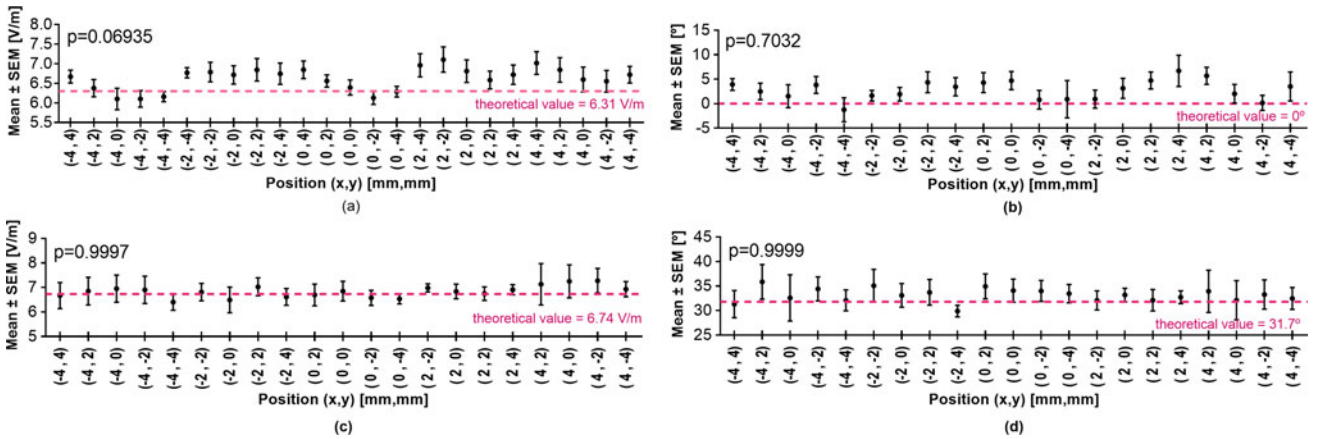

Fig. 3 Experimental results. The red dashed represents the theoretical value. Fig (a) and (b) are the electric field module and phase $\alpha = 0°$, respectively. Fig (c) and (d) are the electric field module and phase para $\alpha = 31.7°$, respectively

Table 2 Computational results

Parameter (Unit)	$\alpha = 0°$	α=31.7°
Chamber resistance in x-axis R_{ch_x} (Ω)	441.42	331.07
Chamber resistance in y-axis R_{ch_y} (Ω)	438.40	328.79
Voltage source in x-axis V_{s_x} (V)	3.45	3.13
Voltage source in y-axis V_{s_y} (V)	0	1.92
Electric field $\lvert E_R \rvert$ (V/m)[a]	6.31	6.74
Phase α (°)[a]	0	31.7

[a]Numerically calculated by Eq. (4)

4 Discussion

To validate the superposition principle in a circular chamber using two insulated electrical pairs of electrodes positioned in orthogonal directions, we mapped the **E** in the work area so we could compare the result with the analytical solution, obtained in [6]. Since the work area that we defined is smaller than in [6], **E** should vary less than 1% in module, and 1° in phase. This was confirmed in our computational study where E varies less than 0,31%. Further, the simulation outcomes at the work area were identical to the analytical solution for electric field intensity and phase.

Moreover, we measured 36 points inside the chamber for simulations at 0° and 31.7°. The expected result for the values found in the work area were 6.31 V/m, for $\alpha = 0°$ and 6.74 V/m, for $\alpha = 31.7°$. When performing the monofactorial ANOVA there was no statistical difference between them, which indicates that the superposition principle is valid when applying stimuli on two pairs of electrodes.

A significant dispersion in the experimental values was noticed, and there were local means that diverged more than 1% or 1°, in magnitude and phase, respectively. Those errors are noticed in the 0° and the 31.7° setup. However, previous works validated the **E** within the work area of 10% of the chamber radius, and they show that there was no differences in **E** greater than 1% and 1° for a single stimulation pair of electrode [6]. Since the errors were noticed for the 0° setup, they should not be given due the superposition principle. We obtained a p-value very close to 0.05 in the 0° setup, which is the case where we are applying stimulus with just one pair of electrodes. The maximum variation in the 0° direction, approximately 14% in magnitude, and the fact that more points varied more than 1% in magnitude, may have contributed to the fact that the p-value is so close to 0.05, which did not occur in the 31.7° direction. Despite this, statistical analysis indicated that there is no significant difference between the data. The errors can be attributed to several factors, such as: electrodes positioning in the reruns of the experiment, electrodes polarization during the experiment, error in determining the height of the solution, the fact that we considered the solution as isotropic, as well as the inherent errors of instrumentation.

Therefore, the fact that there is no statistical difference shows us that the applied model is acceptable, with the exception that the setup developed for this experiment requires improvement to reduce standard error.

5 Conclusions

With this developed work, one can observe that it is possible to apply multidirectional stimuli with only two pairs of electrodes. The electric field was mapped analytically, numerically, and experimentally, applying simultaneous stimuli in two different directions, and we can conclude that the superposition principle was validated inside the work area for 0° and 31.7°. We believe that these results endorse the hypothesis that it is possible to apply a stimuli of any magnitude in any direction, with only two pairs of electrodes. Although it is necessary to improve the experimental setup, we can conclude that our hypothesis is valid, so we can further investigate and develop a setup that allows analyze the electric field for any angle within the four quadrants, for future biological experiments.

Acknowledgements The authors would like to thank CNPq (Proc. N 141289/2018-0) and CAPES (Proc. N 88887.470307/2019-00 and 88887.497724/2020-00) for their financial support.

Conflict of Interest The authors declare that they have no conflict of interest.

References

[1] Guyton AC (2006) Tratado de fisiologia médica. Elsevier Brasil
[2] Li Y, Bihua C (2014) Determinants for more efficient defibrillation waveforms in Anaesthesia, pharmacology, intensive Care and cmergency A.P.I.C.E. In: Antonino G (ed) Springer Milan, Milano, pp 203–218
[3] Oliveira PX, Bassani RA, Bassani JWM (2008) Lethal effect of electric fields on isolated ventricular myocytes. IEEE Trans Biomed Eng 55:2635–2642
[4] Fonseca AVS, Bassani RA, Oliveira PX, Bassani JWM (2012) Greater cardiac cell excitation efficiency with rapidly switching multidirectional electrical stimulation. IEEE Trans Biomed Eng 60:28–34
[5] Viana MA, Bassani RA, Petrucci O, Marques DA, Bassani JWM (2016) System for open-chest. Multidirectional Electr Defibrillation Res Biomed Eng 32:74–84
[6] Bassani RA, Lima KA, Gomes PAP, Oliveira PX, Bassani JWM (2006) Combining stimulus direction and waveform for optimization of threshold stimulation of isolated ventricular myocytes. Physiolog Measur 27:851

Development of a Non-rigid Model Representing the Venous System of a Specific Patient

M. C. B. Costa, S. D. F. Gonçalves, T. C. Lucas, M. L. F. Silva, C. M. P. Junior, J. Haniel, and R. Huebner

Abstract

Regarding the cardiovascular system, in-vitro studies appears as an alternative for experimental assessment of blood flow parameters, in order to validating numerical simulation through particle imaging velocimetry (PIV) or laser Doppler velocimetry (LDV), and assist health professionals in clinical procedure. The aim of this study is to develop a methodology for manufacturing optical silicone models of blood vessels, life size, for the purposes described. A process similar to casting was used. A bipartite mold and a core were manufactured through of the 3D print after the geometry be acquired by computed tomography. The optical silicone was used to manufacture the model. After the cure of the silicone, it was observed that the model showed great transparency and compliance. This procedure showed up a simple and fast way for the manufacturing of optical silicone specimen of blood vessels. The results obtained were ideal for the purpose of the study, however the final model still lacks mechanical characterization for specific applications.

Keywords

Non-rigid anatomical model • Optical silicone • Life size • Cardiovascular system • 3D printing

1 Introduction

Standard hemodynamic in blood vessels can be changed for flow features itself, for example, local vortex generation and turbulence. The flow can also be disturbed due to geometric changes of the lumen or because of pathologic conditions, as aneurysms formation, among other factors. Moreover, instruments and clinical devices insertion, like central venous catheter (CVC) and endoprosthesis, can also cause these disturbances. Furthermore, there may be a variation in shear stress to which blood cells are subjected, changing the hemolytic and thrombogenic potential, which can cause others more grave adversities, like thrombosis [1, 2].

Numerical models based on computational fluid dynamics (CFD) can be used in order to predict these changes [2]. This tool has the advantage of being non-invasive and relatively low cost. The use of CFD has provided useful information to help understand atherosclerosis formation by computing the velocity field and wall shear stress associated with that velocity field in cardiovascular system [3].

However, it is necessary to validate the numeric models by experimental techniques. *In-vivo* experiments have some disadvantages, for example: issues involving patient integrity, in case of invasive technique; and in magnetic resonance imaging (MRI) procedure, where the patient must be immobile during the measurement. Besides, it is not always possible to measure the necessary physical quantities [3, 4]. Thus, in-vitro studies, which use materials that mimic the vascular tissue behavior appears as an alternative [5, 6]. These studies can be performed using a pulsatile flow pump to better simulate the flow and a fluid with the same or similar properties of blood (as a solution of water and glycerin) [7]. This is done in order to compare it with the numerical results for a better understanding of the hemodynamic behavior [8].

Recent researches are using rigid models to perform in-vitro experimentations with several objectives. These models have the advantages of being transparent which

M. C. B. Costa (✉) · S. D. F. Gonçalves · M. L. F. Silva · C. M. P.Junior · J. Haniel · R. Huebner
Departamento de Engenharia Mecânica, Laboratório de Bioengenharia, Universidade Federal de Minas Gerais, Avenida Antônio Carlos, 6627, Belo Horizonte, Brazil

T. C. Lucas
Departamento de Enfermagem, Universidade Federal dos Vales do Jequitinhonha E Mucuri, Diamantina, Brazil

T. F. Bastos-Filho et al. (eds.), *XXVII Brazilian Congress on Biomedical Engineering*, IFMBE Proceedings 83, https://doi.org/10.1007/978-3-030-70601-2_5

allows the visualization and assessment of clinical devices prototypes inserted in specimen. Furthermore, the use of optical techniques to assess the blood flow field is facilitated. Nevertheless, from the engineering point of view, the rigid models are only suitable for fluid dynamics studies, because they do not simulate the behavior of vessels wall due to the blood flow [9–11].

There are many different experimental techniques for measuring flow quantities, however, the most systematically used are optics, such as particle image velocimetry (PIV) and laser Doppler velocimetry (LDV), and acoustics ones, such as ultrasound imaging velocimetry (UIV) [12]. Optical experiments need that the geometry has optical access, that is, the manufacturing material must be transparent and does not exhibits optical deviation, like optical silicone or polyurethane [3]. On the other hand, acoustic tests can employ latex and polyvinyl alcohol, since they do not require optical access [5, 13].

Moreover, these specimens are being used by healthcare professionals as well. Studies about these experimental models are being accomplished with the aim of simulate surgical procedures, as aortic aneurysms, and tests of clinical devices, like robotic catheter for aortic valve implantation [14, 15]. The physical replica of patient-specific anatomy can be used for the training of novice surgeons in robotic surgery. It is fundamental that the model correctly resembles the morphological properties of the vessel [16].

The present study aims to develop a protocol to manufacture simplified models in optical silicone, motivated by the increase of need for anatomical geometric models of the circulatory system. The model used was composed by the right internal jugular vein, left internal jugular vein and superior vena cava.

2 Materials and Methods

The construction of the replica of blood vessel followed the steps below.

2.1 Geometric Model

The geometry used in this work was obtained by the methodology proposed in [17]. Initially, the geometry was acquired by Computed Tomography (CT) of a male healthy patient, 74 years old. The procedure was approved by the Comitê de Ética em Pesquisa/Universidade Federal de Minas Gerais (CEP-UFMG) under process number CAAE 02,405,712.5.1001.5149.

In the InVersalius3®, a medical image processing software, it was imported the DICOM (Digital Imaging and Communications in Medicine) files. The file data were processed to acquire only the region of interest. Figure 1 illustrates the procedure, with the region of interest highlighted in green.

The next step was to edit the geometry in Steriolithography (STL) format in the Autodesk Meshmixer®. This step consisted of smoothing and removing some imperfections on the geometry surface, to improve the surface quality. The subclavian and external jugulars veins were removed to reduce the complexity of the model, since it would be difficult to reproduce an experimental bench. The treated geometry is indicated in Fig. 2a.

With the aim of facilitating the manufacturing process by the silicone casting method (a process similar to casting, but using silicone), the edited geometry of the venous system was simplified in order to make it symmetrical in relation to

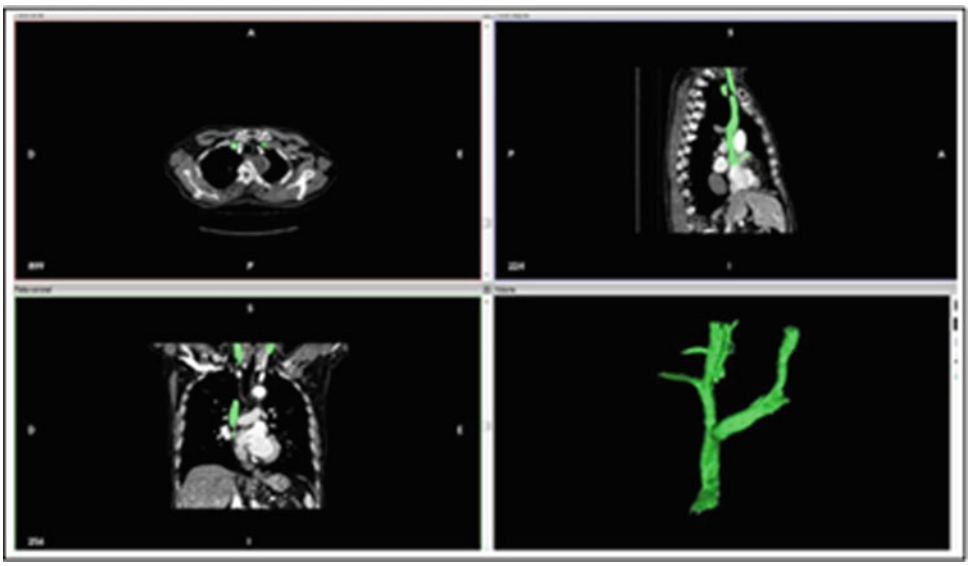

Fig. 1 Image acquisition methodology from CT scan

the XZ plane, represented by Fig. 2b. In this figure, the original geometry is indicated in orange and the simplified geometry in green. The ANSYS SpaceClaim software was used to perform this procedure.

2.2 Bipartite Molds Manufacturing

The geometry acquired by the process previously described was employed to generate the cavity of the bipartite mold, that is, the external surface of the specimen. In the ANSYS SpaceClaim software were inserted cylindrical connections at the inlets and outlet, with standard sizes of ½″ at the border of the internal jugulars and 1″ at the end of the superior vena cava, in order to fixate the models on experimental benches. In addition, fittings were added to ensure that the core was fixed and aligned in the mold during the injection of the silicone. Figure 2c shows the final mold.

For the molds manufacture, a three-dimensional print of Fused Deposition Modeling (FDP) technology, model P350 (3D Factor) was used. The maximum print size is 350 × 350 × 350 mm and the resolution in the vertical direction is 0.01 mm. The printing tolerance is 0.25 mm in all directions. The final molds, in STL format, were converted to Gcode language by Slic3r software. The molds were printed using the lactic polyacid plastic (PLA).

After the mold printing procedure, the cavities, which will be filled with silicone, were sanded and polished in order to reduce the surface roughness with the aim to give the specimen a better transparency and avoid optical deviations to be used in optical tests or flow field visualization technique. Figure 2d indicates the printed mold.

2.3 Core Manufacturing

For manufacturing the core, an offset of 3.0 mm in the geometry acquired in section A was made (mean thickness of the analyzed system). The surface generated through this offset corresponds to the internal surface of the specimen, that is, the external surface of the core. For the core were inserted cylindrical connections, with diameter less than the geometry used to create the molds by 3.0 mm, and fittings as well.

The core was manufactured similarly to the mold. It was used the same printer machine, and the files in STL format were converted to Gcode language. However, the polyvinyl alcohol (PVA), a water-soluble material, was used. This material was employed by ease of removal of the model after of the silicone cure.

After printing procedure, the core was also sanded and polished to ensure that the internal surface of the model has low roughness. Figure 2d shows the printed core.

2.4 Silicone Preparation

In this study, the silicone used for casting procedure was the polydimethylsiloxane (PDMS) of the Sylgard 184 kit (Dow Corning). This material was chosen due to the high degree of transparency.

A curing agent provided by the kit was added in proportion of 10:1 to accelerate the curing reaction. The products were mixed at room temperature.

After preparation, the mixture was taken to a vacuum chamber to eliminate the bubbles that appeared during the process. Figure 2e shows the before and after of the silicone being placed in the vacuum chamber.

2.5 Silicone Injection

First, the core was correctly positioned in the mold, which was closed and properly sealed. The silicone was injected into the injection channel of the mold and filling exclusively due to the gravitational effect.

The mold was left to stand for approximately 24 h, silicone curing time.

3 Results

After the curing process and the removal of the PVA core, by immersing the body in water, the specimen in optical silicone was obtained. Figure 3 indicate the results obtained. It is observed that, the model showed an excellent degree of transparency and a great surface finish. The body also showed good elasticity and compliance.

4 Discussion

The manufacturing of specimens in life sizes is a useful tool in the field of medicine, because they can be used for training trauma correction and surgical simulations. These models help professionals to better understand the patient's anatomy [12]. Furthermore, the specimens can be an alternative for in-vitro experiments, as a way of validating numerical computer simulation.

The transparency and surface finish acquired in the model, Fig. 3, allows medical training to take place in a more didactic way. Visualization of the inside of vessel facilitates the positioning of clinical devices. In addition, it becomes possible to monitor the behavior of the device inserted in the model. Moreover, the transparency is suitable for experimental methods to obtain flow field parameters in the study region, which use optical fundamentals, such as the PIV or LDV. Tests that use only qualitative analysis, such as the use of dyes, can also be performed.

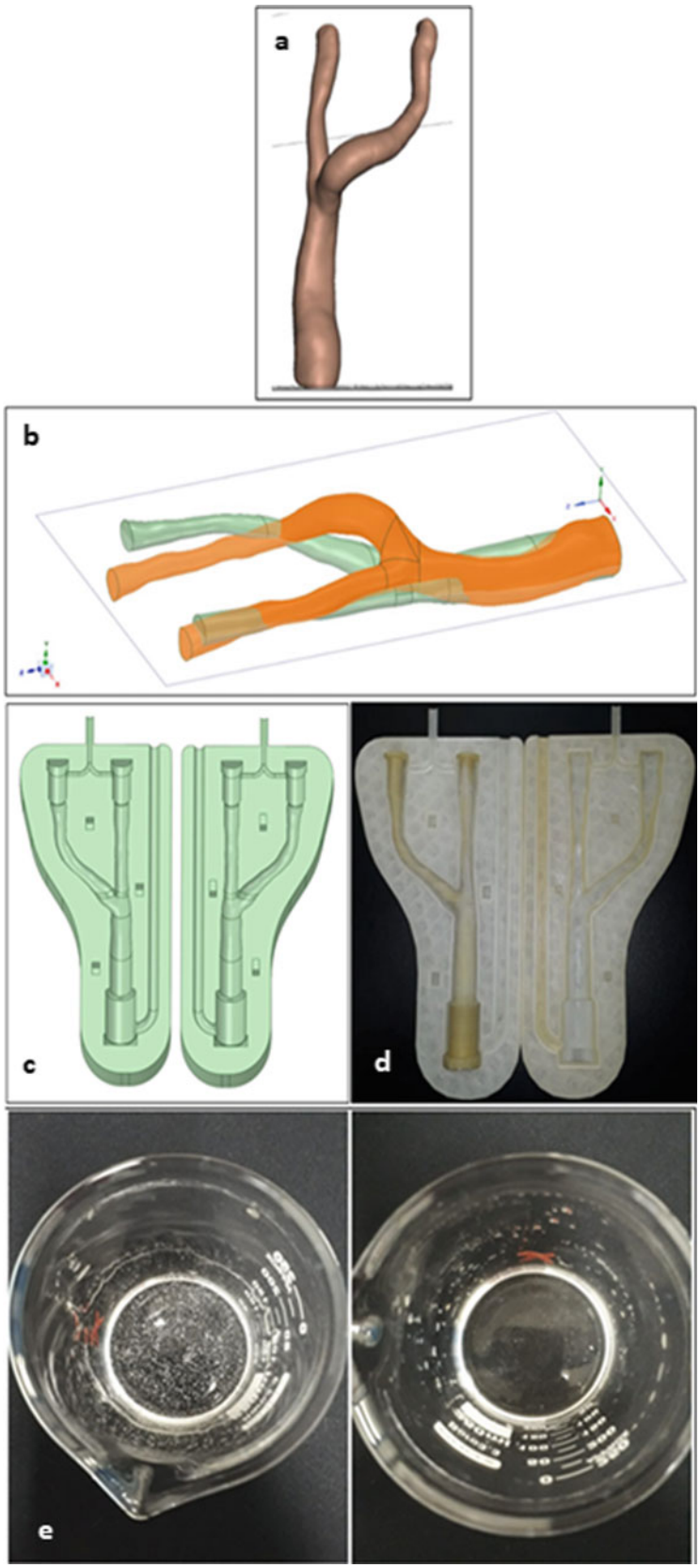

Fig. 2 **a** Edited geometry after CT scan acquisition **b** Simplification of geometry **c** Three-dimensional design of the bipartite mold **d** Bipartite mold and core already printed **e** Removing bubbles in the preparation of the optical silicone

Fig. 3 **a** Result of the process after curing the silicone. **b** Dissolution of the PVA core. **c** Final model of the optical silicone

With respect to elasticity and compliance, the model had plausible results. The specimen showed an appropriate technical feature to be used in practices described above. Thus, the model obtained allows professionals, who work with numerical simulations, to validate their studies from the fluid dynamics point of view. Nevertheless, there is a need for a mechanical characterization to determine a relationship with the real blood vessel wall, because the material used in the manufacture of the model may not have the actual hyperelastic characteristic of the vascular tissue. During the training of surgical procedure, the incision in the specimen is also properly simulated.

In the procedure of manufacturing there is a possibility of leakage during the injection of the silicone in the mold and bubbles formation during the mixing of the silicone with the curing agent. The first problem can be corrected by making the seal more efficient and improving the mold fitting. The second can be adjusted by taking care in the preparing the silicone and using the vacuum chamber.

Finally, the methodology described, presents a limitation because it needs the geometries to be symmetrical in relation to a plane to manufacture the bipartite molds, that is, there cannot be three-dimensional anatomical curvatures.

5 Conclusion

Computational fluid dynamics analysis and in-vitro tests appears as an alternative tool to assess changes in the physical parameters of blood flow due to clinical devices insertions, like CVC and endoprosthesis, furthermore, due to pathologic condition, as aneurysms formation. In this context, is necessary to manufacture models that represent the studied blood vessel and mimics the vascular tissue behavior. Throughout this research, several tests were carried out to develop a methodology capable of manufacturing a specimen in optical silicone, to realize the proposed objective.

Using the silicone casting technique, together with the use of 3D printing, the manufacture of an optical silicone replica of a blood vessel proved to be viable and inexpensive. The developed model allows physiological accuracy for the validation of numerical fluid dynamic studies carried out. In addition, it allows the improvement of surgical procedures, since these models are used to assist surgeons during their training. Finally, tests can be carried out to check whether the presented methodology can be applied to other materials, such as polyurethane, and to other vessels in the circulatory system.

Acknowledgements The authors would like to thank CNPq (401217/2016-7) and FAPEMIG (APQ-02735-17) for their support in this project.

Conflict of Interest The authors declare that they have no conflict of interest.

References

1. Ha H, Ziegler M, Welander M et al (2018) Age-related vascular changes affect turbulence in aortic blood flow. Front. Physiol 9:36. https://doi.org/10.3389/fphys.2018.00036
2. Lucas T, Tessarolo F, Jakitsch V et al (2014) Blood flow in hemodialysis catheters: a numerical simulation and microscopic analysis of in vivo-formed fibrin. Artif Organs 38(7):556–565. https://doi.org/10.1111/aor.12243
3. Lermusiaux P, Leroux C, Tasse J et al (2001) Aortic aneurysm: construction of a life-size model by rapid prototyping. Annals of Vascular Surgery Inc. https://doi.org/10.1007ls100160010054
4. Arcaute K, Palafox G, Medina F et al (2003) Complex silicone aorta models manufactured using a dip-spin coating technique and water-soluble molds. El Paso, Texas
5. Chee A, Ho Chung, Yiu B et al (2016) Walled carotid bifurcation phantoms for imaging investigations of vessel wall motion and blood flow dynamics. IEEE Trans Ultrason, Ferroelectr Freq Cont **63**(11) https://doi.org/10.1109/TUFFC.2016.2591946
6. Le T, Troolin D, Amatya D et al (2013) Vortex phenomena in sidewall aneurysm Hemodynamics: experiment and numerical simulation. Ann Biomed Eng. https://doi.org/10.1007/s10439-013-0811-9
7. Liepsch D (2002) An Introduction to biofluid mechanics-basic models and aplications. J Biomech 35:415–435
8. Arcaute K, Wicker R (2008) Patient-specific compliant vessel manufacturing using dip-spin coating of rapid prototyped molds. El Paso, Texas
9. Amili O, Golzarian J, Coletti F (2019) In vitro study of particle transport in successively bifurcating vessels. Ann Biomed Eng. https://doi.org/10.1007/s10439-019-02293-2
10. Taher F, Falkensammer J, McCarte J (2017) The influence of prototype testing in three-dimensional aortic models on fenestrated endograft design. Soc Vascular Surgery. https://doi.org/10.1016/j.jvs.2016.10.108
11. Geoghegan P, Jermy M (2017) A piv comparison of the flow field and wall shear stress in rigid and compliant models of healthy carotid arteries. J Mech Med Biol 17(4). https://doi.org/10.1142/S0219519417500415
12. Drost S, Alam N, Houston J et al (2017) Review of experimental modelling in vascular access for hemodialysis. Cardiovascular Eng Technol 8(3). https://doi.org/10.1007/s13239-017-0311-4
13. Chaudhuri A, Ansdell L, Richards R et al (2003) (2003) Non-Axisymmetrical (Life-Like) abdominal aortic aneurysm models: a do-It-yourself approach. J Endovasc Ther 10:1097–1100
14. Yuan D, Luo H, Yang H et al (2017) Precise treatment of aortic aneurysm by three-dimensional printing and simulation before endovascular intervention. Sci Rep. https://doi.org/10.1038/s41598-017-00644-4
15. Kvasnytsia M, Famaey N, Böhm M et al (2016) Patient specific vascular benchtop models for development and validation of medical devices for minimally invasive procedures. J Med Rob Res 1(3). https://doi.org/10.1142/S2424905X16400080
16. Marconi S, Negrello E, Mauri V et al (2019) Toward the improvement of 3D-printed vessels' anatoical models for robotic surgery training. Int J Artif Organs. https://doi.org/10.1177/0391398819852957
17. Machado B, Haniel J, Junior C et al (2018) Modelo Complexo Não-Rígido de Tamanho Natural de Grandes Vasos Usando Método de Casting e Impressão em 3D. Águas de Lindóia, São Paulo

Comparative Study of Rheological Models for Pulsatile Blood Flow in Realistic Aortic Arch Aneurysm Geometry by Numerical Computer Simulation

M. L. F. Silva, S. D. F. Gonçalves, M. C. B. Costa and R. Huebner

Abstract

In numerical simulations of blood flow in the aorta, shear rates tend to be higher than $100\,s^{-1}$, making blood behave as a Newtonian fluid, with constant dynamic viscosity. This study proposes a comparative analysis via computational fluid dynamics (CFD) of the Newtonian, Carreau-Yasuda, Power-Law and Casson rheological models for a realistic geometry of the aortic arch obtained by computed tomography (CT) and adapted with an aneurysm. It has been shown that there are instants of time throughout the cardiac cycle in which the blood exhibits non-Newtonian behavior. This behavior leads to a considerable variation in the dynamic viscosity that can influence the flow hemodynamics. It was also possible to detect that the effective viscosity varies over the cardiac cycle, including the Newtonian model, which suggests that the turbulent viscosity is variable. In general, the Carreau-Yasuda and Power-Law models show similar behavior, whereas the Casson model tends to be more closely to the Newtonian model.

Keywords

Rheology • Blood flow • Aneurysm • Non-newtonian models • Aortic arch

1 Introduction

From a rheological point of view, blood has a non-Newtonian behavior of the viscoplastic type. It has characteristics of pseudoplastic fluids, where the apparent viscosity decreases with the increase in the deformation rate, and in addition, it requires an initial shear stress (yield stress), to start its flow [1]. However, the value of the yield stress is very small in a way that the blood throughout the circulation will be fluid and not solid [2].

At low shear rates, blood viscosity decreases due to the "rouleaux" effect, which consists in the aggregation of red cells. On the other hand, above approximately $100\,s^{-1}$, the aggregations are broken by the velocity gradient and the blood assumes Newtonian fluid behavior [3].

Although the shear rate in large arteries is generally high, certain aortic conditions induce flow disorders. This generates regions of recirculation and stagnation that are accompanied by a significant reduction in the shear rate, which may induce non-Newtonian behavior [4].

The shear stress in the artery wall also presents a different behavior according to the rheological model [5]. This variation in shear stress modifies the dynamic of the arterial wall in aortic aneurysms. Bilgi and Atalık [6] demonstrated by fluid structure iteration by assuming blood as Newtonian fluid leads to significant differences in hemodynamic behavior in aneurysms, when compared to the Carreau model. These differences were observed in all structural models of arterial wall analyzed by Bilgi and Atalık [6]: rigid, linearly elastic and hyperelastic.

Although there are not many studies on the blood flow rheology in vivo [7], different investigations through numerical simulations have reached contradictory conclusions. Therefore, the differences between Newtonian and non-Newtonian models has sometimes been subjective [4,8–11].

The research developed here aims to compare the blood flow modeled numerically via computational fluid dynamics (CFD) in a realistic geometry of the aortic arch aneurysm, from the perspective of Newtonian fluid and different non-Newtonian models.

2 Materials and Methods

The geometric model was created from image reconstruction of a computed tomography (CT) scan of a healthy patient. The procedure was approved by the following ethics committee: Comitê de Ética em Pesquisa/Universidade Federal de Minas Gerais (CEP-UFMG) process number CAAE

M. L. F. Silva (✉) · S. D. F. Gonçalves · M. C. B. Costa · R. Huebner
Department of Mechanical Engineering, Universidade Federal de Minas Gerais, Avenida Antônio Carlos, Belo Horizonte 6627, Brazil

T. F. Bastos-Filho et al. (eds.), *XXVII Brazilian Congress on Biomedical Engineering*,
IFMBE Proceedings 83, https://doi.org/10.1007/978-3-030-70601-2_6

02405712.5.1001.5149. After obtaining the solid, a fusiform aneurysm was created in order to exceed at least 50% of the diameter of the aortic arch. The geometry, as well as a three-dimensional reconstitution step by means of digital image processing, can be seen in Fig. 1a, b.

Boundary conditions adapted from Alastruey et al. [12] were adopted. In the ascending aorta (AA), the pulse wave velocity was imposed. In the brachiocephalic trunk (BT), left common carotid artery (LCCA), left subclavian artery (LSA) and thoracic aorta (TA) pulse pressure were imposed. The cardiac cycle considered has a duration of 0.8 s, which represents a heart rate of approximately 72 bpm. 320 time steps of 0.0025 s were used. The boundary conditions are shown in Fig. 1c. Two cardiac cycle were simulated and the first one was discarded.

The mesh convergence test was carried out according to the ASME V&V 20 [13] standard. The mesh selected for the study has 1085072 elements and 360988 nodes, refined in the aortic arch in the region of the aneurysm and branches.

Four rheological models were selected for the comparative study, namely, Newtonian, Power-Law, Casson and Carreau-Yasuda. The rheological properties were the same used by Gonçalves et al. [14] and Shibeshi and Collins [3]. Those properties are represented in Table 1, where: μ: dynamic viscosity (Pa.s), μ_∞: maximum viscosity (Pa.s), μ_0: minimum viscosity (Pa.s), n: Power-Law index, λ: time constant (s), k: consistency index (Pa.s^n), τ_0: yield stress (N) and η: Casson's rheological constant.

ANSYS-Fluent® 2019 R2 software was used to solve the time-dependent continuity and momentum equations. The turbulence model adopted was the $k-\omega$ Shear Stress Transport (SST). For spatial discretization of the momentum and continuity it was used the second order Upwind method. For temporal discretization, the implicit second order algorithm was adopted. The pressure-based coupled algorithm was adopted to solve the pressure-velocity coupling. The second order scheme was used to discretize the pressure equation. Finally, the Least Squares Method Cell-Based Gradient was used for the gradients. As convergence condition, the residual value of 10^{-4} was used for the velocity components, continuity, turbulence kinetic energy (k), and specific dissipation rate (ω). The maximum value of Courant–Friedrichs–Lewy number (CFL) found in numerical simulation was 175.93 and the average was 14.31. Although the CFL were high, numerical instabilities were not found, because an implicit formulation of temporal discretization was used, which is unconditionally stable.

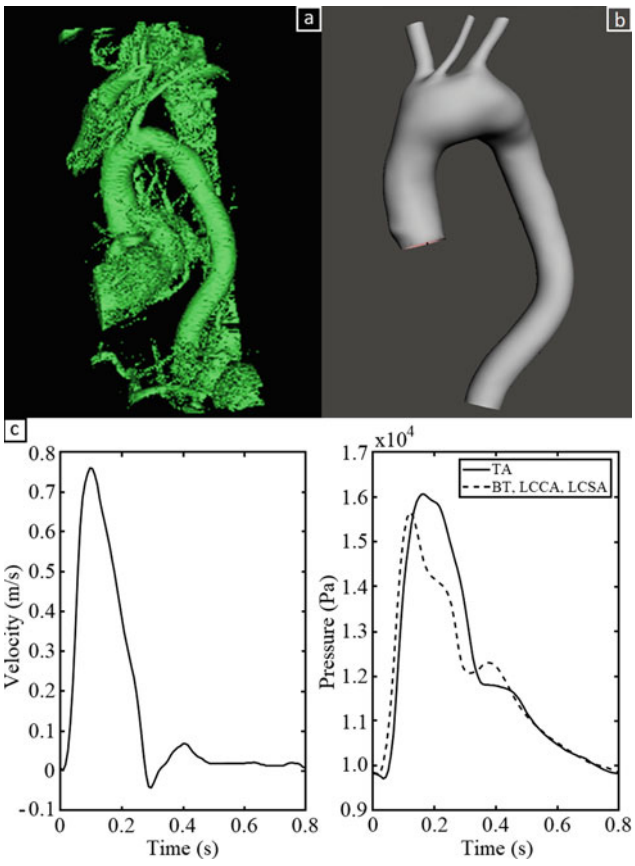

Fig. 1 **a** 3D reconstruction stage; **b** Geometric model; **c** Velocity and pressure pulses

3 Results

The results for analyzing the rheological behavior of the simulated models in different planes can be seen in Fig. 2. The planes were numbered (P1, P2, …, P14) in ascending order from the top of the geometry. For a better comparison of images, the structural similarity index (SSIM) [15] is also shown, which is an index to quantify the percentage difference between images. The comparison was made in relation to the Newtonian model. SSIM is calculated by Equation (1).

$$SSIM\,(x,\,y) = \frac{\left(2\mu_x\mu_y + C_1\right)\left(2\sigma_{xy} + C_2\right)}{\left(\mu_x^2 + \mu_y^2 + C_1\right)\left(\sigma_x^2 + \sigma_y^2 + C_2\right)} \quad (1)$$

where μ_x, μ_y, σ_x, σ_y and σ_{xy} are the local means, standard deviations, and cross-covariance for images x, y. C_1 and C_2 are constants included to avoid instabilities [15].

Figure 2a shows the results of the shear rate of the Newtonian model at the instants of time (t) of 0.10, 0.29, 0.40 and 0.80 s. These instants of time correspond respectively: to the maximum velocity value, which occurs at the systole and it is close to the point of maximum pressure; the moment of closing the aortic valve; approximately half of the diastolic phase; and at the end of the cardiac cycle.

Table 1 Rheological properties of the models selected for the study

	Newtonian	Power-law	Casson	Carreau-Yasuda
μ_∞	–	0.0560	–	0.0560
μ_0	–	0.0035	–	0.0035
n	-	0.7080	–	0.3568
λ	–	–	–	3.3130
k	–	0.0170	–	–
μ	0.0035	–	0.0035	–
τ_0	–	–	0.0050	–
η	–	–	0.0035	–

Figure 2b shows how the dynamic viscosity varies in each model in the aortic arch in the P5, P6, P7 and P8 planes for the instants of time of 0.1 and 0.8 s which are the time of the peak systole velocity and the end of cycle respectively. These instants of time differ each other due to their high and low shear rate, respectively. Figure 2(c) shows the effective viscosity, which is the sum of the dynamic viscosity and the turbulence viscosity, in the same planes for the same instants of time. Finally, Fig. 2(d) shows the velocity field for low shear rates (at t = 0.8 s).

In order to demonstrate once again the behavior of the different rheological models, Fig. 3 shows how the shear rate, dynamic viscosity, effective viscosity, shear stress, velocity and pressure vary in the median plane of the aortic arch (P7). The values correspond to the mass flow weighted average.

Finally, Table 2 shows the mean absolute percentage deviation (MAPD) over time of each model in relation to Newtonian model for the graphs in Fig. 3. MAPD is calculated by Eq. 2. Table 2 also shows the maximum absolute difference (MAD) and the instant of time (t_{mad}) of such difference.

$$MAPD = \frac{1}{n}\sum_{i=1}^{n}\left|\frac{P_{nN_i} - P_{N_i}}{P_{nN_i}}\right| \quad (2)$$

where P_{nN_i} and P_{N_i} are any property of the non-Newtonian and Newtonian model at instant of time i, respectively, and n is the number of time steps.

4 Discussion

It is observed that when the velocity increases, the shear rate also tends to increase. At these instants of time, some part of the aorta has values greater than 100 s^{-1}, as in the systole phase. On the other hand, when the velocity is low, or even in certain regions during systole, the shear rate is less than 100 s^{-1}, which suggests non-Newtonian behavior.

Figure 2b proves that at low velocities, dynamic viscosity tends to vary more than in regions with higher velocities, which cannot be concluded using the Newtonian model. This behavior is also seen in Gonçalves et al. [14] for blood flow in venous catheters that modify the shear rate. This is also shown in Table 2, where the maximum absolute difference between the Newtonian model in relation to the non-Newtonian model occurs at points of low shear rates.

It is important to note that at high shear rates, there were also local variations in viscosity, although smaller. However, in regions where viscosity is predominantly constant, the viscosity value is higher than the Newtonian model. This trend is seen in the three non-Newtonian models analyzed.

At high shear rates, the effective viscosity also tends to vary less, even at different values for different models. At low shear rates, the effective viscosity increases and varies locally, which shows that in addition to the increase in dynamic viscosity, there is an increase in turbulence viscosity.

From the point of view of effective viscosity, Casson's model is the closest to the Newtonian. On the other hand, the Carreau-Yasuda and Power-Law models are more coincident.

Analyzing the hemodynamic behavior of the flow, Fig. 2d shows that in regions of low shear rate and velocity, the velocity field itself can be slightly altered due to the rheological model. In other words, blood rheology can modify the fluid dynamic of the flow. The results of the velocity field are consistent with those found by Karimi et al. [5]. Table 2 shows that the maximum absolute difference coincides with low shear rates. At other instants of time, especially at high shear rates, the velocity difference is small.

In average terms, as shown in Fig. 3, the shear rate in the selected plane is always less than 100 s^{-1}, which suggest that the phenomenon cannot be modeled as Newtonian. In fact, the dynamic viscosity varies throughout the cardiac cycle, at a different value than the Newtonian one. This suggests that for greater agreement with non-Newtonian models, the viscosity must be different from the usual value of 0.0035 Pa.s. It is

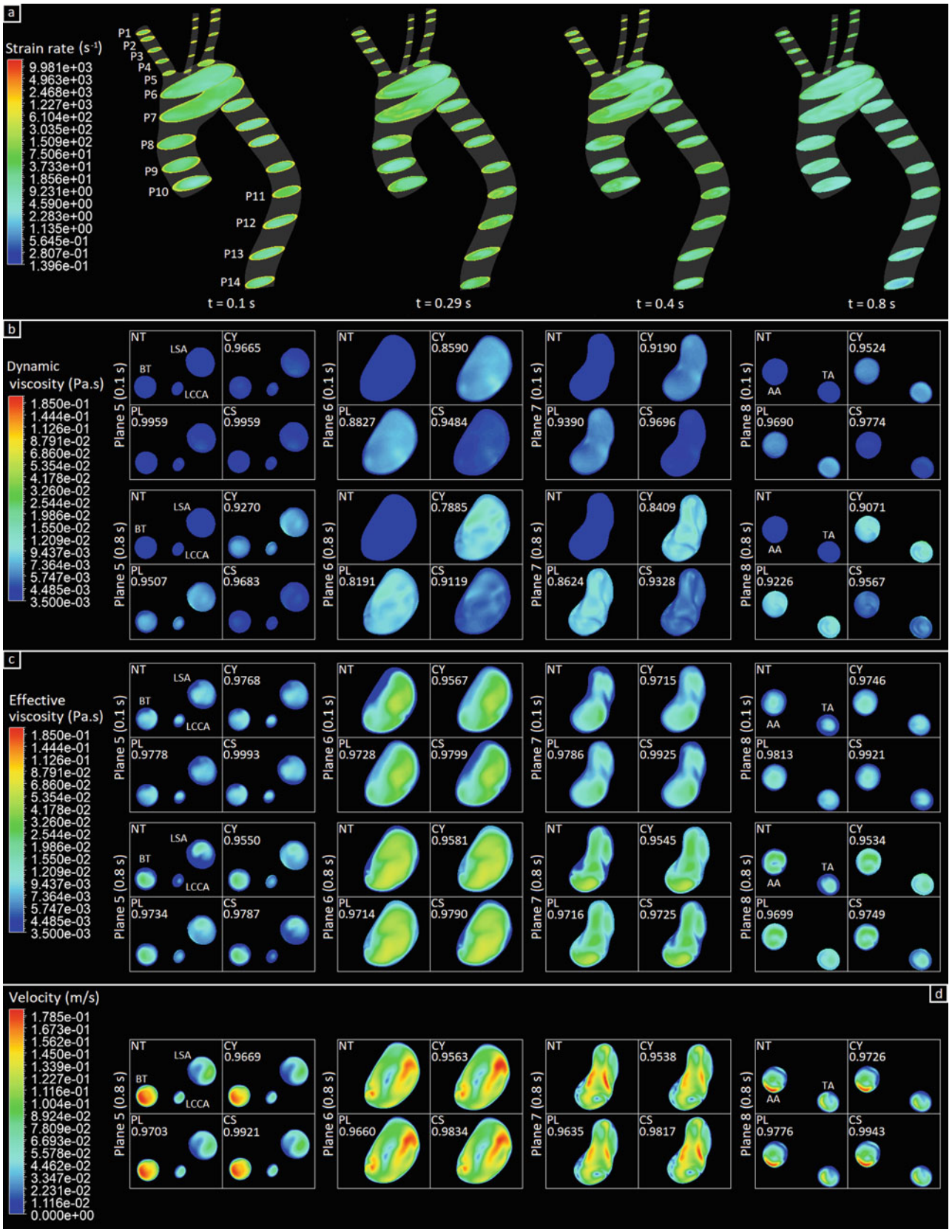

Fig. 2 **a** Strain rate in aorta; **b** Dynamic viscosity at t = 0.1 s and t = 0.8 s; **c** Effective viscosity at t = 0.1 s and t = 0.8 s; **d** Velocity field at t = 0.8 s. NT: Newtonian; CY: Carreau-Yasuda; PL: Power-Law; CS: Casson. BT: brachiocephalic trunk; LCCA: left common carotid artery; LSA: left subclavian artery; TA: thoracic aorta; AA: ascending aorta

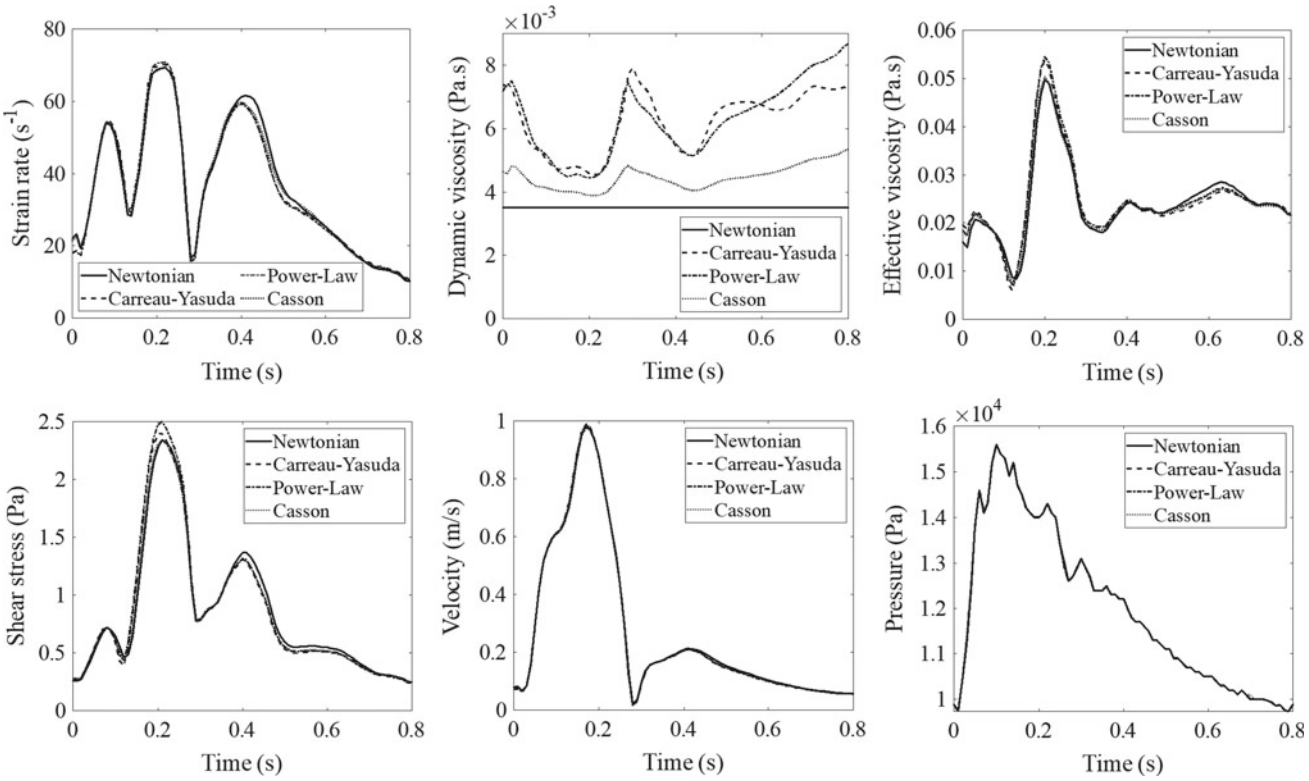

Fig. 3 Average change in the P7 plane of the shear rate, dynamic viscosity, effective viscosity, shear stress, velocity, and pressure over the cardiac cycle

also interesting to note that the highest value in magnitude of the shear rate occurs at the point of maximum velocity in the plane during systole, as expected.

However, from the hemodynamic point of view, the flow behavior does not undergo major changes due to the consideration of the Newtonian model, as shown in the graph of variation in velocity and pressure. However, on average, the biggest differences do not occur at the same instants of time where the viscosity differences are greater.

Figure 3 also shows that the increase in the shear rate leads to a reduction in viscosity, which bring it closer to the Newtonian case. The shear stress peaks occur at these same instants of peak shear rate, despite the reduction in viscosity.

In all models it is shown that the effective viscosity varies over the cycle, as well as it varies from model to model. However, in this case, the Newtonian model follows the trend of the other models. It makes clear that the turbulent viscosity is also different throughout the cycle and it tends to vary more in the Newtonian model. This shows that the turbulence behavior can vary from one model to another. The highest value of effective viscosity occurs during systole, at the same time as the maximum peak shear rate.

It is important to note that the analysis of Fig. 3 is performed in relation to average values, so that occasionally the differences detected can be even greater, as can be seen in Fig. 2 that there are local variations. In addition, although the peak velocity at the exit to the heart (aortic entry) occurs at 0.1 s, the maximum velocity and peaks of the other properties in the plane occur at around 0.2 s.

Finally, in relation to Table 2, it can be said that the maximum differences found are at specific instants of time, especially in regions with low shear rates. On average, the differences between the models are small. Exception for effective viscosity and shear stress, where the greatest differences were in points of higher velocities and shear rates.

5 Conclusion

Although the blood flow in the aorta is systematically treated as Newtonian, when considering the entire cardiac cycle, such a strategy may not represent the behavior of the actual flow. At instants of time where the velocity field has lower values, the shear rate tends to be also lower, leading to a variation in dynamic viscosity, which is not predicted in the Newtonian model, but can be seen in other rheological models, such as demonstrated in this study for a realistic geometry of the aortic arch aneurysm.

Table 2 Difference of non-Newtonian models in relation to the Newtonian model of mass flow weighted average variables in the P7 plane

		CY	PL	CS
Dynamic viscosity	MAPD (%)	42.285	42.484	21.107
	MAD (Pa.s)	0.00442	0.00517	0.00184
	t_{mad} (s)	0.300	0.800	0.800
Effective viscosity	MAPD (%)	6.864	5.337	3.268
	MAD (Pa.s)	0.00612	0.00543	0.00225
	t_{mad} (s)	0.170	0.170	0.010
Strain rate	MAPD (%)	3.969	4.112	1.991
	MAD (s^{-1})	5.312	5.537	3.802
	t_{mad} (s)	0.450	0.450	0.440
Shear stress	MAPD (%)	6.027	5.915	4.094
	MAD (Pa)	0.224	0.255	0.0937
	t_{mad} (s)	0.160	0.160	0.430
Velocity	MAPD (%)	3.031	3.882	2.353
	MAD (m/s)	0.0169	0.00961	0.0113
	t_{mad} (s)	0.140	0.140	0.010
Pressure	MAPD (%)	0.017	0.008	0.009
	MAD (Pa)	12.739	5.072	5.582
	t_{mad} (s)	0.030	0.030	0.030

CY Carreau-Yasuda; *PL* Power-Law; *CS* Casson; *MAPD* Mean Absolute Percentage Deviation; *MAD* Maximum Absolute Difference; t_{mad} Instant of time of maximum absolute difference

In general, the Carreau-Yasuda and Power-Law models show very similar results, while the Casson model tends to get closer to the Newtonian model.

From the rheological point of view, the non-Newtonian models show considerable differences in relation to the Newtonian one. On the other hand, the differences in the hemodynamic field are negligible for regions with higher shear rates, becoming more significant at lower shear rates. Thus, it is advisable to adopt a non-Newtonian model when it is necessary to model regions of low shear rate in aortic blood flow.

Acknowledgements The authors would like to thank Conselho Nacional de Desenvolvimento Científico e Tecnológico—CNPq (312982/2017-8) and Coordenação de Aperfeiçoamento de Pessoal de Nível Superior—CAPES (88882.381154/2019-01) for their support in this study.

Conflict of Interest The authors declare that they have no conflict of interest.

References

1. Irgens F (2014) Rheology and non-newtonian fluids. Springer
2. Chandran Krishnan B, Rittgers Stanley E, Yoganathan Ajit P (2012) Biofluid mechanics: the human circulation. CRC Press
3. Shibeshi Shewaferaw S, Collins William E (2005) The rheology of blood flow in a branched arterial system. Appl Rheol 15:398–405
4. Arzani A (2018) Accounting for residence-time in blood rheology models: do we really need non-Newtonian blood flow modelling in large arteries? J Royal Soc Interface 15:20180486
5. Karimi S, Dabagh M, Vasava P, Dadvar M, Dabir B, Jalali P (2014) Effect of rheological models on the hemodynamics within human aorta: CFD study on CT image-based geometry. J Non-Newtonian Fluid Mech 207:42–52
6. Bilgi C, Atalık K (2019) Numerical investigation of the effects of blood rheology and wall elasticity in abdominal aortic aneurysm under pulsatile flow conditions. Biorheology 56:51–71
7. Ionescu Clara M (2017) A memory-based model for blood viscosity. Commun Nonlinear Sci Numer Simul 45:29–34
8. Razavi A, Shirani E, Sadeghi MR (2011) Numerical simulation of blood pulsatile flow in a stenosed carotid artery using different rheological models. J Biomech 44:2021–2030
9. Steinman DA (2012) Assumptions in modelling of large artery hemodynamics. In: Modeling of physiological flows. Springer, pp 1–18
10. Molla MM, Paul MC (2012) LES of non-newtonian physiological blood flow in a model of arterial stenosis. Med Eng Phys 34:1079–1087
11. Morbiducci U, Gallo D, Massai D et al (2011) On the importance of blood rheology for bulk flow in hemodynamic models of the carotid bifurcation. J Biomech 44:2427–2438
12. Alastruey J, Xiao N, Fok H, Schaeffter T, Alberto FC (2016) On the impact of modelling assumptions in multi-scale, subject-specific models of aortic haemodynamics. J Royal Soc Interface 13:20160073
13. McHale MP, Friedman JR, Karian J (2009) Standard for verification and validation in computational fluid dynamics and heat transfer. Am Soc Mech Eng ASME V&V. 2009:20–2009
14. Gonçalves SF, Lucas TC, Haniel J, Silva MLF, Huebner R, Viana EMF (2019) Comparison of different rheological models for computational simulation of blood flow in central venous access. 25th ABCM international congress of mechanical engineering. Uberlândia, Brasil, pp 1–9
15. Bovik Wang Z, Alan C, Sheikh Hamid R, Simoncelli Eero P (2004) Image quality assessment: from error visibility to structural similarity. IEEE Trans Image Proc 13:600–612

Total Lung Capacity Maneuver as a Tool Screen the Relative Lung Volume in Balb/c Mice

A. E. Lino-Alvarado, J. L. Santana, R. L. Vitorasso, M. A. Oliveira, W. Tavares-Lima and H. T. Moriya

Abstract

Assessment of the mechanical ventilation in rodents is widely performed using a mechanical ventilator for small animals (SAV). One of the main adjustable parameters in SAV is tidal volume, typically 10 mL/kg, which is configured in relation with the animal body weight. Traditionally, the preset TLC maneuver is used for alveolar recruitment; this study aims to explore the data from TLC to screen the relative lung volume in Balb/c mice, in order to analyze its relationship to the body weight of mice. The TLC maneuver allowed us to measure the relative delivered lung volume from PEEP (positive end-expiratory pressure) to 30 cm H_2O. In overall, one hundred twenty-four (124) 13–20 week-old Balb/c mice were used, animals were split into two groups using mean value of the body weight (24g) as a cutoff point. Group H (n =51) had animals with body weight higher than the mean value, while mice with lower body weight belonged to group L (n = 73). Significant positive correlation was found within animals in the group H (r = 0.6137); conversely, animals in group L did not present correlation for relative volume and body weight ($r \approx 0$). Additionally, an analysis of static compliance (Cstat) was conducted for each group using unpaired t-test ($p < 0.05$). Therefore, it was possible to indicate that mice with lower body weight presented lower static compliance compared with those with greater body weight. Results suggest that tidal volume apparently depends on recruitment volume or compliance instead of the mice body weight.

Keywords

Respiratory mechanics • Total lung capacity • Balb/c mice • Static compliance • Ventilator for small animals

1 Introduction

Great advances in the study of the respiratory system of mammals have occurred since the use of small animals became largely implemented in the biomedical research scenario, such as mice, rats and guinea pigs [1–3]. Among these small rodents, mice are currently the main mammals used for in vivo experiments due to some advantages comparing to bigger mammals, for instance, a well understood immunologic system, a short reproductive cycle, they can be easily obtained in large numbers and, also, have perceived economic factors [1,4].

To study the respiratory system, usually, one needs the ability to measure lung function and to understand how lung function changes under conditions likely to be encountered in lung diseases. However, to work with these small animals and successfully assess lung function some practical issues must be overcome, such as the difficulty of measuring the necessary respiratory signals of flow, volume and transpulmonary pressure; difficulties as such, that are mainly attributed to the small magnitude of airflow involved [4].

In order to achieve precision in these measurements, inevitably an invasive approach must be implemented, this a situation very well discussed in [5] where the authors coined "the phenotyping uncertainty principle", which highlights the compromise between the achievement of natural conditions and measurement precision, i.e., the least invasive the method the least precise the measurements and vice versa.

A method capable of assessing lung function with high precision is the one where breathing frequency, tidal volume, mean lung volume and volume history are all under precise experimental control and the influence of the upper airways

A. E. Lino-Alvarado (✉) · J. L. Santana · R. L. Vitorasso · H. T. Moriya
Laboratory of Biomedical Engineering, Escola Politécnica, University of São Paulo, Av. Prof. Luciano Gualberto 158, São Paulo, Brazil

M. A. Oliveira · W. Tavares-Lima
Laboratory of Physiopathology of Experimental Inflammation, Department of Pharmacology, Institute of Biomedical Sciences, University of São Paulo, São Paulo, Brazil

T. F. Bastos-Filho et al. (eds.), *XXVII Brazilian Congress on Biomedical Engineering*, IFMBE Proceedings 83, https://doi.org/10.1007/978-3-030-70601-2_7

has been eliminated. However, to conduct an experiment with all these variables controlled, the animal must be anesthetized, paralyzed and tracheostomized, which put the animal far from its "normal" conditions, due to surgical and pharmacological stresses [4,5].

This method is widely implemented through the use of a mechanical ventilator for small animals (SAV), which uses a piston pump controlled by a computer to transmit airflow to the animal [6]. The computer receives input signals from transducers that measure tracheal pressure and piston displacement and, after correction for gas compression in the piston chamber, it can precisely control the frequency and amplitude of the airflow transmitted to the animal attached to the ventilator [5].

Through a SAV many applications can be performed such as the assessment of respiratory mechanics by positive-pressure ventilation, in the time and frequency-domain [7,8], and analyses of the pressure-volume (P-V) curve relation, which is a classical method to investigate lung elasticity [9] or study the total lung capacity of mice (TLC), which is the aim of this work.

The assessment of the maximum lung volume or TLC of mice has been reported in the literature following no standard experimental procedure [10]. This happens, mainly, because the term TLC is derived from humans, where the maximum volume attributed to TLC is the maximum voluntary inspiration of an individual, which cannot be accomplished by animals [9,10]. For non-human animals, the term TLC as capacity simply indicates maximal lung volume [10,11].

Thereby, the TLC of mice is ideally determined by a limit pressure arbitrarily set by the investigator, at which the inflation limb of the P-V curve starts to plateau (constant lung volume while increasing lung pressure), usually with pressures >20 cm H_2O. Nevertheless, it has already been shown that for much greater values of pressures, such as 90 cm H_2O, in few cases, the inflation limb may not reach a plateau and no lung damage was observed [10]. So, currently, in the lack of a standard, a common practice is to choose a pressure within 25–35 cm H_2O when, in most cases, the inflation curve starts performing a plateau for mice [9].

Working with a specific pressure for TLC, it also means that is possible to investigate another important physiological parameter: one that relates pressure and volume in the absence of flow (i.e., constant pressure and volume), which represents the static compliance (C_{st}) of the respiratory system [12].

The C_{st} is a very useful measurement of lung distensibility, in which several factors might affect it, such as lung size, age, respiratory diseases (e.g. emphysema and asthma), bronchodilator drugs and cardiovascular disease (e.g. mitral stenosis and left ventricular failure) [13], so that it is used as an important tool to investigate different abnormalities involving the respiratory system.

These physiological parameters presented (TLC and C_{st}) are also often subjects of allometric studies to investigate how they are associated with different body sizes. However, although these studies show strong correlations of these parameters with body size, the majority of them are performed with less invasive (i.e., less precise) methods of measuring and controlling airflow and transpulmonary pressure, besides the fact that they are based on interspecies allometric scaling [5,14–16].

Thus, this work aimed to analyze the relationship of the TLC with the body weight of mice of the same strain through the use of a more invasive method to achieve more precision on the assessment of the TLC. For this purpose, a mechanical ventilator for small animals (flexiVent, SCIREQ, Canada) [6], was used to estimate the TLC at a limit pressure of 30 cm H_2O.

2 Materials and Methods

2.1 Animals

All animals were raised under similar conditions in the vivarium with free access to food and water. The experimental procedures conformed to standards of animal welfare and were approved by the Ethics Committee in the Use of Animals of ICB/USP (No 9782280518, 528816021, 95/2017 and 015/2014).

One hundred twenty-four (124) Balb/c mice 13–20 weeks old were used to perform this study. To investigate the relationship of the TLC with the body weight, the animals were divided into two groups: group H (26.6 ± 2.1)(mean ± SD) and group L (18.4 ± 4.2) according to the value of their body weight, whether it is higher (group H) or lower (group L) than a cutoff value of 24 g, which is the average value of all 124 animals.

2.2 Assessment of Total Lung Capacity

To perform the experiments, a mechanical ventilator for small animal (SAV, flexiVent, SCIREQ, Canada) were used to accomplish two task: supply the animals with the necessary airflow to keep them alive and to execute specific maneuvers by controlling pressure and flow to acquire the TLC of each animal.

Before the experiment was conducted, a two-stage calibration had been performed in the SAV. Firstly, the SAV generated a perturbation while the tracheal cannula was closed, this stage permitted to estimate the gas elastance within the cylinder-tubing assembly. Secondly, the same perturbation was started whilst the cannula was totally opened to the atmosphere, at this time, flow resistance and gas inertance were

estimated. Finally, the SAV compensated the airway pressure of the animal by subtracting pressures related to resistances and inertance [17].

The animals were anesthetized with a solution of ketamine (12 mg/kg) and xylazine (12 mg/kg) through an intraperitoneal (i.p.) injection. After, a tracheostomy was performed with a metal cannula 18G (BD Company, USA) and, then the animal was connected to the SAV to be ventilated with a tidal volume of 10 mg/kg [8,18,19], positive end-expiratory pressure (PEEP) of 3 cm H_2O and breathing frequency of 150 breaths/minute.

Following, the right jugular vein was exposed and a needle attached to a flexible PVC tube (Critchley Electrical Products PTY, Australia) was inserted, to be used as a pathway to phosphate-buffered saline (PBS) or bronchoconstrictor drugs used in a concomitant study held by our group. It is worth saying that this study did not interfered in the present work, because the TLC assessments were executed prior any PBS or bronchoconstrictor drug administration.

Finally, the respiratory muscles were blocked with a injection of 1 mg/kg of pancuronium bromide (i.p.). By doing it, possible inferences of the animal breathing on the respiratory system assessment are eliminated, which makes the method more precise [5,7].

2.2.1 Alveolar recruitment maneuvers

To estimate the TLC, we used a preset maneuver available on the SAV, known as alveolar recruitment maneuver (ARM), which is widely implemented in the assessment of respiratory mechanics.

It consists of a pressure-controlled inflation maneuver which starts from a preset PEEP of 3 cm H_2O, with a total duration of 6 s (Fig. 1).

Initially, a linear increase in tracheal pressure (P_{tr}) is made from PEEP value until it reaches the preset value of 30 cm H_2O (approximately 3 s) and, then, this pressure is maintained for more 3 s, creating the plateau observed in Fig. 1a.

In Fig. 1b we can see the amount of air delivered to the lungs through time while the tracheal pressure was increasing and when the plateau condition was reached.

The SAV was adjusted to use as TLC the average value of the delivered volume of air to the lungs (V_{tr}) in the last 100 ms of the inflation maneuver (Fig. 1b), so these were the values used herein to compute the analyses.

The standard protocol of assessing respiratory mechanics in our laboratory performs two ARM for each animal, thereby, to work with as many alveolar units open as possible the second maneuver was chosen for this study.

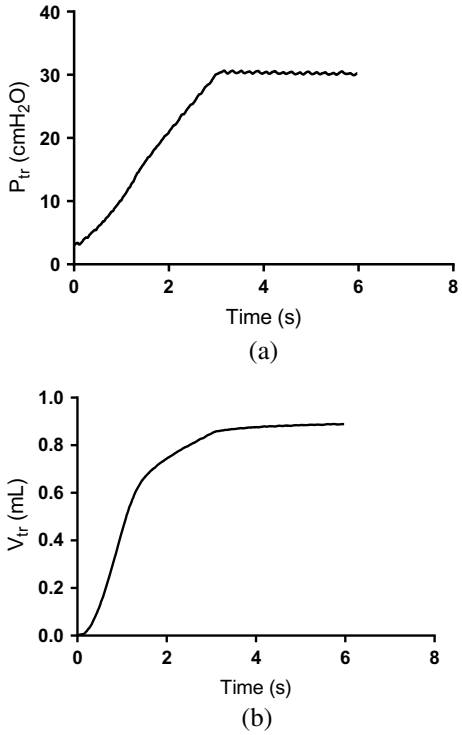

Fig. 1 Inflation maneuver performed in Balb/c mouse by the SAV in the laboratory. In **a** the tracheal pressure is increased and monitored by the SAV until 30 cmH_2O which takes approximately 3 s, then this pressure is maintained for more 3 s. In **b** the corresponding volume of air delivered to the lungs during this maneuver is shown

2.2.2 Static compliance

Cstat was calculated as the measured volume divided by the controlled pressure (30 cm H_2O) during the plateau of the TLC maneuver.

$$Cstat = \frac{\Delta V_{tr}}{\Delta P_{tr}} \quad (1)$$

2.3 Data Analysis

Before statistical analysis was performed, mice had been divided into the following two groups: group H (26.6 ± 2.1) composed of 51 animals with body weight higher than the mean value (24 mg) and group L (18.4 ± 4.2) with 73 animals with body weight below the mean value. To exclude possible outliers, the Tukey method was performed [20].

A Shapiro-Wilk test was used to assess the normality of the data in each group. To evaluate whether or not a significant correlation exists between animal body weight and the TLC (V_{tr}) in the groups H and L, dispersion graphs using the TLC

estimated along with the Pearson coefficient (r) were used. In addition, an unpaired t-test was conducted for the values of Cstat in each group.

3 Results

Figure 2 shows that there is no correlation between the relative volume and body weight ($r \approx 0$) in group L. Otherwise, as it is presented in Fig. 3, a positive correlation was observed in group H ($r = 0.6137$ and $p < 0.0001$).

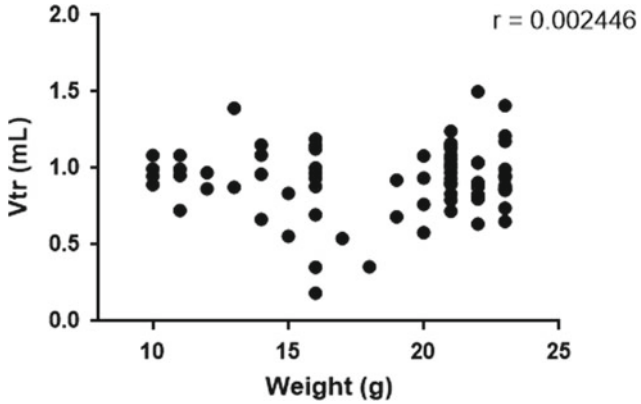

Fig. 2 No correlation was found between the volume during TLC (V_{tr}) and animal weight in group L

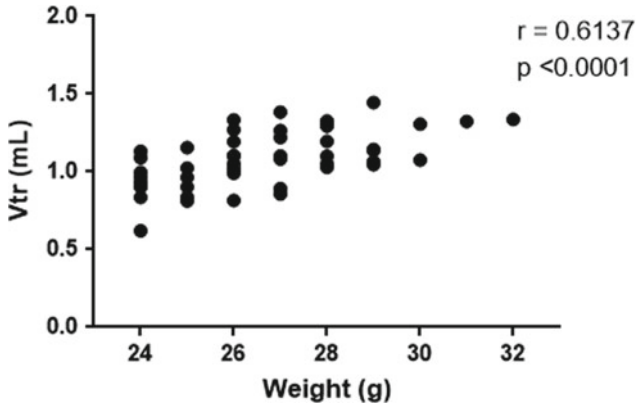

Fig. 3 Significant correlation was observed in group H, involving the volume during TLC (V_{tr}) and animal weight

Figure 4 illustrates the mean value ± SD of Cstat that was calculated for group H and L.

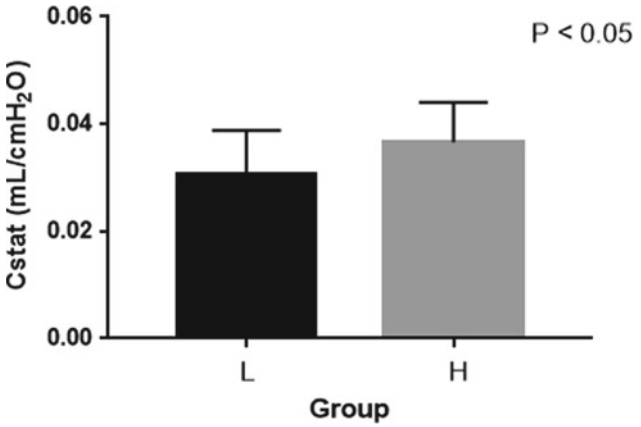

Fig. 4 Mean ± SD of the Cstat for the studied groups: H and L. Animals with lower body weight (group L) presented a lower static compliance; otherwise, animals (group H) had higher static compliance

4 Discussion

ARMs are used, e.g., in Intensive Care Unit (ICU) with the main purpose of recruiting collapsed alveoli, increase gas exchange, and improve arterial oxygenation [21]. Albeit important in clinical practice, ARM must be applied in controlled circumstances such as proper sedation.

However, besides clinical practice, ARMs are present in respiratory mechanics studies with animal models [22,23]. The purpose of ARM is, once more, to recruit collapsed alveoli before the respiratory mechanics evaluation.

Additionally, ARM may be used as a perturbation applied in the respiratory system in order to assess respiratory mechanics with physiological meaning. Herein, the selected ARM from the commercial small animal ventilator was the Total Lung Capacity (TLC), which aims to achieve the homonym lung capacity, the Total Lung Capacity. However, in a new version of the ventilator used in this work the maneuver presents a different name (deep inflation) with the same pressure set.

The TLC as a lung capacity is, for humans, the lung volume at the end of a maximal voluntary inspiration. In the case of non-human animals, the term TLC as capacity refers to the maximal lung volume. The TLC maneuver at 30 cm H_2O may not inflate the animal lung at the maximal capacity [10]; yet, it can bring information regarding the animal respiratory mechanics.

The relative volume referred to the total volume of air delivered into the mice lungs whilst the tracheal pressure increases from PEEP to 30 cm H_2O.

Figure 4 presents that animals with lower body weight had, statistically, a lower static compliance. This compliance was modeled using the TLC maneuver. In addition, it was found that animals with higher body weight and, consequently, greater compliance, presented an association between body weight and volume during TLC (Fig. 3). This association was not observed among the animals with lower body weight.

Therefore, we posit two possibilities: there is, indeed, no association between body weight and volume at the end TLC maneuver for the animals with lower body weight; or the 30 cm H_2O pressure is not sufficient to inflate lower compliance animal lungs up to a point of discriminating animals with lower or higher body weight. Notwithstanding, a pressure screening could fully address this issue.

The implications of these findings are related to animals' life supporting mechanical ventilation and respiratory mechanics. Both tidal volume and perturbation volume are set using body weight. For example, it is common to set the tidal volume as 10 mL/kg and the perturbation's volume amplitude is related numerically with the tidal volume.

Thus, the volume amplitude during perturbation of a larger animal is greater than the volume amplitude of a lower body weight animal. This is intuitive, larger animals would require greater volume amplitude during perturbation. However, since there was no correlation with body weight and volume during ARM for smaller animals, the volume set in the perturbations should not be linearly predicated on animal body weight.

The respiratory impedance and its further modeling is volume dependent [1]. Hence, if animal's tidal volume is not properly adjusted along with adequate perturbation volume amplitude, the modeled parameters and impedance calculations may be inaccurate or unreliable. The impedance calculation and linear models application relies on the linear behavior of the respiratory system [8]. This behavior is only fulfilled with certain conditions and one of them is low amplitude of the perturbation and, clearly, depends on the species and morphological characteristics within.

In this work the body weight cutoff was 24 g based on the group mean. However, another study with a wider body weight range and with a different design could provide a proper cutoff in order to classify the groups. Based on this work findings, the animals with less than 24 g participate in the group with lower compliance. This group had a non-linear distribution of volume at 30 cm H_2O recruitment and this could indicate that the tidal volume and, consequently, perturbation volume amplitudes could be based on recruitment volume or compliance instead of the body weight.

5 Conclusion

Animals with lower body weight presented lower compliance compared with those with greater body weight. Additionally, it was found that animals with higher body weight and, consequently, greater compliance, presented an association between body weight and volume during recruitment, whereas this association was not observed among the animals with lower body weight. These finding could suggest, specially for the lower compliance group, that the perturbation volume amplitude could be based on recruitment volume or compliance instead of the body weight.

Acknowledgements This study was financed in part by the Conselho Nacional de Desenvolvimento Científico e Tecnológico (CNPq)—Brasil (grant numbers 308298/2016-0, 408006/2016-1 and 133814/2019-0); and the Coordenação de Aperfeiçoamento de Pessoal de Nível Superior—Brasil (CAPES)—Finance Code 001 (grant numbers 88882.333327/2019-01 and 88882.333348/2019-01).

Conflict of Interest The authors declare that they have no conflict of interest.

References

1. Sly PD, Collins RA, Thamrin C, Turner D, Hantos Z (2015) Volume dependence of airway and tissue impedances in mice. J Appl Physiol 94(4):1460–1466
2. Aun M, Bonamichi-Santos R, Arantes-Costa F, Kalil J, Giavina-Bianchi P (2017) Animal models of asthma: utility and limitations. J Asthma Allergy 10:293–301
3. Lambrecht BN, Hammad H (2015) The immunology of asthma. Nat Immunol 16:45–56
4. Irvin CG, Bates JHT (2003) Measuring the lung function in the mouse: the challenge of size. Respir Res 4:1–9
5. Bates JHT, Irvin CG (2003) Measuring lung function in mice: the phenotyping uncertainty principle. J Appl Physiol 94:1297–1306
6. Schuessler TF, Bates JHT (1995) A computer-controlled research ventilator for small animals: design and evaluation. IEEE Trans Biomed Eng 42:860–866
7. Bates JHT (2009) Lung mechanics: an inverse modeling approach. Cambridge University Press, New York
8. Moriya HT, Moraes JCTB, Bates JHT (2003) Nonlinear and frequency-dependent mechanical behavior of the mouse respiratory system. Ann Biomed Eng 31:318–326
9. Limjunyawong N, Fallica J, Horton MR, Mitzner W (2015) Measurement of the pressure-volume curve in mouse lungs. J Visualized Exp
10. Soutiere SE, Mitzner W (2004) On defining total lung capacity in the mouse. J Appl Physiol 96:1658–1664
11. Leith DE (1976) Comparative mammalian respiratory mechanics. Physiologist 19:485–510
12. Leith DE (1983) Comparative mammalian respiratory mechanics. Am Rev Respir Disease 128:S77–S82

13. Cotes JE, Chinn DJ, Miller MR (2006) Lung function: physiology, measurement and application in medicine, 6th edn. Wiley-Blackwell, Birmingham
14. Lindstedt SL (1987) Allometry: body size constraints in animal design. In: Pharmacokinet. Risk Assess. Drink. Water Heal, 8th edn. National Academies Press, Washington, D.C
15. Stahl WR (1967) Scaling of respiratory variables in mammals. J Appl Physiol 22:453–460
16. Bennett FM, Tenney SM (1982) Comparative mechanics of mammalian respiratory system. Respir Physiol 49:131–140
17. Bates JHT, Schuessler TF, Dolman C, Eidelman DH (1997) Temporal dynamics of acute isovolume bronchoconstriction in the rat. J Appl Physiol 82:55–62
18. Walder B, Fontao F, Tötsch M, Morel DR (2005) Time and tidal volume-dependent ventilator-induced lung injury in healthy rats. Eur J Anaesthesiol 22:786–794
19. Guivarch E, Voiriot G, Rouzé A et al (2018) Pulmonary effects of adjusting tidal volume to actual or ideal body weight in ventilated obese mice. Sci Rep 8:6439
20. Mosteller F, Tukey JW (1977) Data analysis and regression: a second course in statistics
21. Hartland BL, Newell TJ, Damico N (2015) A systematic review of the literature. Alveolar Recruitment Maneuvers Under General Anesthesia, Respiratory care, p 60
22. Mori V, Oliveira MA, Vargas MHM et al (2017) Input respiratory impedance in mice: comparison between the flow-based and the wavetube method to perform the forced oscillation technique. Physiol Meas 38:992–1005
23. Vitorasso RL, Oliveira MA, Lima W, Moriya HT (2020) Highlight article: respiratory mechanics evaluation of mice submitted to intravenous methacholine: Bolus versus continuous infusion. Exp Biol Med 245:680–689

The Influence of Cardiac Ablation on the Electrophysiological Characterization of Rat Isolated Atrium: Preliminary Analysis

J. G. S. Paredes, S. Pollnow, I. Uzelac, O. Dössel and J. Salinet

Abstract

Atrial fibrillation (AF) is the most common cardiac arrhythmia seen in the clinical practice, and treatments with antiarrhythmic drugs are of limited effectiveness. Radiofrequency catheter ablation (RFA) has been widely accepted as a strategy to treat AF. In this study, we analyzed the electrophysiological impact of different RFA strategies by varying the duration of ablation in a controlled protocol. The electrical activity of the isolated right atrium of rats, under different RFA time strategies, was acquired on the epicardium by electrical Mapping (EM), and simultaneously on the endocardium by Optical Mapping (OM). Analyses were performed in both time and frequency domain, through analysis of signal's morphology, local activation time (LAT), conduction velocity (CV), dominant frequency (DF), and organization index (OI). The morphology of the optical and electrical signals with prolonged ablation time was altered as the ablation time increased. As observed, DF and OI decreased with the increase of the ablation time and resulted in fragmented electrograms. Through the characterization of traditional metrics applied to the electrical and optical data, it was possible to identify the important changes induced by the ablated area.

Keywords

Cardiac electrophysiology • Electrical mapping • Optical mapping • Signal processing • Radiofrequency ablation

1 Introduction

Atrial fibrillation (AF) is the most common cardiac arrhythmia, affecting 1–2% of the worldwide population [1]. It is characterized by the collapse of the synchronized wavefront atria depolarization, experiencing disorganized and self-sustained electrical activation patterns [1]. During AF, the atria do not empty completely between contractions, leading to the formation of blood clots and thromboembolic events, increasing the risk of stroke by five-fold, and doubling mortality [1]. Three different theories were postulated in an attempt to explain the mechanism of AF: multiple and continuous intra-atrial reentries, ectopic foci, and the existence of self-sustained rotors [2,3]. These occurrences vary among patients and can coexist simultaneously, or intercalated with each other in the same patient, favoring a complex atrial activation pattern [2].

The treatment of AF by antiarrhythmic drugs has limited effectiveness, and radiofrequency catheter ablation (RFA) has been widely adopted as a strategy to terminate and prevent recurrence of AF [4]. The primary ablation strategy for AF involves electrical isolation of the pulmonary veins (PVs), aiming to restore and maintain sinus rhythm [4]. Recurrence of AF after RFA occurs in 20–40% of patients when non-conductive cauterized tissue becomes conductive [5]. Permanent PV isolation may not be achieved after a single RFA treatment, and repeated ablation procedure is necessary in such instances [5]. Studies of the electro-physiological characteristics of the ablated tissue allow a better understanding of the ablated area in terms of its excitability and conductivity in order to devise more optimized RFA strategies. This study is based on the analysis of the electrophysiological impact of

J. G. S. Paredes (✉) · J. Salinet
Modelling and Applied Social Sciences Centre, Biomedical Engineering, Federal University of ABC/Engineering, Alameda da universidade, s/n Av.Anchieta, São Bernardo do Campo 09606-045, Brazil

S. Pollnow · O. Dössel
Karlsruhe Institute of Technology (KIT)/Institute of Biomedical Engineering, Karlsruhe, Germany

I. Uzelac
School of Physics,Georgia Institute of Technology, Georgia, USA

T. F. Bastos-Filho et al. (eds.), *XXVII Brazilian Congress on Biomedical Engineering*, IFMBE Proceedings 83, https://doi.org/10.1007/978-3-030-70601-2_8

different RFA time duration through a controlled protocol on isolated mice atria mimicking the clinical practice to treat AF by RFA.

2 Methods

2.1 Experimental Protocol

All animal experiments were carried out in agreement with the European Council guidelines for the care and use of laboratory animals and have been approved by the local Committee for Animal Welfare (Regierungspräsidium Karlsruhe, 35-9185.81/G-104/17). For this study, two adult Fisher rats were used (A Case and B case).

The right atrium was dissected by cutting along the tricuspid valve to the superior vena cava (10 x 10 mm) followed by a bath with a Krebs-Henseleit solution under a controlled temperature of 36.7 $\pm$ 0.5 °C. The sinoatrial node is ablated, and the epicardium stimulated at 6.7 Hz. RFA was performed with a tungsten microdissection electrode connected to an electrosurgical unit (MD1, Micromed) in the center of the atrium epicardium. The RFA strategy is performed as follows: the same area of the tissue is ablated for 0.5, 1, 1.5, 2, 2.5, 3, and 4 s. Before and after each ablation, epicardium atrium unipolar electrograms (EGMs) and Optical Activation Potentials (OAPs) are recorded simultaneously with two-minute intervals between successive ablations. By the end of the ablation protocol, the same area on the epicardium had an accumulative ablation of 14.5 s [6].

2.2 Optical and Electrical Mapping

For optical mapping, the transmembrane voltage-sensitive dye Di-4-ANEPPS (Sigma Aldrich) was used. Two LEDs (525 nm center wavelength) supplied with 4 A and each coupled with the narrow band-pass filters of 530 nm were used as excitation light sources. The excitation light was directed to a glass diffuser and then focused by two plano-convex lenses, propagating to a Dichroic mirror and a Makro-Planar lens before reaching the endocardium. The emitted fluorescence is directed back to the Makro-Planar and Dichroic mirror, followed by a long-pass filter (610 nm) and then to a high-speed focal length lens attached to a camera. Sequences of fluorescence images were acquired at a resolution of 82 $\times$ 82 pixels 868 Hz with a binning factor of 2. The spatial field of view of the camera is approximately 10.5 $\times$ 10.5 mm or 128 $\times$ 128 μm per pixel. Due to the noise around image border, the images were cropped to the resolution of 64 $\times$ 64 pixels. Simultaneously to optical mapping, EGMs were recorded with a circular multielectrode array (MEA) containing eight silver/silver chloride electrodes (3.5 mm of diameter) with a sampling frequency of 100 kHz [6].

Both experiments were made in Karlsruhe Institute of Technology [6], and all the analysis below was calculated with data collected.

2.3 Electrophysiological Characterization

All analyses were performed off-line in MATLAB (R2018b).

Preprocessing: OAPs were filtered with an adaptive multidimensional Gaussian low-pass filter [7]. The baseline of the fluorescence drift was removed with a low-pass Kaiser Window FIR filter, per-pixel basis, subtracting the baseline, and dividing the obtained difference by the baseline [8]. In order to further reduce noise, the signal was smoothed using a Gaussian kernel [9,10] with a matrix's size of 6 $\times$ 6. Finally, for each pixel, signals were normalized from 0 to 1.

EGMs were downsampled to 5 kHz. Pacing artifacts present in the EGMs were removed as follows: as the spectrum of the EGMs is within the region below 1 kHz, the EGMs were high-pass filtered with 3rd-order Butterworth (fc = 1 kHz) filter in order to detect only the pacing peak. After peak detection, a segment with length covering 2 ms before and after the detected pacing peak was removed and replaced by a cubic spline interpolation. Afterwards, the EGMs were band-pass filtered with 3rd-order low-pass (fc = 743 Hz), and high-pass (fc = 0.6 Hz) Butterworth filters. A 50 $\pm$ 1 Hz notch filter was used to remove the power line noise.

Signal Morphology: 10 OAPs were selected (eight of them near the location of the MEA's electrodes, one far away from the ablated area, and one in the center of the RFA area). The comparison of the morphology between OAPs recorded at baseline (BL) and after each RFA was performed with Pearson Correlation (PC). The analysis was also expanded to the EGMs' morphology.

Time analysis: The activation and repolarization times were considered as the time at which the upstroke reaches 50% and recovers to 90% of its maximum amplitude, respectively [11]. LATs were calculated for the optical signals, with a duration of 4 s, underneath the MEA's electrodes. For the eight pixels, the differences between maximal and minimal LATs were calculated. The mean dispersion ($\triangle$LAT) was calculated as the mean value of the obtained differences. With the LATs, the isochronous maps are generated to distinguish patterns of wave-front propagation and provide information on the longitudinal conduction velocity (CV) calculated through the single vector method [12] where it was selected a point at approximately 80% of the distance between the stimulation site to the border for the longitudinal direction [13]. The mean OAP pattern for each pixel under the MEA was upsampled [14] and used to find the action potential duration (APD),

between the time shift from the LAT to the time where the amplitude decays 30, 50, and 90% from highest OAP positive peak [15]. The LATs from EGMs were obtained with the minimum downstroke derivative (-dV/dt) [6]; after that, the △LAT values are calculated.

Frequency analysis: the Fast Fourier Transform (FFT) is applied to characterize the frequency spectrum. A Hamming window was used to reduce spectral leakage. FFT was performed with a zero-padding factor of 5, resulting in a frequency step of 0.05 Hz. Dominant frequency (DF) is identified as the frequency peak in the power spectrum within the range of 4–12 Hz. The organization index (OI) [16] allows us to characterize the spread of the DF peaks and its harmonics due to the dispersion of CV and action potential upstroke caused by ablation. For the OI calculation, an area with 0.5 Hz on either side of the DF and its harmonics (in the range up 20 Hz) is divided by the total area under the power frequency spectrum within a range of 2–20 Hz.

3 Results

Figure 1a shows two consecutive OAPs at the center of the ablated area for BL, 2.5 s, and 4 s of RFA, with LATs marked in the signals. With RFA time increase, the morphology of OAPs deteriorates with increased fractionation, leading to dispersion of LATs. Figure 1b shows OAPs at the location underneath the 3rd MEA electrode located around the center of ablated area, characterized with lower fractionation than inside the ablated area. Figure 1c shows the 3rd electrode's EGMs, with noticeable absence of the negative segment of the S wave (down deflection). This feature indicates tissue damage due to ablation, with complete wave propagation block after 2.5 s of ablation. The absence of negative S wave segment indicates that wavefront is not passing through the ablated region.

Table 1 shows PC values obtained from 8 OAPs underneath the MEA's electrodes (2nd and 5th column), one OAP at the center, and far away from the ablated area (in and out columns), for the different time RFA strategies. The corresponding PC values from EGMs are shown in the lower part of the table. Inside the ablated area, and at the MEA's electrodes, the PC decreases with RFA time increase.

3.1 Time Analysis

The △LAT time across the OAPs recorded underneath the MEAs electrodes increased (in ms) from 4.3 ± 0.5 (baseline) to 8.4 ± 2.2 (2.5 s) and 9.8 ± 4.2 (4 s). The EGMs presented a similar trend, increasing from 6.0 ± 1.2 to 11.7 ± 2.5 and 12.6 ± 2.7, respectively. The ablation affected APD values, for "A" case, specifically, with decreased APD90 towards the end of RFA ablation protocol indicating abscence of repolarization due to wavefront block (Fig. 2a).

The isochronous maps show a pattern of wavefront propagation from the bottom right to the upper left for case A (Fig. 2b). After 4 s of RFA, compressed isochrone lines around the ablation area indicate CV reduction, where the ablated area acts as a functional block. The CV was 87 cm/s in BL and 65 cm/s after 4 s of RFA with an estimated CV of 48 cm/s in the center of the ablation area. For Case B, the propagation is from the left to the right. The CV was 69 cm/s at BL, 37 cm/s after 4 s of RFA, and eximated to be 0.8 cm/s in the center of the ablation area (Fig. 2c).

3.2 Dominant Frequency and Organization Index

The DF analysis for the A case shows large areas of 6.7 Hz until 2.5 s, decreasing in the ablated area to 5.4 Hz after 4 s of RFA. The DF obtained from EGMs went down from 6.7 to 4.7 Hz. The respective OI maps are displayed in Fig. 3a. The overall OI values for the OAPs in the ablated area are reduced, in contrast to the EGMs. For B case, the DF decreases from 6.7 Hz to 5.7 Hz after 2.5 s of RFA. Figure 3b shows that the OI maps have similar patterns as A case, with lower values of OI in the middle of the ablated area after 2.5 s. The EMGs show partially correlated OI values to the OI map.

4 Discussion

Similar to our observations, a recent study also showed that EGMs and OAPs change in their morphology, by increasing levels of fractionation, are associated with prolonged RFA time [17]. Specifically, EGMs are useful to detect wave-block in the ablated region, as successful ablation, through the absence of the negative S-wave segment [17]. Several authors use the first derivative of the AP in order to find the activation time [14,18]; but this method presented problems in the ablated area, and alternatively, time activation was determined as the time point at which the upstroke reaches 50% [11].

In optical mapping due to inherited spatial averaging, waveblocks are characterized by the dispersion of LATs around the ablated area, and randomness of LATs corresponding to successive wavefronts in the ablated region. According to Chorro et al. [19] the distal tissue has its activation delayed by the ablated lesions.

With both OAP and EGM methods, PC values are highly correlated, consistent, and can be used as markers to characterise successful or failed ablation [17]. For more detailed ablation analysis, OAPs are advantageous due to a higher resolution.

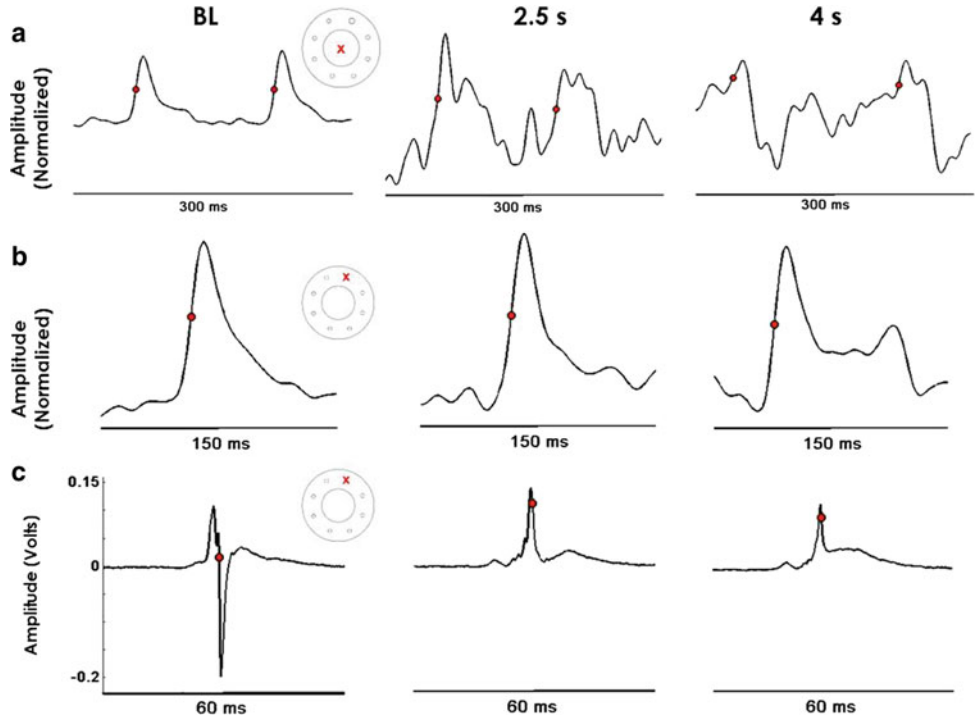

Fig. 1 **a** OAPs at BL, 2.5 s and 4 s after RFA obtained in the ablated area. **b** OAP acquired underneath MEA electrode 3. **c** EGM for electrode

Table 1 OAPs and EGMs's Pearson Correlation

	A case			B case		
Time	Mean ± SD	In	Out	Mean ± SD	In	Out
			OAP			
0.5 s	0.94 ± 0.02	0.91	0.96	0.88 ± 0.05	0.87	0.95
2.5 s	0.91 ± 0.03	0.60	0.97	0.87 ± 0.04	0.70	0.96
4 s	0.01 ± 0.03	0.01	−0.01	0.77 ± 0.09	0.53	0.96
			EGM			
0.5 s	0.95 ± 0.04			0.52 ± 0.31		
2.5 s	0.05 ± 0.15			0.10 ± 0.31		
4 s	0.06 ± 0.03			0.03±0.28		

In the border zone surrounding the lesion, the RF energy resulted in a significant APD shortening [20] presented at the end of the RFA strategy, (Fig. 2a). Some authors found no significant modifications in atrial CV in the proximal areas to the ablation site [19].

APD markers (to study repolarization) and CV can be calculated across entire tissue to study the effects of RFA not only on the ablated area but also at surrounding tissue to limit the RFA damage where it is not necessary. OI is the marker of choice to identify focal sources during persistent atrial fibrillation. However, in this study, the randomness of the OIs from EGMs and poor correlation with respective OI values from OAPs, render OIs from EGMs as poor markers for ablation characterization. OIs from OAPs are much better suited [21]; however optical mapping cannot be used in clinical settings.

5 Conclusion

This study aimed to identify the effect of the ablation time duration on the atrium substrate. The effect on heart electrophysiology at the ablation site and surrounding tissue was quantified by simultaneously optical and electrical signals. Many factors can influence the observed difference between cases A and B during the experimental phase such as: wall thickness, force, time, temperature, size of electrode, and the pacing location. Statistically the most important limitation was the number of cases, a bigger number of samples would be helpful to explain also the differences among experiments. Future studies will include more experimental data, including different animal species and different RFA strategies, to identify the important physiological changes at the ablated area.

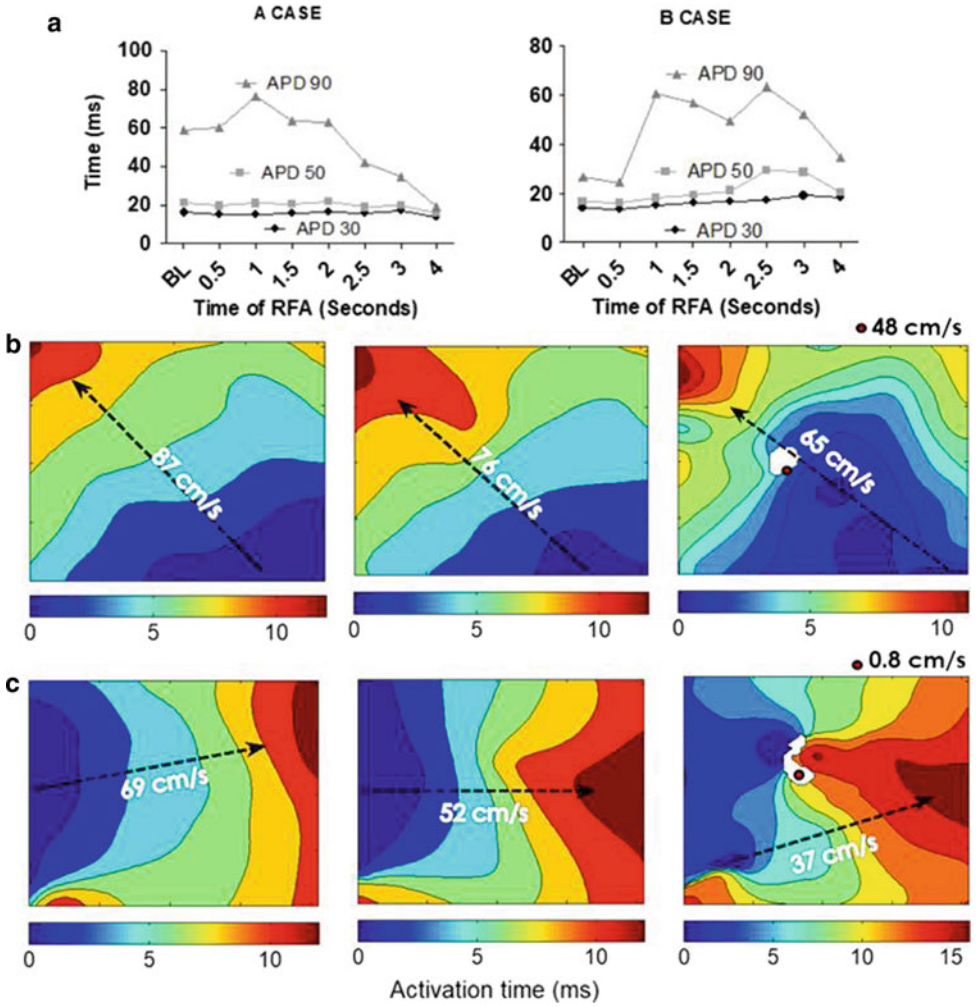

Fig. 2 **a** APD30, APD50 and APD90 for RFA strategy for A and B cases inside the ablated area. **b** LAT map generated at BL, after 2.5 s, and 4 s of RFA for A case. **c** LAT maps for B case

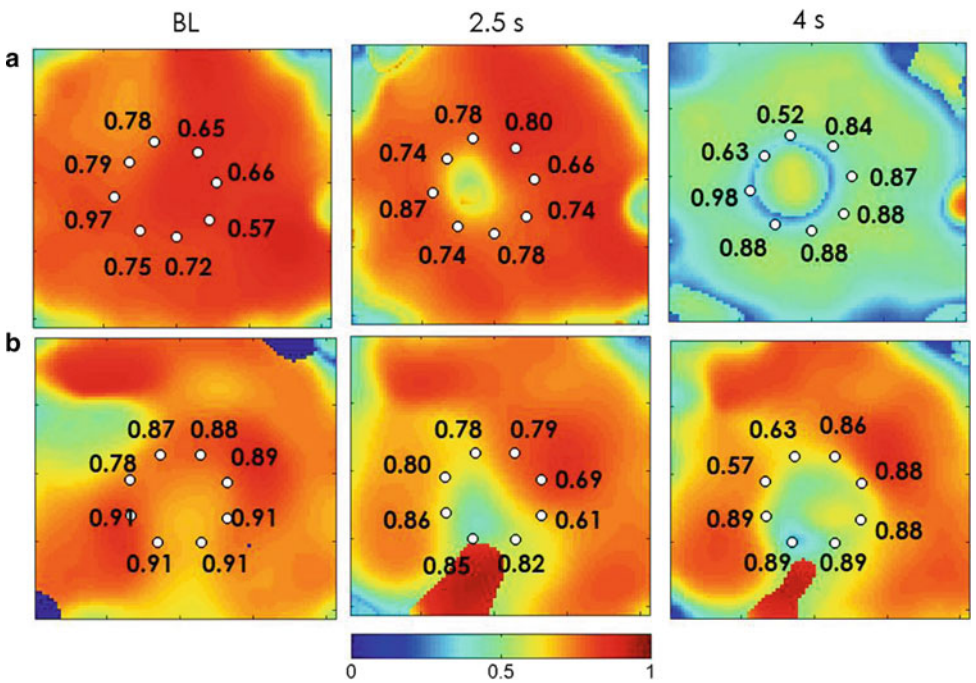

Fig. 3 **a** OI maps with the OI values for the EGMs for A case. **b** OI maps for B case

Acknowledgements Financial support: Program of Alliances for Education and Training (Scholarship Brazil - PAEC OEA-GCUB-2017).
Conflict of Interest The authors declare no conflict of interest.

References

1. January CT, Wann L, Calkins H et al (2019) Guideline for the management of patients with atrial fibrillation: a report of the american college of cardiology. J. Am College Cardiol. 74:104–132
2. Konings KT, Kirchhof CJ, Smeets JR, Wellens HJ, Penn OC, Allessie MA (1994) High-density mapping of electrically induced atrial fibrillation in humans. Circulation, Philadelphia
3. Zipes DP, Jalife J (2004) Cardiac electrophysiology from cell to bedside. SAUNDERS, Philadelphia
4. Kirchhf P, Eckardt L (2013) Ablation of atrial fibrillation: for whom and how? Heart 96:1325–1330
5. Darby AE (2016) Recurrent atrial fibrillation after catheter ablation: considerations for repeat ablation and strategies to optimize success. J Atr Fibrillation 9
6. Pollnow S (2018) Characterizing cardiac electrophysiology during radiofrequency ablation; 24. Karlshure Transactions on Biomedical Engineering, Karlsruhe, Germany
7. Pollnow S, Pilia N, Schwaderlapp G et al (2019) An adaptive spatiotemporal Gaussian filter for processing cardiac optical mapping data. Comput Biol Med 102:267–277
8. Uzelac I, Iravanian S, Fenton FH (2019) Parallel acceleration on removal of optical mapping baseline wandering. Comput Cardiol 46
9. Sung D, Omens JH, Mcculloch AD (2000) Model-based analysis of optically mapped epicardial activation patterns and conduction velocity. Annal Biomed Eng 28:1085–1092
10. Gurevich DR, Herndon C, Uzelac I, Fenton FH, Grigoriev RO (217) Level-set method for robust analysis of optical mapping recordings of fibrillation. Comput Cardiol 44
11. Efimov IR, Nikolski VP, Salama G (2004) Optical imaging of the heart. Circulation 95:21–33
12. Doshi AN, Walton RD, Krul SP et al (2015) Feasibility of a semi-automated method for cardiac conduction velocity analysis of high-resolution activation maps. Comput Bio Med 177–183
13. Linnenbank AC, Bakker JMT, Coronel R (2014) How to measure propagation velocity in cardiac tissue: a simulation study. Front Physiol
14. O'Shea C, Holmes AP, Yu TY et al (2019) ElectroMap: high-throughput open-source software for analysis and mapping of cardiac electrophysiology. Sci Rep 9–1389
15. Yu TY et al (2014) An automated system using spatial oversampling for optical mappingin murine atria. Development and validation with monophasic andtransmembrane action potentials. Prog Biophy Molecular Biol 1–9
16. Salinet JL (2013) High density frequency mapping of human intracardiac persistent atrial fibrillation electrograms. University of Leicester
17. Pollnow S, Schwaderlapp G, Dössel O et al (2019) Monitoring the dynamics of acute radiofrequency ablation lesion formation in thin-walled atria–a simultaneous optical and electrical mapping study. Biomed Eng Biomed, Technik, p 65
18. Efimov IR, Huang DT, Rendt JM, Salama G (1994) Optical mapping of repolarization and refractoriness from intact hearts. Circulation 90
19. Chorro FJ et al (1998) Acute effects of radiofrequency ablation upon atrial conduction in proximity to the lesion site PACE 21:1659–1668
20. Wu CC et al (1999) Sequential change in action potential of rabbit epicardium during and following radiofrequency ablation. J Cardiovasc Etectrophxsiol 10:1252–1261
21. Jarman JWE et al (2014) Organizational index mapping to identify focal sources during persistent atrial fibrillation. J Cardiovasc Etectrophxsiol 25:355–363

Evaluation of the Surface of Dental Implants After the Use of Instruments Used in Biofilm Removal: A Comparative Study of Several Protocols

D. P. V. Leite, G. E. Pires, F. V. Bastos, A. L. Sant'ana, L. Frigo, A. Martins e Silva, J. E. P. Nunes, M. H. B. Machado, A. Baptista, R. S. Navarro, and A. T. Araki

Abstract

It is extremely important to check the morphological changes on the surfaces of the implants that will have an impact on their osseointegration and clinical longevity of the implant. For this reason, the purpose of this in vitro study was evaluated the damage caused to the surface of dental implants after different conditions of simulation of mechanical removal of the biofilm and scraping using several different protocols. There was no formation and removal of biofilm. Twenty-five implants of the Singular Implants® brand (Parnamirim, Brazil) were divided into 05 groups: G1 control- C (n = 5), G2 Ultrasound- US (n = 5), G3 Stainless Curette- INX (n = 5), G4 Teflon®-TF curtain (n = 5), G5 Laser-L (n = 5). Scraping was performed on the first three turns of the G2, 3 and 4 implants. The G5-L received irradiation with Laser Er: YAG (50 J, 1.5 W, 30 Hz). After the procedures, the implants were evaluated in SEM (1500–3000 X). It can be observed that in G4-TF there was no change in surface morphology and roughness, however residues of TF were deposited on the surface; in G3-INX important morphological changes were observed, with impression on the titanium of parallel striations typical of the use of curettes; in G5-L, flattening of the roughness peaks was observed, but not in the valleys; in G2-US several morphological changes were observed: total kneading of the roughness in some areas and fine scratches in others. It is concluded that of the protocols used, the least harmful to roughness was the laser, followed by stainless steel curettes and ultrasound. Teflon curettes did not change the surface roughness, but added material residues to the surface.

Keywords

Dental implants • Peri-implantitis • Ultrasound • Laser • Curettes

1 Introduction

In 1954, Branemark discovered, indirectly, through his classic study that checked blood circulation in rabbit tibias, what he called osseointegration. This allowed for further research on animal models, leading to results that enabled the treatment of edentulism, using prostheses connected to dental implants [1]. The osseointegration process is decisive for obtaining success in prosthetic rehabilitation of totally or partially edentulous edges, using dental implants. Direct and stable contact between the implant and the surrounding bone determines this success [2]. Effective osseointegration is dependent on characteristics such as implant shape (macroscopic and microscopic), titanium quality surface and its chemical-biological interaction with bone tissue [3, 4]. Characteristics such as topography, wettability, surface load and surface chemical composition, in contact with bone tissue, define the speed and quality of osseointegration. These properties provide bone-implant interactions, such as ionic adsorption, protein absorption, communication between cells and implant surface, in addition to signaling for differentiation of these cells, leading to the union of the biomaterial with the bone [5, 6]. Surface treatment

D. P. V. Leite (✉) · G. E. Pires · A. T. Araki
Dentistry Post Graduation Program, Universidade Cruzeiro do Sul, Galvão Bueno Street, 868 – Liberdade, São Paulo, 01506-000, Brazil

M. H. B. Machado · A. Baptista · R. S. Navarro
Bioengineering Post Graduation Program, Universidade Brasil, São Paulo, Brazil

A. L. Sant'ana · A. M. eSilva · J. E. P.Nunes · R. S. Navarro
Biomedical Engineering Post Graduation Program, Universidade Brasil, São Paulo, Brazil

F. V. Bastos
Dentistry Post Graduation Program, Universidade Anhanguera, São Paulo, Brazil

L. Frigo
Dentistry Post Graduation Program, Universidade Guarulhos, Guarulhos, Brazil

T. F. Bastos-Filho et al. (eds.), *XXVII Brazilian Congress on Biomedical Engineering*, IFMBE Proceedings 83, https://doi.org/10.1007/978-3-030-70601-2_9

techniques have been proposed in order to create a biochemical union capable of accelerating the initial phases of bone neoformation on the implant [4, 7].

The purpose of this in vitro study was evaluated the damage caused to the surface of dental implants after different conditions of simulation of mechanical removal of the biofilm and scraping using several different protocols.

2 Material and Methods

This is a comparative in vitro study to evaluate the damage caused to the surface of dental implants after the simulation conditions of mechanical removal of the biofilm and scraping using several different protocols. There was no formation and removal of biofilm. Twenty-five sterile implants from the Singular Implants® brand (Parnamirim-RN, Brazil) were divided into 5 groups: G1 control (n = 5), G2 Ultrasound (n = 5), G3 Stainless Curette (n = 5), G4 Teflon® curette (n = 5), G5 Er:YAG Laser (n = 5).

To perform the laboratory study, dental implants were attached to implant support braces to perform a simulation of the clinical scraping and cleaning procedure to assess damage to the implant surface. Treatments were performed on the first three turns of the implants (Fig. 1). In the control group (G1) no treatment was performed, in the Groups 2 and 3 were performed scraping with different types of curettes, in the Group 4 scraping with ultrasound was performed in P mode (Periodontics) at intensity 3, in the Group 5 received irradiation with an Er:YAG high power laser in the parameters: 50 J, 1.5 W, 30 Hz. After performing the procedures, the implants were evaluated in SEM (1500 X and 3000 X) at the LCT-POLI/USP-SP laboratory.

Fig. 1 Illustrative image of laboratory performance of the treatment on the implant surface

3 Results

It was observed that in G4 Teflon® there was no morphological change in the roughness, but Teflon® residues were blunted on the surface; in the G3 Inox, important morphological changes were noted, with printing on the titanium of parallel striations typical of the use of curettes; in the G5-Laser, flattening of the roughness peaks was observed, but not in the valleys; in G2-ultrasound, more varied morphological changes were observed: total kneading of the roughness in some areas and fine scratches in others (Fig. 2).

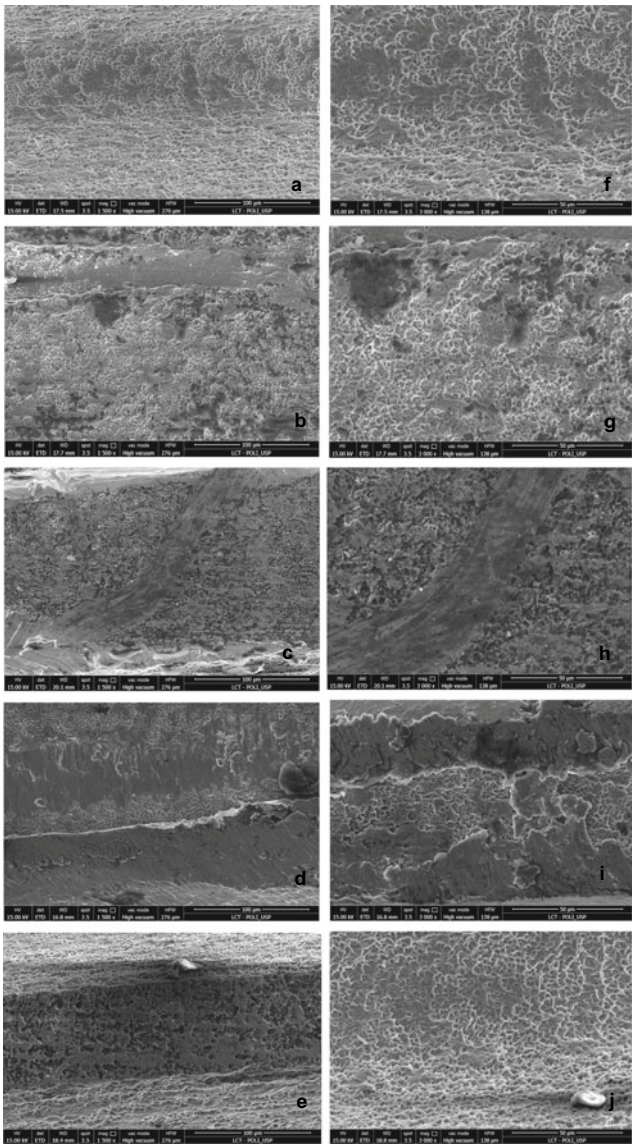

Fig. 2 Representatives SEM photomicrographs of the surface morphology of the implants after different treatments. A: G1 control, B: G2 Ultrasound; C: G3 Stainless Curette; D: G4 Teflon® curette; E: G5 Laser. Original magnification at 1500X. F: G1 control, G: G2 Ultrasound; H: G3 Stainless Curette; I: G4 Teflon® curette; J: G5 Laser. Original magnification at 3000X

4 Discussion

Effective osseointegration is dependent on characteristics such as implant shape, titanium quality and its chemical-biological interaction with bone tissue. This analysis will guide appropriate clinical choices, providing better quality and speed to osseointegration [3, 4]. These properties provide bone-implant interactions with tissues leading to the union of the biomaterial with the bone [5, 6]. Surface treatment techniques have been proposed in order to create a biochemical union capable of accelerating the initial phases of bone neoformation on the implant [4, 7].

The purpose of this in vitro study was evaluated the damage caused to the surface of dental implants after different conditions of simulation of mechanical removal of the biofilm and scraping using several different protocols**.**

According to Louropoulou et al. [8], dental implants must integrate with three different types of tissues: epithelial, connective and bone, so that they can, in a predictable way, be really durable. For Davies [9], there are several factors that influence the success of the dental implant, these being the primary stability, quality and bone quantity [9]. Sangata [10] states that primary stability is essential for osseointegration, therefore, an implant with high primary stability will be successful and the opposite will lead to the failure of this implant. For Goiato et al. [11], the factors that influence osseointegration are bone density, the location of the implant in the maxilla and/or mandible and the length of the implant, so that primary stability was not considered as the main requirement for osseointegration.

For Thakral et al. [11], texturing techniques in dental implants can influence the establishment of osseointegration, both for cell differentiation, after implant insertion, and in the calcified bone matrix. Also according to Wennerberg and Albrektsson [12], the treated surfaces result in greater bone/implant contact (BIC), in relation to smooth implants. Thus, implants with textured surfaces are indicated for locations with lower BIC at the end of surgery. In contrast, Att et al. [13] state that the bone is deposited indistinctly on porous or smooth surfaces. Thus, porosity, then, would not be a necessary condition for bone apposition to occur. Park et al. [14] and Yan et al. [15] showed that Ti implants covered with hydroxyapatite spray plasma had a greater amount of bone at the bone/implant interface, when compared to implants with a smooth surface. According to De Groot et al. [16], hydroxyapatite spray plasma implants have been extensively studied and considered to have high potential for osseointegration. The force used to remove HA-coated implants in the bed requires 55 MPa in 3 months and 62 MPa in 6 months, which suggests high bone remodeling.

With the aid of scanning microscopy, it was identified that each surface accumulated a different amount of organic and inorganic matter in the formation of bone matrix. This suggests that cellular responses occur regardless of the physicochemical properties of surface conditioning [17]. In this line of reasoning, Rupp et al. [16] confirm that the SLActive and SLA surfaces did not show any apparent differences when both had the same topography, however, statistically significant differences were observed with two or four weeks of BIC repair (bone/implant contact). This reports that the changes were not the result of topography, but that they probably occurred due to changes in chemical structures [18]. Proving the study by Rupp et al. [18], a new study carried out in Sweden by Oates et al. [19] demonstrated that the increase in the speed of bone formation can influence the stability of the implant. The SLA and SLActive surfaces were analyzed using a resonance frequency for osseointegration. The authors noted that the transition time from primary stability to secondary stability was two weeks for SLActive surface and four weeks for SLA. These results demonstrate that the speed of bone formation directly influences the stability of the implant [18]. Huang et al. [19] studied the effect of chemical and nanotopographic changes in the early stages of osseointegration. The sandblasting surface modifications with Ti oxide, fluoride treatment and modifications with nanohydroxyapatite were investigated, analyzed by means of removal torque and histological analyzes after four weeks. Analyzes of SEM images indicated the presence of nanostructures on chemically modified implants, confirming the presence of Ti, O_2, C and N in all studied groups. The removal torque was higher for implants with chemical nanotopographic modifications. It is concluded that nanotopographically modified surfaces produced a differentiated surface with greater bone apposition, thus explaining the greater results for removal torque on that surface [19]. In the preset study, the Fig. 2 demonstrated that in the group 4 Teflon® there was no morphological change in the roughness, but Teflon residues were blunted on the surface; in group 3 Inox important morphological changes were noted, with imprint on the titanium of parallel streaks typical of the use of curettes; in Group 5 Laser there was a flattening of the roughness peaks, but not of the valleys; in group 2 Ultrasound the most varied morphological changes were observed: total kneading of the roughness in some areas and fine scratches in others.

5 Conclusion

Based on the findings, it can be concluded that all tested protocols for scraping and simulation of biofilm removal, promoted changes in the surface of implants. The treatment with Er:YAG laser promoted less roughness and morphological damages, followed by stainless steel curettes and ultrasound.

Acknowledgements The authors thank the Universidade Cruzeiro do Sul.

Conflict of Interest The authors declare that they have no conflict of interest.

References

1. Albrektsson T, Pi B, Ha H, Lindstrom J (1981) Osseointegrated titanium implants. Requirements for ensuring a long-lasting, direct bone-to-implant anchorage in man. Acta Orthop Scand 52:155–170
2. Vargas E, Dw B, Cl S (2006) Beneficial neurocognitive effects Bernardes SR, Claudino M, Sartori IAM. Análise fotoelástica da união de pilar a implantes de hexágono externo e interno. Implant News 3:355–359
3. Pi B (1983) Osseointegration and its experimental background. J Prosth Dent 50:399–410
4. Skalak R (1988) Stress transfer at the implant interface. J Oral Implantol 13:581–593
5. Ce M (1999) Implant design considerations for the posteriorregions of the mouth. Imp Dent 8:376–385
6. Kasemo B, Lausmaa J (1988) Biomaterial and implant surfaces:on the role of cleanliness, contamination, and preparation procedures. J Biomed Mater Res 22:145–158
7. Buser D, Nydegger T, Oxland T, Dl C, Rk S, Hp H et al (1999) Interface shear strength of titanium implantswith sandblasted and acid-etched surface: a biomechanical study in the maxilla of miniature pigs. J Biomed Mater Res 45:75–83
8. Louroupou A, Vander W (2015) Influence of mechanical instruments on the biocompatibility of titanium dental implants surfaces: a systematic review. Clin Oral Implants Res 26:841–850
9. Je D (1998) Mechanisms of endosseous integration. Int J Prosthodont 11:391–401
10. Sangata M (2010) Immediate loading of dental implant after sinus floor elevation with osteotome technique: a clinical report and preliminary radiographic results. J Oral Implantol 36:485–489
11. Thakral G, Thakral R, Shrama N, Seth J, Vashisht P (2014) Nanosurface the future of implants. J Clin Diagn Res 8:07–10
12. Att W, Yamada M, Ogawa T (2009) Effect of titanium surface characteristics on the behavior and function of oral fibroblasts. Int J Oral Maxillofac Implants 24:419–431
13. Park EJ, Song Yh, Hwnag MJ, Song HJ, Park YJ (2015) Surface characterization and osteoconductivity evaluation of micro/nano surface formed on titanium using anodic oxidation combined with H_2O_2 etching and hydrothermal treatment. J Nanosci Nanotechnol 15:6133–6136
14. Yan J, Jf S, Pk C, Han Y, Ym Z (2013) Bone integration capability of a series of strontium-containing hydroxyapatite coatings formed by micro-arc oxidation. J Biomed Mater Res 101:2465–2480
15. De Groot K, Geesink R, Cpa K (1987) Plasma sprayed coatings of hydroxylapatite. J Biomed Mat Res 21:1375–1381
16. Rupp F, Ra G, Scheideler L, Marmur A, Boyan Bd, Schwartz Z et al (2014) A review on the wettability of dental implant surfaces I: theoretical and experimental aspects. Acta Biomater 10:2894–2906
17. Tw O, Valderrama P, Bischof M, Nedir R, Jones A, Simpson J et al (2007) Enhanced implant stability with a chemicallymodified SLA surface: a randomized pilot study. Int J Oral Maxillofac Implants 22:755–760
18. Huang Y, He J, Gan L, Liu X, Wu Y, Wu F, Gu ZW (2014) Osteoconductivity and osteoinductivity of porous hydroxyapatite coatings deposited by liquid precursor plasma spraying: *in vivo* biological response study. Biomed Mater 9:065007
19. Ke H, Ducheyne P (1992) Hydration and preferential molecular absorption on titanium in vitro. Biomaterials 13:553–647
20. Wennerbeg A, Albrektsson T (2009) Effects of titanium surface topographyon bone integration: a systematic review. Clin Oral Impl Res 20:172–184

Comparison of Hemodynamic Effects During Alveolar Recruitment Maneuvers in Spontaneously Hypertensive Rats Treated and Non-treated with Hydralazine

L. C. Ferreira, R. L. Vitorasso, M. H. G. Lopes, R. S. Augusto, F. G. Aoki, M. A. Oliveira, W. Tavares-Lima and H. T. Moriya

Abstract

This article aims to evaluate the behavior of the arterial pressure response during alveolar recruitment maneuvers in spontaneously hypertensive rats (SHR). Such study can lead to a better understanding of arterial pressure behavior, which is relevant in the context of hypertension being a health condition. The animals were separated into groups: with and without Hydralazine treatment (20 mg/kg dissolved in drinking water) and two ages (17 weeks—2 weeks treatment and 21 weeks—6 weeks treatment). For the experiment, the animals were anesthetized, tracheostomized and connected to a small animal ventilator (*flexiVent* legacy, SCIREQ, Canada). The animals were connected to a custom-built arterial pressure monitor device. Arterial pressure and volume of the respiratory system were analyzed during two consecutive alveolar recruitment maneuvers. The results indicated that there is no statistically significant difference in arterial pressure during alveolar recruitment maneuvers, although respiratory system volume showed significant difference ($p < 0.0001$, ANOVA) among different groups. Regarding the percentage comparison between the period before ARM and the second ARM, there was statistical ($p < 0.0001$, ANOVA) difference in 17 weeks treated versus 21 weeks non-treated and 21 weeks treated versus ($p > 0.05$ for all). These findings could indicate that the drug, with the present dose and administration time, was not sufficient to decrease the basal pressure, however it influenced on the cardiovascular response during alveolar recruitment. Since there was no difference in the total air volume displacement in alveolar recruitment maneuvers among groups, the explanation to the influence on the cardiovascular response during alveolar recruitment is solely related with the cardiovascular system.

Keywords

Arterial pressure • Alveolar recruitment maneuver • Hydralazine • Hypertension • Rats

1 Introduction

Arterial Hypertension (AH) is a cardiovascular disease that affects the health system globally [1,2]. In the 2000s, 26.4% of the world's adult population had hypertension. This number becomes even higher in the forecast for the year 2025, where 29.2% of people will be affected by the condition [3]. Currently, in Brazil, about 35% of the population over 40 years old suffers from heart problems related to increased arterial pressure. To reduce this number, it is possible to use antihypertensive drugs to prevent or treat the condition, since its efficiency compared to non-pharmacological treatments is approximately 5 times greater [2,4].

Animal model studies of AH have been very useful in understanding this pathology. Such studies aim to better understand the pathophysiology of AH in humans, by reproducing this condition in animal models in order to observe their hemodynamic response. Data obtained from these researches can later on be useful in translational medicine [5,6]. In addition, hypertensive behavior and its hemodynamic parameters have been occasionally studied associated with mechanical ventilation [7,8] and in comparison studies involving normotensive individuals [9].

L. C. Ferreira (✉) · R. L. Vitorasso · M. H. G. Lopes · R. S. Augusto · H. T. Moriya
Biomedical Engineering Laboratory, Escola Politécnica of the University of São Paulo, Av. Prof. Luciano Gualberto, 380-Cidade Universitária, São Paulo/SP, Brazil

F. G. Aoki
Institute of Science and Technology, Federal University of São Paulo, São José dos Campos/SP, Brazil

M. A. Oliveira · W. Tavares-Lima
Department of Pharmacology, Institute of Biomedical Sciences, University of São Paulo, São Paulo/SP, Brazil

T. F. Bastos-Filho et al. (eds.), *XXVII Brazilian Congress on Biomedical Engineering*, IFMBE Proceedings 83, https://doi.org/10.1007/978-3-030-70601-2_10

Alveolar Recruitment Maneuver (ARM) is normally used in mechanical ventilation as a short-term increase in airway pressure in order to recruit collapsed alveoli [10,11]. This technique is used in clinical practices and also in studies of ventilatory mechanics [12]. There are several techniques of recruitment maneuvers discussed in the literature [13], but it is known that this technique can prevent the collapse of alveolar units, thus increasing the available lung area for an effective gas exchange and better arterial oxygenation, through an insufflation pressure corresponding to the total lung capacity applied repeatedly for a period of time [13–16].

Since one of the characteristics of antihypertensive drugs is decreasing the effects of AH through vasodilation [3,4], it is expected that its use could be beneficial in these conditions when associated with the use of lung ventilation through ARM, which means having a significant decrease in arterial pressure, although the ARM promotes an increase in lung volume, that can affect the arterial pressure measurements due to lung expansion.

The present study aimed to evaluate the arterial pressure behavior during the performance of ARMs in two groups of Spontaneously Hypertensive Rats (SHR) for the purpose of understanding the consequences of treatment with antihypertensive substance and how it affects the hemodynamic response of animals. These groups were divided into two categories: rats treated with the antihypertensive drug hydralazine and those that were not treated.

2 Materials and Methods

2.1 Animals

SHR (n = 36) were used for this research. Hydralazine-treated (n = 20, 20 mg/kg dissolved in drinking water) and non-treated (n = 16, naïve) animals were divided into two groups according to their age: 17 weeks old (hydralazine-treated, n = 12, and non-treated, n = 10) received a 2-week treatment, and 21 weeks old (hydralazine-treated, n = 8, and non-treated, n = 6) received a 6-week treatment (Table 1).

During the procedure, the animals were anesthetized with an intravenous (i.v.) injection of ketamine (110 mg/kg) and xylazine (10 mg/kg).

Table 1 Groups of animals

Group	Age (weeks)	n	Weight (g)
Treated with hydralazine	17	12	308.5±28.3
Treated with hydralazine	21	8	333.8±42.1
Non-treated	17	10	331.9±40.9
Non-treated	21	6	347.0±39.2

2.2 Experimental Protocol

A 2.5 cm long 14G cannula was inserted into the animal's trachea (Höppner, Brazil), which was connected to a small animal ventilator (SAV) (*flexiVent* legacy, SCIREQ, Canada) and ventilated with a tidal volume of 10 mL/kg, respiratory rate of 120 cycles per minute and PEEP (Positive end-expiratory pressure) of 3 cmH_2O. Although smaller tidal volumes are used for protective mechanical ventilation, higher tidal volumes are also applied for evaluating physiological parameters [17–19]. Through SAV the respiratory system volume was measured. The jugular vein was dissected and then a flexible PVC tube (Critchley Electrical Products PTY, Australia) was inserted during ventilation. Furthermore, the right carotid artery was cannulated with a polyethylene catheter to measure the animal's arterial pressure. The respiratory musculature was blocked with pancuronium bromide (1 mg/kg i.v.). After that, the standard SAV protocol for ARM was performed [18], which consists in two alveolar recruitment maneuvers up to 30 cmH_2O (the pressure was increased in ramp for 3 seconds until it reached 30 cmH_2O and then maintained at this pressure for another 3 seconds) with an interval of 5 seconds between the two ARMs.

2.3 Data Acquisition

An analog to digital 24-bit converter module (HX711, Avia Semiconductor, China) was used to acquire arterial pressure data with an invasive arterial pressure sensor (New NPC 100 Sensor, Amphenol, USA). A custom-made software routine was implemented in order to perform the calibration of the device using as references pressures 0 mmHg and 200 mmHg, to which the device was subjected through a mercury column. The data were exported at a rate of 50 samples per second and with a resolution of 0.01 mmHg.

The data output from SAV provided the airway pressure and tracheal volume signals with a sampling frequency of 256 Hz.

2.4 Data Analysis

Arterial pressure data were treated using the Tukey criterion for outlier detection [20]. Then, in order to facilitate the visualization of the stabilization segments, the signal was filtered through a moving average with 21 samples in length ($N = 21$ in Eq. (1)).

$$PA_i = \frac{1}{N}\sum_{j=1}^{N} PA_{i+j} \tag{1}$$

After filtering the arterial pressure signal, certain sections were selected for analysis: Before ARM and during ARM (in order to adopt a standard, we selected 1 s in the three mentioned sections), since the objective is to evaluate if hydralazine treatment promotes a significant impact on arterial pressure decrease, and, if so, when this impact is more critical (before or during the recruitment). The absolute arterial pressures of the animals before and during ARM were then compared in terms of percentages.

A statistical package (Prism 8, GraphPad Software, USA) was used. For the analysis of tracheal volumes in the different groups studied, during ARM, we used Two-Way ANOVA (ANOVA—Analysis of Variance), with Bonferroni *post-hoc*. Regarding the arterial pressure data, the data were submitted to a normality test (Shapiro-Wilk) and in case of adherence to the normal distribution curve, parametric analysis (One-Way ANOVA) or non- parametric (Kruskal-Wallis) was used. For such analyses, statistical significance of $p < 0.05$ was adopted.

3 Results

Figure 1 shows the profile of a representative arterial pressure measurement during data collection. It is possible to notice the absence of stabilization (plateau) during the first ARM.

Regarding the measured respiratory system volumes (Fig. 2), between the first and second ARMs, a significant difference was verified ($p < 0.0001$). In terms of *post-hoc* analysis, significant difference between ARMs was found on the following groups: 17 weeks and 21 weeks treated, and 21 weeks non treated ($*p < 0.05$).

The graphs on Fig. 3 represent the absolute values of arterial pressure before the second ARM (a), the absolute values of arterial pressure during the second ARM (b) and the percentage of arterial pressure decrease during ARM (c). In terms of absolute values of arterial pressure before ARM, there was no significant difference among the groups observed, both for analysis of variance and *post-hoc* analysis. For absolute values of arterial pressure during ARM, the analysis of variance showed a significant difference among the groups observed ($p < 0.05$), while in the *post-hoc* analysis there was no significant difference among groups ($p > 0.05$). Regarding the percentage comparison between the period before ARM and the second ARM, a significant difference was observed between the groups in the analysis of variance ($p < 0.05$). It was found statistical difference in 17 weeks treated versus 21 weeks non-treated and 21 weeks treated versus 21 weeks non-treated comparisons ($p > 0.05$).

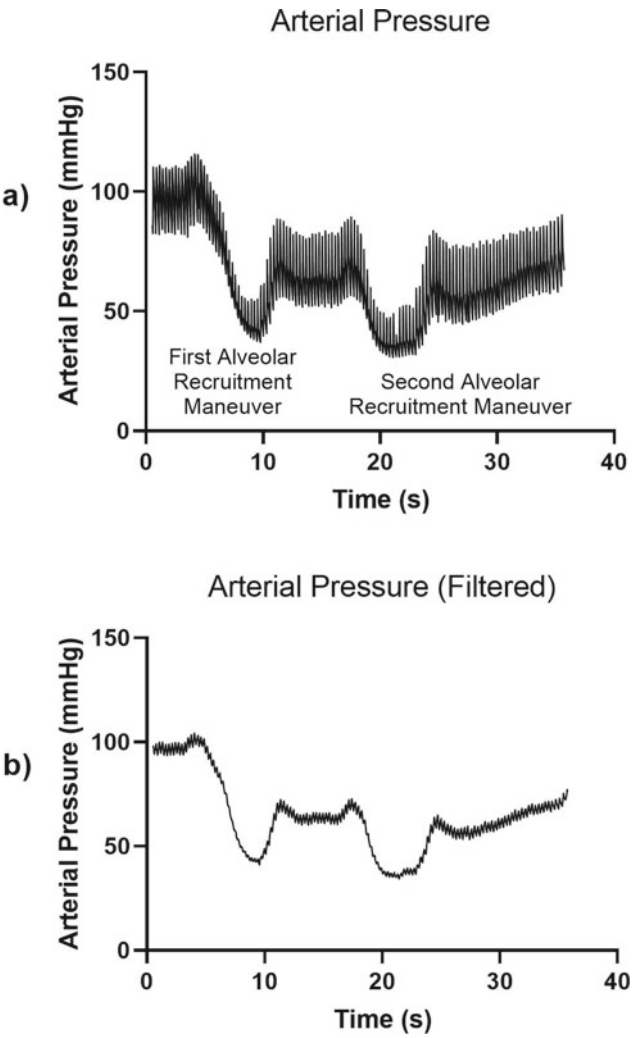

Fig. 1 Arterial pressure behavior during the alveolar recruitment maneuvers. Graph **a** is the signal extracted from the custom-built arterial pressure measurement device and **b** is the same signal after being filtered by a moving average of 21 samples

4 Discussion

In our study, we aimed to verify a possible influence of the ARM on arterial blood pressure using a strain of SHR, commonly used in arterial hypertension research [21–23]. The ARM is often used in animal models to homogenize lung volume history prior to assessment of respiratory mechanics procedures. Clinically, this technique is used to improve oxygenation by opening previously collapsed airways [24].

Since the arterial pressure is a vital signal and the alveolar recruitment may present cardiovascular repercussions [12,25] such as hypotension, the main objective of this work was

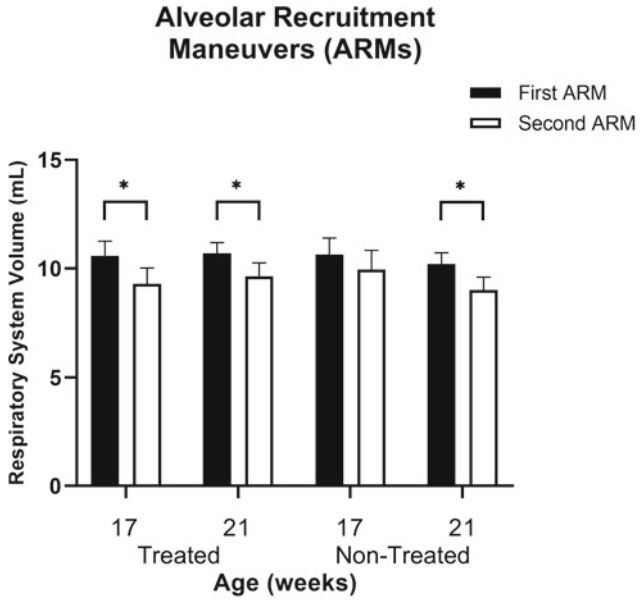

Fig. 2 Comparison between ARM volumes (information expressed in terms of means and standard deviations), where there was significant difference between the first and second ARMs in the analysis of variance ($p < 0.0001$, Two-way ANOVA). In *post-hoc* analysis, there was significant difference between ARMs on the following groups: 17 weeks and 21 weeks treated, and 21 weeks non treated ($*p < 0.05$)

to study the arterial blood pressure in SHR during alveolar recruitment.

In order to collect the data in a standardized way, it was decided to use the second ARM instead of the first to which the animals were submitted. This is because during the first ARM, not all animals showed arterial pressure stabilization, making it not possible to collect physiologically relevant information in this context (Fig. 1).

It was found that, statistically, the volume displacement of the respiratory system during the second ARM was lower than the first ARM (Fig. 2). The hypothesis is that this happens because between the first and the second ARM there is not enough time to reach Functional Residual Capacity (FRC), thus the remaining volume above FRC of the first ARM influences the volume measured in the second ARM. This phenomenon may influence on the assessed compliance/elastance, once the compliance may be obtained simply dividing the volume displacement by the difference in pressure.

Besides the volume displacement repercussion, this work studied the arterial blood pressure during those maneuvers. There was no difference in the basal arterial pressure among treated and non-treated in different age animal groups (Fig. 3).

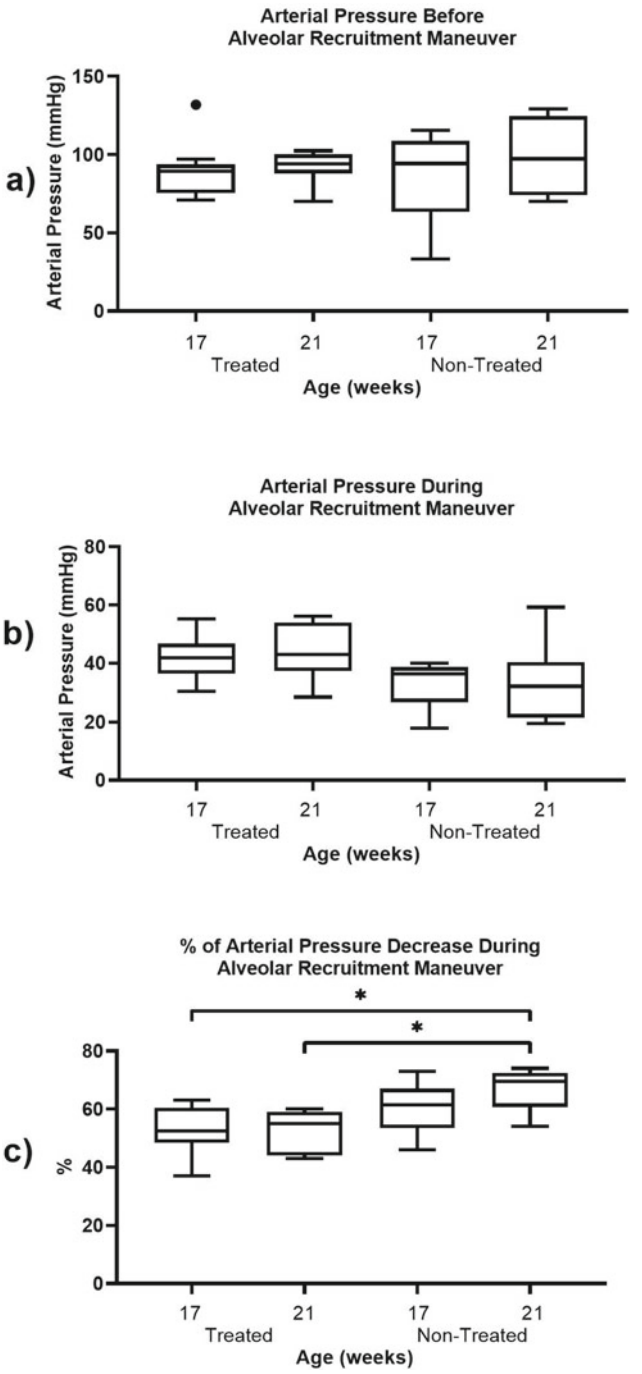

Fig. 3 Arterial pressure comparisons. **a** Absolute arterial pressure value before ARMs ($p > 0.05$, ANOVA). **b** Absolute arterial pressure value during the second ARM ($p < 0.05$, ANOVA). In *post-hoc* analysis, no significant differences were observed **c** pressure decrease percentage when comparing the period before the two ARMs and the pressure value during the second ARM ($p < 0.05$, ANOVA). $*p < 0.05$

This finding was not expected. However, one possible explanation is related with the hydralazine administrated time and dose. Notwithstanding, the pressure during recruitment was not different among groups in post-hoc analysis, only in the analysis of variance, despite being, visually (Fig. 3), lower in the non-treated groups.

However, the treated groups presented a lower decrease during the recruitment, which is a desirable physiological response. Thus, the treated groups cardiovascular system was less impacted by the intrinsic transitory hypotension during ARM than the non-treated groups. The arterial blood pressure is directly influenced by the recruitment since the heart is mechanically compressed within the lung expansion, hence impacting on the amount of blood entering in the atrium and on the output blood resistance [26].

These findings could indicate that the drug, with the present dose and administration time, was not sufficient to decrease the basal pressure, however it influenced on the cardiovascular response during alveolar recruitment. Since there was no difference in the total air volume displacement in ARMs among groups (Fig. 2), the explanation to the influence on the cardiovascular response during alveolar recruitment is solely related with the cardiovascular system. Therefore, the cardiovascular compliance or resistance rather than the respiratory compliance played a major role on the results found herein.

5 Conclusion

There was no difference in basal arterial blood pressure between treated and non-treated animals with the present hydralazine doses and time set. However, the treated groups cardiovascular system was less impact by the intrinsic transitory hypotension during ARM than the non-treated groups which is a desirable physiological response. Furthermore, since there was no difference in the total air volume displacement in ARMs among groups, the explanation to the influence on the cardiovascular response during alveolar recruitment is solely related with the cardiovascular system.

6 Compliance with Ethical Requirements

6.1 Conflict of Interest

The authors declare that they have no conflict of interest.

6.2 Statement of Human and Animal Rights

All experiments involving laboratory animals were evaluated and approved by the "Ethics Committee for Animal Use" of the Institute of Biomedical Sciences of the University of São Paulo (CEUA protocol number 1936211117)

The procedures comply with Law number 11794 (08/10/2008), which regulates all research activities involving the use of animals in Brazil.

Acknowledgements This study was financed in part by the Coordenação de Aperfeiçoamento de Pessoal de Nível Superior (CAPES—Brazilian Coordination for the Improvement of Higher Education Personnel)—Brazil—Finance Code 001 (88882.333348/2019-01) and the Conselho Nacional de Pesquisa e Desenvolvimento Científico e Tecnológico (CNPq—Brazilian National Council of Scientific and Technological Development)—Brazil (308298/2016-0 and 408006/2016-1).

Conflict of Interest The authors declare that they have no conflict of interest.

References

1. Castrillón-Spitia JD, Franco-Hurtado A, Garrido-Hernández C et al (2018) Utilización de fármacos antihipertensivos, efectividad e inercia clínica en pacientes. Rev Colomb Cardiol 25(4):249–256
2. Souza AC, Borges JWP, Moreira TMM (2016) Qualidade de vida e adesão ao tratamento em hipertensão: revisão sistemática com metanálise. Rev Saúde Pública 2016:50–71
3. Kearney P, Whelton M, Reynolds K et al (2005) Global burden of hypertension: analysis of worldwide data. The Lancet 365(9455):217–223
4. Limas C, Westrum B, Limas CJ (1984) Comparative effects of hydralazine and captopril on the cardiovascular changes in spontaneously hypertensive rats. Am J Pathol 117:360–371
5. Doggrell S (1998) Rat models of hypertension, cardiac hypertrophy and failure. Cardiovasc Res 39(1):89–105
6. Garutti I, Martinez G, Cruz P et al (2009) The impact of lung recruitment on hemodynamics during one-lung ventilation. J Cardiothoracic Vasc Anesth 23(4):506–508
7. Bento AM, Cardoso LF, Tarasoutchi F et al (2014) Hemodynamic effects of noninvasive ventilation in patients with venocapillary pulmonary hypertension Arq. Bras Cardiol 103(4):410–417
8. Zamanian R, Haddad F, Doyle R et al (2007) Management strategies for patients with pulmonary hypertension in the intensive care unit. Crit Care Med 35(9):2037–2050
9. Ferreira L, Vanderlei L, Valenti V (2014) Efeitos da Ventilação Mecânica não Invasiva sobre a Modulação Autonômica Cardíaca Revista Brasileira de. Cardiologia 27:53–58
10. Rosa RG, Rutzen W, Madeira L et al (2015) Uso da tomografia por impedância elétrica torácica como ferramenta de auxílio às manobras de recrutamento alveolar na síndrome do desconforto respiratório agudo: relato de caso e breve revisão da literatura. Rev bras ter intensiva 27(4):406–411
11. Costa DC, Rocha E, Ribeiro TF (2009) Associação das manobras de recrutamento alveolar e posição prona na síndrome do desconforto respiratório agudo. Rev Bras Ter Intensiva 21(2):197–203
12. Hartland B, Newell T, Damico N (2015) Alveolar recruitment maneuvers under general anesthesia: a systematic review of the literature. Respir Care 60(4):609–620
13. Doras C, Guen ML, Ferenc P et al (2015) Cardiorespiratory effects of recruitment maneuvers and positive end expiratory pressure in an experimental context of acute lung injury and pulmonary hypertension. BMC Pulm Med 15(2015):82
14. Pinto A, Reis M, Teixeira C et al (2015) Alveolar recruitment: who needs? how? when? Revista Médica de Minas Gerais 2015:25
15. Barbas CSV, Bueno MAS, Amato MBP et al (1998) Interação cadiopulmonar durante a ventilação mecânica. Rev Soc Cardiol Estado de São Paulo 3:28–41

16. Rodrigues YCSJ, Studart RMB, Andrade IRC et al (2012) Ventilação mecânica: evidências para o cuidado de enfermagem. Esc Anna Nery 16(4):789–795
17. Severgnini P, Selmo G, Lanza C et al (2013) Protective mechanical ventilation during general anesthesia for open abdominal surgery improves postoperative pulmonary function. Anesthesiology 118:6
18. Barros A, Takeuchi V, Fava F et al (2020) (2019) Effects of arterial and tracheal pressures during a respiratory mechanics protocol in spontaneously hypertensive rats. MEDICON 76:551–558
19. Santos C, Moraes L, Santos R et al (2012) Effects of different tidal volumes in pulmonary and extrapulmonary lung injury with or without intraabdominal hypertension. Intensive Care Med 38:499–508
20. Tukey JW (1970) Exploratory data analysis. Addison-Wesley, Reading, Massachusetts
21. Doris P (2017) Genetics of hypertension: an assessment of progress in the spontaneously hypertensive rat. Physiol Genom 49(11):601–617
22. Jennings DB, Lockett HJ (2000) Angiotensin stimulates respiration in spontaneously hypertensive rats. Regul Integr Phys 287(5):R1125–R1133
23. Iriuchijima J (1973) Cardiac output and total peripheral resistance in spontaneously hypertensive rats. Jpn Heart J 14(3):267–272
24. Reiss LK, Kowallik A, Uhlig S (2011) Recurrent recruitment manoeuvres improve lung mechanics and minimize lung injury during mechanical ventilation of healthy mice. PLoS One 6(9):1–15
25. Hess DR (2015) Recruitment maneuvers and PEEP titration. Respir Care 60(11):1688–1704
26. Lovas A, Szakmány T (2015) Haemodynamic effects of lung recruitment manoeuvres. BioMed Res Int 2015

Experimental Study of Bileaflet Mechanical Heart Valves

Eraldo Sales, M. Mazzetto, S. Bacht, and I. A. Cestari

Abstract

Biological or mechanical heart valve prostheses are used as a treatment to replace failing native heart valves. The goal of this study is to investigate the hydrodynamic performance of small sizes bileaflet mechanical heart valves (BMHVs) considering their use to control flow direction on a pulsatile pediatric ventricular assist device (VAD) [1]. Small size BMHVs of 17, 19 mm were tested in vitro and compared to 23 mm prosthesis. Each prosthesis was placed on a pulse duplicator (4–90 bpm, 2.0–4.0 L/min flow range) and pressure and flow signals were recorded to determine pressure gradient, flow regurgitation and effective orifice area (EOA). Pressure gradients (maximum/minimum; mmHg) were (12.2/8.5), (8.4/6.3) and (8.2/5.8), for 17, 19 and 23-mm, respectively. Valve effective orifice areas (maximum/minimum; cm^2) were (1.05/1.02), (1.37/1.24) and (1.55/1.35) for 17, 19 and 23-mm sizes, respectively. The regurgitation fractions (maximum/minimum; %) obtained were (6.91/5.29), (10.47/6.08), and (14.63/10.04), for 17, 19 and 23-mm sizes, respectively. The results suggest that the mechanical valves have adequate performance according to the requirements of the ISO 5840:2015 standards and that they can be used to effectively control flow direction on a pediatric pulsatile ventricular assist device.

Keywords

Hydrodynamic performance • Cardiac simulator • Artificial heart valves • Mechanical prosthesis

E. Sales (✉) · M. Mazzetto · S. Bacht · I. A. Cestari
Laboratorio de Bioengenharia, Instituto do Coracao, Hospital das Clinicas HCFMUSP, Faculdade de Medicina, Universidade de Sao Paulo, Sao Paulo, SP, Brazil
e-mail: eraldo.sales@hc.fm.usp.br

1 Introduction

The function of heart valves is to ensure that blood flow occurs unidirectionally through the cardiac chambers. When these valves fail, they need to be replaced by a cardiac prosthesis. The currently available prostheses include two main categories: mechanical valves and bioprostheses [2]. In vitro characterization of the dynamic performance of these prostheses is necessary to predict their hemodynamic behavior prior to implantation [3].

In this study, in vitro tests of BMHVs of sizes #17, #19 were performed and compared to #23 regular size valve. The minimum requirements for the hydrodynamic performance of cardiac prostheses as determined by ISO 5840:2015 are shown in Table 1 for valves of sizes 17–25 mm.

2 Materials and Methods

2.1 Experimental Set Up and Data Collection

The characterization of the hydrodynamic performance of cardiac prostheses is performed by measuring the pressure gradient and the flow through the prosthesis. We utilized a pulse duplicator ("The Shelhigh Pulse Duplicator®", Shelhigh Inc, New Jersey, USA) to simulate physiological conditions as shown in Fig. 1.

BMHV were positioned in the aortic position of the pulse duplicator adjusted to generate flows in the range of 2.0–4.0 L/min with a stroke volume of 65 ml and pulse rates varying from 40 to 90 cycles per minute. The pulse duplicator was filled with a blood analog fluid (33.33% of glycerin and 66.67% of physiological saline solution). A 25 mm BMHV (St. Jude Medical® Regent®, USA) was positioned in the mitral position of the pulse duplicator in all tests.

Flow and pressure signals were recorded using DataQ WinDaq DI-220 acquisition system (DataQ Instruments, USA) at a sampling rate of 500 samples per second per channel.

T. F. Bastos-Filho et al. (eds.), *XXVII Brazilian Congress on Biomedical Engineering*, IFMBE Proceedings 83, https://doi.org/10.1007/978-3-030-70601-2_11

Table 1 Minimum requirements for an aortic prosthesis hydrodynamic performance according to ISO 5840:2015

Parameter	Aortic				
Diameter (mm)	17	19	21	23	25
EOA (cm^2)	≥ 0.70	≥ 0.85	≥ 1.05	≥ 1.25	≥ 1.45
Regurgitation fraction (%)	≤ 10	≤ 10	≤ 10	≤ 10	≤ 15

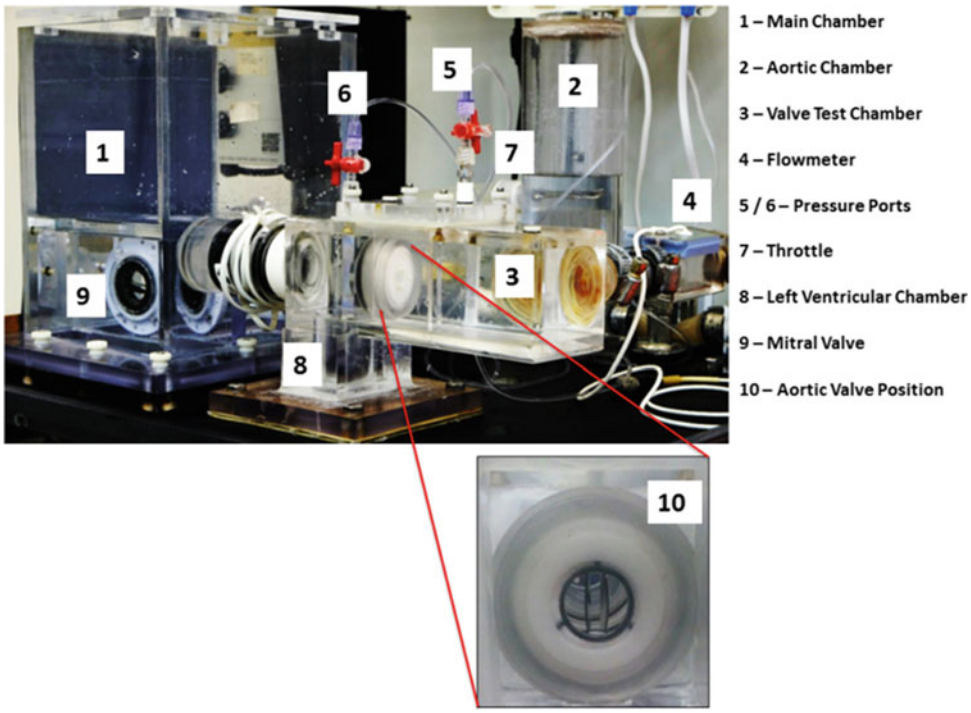

Fig. 1 Circuit for in vitro characterization of the hydrodynamic performance of mechanical valve prostheses

The pressure gradient was obtained by a differential transducer with input and output pressure ports positioned before and after the valve, respectively. The pressure gradient was calculated from the average value in the positive differential pressure signal recorded in each pulse, that is, when ventricular pressure (before the aortic prosthesis, following the flow direction) is greater than the aortic pressure (after the prosthesis).

The difference between ventricular and aortic pressure, was measured with differential pressure transducer Validyne DP15-TL (Validyne Engineering Corporation, USA) and an ultrasonic flow meter was used to measure instantaneous flow (Transonic System Inc., Transonic, USA).

Pressures in the so-called ventricular and aortic compartments of the Pulse duplicator were measured (Edwards PX12N absolute pressure transducers, Edwads LifeScience, USA).

2.2 Data Analysis

To obtain the effective orifice area, the equation proposed by Gorlin and Gorlin was used [4, 5]:

$$EOA = \frac{q_{V_{RMS}}}{51,6\sqrt{\frac{\Delta p}{\rho}}} \quad (1)$$

where Δp is the mean differential pressure (positive differential pressure, in mmHg), ρ is the density of the test fluid (g/cm^3) and $q_{V_{RMS}}$ is the root mean square of the anterograde flow (ml/s).

Pressure and flow measurements made in ten cycles were used for determination of pressure gradient, regurgitation fraction and effective orifice area for each BMHV studied. Uncertainties were determined by the standard deviation of the measures.

Root mean square of the anterograde flow along a pulse is given by:

$$q_{V_{RMS}} = \sqrt{\frac{\int_{t_1}^{t_2} q_V(t)^2 dt}{t_2 - t_1}} \quad (2)$$

where $q_v(t)$ is the pulsatile flow (ml/s) and, t_1 and t_2 are the initial and final instants of the positive differential pressure period, respectively.

Table 2 Characteristics of the BMHVs prostheses

Model	17 AHPJ-505	19 AHPJ-505	23 AHPJ-505
Type	Aortic	Aortic	Aortic
Tissue annulus diameter (mm)	17	19	23
Geometric orifice area (cm^2)	1.6	2.1	3.1
Implant height open (mm)	4.8	5.2	6.7
Overall height open (mm)	9.9	10.6	13.3
Cuff OD (standard/expanded) (mm)	23/24	25/26	29/31

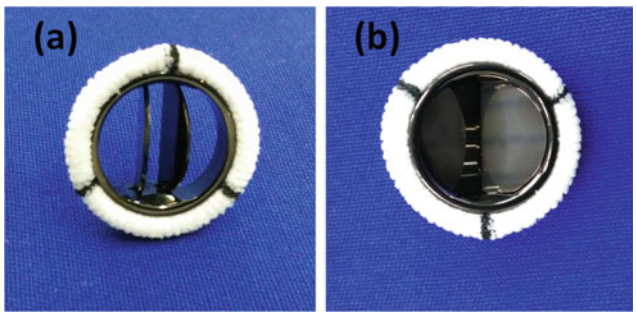

Fig. 2 BMHV in open position **(a)** and closed position **(b)**

The regurgitant fraction (R_F) as a function of closing volume (CV), leakage volume (LV) and the total forward volume (FV) is given by [5]:

$$R_F = \frac{C_V + L_V}{F_V} \cdot 100 \quad (3)$$

2.3 BMHVs

Nominal characteristics of BMHVs (St. Jude Medical® Regent®, USA) sizes #17, #19 and #23 are shown in Table 2. An image of a BMHV is shown in Fig. 2 in the fully open (a) and closed position (b).

3 Results

Figure 3 shows representative signals recorded for different flow rates (2.0–4.0 L/min). Pressure gradient values for the three evaluated prostheses are presented in Table 3.

Effective orifice areas obtained (mean ± SD) for the BMHV studied are shown in Fig. 4.

The regurgitation fractions versus flow are shown in Fig. 5 for prostheses #17, #19 and #23.

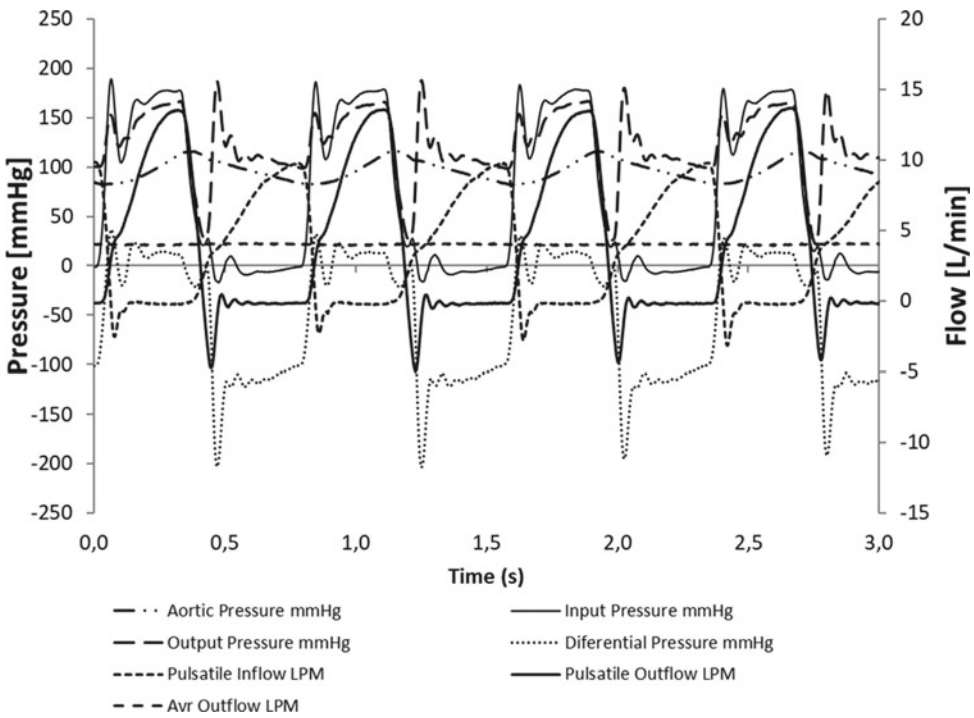

Fig. 3 Representative hydrodynamic curves for BMHV

Table 3 Pressure gradients (P, mmHg) for #17, #19 and #23 sizes BMHVs

Flow rate (L/min)	P (#17, mmHg)	P (#19, mmHg)	P (#23, mmHg)
2.0	12.2 ± 0.2	7.0 ± 0.2	5.8 ± 0.1
2.5	11.9 ± 0.1	8.4 ± 0.4	6.2 ± 0.3
3.0	9.4 ± 0.4	8.3 ± 0.3	6.6 ± 0.3
3.5	8.5 ± 0.3	6.3 ± 0.3	8.2 ± 0.5
4.0	9.4 ± 0.3	6.6 ± 0.3	7.0 ± 0.4

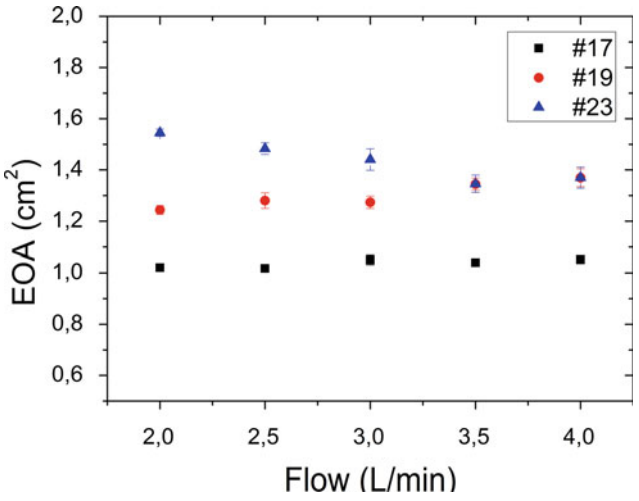

Fig. 4 Effective orifice area for #17 (1.04 ± 0.01 cm^2), #19 (1.30 ± 0.05 cm^2) and #23 (1.44 ± 0.08 cm^2) bileaflet mechanical prostheses

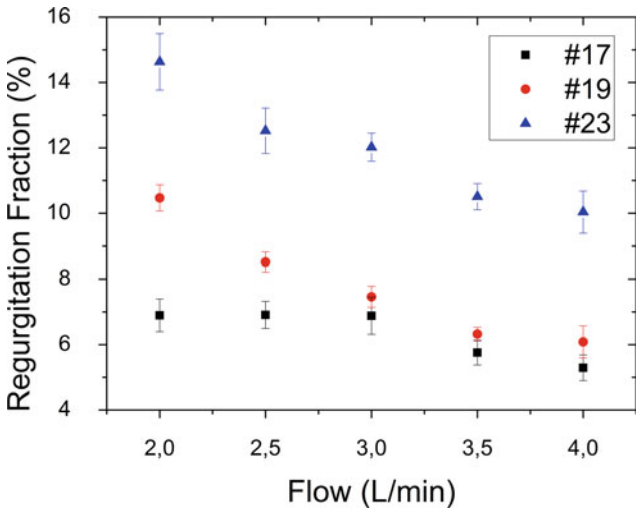

Fig. 5 Regurgitation fraction for BMHVs sizes 17 (6.4 ± 0.8%), 19 (8 ± 1%) and 23 (12 ± 2%) versus flow (L/min)

4 Discussion

There are several studies in the literature reporting the characterization of BMHVs [6, 7]. However, the performances of BMHVs of smaller sizes have not been reported. Lee et al. [8] investigated the application of 21 mm size cardiac BMHV scaled to pediatric VAD. The tests reported did not take into account the metrics of interest for the specific VAD application, including the pressure gradient, effective orifice area and regurgitant fraction. Dasi et al. [6] studied flow through a 25 mm BMHV which is suitable only for ventricular assist devices of larger volumes. Yun et al. [7] reported a model of BMHV for assessment of blood damage which was scaled in size for pediatric patients.

To the best of our knowledge there are no reports of 17 and 19 mm BMHV compatible with pediatric VADs considering the measurements of all the parameters of interest for this specific application.

According to the requirements of the ISO 5840:2015 for #17, #19 and #23 the EOA (cm^2) must be greater than or equal to 0.70, 0.85 and 1.25, respectively. The average values obtained and uncertainties were 1.04 ± 0.01 cm^2, 1.30 ± 0.05 cm^2, and 1.44 ± 0.08 cm^2, respectively. According to the same standards the regurgitation fraction must be equal or less than 10%. The average regurgitation fractions and uncertainties obtained in our measurements for #17, #19 and #23 BMHV were 6.4 ± 0.8%, 8 ± 1%, 12 ± 2%, respectively.

Both EOA and regurgitation fraction obtained demonstrate that the mechanical valves tested have adequate performance according to the minimum requirements established by ISO 5840:2015.

5 Conclusions

Three bileaflet mechanical prostheses used as replacements for heart valves were evaluated. The results showed that the hydrodynamic performance of these devices is in accordance with the requirements established by the regulatory test standards for the characterization of these prostheses (ISO 5840:2015).

Our results suggest that the BMHVs tested can be used to effectively control flow direction as needed for pediatric pulsatile ventricular assist device.

Acknowledgements We thank FAPESP (2012/5083-6), FINEP (1253/13),) and CNPQ (467270/2014-7; 311191/2017-7) for the financial support.

Conflict of Interest The authors declare that they have no conflict of interest.

References

1. Cestari IA, Mazzetto M, Oyama HT, Bacht S, Jatene MB, Cestari IN, Jatene FB (2019) Design and hydrodynamic performance of a pediatric pulsatile pump. In: Costa-Felix R, Machado J, Alvarenga A (eds) Proceedings on 26th Brazilian congress on biomedical engineering, vol 70/1. IFMBE. Springer, Singapore, pp 85–88
2. Burriesci G, Marincola FC, Zervides C (2010) Design of a novel polymeric heart valve. J Med Eng Technol 34(1):7–22
3. Rahmani B et al (2012) Manufacturing and hydrodynamic assessment of a novel aortic valve made of a new nanocomposite polymer. J Biomech 45:1205–1211
4. Gorlin R, Gorlin SG (1951) Hydraulic formula for calculation of area of the stenotic mitral valve, other cardiac valves, and central circulatory shunts. Am Heart J 41:1–29
5. Claiborne TE et al (2013) In vitro evaluation of a novel hemodynamically optimized trileaflet polymeric prosthetic heart valve. J Biomech Eng 135:021021-1–021021-8
6. Dasi LP et al (2008) Passive flow control of bileaflet mechanical heart valve leakage flow. J Biomech 41(6):1166–1173
7. Yun BM et al (2014) Computational simulations of flow dynamics and blood damage through a bileaflet mechanical heart valve scaled to pediatric size and flow. J Biomech 47(12):3169–3177
8. Lee H et al (2007) Hydrodynamic characteristics of bileaflet mechanical heart valves in an artificial heart: cavitation and closing velocity. Artif Organs 31:532–537

Preliminary Results of Structural Optimization of Dental Prosthesis Using Finite Element Method

M. M. Togashi, M. P. Andrade, F. J. dos Santos, B. A. Hernandez, and E. A. Capello Sousa

Abstract

Despite the high success rate of dental prostheses in treating patients, mechanical failures still occur. Studies about the biomechanical behaviour of dental prostheses are thus important to avoid such failures and to ensure patient's well-being. This study proposed a parametric and optimization analysis of a dental implant to investigate which implant's structural parameters are more relevant to prevent failure and improve osseointegration. A mathematical function called response surface was obtained based on Von Misses stresses in the cortical bone, RSM (Response Surface Methodology), DOE (Design of Experiments), and finite element models. A structural optimization analysis was conducted with the objective of minimizing stresses in the cortical bone. In addition to the sensitivity analysis of the parameters, a more agile process to estimate critical stress through equations was presented, providing a faster way of identifying potential failure causes.

Keywords

Biomechanics • Dental prosthesis • Finite element method • Parametric analysis • Optimization

1 Introduction

Dental prostheses are biomechanical structures responsible for restoring the mechanical function of natural and damaged/lost teeth. The use of osseointegrated implants has become a common practice in dentistry due to countless success reports. However, dental implants still present long-term problems, mostly because they are mechanical components, which are subject to failures [1].

External loads are constantly applied to the implant's system, which generates stress and strains in the implant and its surrounding bone. Within certain levels, they are beneficial and contribute to osseointegration; when they are excessive or insufficient, they can cause system instability and bone loss, affecting implant stability [2].

Studies in biomechanics present complexities, such as inhomogeneous mechanical properties and non-linear geometries, which make an analytical solution unfeasible. As a result, numerical methods, especially the Finite Element Method (FEM), are widely applied in this area [3–6]. For example, a study reported that it is possible to evaluate, with good precision, the mechanical behaviour of dental prosthesis using the Finite Element Method [7].

In order to develop new and better implants, it is necessary to investigate the influence of the different parameters that will affect the structural behaviour of the prosthesis, such as the mechanical properties of the bone and implant's design. However, if such analysis is conducted manually, by individually comparing each parameter, it certainly will be a time-consuming process. When a structural analysis becomes too complex, with different parameters and constraints, a manual analysis limits the possibility of a wider exploration of the modelling options. An alternative methodology for this analysis must then be explored [8].

One way of evaluating several parameters is through the Response Surface Methodology (RSM). RMS is a set of statistical and mathematical techniques applied in the development, improvement, and optimization of parameters [9]. The purpose of this methodology is to find a mathematical equation, via response equations or functions and based on the initial variables, so that, given a set of new independent variables, the approximate answer is

M. M. Togashi · M. P. Andrade (✉) · F. J. dos Santos · B. A. Hernandez · E. A. Capello Sousa
Department of Mechanical Engineering, Engineering College of Bauru, São Paulo State University - UNESP, Bauru, Brazil
e-mail: matheus.prevelato@unesp.br

T. F. Bastos-Filho et al. (eds.), *XXVII Brazilian Congress on Biomedical Engineering*, IFMBE Proceedings 83, https://doi.org/10.1007/978-3-030-70601-2_12

instantaneously found. RSM uses the Design of Experiments (DOE) technique to create the response surface. The DOE is based on experimenting several combinations of parameters and measuring the responses provided. Each experiment, with a specific combination of parameters, is then translated to the finite element models and the output results are used to create the response curve [10].

This study presents the preliminary results of an optimization analysis of a dental prosthesis and an analysis of the influence of the main structural parameters in the implant structural behaviour using the Finite Element Method and the Response Surface Methodology.

2 Materials and Methods

The finite element model developed in this study is similar to the prosthesis used elsewhere [11]. The prosthesis consists of a Branemark single implant (Nobel Biocare−Götemburg, Sweden), in which a 5 mm abutment (Nobel Biocare −Götemburg, Sweden) was screwed in with a titanium screw. A prosthetic crown, composed of a cobalt–chromium (Co–Cr) alloy and coated with a feldspathic ceramic (CNG solutions prosthetics, São Paulo, SP, Brazil), was placed on the top of the abutment, using another titanium screw.

A previously developed finite element (FE) model of the mandible, containing both cortical and cancellous bone, was used to insert the implant and its components [12]. The mandibular bone was then imported into the finite element software Ansys (Ansys 15.0, Swanson Analysis System, Houston, Pa, USA). A hole was made in the bone through Boolean operation, which consists of generating a cylinder with the same diameter of the implant in the centre of the bone and then extracting this volume from the bone, generating a hole, making it possible to insert the implant in it.

The internal components of the prosthesis (implant, screws and abutment) were modelled directly in the finite element software, using the programming language APDL (Ansys Parametric Design Language). The crown geometry was obtained through 3D scanning and CAD manipulation [12]. The outer (feldspathic porcelain) and the inner layer (Co–Cr alloy) of the crown were built based on micro-CT images. The central hole in the crown (to place the screws) was also obtained by Boolean operation. Figure 1 illustrates the final volume of the prosthesis into the bone.

After modelling of the geometry, homogeneous, isotropic and linearly elastic material properties were applied to each component, as shown on Table 1.

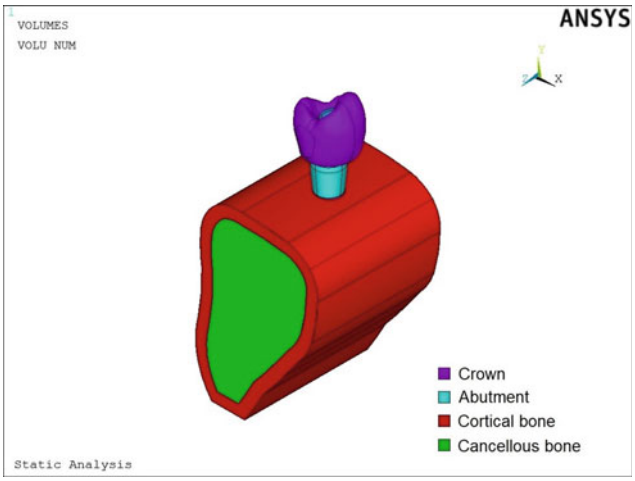

Fig. 1 Final structure composed of the prosthesis incorporated into the bone

Table 1 Properties of the components used in the model

Material	Young's modulus (GPa)	Poisson's coefficient	References
Cortical bone	14	0.3	[13]
Cancellous bone	1	0.3	[13]
Implant	110	0.34	[14]
Abutment	110	0.34	[14]
Fixation screw	100	0.34	[14]
Abutment screw	100	0.34	[14]
Metallic crown	218	0.33	[15]
Ceramic crown	68.9	0.28	[16]

The element SOLID187 was used to discretize the components in the FE software. It is a solid 3D quadratic element, with ten nodes and three degrees of freedom per node. After generating the mesh, a load of 75 N was applied in the negative direction of the y-coordinate (vertical) on top of the crown. Movement restrictions were applied in all degrees of freedom in the mandibular bone in order to simulate its real fixation. Such configuration is illustrated in Fig. 2.

Contact elements were inserted into the sharing surfaces between implant and abutment and between abutment and crown. Preloads of 100 N mm and 200 N mm were applied to the implant and crown screws, respectively, to simulate the tightening torque.

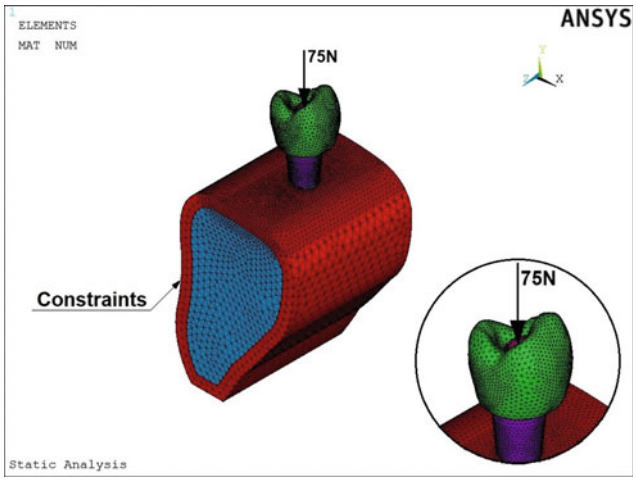

Fig. 2 Discretized volume and loading application

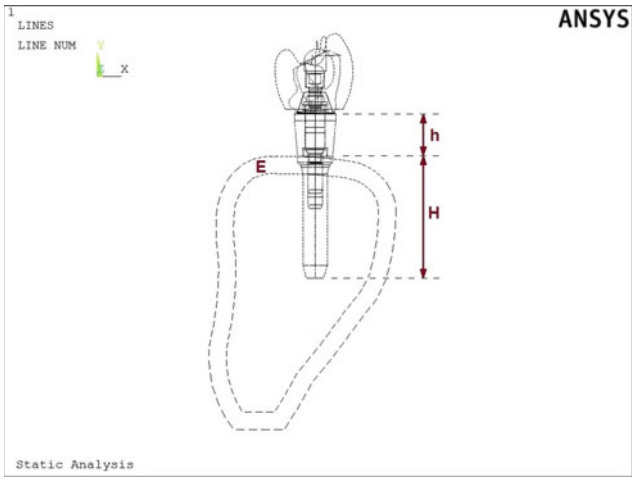

Fig. 3 Parametrized parameters

The parametric and optimization analyses were conducted using Response Surface Methodology (RSM), Design of Experiments (DOE), and the Box-Behnken model. The Box-Behnken approach uses an independent cubic model in which the possible combinations are represented at the midpoints of a cube's edges. This model can rotate and requires at least three levels, or options, on each parameter.

Figure 3 illustrates the parameters assessed in this study: implant length (H), abutment height (h), and Young's modulus of the cortical bone (E). Figure 4 presents the geometrical representation of the coded values for each variable: (+1) for maximum values, (0) for average values, and (−1) for minimum values. Table 2 depicts the real and coded values for each parameter.

Each analysis shown in Table 2 was carried out by adapting the finite element model to that combination of parameters. By means of this parametric analysis, a function called response surface was obtained and it described the Von Mises stress on the cortical bone, acquired from the finite element models, as a function of the selected parameters.

3 Results and Discussion

After running 13 different model combinations, Von Mises stresses around the implant hole and on the cortical bone were obtained as illustrated in Fig. 5 and listed on Table 3.

Based on the obtained stress values, three different regressions equations were created using Microsoft Office Excel software to determine which response curve best represented the model. These equations were (i) a linear regression without interaction, (ii) a linear regression with interaction, and (iii) a non-linear regression. The best results, in terms of adjusted R^2, were obtained from the non-linear regression as a function of the coded parameters (H, implant height; h, abutment height; E, Young's modulus of the cortical bone).

The response surface obtained was presented and evaluated from a statistical point of view and it is shown on Eq. 1:

$$S = 28,726 - 3153H - 3043h + 6319E + 6058H^2 + 4847h^2 \quad (1)$$

In order to assess the precision of the response curve, von Mises stress values were estimated using the response surface and compared to the calculated stress values obtained by the finite element models. A correlation of $R^2 = 0.93$ was found for a relationship of $y = 0.98x + 0.13$ (Fig. 6).

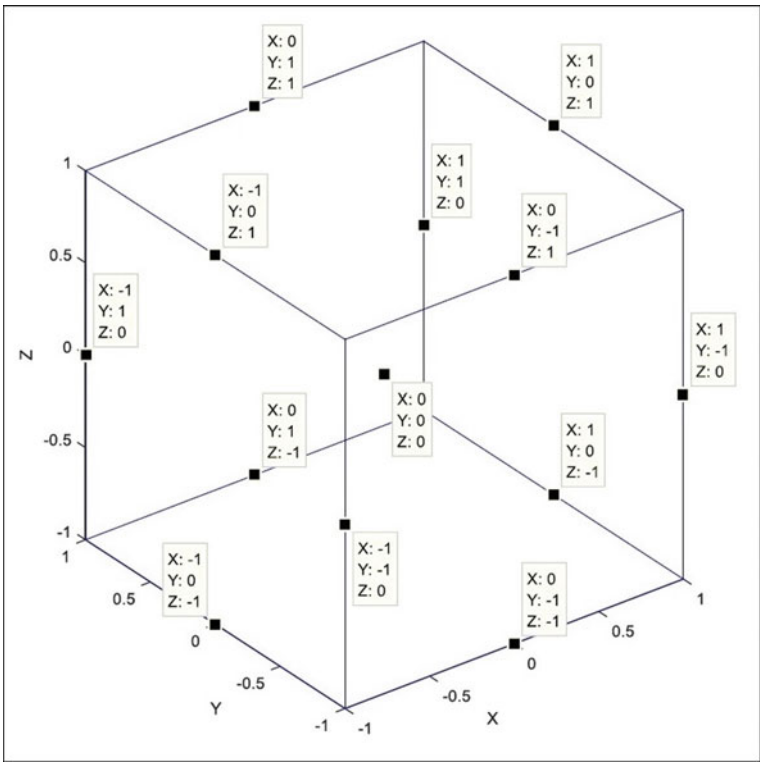

Fig. 4 Representation of Box-Behnken model

Table 2 Coded and real values for each parameter

Experiment/model	Hcod	hcod	Ecod	Hreal (mm)	Hreal (mm)	Ereal (MPa)
1	0	1	1	11	5	20,000
2	0	−1	1	11	1	20,000
3	0	1	−1	11	5	8000
4	0	−1	−1	11	1	8000
5	1	0	1	15	3	20,000
6	−1	0	1	7	3	20,000
7	−1	0	−1	7	3	8000
8	1	0	−1	15	3	8000
9	1	1	0	15	5	14,000
10	−1	1	0	7	5	14,000
11	1	−1	0	15	1	14,000
12	−1	−1	0	7	1	14,000
13	0	0	0	11	3	14,000

Hcod is the coded value for the implant's height, *Hreal* is the real value for the implant's height in mm, *hcod* is the coded value for the abutment's height, *hreal* is the real values for the abutment's height in mm, *Ecod* is the coded value for the Young's modulus of the cortical bone, and *Ereal* is the real value for Young's modulus of the cortical bone in MPa

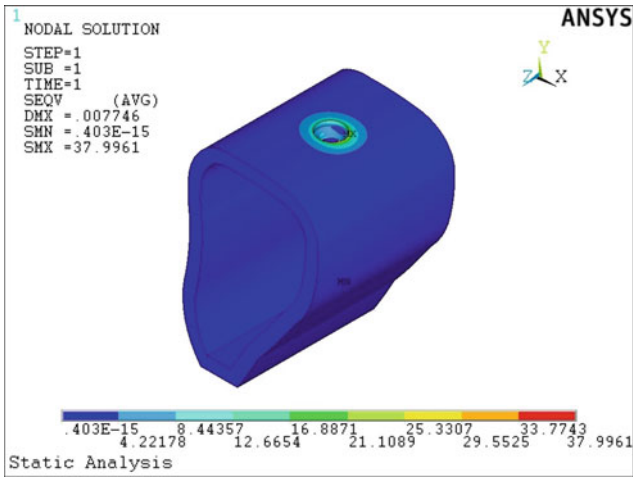

Fig. 5 Von Mises stress on the cortical bone

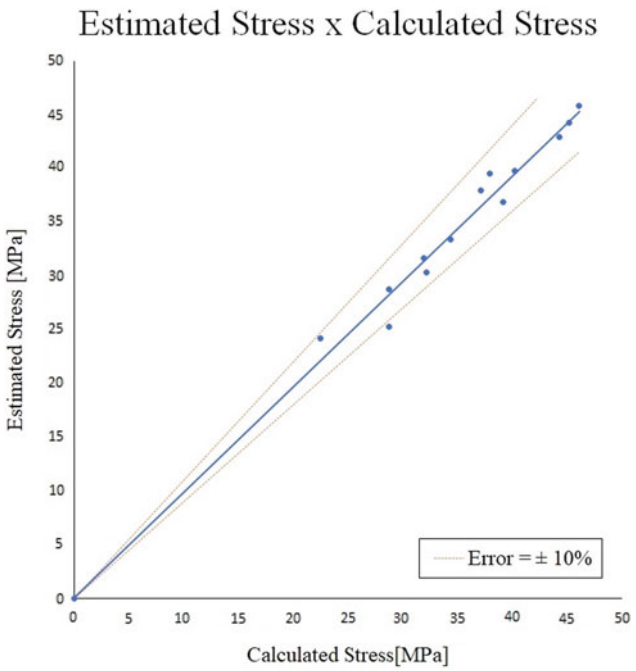

Fig. 6 Estimated stress and real stress correlation plot. Dashed lines represent a deviation of 10%

Table 3 Von Mises stress in the cortical bone obtained in the 13 analyses

Experiment/model	Stress [MPa]
1	39.174
2	44.307
3	22.457
4	32.107
5	37.100
6	45.163
7	31.883
8	28.746
9	34.304
10	40.177
11	37.944
12	46.098
13	28.726

4 Conclusions

A response surface representing the von Mises stress distribution on the cortical bone as a function of the structural parameters h, H, and E was created. A good correlation between calculated and estimated von Mises stress was found. Among the analysed parameters, the most sensitive, i.e. the one in which a small change significantly affects the cortical bone stress distribution, is the height of the implant.

The use of response curves (or surfaces) in structural optimization of dental implants sped up the analysis process, as the best parameter, which minimises the stress on the bone, is found directly from a polynomial, not requiring intense and time-consuming interactive processes, which would include the generation of new geometries, meshes and finite element calculations.

It is worth mentioning that, for simplification purposes, some other conditions were not assessed in this study, such as the stress on the prosthesis, the stress on the cancellous

bone, etc. However, this preliminary study adds confidence in the use of optimization techniques and finite element models in the design of new dental implants.

Acknowledgements The authors gratefully acknowledge the support of the Brazilian Government and CAPES for a Master of Science Scholarship and CNPq for an Undergraduate Research Scholarship.

Conflict of Interest The authors declare that they have no conflict of interest.

References

1. Franciosa P, Martorelli M (2012) Stress-based performance comparison of dental implants by finite element analysis. IJIDeM 6(2):123–129. https://doi.org/10.1007/s12008-012-0155-y
2. Frost HM (1994) Wolff's Law and bone's structural adaptations to mechanical usage: an overview for clinicians. Angle Orthod 64 (3):175–188
3. Chen L-J, Hao HE, Li Y-M et al (2011) Finite element analysis of stress at implant-bone interface of dental implants with different structures. Trans Nonferrous Met Soc China 21(7):1602–1610. https://doi.org/10.1016/s1003-6326(11)60903-5
4. Winter W, Möhrle S, Holst S et al (2010) Bone loading caused by different types of misfits of implant-supported fixed dental prostheses: a three-dimensional finite element analysis based on experimental results. Int J Oral Maxillofac Implants 25(5):947–952
5. Perez M (2012) Life prediction of different commercial dental implants as influence by uncertainties in their fatigue material properties and loading conditions. Comp Meth Prog Bio 108 (3):1277–1286. https://doi.org/10.1016/j.cmpb.2012.04.013
6. Tian K, Chen J, Han L et al (2012) Angled abutments result in increased or decreased stress on surrounding bone of single-unit dental implants: a finite element analysis. Med Eng Phy 34 (10):1526–1531. https://doi.org/10.1016/j.medengphy.2012.10.003
7. Baiamonte T, Abbate MF, Pizzarello F et al (1996) The experimental verification of the efficacy of finite element modelling to dental implant systems. J Oral Implantol 22(2):104–110
8. Szajek K (2013) Optimization of a two-component implantology system using genetic algorithm, Thesis (Ph.D. in Structural Engineering). Posznan University of Technology, Faculty of Civil and Environmental Engineering
9. Myers R, Montgomery D, Anderson-Cook C (2009) Response surface methodology, process and product optimization using designed experiments. Wiley, New Jersey
10. Nist/Sematech at https://www.itl.nist.gov/div898/handbook
11. Albarracín ML (2011) Evaluation of the deformation of the abutment and perimplantar region as a function of the load applied to screw-retained implant-supported single crowns. Master of Science dissertation (Master of Science in dentistry)—College of Dentristy of Bauru, University of São Paulo–USP, Bauru, SP
12. Hernandez BA, Capello Sousa E (2010) Analysis of mechanical contact problems using finite element method in two-dimensional and three-dimensional models of dental prostheses. Final Research Report to PIBIC. Bauru, SP
13. Juodzbalys G, Kubilius R, Eidukynas V et al (2005) Stress distribution in bone: single-unit implant prostheses veneered with porcelain or a new composite material. Implant dent 14(2):166–175. https://doi.org/10.1097/01.id.0000165030.59555.2c
14. Aoki T, Okafor ICI, Watanabe I et al (2004) Mechanical properties of cast Ti-6Al-4V-XCu alloys. J Oral Rehabil 31(11):1109–1114. https://doi.org/10.1111/j.1365-2842.2004.01347.x
15. Craig RG, Powers JM (1989) Restorative dental materials. Mosby, St. Louis
16. Geng JP, Tan KB, Liu GR (2001) Application of finite element analysis in implant dentistry: a review of the literature. J Prost Dent 85(6):585–598. https://doi.org/10.1067/mpr.2001.115251

Biomaterials, Tissue Engineering and Artificial Organs

Tribological Characterization of the ASTM F138 Austenitic Stainless-Steel Treated with Nanosecond Optical Fiber Ytterbium Laser for Biomedical Applications

Marcelo de Matos Macedo, Giovanna Vitória Rodrigues Bernardes, Jorge Humberto Luna-Domínguez, Vikas Verma, and Ronaldo Câmara Cozza

Abstract

This study investigated the tribological behavior of the ASTM F138 austenitic stainless-steel – which is generally used in biomedical applications – treated with laser. Metallic biomaterial surfaces were treated under different nanosecond optical fiber ytterbium laser pulse frequencies, with the purpose to increase their surface hardness. Further, ball-cratering wear tests were conducted to analyze their tribological behavior on the basis of their wear volume and coefficient of friction. The obtained results showed that the nanosecond optical fiber ytterbium laser pulse frequency influenced the surface hardness of each specimen and, consequently, on the wear resistance of the ASTM F138 austenitic stainless-steel biomaterial. With an increase of laser pulse frequency, a decrease in the wear volume of the worn biomaterial was observed – which is the main tribological parameter to study the wear resistance of a metallic biomaterial. In contrast, the coefficient of friction values were found to be independent of the laser pulse frequency, surface hardness and the wear volume of the specimen.

Keywords

Biomaterial • Austenitic stainless-steel • Laser treatment • Wear resistance • Wear volume • Coefficient of friction

1 Introduction

Orthopedic devices, because of friction against mobile implants, bones, or other body parts, detach particles in contact with body fluids, which are placed in locations far from the removed source causing complications to the patients [1]. Metallic particles released from the wear process may move passively, through tissue and/or the circulatory system or, can be actively transported [2], compromising the biomaterial's biofunctionality.

ASTM F138 austenitic stainless-steel is one of the metallic materials used for the manufacturing of orthopedic implants, because of its unique mechanical properties and low cost. Additionally, a surface treatment with a laser technique can be adopted to increase the wear resistance of a metallic implant manufactured with biomaterial.

In other line of research, generally, the *ball-cratering wear test* is a practical tribological method used by various researchers, to analyze the wear resistance of different materials [3–10].

Figure 1 presents a schematic representation of the principle of this wear test.

In this mechanical configuration of the wear test, a rotating ball is forced against the specimen being tested and a liquid solution is supplied between the ball and the specimen during wear experiments.

The purpose of the *ball-cratering wear test* is to generate wear craters on the surface of the specimen; the wear volume (V) may be determined using Eq. 1 [5], where "d" is the diameter of the wear crater and "R" is the radius of the ball.

M. de Matos Macedo
Department of Materials Science, UFABC – Federal University of ABC, Santo André, Brazil

G. V. R. Bernardes · R. C. Cozza (✉)
Department of Mechanical Engineering, University Center FEI – Educational Foundation of Ignatius "Priest Sabóia de Medeiros", São Bernardo do Campo, Brazil
e-mail: rcamara@fei.edu.br; ; ronaldo.cozza@fatec.sp.gov.br

J. H. Luna-Domínguez
Facultad de Odontología, Universidad Autónoma de Tamaulipas, Ciudad Victoria, Mexico

V. Verma
Thermochemistry of Materials SRC, National University of Science and Technology, Moscow, Russia

R. C. Cozza
FATEC-Mauá – Department of Mechanical Manufacturing, CEETEPS – State Center of Technological Education "Paula Souza", Mauá, Brazil

T. F. Bastos-Filho et al. (eds.), *XXVII Brazilian Congress on Biomedical Engineering*, IFMBE Proceedings 83, https://doi.org/10.1007/978-3-030-70601-2_13

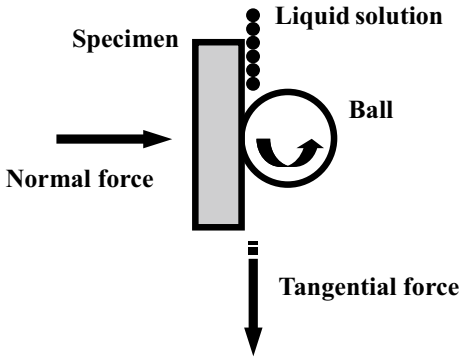

Fig. 1 Micro-abrasive wear testing by rotating ball: schematic representation of its principle

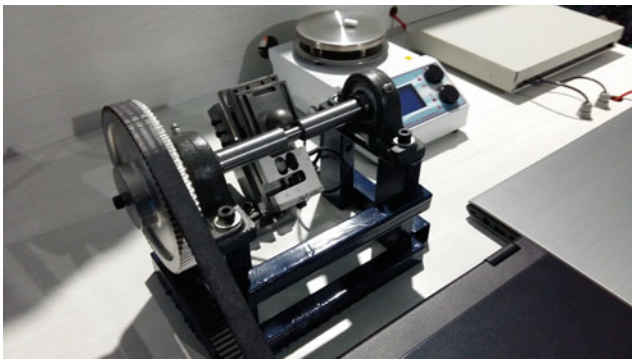

Fig. 2 Ball-cratering wear test equipment with free-ball mechanical configuration used for the ball-cratering wear tests

$$V \approx \frac{\pi d^4}{64R} \quad (1)$$

The friction coefficient (μ) acting on the tribological system "*specimen + ball*" can be calculated using Eq. 2, where "*N*" is the *normal force* applied on the specimen and "*T*" is the *tangential force* measured during the wear tests.

$$\mu = \frac{T}{N} \quad (2)$$

Observing the importance of the *biomaterials* in terms of the social factor and considering the acceptance of the *ball-cratering wear tests* to study the wear behavior of materials, in the present work, we aimed to evaluate the tribological behavior of ASTM F138 austenitic stainless-steel treated with different laser processes – to increase its hardness, by using the "ball-cratering wear test method".

2 Experimental Procedure

2.1 Ball-Cratering Equipment

An equipment with a free-ball mechanical configuration (Fig. 2) has been used for the wear tests, in which its design, building and technical functionality has been detailed in a previous work [11].

Additionally, this ball-cratering wear test equipment has also been previously evaluated by other researchers [11–15], who selected different test conditions and whose tribological apparatus presented excellent functionality during the experiments.

Two load cells were used in the ball-cratering wear test equipment: one load cell to control the "*normal force – N*" and the other load cell to measure the "*tangential force – T*" developed during the experiments. These "*normal*" and "*tangential*" force load cells used had a maximum capacity of 50 N and an accuracy of 0.001 N. The values of "*N*" and "*T*" were read by a readout system, continuously, during the tests.

2.2 Materials

The tested material was an ASTM F138 austenitic stainless-steel biomaterial with the following chemical composition – Table 1.

It was treated with a nanosecond optical fiber ytterbium laser, under four different pulse frequencies, with the purpose to increase its hardness, as presented in Table 2.

One ball made of AISI 316L austenitic stainless-steel, with diameter of $D = 25.4$ mm ($D = 1$" – *standard size*), was used as the counter-body.

Table 3 shows the hardness (H) of the materials used in this work (specimen and ball). For the sake of comparison, the surface of this biomaterial without laser treatment – under the condition of "*as received*" – was also evaluated, totaling five specimen tested.

2.3 Wear Tests

Table 4 presents the test conditions defined for the ball-cratering wear experiments.

One value of normal force (N) was defined for the wear experiments: $N = 0.25$ N.

The ball rotational speed was $n = 50$ rpm and with the diameter $D = 25.4$ mm, the tangential sliding velocity of the ball was equal to $v = 0.066$ m/s.

The wear experiments were conducted under a test time of $t = 2$ min and with the value of $v = 0.066$ m/s, was calculated a value of sliding distance (S) between the specimen and the ball of $S = 8$ m.

All the experiments were conducted without interruption and a Phosphate Buffered Saline (PBS) chemical solution –

Table 1 Chemical composition of the ASTM F138 austenitic stainless-steel biomaterial

Chemical element	% (in weight)
C	0.023
Si	0.78
Mn	2.09
P	0.026
S	0.0003
Cr	18.32
Mo	2.59
Ni	14.33
Fe	Balance

Table 2 Nanosecond optical fiber ytterbium laser pulse frequencies used for surfaces treatments of the specimen

Specimen	Laser frequency – f
1	f_1 = 80 kHz
2	f_2 = 188 kHz
3	f_3 = 296 kHz
4	f_4 = 350 kHz

Table 3 Hardness of the materials used in this research – specimen and ball

Specimen condition – counter-body		Hardness – H	
Specimen – "*as received*"		199.3 HV	(H_0)
Specimen 1	Treated ⇒ f_1 = 80 kHz	204.3 HV	(H_1)
Specimen 2	Treated ⇒ f_2 = 188 kHz	215.4 HV	(H_2)
Specimen 3	Treated ⇒ f_3 = 296 kHz	226.1 HV	(H_3)
Specimen 4	Treated ⇒ f_4 = 350 kHz	239.9 HV	(H_4)
Ball – AISI 316L austenitic stainless-steel		380 HV	(H_B)

Table 4 Test conditions selected for the ball-cratering wear experiments

Experimental parameter	Value
Normal force – N	0.25 N
Ball rotational speed – n	50 rpm
Tangential sliding velocity – v	0.066 m/s
Test time – t	2 min
Sliding distance – S	8 m

which simulates body fluid – was continuously fed between the specimen and the ball during the wear experiments, at a frequency of 1 drop/2 s. Additionally, both the normal force (N) and the tangential force (T) were monitored and registered constantly during the wear tests.

Then, after the tests, the diameters (d) of the wear craters were measured by optical microscopy.

Finalizing the step of data acquisition, the wear volume and the coefficient of friction were calculated from Eqs. (1) and (2), respectively and the maximum standard-deviation reported was informed on the plots of V and μ.

3 Results and Discussion

3.1 Scanning Electron Micrograph

Figure 3 presents a scanning electron micrograph of the surface of a wear crater generated during the ball-cratering wear experiments.

Analyzing Fig. 3, presence of grooves was reported due to the sliding movement between the ball and the specimen during the wear test. In fact, the occurrence of grooves along

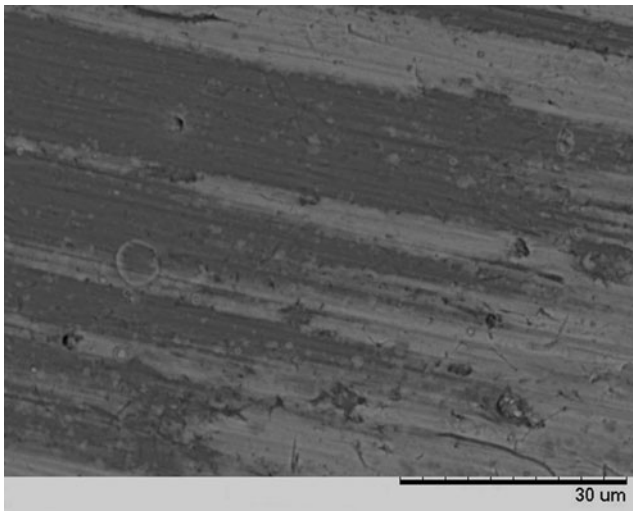

Fig. 3 Example of surface of a wear crater obtained during the ball-cratering wear tests

the surface of a worn material is a characteristic tribological behavior of two metallic materials under relative movement.

3.2 Wear Volume Behavior

Figure 4 shows the results obtained for the behavior of the wear volume (V) as a function of the nanosecond optical fiber ytterbium laser pulse frequency (f) and specimen hardness (H) − V = f(f,H), along with the result obtained from "*as received*" specimen.

We observed that with an increase in the nanosecond optical fiber ytterbium laser pulse frequency (f) and, consequently, an increase in the superficial hardness of the ASTM F138 austenitic stainless-steel, the wear resistance of the specimen increased, as characterized by decrease in the wear volume (V).

The tribological behavior reported in this work is in qualitative agreement with Archard's Law, where the material hardness (H) is inversely proportional to wear volume (V), expressed by Eq. (3):

$$V = \frac{K}{H} SN \tag{3}$$

K is dimensionless constant, as a function of the type of material.

3.3 Friction Coefficient Behavior

Figure 5 shows the behavior of the coefficient of friction (μ) for the "*as received*" specimen and the specimen treated by nanosecond optical fiber ytterbium laser pulse frequency (f) − μ = f(f).

Analyzing the behavior of the coefficient of friction (μ) as a function of the nanosecond optical fiber ytterbium laser pulse frequency (f) and specimen hardness (H) − μ = f(f, H), it is possible to observe that the coefficient of friction did not present a direct relationship with f, i.e., the coefficient of friction was independent of the laser pulse frequency and specimen hardness.

3.4 Wear Resistance Analysis

No direct relationship between the wear volume (V) and the coefficient of friction (μ) was observed, i.e., the highest value

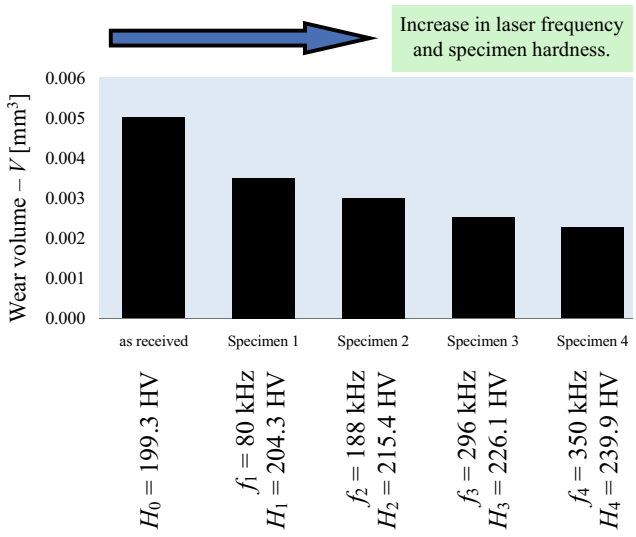

Fig. 4 Wear volume (V) as a function of the nanosecond optical fiber ytterbium laser pulse frequency (f) and specimen hardness (H) − V = f(f, H). maximum standard-deviation reported: 0.001 mm^3

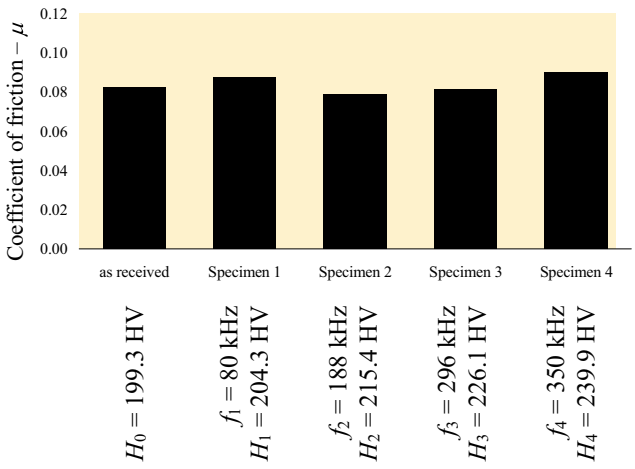

Fig. 5 Friction coefficient (μ) as a function of the nanosecond optical fiber ytterbium laser pulse frequency (f) and specimen hardness (H) − μ = f(f,H). Maximum Standard-Deviation reported: 0.02

of the wear volume was not related to the higher value of the coefficient of friction.

However, considering the wear resistance of the ASTM F138 austenitic stainless-steel, we observed that the important tribological behavior was the decrease in the wear volume (V), which was directly related to the longer service life of the orthopedic implant.

In fact, a longer service life of an orthopedic implant is important to improve the quality life of the patients, avoiding unnecessary surgical operations.

4 Conclusions

The following are the major conclusions drawn from the results obtained in this work, regarding the tribological characterization of the ASTM F138 austenitic stainless-steel biomaterial:

(1) The tribological behavior was influenced by frequency of the nanosecond optical fiber ytterbium laser, in terms of "wear volume";
(2) The laser treatment increased the wear resistance of the biomaterial, quantified by decrease in "wear volume";
(3) The coefficient of friction behavior was independent of the nanosecond optical fiber ytterbium laser pulse frequency;
(4) No direct relationship was found between the wear volume and the coefficient of friction.

Acknowledgements The Authors acknowledge University Center FEI – Educational Foundation of Ignatius "Priest Sabóia de Medeiros" and CEETEPS – State Center of Technological Education "Paula Souza" by financial support to conduct this work.

Conflict of Interest The Authors of this work declare that they do not have "conflict of interest".

References

1. Blac J (1984) Systemic effects of biomaterials. Biomater 5(1):11–18. https://doi.org/10.1016/0142-9612(84)90061-9
2. Okazaki Y (2002) Effect of friction on anodic polarization properties of metallic biomaterials. Biomater 23(9):2071–2077. https://doi.org/10.1016/S0142-9612(01)00337-4
3. Adachi K, Hutchings IM (2003) Wear-mode mapping for the micro-scale abrasion test. Wear 255(1–6):23–29. https://doi.org/10.1016/S0043-1648(03)00073-5
4. Allsopp DN, Hutchings IM (2001) Micro-scale abrasion and scratch response of PVD coatings at elevated temperatures. Wear 251(1–12):1308–1314. https://doi.org/10.1016/S0043-1648(01)00755-4
5. Rutherford KL, Hutchings IM (1997) Theory and application of a micro-scale abrasive wear test. J Test Eval 25(2):250–260. https://doi.org/10.1520/JTE11487J
6. Cozza RC, Tanaka DK, Souza RM (2009) Friction coefficient and abrasive wear modes in ball-cratering tests conducted at constant normal force and constant pressure–preliminary results. Wear 267:61–70. https://doi.org/10.1016/j.wear.2009.01.055
7. Cozza RC (2014) Influence of the normal force, abrasive slurry concentration and abrasive wear modes on the coefficient of friction in ball-cratering wear tests. Tribol Int 70:52–62. https://doi.org/10.1016/j.triboint.2013.09.010
8. Umemura MT, Varela LB, Pinedo CE, Cozza RC, Tschiptschin AP (2019) Assessment of tribological properties of plasma nitrided 410S ferritic-martensitic stainless steels. Wear 426–427:49–58. https://doi.org/10.1016/j.wear.2018.12.092
9. Cozza RC, de Mello JDB, Tanaka DK, Souza RM (2007) Relationship between test severity and wear mode transition in micro-abrasive wear tests. Wear 263:111–116. https://doi.org/10.1016/j.wear.2007.01.099
10. Gee MG, Wicks MJ (2000) Ball crater testing for the measurement of the unlubricated sliding wear of wear-resistant coatings. Surf Coat Technol 133–134:376–382. https://doi.org/10.1016/S0257-8972(00)00966-X
11. Cozza RC, Suzuki RS, Schön CG (2014) Design, building and validation of a ball-cratering wear test equipment by free-ball to measure the coefficient of friction. Tecnologia em Metalurgia Materiais e Mineração 11(2):117–124. https://doi.org/10.4322/tmm.2014.018
12. Wilcken JTSL, Cozza RC (2014) Influence of the abrasive slurry concentration on the coefficient of friction of different thin films submitted to micro-abrasive wear. In: 2nd International conference on abrasive processes—ICAP 2014, 8–10 Sept 2014, University of Cambridge, UK
13. Cozza RC, Rodrigues LC, Schön CG (2015) Analysis of the micro-abrasive wear behavior of an iron aluminide alloy under ambient and high-temperature conditions. Wear 330–331:250–260. https://doi.org/10.1016/j.wear.2015.02.021
14. Macedo MM, Cozza RC (2019) Tribological behavior analysis of the ISO 5832-1 austenitic stainless-steel treated by optical fiber laser used for biomedical applications. J Mater Appl 8(2):91–96. https://doi.org/10.32732/jma.2019.8.2.91
15. Macedo MM, Verma V, Luna-Domínguez JH, Cozza RC (2020) Biotribology of mechanically and laser marked biomaterial. Corrosion, 1st edn. IntechOpen, London, pp 1–11. https://doi.org/10.5772/intechopen.92564

Computational Modeling of Electroporation of Biological Tissues Using the Finite Element Method

M. A. Knabben, R. L. Weinert and A. Ramos

Abstract

This article presents experimental and computational results of electroporation in rabbit liver. Therefore, an empirical electroporation model was used, able to describe the dynamic behavior of electroporation. The experiments were perform with a cylindrical electrode system, where voltage pulses with three different levels were applied. For the numerical simulation of electroporation, a finite element software in MatLab® was developed, intended for academic research. The electroporation model combined with the Finite Element Method proved to be an appropriate simulation tool for the study of biological electropermeabilization.

Keywords

Electropermeabilization of biological tissues • Dynamic modeling of electroporation • Rabbit liver • Computational electromagnetic field calculation • Finite element method

1 Introduction

Biological electropermeabilization is a non-linear physical phenomenon that causes the opening of pores in the plasma membrane, for isolated cells, cell suspension or biological tissue, when these are subjected to high intensity electric fields. The electric field applied on the tissue causes the movement of ions near the cell membrane, increasing the potential difference between the intracellular and extracellular environment, known as transmembrane potential V_m [1].

This electrical polarization mechanism creates pores in the cell membrane, facilitating the flux of ions from the intracellular environment to the extracellular environment, resulting in the increase of tissue conductivity. Biological electropermeabilization occurs if V_m reaches values between 200 mV and 1 V. If V_m exceeds the value of 1 V, irreversible electropermeabilization occurs, causing the cell death [2].

Although electroporation has been a phenomenon studied for several decades and is already used in important applications in medicine, biology and biochemistry, there are still fundamental questions to be investigated. Due to the complex mathematical process associated, the field calculation by computational methods comes up as the only available resource to evaluate the effects of electroporation on biological material. However, this requires the use of models able to describe the temporal variation in tissue conductivity, as a function of the local applied electric field.

Electroporation models can be characterized as static or dynamic. In static models, the simulation is performed in stages, where the conductivity is updated in the analysis domain according to the distribution of the electric field obtained in the previous stage, fallowing a specific mathematical relation. The process is repeated until the conductivity stabilizes in the entire domain through a convergence criterion. In dynamic models, interest case of this article, as the program calculates the local electric field, the conductivity value in each region is increased at each step time of the simulation, according to the electroporation model [3,4].

Currently, some published papers have dealt with the inclusion of electroporation models in finite element programs. The preference for using the Finite Element Method (FEM) is justified because it allows a better discretization of the objects involved in the analysis domain, when compared to the other numerical methods [4,5].

In this article, the calculation of field distribution and current density were obtained using a software based on the Finite Element Method, that were built in MatLab® for academic research, which allows the inclusion of the dynamic electroporation model obtained from [3].

The adjustment of model parameters is made by comparing the simulated results with the experimental results, performed on rabbit liver.

M. A. Knabben (✉) · R. L. Weinert · A. Ramos
Department of Electrical Engineering, University of Santa Catarina State, Joinville, SC, Brazil

T. F. Bastos-Filho et al. (eds.), *XXVII Brazilian Congress on Biomedical Engineering*, IFMBE Proceedings 83, https://doi.org/10.1007/978-3-030-70601-2_14

2 Materials and Methods

2.1 Electropermeabilization in Biological Tissues

The electroporation equipment consists of a switched-mode power supply to generate the pulsed voltage waveform of up to 800 V and 10 A, and an instrumentation circuit for measuring the applied voltage and the current that flows through the sample of biological material.

Rabbit liver samples were used from the Leporidae strain, Oryctolagus cuniculus, between 4 and 6 months of life. The reason why we chose rabbit liver in this work is to verify if the dynamic electroporation model in [3] is able to represent the biological electropermeabilization in the same organ (liver), but on a different species of animal (rabbit). The tests were performed about 30 min after the organs were removed. Three rabbits were used in the experiments. The liver of each animal was divided into standard formats (20 mm wide and 10 mm high), where each organ resulted in five samples, resulting in five experiments for each voltage level applied.

For the application of the electric field, a system of cylindrical steel electrodes with 0.6 mm of diameter and 15 mm of high was used, separated by a distance of 5.4 mm center to center. The electroporation protocol used in the experiments consists in the application of 10 consecutive voltage pulses. The tests were carried out for three different voltage levels, 200 V (case A), 500 V (case B) and 800 V (case C). The time duration of each pulse is 93 μs at high level and 95 μs at low level. The rise and fall times are 3 μs and 100 *n*s, respectively. The room temperature was controlled at 22 °C.

The dynamic electroporation model used in computer simulations is an empirical model proposed in [3], where the model has been validated for rat liver. Equations (1) and (2) combined result in rate of time variation of the electroporation conductivity.

$$\frac{d\sigma_p}{dt} = \frac{(\sigma_{eq} - \sigma_p)}{\tau_o + \Delta\tau e^{-(\frac{E}{E_{p2}})^2(\frac{\sigma_t}{\sigma_t+\sigma_p})^2}} \tag{1}$$

$$\sigma_{eq} = \frac{\sigma_o\sigma_t}{\sigma_o + \sigma_t e^{-(\frac{E}{E_{p1}})^2(\frac{\sigma_t}{\sigma_t+\sigma_p})^2}} \tag{2}$$

This model can be understood as a relaxation equation, where σ_p is the electroporation conductivity, σ_o is the initial value of the electroporation conductivity, σ_{eq} is the final conductivity of the tissue, whose value depends of the intensity of the applied field and σ_t is the conductivity of the region near to the cell membranes. τ_o and $\tau_o + \Delta\tau$ are, respectively, the minimum and maximum relaxation times of the electroporation process. E is the local electric field and E_{p1} and E_{p2} are the electric field thresholds.

The initial values of the parameters were taken from [3]. Then, successive simulations were performed using the "trial & error" method, minimizing the percentage of error from pulse to pulse, between the experimental and simulated curves. In this study' modeling, the parameters σ_t, $\Delta\tau$ and E_{p2} were adjusted for each of the applied voltage amplitudes. The remaining parameters of the model were maintained.

2.2 Finite Element Method

The analysis domain consists of the plane that intercepts the medium height of the electrodes. Due to the cylindrical geometric shape of the electrodes, the electric field distribution on this surface is non-uniform. However, along the normal direction of the surface (direction of tissue thickness) the field distribution is approximately uniform. Therefore, the FEM in two dimensions is appropriated to perform computational calculations, considering this type of geometry.

The geometric model explored in this article is shown on Fig. 1.

The construction of the finite element software requires the follow steps in sequence:

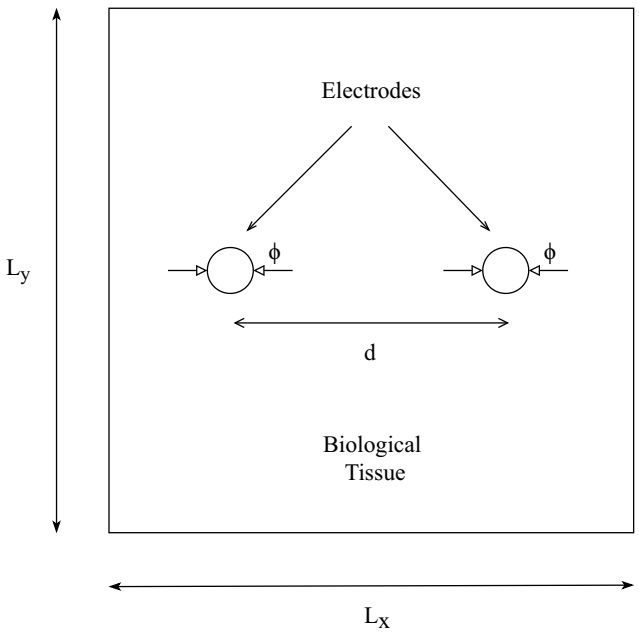

Fig. 1 Geometric model analyzed

1. Discretization of the analysis domain in a finite number of triangular elements, filling the discretization mesh;
2. Organize the set of equations that allow the calculation of the electrical potential within each element as a linear function of spatial coordinates;
3. Perform the superposition of all elements of the mesh to obtain an expression for the electrical potential in the entire domain of analysis;
4. Create a loop for the development of simulation's dynamic where, at each k iteration, the follow steps in the follow order are required:

4.1. Update the potential in electrode nodes;
4.2. Solve the system of linear equations to obtain the potential of nodes in the analysis domain;
4.3. Obtain the electric field in each element through the potential of the nodes;
4.4. Update the conductivity in the elements using the electroporation model, with the electric field as input.

The FEM allows writing the potential as a linear function of the spatial coordinates. Thus, the potential inside of each element of the mesh is then written as a system of linear equations, which depends of the potential of its vertices (local nodes). With the superposition of all elements, the potential is then obtained in the entire domain of analysis [6].

Then, it is necessary to identify the local nodes of each element according to a global numbering. Thus, Eq. (3) is obtained,

$$\tilde{V}(x, y) = \sum_{n=1}^{N_p} f_n V_n \tag{3}$$

where $\tilde{V}(x, y)$ is the potential at any position in the analysis domain, V_n are the potentials of the nodes and f_n are functions resulted from combination of linear equations of the local nodes, only for elements that share the considered node [6].

Equation (3) suggests that the solution for the electrical potential $\tilde{V}(x, y)$ may be write through the expansion in the f_n function base, where the coefficients of this series are the potentials of the V_n nodes.

The problem consider in this article consist in solve the continuity equation. Therefore, the divergence of the current density is zero, as shown in (4),

$$-\nabla \cdot \left[\sigma(x, y)\nabla\tilde{V}(x, y)\right] = 0 \tag{4}$$

where σ (s/m) is the conductivity of the environment. In this study, it was assumed that the conduction current in the tissue is much greater than the displacement current. In addition, the tissue was considered homogeneous and the dielectric dispersion was negligible in the frequency range used. These are approaches commonly used in the analysis of electroporation in biological tissues [1,4,5].

The potential is then calculated using the weighted residuals method between the expected response of Equation (3) and the numerically response, where weighting functions are used to the minimize the average error (residual). Thus, the Galerkin method was adopted, where the weighting functions are the $f_n{}'$ functions of the potential expansion base [6].

The Neumann boundary condition was adopted, which establishes that the normal electric field on the boundary surfaces of the analysis domain is null. Thus, a homogeneous system of equations appears, which when solved, allows obtaining the potential of the V_n nodes. This system was solved by the LU factor method, available in MatLab® through the command *linsolve*. However, it is necessary to simplify the system by using the electrodes nodes as an independent term (source of the system), since their potential are imposed by the voltage source. Therefore, they should not be calculated. The potential in the analysis domain is then obtained by (3).

The electric field is then calculated for each element using the negative of the gradient of the potential, as written in (5).

$$\mathbf{E} = -\sum_{n=1}^{N_p} V_n \nabla f_n \tag{5}$$

The next step is to use the Equations (1) and (2) to calculate the increment in electroporation conductivity $\sigma_P(k)$ in the mesh elements, at each time step Δt, as shown in (6).

$$\sigma_P(k) = \sigma_P(k-1) + \frac{d\sigma_p}{dt}(k)\Delta t \tag{6}$$

Thus, Eq. (7) provides the conductivity value $\sigma(k)$ that must be updated in each element, for the new calculation of the electric field in the next iteration,

$$\sigma(k) = \sigma_S + \sigma_P(k) \tag{7}$$

where σ_S is the conductivity of the intact tissue.

The current can be obtained by integrating $|\mathbf{J}(k)|$ along the median line between the electrodes, as shown in (8),

$$I(k) = h\int_0^{L_y} \sigma\left(\frac{L_x}{2}, y, k\right)\left|\mathbf{E}\left(\frac{L_x}{2}, y, k\right)\right| dy \tag{8}$$

where h is the height of the sample and k is an iteration.

3 Results

Simulations were performed on regular meshes with a certain number of elements and nodes. It was verified that, as more well-resolved meshes were being used, more irrelevant the differences between the curves were, which led to the use of a uniform mesh with 24336 elements and 12325 nodes. The software was run on a personal computer (Intel® Core i7-9700, 3 GHz, 16 GB RAM) with Windows 10 operating system. The simulation time for each of the three voltage levels took about 80 h, all with 5001 time steps.

Table 1 presents the numerical parameters used in the computer simulation and the parameters of the electroporation model that provided the best results.

Figure 2 shows the experimental and computational results obtained for the electric current that circulates in the tissue for the three cases treated in this article.

The electric current has a well-characterized behavior, increasing during the intervals corresponding to the application of voltage pulses. This happens because the conductivity of the tissue is also increasing, due to electroporation. Note that the dynamic electroporation behavior changes significantly in the initial pulses, however it acquires a stable and repetitive behavior in the final pulses. The proposed model is able to reproduce this behavior very close to the experimental reality, especially for the pulses of greater amplitude [7,8].

Table 1 Simulation parameters

Parameter	Greatness	Value
Length of x edge	L_x	10 mm
Length of y edge	L_y	10 mm
Distance between electrodes	d	5.4 mm
Electrode diameter	ϕ	0.6 mm
Applied voltage levels	V_o	200/500/800 V
Total simulation time	T	1.94 ms
Number of pulses	N_p	10
Time step	Δt	382.2 ns
Initial conductivity	σ_o	$1\text{x}10^{-8}$ s/m
Conductivity of intact tissue	σ_S	$47\text{x}10^{-3}$ s/m
	σ_{t_A}	0.101 s/m
Maximum conductivity	σ_{t_B}	0.286 s/m
	σ_{t_C}	0.387 s/m
Minimum relaxation time	τ_o	1 µs
	$\Delta\tau_A$	7 ms
Maximum relaxation time	$\Delta\tau_B$	2.5 ms
	$\Delta\tau_C$	3.5 ms
Electric field threshold	E_{p1}	2.3 kV/m
	E_{p2_A}	8.5 kV/m
Electric field threshold	E_{p2_B}	27 kV/m
	E_{p2_C}	40 kV/m

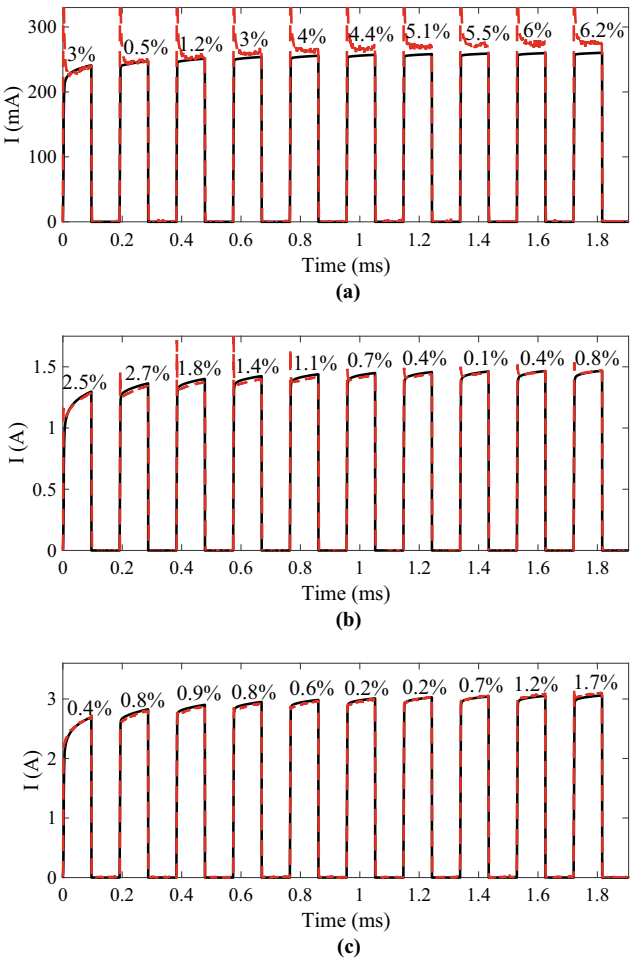

Fig. 2 Comparison between experimental (- -) And simulated (-) currents, with the percentage of relative error to each pulse, for applied voltage levels of: **a** 200 V; **b** 500 V; **c** 800 V

Figure 2 also shows the distribution of the percentage error for each pulse, related to the experimental and simulated current, for the three voltage levels applied. The experimental current peaks present at the beginning of each new pulse occur mainly because of the displacement current and dielectric dispersion in the biological tissue sample. Note that the simulated current curves do not show such peaks, since the displacement current and dispersion were not consider in the computational modeling. Therefore, for the calculation of the error distribution, the current peaks were neglected.

Figure 3 shows the distribution of conductivity and the electric field module in the analysis domain for 500 V applied voltage (case B), generated in a 100 × 100 nodes in the grid, distributed uniformly throughout the domain, at the instant of time equal to 1,815 ms, which corresponds to the last instant of time at high level of the last pulse.

Figure 3a Shows a uniform region with an approximately elliptical shape containing the electrodes, where the conductivity has its maximum value equal to 0.33 S/m, which indicates the occurrence of electroporation in this region.

Figure 3b shows some values of the electric field module in the analysis domain, with the maximum value equal to 286 kV/m, near to the surface of the electrode on the left side, and the minimum equal to 22 kV/m, near to domain's contour. It indicates that the electric field module tends to be more intense in the region next to the electrodes, which justifies the greater values of conductivity in this region as well.

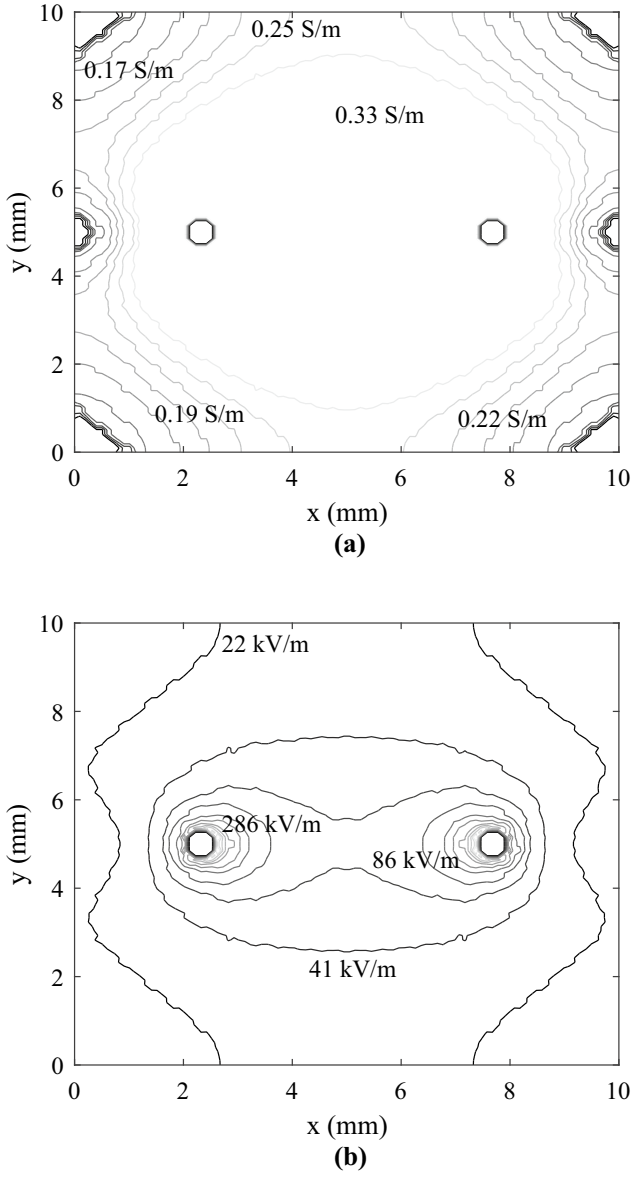

Fig. 3 **a** Distribution of conductivity in analysis domain for $V_o = 500$ V; **b** Distribution of electric field module in analysis domain for $V_o = 500$ V

Comparing the results of this work with the results of [4], where the FEM was also applied to the geometry of cylindrical electrodes, we note that both dynamic models of electroporation are able to represent the experimental current curves and resulted in similar conductivity distributions. However, we must consider that the model proposed in [4] needs the adjustment of 14 parameters, while the model proposed in this work needs the adjustment of only six.

4 Conclusion

The software developed based on the Finite Element Method allowed the inclusion of a dynamic model of electroporation for the analysis of the current and the conductivity and electric field distribution in rabbit liver samples. The electroporation model proved to be appropriate, as it involved only six parameters, which three of them remained the same for both three voltage levels applied. Studies still need to be performed in the future to include the displacement current and dielectric dispersion in the computational software, to faithfully model the physical phenomena that occur in biological tissues. The electroporation model combined with the Finite Element Method proved to be an appropriate simulation tool for the study of biological electropermeabilization.

Conflict of interest The authors declared no conflicts of interest for this article.

Ethics All animal procedures were conducted only after the project was approved by the Committe of Ethics in Animal Use of the UNIVILLE—Universidade da Região de Joinville [University of the Joinville Region]—CEUA/UNIVILLE, (UNIVILLE process 02/2019). The works analyzed by CEUA/UNIVILLE agree to the Brazilian Law 11.974 (1998), which establishes the procedures for the scientific use of animals according to the guidelines of the National Couneil for Animal Experimentation Control (CONCEA).

References

[1] Suzuki D, Anselmo J, Oliveira K et al (2014) Numerical model of dog mast cell tumor treated by electrochemotherapy. Artif Organs 39:192–197

[2] Chen C et al (2006) Membrane electroporation theories: a review. Med Biol Eng Comput 44:5–14

[3] Weinert R, Pereira E, Ramos A (2018) Inclusion of memory effects in a dynamic model of electroporation in biological tissues. Artif Organs 1–6
[4] Langus J, Kranjc M, Kos B, Šuštar T, Miklavčič D (2016) Dynamic finite-element model for efficient modelling of electric currents in electroporated tissue. Sci Rep 6
[5] Voyer D, Silve A, Mir L, Scorretti R, Poignard C (2018) Dynamical modeling of tissue electroporation. Bioelectrochemistry 119:98–110
[6] Bondeson A, Rylander T (2006) Ingelström Pär. Springer, Computational Electromagnetics
[7] Teissie J, Golzio M, Rols M (1724) Mechanisms of cell membrane electropermeabilization: a minireview of our present (lack of ?) knowledge. Bio-chimica et Biophysica Acta 205:270–280
[8] Chang D, Chassy B, Saunders J, Sowers A (1992) Guide to electroporation and electrofusion. Strut Dynam Electr Field 1

The Heterologous Fibrin Sealant and Aquatic Exercise Treatment of Tendon Injury in Rats

S. M. C. M. Hidd, E. F. Dutra Jr, C. R. Tim, A. L. M. M. Filho, L. Assis, R. S. Ferreira Jr, B. Barraviera, and M. M. Amaral

Abstract

Acute rupture of the calcaneus tendon is relatively common, usually related to sports practice. In recent years, the number of researches in search of more efficient techniques, which induce the healing process, has been growing. The Fibrin Sealant Derived from Snake Venom (FSDSV) or Heterologous Sealant has been standing out in animal and human application for accelerating the repair of lesions, reducing the likelihood of hemorrhage and infectious diseases and having low production cost. Aquatic exercise also presents itself as an efficient strategy for rehabilitation, reducing pain and edemas, improving muscle properties and enhancing the repair process due to the numerous beneficial effects provided by the liquid medium. The aim of this research is to evaluate the use of fibrin sealant derived from snake venom associated with aquatic exercise in tendon repair. We used 84 rats of the Wistar strain, weighing between 170 and 250 g of weight who underwent surgery to induce partial rupture of the calcaneus tendon. The animals were randomly separated into four experimental groups. The technique used was the application of fibrin sealant and aquatic exercises according to the studied group. There was a greater reduction in the edema of the animals' paws from the seventh day on in all treatments ($p < 0.002$), when compared to the control group. After 7 and 14 days of treatment, LE showed a greater reduction in the volume of edema ($p = 0.03041$) compared to the control. After 21 days, the (LS) showed a greater reduction in edema compared to the control group. It was possible to verify a higher collagen to LSE ratio in the evaluated period after 21 days of treatment. Thus, the heterologous fibrin sealant associated or not with aquatic exercise has a beneficial influence on tendon repair, becoming a propitious technique for future clinical applications.

Keywords

Edema • Calcaneus tendon • Fibrin sealant • Aquatic exercises

1 Introduction

The calcaneus tendon is the largest tendon in the human body, formed by connective tissue compact, composed of fibroblasts and extracellular matrix, which by function connects to calf muscles to heel bone, with spontaneous regeneration capacity [1]. Despite its high biomechanical resistance, it breaks frequently, usually due to the practice of repetitive sports and intense mechanical loads, with predominant involvement in the age group between 30 and 50 years and in men [2].

After a tendon injury, the healing tissue formed in regeneration can hinder habitual mobility, heal slowly and hardly maintain the structural integrity and mechanical strength of a healthy tissue, which often results in challenges in choosing a better form of treatment. The most used treatment for tendon injuries has been the surgical and conservative (non-surgical) methods. However, these methods can cause a series of complications to the patient, such as

S. M. C. M. Hidd · E. F. Dutra Jr · C. R. Tim · L. Assis · M. M. Amaral
Universidade Brasil, São Paulo, Brazil

A. L. M. M.Filho
Núcleo de Pesquisa em Biotecnologia e Biodiversidade, UESPI, Teresina, Brazil

R. S. Ferreira Jr
Centro de Estudos de Venenos e Animais Peçonhentos CEVAP-UNESP, Botucatu, Brazil

B. Barraviera
Faculdade de Medicina de Botucatu, UNESP, Botucatu, Brazil

S. M. C. M. Hidd (✉)
Biomedical Engineering, Universidade Brasil, Rua Carolina Fonseca 235, São Paulo, Brazil
e-mail: silviahidd@terra.com

T. F. Bastos-Filho et al. (eds.), *XXVII Brazilian Congress on Biomedical Engineering*, IFMBE Proceedings 83, https://doi.org/10.1007/978-3-030-70601-2_15

tissue necrosis, injury recurrence, infections preventing the integral restructuring of the tendon [3].

In the search for the replacement of traditional treatments, FSDSV is a promising alternative due to its hemostatic and adhesive potential. This sealant is a biologic product obtained through the combination of concentrated fibrinogen and reestablished bovine thrombin of calcium chloride, which assists in tissue regeneration, acting as a substrate for cell growth, with total biocompatibility in studies carried out in both animals and humans [4].

The exercise performed in the liquid medium is another alternative to improve the prognosis of the lesion due to the benefits that the physical properties of water provide to the practitioner. This helps in the range of motion, flexibility and consequently provides muscle relaxation, thus avoiding complications such as edemas, pain, and muscle spasms, in addition to reducing the recovery time of tendon injury [5].

Thus, the present study proposes to analyze the reduction of edema, the scar response, and possible changes in the amounts of total collagen in the tendons of the different groups, with the use of FSDSV in association with aquatic exercise.

2 Methods

The study was approved by the ethics committee (CEUA/UESPI), no. 6,899, of July 15, 2019.

To carry out this study, 84 female *Rattus norvegicus* of the Wistar strain were used, obtained in the biotherium of UESPI. Rats weighing between 170 and 250 g were underwent to partial injury of the right calcaneus tendon. The rats were kept in a light–dark photoperiod of 12 h, with a temperature of 24 ± 1 °C, with free access to water and food.

The animals were randomly separated into four experimental groups, containing 21 rats divided into each of the following 4 groups: Control Group (L), group in which the rats underwent partial tendon injury, without receiving any type of treatment; Fibrin Sealant Group Derived from Snake Venom (LS), a group that rats underwent partial tendon injury and treated with sealant; Aquatic Exercise Group (LE) group in which the rats underwent partial tendon injury and treated with aquatic exercise; Fibrin Sealant Group Derived from Snake Venom plus Aquatic Exercises (LSE) group in which the rats underwent partial tendon injury and treated with the sealant and aquatic exercises. Each group was subdivided into 3 other subgroups, containing 7 rats each, related to the evaluation times: 7, 14 and 21 days [6].

The treatment was performed with the application of fibrin sealant and aquatic exercises, according to the experimental group described.

2.1 Surgical Procedure

Prior to the surgical procedure, trichotomy and asepsis were performed (alcohol 70%) on the right lower paw of each rat. Then, a longitudinal incision of 3 cm was made in the animal's skin for exposure of the calcaneus tendon. Soon afterwards, under a surgical, a partial rupture of the calcaneus tendon was done and then applied the fibrin sealant to the injured area [1].

The fibrin sealant composed of the thrombin-like fraction of the venom of *Crotalus durissus terrificus*, cryoprecipitate of buffalo blood and calcium chloride, was provided by the Center for The Study of Venomous Poisons and Animals of UNESP (State University of São Paulo–Brazil).

The heterologous fibrin compound was made available in three microtubes stored at a temperature (−20 ºC). At the time of application, they were thawed, reconstituted, mixed and applied (9 µL in each transected tendon) to form a stable clot with a dense fibrin network [6].

2.2 Aquatic Exercise Protocol

All animals went through a period of adaptation to the liquid medium, for 15 days preceding the surgical process. The duration of the exercises was 10 min a day, 5 times a week and with a load equivalent to 10% of body weight [7].

Only groups (LE), and (LSE) to went through aquatic exercise training after the third postoperative day [8]. The exercises were done in an oval tank, with 50 cm depth and capacity for 100 L, with water level of 40 cm depth and water temperature controlled at 32 °C.

2.3 The Evolution of Edema

The edema volumes were measured in five moments: before the tendon injury, 24 h, 7, 14 and 21 days after the tendon injury.

The right paw of the animal was introduced in the plethysmometer. A pencil mark was made on the animal paw to standardize the measurements position. The plethysmometer measures the volume of the paw. The edema volume was calculated by the difference between the measurements before and after the tendon injury [10].

2.4 Euthanasia

All animals were humanely killed on the scheduled dates by a lethal dose of anesthetic of sodium Thiopental (100 mg/kg), by intraperitoneal injection [9].

2.5 Collagen Quantification

Collagen quantification was performed through the slides stained with picrosirius red. After the random choice of one cut per blade, it was photographed in 3 distinct graft fields, using an optical microscope (Olympus, Optical Co. Ltd, Tokyo, Japan) equipped with filters to provide polarized lighting.

The images were obtained at a 400× increase with a digital camera coupled to the microscope (Sony DSCs75, Tokyo, Japan) and analyzed using MatLab R2019b image analysis software. The analysis methodology was carried out in accordance with Castro et al. [13].

2.6 Statistical Analyses

The statistical analyses were performed using the Minitab 18 statistical software. To analyse the distribution of the groups, the Anderson–Darling normality test was used. The Quantitative variables were presented and standard deviator minimum, maximum, median and quartiles. The Kruskall-Wallis nonparametric test was used for comparison between the groups. For all analyses, a significance level of 5% was considered. Analysis of the animal weight, the volume of edema 24 h after surgery, the final edema volume, and total collagen were performed.

3 Results and Discussions

The mean and standard deviation of the weight of the animals was 206 ± 24 g, there was no statistical difference between the groups studied.

In the analysis of the volume of edema 24 h after surgery, the statistical comparison between the groups showed that there is no difference between their values (p-value = 0.023). Thus, the surgical injury procedure induced the inflammatory process equally in all the paws of the animals of all groups.

Figure 1 shows the volume of the final edema of each of the groups studied. It was observed that after 7 days of treatment, the treatment groups (LE7, LS7 and LSE7) presented statistically lower edema volume (p-value < 0.002), compared to the group without treatment application.

In the intragroup comparison, it was observed that the control group (without treatment) presented a volume of edema for the period of 21 days statistically greater than 14 days (p-value = 0.04), showing that the lesion without treatment does not progress satisfactorily. The group treated only with aquatic exercise showed greater statistical differences between the LE7 and LE21 (p-value = 0.0090) and between LE14 and LE21 (p-value = 0.0096), showing that there was an increase in the volume of edema for this treatment.

Among the groups treated only with fibrin sealant, there were greater statistically differences between LS14 and LS21 groups (p-value = 0.0014). Finally for groups treated with fibrin sealant and aquatic exercise, statistically smaller differences were observed between LSE7 and LSE21 (p-value = 0.0048).

Figure 2 presents the representative images of collagen stained by picrosirius red for each studied group.

The results of this analysis for each group are shown in Fig. 3. When comparing the intragroup results of the total collagen ratio, it is observed that the proportion of collagen ratio for the L7 control group is significantly higher than in the L21 group (p-value = 0.013).

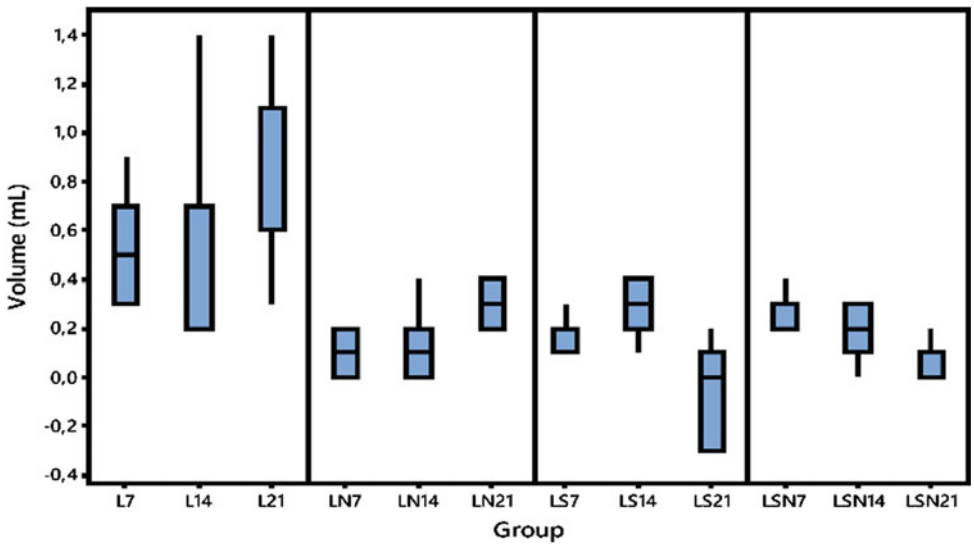

Fig. 1 Edema volume

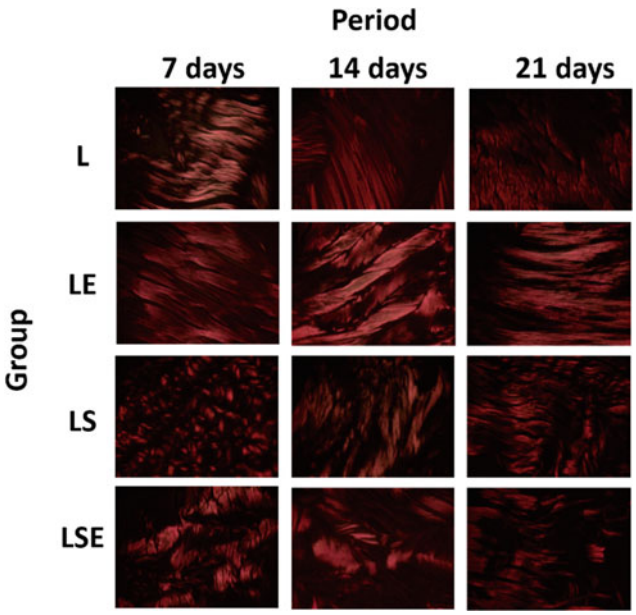

Fig. 2 Representative images of picrosirius red collagen stained

For the groups treated with aquatic exercise LE, no statistical difference was observed in the amount of collagen (p-value > 0.4). In the groups treated with LS sealant, a statistical difference was observed between groups LS7 and LS21 (p-value = 0.012) and between LS14 and LS21 (p-value = 0.007). The collagen content of the LS21 group is statistically higher compared to the LS7 and LS14 groups. However, no statistical difference was observed between groups LS7 and LS14. For the groups treated with sealant plus aquatic exercise, no statistical difference was observed in the amount of collagen between the groups (p-value > 0.27).

In the intergroups comparison by period, it was observed that, after 7 days of injury induction, the groups treated with aquatic exercise LE7 showed a statistically higher value than the control group L7 (p-value = 0.04). After the 14 days of injury induction, the LE14 group showed a statistically lower value than the control group L14 (p-value = 0.0006). For 21 days after the injury, the LE21 group has a statistically lower value than the L21 group (p-value = 0.0002).

This study tested the effects of FSDSV associated with aquatic exercise in the partial tendon repair process in rats, aiming to analyze the reduction of edema, scar response and possible changes in the amounts of total collagen in the tendons of the different groups.

It was observed that there was a statistically significant reduction in edema for the group treated with fibrin sealant associated with aquatic exercise (LSE21) compared to the control group. Indicating that in the first day after the induced partial injury, the rats showed a greater volume of edema, resulting from the greater accumulation of macrophages at the injury site [10].

Rats that underwent to aquatic exercise for a period of 7, 14 or 21 days showed progress in reducing the volume of edema. It is known that physical exercise acts as a stressful stimulus that can promote changes and reorganize the responses of the neuroendocrine system [11]. Corroborating these results, Antunes et al. (2012) evaluated the effect of resistance exercise in aquatic environment in experiments with 18 Wistar rats and found that physical exercise was somewhat beneficial in reducing edema.

In the present study, the association of fibrin sealant with aquatic exercise in the acute phase of tendinopathy recovery was an effective therapeutic modality in improving edema from the inflammatory process, although treatment with aquatic exercise or sealant, when applied alone, has also been effective in reducing the volume of edema, contributing to the regenerative process, aiming at the return of functionality to the patient.

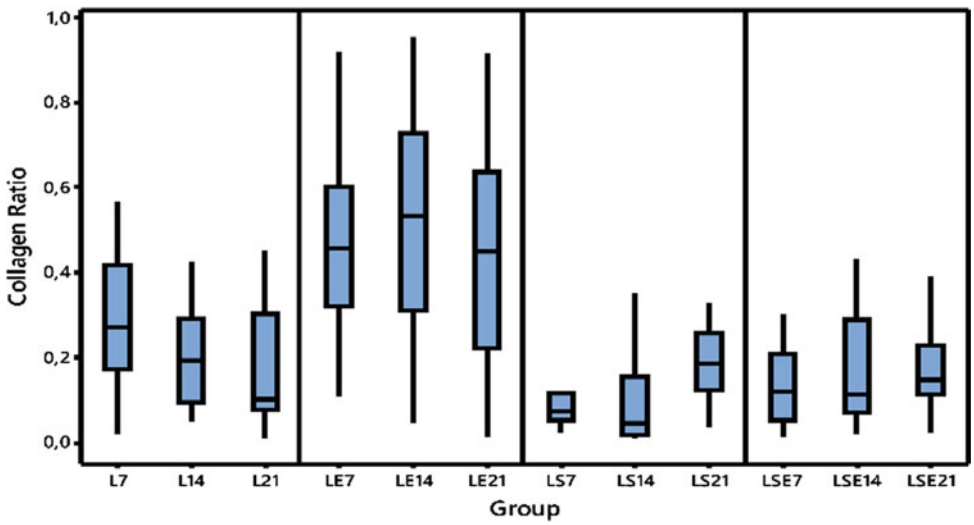

Fig. 3 Comparison p-value intergroups and intragroup

However, these same authors found that when comparing the results of intragroup edema, it was not possible to observe a statistically significant difference, unlike this study, where there was a significant difference in the volume of edema in the groups that underwent to more days of exercise.

Regarding the amounts of collagen in the intragroup comparison, only the group treated with fibrin sealant by LS21 presented a significant amount when compared to groups LS7 and LS14. The data in the intergroup comparison suggest that the FSDSV and aquatic exercise may be an excellent support for treatment during tendon repair (LSE14) followed by LE7 and finally LS21, because they presented satisfactory results in relation to the recovery of tendon organization, with the time and types of treatments applied.

4 Conclusions

To the best of our knowledge, this work is the first experimental model of tendinopathy associating fibrin sealant derived from snake venom associated with aquatic exercise, thus providing innovative options for the treatment of tendon lesions.

In this work, the groups treated with aquatic exercise, with fibrin sealant and sealant associated with aquatic exercise presented statistically lower edema volume than the control group. It was found that the group treated with fibrin sealant associated with physical exercise obtained a better reduction of edema when compared with the other treatment groups.

The association of sealant with aquatic exercise promoted the regeneration of the calcaneus tendon of the animals, as well as stimulating the early organization of collagen fibers.

Acknowledgements This work was supported by FAPESP 2017/21851-0.

Conflict of Interest The authors declare that they have no conflict of interest.

References

1. Holm C, Kjaer M, Eliasson P (2014) Achilless tendon rupture–treatment and complications: a systematic review. Scand J Med Sci Sports 25(1):e1-10
2. Frauz K et al (2019) transected tendon treated with a new fibrin sealant alone or associated with adipose-derived stem cells. Cells 8:56
3. Rosa LFPBC, Vaisberg MW (2002) Influências do exercício na resposta imune. Rev Bras Med Esporte. 8(4):167–172
4. Walden G et al (2017) A clinical, biological, and biomaterials perspective into tendon injuries and regeneration. Tissue Eng Part B Rev 23(1):44–58
5. Grinsell D, Keating CP (2014) Peripheral nerve reconstruction after injury: a review of clinical and experimental therapies. Biomed Res Int 2014:13
6. Dietrich F (2012) Comparação do efeito do plasma rico em plaquetas e fibrina rica em plaquetas no reparo do tendão de Aquiles em ratos. Faculdade de Medicina, Pontifícia Universidade Católica do Rio Grande do Sul, Porto Alegre, RS
7. Ferreira JR (2017) Selante de fibrina heterólogo derivado do veneno de cobra: do banco ao leito-uma visão geral. J Venom Anim Toxins Incl Trop Dis
8. Peres VS (2013) Efeito do selante de fibrina derivado de peçonha de serpente associado a células-tronco mesenquimais na cicatrização de feridas cirúrgicas em ratos. Dissertation-Faculdade de Medicina de Botucatu, Universidade Estadual Paulista, Botucatu
9. Rajabi H et al (2015) Os efeitos curativos das atividades aquáticas e injeção alogênica do plasma rico em plaquetas (PRP) nas lesões do tendão de Aquiles em ratos experimentais. World J Plast Surg 4 (1):66–73
10. Karvat J, Antunes JS, Bernardino GR, Kakihata CMM, Bertolini GRF (2014) Effect of low-level laser and neural mobilization on nociceptive threshold in experimental sciatica. Revista Dor 15 (3):207–210
11. Pestana PRD, Alves AN, Fernandes KPS, Silva JA Jr, França CM, Martins MD, Bussadori SK, Mesquita-Ferrari RA (2012) Efeito da natação na expressão de fatores regulatórios miogênicos durante o reparo do musculoesquelético de rato. Rev Bras Med Esporte 18 (6):419–422
12. Silva ASD, Lima AP (2011) Os benefícios da reabilitação aquática para grupos especiais. Lecturas Educación Física y Deportes, Buenos Aires 16:159
13. Castro TNS, Martignago CCS, Assis L, de Alexandria FED, Rocha JCT, Parizotto NA, Tim CR (2020) Effects of photobiomodulation therapy in the integration of skin graft in rats. Lasers Med Sci 35:939–947

Myxomatous Mitral Valve Mechanical Characterization

A. G. Santiago, S. M. Malmonge, P. M. A. Pomerantzeff, J. I. Figueiredo and M. A. Gutierrez

Abstract

The mitral valve (MV) along with the tricuspid valve are part of the atriovalvar complex and, when committed by myxomatous disease, suffers from tissue degeneration with severs changes in its mechanical properties, consequently loosing its coaptation capability, resulting in the well known Mitral Regurgitation (MR). This paper presents the results of stress × strain tests of 19 mitral valve posterior leaflets committed by myxomatous disease extracted from patients undergoing MV repair surgery. Due to their dimensions, only uni axial testes were performed, i.e., only the radial direction was considered. Are presented the Young Modulus, Yielding and Linearity limits. The Young Modulus obtained for myxomatous MV are compared to normal values found in the literature.

Keywords

Mitral valve • Myxomatous disease • Mechanical properties

1 Introduction

The mitral valve (MV) is responsible for maintaining one directional blood flow inside the cardiac cavity. The MV possesses a complex set of structures such as the *chordae thendinae*, papillary muscles and the mitral annulus. The papillary muscle is attached to the leaflets via several *chordae thendinae*, controlling their opening and closing movements, while the mitral annulus is responsible for maintaining the circumferential tension of the MV.

The VM proper behavior allows the one directional blood flow, from the left atrium to the left ventricle, with no considerable re-flux. However, its behavior may be compromised by myxomatous disease, causing a degeneration of the *chordae thendinae* and leaflets tissues and, consequently, changing their mechanical properties [1], implying in a coaptation failure, causing the well known Mitral Regurgitation (MR).

Valve replacement and valve repair are the two techniques employed to solve MR problem, with the latter being the most used with better post-surgical results. This technique consists in removing the most damaged portion of the leaflet, reducing its area. Literature presents several numerical models for MV simulations [2–5], which are crucial for better surgical planning and understanding of the MV post-surgical behavior. Such simulations depends upon the knowledge of the mechanical properties of the structure being analyzed, thus, relies on the proper characterization of myxomatous mitral valves.

The MV internal structure is composed by conjunctive tissue and collagen fibers circumferential oriented [6], hence, the material can be classified as a transversely isotropic, having distinct characteristics in circumferential and radial directions. Several studies have been made in order to characterize its different structures, such as the paper presented by Ritchie et al. [7] and Chen et al. [8], that aim to determine the mechanical properties of the *chordae thendinae*; Liao et al. [9] performed a study in which the authors determined the influence of the MV anterior leaflet collagen fibers in the MV movements. A main issue concerning the mentioned papers is that they did not use human specimen for testing, which may lead to considerable divergences in numerical simulations. Barber et al. [10] presents an extensive study considering normal and mixomatous MV.

This paper presents the characterization a first study, consisting of 19 myxomatous mitral valve samples (posterior leaflet) considering a brazilian population, which can lead to important insights concerning its demographics particularities. Are presented the Young Modulus, Stress at Break, Stress

A. G. Santiago (✉) · S. M. Malmonge
Engineering and Social Sciences, Federal University of ABC/ Center for Modeling, Alameda da Universidade s/n, São Bernardo do Campo, Brazil
e-mail: gabriel.santiago@ufabc.edu.br

P. M. A. Pomerantzeff · J. I. Figueiredo · M. A. Gutierrez
Medical School,University of São Paulo/ Heart Institute, São Paulo, Brazil

T. F. Bastos-Filho et al. (eds.), *XXVII Brazilian Congress on Biomedical Engineering*,
IFMBE Proceedings 83, https://doi.org/10.1007/978-3-030-70601-2_16

at Yield, Peak Stress, Stress at Break and Strain at Break, since these parameters are needed for plotting the Stress-Strain ($\sigma \times \epsilon$) material characteristic curve. All 19 samples were extracted from patients undergoing MV repair surgery at the Heart Institute of the University of São Paulo (InCor-FMUSP) and due to their size and shape, only the radial tensile test was performed. This research was approved by InCor's Institutional Review Board (IRB) under number 4704/18/056.

This is the first study known so far that aims the characterization of myxomatous MV specific for brazilian population and also, the first to use samples from surgical procedures.

2 Methodology

All 19 myxomatous mitral valve samples (posterior leaflet) were extracted from patients undergoing mitral valve repair surgery with age ranging from 44 to 83 years old, with mean age $63.31 \pm 9.35\ years$. Transesophagial Echocardiography Ultrasound (TEE-US) was used to evaluate the patients condition before the surgery. The samples were sectioned from the mitral annulus to the free edge and each one was placed in a plastic container filled with glycerin in order to preserve its integrity and taken to the tensile test. In order to proceed with the tension tests, each one of them was immersed into a saline solution for 10–15 min before placed in the tension machine.

All tension tests were performed using the *MTS Tryton 250* located at the Laboratory of Biomaterials of the Federal University of ABC. In order to guarantee the stability of the samples, four adapters were used, each one designed to avoid the samples to slip over the machines grips. Figure 1 shows one sample placed on the machine.

The horizontal gap between each grip was carefully adjusted according the length of each sample, avoiding any pre-tension.

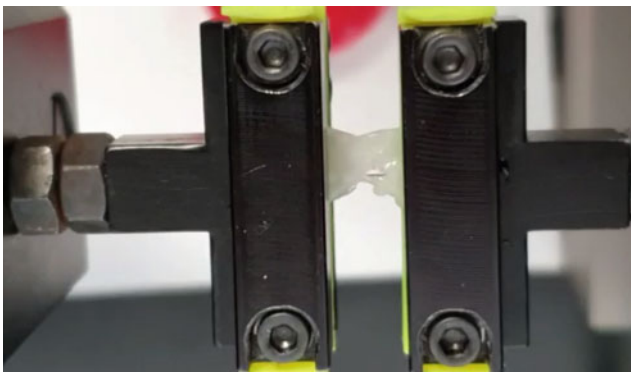

Fig. 1 Mitral Valve sample placed on tension machine for testing

The *TestWorks* proprietary software was used to perform the tests and the results of load × displacements were recorded and used to determine the Young Modulus (E), Stress at Yield (σ_e), Peak Stress (σ_M) as well as Stress at Break (σ_R) and Strain at Break (ε_R). A Python 3.7 Application Programming Interface (API) was developed in order to read and convert the data from each generated file to a `pandas` library, which posses statistical and graphical resources. It must be mentioned here, that all stress-related values are considered as engineering stress, i.e., $\sigma = F/A\ [Pa]$, with A the cross-section area of the specimen, considered to be constant.

3 Results

Figure 2a shows the boxplot for the samples Young Modulus parameter and considering the Young Modulus over $1.84\ [MPa]$ as an outlier, it can be excluded from the parameters statistics. Figure 2b, c present the histogram and the gaussian distribution for the Young Modulus. It must be noted that Fig. 2c was evaluated considering only those values below $1.8\ [MPa]$. Table 1 presents the mean values along the standard deviation for the analyzed properties.

Figure 3 present the Young Modulus (E), Stress at Yield (σ_e), Stress at Break (σ_R) and Strain at Break (ϵ_R) parameterized by the patients age. The p-values and Pearson coefficients (r^2) are presented in Table 2.

4 Discussion

This paper presented a study of 19 myxomatous mitral valve samples extracted from patients undergoing MV repair surgery. An analysis concerning the Young Modulus values is presented along some other important characteristics such as Strain at Break, Stress at Break, Peak Stress and Stress at Yield. It is also presented an attempt to correlate the variation of the mentioned parameters with the patients age.

As stated by Fig. 2a, b, Young Modulus over $1.84\ [MPa]$ can be considered as outliers, hence, they were not considered for estimating the mean value for myxomatous MV Young Modulus (Fig. 2c).

The presented results in Fig. 2c and Table 1 shows that the Young Modulus for myxomatous MV is higher than those for healthier MV, as presented by Pham et al. (2017) [11], with $E = 180.05 \pm 71.50\ [KPa]$.

From the parametric properties shown in Fig. 3 and the results in Table 2, it can be observed a low correlation between the given properties and the patients age for the considered age range, meaning that no significant change in the myxoid MV properties can be noticed in the age span analysed.

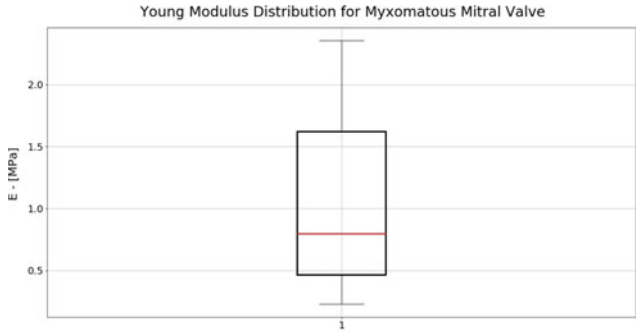

(a)

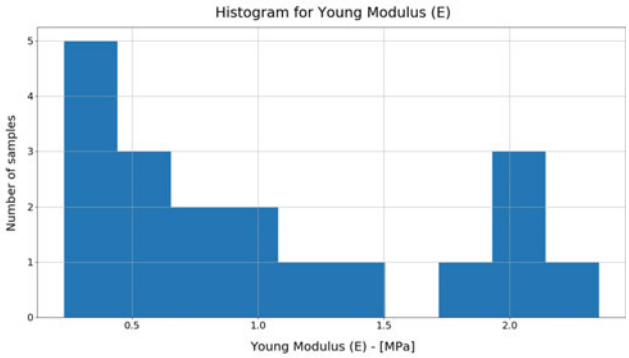

(b)

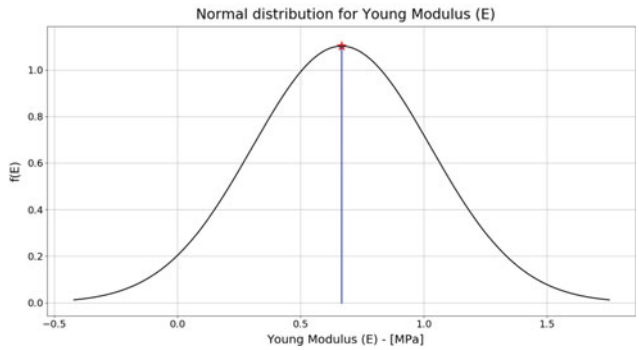

(c)

Fig. 2 Analysis for myxomatous Young Modulus: **a** Boxplot for Young Modulus values in MPa; **b** Young Modulus histogram; **c** Normal distribution for Young Modulus

Table 1 Tension tests results: Mean value and Standard deviation

Property	Mean Value	Std. deviation
Thickness (mm)	2.084	671.03×10^{-3}
Width (mm)	6.474	1.144
Area (mm^2)	13.45	4.739
Modulus (E) (KPa)	666.18	361.60
Stress at Yield (σ_e) (KPa)	822.71	558.00
Peak stress (σ_M) (KPa)	983.77	579.90
Break stress (σ_R) (KPa)	632.00	549.60
Strain at break (ϵ_R) (%)	230.50	158.90

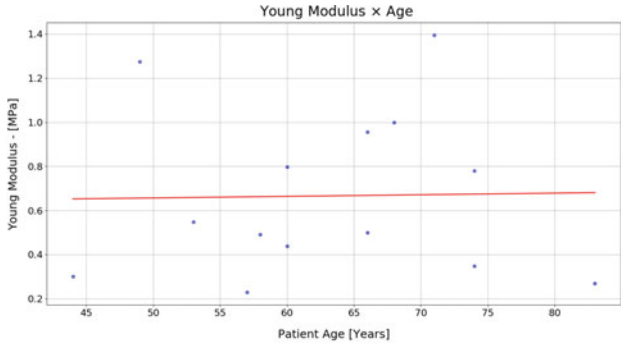

(a)

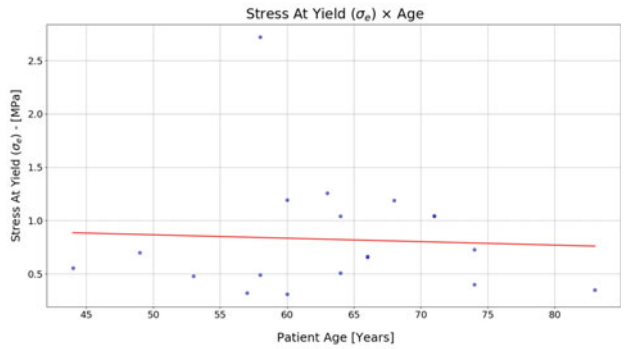

(b)

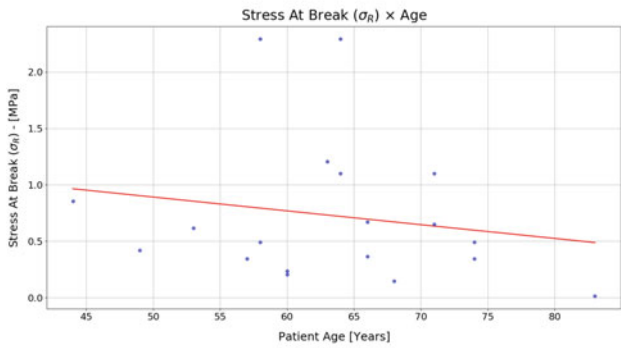

(c)

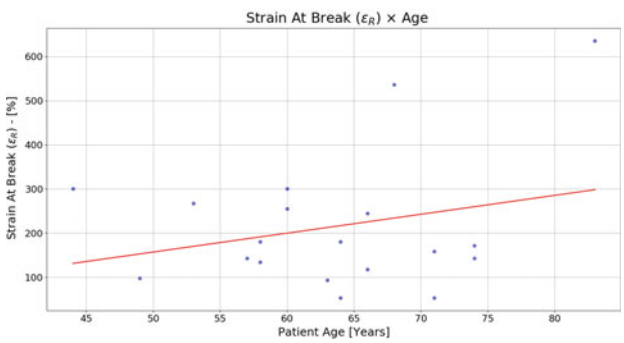

(d)

Fig. 3 Properties parameterized by the patients age: **a** Young Modulus; **b** Stress at yield; **c** Stress at break; **d** Strain at break

Table 2 Tension tests results: p_{value} and Pearson coefficient

Property	p_{value}	r^2
Modulus (E)	943.97×10^{-3}	428.98×10^{-6}
Stress at Yield (σ_e)	826.90×10^{-3}	2.89×10^{-3}
Stress at Break (σ_R)	465.43×10^{-3}	31.75×10^{-3}
Strain at Break (ϵ_R)	275.03×10^{-3}	69.62×10^{-3}

Conflict of Interest

The authors declare that they have no conflict of interest.

References

[1] Lazar F, Marques LC, Aiello VD (2018) Myxomatous degeneration of the mitral valve. Autopsy Case Rep 8

[2] Gao H, Qi N, Feng L et al (2017) Modelling mitral valvular dynamics–current trend and future directions. Int J Numerical Methods Biomed Eng 33

[3] Khodaei S, Fatouraee N, Nabaei M (2017) Numerical simulation of mitral valve prolapse considering the effect of left ventricle. Math Biosci 285:75–80

[4] Sturla F, Onorati F, Votta E et al (2014) Is it possible to assess the best mitral valve repair in the individual patient? Preliminary results of a finite element study from magnetic resonance imaging data. J Thoracic Cardiovascular Surg 148:1025–1034

[5] Voigt I, Ionasec RI, Georgescu B et al (2009) Model-driven physiological assessment of the mitral valve from 4D TEE medical imaging 2009: visualization. Image-Guided Procedures Modeling 7261:72610R

[6] Kunzelman RP, Cochran (1992) Stress/strain characteristics of Porcine mitral Valve tissue: parallel versus perpendicular Collagen orientation. J Cardiac Surg 7:1–20

[7] Ritchie J, Jimenez J, He Z, Sacks MS, Yoganathan AP (2006) The material properties of the native porcine mitral valve chordae tendineae: an in vitro investigation. J Biomech 39:1129–1135

[8] Chen L, Yin FCP, May-Newman K (2004) The structure and mechanical properties of the mitral valve Leaflet-Strut chordae transition zone. J Biomech Eng 126:244–251

[9] Liao J, Yang L, Grashow J, Sacks MS (2007) The relation between collagen fibril kinematics and mechanical properties in the mitral valve anterior leaflet. J Biomech Eng 129:78–87

[10] Barber JE, Kasper FK, Ratliff NB, Cosgrove DM, Griffin BP, Vesely I (2001) Mechanical properties of myxomatous mitral valves. J Thoracic Cardiovascular Surg 122:955–962

[11] Pham T, Sulejmani F, Shin E, Wang D, Sun W (2017) Quantification and comparison of the mechanical properties of four human cardiac valves. Acta Biomaterialia 54:345–355

Qualitative Aspects of Three-Dimensional Printing of Biomaterials Containing Devitalized Cartilage and Polycaprolactone

I. M. Poley, R. Silveira, J. A. Dernowsek, and E. B. Las Casas

Abstract

The aim of this study was to investigate the printability of different compositions of biomaterials to be potentially used in bioprinting of cartilaginous substitutes. Part of the compositions contained pulverized devitalized cartilage (DVC), which confers the necessary biochemical complexity for bioprinted scaffolds, and some compositions contained granulated polycaprolactone (PCL), that provides greater mechanical resistance to the scaffolds. An additive manufacturing equipment specially customized for bioprinting was used in the printing tests. In addition to bringing biochemical advantages, DVC increases consistency of scaffolds. PCL, on the other hand, has to be reduced to smaller granulometries for better results, since it has obstructed the printing needles. Modifications to the printer design have been suggested to make printing viable using high viscosity biomaterials and 0.41 mm or thinner needles, which may provide greater resolution and shorter distances for diffusion of nutrients and oxygen inside the scaffolds.

Keywords

Bioprinting • Bioink • DVC • PCL • Printability

1 Introduction

Bioprinting is a promising area of tissue engineering. It aims to biofabricate complete rejection-free organs and tissues by using computer-controlled three-dimensional printing devices to accurately deposit cells and biomaterials, for the purpose of creating anatomically correct structures. Cell-embedded biomaterials used in bioprinting comprise the so-called bioinks, whereas those without cells are considered biomaterial inks.

Extracellular matrices have already been used as biomaterials in biofabrication of substitutes for cartilaginous tissues due to their chondroinductive potential [1]. The biochemical complexity of those structures helps to mimic a natural cellular microenvironment in the scaffolds, promoting cell growth, multiplication, and correct differentiation.

According to Kiyotake et al. [1], extracellular cartilage matrices are used in two different presentations, those being DCC (decellularized cartilage) and DVC (devitalized cartilage). Decellularization is done to avoid immunogenicity of the material; that process, however, damages the biochemical content and consequently the chondroinductivity of the scaffolds. Devitalization, on the other hand, disrupts the chondrocytes membranes by ice crystals formation due to freezing and thawing processes—in this case, the cellular debris remains in the middle of the extracellular matrix. In addition to greater chondroinductive potential, DVC has a mechanical advantage over DCC due to its greater biochemical complexity. Clinical evidence suggests that cartilage presents a low risk of immune response, and therefore cell debris need not to be removed [2].

Polycaprolactone (PCL) is a biocompatible polymer that melts at about 60 °C. Under physiological conditions, as in implants in the human body, it is degraded by hydrolysis of its esters, making room for collagen produced by chondrocytes that can be added to the scaffolds. In bone and cartilage substitutes, it provides the necessary structural reinforcement to support cells [3, 4].

I. M. Poley (✉)
Laboratório de Bioengenharia/Departamento de Engenharia Mecânica, Universidade Federal de Minas Gerais, Belo Horizonte, Brazil
e-mail: poley@ufmg.br

R. Silveira
3DLopes, Belo Horizonte, Brazil

J. A. Dernowsek
CTI Renato Archer, Campinas, Brazil

E. B.L. Casas
Departamento de Engenharia de Estruturas, Universidade Federal de Minas Gerais, Belo Horizonte, Brazil

T. F. Bastos-Filho et al. (eds.), *XXVII Brazilian Congress on Biomedical Engineering*, IFMBE Proceedings 83, https://doi.org/10.1007/978-3-030-70601-2_17

In this study, different biomaterials with potential to be used in bioprinting of cartilaginous substitutes and their variations containing DVC and/or PCL were tested on a 3D printer for their printability and consistency of the resulting printed scaffolds.

2 Materials and Methods

Twelve different biomaterials have been formulated to be tested for their potential use in bioprinting. The formulations started from compositions previously tested by Paxton et al. [5]. Pulverized DVC and/or granulated PCL were added to some formulations.

The exogenous pulverized DVC added to the compositions is commercially available and produced from shark cartilage by the Tiaraju™ Laboratory (Santo Ângelo, RS, Brazil) under the name of "Cartilagem de Tubarão". Its maximum particle size is 0.25 mm. At first, preference was given to the use of porcine DVC due to its greater physiological similarity with human cartilage, but difficulties related to grinding that material and obtaining it in sufficient quantities for the tests justified the replacement by shark DVC only for mechanical tests. Anyway, the use of exogenous material is justified by clinical evidence that cartilaginous tissues are immunoprivileged [1]. Future immunohistochemical evaluation of the printed scaffolds is suggested to verify biocompatibility.

PCL (average Mn 80,000, 440,744-250G), poloxamer 407 (Pluronic F-127, P2443-250G), sodium alginate (W201502-1 KG), gelatin (48,723-500G-F), and Dulbecco's Modified Eagle's Medium (D5921-500ML) were purchased from Sigma-Aldrich (St. Louis, Missouri, USA). Calcium chloride (102,392) was purchased from Merck Millipore (Burlington, Massachusetts, USA).

Granulated PCL was obtained by grating. Average particle diameter of 1 mm was achieved. Thinner comminution is suggested for future tests, making it possible to use printing needles with 0.41 mm or smaller diameter. 0.41 mm is the largest recommended diameter for bioprinted filaments, since the diffusion of oxygen and nutrients through the material requires a maximum radius of 0.2 mm.

The formulations by Paxton et al. [5] reproduced in this study were:

- Poloxamer 407 30% wt in aqueous solution
- Sodium alginate 8% w/v in PBS (phosphate buffered saline), with pre-crosslinking promoted by 1% w/v $CaCl_2$ solution, mixed with the alginate gel in a proportion of 7:3 volume mixing ratio (that composition is hereafter referred to as 8%/1% alginate, as in Paxton et al. [5])
- 2%-10% alginate-gelatin, formulated from a mixture of 4% w/v sodium alginate in PBS and 20% w/v gelatin in PBS (that composition was first tested by Wüst et al. [6] and then reproduced by Paxton et al. [5])

The resulting compositions are listed in Table 1.

The biomaterials were tested using a customized 3D printer by 3DLopes™. The equipment uses the FDM (fused deposition modeling) technique, and was adapted to function with a syringe filled with biomaterial, with the piston being pressed by a screw system whose stepper motor (Nema 17, 3 W, 1.33 A) is controlled by a processing board. At the tip of the syringe, needles with various diameters can be adapted. For this study, 1.54 mm needles were used.

Scaffolds with overlapping layers of parallel filaments, rotated by 90°, forming a checkerboard pattern, were printed to assess the uniformity and consistency of the filaments.

The scaffolds made with biomaterials from 1 to 8 received calcium chloride 2% w/V solution to have the

Table 1 Compositions of biomaterials tested on the 3D printer

Biomaterial	Composition
1	8%/1% alginate mixed with poloxamer 407 30% wt in a 1:1 volume mixing ratio
2	Same composition of biomaterial ink 1 with additional DVC 3% wt
3	Same composition of biomaterial ink 1 with additional PCL 3% wt
4	Same composition of biomaterial ink 1 with additional DVC 1.5% wt and PCL 1.5% wt
5	Pure alginate 8%/1%
6	Same composition of biomaterial ink 5 with additional DVC 3% wt
7	Same composition of biomaterial ink 5 with additional PCL 3% wt
8	Same composition of biomaterial ink 5 with additional DVC 1.5% wt and PCL 1.5% wt
9	2% - 10% alginate-gelatin
10	Same composition of biomaterial ink 9 with additional DVC 3% wt
11	Same composition of biomaterial ink 9 with additional PCL 3% wt
12	Same composition of biomaterial ink 9 with additional DVC 1.5% wt and PCL 1.5% wt

alginate crosslinking completed after deposition. Biomaterials numbered 9 to 12, which are heat-responsive, were transferred from the printhead heated to 37 °C to a cooled plate (0–4 °C) when deposited, following the same procedure as Paxton et al. [5].

3 Results and Discussion

3.1 Biomaterials Based on Alginate and Poloxamer 407 (Compositions 1 to 4)

Biomaterial 2, which contains DVC, presented filaments with greater consistency and, in general, less irregularities, when compared to biomaterial 1, as shown in Fig. 1.

When printing using biomaterial 3, which contains the largest amount of particulate PCL among compositions 1 to 4, clogging occurred due to the gradual accumulation of PCL particles at the syringe outlet. As shown in Fig. 1, the resulting scaffold became very irregular and it was not possible to print overlapping layers.

Biomaterial 4, with lower amounts of PCL compared to biomaterial 3, allowed to print a complete scaffold, shown in Fig. 1, but with more irregular filaments compared to biomaterials 1 and 2. Partial obstruction of the syringe outlet by PCL particles contributed to the irregularities.

Due to the presence of poloxamer 407 in the compositions, during periods of refrigerated storage before impressions, those biomaterials liquefied and decanted, decreasing the presence of air bubbles that remained mixed in those biomaterials after the preparation of the compositions.

Centrifugation procedures for removal of air bubbles were not successful due to the unwanted decanting of the particulate additives of the compositions.

3.2 Biomaterials Based on Alginate (Compositions 5 to 8)

Biomaterial 5, which is 8%/1% pure alginate, presented a more irregular printed pattern, shown in Fig. 2, when compared to biomaterial 1, the mixture of 8%/1% alginate and poloxamer 407 30% w/w in equal parts. This is because biomaterial 5 does not liquefy when stored in the refrigerator and, therefore, does not release air bubbles by decantation. For comparative purposes, none of the biomaterials was centrifuged prior to printing, but biomaterial 5, which was also prepared and tested by Paxton et al. [5], does require centrifugation for better results.

Similarly, biomaterial 6 showed a more irregular printed scaffold compared to its equivalent with poloxamer 407

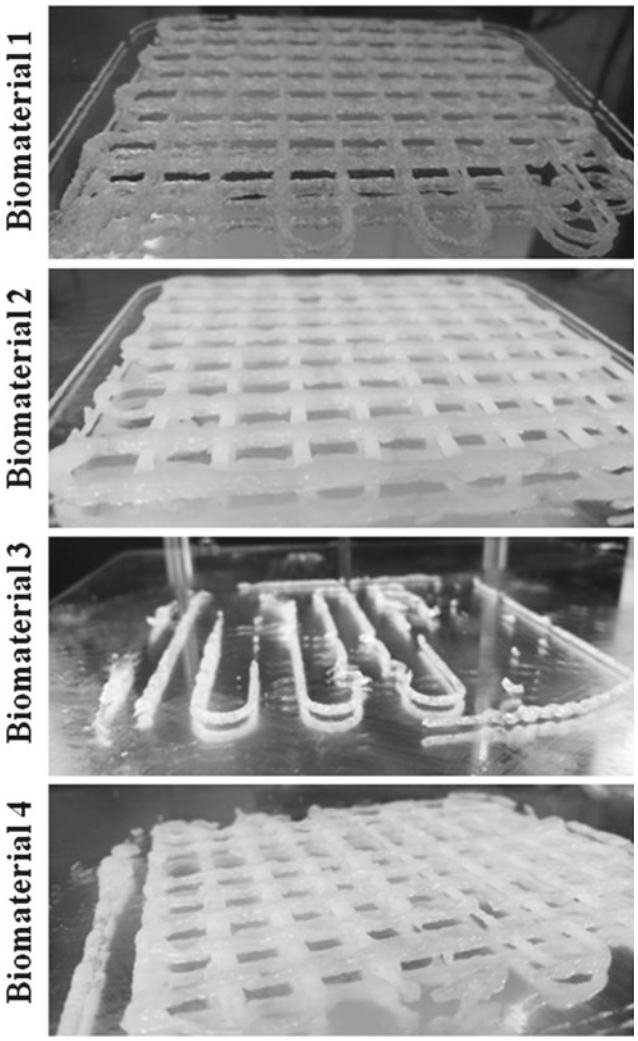

Fig. 1 Printing results for biomaterials 1 to 4

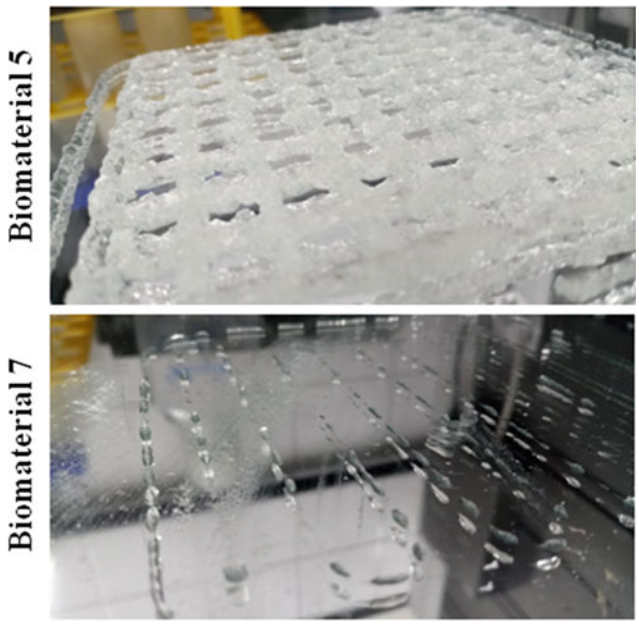

Fig. 2 Printing results for biomaterials 5 and 7

(biomaterial 2) due to the presence of air bubbles. However, the use of centrifugation for biomaterial 6 would separate its particulate DVC from its content.

Biomaterial 7, as well as its equivalent with poloxamer 407 (biomaterial 3), caused clogging by PCL particles at the syringe outlet. Drip was observed when increasing the printhead temperature, because the biomaterial became less viscous, as seen in Fig. 2, and passed between the PCL particles instead of carrying them.

Biomaterial 8 printing results were very similar to those of its equivalent with poloxamer 407, biomaterial 4.

3.3 Biomaterials Based on Alginate and Gelatin (Compositions 9 to 12)

Biomaterials 9 to 12, which are thermoresponsive, were deposited on cooled plates to acquire consistency. Figure 3 shows the advantage of the presence of DVC in biomaterial 10 when compared to biomaterial 9, which does not have DVC. The filaments of biomaterial 10 maintain the tubular characteristic to a greater degree, as they are more consistent.

Biomaterial 11, shown in Fig. 3, generated a problem similar to that presented in Fig. 2 for biomaterial 7. There was also clogging with PCL particles at the syringe outlet, but the low viscosity of the gel containing gelatin at 37 °C allowed the gel to pass through the interstices between the particles and through the needle. The result was a scaffold poor in PCL particles. The scaffold of biomaterial 12, shown in Fig. 3, on the other hand, also presented some irregularities, due to some clogging, but the filament consistency was improved due to the presence of particles from both DVC and PCL.

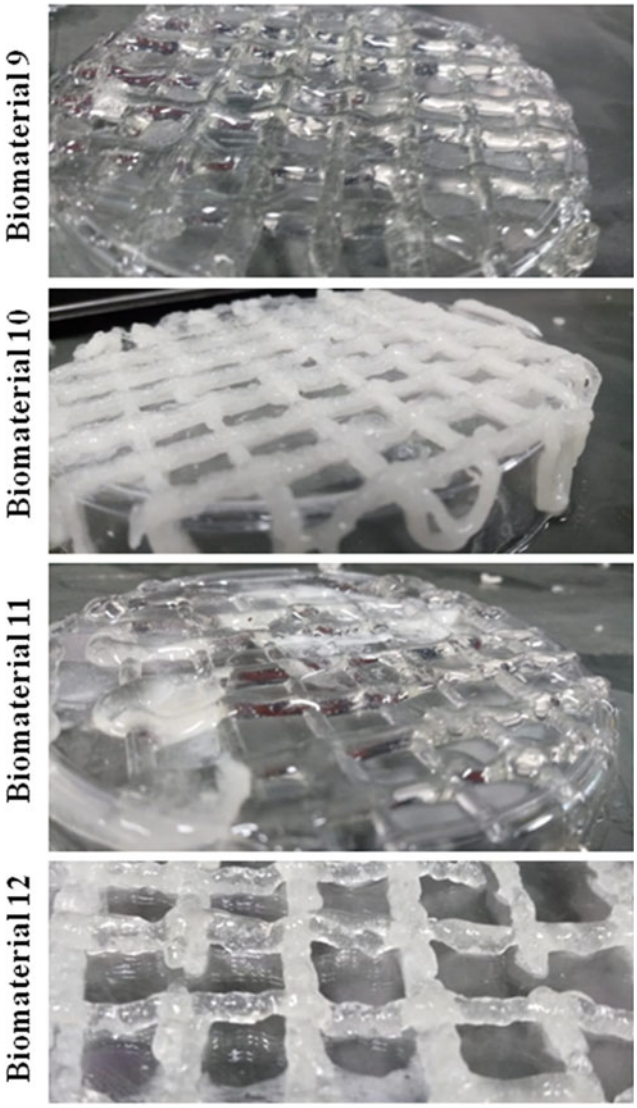

Fig. 3 Printing results for biomaterials 9–12

4 Conclusions

The high viscosities of the biomaterials make it necessary to replace the printer's central axis motor. The currently used motor is not potent enough to keep the thread turning in attempts to print using thinner needles. More potent motors are larger, so their use would require to redesign the entire central axis. With a more potent motor, printing needles with a diameter of 0.41 mm can be used. Also for the use of thinner needles, it will be necessary to obtain PCL with smaller particle sizes.

The high viscosities of the tested biomaterials favor the gradual carrying, without accumulation, of their particulated components along the printing. Lower viscosities would give PCL particles greater freedom to settle to the bottom of the syringe and to accumulate. However, it is necessary for the particulated material to be, in any case, sufficiently fine to avoid clogging.

The addition of DVC to the compositions, besides conferring biochemical advantages, also brought mechanical advantages to the consistency of the scaffolds. The effect of adding PCL, on the other hand, will be better evaluated when testing PCL with smaller particle sizes.

The use of poloxamer 407 in conjunction with alginate favors the escape of bubbles by decantation during refrigerated storage. The decantation of compositions containing gelatin at temperatures just above room temperature has the same effect. In such cases, centrifugation may not be necessary when preparing biomaterials. However, it is recommended to gently stir these compositions before use to redistribute the particulate material with a minimum mixing with air.

Rheometry analysis of the twelve tested biomaterials, in conjunction with computational fluid dynamics simulations, will be useful to predict the shear stresses to which cells may

be subjected when added to biomaterials for bioprinting. Shear stresses must be low enough to minimize disruption of cell membranes.

Acknowledgements The authors would like to thank the Brazilian agencies CNPq (Conselho Nacional de Desenvolvimento Científico e Tecnológico) and FAPEMIG (Fundação de Amparo à Pesquisa do Estado de Minas Gerais) for their support.

Conflict of Interest The authors declare that they have no conflict of interest.

References

1. Kiyotake E, Beck E, Detamore M (2016) Cartilage extracellular matrix as a biomaterial for cartilage regeneration. Ann NY Acad Sci 2016:139–159
2. Farr J, Yao J (2011) Chondral defect repair with particulated juvenile cartilage allograft. Cartilage 2:346–353
3. Kang H, Lee S, Ko I et al. (2016) A 3D bioprinting system to produce human-scale tissue constructs with structural integrity. Nat Biotechnol, 1–11
4. Garrigues N, Little D, Adams J et al (2014) Electrospun cartilage-derived matrix scaffolds for cartilage tissue engineering. J Biomed Mater Res 102a: 3998–4008
5. Paxton N, Smolan W, Böck T et al (2017) Proposal to assess printability of bioinks for extrusion-based bioprinting and evaluation of rheological properties governing bioprintability. Biofabrication 9. https://doi.org/10.1088/1758-5090/aa8dd8
6. Wüst S, Müller R, Hofmann S (2015) 3D Bioprinting of complex channels-effects of material, orientation, geometry, and cell embedding. J Biomed Mater Res A 103:2558–2570

Chemical Synthesis Using the B-Complex to Obtain a Similar Polymer to the Polypyrrole to Application in Biomaterials

Lavínia Maria Domingos Pinto, Mariane de Cássia Rodrigues dos Santos, Mirela Eduarda Custódio, F. E. C. Costa, Larissa Mayra Silva Ribeiro, and Filipe Loyola Lopes

Abstract

This research aimed to perform chemical synthesis using the B-complex to obtain similar conductive and magnetic characteristics to the Polypyrrole polymer, which presents biocompatible properties. The technique, characterized as low-cost, can be used in many applications, since as biomaterials in biomedical area until telecommunications area. To obtain the Polypyrrole, it was chosen two methods and four treatments to achieve the powder. The conductive properties of the resulting powders were verified using the four-probe technique to measure the voltage; the conductivity was performed using a conductivity meter, and the HD magnet was used to check the magnetic properties of the synthesized powder. The results obtained for the conductivity was ≈ 1.68 μS/cm, and the voltage was about 1.31 mV. The use of B-complex as a substitute of the Polypyrrole shows similar results to its conductive characteristics, been a viable alternative as biomaterial application.

Keywords

Biosensors • B-complex • Conductive

1 Introduction

The Polypyrrole (PPy) is an organic polymer performed by the polymerization of pyrrole discovered by Dall'Olio in 1968. Dall'Olio obtained a black powder adhered to the electrode surface through the electrolysis process of a solution of PPy in sulfuric acid. A few years later, Diaz and Col obtained a PPy black film from the electrolysis of pyrrole in acetonitrile and tetramethylammonium tetrafluorborate. This process resulted in a high conductivity of the polymer (≈100 S. cm $^{-1}$), caused by the oxidation–reduction between the polymeric chain and the doping agent [1]. Since then, the PPy synthesis has been used due to the high electric conductivity, adhesion, mechanical strength, chemical activity, and it is used as metals coating, protecting it from the corrosion processes. Besides, the PPy synthesis is obtained easily [2]. Furthermore, this polymer is often used in biosensor manufacturing, showing better characteristics of sensibility, lifetime, fast response time, high conductivity, and biocompatibility [3, 4].

However, it is necessary to search for substances with new physicochemical properties, which presents a low impact on the environment and low-cost fabrication for innovative materials. The choice of new polymeric material is necessary to select the chemical synthesis route that best suits the process [5].

The most revolutionary applications of the conductive polymers concern in the biomedicine field, being applied in tissue engineering, artificial nerves, and biosensors [5]. The PPy electrodes biosensors can be used to receive biological and electrical signals and also in the manufacturing of neural prosthesis for nerve regeneration [6–9].

L. M. D. Pinto · M. de CássiaR. dos Santos · M. E. Custódio · F. E. C. Costa · F. L. Lopes (✉)
National Institute of Telecommunication, Santa Rita do Sapucai, Brazil
e-mail: filipeloyola@geb.inatel.br

L. M. D. Pinto
e-mail: laviniamaria@geb.inatel.br

M. E. Custódio
e-mail: mirelaeduarda@geb.inatel.br

F. E. C. Costa
e-mail: costafec@inatel.br

L. M. S. Ribeiro
Federal University of Itajubá, Itajubá, Brazil
e-mail: larissa.ribeiro@geb.inatel.br

T. F. Bastos-Filho et al. (eds.), *XXVII Brazilian Congress on Biomedical Engineering*, IFMBE Proceedings 83, https://doi.org/10.1007/978-3-030-70601-2_18

To obtain a conductive material through the PPy synthesis, some researchers used oxidizing agents, surfactants, and conventional PPy. These works present good conductive results, but the high cost may prevent its use [1].

The cost analysis demonstrates that 250 g of doped PPy costs R$ 2.1800,00 and non-doped general PPy costs about R$ 640,00 [10]. The doped polymer presents high conductive than the non-doped polymer due to the use of oxidizing or reductive agents in the doping process, leading to deformations on the polymeric chain known as polarons and bipolarons resulting on the better conductivity properties [5]. Also, the oxidizing or reductive process of PPy causes the appearance of magnetic characteristics, and the higher is the doping level, the better is its magnetic sensibility [11].

For these reasons, this research aims to develop and test two methods of chemical synthesis, which presents a conductive effect similar to conventional PPy using the same oxidizing and surfactants agents, but substituting the PPy by the B-complex (group of vitamins that contains pyrrolic rings in its chemical structure).

2 Materials and Methods

This study was realized in the biochemistry lab of the National Institute of Telecommunications in June-November of 2019. The research was divided into two methods, developed in the following steps: (A) Definition of the methods I and II to obtain the pyrrole monomer from natural substrates that present chemical pyrrolic structures; (B) B-complex First Treatment; (C) B-complex Second Treatment; (D) B-complex Third Treatment; (E) B-complex Fourth Treatment and (F) Conductive Properties Assay.

2.1 Definition of the Methods and Reagents

The Method I consist of the following reagents: sodium lauryl sulfate (SLS) (0.08 mol/L), ammonium sulfate (0.05 mol/L), acetone, methanol, distilled water, and the B-complex.

Method II consists of the following reagents: iron (III) sulfate (0.05 mol/L), iron perchloride (0.1 mol/L), acetone, methanol, distilled water, and the B-complex.

The B-Complex is a group of eight vitamins compound by: 16 mg of Niacin (B3), 5.0 mg of Pantothenic Acid (B5), 1.3 mg of Pyridoxine (B6), 1.3 mg of Riboflavin (B2), 1.2 mg of Thiamine (B1), 2.4 mg of Cyanocobalamin (B12), 240 µg of Folic Acid (B9) and 30 µg of Biotin (B7) [12]. In the B-Complex is possible to find the union of four pyrrole groups (C4H5N) that are present in the vitamin B12 [13].

The oxidazings agents (Ammonium Sulfate, Iron (III) Sulfate and Iron Perchloride) and the surfactant (SLS) were used in the synthesis to realize the polymer doping and consequently increase its conductivity.

2.2 B-complex First Treatment

For the First Treatment were used the reagents of Method I. An aqueous solution was prepared, dissolving the SLS reagent in 1L of distilled water in stirring for 30 min. This solution was divided into twice: Solution 1 (S_1) and Solution 2 (S_2) with 500 mL each. In S_1 was added 5.04 g of B-complex and in S_2 was added 3.30 g of ammonium sulfate. S_1 and S_2 solutions were stirring for 15 min. After these processes, the S_1 solution was added in S_2 solution and stirred for 1h05 resulting in Solution 3 (S_3). In 40 mL of S_3, it was added 16 mL of acetone and 16 mL of methanol. This new solution was stirring for 30 min and centrifuged for 10 min posteriorly. Figure 1 represents the S_3 solution with the black powder resulting from the centrifugation process. After this process, the liquid was disposed of and the first washing was done.

For the first washing, were used 16 mL of ethanol, 16 mL of acetone, and 20 mL of distilled water distributed in 5 test tubes. All tubes were centrifuged for 10 min. For the second washing, were used 16 mL of acetone and 32 mL of distilled water. The solution was centrifuged for more 10 min and was obtained a clear liquid. The liquid of the tubes was filtered in quantitative filter paper.

The powder achieved was removed from the filter paper, placed on a porcelain vessel, and was taken to the oven for 72 h at 75 °C. After the drying process, the powder was weighed.

2.3 B-complex Second Treatment

The second treatment with the B-complex was realized using the reagents of Method II.

An aqueous solution was prepared to dissolve 1.999 g of iron (III) sulfate in 50 mL of distilled water, forming the Solution 1 (S_1). Another solution was made dissolving 1.059 g of B-complex in 50 mL of distilled water, creating

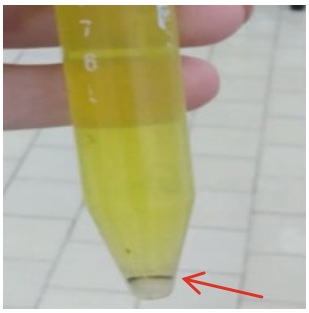

Fig. 1 Black powder obtained after the first centrifugation process

the Solution 2. The S_1 and S_2 solutions were added in each other using a pipette and stirred for 3h30, resulting in Solution 3 (S_3). The S_3 solution was centrifuged for 10 min. It was realized three washing with distilled water and four centrifugation process until obtaining a clear liquid.

After the fourth centrifugation, the solution was filtered and taken to an oven for 16 h at 75 °C to obtain a dry powder.

To verify the magnetic properties, an HD magnet was used to attract the black powder, as seen in Fig. 2.

2.4 B-complex Third Treatment

The third treatment using the B-complex was made using the reagents of Method II. An aqueous solution was prepared dissolving 1.622 g of iron perchloride in 50 mL of distilled water, forming Solution 1 (S_1). Solution 2 (S_2) was obtained dissolving 1.059 g of B-complex in 50 mL of distilled water. The S_1 and S_2 solutions were added in each other using a pipette and stirred for 3h30, resulting in Solution 3 (S_3).

The centrifugation, washing, drying, and verification of magnetic properties processes were the same as the second treatment with the B-complex.

2.5 B-complex Fourth Treatment

The B-complex fourth treatment was realized using the reagents of Method I. In this treatment, the concentrations of the SLS and ammonium sulfate reagents were increased to 46.137 g and 6.606 g, respectively. An aqueous solution was prepared dissolving the SLS reagent in 500 mL of distilled water and stirred for 30 min. This solution was divided into two, Solution 1 (S_1) and Solution 2 (S_2), with 250 mL each.

In S_1, was added 5.0428 g of B-complex, and the ammonium sulfate was added in S_2. Both solutions were stirring for 15 min. After this process, S_1 and S_2 were added in each other using a pipette and stirred for 1 h, resulting in Solution 3 (S_3).

In 40 mL of S_3 was added 32 mL of methanol and it was stirring for 30 min. Subsequently, the S_3 was dispensed in 5 test tubes and taken to the centrifuge process for 10 min. To increase the powder concentration in the tubes was removed the liquid of each tube and added more of S_3 solution to it. The tubes were centrifuged for more 10 min before the first washing process.

The washing process was realized using 50 mL of methanol in 30 mL of distilled water distributed in test tubes centrifuged for 10 min. After the last centrifugation, it could be seen a considerable quantity of powder at the bottom of the tube, which was refrigerated for seven days.

The centrifugation, washing, drying, and verification of magnetic properties processes were the same as the second treatment with the B-complex.

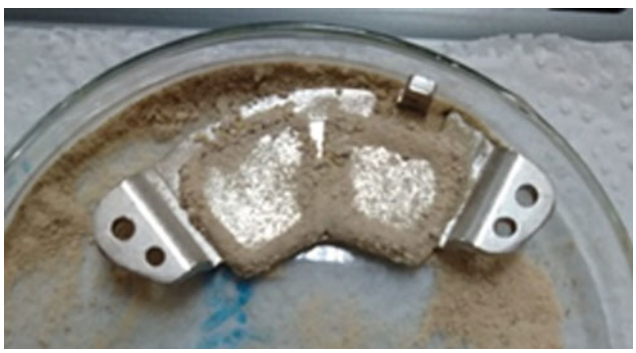

Fig. 2 Black powder attracted for the HD magnet

2.6 Conductive Properties Assay

The first technique used to assay the conductive characteristics of the chemical synthesis using the Method I and II described previously was the four-probe method. This technique consists of four electrically conductive probes arranged in lines, which are positioned in contact with the sample surface. The probes are equally spaced with each other for a known distance (S). An electrical charge (i) is provided to the sample through the external probes, and the potential difference (V) is measured through the internal probe [9, 14].

To measure the voltage, a colorless nail base coat was used because it is an electrical insulator and does not interfere with the conductivity of the material. Therefore, the obtained powders were mixed with the nail base and were deposited separately in 5 cm lines drawn in a paper, as seen in Fig. 3a.

For each sample, it was used four reference points with the distance of 1.5 cm between then. A 5 V DC (1A) source powered the peripheral region, and the multimeter test probes (Minipa ET—2042D) were placed in the central points of each sample.

The second technique to check the conductive characteristics of the powders obtained in Method I and II was realized using a Siemens conductivity meter with a range of 40 mΩ to 1 kΩ, as shown in Fig. 3b.

For the third technique, a conductivity meter (HANNA Instruments Brasil) was used. This device is used to measure the hemodialysis water conductivity from the Teaching Hospital of Itajubá—MG. In this test, due to the amount of powder, there were realized measurements with the powder obtained from the second and fourth treatments only. To

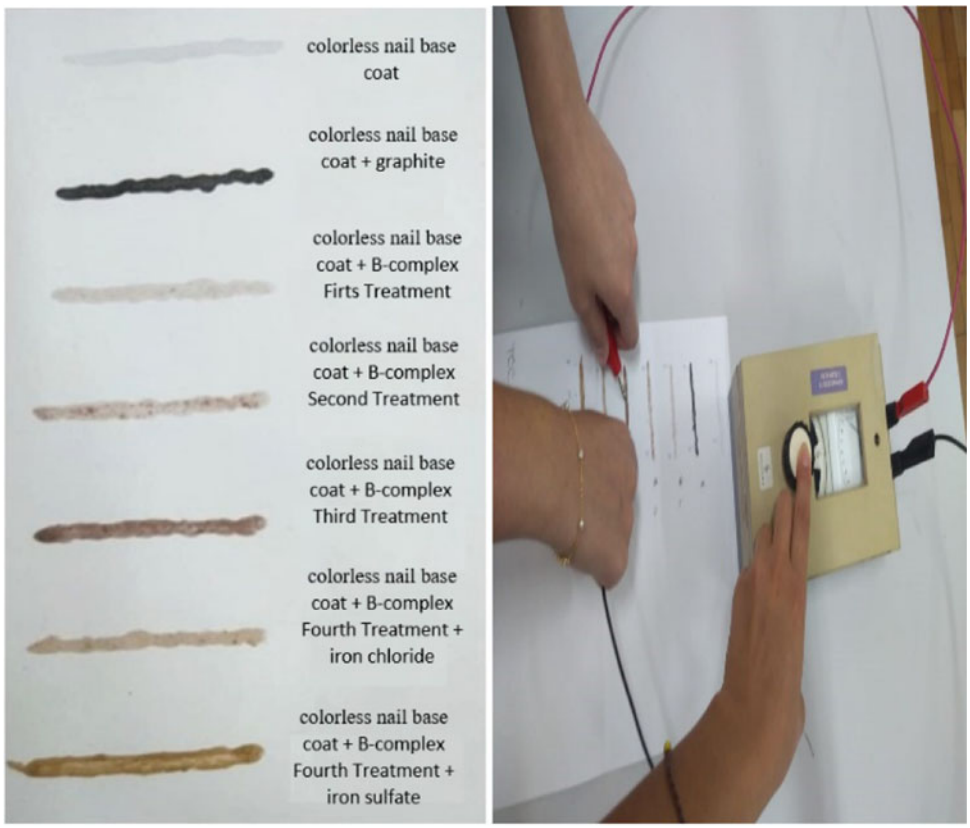

Fig. 3 **a** Colorless nail base mix with the powders obtained in Method I and II. **b** Conductivity measurement of the powders mix with the nail base using the Siemens Conductivity Meter

measure the conductivity, three beckers with 100 mL of hemodialysis water were used: one becker with 0.05 g of graphite for the control sample and the others two with 0.05 g of the powder obtained in the second and fourth treatment.

3 Results

To verify the conductive properties of the powders of each treatment, it was necessary to produce adequate amounts of powder. Table 1 represents the amount of powder obtained in each treatment.

Observing the Table 1, the first and third treatment presented a small amount of powder, so it could not be used to verify the conductive characteristics in the conductivity meter. Although, it was realized the measurements using the four-probe technique of each sample in triplicate, and the results are presented in Table 2.

The resistance of the samples was not measurement because the resistance values were out of the scale reading for the multimeter.

Tables 3, 4, and 5 present the values obtained of the measurement realized in quintuplicate.

After confirming the conductivity of the powders obtained of the PPy synthesis in the laboratory, it was realized the arithmetic average for the control sample, second and third treatment, as shown in Table 6.

The results obtained in the tested methods were satisfactory for the second and fourth treatments due to the possibility of verifying the conductivity properties using all techniques of measurement and also the magnetic properties using the HD magnet.

Table 1 Amount of obtained powder

Treatments	Amount powder (g)
First treatment	0.0436
Second treatment	0.7139
Third treatment	0.0682
Fourth treatment	0.1996

4 Discussion

Comparing the results obtained in Table 6 with the literature, as shown in Table 7, it was possible analyzing the conductivity of the PPy and its synthesis. The product obtained in the present study presents several characteristics of PPy that

Table 2 Potential difference obtained in each sample

Measurements of the Potential Difference (mV)			
Samples	1º	2º	3º
Base Nail	0	0	0
Base + Graphite	6.4	4.2	3.9
Base + Firts Treatment	3.7	5.8	3.3
Base + Second Treatment	1.7	1.2	2.2
Base + Third Treatment	10.6	12.4	9.8
Base + Fourth Treatment	1.2	0.9	1.5

Table 3 Graphite conductivity measurement

Measurements of the conductivity (μS/cm)					
Samples	1º	2º	3º	4º	5º
Water hemolialysis conductivity	2.8	2.9	3.0	3.0	3.0
Water hemodialisys + powders conductivity	3.5	3.4	3.4	3.4	3.5

Table 4 Second treatment conductivity measurement

Measurements of the conductivity (μS/cm)					
Samples	1º	2º	3º	4º	5º
Water hemolialysis conductivity	2.8	2.9	2.9	2.8	2.9
Water hemodialisys + powders conductivity	4.1	4.8	4.7	4.8	4.8

Table 5 Fourth treatment conductivity measurement

Measurements of the conductivity (μS/cm)					
Samples	1º	2º	3º	4º	5º
Water hemolialysis conductivity	2.8	2.7	2.9	2.8	2.9
Water hemodialisys + powders conductivity	4.2	4.3	4.2	4.5	4.4

Table 6 Average of the potential difference and conductivity

	Potential difference (mV)	Conductivity (μS/cm)
Graphite	4.83	0.50
Second Treatment	1.7	1.79
Fourth Treatment	0.93	1.57

Table 7 Conductivity according to other authors

Authors	Conductivity (mS/cm)
Campos et al. [1]	12600 ± 2330
Santim, 2011 [15]	0.0334
Sowmiya et al. [16]	8.21
Kim et al. [17]	280

characteristics differ from those of the substrates used in chemical reaction. However, it cannot be possible to compare the results due to the measurement of this research be made in an aqueous medium. For the comparison be realized, it will be necessary a hydraulic press and manual press to prepare the sample, according to the authors.

The use of the B-complex as a substitute of PPy is viable due to the low-cost and the presence of conductive and magnetic properties similar to the polymer. For this reason, the synthesis obtained in this work can be used in applications as biosensors for disease diagnostics as cancer, which present different electrical responses in the ill cells to the

healthy cells. Also, it can be used as a controlled drug release, synthetic membranes, artificial muscles, tissue engineering, and neural probes [5, 15, 18]. Notwithstanding, the PPy can be destinate as electromagnetic Shielding for electromedical equipment with needs this protection for an excellent performance.

As future research, the synthesis can be realized with baker's yeast, which presents pyrrolic rings in their chain and low-cost.

5 Conclusion

The chemical synthesis of the second and fourth treatment obtained in this work showed good results due to present conductive and magnetic properties similar to the PPy.

From this research, future and promising works will be continued with more tests, including biocompatibility assay and the physicochemical characterization of the B-complex synthesis.

Acknowledgements The authors would like to thank the FAPEMIG (Foundation for Research Support of State of Minas Gerais), and all other agencies from the Brazilian government.

Conflict of Interest The authors announce no potential conflicts of interest with respect to the research, authorship, or publication of this article.

References

1. Campos RM, Rezende MC, Faez R (2009) Chemical synthesis of polypyrrole: influence of anionic surfactants on thermal and conductive properties. In: Proceedings of the 10th Brazilian Polymer Congress, Foz do Iguaçu
2. Ramôa SDAS, Merlini C, Barra GMO (2014) Obtaining Montmorillonite/Polypyrrole conducting nanocomposites: effect of incorporating surfactant on structure and properties, Scielo Polímeros, vol. 24, n spe, pp 57–62. Epub Apr 18, 2014. ISSN 0104-1428. https://doi.org/10.4322/polimeros.2014.051
3. Júnior LR, Neto GO, Kubota LT (1997) Conductive polymer-based potentiometric transducers: analytical applications. New Chem 1997:519–527
4. Fahlgren A, Bratengeier C, Gelmi A, Semeins CM, Klein-Nulend J, Jager EWH et al (2015) Biocompatibility of polypyrrole with human primary osteoblasts and the effect of dopants. J Plos One, 1–18
5. Nogueira FAR (2010) Synthesis and characterization of polypyrrole derivatives for application in electrochemical devices, Post-Graduation Dissertation, Federal University of Alagoas, Maceió, AL, 2010
6. Gomez N, Schmidt CE (2007) Nerve growth factor-immobilized polypyrrole: Bioactive electrically conducting polymer for enhanced neurite extension. J Biomed Mater 81A(2007):135–149
7. Fonner JM, Forciniti L, Nguyen H, Byrne JD, KouL Y (2008) Nawaz J S (2008) Biocompatibility implications of polypyrrole synthesis techniques. Biomed Mater 3:1–12
8. Ferreira CL (2017) Synthesis of polymeric nanocomposites PCL/PLGA/Polypyrrole nanofibers for application in biocompatible conduit for nerve regeneration, Master's Dissertation, Eng. Tec. Materials, Pontifical Catholic University of Rio Grande do Sul, Porto Alegre, RS
9. Noeli S (1998) Photochemical synthesis, electrical and morphological characterization of PPy/PVDF composites, Master's Dissertation, Faculty of Chemical Engineering of Campinas, SP
10. Polypyrrole Price at https://www.sigmaaldrich.com/catalog/product/aldrich/482552?lang=pt&region=BR&gclid=Cj0KCQjwgezoBRDNARIsAGzEfe6O5DxbAli8qLqJ_LRr_q0QYYRQqt1XEQR5wwE73G_Vb6fW_EDUA8waApTCEALw_wcB
11. Marchesi LFQP (2010) Study of the electrochemical and magnetic properties of Polypyrrole, PhD Thesis Federal University of São Carlos, SP
12. VITGOLD at https://www.vitgold.com.br/b-complex
13. Silva MT (2019) Concentrations of vitamins B6, folate and B12 and their association with serum lipids in pregnancy: a prospective study, Postgraduate Master's Dissertation, University Federal of Pelotas, Pelotas, RS
14. Okoa MM (2000) Four Point Measure at https://www.lsi.usp.br/~dmi/manuais/QuatroPontas.pdf
15. Santim RH (2011) Synthesis and characterization of Polypyrrole (PPy) obtained by the conventional chemical process and microemulsion, Post-Graduation Dissertation, Universidade Estadual Paulista, Faculty of Engineering of Ilha Solteira, SP, Ilha Solteira
16. Sowmiya G, Anbarasan PM, Velraj G (2017) Synthesis, characterization and electrical conductivity study of conductive polypyrrole doped with nano Tin composite for antibacterial application. IRJET 4(2017):127–131
17. Kim S et al (2016) Electrochemical deposition of conductive and adhesive polypyrroledopamine films. Sci Rep 6:30475
18. Hocevar MA (2011) Development of amperometric enzyme biosensors using polypyrrole nanoparticles, Postgraduate Master's Dissertation in Mines, Metallurgy and Materials, Federal University of Rio Grande do Sul, Porto Alegre, RS

Evaluation of the Effect of Hydrocortisone in 2D and 3D HEp-2 Cell Culture

M. O. Fonseca, B. H. Godoi, N. S. Da Silva, and C. Pacheco-Soares

Abstract

Cancer is one of the diseases with the highest incidence in the world and that associated with the patient's emotional state, can act positively or negatively in the treatment. Cortisol is described as a primary stress hormone in the human body. Studies show a positive correlation of elevated cortisol levels and cancer progression. The corticoids can increase cell proliferation and increased reactive oxygen species that contribute to DNA damage. Prolonged exposure to stress can contribute to tissues becoming insensitive to cortisol, the primary human stress hormone. This study explores the influence of cortisol, an important hormone involved in stress, on tumor cell development, particularly in human cells of carcinoma of human laryngeal (HEp-2). HEp-2 cells were exposed to increasing cortisol (hydrocortisone) concentrations for 24 or 48 h and cytotoxicity (MTT assay [3-(4,5-dimethylthiazolyl-2)-2,5-diphenyltetrazio bromide], proliferation assay (crystal violet assay), and immunolabeled 3D culture for fibronectin and FAK were investigated. Corticosteroids and stress in cancer patients may inter-fere with cancer treatments because these may cause tumor cells to progress instead of reduce depending on the cell type. Although some cases favored corticosteroids use in cancer patients, a more detailed analysis is necessary be-fore prescribing them. Moreover, it is important to assess the patient's cortisol level before and after treatment as well.

Keywords

Stress • Carcinoma • 3D culture • Hydrocortisone

1 Introduction

Cancer is one of the most feared diseases of the twentieth century and spreads with increasing incidence in the twenty-first century [1]. As regards occurrences of cancer, several factors have been identified as contributing factors, including genetic predisposition, exposure to environmental risk factors, contagion by certain viruses, cigarette use, and the ingestion of carcinogens [2].

Psychological factors can contribute to the development of cancer, given the effects of emotional states on hormonal modification and the alteration of the immune system [3]. From these possibilities, we increasingly find studies that seek to relate or measure possible influences of psychological and social aspects in the development and possible aggravation of oncological pathologies.

The disease's symptoms and the related characteristics of the different forms of treatment used to fight cancer significantly interfere with patients' routines and quality of life, characterizing significant stressors in many cases [4].

Studies relate factors associated with stress to tumor biology; those that relate the effects of glucocorticoids and their relationship with the biology of tumor cells stand out [5–7]. The dysregulation of cortisol levels, a symptom associated with stress, also contributes to factors related to the morbidity, severity, and mortality of the disease process. This includes numerous types of oncological diseases such as tumor progression in breast cancer [8, 9].

M. O. Fonseca · B. H. Godoi · C. Pacheco-Soares (✉)
Laboratório de Dinâmica de Compartimentos Celulares, Universidade do Vale do Paraíba, Av Shishima Hifumi 2911, São Jose dos Campos, Brazil
e-mail: cpsoares@univap.br

N. S. Da Silva
Laboratório de Biologia Celular e Tecidual, Universidade do Vale do Paraíba, São Jose dos Campos, Brazil

T. F. Bastos-Filho et al. (eds.), *XXVII Brazilian Congress on Biomedical Engineering*, IFMBE Proceedings 83, https://doi.org/10.1007/978-3-030-70601-2_19

2 Materials and Methods

2.1 Cell Culture

HEp-2 (carcinoma of human larynges) were obtained from cell bank of Rio de Janeiro and cultured at 37 °C under 5% CO_2 in Dulbecco's Modified Eagle Medium (DMEM, Gibco BRL, Grand Island, NY, USA) supplemented with 10% fetal bovine serum (FBS) (Gibco BRL, Grand Island, NY, USA), and 1% penicillin and streptomycin (Invitrogen Life Technologies, Carlsbad, CA, USA).

2.2 Incubation with Hydrocortisone

HEp-2 cells were plated (1×10^5 cells/mL) in 24-well microplates, with MEM culture medium supplemented with 10% fetal bovine serum (SFB) for cell adhesion in a 5% CO_2 oven and temperature of 37 °C and incubated overnight. The next day, the cells were subjected to treatment with Hydrocortisone 500 mg, diluted in PBS, for periods of 24 and 48 h in the following concentrations: 0.5, 1.0, 1.5, 2, and 2.5 μM [10].

2.3 Mitochondrial Metabolic Activity (MTT Assay)

HEp-2 cells submitted to treatment with hydrocortisone in the periods of 24 and 48 h were washed with PBS three times incubated with MTT (0.5 mg/ml) for 1 h at 37 °C in an atmosphere of 5% CO_2. Over the precipitates of formazan, the organic solvent DMSO (50 μL) was added to each well. The plate is kept under shaken for 10 min, for solubilization of the formazan crystals, and the absorbance reading was performed on a Packard SpectraCount wavelength of 570 nm. The data obtained were plotted in a graph by the GraphPad 6.0 program.

2.4 Crystal Violet Assay

Crystal Violet staining is used to infer population density, a clonogenic test. The method is described as colorimetric for determining appropriate cells, as described by Fernandes et al. Cristal Violeta, a substance used for the test, crosses cell and nuclear membranes, binding to DNA, RNA, and proteins, which provides the identification of viable cells. In its outline, the spectrophotometric quantification of adherent cells indirectly identifies the number of viable cells used in this study to measure the population variation of the strains.

The HEp-2, subjected to treatment with cortisol at the mentioned times, had the culture medium removed afterward and incubated with 100 μL of Crystal Violet for 3 min at room temperature. Afterward, the plate was washed with running water and incubated for 1 h with 100 μL of DMSO, to then read on the photometer spectrum at 570 nm.

2.5 3D Culture

Cultures were performed using the Bio-Assembler™ kit designed for 24-well plates (n3D-Biosciences Inc, Houston, TX, USA) [11]. In summary, NanoShuttlesTM was added to a T-25 culture flask with a ratio of 1 μL of NanoShuttlesTM per 20,000 cells and incubated at 37 °C and 5% CO_2 overnight. Then, the cells were detached by treating them with 5 mL of trypsin for 5 min and washed by centrifugation (600 g/5 min) with a balanced saline solution (PBS). Cell viability was determined by the trypan blue exclusion method (1% w/v in PBS), and the density was adjusted to 106 cells/mL in the medium supplemented with RPMI-1640.

HEp-2 cells conjugated to NanoShuttlesTM were seeded on a 24-well ultralow-attachment plate (ULA, Cellstar® Greiner Bio-one, Kremsmünster, Austria) in 10^5 cells and a final volume of 400 μL/well.

The 3D culture was achieved by incubating (at 37 °C and 5% CO_2) the plates under the magnetic field, first using a bioprinting unit for 3 h, followed by the levitation unit during the entire culture period. This procedure allows for the growth of the cellular spheroid. The 3D culture plate was replenished with fresh medium every two days until the time of using the spheroid.

2.6 Immunostaining

After seven days of culture, HEp-2 cell spheroids were divided into two groups: (i) a cells-only control group and (ii) a treatment group, in which the cells were incubated with cortisol (2.5 μM) for 48 h at 37 °C in a 5% atmosphere of CO_2. After this, the spheroids were fixed with 4% paraformaldehyde in PBS for 15 min at room temperature. The cells were then permeabilized with 0.2% Triton X-100 in PBS for 10 min and then blocked with 1% bovine albumin serum (BSA) in PBS for 30 min. Thereafter the spheroids were incubated with anti-human monoclonal antibody mouse against fibronectin antibody (1:500/1 h) and rabbit anti-human monoclonal antibody against FAK (1:500/1 h), and then incubated with antibodies. Anti-mouse polyclonal secondary antibody was conjugated to FITC, and goat anti-rabbit polyclonal secondary antibody was conjugated to TRITC (all antibodies from Sigma Aldrich, Co). The nuclei

were marked with DAPI (4′,6-diamidino-2-phenylindole). Samples were visualized using a fluorescence microscope (DMIL, Leica).

2.7 Statistical Analysis

The data presented are in the form of mean and standard deviation, compared by the two-way ANOVA test and confirmed by the Tukey test. Statistical significance was admitted with $P < 0.05$ with *$P < 0.05$; **$P < 0.01$; ***$P < 0.001$; ****$P < 0.0001$ being considered significant. Experiments were performed in three independent replications with n = 8. GraphPad Prism 6® software was used to perform statistical and graphical analyzes.

3 Results

The mitochondrial evaluation by MTT aimed to measure possible influences of incubation with hydrocortisone, in concentrations of 0.5, 1.0, 1.5, 2.0, and 2.5 μM, in HEp-2 cell culture, relating possible findings to the population density results which were then analyzed. Figure 1 presents the results of the mitochondrial activity.

Compared with the control group, the other groups with increasing concentrations of hydrocortisone do not show a statistical difference within 24 h. The comparative analysis of the control group with the other groups in the 24 h period shows a statistically significant increase in mitochondrial activity, mainly in the control, with concentrations of 0.5 to 2.0 μM ($p < 0.0001$), while the comparison between different concentrations of hydrocortisone results in a significant increase in mitochondrial activity between groups 0.5 versus 2.5 μM ($p < 0.0001$), 1.0 versus 2.0 μM ($p < 0.0003$), 1.0 versus 2.5 μM ($p < 0.0001$), 1.5 versus 2.5 μM ($p < 0.0001$), and 2.0 versus 2.5 μM ($p < 0.0001$).

Within 48 h, a significant increase was observed in all concentrations when compared to the control.

Population growth was assessed using the Crystal Violet test. The data described in Fig. 2 reveal that even under exposure to increasing hydrocortisone concentrations, there was no population reduction in the two distinct periods, except for the group incubated at 2.5 μM in the 24 h period, where a slight but not significant population reduction was observed.

The 3D growth assessment of HEp-2 cell culture under the action of hydrocortisone (2.5 μM) after 24 and 48 h of incubation is shown in Figs. 3 and 4.

In 24 h, the interaction with hydrocortisone was observed to be interfering with cells' spheroid formation, showing a very significant dispersion of cells marked with DAPI ($p = 0.0004$). Compared to the control, the immunolabeled for fibronectin exhibited a significant reduction ($p = 0.0192$) in the staining intensity (Fig. 3b).

Within 48 h, there was no significant change in fluorescence intensity among the immunolabeling (Fig. 4b).

4 Discussion

The disclosure of cancer diagnosis and treatment is usually a traumatic experience for the patient, causing the release of cortisol in response to stress associated with physical and mental comorbidities.

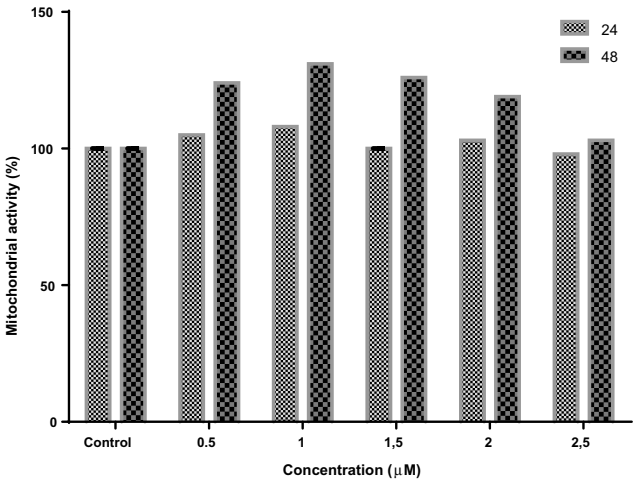

Fig. 1 Mitochondrial activity (MTT) assay of the HEp-2 cells. Cellular activity of the HEp-2 cells MTT assay at 24 and 48, after incubation of increasing concentrations of hydrocortisone, showing increase in cell numbers with increase in time. All values are expressed as mean ± standard error of the mean (SEM) from three different samples

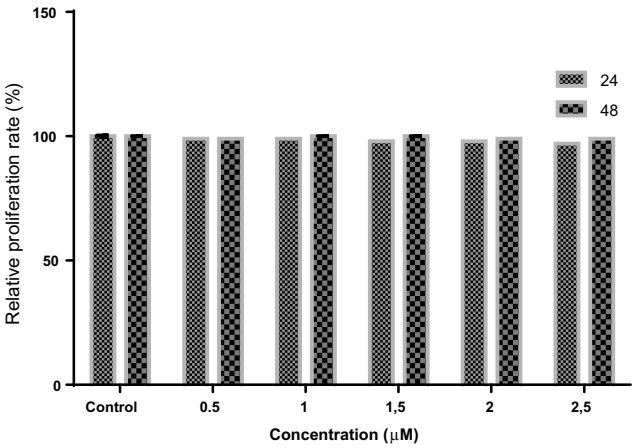

Fig. 2 Crystal violet assay. Crystal violet assay of HEp-2 cells, 24 to 48 h incubation with increasing concentrations of hydrocortisone. All values are expressed as mean ± standard error of the mean (SEM) from three different samples

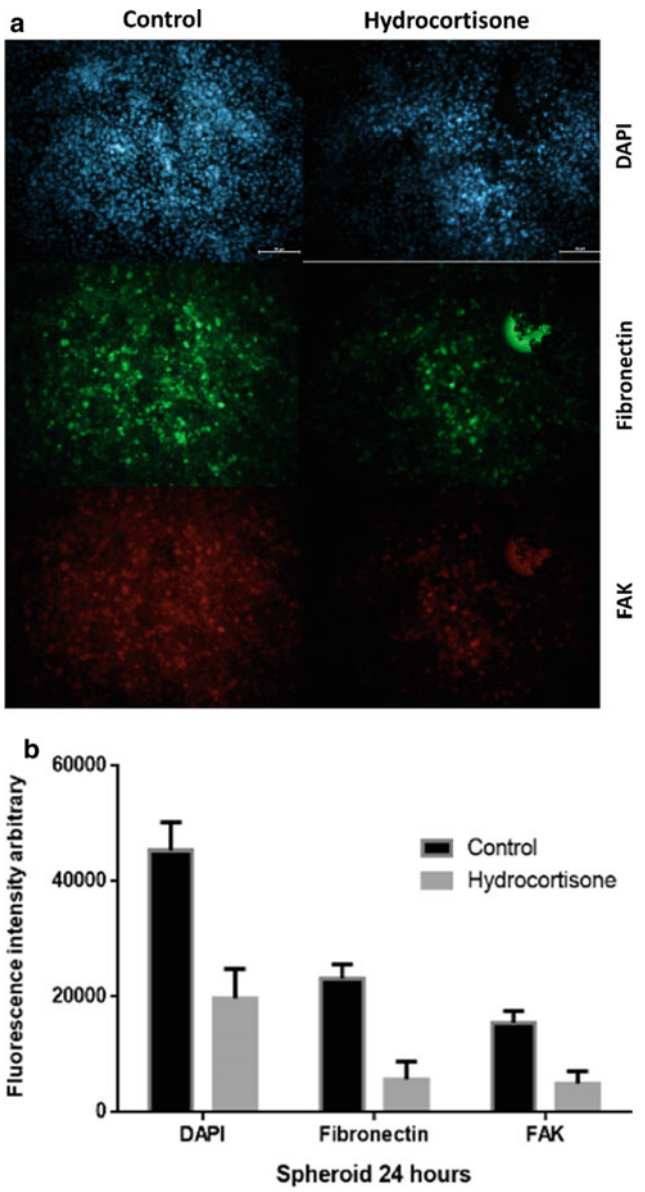

Fig. 3 Tumor spheroids immunolabeled for fibronectin and FAK. Cell proliferation and morphology of tumor spheroids at day 7 of culture, and after 24 h incubation with 2.5 µM of hydrocortisone, **a** photomicrography of spheroids after immunolabeled with ant-fibronectin and anti-FAK, nuclei labeled with DAPI, bar 50 µm. **b** Graphic fluorescence intensity for DAPI, fibronectin and FAK

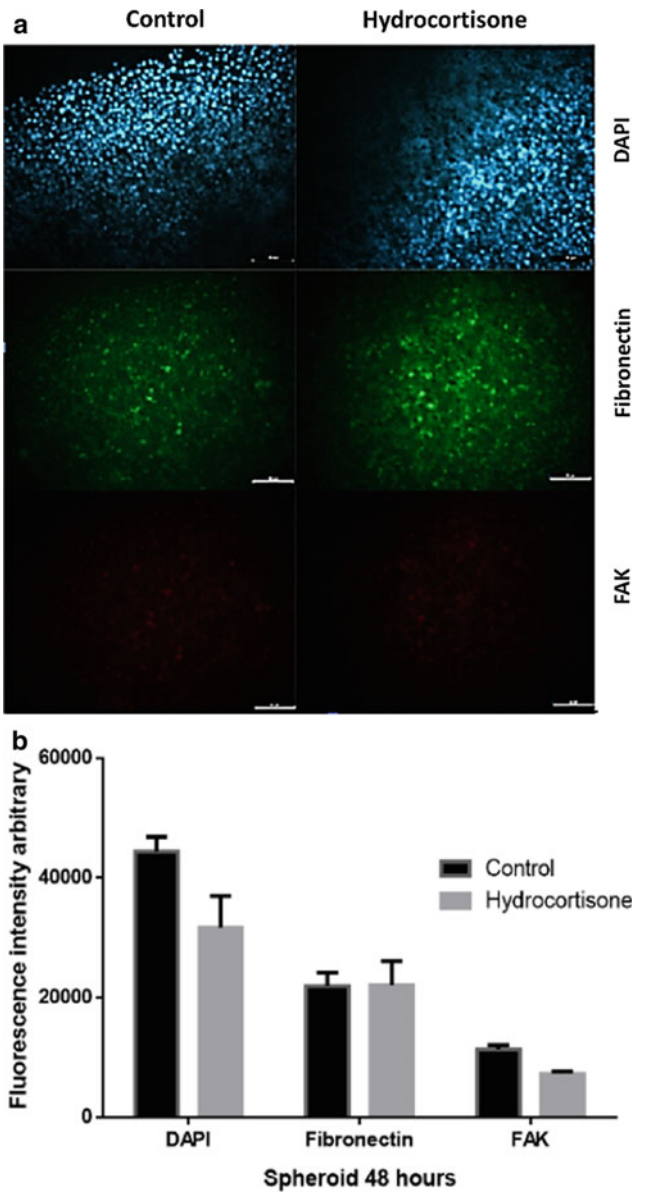

Fig. 4 Tumor spheroids immunolabeled for fibronectin and FAK. Cell proliferation and morphology of tumor spheroids at day 7 of culture, and after 48 h incubation with 2.5 µM of hydrocortisone, **a** photomicrography of spheroids after immunolabeled with ant-fibronectin and anti-FAK, nuclei labeled with DAPI, bar 50 µm. **b** Graphic fluorescence intensity for DAPI, fibronectin and FAK

To investigate the effects of cortisol on mitochondrial activity and cell proliferation, we exposed HEp-2 cells to 0.5–2.5 µM cortisol for 24 and 48 h and subjected them to MTT and crystal violet assays. The 3D culture was also tested to evaluate the extracellular matrix.

The results of the evaluation of the mitochondrial activity show that after 24 h of exposure to increasing concentrations of hydrocortisone, the cells presented a significant increase at 0.5 and 1.0 µM and a reduction at 2.5 µM. There is a significant increase in mitochondrial activity within 48 h, indicating intense cellular activity, as verified by Bomfim et al. and Peterson et al. [12, 13].

The behavior of HEp-2 cells (laryngeal carcinoma), was different from that of K562 cells (chronic myeloid leukemia) [14]. Within 24 h, the latter showed reduced mitochondrial activity. However, both strains showed similar behavior after 48 h.

The crystal violet assay shows DNA duplication. It can be verified that the decrease observed within 24 h is insignificant and that the duplication of the genetic material and,

consequently, the cell proliferation within 48 h remain similar to the control. These results are corroborated by Peterson et al. and Dong et al. [13, 15].

The evaluation of 3D growth HEp-2 cells and interaction with a concentration of 2.5 μM demonstrates that such concentration interferes with the interaction between cells after 24 h of incubation. There was no significant change in the interaction and spheroid formation after 48 h. Similar results were obtained by Chen et al. and Al-natsheh [16].

5 Conclusion

Corticosteroids and stress in cancer patients may interfere with cancer treatments because these may cause tumor cells to progress instead of reduce depending on the cell type. Although some cases favored corticosteroids use in cancer patients, a more detailed analysis is necessary before prescribing them. Moreover, it is important to assess the patient's cortisol level before and after treatment as well.

Acknowledgements This study had financial support of the Fundação de Amparo à Pesquisa de São Paulo (FAPESP) under Partnership Grant Number 16/17984-1.

Conflict of Interest The authors declare that they have no conflict of interest.

References

1. Roy PS, Saikia BJ (2016) Cancer and cure: a critical analysis. Indian J Cancer 53. Available from https://www.indianjcancer.com/text.asp?2016/53/3/441/200658
2. Brian C, Clarke B, Blackadar B, Blackadar CB, Researcher V (2016) Historical review of the causes of cancer. Accessed 17 May 2020. Available from https://dx.doi.
3. Chae J, Lee CJ (2019) The psychological mechanism underlying communication effects on behavioral intention: focusing on affect and cognition in the cancer context. Commun Res 46(5):597–618. https://doi.org/10.1177/0093650216644021
4. Bedillion MF, Ansell EB, Thomas GA (2019) Cancer treatment effects on cognition and depression: the moderating role of physical activity. Breast 44:73–80. https://doi.org/10.1016/j.breast.2019.01.004
5. Reiche EMV, Nunes SOV, Morimoto HK (2004) Stress, depression, the immune system, and CACER. Lancet Oncol 5:617–625. https://doi.org/10.1016/S1470-2045(04)01597-9
6. Spiegel D, Giese-Davis J (2003) Depression and cancer: mechanisms and disease progression. Biol Psychiatry 54:269–282. https://doi.org/10.1016/S0006-3223(03)00566-3
7. Vitale I, Manic G, Galassi C, Galluzzi L (2019) Stress responses in stromal cells and tumor homeostasis. Pharmacol Therapeut 200:55–68. https://doi.org/10.1016/j.pharmthera.2019.04.0048.mcewen1998
8. Lillberg K, Verkasalo PK, Kaprio J, Teppo L, Helenius H, Koskenvuo M (2003) Stressful life events and risk of breast cancer in 10,808 women: A cohort study. Am J Epidemiol. 157:415–423. https://doi.org/10.1093/aje/kwg002
9. Sephton SE, Sapolsky RM, Kraemer HC, Spiegel D (2000) Diurnal cortisol rhythm as a predictor of breast cancer survival. J Natl Cancer Inst 92(12):994–1000. https://doi.org/10.1093/jnci/92.12.994
10. Abdanipour A, Tiraihi T, Noori-Zadeh A, Majdi A, Gosaili R (2014) Evaluation of lovastatin effects on expression of anti-apoptotic Nrf2 and PGC-1α genes in neural stem cells treated with hydrogen peroxide. Mol Neurobiol 49(3):1364–1372. https://doi.org/10.1007/s12035-013-8613-5
11. Natânia de Souza-Araújo C, Rodrigues Tonetti C, Cardoso MR, Lucci de Angelo Andrade LA, Fernandes da Silva R, Romani Fernandes LG et al (2020) Three-dimensional cell culture based on magnetic fields to assemble low-grade ovarian carcinoma cell aggregates containing lymphocytes. Cells 9(3):635. https://doi.org/10.3390/cells9030635
12. Bomfim G, Merighe G, de Oliveira S, Negrao J (2018) Effect of acute stressors, adrenocorticotropic hormone administration, and cortisol release on milk yield, the expression of key genes, proliferation, and apoptosis in goat mammary epithelial cells. J Dairy Sci 101:6486–96. Available from https://doi.org/10.3168/jds.2017-14123
13. Petersen A, Carlsson T, Karlsson J-O, Jonhede S, Zetterberg M (2008) Effects of dexamethasone on human lens epithelial cells in culture
14. De M, Fonseca O, Soares Da Silva N, Soares CP (2019) Effect of cortisol on K562 leukemia cells. O Mundo Da Saúde, São Paulo 43(4):854–869. https://doi.org/10.15343/0104-7809.20194304854869
15. Dong J, Li J, Li J, Cui L, Meng X, Qu Y et al (2019) The proliferative effect of cortisol on bovine endometrial epithelial cells. Reprod Biol Endocrinol 17(1):97. Accessed 27 May 2020. Available from https://doi.org/10.1186/s12958-019-0544-1
16. Chen YX, Wang Y, Fu CC, Diao F, Song LN, Li Z et al (2010) Dexamethasone enhances cell resistance to chemotherapy by increasing adhesion to extracellular matrix in human ovarian cancer cells. Endocr Relat Cancer 17(1):39–50. https://doi.org/10.1677/ERC-08-0296

Surface Topography Obtained with High Throughput Technology for hiPSC-Derived Cardiomyocyte Conditioning

Lucas R. X. Cortella, I. A. Cestari, M. S., M. Mazzetto, A. F. Lasagni, and Ismar N. Cestari

Abstract

The use of human induced pluripotent stem cell-derived cardiomyocytes (hiPSC-CM) to replace myocardial tissue after an infarct holds great promises. However, hiPSC-CM are phenotypically immature when compared to cells in the adult heart, hampering their clinical application. We aimed to develop and test a surface structuring technique that would improve hiPSC-CM structural maturation. Laser ablation was used to fabricate a micron-pattern on polyurethane surface and evaluated cell morphology, orientation and F-actin assemblage to detect phenotypic changes in response to the microtopography. This topography positively influenced cell morphology regarding to spreading area and elongation, and hiPSC-CM orientation, improving their structural maturation. The methodology thus presented has relatively low cost and is easily scalable, making it relevant for high-throughput applications such as drug screening for the pharma industry.

Keywords

hiPSC-CM • Cardiomyocytes • Surface topography • Direct laser interference patterning • Polyurethane

L. R. X. Cortella (✉) · I. A. Cestari · M. Mazzetto · I. N. Cestari
Bioengineering Department, Heart Institute (InCor), University of São Paulo Medical School, Av. Dr. Enéas de Carvalho Aguiar, 44, 05403-900 São Paulo, Brazil
e-mail: lucas.cortella@hc.fm.usp.br

M. S. · A. F. Lasagni
Institute for Manufacturing Technology, Technische Universität Dresden, George-Baehr-Str. 3c, 01069 Dresden, Germany

M. S.
PROBIEN-CONICET, Dpto. de Electrotecnia, Universidad Nacional del Comahue, Buenos Aires 1400, 8300 Neuquén, Argentina

A. F. Lasagni
Fraunhofer-Institut für Werkstoff-und Strahltechnik IWS, Winterbergstr. 28, 01277 Dresden, Germany

1 Introduction

The use of human induced pluripotent stem cell-derived cardiomyocytes (hiPSC-CM) holds great promises for the development of physiologically relevant in vitro models for drug screening and mechanistic studies of cardiac development [1, 2]. Furthermore, tissue-engineering strategies using hiPSC-CM are actively sought for therapy after myocardial ischemia and infarction. These strategies seek to create viable tissue constructs to repair, replace or augment the function of injured or diseased myocardial tissue [3]. However, hiPSC-derived cardiac constructs have technical limitations that hamper its application on cardiac regeneration. These stem cell-derived cardiomyocytes are phenotypically immature compared to those present in the adult heart [4]. When hiPSC-CM are cultured in vitro, they present a random spatial distribution, circular morphology and an isotropic actin organization, which results in an immature contractility pattern [5]. In turn, in the native myocardium, cardiomyocytes are longitudinally aligned rod-shaped cells with anisotropic actin distribution that communicate and contract in a specific directional manner [6]. Proper alignment of cardiomyocytes provides optimal coupling for electrical signal propagation and synchronous cell contractions required for good cardiac function [7]. As a consequence, achieving proper orientation of elongated hiPSC-CM is a fundamental goal in cardiac tissue engineering. One way to achieve similar physiological cellular organization in vitro is to use topographical cues to induce cell elongation and orientation [8].

There are many techniques available to create microtopographies with potential to direct cell behavior. We previously demonstrated that grooves and ridges produced by Direct Laser Interference Patterning (DLIP) were able to promote elongation and alignment of endothelial cells [8]. DLIP permits the direct fabrication of periodic structures in

T. F. Bastos-Filho et al. (eds.), *XXVII Brazilian Congress on Biomedical Engineering*, IFMBE Proceedings 83, https://doi.org/10.1007/978-3-030-70601-2_20

the low micrometer to sub-micrometer scale on different types of solid materials such as polymers, metals and ceramics [9]. DLIP has significant advantages over other methods, since it is possible to process large areas with reproducibility and accuracy in a single step with throughputs approaching 1 m^2/min [10].

In this study, we have hypothesized that a microtopography produced by DLIP will positively influence the morphology and orientation of hiPSC-CM statically cultured in vitro. We demonstrated that it is possible to use DLIP to pattern polymeric polyurethane (PU) surface useful in conditioning hiPSC-CM. Using this methodology, we showed that hiPSC-CM cultured onto aligned grooves were more elongated and oriented themselves according to the underlying topography when compared to those cells cultured on non-patterned surfaces.

2 Materials and Methods

2.1 Polyurethane Substrate Preparation

Polyurethane was prepared following the instructions from the manufacturer (Cequil™, Araraquara, Brazil) by mixing the pre-polymer and polyol components and casting over an inert mold. Equal parts of the two liquid components were weighed, placed in a heating oven (Quimis, Brazil) at 75 °C for 30 min to eliminate humidity and immediately mixed in equal stoichiometric ratio and poured on the mold at 30 °C, under vacuum (8 kPa) to remove air bubbles during polymerization and curing process (approximately 30 min). The reaction between pre-polymer and polyol components resulted in PU films of 1.3 mm (±0.2 mm) thickness. The pre-polymer was industrially synthesized from 4, 4′-diphenylmethanodiisocyanate in molar excess with the polyol, keeping a percentage of free isocyanate for later reaction. The polyol is polyester derived from castor oil, a natural oil with 90% of its fatty acid content consisting of ricinoleic acid.

2.2 DLIP on Polyurethane

Line-like structures with a spatial period of 3 µm were produced using a high-power Nd:YAG laser (Quanta Ray, Spectra Physics) with a pulse duration of 10 ns and a fundamental wavelength of 1064 nm. The repetition rate of the laser system was 10 Hz. Due to the high absorption of PU in the UV-spectral region, a wavelength of 266 nm was selected, which corresponds to the 4th harmonic of 1064 nm. The fluence, defined as the average optical energy per unit area, was set to 0.7 J cm^{-2}. A detailed description of the experimental setup can be found elsewhere [11].

2.3 DLIP-Modified PU Surface Characterization —Atomic Force Microscopy (AFM) and Scanning Electron Microscopy (SEM)

Surface micropattern produced on PU was characterized by AFM with a Nanoscope IIIA (Digital Instruments, USA) and the measurements were conducted using tapping mode. The measured features were spatial period (Λ), defined as the distance between two consecutive ridges; groove depth, which was measured from ridge top to groove bottom and ridge width, determined as full width at half maximum of groove depth. The topographies were further inspected with a scanning electron microscope TM 3000 (Hitachi, Japan) at an acceleration voltage of 5 kV.

2.4 hiPSC-CM Cell Culture on DLIP-Modified PU Substrate

Human induced pluripotent stem cells derived cardiomyocytes were purchased from Pluricell Biotech (São Paulo, Brazil) and cultivated following manufacturer's instructions. Cells were firstly plated at 15th day of differentiation on 24-well plate (Sarstedt), previously coated with extracellular matrix (Geltrex™, Thermo Fisher), at a density of 137 × 103/cm^2 and cultured at 37 °C and 5% CO^2 atmosphere with RPMI (Thermo Fisher) supplemented with plating medium supplement (PluriCardio™ PMS). Culture medium was replaced by RPMI containing maintenance medium supplement (PluriCardio™ MMS) every 24 h.

In order to perform the experiments, sterile DLIP-modified and unmodified PU samples were placed inside a 96-well microplate (Sarstedt) and allowed to equilibrate with RPMI containing Geltrex™ for two hours prior to cell seeding. At 19th day of differentiation cells were harvested from 24-well plate with 0.35% trypsin/EDTA solution (Gibco); centrifuged at 250 × g for 5 min, suspended in RPMI with PMS and seeded on PU at a density of 17 × 103/cm^2 for morphology and orientation analysis and at a density of 34 × 103/cm^2 for immunocytochemistry assay, under same culturing conditions. Culture medium was replaced with RPMI containing MMS every 24 h. Experimental groups were defined as follows: (a) unmodified PU (control) and (b) PU-L3 (line-like pattern featuring spatial period of 3 µm).

2.5 Cell Morphology and Orientation—SEM and Fluorescent Staining

The influence of microtopography on hiPSC-CM morphology and alignment was investigated. Cells at the 19th day of

differentiation were cultured on DLIP-modified PU for 48 h and fixed with 4% paraformaldehyde (PFA) (Sigma) for one hour at 4 °C. Then they were washed with phosphate buffered saline (PBS) (Gibco) and dried at room temperature, before placing them in the scanning electron microscope vacuum chamber.

F-actin and cell nucleus were visualized by fluorescent staining using a fluorescence microscope (TM300, Nikon, Japan) equipped with an AxioCam MRC camera (Zeiss, Germany). Cells were fixed with 4% PFA in PBS for two hours at 4 °C, permeabilized by 0.1% Igepal (Sigma, Brazil) at 37 °C for 30 min and blocked with 2% bovine serum albumin (BSA) (Sigma, Brazil) in PBS for one hour. F-actin fibers were stained with alexa-488-phalloidin (A12379, Life Tech., USA) at 1:100 and nuclei were stained with Hoechst 33,342 (B2261, Sigma, Brazil) at 1:50. PU samples were maintained in PBS/glycerol (1/1) solution and protected from light prior to viewing under the microscope.

SEM and fluorescent images were used to estimate cell morphology with ZEN 2012 software (Zeiss, Germany) and orientation of cells with Image J (NIH, USA). A total of six samples from each experimental group were examined and at least 150 cells per sample were imaged. Based on the outline of isolated cells we estimated values of spreading area (filled region by projected cell boundary) and aspect ratio, which gives an indication for cellular elongation. Aspect ratio is defined as the ratio between the breadth (minimum feret) and length (maximum feret) of each cell and varies from zero to one. A value of 1 approximates the shape of a circle and a value of zero depicts that of a straight line.

Cell orientation, defined as the angle between the major axis of the cell and the axis of the grooves was estimated and cells were considered aligned when this angle was lower than 10°. A minimum angle of 0° indicated parallel alignment from the groove axis; a maximum angle of 90° suggested perpendicular alignment and an average angle of 45° was expected for random orientation. For quantification of cell orientation on control, an arbitrary axis was selected.

2.6 Statistical Analysis

All values were obtained from datasets of three independent experiments performed in duplicates. Statistical comparison between DLIP-modified PU and unmodified PU groups was carried out by Mann–Whitney rank sum test using SigmaStat statistical software (Jandel Scientific). Statistical significance was accepted at $P < 0.05$. Data are expressed as mean ± standard deviation (S.D).

3 Results

3.1 Surface Characterization of DLIP-Modified PU—AFM and SEM

A two beams configuration in the DLIP system was used to fabricate well defined and homogeneous line-like micropatterns consisting in periodic and parallel ridges and grooves on PU substrate. Figure 1a displays an AFM image from a 3D projection of the micropattern from structured PU and Fig. 1b represents schematically the topographical features measured by AFM. Average values of spatial period, ridge width and groove depth are summarized in Table 1. The SEM images of Fig. 2 show a laser irradiated PU with

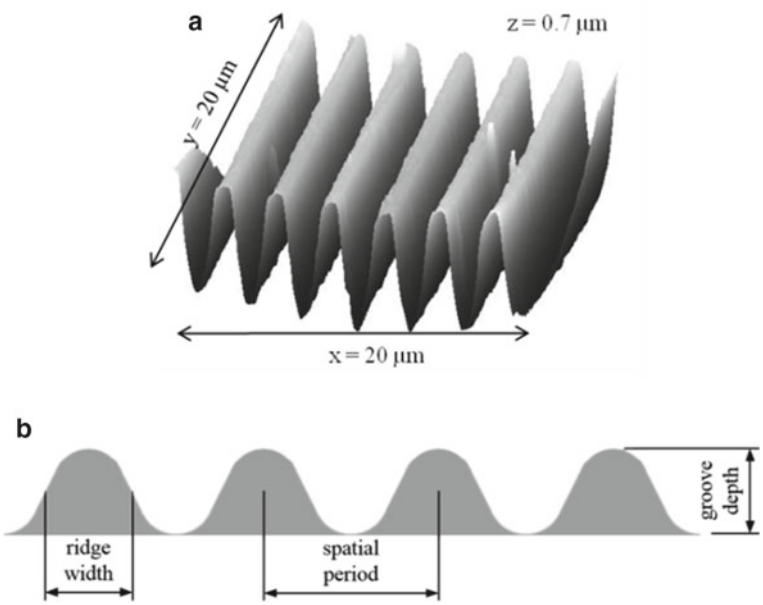

Fig. 1 **a** AFM characterization of surface micropattern produced on PU represented by 3D projection obtained with NanoScope Analysis software. The X and Y axes indicate width and length of the sections, respectively. Note that Z-axis is expanded for better visualization (aspect ratio = 0.4). **b** Schematic representation of the topographical features measured by AFM

Table 1 AFM measurements of spatial period, ridge width and groove depth. Mean values ± S.D are shown in (μm)

AFM measurements	PU-L3
Spatial period	3.0 ± 0.01
Groove depth	0.7 ± 0.03
Ridge width	1.7 ± 0.01

no interference pattern that was used as control group (Fig. 2a), as well as the DLIP-patterned PU substrate with a spatial period of 3.0 μm (Fig. 2a).

3.2 Alignment of hiPSC-CM in Response to DLIP-Modified PU

We investigated hiPSC-CM orientation as a measure of the degree to which hiPSC-CM responded to the underlying topography. Figure 3 shows the distribution of orientation angles of cells cultured on DLIP-modified PU and control. Table 2 summarizes the values of average orientation angle and percentage of aligned cells. hiPSC-CM cultured on non-patterned PU were randomly orientated, resulting in an expected average angle of 47° ± 26°. Differently, the interaction of hiPSC-CM with the topography narrowed the distribution of orientation angles, with 50% of aligned cells at angles lower than 10°. Figure 4 shows aligned hiPSC-CM following the groove direction.

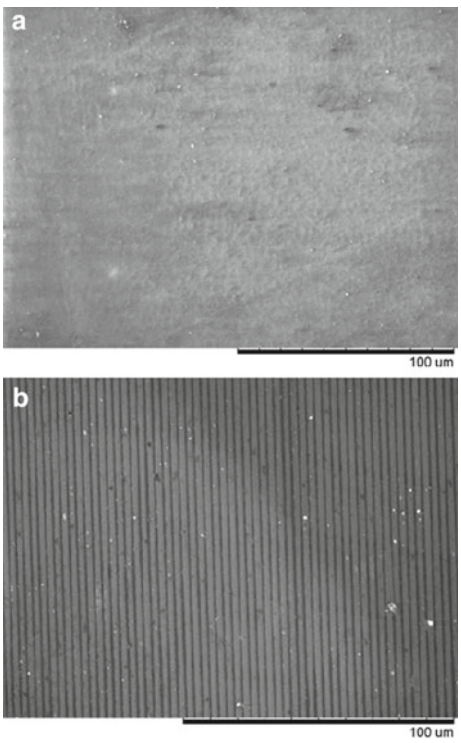

Fig. 2 SEM visualization of non-patterned surface Control PU **a** and micropatterned PU-L3 **b**. Scale bar: 100 μm

3.3 Differential Morphology of hiPSC-CM Cultured on DLIP-Modified PU—aspect Ratio and Spreading Area

In order to evaluate the development of structural anisotropy of cells, aspect ratio and cell area were determined. The contact of hiPSC-CM with the microtopography resulted in a more elongated shape than cells in contact with non-patterned PU, showing a 29% difference ($P < 0.001$) in elongation (Fig. 5) and a 21% reduction in spreading area (Fig. 6) ($p < 0.001$).

3.4 Alignment of F-Actin Myofibrils

hiPSC-CM cultured on DLIP-modified PU exhibited a parallel assemblage of F-actin filaments to groove direction (Fig. 7b), whereas cells on control surface displayed a random disposition of actin fibers across the cytoplasm (Fig. 7a).

4 Discussion

In this work, we showed a microtopography produced by DLIP technique on the surface of a polymeric polyurethane substrate capable to induce a distinct morphology and orientation of hiPSC-CM in vitro. Using this methodology, we demonstrated that hiPSC-CM cultured onto aligned ridges and grooves were more elongated with smaller spreading area and oriented themselves according to the underlying topography, when compared to those cells cultured on non-patterned surface. These phenotypic changes may be associated to maturation aspects that are clinically relevant in the eventual production of myocardial tissue implants. This methodology is easily scalable and can be implemented with relative low cost and high throughput. Our results indicate the feasibility of using DLIP to create precise and relevant topographical patterns in order to induce phenotypic characteristics of interest for the large scale production of hiPSC-CM, important for obtaining functional cardiac tissue substitutes.

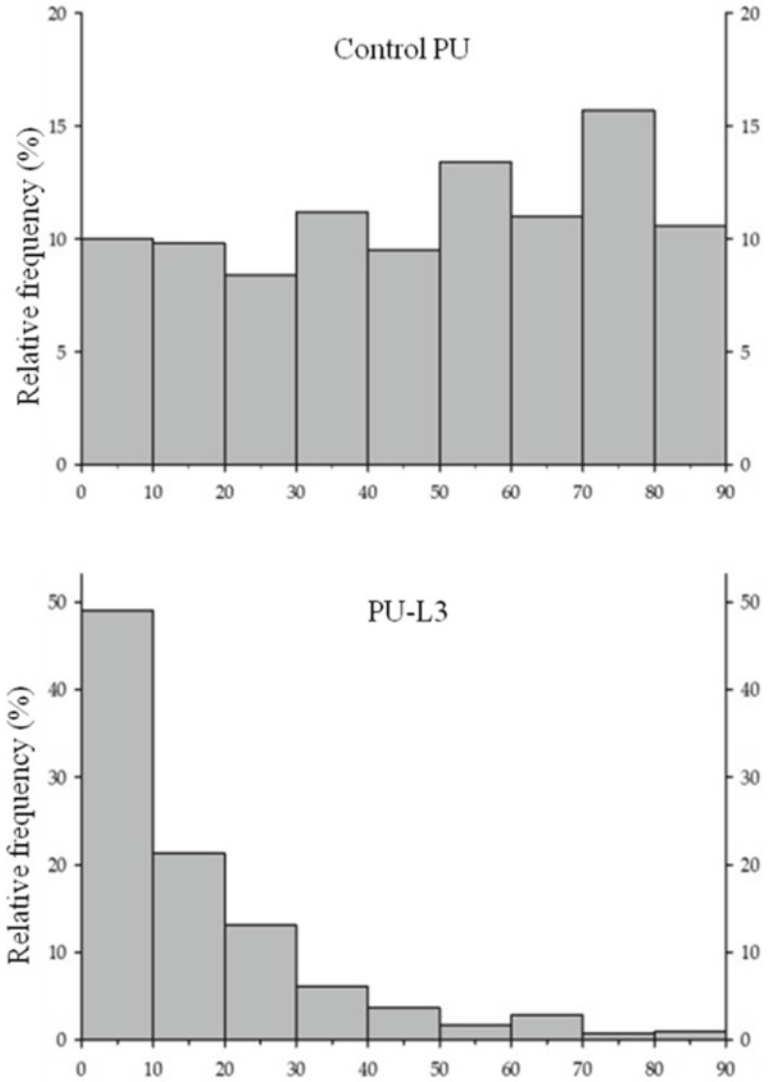

Fig. 3 Histograms report the distribution of orientation angles in degrees (x axis) and their relative frequency (%) (y axis) of hiPSC-CM cultured for 48 h on control (top) and DLIP-modified PU (bottom)

Table 2 Values of mean orientation angles and percentage (%) of aligned cells on micropatterned PU and control. Cells oriented with angle lower than 10° in relation to the groove direction were considered aligned. (*) indicates statistical significance ($P < 0.001$) between groups

	Mean orientation angle (°)	% aligned cells (<10°)
Control PU	47	12
PU-L3	11*	49*

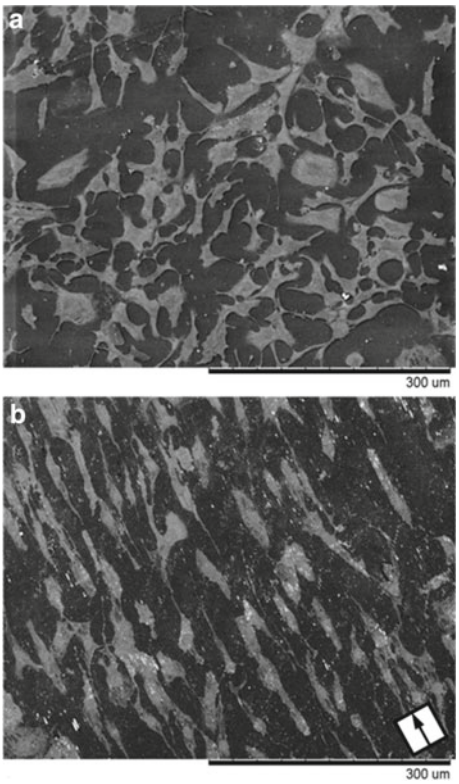

Fig. 4 SEM images showing hiPSC-CM with distinct orientation in response to the underlying topography after 48 h of cell plating. **a** control PU; **b** PU-L3. Scale bar: 300 μm. The arrow inside the box indicates the direction of the grooves

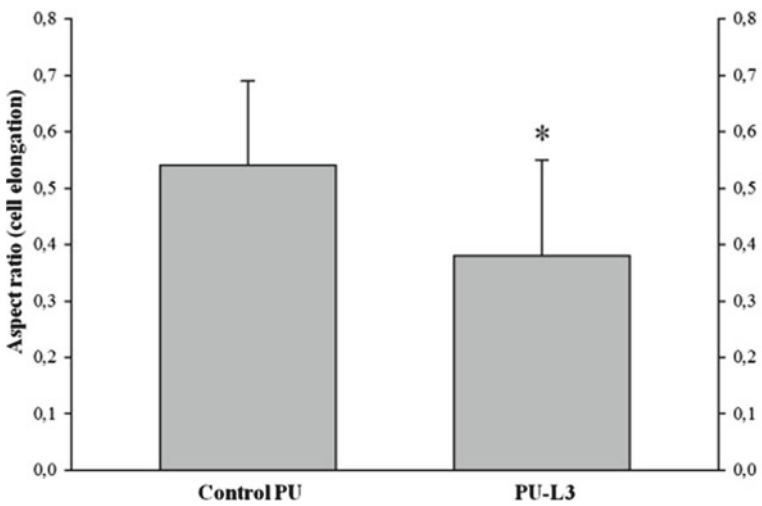

Fig. 5 Values of aspect ratio (elongation) from hiPSC-CM cultured for 48 h on control (left) and DLIP-modified PU (right). (*) indicates statistical significance ($P < 0.001$) between groups

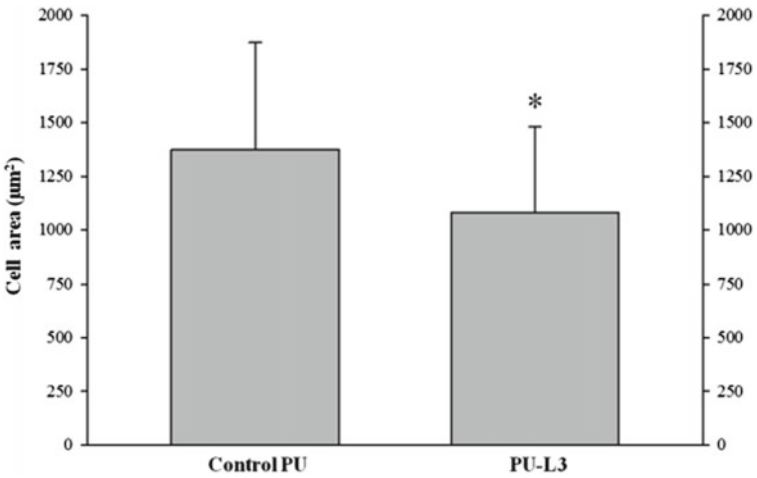

Fig. 6 Values of spreading area (μm^2) from hiPSC-CM cultured for 48 h on control PU (left) and DLIP-modified PU (right). (*) indicates statistical significance ($P < 0.001$) between groups

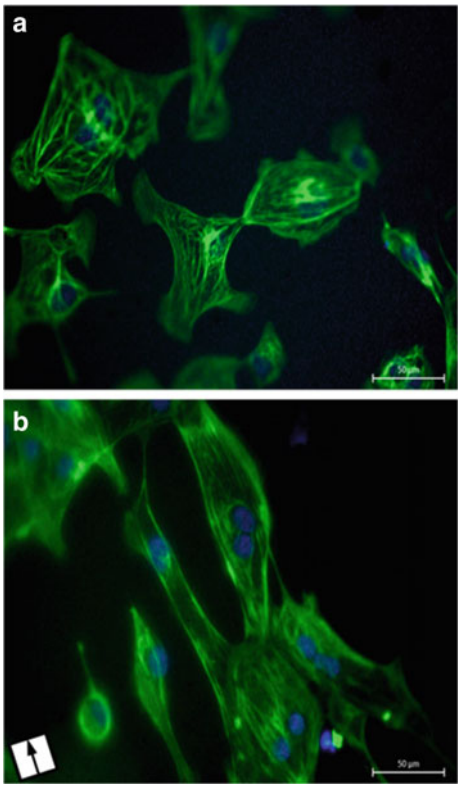

Fig. 7 Representative fluorescent images of hiPSC-CM cultured on control PU **a** and PU-L3 **b**. F-actin (green) stained with alexa-488-phaloidin and nucleus (blue) with Hoechst 333,432. The arrow inside the box indicates the direction of the grooves. Scale bar: 50 μm

5 Conclusions

The interaction of hiPSC-CM with 3 μm line-like surface pattern, produced by DLIP, during in vitro static culture promoted specific cell orientation, morphological alterations regarding to cell elongation and spreading area and induced an organized F-actin assemblage.

Acknowledgements This work was supported by FAPESP (12/50283-6); Finep (1253/13) and National Council for Scientific and Research Development—CNPq (467270/2014-7 and 311191/2017-7). M.S. acknowledges the support of the Alexander von Humboldt Foundation.

Conflict of Interest The authors declare that they have no conflict of interest.

References

1. Liu WH, Chang YL, Lo WL et al (2015) Human induced pluripotent stem cell and nanotechnology-based therapeutics. Cell Transplant 24:2185–2195. https://doi.org/10.3727/096368914X685113
2. Acimovic I, Vilotic A et al (2014) Human pluripotent stem cell-derived cardiomyocytes as research and therapeutic tools. BioMed Res Int 14. https://doi.org/10.1155/2014/512831
3. Parrag IC, Zandstra PW, Woodhouse KA (2012) Fiber alignment and co-culture with fibroblasts improves the differentiated phenotype of murine embryonic stem cell-derived cardiomyocytes for cardiac tissue engineering. Biotechnol Bioeng 109:813–822. https://doi.org/10.1002/bit.23353
4. Gherghiceanu M, Barad L, et al (2011) Cardiomyocytes derived from human embryonic and induced pluripotent stem cells: comparative ultrastructure. J Cell Mol Med 15:2539−2551. https://doi.org/10.1111/j.1582-4934.2011.01417.x
5. Ribeiro AJ, Ang YS et al (2015) Contractility of single cardiomyocytes differentiated from pluripotent stem cells depends on physiological shape and substrate stiffness. Proc Natl Acad Sci USA 112(41):12705–12710. https://doi.org/10.1073/pnas.1508073112
6. Hooks DA, Trew ML et al (2007) Laminar arrangement of ventricular myocytes influences electrical behavior of the heart. Circ Res 101(10): E103–E112. https://doi.org/10.1161/CIRCRESAHA.107.161075

7. Parker KK, Ingber DE (2007) Extracellular matrix, mechanotransduction and structural hierarchies in heart tissue engineering. Philos Trans R Soc Lond B Biol Sci 362:1267–1279. https://doi.org/10.1098/rstb.2007.2114
8. Cortella LRX, Cestari IA et al (2017) Endothelial cell responses to castor oil-based polyurethane substrates functionalized by direct laser ablation. Biomed Mater 12. https://doi.org/10.1088/1748-605X/aa8353
9. Langheinrich D, Yslas E et al (2012) Control of cell growth direction by direct fabrication of periodic micro and submicrometer arrays on polymers. J Polym Sci B 50:415–422. https://doi.org/10.1002/polb.23017
10. Lang V, Teja R, Lasagni AF (2016) World record in high speed laser surface microstructuring of polymer and steel using direct laser interference patterning. Proc SPIE 9736:8. id. 97360Z. https://doi.org/10.1117/12.2216203
11. Estevam-Alves R, Gunther D, Dani S et al (2015) UV direct laser interference patterning of polyurethane substrates as tool for tuning its surface wettability. Appl Surf Sci 374:222–228. https://doi.org/10.1016/j.apsusc.2015.11.119

The Effect of Nitrided Layer on Antibacterial Properties of Biomedical 316L Stainless Steel

M. Benegra, G. H. Couto, and E. A. Bernardelli

Abstract

This study investigates the effect of the nitrided layer on antibacterial properties of biomedical stainless steel, grade 316L. The surfaces were sanded #1200 mesh papers, subsequently plasma-nitrided at a temperature of 400 °C for 2 h, which resulted in a 4.5 μm thick layer. The characterization was made using optical and scanning electron (SEM) microscopies, energy dispersive spectrometry (EDS) X-ray diffraction, and Vickers hardness testing. The antibacterial characteristic of the untreated steel and the nitrided layer was evaluated using Gram-negative *Escherichia coli* ATCC8739, according to Japanese International Standard (JIS) no. Z2801:2000. A single γ-phase layer was formed, supersaturated in nitrogen, increasing the surface hardness significantly by 35%. The bacterial test demonstrated that the nitrided layer presented suitable antibacterial characteristics.

Keywords

Plasma nitriding • Stainless steel • Antibacterial

1 Introduction

The biocompatible properties of 316 austenitic stainless steel promote its use as orthopedic and orthodontic implants. The integration of the metal with the human body occurs on the surface of the component, a region that suffers a high loading, becoming the most susceptible to degradation. Plasma nitriding is a surface treatment usually employed to improve the wear and corrosion resistance of stainless steel [1–4]. Some studies indicate that the nitrided layers exhibited an excellent ability to inhibit E. coli in 303 stainless steel [5]. At temperatures between 300 and 500 °C, a supersaturated phase (γN phase or S-phase) can be formed, with nitrogen and Carbon in octahedral interstices of face-centered cubic (fcc) lattice, without any precipitation. The diffused nitrogen expanded the lattice parameter of the austenite, keeping the fcc crystallographic structure. It resulted in a nitride phase responsible for increasing the hardness, with no loss in the corrosion resistance [5, 6]. Considering that the previous study [5] applied the nitriding treatment only on 303 steel, this study aims to evaluate the antibacterial effect of 316L stainless steel—a widely used material for implants—against E. coli using DC plasma nitriding.

2 Materials and Methods

AISI 316 L austenitic stainless steel was used as a substrate material. Its nominal and experimentally quantified compositions are listed in Table 1. A rolled round bar (20-mm diameter) was cut into slices (5 mm thick). The as-cut samples were wet ground with SiC emery paper from grit #120 to #1200, cleaned with soapy water and acetone ultrasonically, and dried in hot air before the plasma nitriding.

Plasma nitriding was carried out in a pulsed DC glow discharge under a gas mixture composed of 50% Ar, 25% N_2, and 25% H_2 (gas flow 200 sccm). The nitriding treatments were performed at 400 °C for 2 h under the pressure of 3 Torr. Before nitriding, the samples are cleaned by sputtering carried out to remove the oxides comprising the external passive layer, utilizing the conditions: 50% Ar and 50% H_2, flow 150 sccm, pressure 2 Torr, temperature 300 °C, time 30 min. A complete description of the reactor can be obtained in [7]. Scanning electron microscopy (SEM) and optical microscopy (OM) were used for observing the surface morphology and microstructure. Cross-sectional areas were etched with a solution of (50% HCl + 25%

M. Benegra (✉) · G. H. Couto · E. A. Bernardelli
Universidade Tecnológica Federal do Paraná, Curitiba, Brazil
e-mail: marjorieb@utfpr.edu.br

T. F. Bastos-Filho et al. (eds.), *XXVII Brazilian Congress on Biomedical Engineering*,
IFMBE Proceedings 83, https://doi.org/10.1007/978-3-030-70601-2_21

Table 1 Chemical composition of AISI 316 L stainless steel

Element	Mn	Mo	Si	Cr	Ni
Wt% (nominal)	≤ 2.0	≤ 2.0	≤ 1.0	16 ~ 18	10 ~ 14
Wt% (EDS)	2 ± 0.2	2.3 ± 0.4	0.4 ± 0.2	16.5 ± 0.3	8.8 ± 0.3

Fe: balance, Carbon less 0.08 (nominal)

HNO_3 + 25% H_2O). The chemical composition of the treated layers was analyzed using energy dispersive spectrometry (EDS). Shimadzu XRD 7000 Diffractometer (Cu-K radiation λ = 0.154 nm) was used to obtain XRD patterns with a scanning angle from 30 to 60° at a speed of 0.02 s^{-1}. Surface hardness was measured using a Shimadzu Micro Hardness Tester, under a load of 50 g.

The nitrogen concentration within the nitrided layer was determined by the method proposed by Öztürk and Williamson [8]. According to this method, the amount of nitrogen is based on the lattice expansion, which can be determined by the shift of peaks corresponding to the austenite phase ($\gamma \rightarrow \gamma N$, where γ is the unexpanded austenite phase, and γN is the expanded austenite phase). Equations 1 and 2 should be used in order to calculate the nitrogen concentration:

$$a_{\gamma_N} = a_\gamma + \alpha C_N \quad (1)$$

$$d_{hkl} = \frac{a}{\sqrt{h^2 + k^2 + l^2}} \quad (2)$$

where:

a_γ = lattice parameter of austenite [Å];
C_N = nitrogen concentration [at. %].
α = Vegard constant (considered value: 0.0078 [Å / at. % N]);
a_{γ_N} = lattice parameter of expanded austenite [Å];
d_{hkl} = interplanar spacing.

All culture media in the test were purchased from HiMedia, India. The effect of plasma nitrided layer on antibacterial properties for steel AISI 316 L was tested in triplicate using Gram-negative bacterium *Escherichia coli* ATCC 8739, according to Japanese International Standard (JIS) no. Z 2801:2000. Six steel specimens were tested or used as controls, three to measure viable *E. coli* cells just after dropped onto specimens, and three to measure the variation of viable cells on specimens after incubation for 24 h. Test inoculum was prepared by diluting a suspension of fresh cultured *E. coli* cells with 1/500 nutrient broth at a concentration of $\sim 4.0 \times 10^5$ cells/mL. A bacterial suspension of 0.2 mL was dropped on the surface of each specimen (20 mm-diameter, five mm-thick). It was placed on a sterilized Petri dish containing a cotton pad saturated with distilled water to maintain ~90% humidity. Droplets were covered with a sterile glass coverslip to prevent evaporation of the suspensions and maintain the cells in close contact with specimens. These were subsequently incubated at 35 °C for 24 h and placed into sterilized plastic bags followed by washing with sterile phosphate buffer solution (PBS) in a final volume of 10 mL to dislodge the cells inside the bags. Serial dilutions of PBS-bacterial suspension were carried out, and 100 µL aliquots of each dilution were transferred to Petri dishes containing Plate Count Agar (PCA) medium. After incubation at 37 °C for 24 h, colony-forming units (cfu) were counted. For the control specimens, all steps (incubation, harvest, and counting cfu) were carried out simultaneously as those for sample specimens.

3 Results

Figure 1 shows the microstructure of the plasma nitrided layer, and Table 2 shows its respective EDS analyses. The layer thickness is 4.5 µm. The nitrogen concentration observed by EDS is 6.4 ± 1.2 wt%.

Using the method proposed by Öztürk and Williamson [8], the nitrogen concentration is 4.83%wt. Considering that the EDS technique is not the most suitable for analyzing light elements, such as nitrogen, the result obtained by the method proposed by Öztürk and Williamson [8] should better represent the nitrogen concentration of this nitrided layer. If compared to the nitrogen concentration values obtained by Reis et al. [9] nitriding the stainless steel in similar conditions, the results are very close.

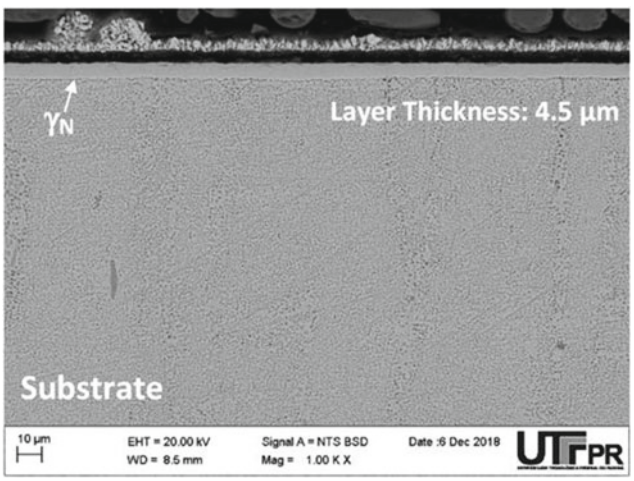

Fig. 1 Cross-section image obtained in SEM of plasma nitrided layer

Table 2 EDS analysis of the nitrided layer

Element	Wt%
N	6.4 ± 1.2
Mn	1.7 ± 0.1
Mo	2.3 ± 0.4
Si	0.4 ± 0.2
Cr	15.3 ± 0.4
Ni	9.1 ± 0.3
Fe	Bal

Plasma nitriding resulted in a higher hardness, 759 HV. The increase promoted about the original hardness—261 HV—can be directly related to the supersaturated austenite constituents (S-phase), as revealed by XRD (Fig. 2).

Two left-shifted and broadened peaks from the γ-fcc phase were observed for nitrided samples (Fig. 2). They are defined as S-phase and denoted as S111, S200. The S-phase peaks are increasingly shifted to left as the results of increased nitrogen super-saturation in fcc lattice. The presence of α-phase is attributed to metallographic preparation, where the ɣ phase originates α phase by plastic deformation.

To be considered an antibacterial coating, the number of cfu after 24 h must be lower than the one at zero hours. Figure 3 shows the number of bacterial colonies grown on PCA plates counted at zero and 24 h of incubation when approximately 4.10^5 cfu's were applied to the steel samples.

The presence of the nitrided layer on steel decreased the number of colonies to $2.7.10^4$ after 24 h of incubation (Fig. 3, red bar). Tests were carried out in parallel with the same *E. coli* inoculum on untreated steel samples to verify

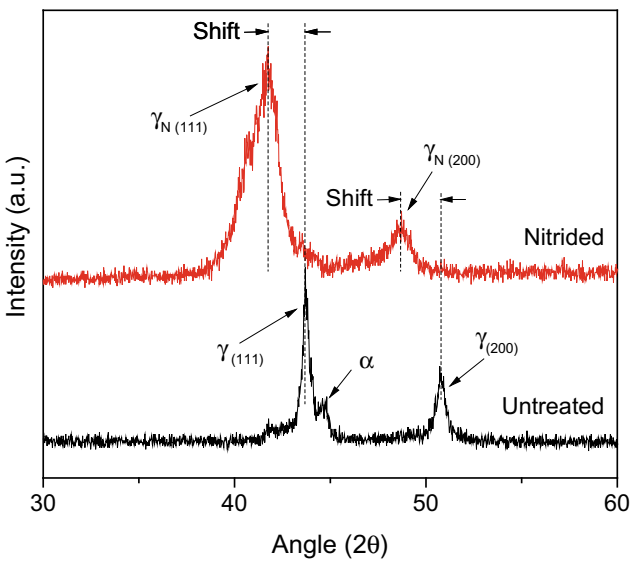

Fig. 2 XRD of stainless steel AISI 316 nitrided and untreated

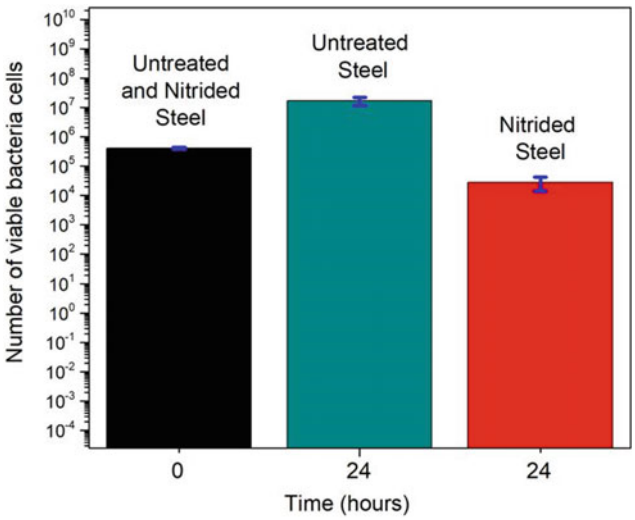

Fig. 3 Number of viable E. coli cells immediately after inoculation (0 h) and after incubation for 24 h

that the antibacterial effect only comes from this nitrided layer. For this, the number of bacteria increased from 4.10^5 to more than $1.6.10^7$ cfu's after 24 h of incubation, indicating that this difference in the number of viable cells was due the nitrided layer (Fig. 3, green bar and Fig. 4). Hence, based on the tests, the nitrided layer was useful to provide either bacteriostatic and/or bactericidal properties by inhibiting growth and/or cell killing, respectively. Similar results were observed by Li-Hsiang et al. [5], Hung et al. [10], Ou et al. [11] and Li et al. [12], nitriding austenitic and martensitic stainless steels.

A hypothesis to explain the results was provided by Li-Hsiang et al. [5] and corroborated by Hung et al. [10], Ou et al. [11] and Li et al. [12]. They supposed that the nitrided surface becomes antibacterial mainly because of the more straightforward dissolution of Fe^+ and Cr^+ ions when the surface of stainless steels is nitrided. These are suspended in the solution containing bacteria, for example, *E. coli* bacteria, killing them. To prove this hypothesis, it is necessary to analyze the chemical composition of the solution, which will be the object of study in the next work.

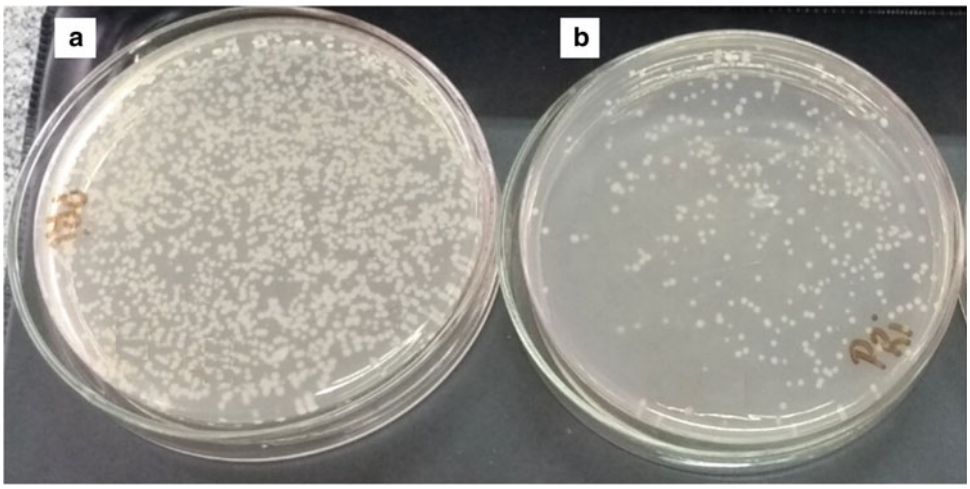

Fig. 4 Example of Petri dishes after incubation at 35 °C during 24 h showing ufc´s in the **A** untreated steel, (10^{-3} dilution), and **B** plasma nitriding surface steel (10^{-1} dilution)

Considering the dissolution of the metal to form ions, this hypothesis should not corroborate with the increase in corrosion resistance when occurs the formation of expanded austenite at low temperature (<400 °C) plasma nitriding, since the increase in corrosion resistance is attributed to the higher resistance to dissolution of the metal in the corrosive medium. However, the primary mechanism for increasing the corrosion resistance of nitrided stainless steel is associated with the release of NH_4^+, neutralizing the acidity within the pitting. Thus, a possible explanation for a more significant release of Fe^+ and Cr^+ ions may be the formation of $Fe_{2\text{-}3}$ N and Cr_xN_y nanoprecipitates, even when the nitriding temperature is low (<400 °C). Such nanoprecipitates were observed by Zagonel et al. [13] plasma nitriding H13 steel at 400 °C. Considering the presence of nanoprecipitates, a higher dissolution of the metal could occur around them, which would probably be a factor that alters less resistance to corrosion when compared to the formation of $NH4^+$.

4 Conclusions

The plasma nitriding applied on AISI 316L steel caused a microstructural change, converting the previous austenite into expanded austenite (S-phase) with a particular nitrogen concentration. The S-phase has been shown to have an excellent antibacterial property against *E. coli*, confirming findings described for another grade of stainless steel. A study that aims to study the influence of different concentrations of nitrogen in the expanded austenite layer (S-phase) on antibacterial properties would be necessary for the development as a potential biomedical material.

Acknowledgements The authors thank the Multi-User Center for Materials Characterization (CMCM) of the UTFPR for XRD and SEM analysis, and Professor G. Pintaude for his revisions and suggestions.

Conflict of Interest The authors declare that they have no conflict of interest.

References

1. Olzon-Dionysio M, Campos M, Higa OZ et al (2013) Investigating the correlation between some of the properties of plasma nitrided AISI 316L stainless steel. Mater Res 16(5):1052–1057. https://doi.org/10.1590/S1516-14392013005000081
2. Mendes AF, Scheuer CJ, Joanidis IL et al (2014) Low-temperature plasma nitriding of sintered PIM 316L austenitic stainless steel. Mater Res 17(Supl.1):100–8. https://doi.org/10.1590/S1516-14392014005000064.
3. Reis RF, Maliska AM, Borges PC (2011) Nitrogen surface enrichment of austenitic stainless steel ISO 5832–1. J Mater Sci 46 (3):846–854. https://doi.org/10.1007/s10853-010-4827-3
4. Bernardelli EA, Borges PC, Fontana LC et al (2010) Role of plasma nitriding temperature and time in the corrosion behaviour and microstructure evolution of 15–5 PH stainless steel. Kovové Materiály 48(2):105–116. https://doi.org/10.4149/km_2010_2_105
5. Li-Hsiang L, Shih-Chung C, Ching-Zong W et al (2011) Microstructure and antibacterial properties of microwave plasma nitrided layers on biomedical stainless steels. App Surf Sci 257:7375–7380. https://doi.org/10.1016/j.apsusc.2011.01.065
6. Dong Y, Li X, Bell T et al (2010) Surface microstructure and antibacterial property of an active-screen plasma alloyed austenitic stainless steel surface with Cu and N. Bio Mater 5:054105. https://doi.org/10.1088/1748-6041/5/5/054105
7. Sphair AC (2017) Nitretação por plasma de aço inoxidável austenítico com fluxo pulsado de nitrogênio [dissertação]. Curitiba: Programa de Pós-graduação em Engenharia Mecânica e de Materiais, Universidade Tecnológica Federal do Paraná
8. Öztürk O, Williamson DL (1995) Phase and composition depth distribution analysis of low energy, high flux N implanted stainless steel. J Appl Phys 77:3839–3850. https://doi.org/10.1063/1.358561
9. Reis RF, Silva PGHM, Villanova RL et al (2020) Plasma nitriding of ISO 5832-1 stainless steel with intermittent nitrogen flow at 450 °C. Mater Res 23(1):e20190501. https://doi.org/10.1590/1980-5373-MR-2019-0501

10. Hung CF, Wu CZ, Lee KL et al (2012) The effect of nitrided layer on antibacterial properties for biomedical stainless steel. Phys Procedia 32:914–919. https://doi.org/10.1016/j.phpro.2012.03.656
11. Ou KL, Chou HH, Liu CM et al (2011) Surface modification of austenitic stainless steel with plasma nitriding for biomedical applications. Surf Coat Technol 206:1142–1145. https://doi.org/10.1016/j.surfcoat.2011.08.001
12. Li J, He X, Zhang G et al (2018) Effect of nitriding on antibacterial performance of 8Cr17 and 4Cr13 martensitic stainless steel. Mater Perform Charact 7(1):70–77. https://doi.org/10.1520/MPC20170058
13. Zagonel LF, Bettini J, Basso RLO et al (2012) Nanosized precipitates in H13 tool steel low temperature plasma nitriding. Surf Coat Technol 207:72–78. https://doi.org/10.1016/j.surfcoat.2012.05.081

Biomechanical Analysis of Tissue Engineering Construct for Articular Cartilage Restoration—A Pre-clinical Study

R. R. de Faria, M. J. S. Maizato, I. A. Cestari, A. J. Hernandez, D. F. Bueno, R. Bortolussi, C. Albuquerque, and T. L. Fernandes

Abstract

The chondral lesion and osteoarthritis are conditions associated with an economic burden, since if left untreated may cause changes in the biomechanics of the joint and result in several injuries considered highly disabling to the individual. Mesenchymal Stem Cells (MSCs) have the immunomodulatory capacity and paracrine signaling that are useful for tissue bioengineering to treat bone and cartilage injuries. To the best of our knowledge, there is no institution in Brazil studying cartilage biomechanical properties in Good Manufacturing Practice (GMP) technique. Therefore, this study aims to describe biomechanics analysis for cartilage restoration by tissue engineering and cell therapy treatments in a GMP translational large animal model. A controlled experimental study in fourteen Brazilian miniature pigs was performed, using scaffold-free Tissue Engineering Construct (TEC) from dental pulp and synovial MSCs with 6 months follow-up. To compare the cartilage with and without TEC, indentation and maximum compressive tests were performed, as well as Finite Element model to simulate the osteochondral block and characterize its properties. The Young's Modulus of each sample was determined, and the outcomes of maximum compressive test demonstrated the cartilage integrity. The proposed method was feasible and capable to properly evaluate articular cartilage restoration.

Keywords

Mechanical testing • Biomechanics • Indentation test • Cell therapy • Mesenchymal Stem Cells • Articular cartilage

1 Introduction

It is known that cartilage injuries and osteoarthritis are very prevalent and considered a public health problem, since it is highly disabling and is expected to grow due to population aging. Cartilage defects can generate several complications to the individual, such as changes in the biomechanics and homeostasis of the joint, lesions in the adjacent subcentral bone, loss of mobility, degeneration and osteoarthritis of the knee, directly affecting quality of life [1–3].

In 2020, it is believed that osteoarthritis (OA) will be the major cause of morbidity and physical limitation among individuals over 40 in the United States. Therefore, the treatment of patients with symptomatic cartilage injuries is a necessity and studies related to new therapies are extremely important [4–6].

Currently, the gold standard for cellular treatment of cartilage injuries includes the Autologous Chondrocyte Implant (IAC), but this procedure requires previous surgery to collect the cartilage from the patient and the number of available cells decreases with age, both with respect to quantity as to quality [7].

Therefore, the tissue engineering using cell architecture and Mesenchymal Stem Cells (MSCs) has been highlighted in current research for several reasons, including ease of harvesting, capacity for cell proliferation and differentiation,

R. R. de Faria · A. J. Hernandez · T. L. Fernandes (✉)
Institute of Orthopedics and Traumatology, Hospital das Clínicas, Faculdade de Medicina da Universidade de São Paulo, 333 Dr. Ovídio Pires de Campos, 05403-010 São Paulo, SP, Brazil
e-mail: tiago.lazzaretti@usp.br

D. F. Bueno · T. L. Fernandes
Hospital Sírio Libanês, São Paulo, SP, Brazil

R. R. de Faria
Pontifícia Universidade Católica de São Paulo (PUC-SP), São Paulo, SP, Brazil

M. J. S. Maizato · I. A. Cestari
Instituto do Coração (InCor)/Bioengenharia, Hospital das Clínicas da FMUSP, São Paulo, Brazil

R. Bortolussi · C. Albuquerque
Centro Universitário FEI, São Paulo, Brazil

T. F. Bastos-Filho et al. (eds.), *XXVII Brazilian Congress on Biomedical Engineering*, IFMBE Proceedings 83, https://doi.org/10.1007/978-3-030-70601-2_22

not rejection by the patient and paracrine effect in local cell machinery [7].

The stem cells can be isolated from different tissues, such as bone marrow, synovial membrane, adipose tissue, dental pulp, and others. Dental Pulp Stem Cells (DPSCs) have the capacity to differentiate into chondroblasts and osteoblasts, suggesting that this stem cell type is useful for tissue engineering to treat bone and cartilage injuries. Moreover, cells from adipose tissue and synovial membrane can be easily accessed through routine arthroscopy and can be harvested with minimum complications in the donation area. Isolated synovial and fat pad cells have an ability to synthesize molecules that are considered markers specific for musculoskeletal tissue, such as collagen and proteoglycan [8–10].

The articular cartilage is a viscoelastic material that can undergone structural and compositional changes, so it is common to apply in vitro, in situ, in vivo and ex vivo approaches to assess the cartilage restoration. However it is also important to assess the physical properties of the new tissue formed, since they provide the biomechanics functions, such as stiffness, load bearing, shock absorption and wear resistance. Therefore, mechanical evaluation is essential and is described in this study [11, 12].

2 Materials and Methods

This is a controlled experimental study in animals that was developed from 2017 to 2020. Fourteen Brazilian miniature pigs (BR-1) with the specifications of being adults aged 8–12 months and weighing 19–22 kg (Minipig Pesquisa e Desenvolvimento, Ltda., Campina do Monte Alegre, SP, Brazil) were used in the present study, totaling 28 surgeries, two knees per animal.

2.1 Cell Culture: Harvesting, Isolation, Expansion and Differentiation of MSCs

The harvesting of synovial tissue from human knees included seven patients who undergone arthroscopic surgery for anterior cruciate ligament or meniscus injuries. Patients with previous history of surgery, infection, inflammatory arthritis and pregnant women were excluded.

Knee synovia was harvested in the beginning of arthroscopy, through the antero-lateral portal. A sample up to 1 g of synovia was stored in a 50 ml falcon flask containing saline solution 0.9% and was sent immediately to the Advanced Cellular Technology Laboratory at Sírio-Libanês Hospital (São Paulo, Brazil) and processed up to 6 h after harvesting.

The harvesting of dental pulp was collected from a deciduous tooth. The deciduous tooth used were those that occurred spontaneously and would be discarded. No extraction of tooth was performed. The tissue was washed and digested for 90 min at 37 °C, followed by centrifugation and plated in culture bottles [13].

The MSCs obtained were isolated and cultivated in a Good Manufacturing Practice (GMP) Laboratory. All this harvesting, isolation and expansion of MSCs from knee synovia and also dental pulp process was better described in previous article [13, 14].

The MSCs strains were induced in vitro to undergo osteogenic, chondrogenic, and adipogenic differentiation, showing that these strains had mesenchymal origins and maintained multipotentiality [13]. They also were fibroblast-like cells and were tested to express specific stem cell markers.

2.2 Development of a Tissue Engineering Construct Compound of Cell and Extracellular Matrix (TEC)

The derived MSCs were plated on a six-well culture dish at a density of 4.0×10^5 cm^2 in the growth medium with 0.2 mM ascorbic acid 2-phosphate (Asc-2P; Sigma-Aldrich, St. Louis, MO). Within some days, the cells became confluent. After approximately 15 days, a complex of the cultured cells and extracellular matrix synthesized by the developed cells were detached from the substratum by application of shear stress at the cell–substratum interface using gentle pipetting. The detached complex was left in suspension to form a 3D structure by active tissue contraction. This contracted tissue was termed TEC.

2.3 Animal Model

Information on the characteristics, care and procedures related to animals in this research was collected following the ARRIVE Guideline Checklist [15] and kept in a digital repository [16]. The animals were kept in individual bays and were fed twice a day with food and water ad libitum.

At the time of surgery, the surgeon was told which side would receive the TEC. Therefore, in the other knee, the defect was left empty. Randomization was performed by a researcher not involved in the surgical procedure [17].

A full-thickness cartilage defect measuring 6 mm in diameter was performed in the loading area of the medial femoral condyle, on the two hind limbs of each animal, using a biopsy punch and then the calcified basal layer of the cartilage was removed with a scalpel. Following, the TEC was placed into the defect [17].

The pigs were able to weight-bear within 12 h and walked normally in few days. At 6 months post-surgery,

each animal was euthanized with an overdose of propofol and potassium chloride. The hind limbs were disarticulated at the hip.

2.4 Mechanical Evaluation

The mechanical evaluation of the cartilage with and without TEC was performed using an universal test equipment INSTRON 3365 which works with own Bluehill 3™ software (Instron, USA). The accessory BioPuls™ temperature controlled bath was used (Fig. 1a). The compression test conducted at 0.5 mm/min speed, with 100 N load cell. To analyze the mechanical properties of solid matrix in this study were applied indentation test and maximum compression test [18].

The test samples were constructed using 5 mm height of subchondral bone. The bone density and average of four main measures (cartilage thickness, weight, width and height of the total sample) of osteochondral block which consists of the bone and cartilage set were obtained and inserted in the Bluehill 3™ program to process the test. This block was placed on a support with the cartilage part facing up and positioned on the Instron (Fig. 1b). To perform the test the structure was immersed saline solution (0.9% NaCl) bath at 36 °C to simulate the physiological condition of the body (Fig. 1a) [19].

A minimum load was applied to ensure alignment and total contact between the cartilage surface and the spherical tip indenter (2 mm diameter). The indentation test consisted of three cycles of strain stress-relaxation that was performed at a constant loading rate with a fixed displacement of 5% of the cartilage thickness' average. Followed this, the maximum compression test was performed with a fixed displacement of 50% of the total height [19].

The Young's Modulus was determined based on the second ramp of the stress-relaxation indentation test, as this step presents a more linear behavior and the lowest amount of error. The elasticity module depends on the straight slope value, which is associated with the cartilage elasticity (N/mm) [20].

3 Results

Indentation test (Fig. 2a) and maximum compressive test (Fig. 2b) assessed the properties of the solid matrix and mechanical proprieties of the tissue repair in control and treatment groups.

A Finite Element (FE) model was created for the indentation test using the ANSYS R17.2 software (Fig. 3). To simulate the osteochondral block, the Young's Modulus found in the mechanical analysis was inserted in the program. The cartilage, characterizing a viscoelastic material, was modeled as a thin layer over the bone structure and the spherical indenter was created as a rigid material with 2 mm diameter [21].

In preliminary analysis, the samples presented different cartilage thickness, which directly affects the indentation response and so, the Young's Modulus [20]. However, it is possible to observe in all results the hysteresis phenomenon when applying the three cycles of strain stress-relaxation, evidencing the viscoelastic property of the articular cartilage.

4 Discussion

To the best of our knowledge, this is the first study in Brazil describing mechanical tests and properties of cartilage treatment after tissue engineering in GMP technique.

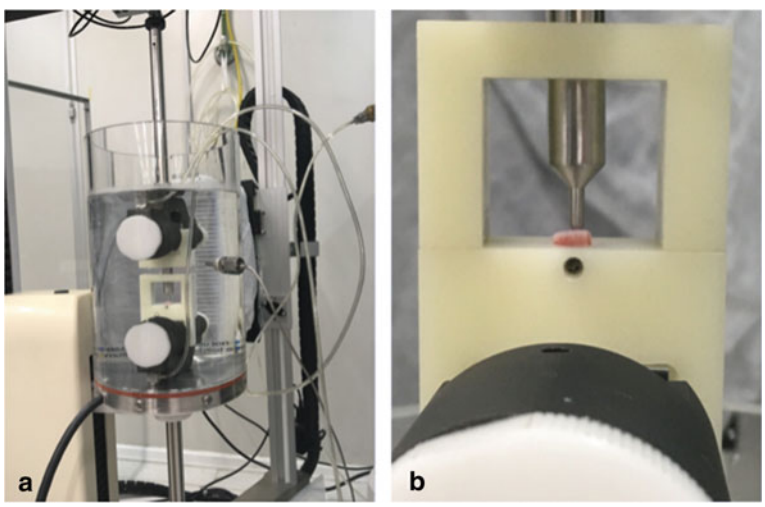

Fig. 1 Indentation test set up. **a** Structure immersed in saline solution (0.9% NaCl) at a temperature of 36 °C. **b** Sample placed on a support with the cartilage part facing up and positioned on the equipment

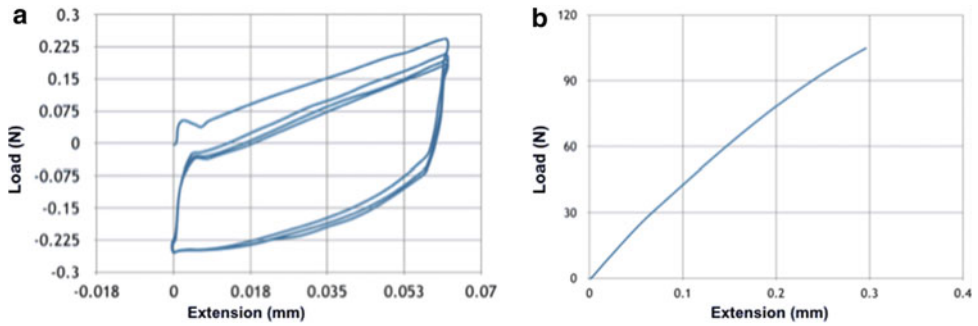

Fig. 2 Biomechanical analysis of one sample. **a** Indentation test: load (N) × extension (mm) showing the three cycles of 5% tension relaxation. **b** Maximum compression test: load (N) × extension (mm) showing the linear behavior of the cartilage

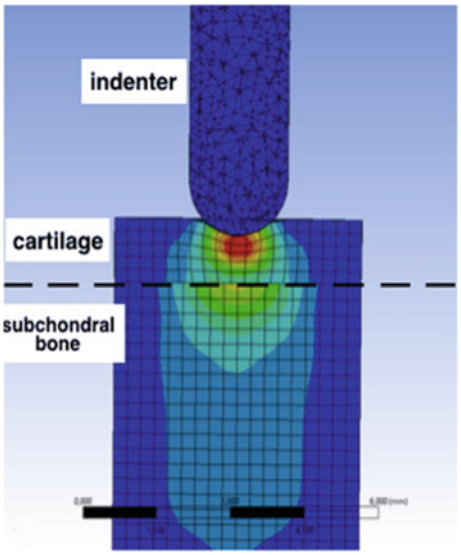

Fig. 3 Finite element analysis image representing the force distribution caused by the indenter in the osteochondral block, indicating the cartilage above the dashed line and the subchondral bone below

Comparisons of the Young's Modulus and maximum compressive test of the osteochondral block with and without TEC will be performed in a near future to demonstrate the structure integrity of the articular cartilage as the chondrocytes distribution and the extracellular matrix changes when the sample is deformed.

5 Compliance with Ethical Requirements

5.1 Statement of Informed Consent and Human Rights

This study was approved by the Ethics Committee at the Hospital das Clínicas, University of São Paulo, Medical School (protocol: CAPPesq nº 15428, IOT nº 1216). All patients signed informed consent terms to participate in this research.

5.2 Statement of Animal Rights

The Ethics and Research Committee at Sírio-Libanês Hospital (São Paulo, Brazil) approved the animal study (protocol: CEUA-P 2015-08).

6 Conclusions

This study showed that mechanical evaluation was feasible and capable to properly evaluate articular cartilage restoration by determining the Young Modulus of the cartilage with and without tissue engineering (TEC) treatment.

Acknowledgements This study was supported by Fundação de Amparo a Pesquisa do Estado de São Paulo (FAPESP–Process 2017/05774-5), Coordenação de Aperfeiçoamento de Pessoal de Nível Superior (CAPES–Process 88881.171651/2018-01), grant from the International Society of Arthroscopy, Knee Surgery and Orthopaedic Sports Medicine and the Orthopaedic Research and Education Foundation (ISAKOS Osteoarthritis Grant—2018). This study was performed at Hospital Sírio Libanês, São Paulo, SP, Brazil; Hospital das Clínicas HCFMUSP, Faculdade de Medicina, Universidade de São Paulo, São Paulo, SP, Brazil; and Instituto do Coração INCOR, São Paulo, SP, Brazil.

Conflict of Interest
The authors declare that they have no conflict of interest.

References

1. Perera JR, Gikas PD, Bentley G (2012) The present state of treatments for articular cartilage defects in the knee. Ann R Coll Surg Engl 94(6):381–7. [cited 2016 Dec 30]. https://www.ncbi.nlm.nih.gov/pubmed/22943326
2. Curl WW, Krome J, Gordon ES, Rushing J, Smith BP, Poeh-ling GG (1997) Cartilage injuries: a review of 31,516 knee arthroscopies. Arthrosc J Arthrosc Relat Surg 13(4):456–60. [cited 2016 Dec 30]. https://www.arthroscopyjournal.org/article/S0749806397901249/fulltext

3. Flanigan DC, Harris JD, Trinh TQ, Siston RA, Brophy RH (2010) Prevalence of chondral defects in Athletes' knees: a systematic review. Med Sci Sports Exerc 42:1795–1801
4. Gomoll AH, Madry H, Knutsen G, van Dijk N, Seil R, Brittberg M et al (2010) The subchondral bone in articular cartilage repair: current problems in the surgical management. Knee Surg Sport Traumatol Arthrosc. 18(4):434–447
5. Showery JE, Kusnezov NA, Dunn JC, Bader JO, Belmont PJ, Waterman BR (2016) The rising incidence of degenerative and posttraumatic osteoarthritis of the knee in the United States Military. J Arthroplasty 31(10):2108–14. [cited 2017 Jan 14]. https://linkinghub.elsevier.com/retrieve/pii/S0883540316003028
6. Shen J, Chen D (2014) Recent progress in osteoarthritis research. J Am Acad Orthop Surg 22:467–468
7. Ando W, Tateishi K, Katakai D, Hart DA, Higuchi C, Nakata K et al (2008) In vitro generation of a scaffold-free tissue-engineered construct (TEC) derived from human synovial mesenchymal stem cells: biological and mechanical proper-ties and further chondrogenic potential. Tissue Eng Part A 14:2041–9
8. Hilkens P, Gervois P, Fanton Y, Vanormelingen J, Martens W, Struys T et al (2013) Effect of isolation methodology on stem cell properties and multilineage differentiation potential of human dental pulp stem cells. Cell Tissue Res 353:65–78
9. Shimomura K, Ando W, Moriguchi Y, Sugitan N, Yasui Y, Koizumi K, Fujie H, Hart DA, Yoshikawa H, Nakamura N (2015) Next generation mesenchymal stem cell (MSC)-based cartilage repair using scaffold-free tissue engineered constructs generated with synovial mesenchymal stem cells. Cartilage 6(2Suppl):13S–29S. https://doi.org/10.1177/1947603515571002. https://www.ncbi.nlm.nih.gov/pmc/articles/PMC4481383/
10. Wickham MQ, Erickson GR, Gimble JM, Vail TP, Guilak F (2003) Multipotent stromal cells derived from the infrapatellar fat pad of the knee. Clin Orthop Relat Res 412:196–212
11. Patel JM, Wise BC, Bonnevie ED, Mauck RL (2019) A systematic review and guide to mechanical testing for articular cartilage tissue engineering. Tissue Eng Part C Methods 25(10):593–608. https://doi.org/10.1089/ten.tec.2019.0116
12. Lu XL, Mow VC (2008) Biomechanics of articular cartilage and determination of material properties. Med Sci Sports Exerc 40 (2):193–199. https://doi.org/10.1249/mss.0b013e31815cb1fc
13. Fernandes TL, Kimura HA, Pinheiro CCG, Shimomura K, Nakamura N, Ferreira JR et al (2018) Human synovial mesenchymal stem cells good manufacturing practices for articular cartilage regeneration. Tissue Eng Part C Methods 24(12):709–716
14. Bueno DF (2018) Bone tissue engineering with dental pulp stem cells for alveolar cleft repair—Full text view—ClinicalTrials.gov hospital Sirio-Libanes. [cited 2019 Jan 29]. https://clinicaltrials.gov/ct2/show/NCT03766217?id=NCT03766217&rank=1&load=cart
15. Kilkenny C, Browne W, Cuthill IC, Emerson M, Altman DG, NC3Rs Reporting Guidelines Working Group (2010) Animal research: reporting in vivo experiments: the ARRIVE guide-lines. Br J Pharmacol 160(7):1577–9. [cited 2020 Mar 8]. https://www.ncbi.nlm.nih.gov/pubmed/20649561
16. Harris PA, Taylor R, Thielke R, Payne J, Gonzalez N, Conde JG (2009) Research electronic data capture (REDCap)—a metadata-driven methodology and workflow process for providing translational research informatics support. J Bio-med Inform 42 (2):377–81. [cited 2020 Mar 24]. https://www.sciencedirect.com/science/article/pii/S1532046408001226?via%3Dihub
17. Kuo CK, Li W-J, Mauck RL, Tuan RS (2006) Cartilage tissue engineering: its potential and uses. Curr Opin Rheumatol 18 (1):64–73. [cited 2020 Mar 11]. https://journals.lww.com/00002281-200601000-00011
18. Knecht S, Vanwanseele B, Stüssi E (2006) A review on the mechanical quality of articular cartilage—implications for the diagnosis of osteoarthritis. Clin Biomech 21(10):999–1012. https://doi.org/10.1016/j.clinbiomech.2006.07.001
19. Meloni GR, Fisher MB, Stoeckl BD, Dodge GR, Mauck RL (2017) Biphasic finite element modeling reconciles mechanical properties of tissue-engineered cartilage constructs across testing platforms. Tissue Eng Part A 23(13–14):663–674. https://doi.org/10.1089/ten.tea.2016.0191. [cited 2020 May 27]. https://www.ncbi.nlm.nih.gov/pmc/articles/PMC5549831/
20. Töyräs J, Lyyra-Laitinen T, Niinimäki M, Lindgren R, Nieminen MT, Kiviranta I, Jurvelin JS (2001) Estimation of the Young's modulus of articular cartilage using an arthroscopic indentation instrument and ultrasonic measurement of tissue thickness. J Biomech 34(2):251–256. https://doi.org/10.1016/S0021-9290(00)00189-5
21. Armitage OE, Oyen ML (2017) Indentation across interfaces between stiff and compliant tissues. Acta Biomater 56:36–43. https://doi.org/10.1016/J.ACTBIO.2016.12.036

Cytotoxicity Evaluation of Polymeric Biomaterials Containing Nitric Oxide Donors Using the Kidney Epithelial Cell Line (Vero)

V. C. P. Luz, F. N. Ambrosio, C. B. Lombello, A. B. Seabra, and M. H. M. Nascimento

Abstract

Nitric oxide (NO) is a small diatomic molecule, endogenously produced, and plays important roles in many vital biological processes including angiogenesis, antioxidant/antitumor/antimicrobial actions and tissues regeneration such as skin, cartilage and bone. For being a free radical, NO is relatively instable in biologic system and it can be rapidly inactivated. Among then, the S-nitrosothiols (RSNOs) are prominent, which spontaneously decompose releasing NO. The combination of RSNOs and biomaterials represent a promising strategy to increase the therapeutic efficiency of these NO donors. In this way, the main objective of this study was to evaluated cytotoxicity of thermosensitive poloxamer/hyaluronic acid hydrogels (PL/HA) and chitosan nanoparticles (CS NPs) containing NO donors (RSNOs), using the kidney cells of African green monkey (Vero). The results obtained by quantitative MTT assays showed cell viability dependent on the concentrations of SNAC and polymeric biomaterials. Thus, these results point the in vitro biocompatibility of PL/HA and CS NPs systems containing NO donors and their possible application in bone tissue regeneration and also contribute to studies using Vero cells.

Keywords

Nitric oxide • Nitric oxide donors • Hydrogels • Nanoparticles • Cytotoxicity

V. C. P. Luz · F. N. Ambrosio · A. B. Seabra · M. H. M. Nascimento (✉)
Center for Natural and Human Sciences (CCNH), Federal University of ABC (UFABC), Santo André, SP, Brazil
e-mail: monica.nascimento@ufabc.edu.br

C. B. Lombello
Center for Engineering, Modeling and Applied Social Sciences (CECS), Federal University of ABC (UFABC), Santo André, SP, Brazil

1 Introduction

Nitric oxide (NO) is a small diatomic molecule, endogenously produced, and plays important roles in many vital biological processes including angiogenesis, skin healing, antioxidant/antitumor/antimicrobial actions and tissues regeneration such as skin, cartilage and bone [1]. Deficiencies on this endogenous production are associated with several pathologic conditions, such as cancer, diabetes and neurodegenerative effects [2]. The effects of NO are related to its concentration, location and on environment where it is produced. Generally, lower concentrations are related to cytoprotective effects and higher concentration are related to toxic effects [3].

Being a free radical, NO is relatively instable in biologic system and it can be rapidly inactivated. Consequently, there is a strong interest on the development of relatively stable NO donors, such as biomaterial who can delivery NO in a sustained manner, for biomedical applications [4].

There are several molecules with low molecular mass that act as NO donors, preserving their bioactivity [5]. Molecules as S-nitrosothiols (RSNOs) act as NO donors preserving the molecule bioavailability and bioactivity when they decompose and release NO. The combination between biomaterials and RSNOs represent a promising strategy to increase the therapeutic efficiency of these NO donors [6, 7]. The success from biomaterial application in organism depends primarily on its biocompatibility, being necessary to perform in vitro cytotoxicity assays to evaluate and identify the biomaterials that exhibit cytotoxic behavior. Therefore, it is possible to select only the most suitable biomaterial for clinic studies, in vivo application, thus minimizing the number of experiments animals [8].

This research studied the cytotoxicity of thermosensitive polaxamer/hyaluronic acid hydrogel (PL/HA) and chitosan nanoparticles (CS NPs) containing NO donors (RSNOs), using Vero cell line, with the purpose of studying these harmful properties about these interactions among biomaterials and cell cultures.

T. F. Bastos-Filho et al. (eds.), *XXVII Brazilian Congress on Biomedical Engineering*, IFMBE Proceedings 83, https://doi.org/10.1007/978-3-030-70601-2_23

2 Methodology

2.1 Biomaterials Synthesis

The biomaterials containing NO donors were synthesized in collaboration with researcher's group by Dra. Amadea Seabra (CCNH-UFABC). The NO donors, RSNOs, were incorporated in hydrogels and nanoparticles, synthesized from the nitration of their respectively thiol groups (RSHs). Nitrosation occurs by adding an equimolar amount of sodium nitrite ($NaNO_2$), in relation to RSH, in an acidic aqueous solution. The formation of RSNOs was confirmed by detecting the absorption bands characteristic of RSNOs at 333 nm ($\pi \rightarrow *$) and 545 nm ($n_N \rightarrow \pi^*$), using a spectrophotometer in the ultraviolet-visible (Agilent 8454). The following RSNO was synthesized: S-nitroso-N-acetylcysteine (SNAC) from N-acetylcysteine (NAC).

2.2 Incorporation of RSNOs in Polaxamer/hyaluronic Acid Hydrogels and Chitosan Nanoparticles

Poloxamer thermo-sensitive hydrogels/hyaluronic acid (PL-HA) were prepared by direct dispersion of RSNOs (SNAC), in solutions of polaxamer 407 forming a binary system with hyaluronic acid. An aqueous solution of Poloxamer 407 (18%) was prepared and maintained at 4 °C. Hyaluronic Acid (1%) were added to the poloxamer 407 solution, previously prepared, in an ice bath, under stirring. The solutions were kept at temperatures below 10 °C, for a period of 10 h, in order to obtain the equilibrium of dissolution of the copolymer in water. Known amounts of free SNAC solutions were added to Poloxamer 407/Hyaluronic Acid solutions. After preparation, the samples were stored at 4–8 °C until further use. Samples of hydrogels used on tests were sterilized by autoclaving with 15 lb per square inch of pressure and 121 °C for 15 min.

The synthesis of CS nanoparticles involves the process of ionotropic gelation that occurs through the interaction of opposite charges of the molecules. The NH^3 + functional groups present in the CS chains interact with the O-tripolyphosphate (TPP) functional groups, which results in the formation of nanoparticles. To synthesize the nanoparticles, a solution of CS (1 mg mL^{-1}) in 1% acetic acid (pH ≈ 3) containing NAC (163.2 g/mol) was submitted a mechanical agitation using a magnetic bar for 90 min. After the end of the stirring, a TPP solution (0.6 mg mL^{-1}) was dripped into the CS solution containing NAC (1 drop every 20 s) respecting the volume ratio of 1 mL of CS to 3 mL of TPP. With this, an aqueous suspension of nanoparticles (1 g L^{-1} CS) was formed containing NAC, which were called CS NPs.

2.3 Cells Viability Assays

Cell Culture: Vero cells lineage, established from kidney epithelial cells of African green monkey, (CCIAL 057, Adolfo Lutz Institute, São Paulo) were cultivated in HamF10 medium (Sigma-Aldrich), with fetal bovine serum (10%; Sigma Aldrich), 100 µg/ml penicillin, maintained at 37 °C with 5% CO_2. The cells were observed by inverted light microscope (A1 Axiovert, Zeiss).

Cytotoxicity by direct method: the tests were performed according to ISO 10993-5 (2009) and used to obtain a qualitatively evaluation of cells cytotoxicity [9]. The cells had been seeded in 96-well plates and maintained for 24 h until the monolayer was formed, at a confluence of 80%. After this, the culture medium was removed and substituted by 100 µL of elution medium containing the biomaterials samples (the concentrations of each biomaterial are shown at Table 1). After 24 h the cells were maintained in this direct contact. For the negative control, non-cytotoxicity, it was only used the culture medium as described above. For the positive control, cytotoxic, it was used 0.25% solution of phenol in the culture medium. The assays were performed in quintuplicate of samples.

MTT assays: The cells cultivated in direct cytotoxicity conditions in contact with biomaterial samples were evaluated after 24 h by MTT (3-(4,5-dimethylthiazol-2-yl)-2,5-diphenyltetrazolium bromide) methodology. It was added 100 µl of MTT solution (0.5 mg/mL) to each well, and the cells were incubated for 4 h. After that, the MTT solution was removed and 50 µl of dimethyl sulfoxide (Synth) was added to each well for 10 min, and the absorbance was

Table 1 Corresponding concentrations of NAC/SNAC in hydrogels and nanoparticles evaluated for cell viability

Concentration of NAC/SNAC (mmol L^{-1})	Concentration of hydrogel (m/v %)	Concentration of CS NPs (µg/mL)
2	3.6	0.2
1	1.8	0.1
0.5	0.9	0.05
0.125	0.18	0.0125
0.05	0.09	0.005

measured with an automated spectrophotometric microtiter plate reader (SpectraMax M5), using a 570 nm filter and considering the negative control as 100% cells viability.

Statistical analysis: The experimental data were analyzed using GraphPad Prism software, version 8.0 and Microsoft Excel. All results are presented with mean and standard deviation (SD), using the ANOVA (one-way) variance test and post Tukey-Krammer test for comparing the groups. Statistical significance was set at a p-value of ≤ 0.05.

3 Results

The MTT assay has a quantitative character used specifically for the mitochondrial functionality. MTT analyzes quantitatively the reduction of tetrazolium salt (yellow coloring) by the pyruvate dehydrogenase enzyme complex present in mitochondria with the formation of a final product of formazan crystals (purple) that are measured in a spectrophotometer at 570 nm (Fig. 1). In this way, this reaction occurs only in viable cells that have their mitochondria active, thus configuring a versatile method for assessing cell.

The first cytotoxicity test was performed varying the precursor and donors' molecules of NO (NAC and SNAC) shown at Fig. 2A. These results showed over 70% cells viability (represented with a red line) for all concentrations of NAC, and therefore considered viable for the tested cell line. While the treatment with the NO donor (SNAC), promoted a dose dependent cell viability, in which cytotoxicity (44%) is noted in concentrations below 1 mmol L^{-1} (Fig. 2A).

The combination between polaxamer/hyaluronic acid hydrogel (PL/HA) and RSNOs showed a non-cytotoxicity effect for all concentrations in the presence of NAC (Fig. 2B). The last hydrogel concentration (3.6%) in the presence of NO donor (SNAC) showed a viability of 70%, remaining within the limit of cell viability (Fig. 2B). By the ANOVA test all concentrations of PL/HA, with precursor and NO donor showed statistical difference.

The last association between chitosan nanoparticles and RSNOs (Fig. 2C) the cytotoxicity effect showed concentration dependent, in which is possible to see that the concentrations higher than 0.0125 µm mL^{-1} presented a viability less than 70% in relation to the negative control. Like the previous one, all the concentrations of NAC and SNAC in association with NPs showed statistical difference by the test.

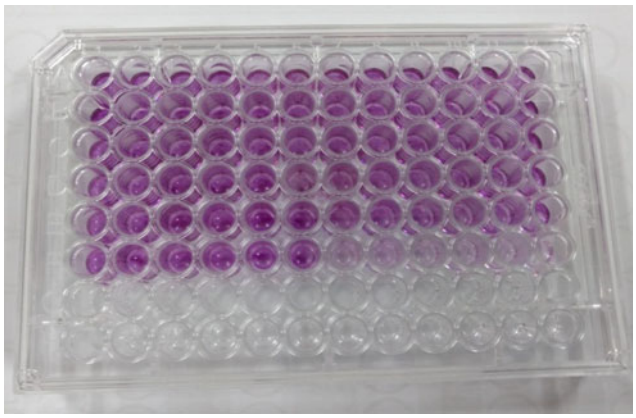

Fig. 1 Final step of MTT reduction test, after 50 µl of dimethyl sulfoxide was added to each well to form formazan crystals

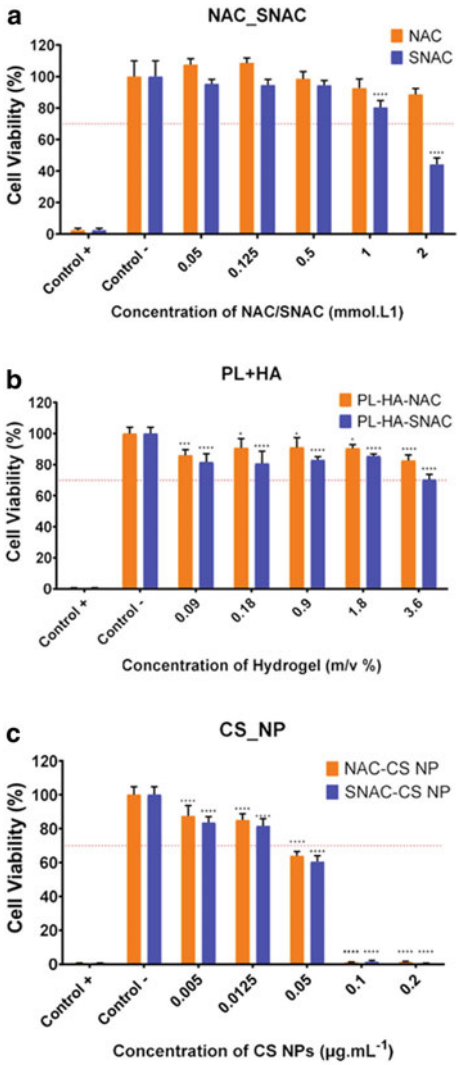

Fig. 2 Effects of samples at different concentration on Vero cells evaluated by MTT reduction test. **A** NAC/SNAC; **B** PL/HA hydrogel, **C** CS NPs. Values are reported as mean +− standard deviation (SD) (n = 3). Statistical differences relatively to positive control, *p < 0.05, **p < 0.001 e ****p < 0.0001

4 Discussion

Related to cytotoxicity assays the Vero cells lineage is one of the international standard lines used for this cytotoxicity studies with biomaterials [9, 10].

As mentioned before the NO effects in biologic environment are related to its respective concentration [3]. Thereby, the NO donor used in this research (SNAC) showed a dependent concentration for concentrations higher than 1 mmol L^{-1} (Fig. 2A).

For all concentrations, the combination between the polymer PL-HA showed a non-cytotoxicity effect. The hyaluronic acid is known to be a highly biocompatible, biodegradable, bioactive, non-immunogenic and non-thrombogenic. The HA is a polymer knowing for its importance in control and regulate the cells behavior, such as the interaction between cell to cell [11]. However, the Pluronic's cytotoxicity, among other cells lineage, has been demonstrated in literature and appears to be directly related to the concentration of the polymer.

Nascimento (2019) demonstrated cytotoxicity effects in chondrosarcoma cell lineage (SW1353) treated with formulations of 0.5% of PL [12]. Although, this association between hydrogels of PL and NO donors, in concentrations among 0.09 and 3.6%, demonstrated to be a biocompatible biomaterial for Vero cells line (Fig. 2B).

The combination of chitosan nanoparticles and RSNOs showed a non-cytotoxicity effect to concentrations below 0.125 μg ml^{-1} of NAC-CS NPs and SNAC-CS NPs. Then, the synergic effect among CS NPs and RSNO's was observed (Fig. 2C). It is believed that the cytotoxic effect observed being intrinsically related to incorporation of NO donors once Pelegrino et al. (2017) showed assays with CS NPs in concentrations of 0.2 μg ml^{-1} that showed no degree of cytotoxicity [1]. It is known that he cytotoxicity about NO donors are related with inhibition of cell proliferation and apoptosis induction [13]. Therefore, according with literature, the CS NPs are biocompatible and biodegradable, approved by the Food and Drug administration for different therapeutic purposes [14].

To know more details about the biocompatibility between VERO cells and these biomaterials—CS NPs and PL-HA—qualitative studies, such as morphologic assays, and characterization studies of these biomaterials are critical to improve in vitro tests and it is fundamental for all biomaterial aimed at clinical application.

5 Conclusions

The evaluation of cellular interaction with NO donors and polymeric biomaterials, chitosan nanoparticles (NAC-CS NPs and SNAC-CS NPs) and hyaluronic acid hydrogels (PL-HA/NAC and PL-HA/SNAC), using the quantitative method (MTT) allowed to verify that the Vero cells showed different degree of cytotoxicity between the concentration of these biomaterials. The NO donors demonstrated a cell viability dependent of concentrations higher than 3.6% to PL-HA/SNAC and higher than 0.05 μg ml^{-1} to SNAC-CS NPs. With this, these results appoint PL/HA and CS NPs biocompatibility containing NO donors and showed that they are a promising polymerics biomaterial aiming therapeutics application.

6 Compliance with Ethical Requirements

6.1 Conflict of Interest

The authors declare that they have no conflict of interest.

Acknowledgements This research is supported by Federal University of ABC, CAPES and CNPq.

References

1. Pelegrino MT, Silva LC, Watashi CM et al (2017) (2017) Nitric oxide-releasing nanoparticles: synthesis, characterization, and cytotoxicity to tumorigenic cells. J Nanopart Res 19:57
2. Seabra AB, Durán N (2017) Nanoparticulated nitric oxide donors and their biomedical applications. Bentham Sci 17:216–223
3. Basudhar D, Cheng R et al (2015) (2015) Chemotherapeutic potential of diazeniumdiolate-based aspirin produgs in breast cancer. Free Radic Biol 83:101–114
4. Kollau A, Russwurm M et al (2016) Scavenging of nitric oxide by hemoglobin in the tunica media of porcine coronary arteries. Nitric Oxide 54:8–14
5. Silva RS, Lima RG, Machado SP (2016) Adv Inorg Chem 64:225–292
6. Broniwska KA, Hogg N (2012) (2012) The chemical biology of S-nitrosothiols. Antioxid Redox Sig 17:969–980
7. De Oliveira MG (2016) (2016) S-nitrosothiols as platforms for topical nitric oxide delivery. Basic Clin Pharmacol Toxicol 119:49–228
8. Massom AO, Nascimento MHM, Lombello CB. (2014) Análise comparativa de diferentes métodos de citotoxicidade *in vitro*. CBEB 2014.

9. International Standards Organization (2019) Biological evaluation of medical devices—Part 5: tests for in vitro cytotoxicity. ISO 10993-5
10. Mosmann T (1983) Rapid colorimetric assay for cellular growth and survival: Application to proliferation and cytotoxicity assays. J Immunol Meth 65:55–63
11. Nascimento MHM (2016) Lombello CB (2016) Hidrogéis a base de ácido hialurônico e quitosana para engenharia de tecido cartilagisono. Polímeros 26:360–370
12. Nascimento MHM (2019) Hidrogéis de poloxamer-ácido hialurônico como sistemas para liberação de sulfarofano no tratamento de osteoartrite. UFABC
13. Ferraz LS, Watashi CM, Pelegrino MT et al (2018) Antitumor potential of S-nitrosothiol-containing polymeric nanoparticles against melanoma. Mol Pharmaceut 15:1160–1168
14. Ferreira DM, Saga YY et al (2013) Cchitosan nanoparticles for melanoma cancer treatment by photodynamic therapy and electrochemotherapy using aminolevulinic acid derivates. Curr Med Chem 20(4):1904–1911

Cellular Interaction with PLA Biomaterial: Scanning Electron Microscopy Analysis

L. H. S. Mazzaron and C. B. Lombello

Abstract

Polymeric biomaterials are used in tissue repair due to characteristics as biocompatibility and cell interaction. In the category of synthetic polymers, poly lactic acid (PLA) is especially used in several clinical applications. This biomaterial can be prepared in the form of dense and porous membranes, in order to characterize the interaction with Vero cells in culture, using scanning electron microscopy (SEM). For this purpose, dense and porous PLA membranes were previously prepared, sterilized by ultraviolet light (UV) and used as a substrate for cultivation of Vero cells, for periods of 2 h and 7 days. To observe the cell interaction with the membranes, different methodologies for processing the samples for observation by SEM were considered, and a comparative analysis of the results was performed. There was no significant difference in cell morphology comparing samples with and without osmium tetroxide, however samples that underwent drying at a critical point had better preservation of cell morphology compared to samples in chemical drying. Osmium tetroxide is not a major factor in the processing of cells for SEM, and that the type of drying is the factor that most affects cell morphology in this process. It was possible to observe cell adhesion after 2 h of culture, with morphological changes such as cytoplasmic transition to a more flat aspect being more characteristic for 7 days of culture.

Keywords

Biomaterial • PLA • Scanning electron microscopy • Vero cell

L. H. S. Mazzaron (✉) · C. B. Lombello
Biomedical Engineering/CECS, Federal University of ABC (UFABC), Alameda da Universidade, s/n, São Bernardo do Campo, SP, Brazil

1 Introduction

Tissue engineering is a multidisciplinary science that aims to maintain, repair or improve tissue function. In this concept, three elements are fundamental: biomaterials (such as scaffolds, supports or membranes), cells and a specific microenvironment [1, 2]. In this context, polymers are biomaterials widely used as scaffolds due to their characteristics, mainly of biocompatibility [3, 4].

Polymeric biomaterials, such as poly (α-hydroxy acids), the poly (lactic acid) (PLA) [5, 6], are used for the repair of soft tissue functions, such as tendon and cartilage, and of hard tissues, such as bones [3, 7]. The ease of synthesis, the possibility to control the properties of the biomaterial and the improvement of the mechanical and degradation properties are advantages of synthetic polymers, when compared with natural polymers [3, 8].

The clinical application of a biomaterial must attend the safety and efficacy of its use. The interaction of these biomaterials with living tissues must allow an adequate biological response [9]. In addition to biocompatibility, bioreabsorption and mechanical resistance, the interaction with cells that make up living tissues with biomaterials is modulated by the biomaterial surface characteristics [10, 11]. The presence of pores, electrical charges and hydrophilicity may influence contact with cells, both in vitro experimentation and in vivo applications [11–14].

The cell culture technique is applied as an initial step to assess the biomaterials biocompatibility, and may include cytotoxicity tests, cell interaction and tissue engineering techniques. The Vero cell line, isolated from the epithelium of the African green monkey kidney, is used for the mentioned purposes. They are anchorage-dependent cells, with effective cell adhesion and spreading on favorable surfaces, and with a high mitotic index [15].

The interaction between cells and biomaterials can be evaluated by different techniques. Microscopy techniques are widely used, mainly for qualitative analysis of this

T. F. Bastos-Filho et al. (eds.), *XXVII Brazilian Congress on Biomedical Engineering*, IFMBE Proceedings 83, https://doi.org/10.1007/978-3-030-70601-2_24

interaction [13, 14, 16]. Phase contrast light microscopy is used to accompany cells in culture during experiments on two-dimensional substrates, and some three-dimensional substrates, especially translucent ones. Electron microscopy, both scanning and transmission, are complementary tools for analyzing cell-substrate interaction, as they allow the analysis of substrates of different shapes and thicknesses, with higher resolution. However, the processing of biomaterials, specially containing cells on their surface (from in vitro experimentation or even in contact with living tissue) can lead to changes, artifacts, which affect the quality and objectivity of the results [17].

The objective of this project is to characterize the interaction of Vero cells in culture on PLA membranes by scanning electron microscopy (SEM), evaluating cell interaction and the sample preparation protocol, thus providing a modified protocol for this kind of analysis that can optimize time, and diminish material usage and costs, in other experiments.

2 Materials and Methods

2.1 Biomaterial Preparation and Sterilization

The PLA membranes (NatureWorks®, Cargill) were obtained by dissolving the PLA polymer in chloroform (Synth), at a concentration of 10% (w/v) by weight of the polymer in relation to the solvent volume, at room temperature. The solution was poured into glass Petri dishes until the solvent evaporated, in an exhaust hood, at room temperature. The porous membranes were obtained with the addition of NaCl (Synth) to the polymer solution, 5 g of NaCl for 10 mL of polymeric solution. The dense and porous samples of PLA were sterilized by ultraviolet (UV) light for 30 min each face [3, 18].

2.2 Vero Cell Culture

The Vero cell culture (Instituto Adolfo Lutz/SP, CCIAL 057) was performed in HAM F10 medium, with 10% fetal calf serum (FCS), and 100 µg/ml of penicillin/streptomycin, and was maintained at 37 °C with 5% CO_2. The cultures were monitored by phase microscopy, using an inverted light microscope (Axiovert A1/Zeiss). This cell line is considered a standard for cell cytotoxicity tests, and is also used as a standard for studies of cell-biomaterials interaction [15, 19].

2.3 Cell Interaction—Scanning Electron Microscopy

Vero cells were inoculated on sterile PLA membranes, cut into squares of approximately 0.25 cm^2, by direct deposition of a suspension containing 2×10^5 cells/mL, and cultures were maintained for periods of 2 h and 7 days in a 24-well cell culture plate. After the culture period, different sample preparation protocols were performed. As a basic protocol, the samples were fixed with 2.5% glutaraldehyde, in phosphate buffer (PBS, pH 7.4, 0.1 M), for 1 h, washed in PBS, for 1 h, followed by washing in distilled water (30 min) and dehydration in an increasing series of ethanol (30, 50, 70, 90, 96 and 100%), followed by critical point drying (EM CPD300, Leica).

As an alternative to this protocol, modifications related to post-fixation and dehydration were included. In the post-fixation stage, samples of biomaterials with cultured cells were treated with 1% osmium tetroxide for 1 h. In the dehydration stage, critical point drying was replaced by chemical drying, with evaporation of the dehydrating agent, ethanol.

The PLA samples with cultured cells were then covered with 15 nm gold in sputtering (AC200, Leica) and observed with a scanning electron microscope (Quanta 250, FEI). The images were analysed for cellular morphology, and the cell perimeter and area were measured with software Image J (NHI, Bethesda, MD, USA).

3 Results and Discussion

During the culture, Vero cells were observed under a light microscope, with phase contrast (Fig. 1) [19]. The cells showed rounded morphology, without spreading, in both dense and porous PLA. The opacity and the thickness of the biomaterial samples leads to difficulty of visualizing the cells on the biomaterial, impairing the proper characterization of cellular interaction, a fact that motivated the use of the SEM for more accurate analyzes.

After 24 h of cell culture, the samples were observed under a light microscope, both on the surface of the biomaterials (Fig. 1) and on the bottom of the culture plate (Fig. 2). The observation of the cells growing on the culture plate near biomaterial samples can be used to verify a possible cytotoxic cellular response, the PLA samples were considered non-cytotoxic, once the cells showed typical morphology [15, 16, 20] (Fig. 2).

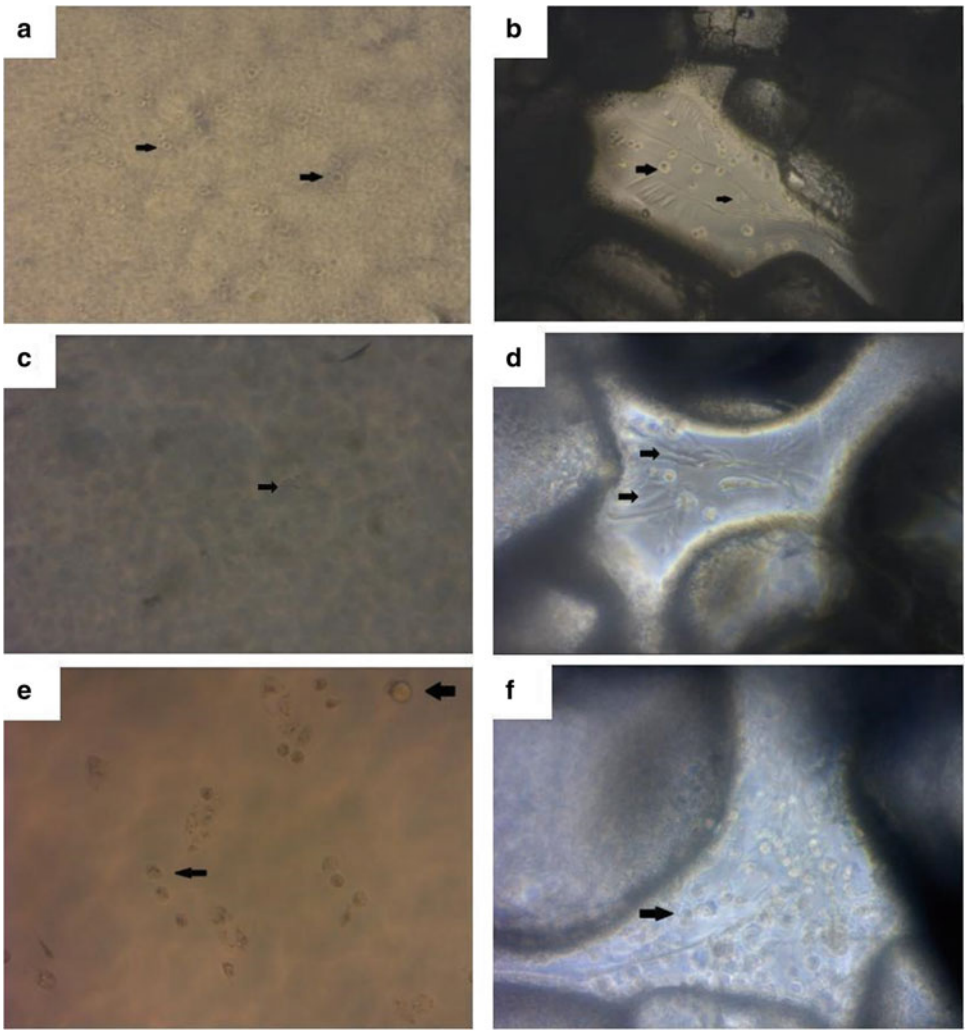

Fig. 1 Vero cells cultured on PLA biomaterial. **A**, **B**: 30 min, **C**, **D**: 24 h; **E**, **F**: 7 days. **A**, **C**, **E**: dense PLA; **B**, **D**, **F**: porous PLA. The arrows indicate the presence of the cells. Magnification: 200×

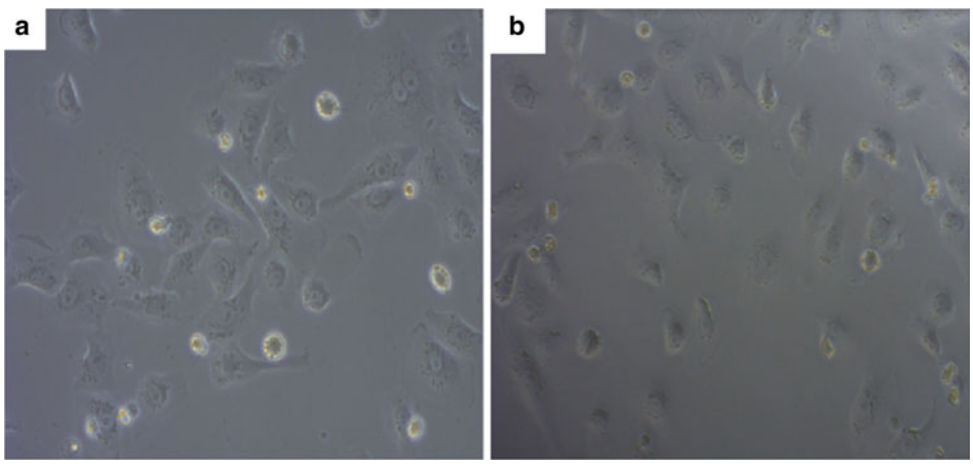

Fig. 2 Vero cells cultured on PLA biomaterials after 24 h, a representative result of the non-cytotoxicity of dense **A** and porous **B** samples. Magnification: 200×

For electron microscopy, biomaterials, and biological materials, are exposed to an electron beam as a source to form the image, allowing a high resolution image. In scanning electron microscopy (SEM) this electron beam interacts with the surface of the sample, in a high or low vacuum environment. The samples are exposed to high acceleration voltage (kV), and must be able to interact with the beam of electrons generating backscatter or secondary electrons, for example [21].

For electron microscopy, biomaterials, and biological materials, are exposed to an electron beam as a source to form the image, allowing a high resolution image. In scanning electron microscopy (SEM) this electron beam interacts with the surface of the sample, in a high or low vacuum environment. The samples are exposed to high acceleration voltage (kV), and must be able to interact with the beam of electrons generating backscatter or secondary electrons, for example [21].

The preparation of samples of biomaterials containing cells is necessary in order to preserve the structures to be observed with a SEM. The preparation includes fixation, post-fixation, washing, dehydration, drying and metallization steps [16, 20, 22].

The chemical fixation process aims at the preservation of the cellular structure, creating crosslinking and chemical bonds that allow the stabilization of the cell morphology as close to its natural and functional state [23]. Glutaric aldehyde, or glutaraldehyde, is generally used as a primary fixative, which acts on the fixation of proteins by divalent bonds with amino groups. Other fixatives, such as paraformaldehyde, can be used in association with glutaraldehyde (the Karnovsky's Mixture).

The post-fixation step with osmium tetroxide (OsO_4) can be used to preserve lipid structures, such as cell membranes. However, OsO_4 has a strong oxidizing effect, in addition to its toxic, carcinogenic, mutagenic and teratogenic effects, as well as it is a high-cost reagent [24].

After the fixation, the washing is important to eliminate fixatives, mainly if they may form precipitations in contact with the dehydration solution. The dehydration step is made in increasing concentrations of ethanol or acetone, with the function of replacing the water present in the biological samples, as the observation by SEM usually occurs in a vacuum condition [22]. The final drying can be done in air, allowing the agent used in the dehydration to dry naturally. However, during this process it is common to observe morphological changes in biological structures, such as shrinking, destruction of surface structures, and even collapse of the sample, due to the surface tension of the chemical drying agent, creating artifacts that prevent the correct morphological observation of the sample. It can alternatively be used as the technique of critical point drying, which establishes a condition of low temperature and high pressure, to replace the dehydration agent with liquid CO_2. The transition from the liquid to the gaseous phase occurs with a minimum of surface tension [25], preserving biological samples [26].

All the described processing aims at the ultrastructural preservation of biological structures, cells, tissues or organs, with the least possible deformation (or artifact), and the proper interaction with the electron beam [27, 28]. For this study, the standard mentioned protocol was altered in the post-fixation and dehydration phases, to observe the impact that the absence of a post-fixator and different dehydration agents can bring to the analysis.

In this study the cells cultured on PLA samples for the period of 2 h showed cell adhesion, with few cells widely spread among themselves, with rounded morphology (Fig. 3). In some areas it was possible to observe cell spreading, with cytoplasmic expansions contact with the biomaterial (Fig. 3B). The cells were well preserved with glutaraldehyde fixation, and the post-fixation with osmium tetroxide did not result in improved cell morphological preservation (Fig. 3C, D, G, H). However the use of a critical point for dehydration results in better cytoplasmic preservation of expansions in areas of cell adhesion (Fig. 3 B, D, F, H), which was expected for this kind of technique, as the liquid CO_2 transitions to gas and it occurs with a minimum of surface tension, bringing less harm to the biological samples [25, 26].

Regarding the biomaterial, the processing allowed a good preservation, without structural modifications. In porous PLA samples, it can be observed that the cell deposition inside the pores, where they showed rounded morphology, with focal contact with the biomaterial, indicative of the beginning of the cell adhesion process, the morphology is distinct from cells in dense samples (Fig. 3).

The observation of cells cultured on PLA biomaterials at 7 days allowed the verification of their proliferation pattern (Fig. 4). The cells cultured on samples of dense PLA after 7 days of cultivation showed very spread morphology, with well-preserved cytoplasmic expansions, and few scattered cells were observed, indicating little cell proliferation (Fig. 4 B–D).

For the porous samples, small cell clusters were observed, two or few cells, isolated from each other, preferably in areas of depression or biomaterial surface (Fig. 4A). The cells maintain a rounded shape, little scattered, indicating little interaction with the biomaterial.

The presence of isolated cells, or small groups of these, demonstrates that proliferation is not favored. The rounded morphology of the cells, without cytoplasmic breaks or interruptions, also reveals that they are in good morphological preservation conditions (Fig. 4).

The samples fixed only with glutaraldehyde showed cells with very visible cytoplasmic expansions, with good

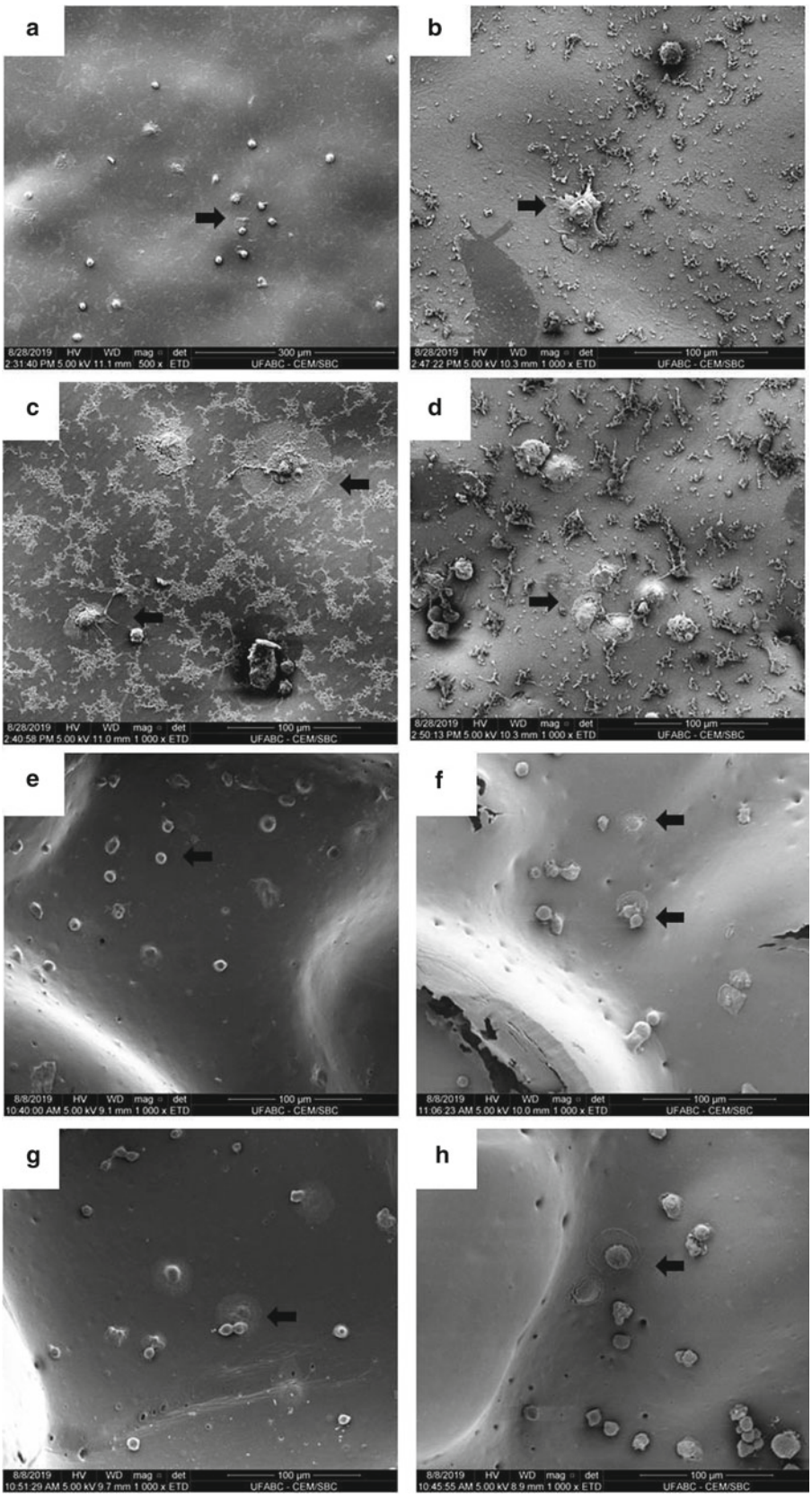

Fig. 3 Vero cells cultured on PLA biomaterials after 2 h, fixed with glutaraldehyde. Arrows indicate the presence of cells. **A**–**D**: dense samples; **E**–**H**: porous samples; **C**, **D**, **G**, **H**: post-fixed in osmium tetroxide; **A**, **C**, **E**, **G**: chemically dehydrated; **B**, **D**, **F**, **H**: critical point drying

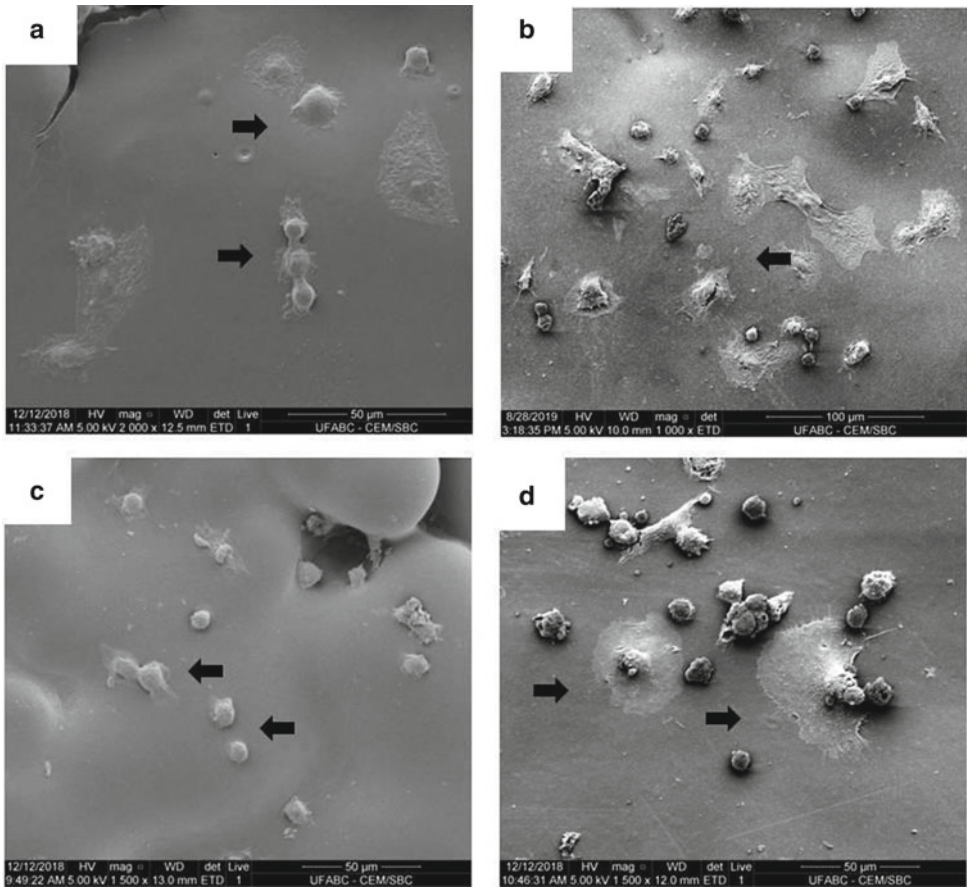

Fig. 4 Vero cells cultured on PLA biomaterials after 7 days, fixed with glutaraldehyde. Arrows indicate the presence of cells. **A**: porous sample, flattened pore surface; **B–D**: dense samples; **C**, **D**: post-fixed in osmium tetroxide; **A**, **C**: chemically dehydrated; **B**, **D**: critical point drying

morphological preservation (Figs. 3 and 4). This finding corroborates data presented in the literature. In general, porous substrates, even with larger pores, favor the differentiated state of cells, and little proliferative activity [13]. It was possible to evaluate that despite a slight improvement in the preservation of cell membranes, the presence of osmium tetroxide did not cause a significant improvement in cell morphology preservation. Due to the extreme toxicity and the high course, we do not consider it necessary to use this post-fixative. Other reports also consider the possibility of dispensing this reagent in the processing of biological samples for SEM [24, 29].

However, the preservation of samples with critical point drying was shown to be effectively superior than chemical drying (Fig. 5) to avoid technical artifacts, in concordance with the literature [30–32]. The samples dehydrated by ethanol, we can observe less cellular flattening and adhesion when compared with the ones dehydrated with critical point, as can be seen comparing Fig. 5C, D, for example, which indicates that the latter is more efficient in preserving cellular structure. This can be observed in Fig. 3, comparing Fig. 3 E, F, for example, it can be observed that cells dehydrated by ethanol present a slightly more polygonal morphology and are more scattered, while in the ones dehydrated by critical point present more round and clustered cells, which indicates better preservation of cellular morphology and interaction with the biomaterial.

The results shown in Figs. 4A, D, and 5B, E were used to evaluate cell perimeter and area (Table 1). It was observed that cell area was 45,45% larger in the preparations submitted to critical point drying. This result corroborates with the morphological description for the figures, showing a better preserved morphology with this protocol.

4 Conclusion

Analyzing the results we concluded that the most impacting factor for the good preservation of both the biomaterial and the cells was the dehydration protocol. The use of critical point drying for both types of PLA samples, dense and porous, resulted in fewer biomaterial failures and better preservation of cell morphology. As for the use of post-fixative osmium tetroxide, there was no significant improvement in the morphological preservation of the cells. There were also no alterations in the PLA samples used for cell cultures. Therefore, it can be proposed that there is no need for post-fixation PLA samples with cultured cells, thus

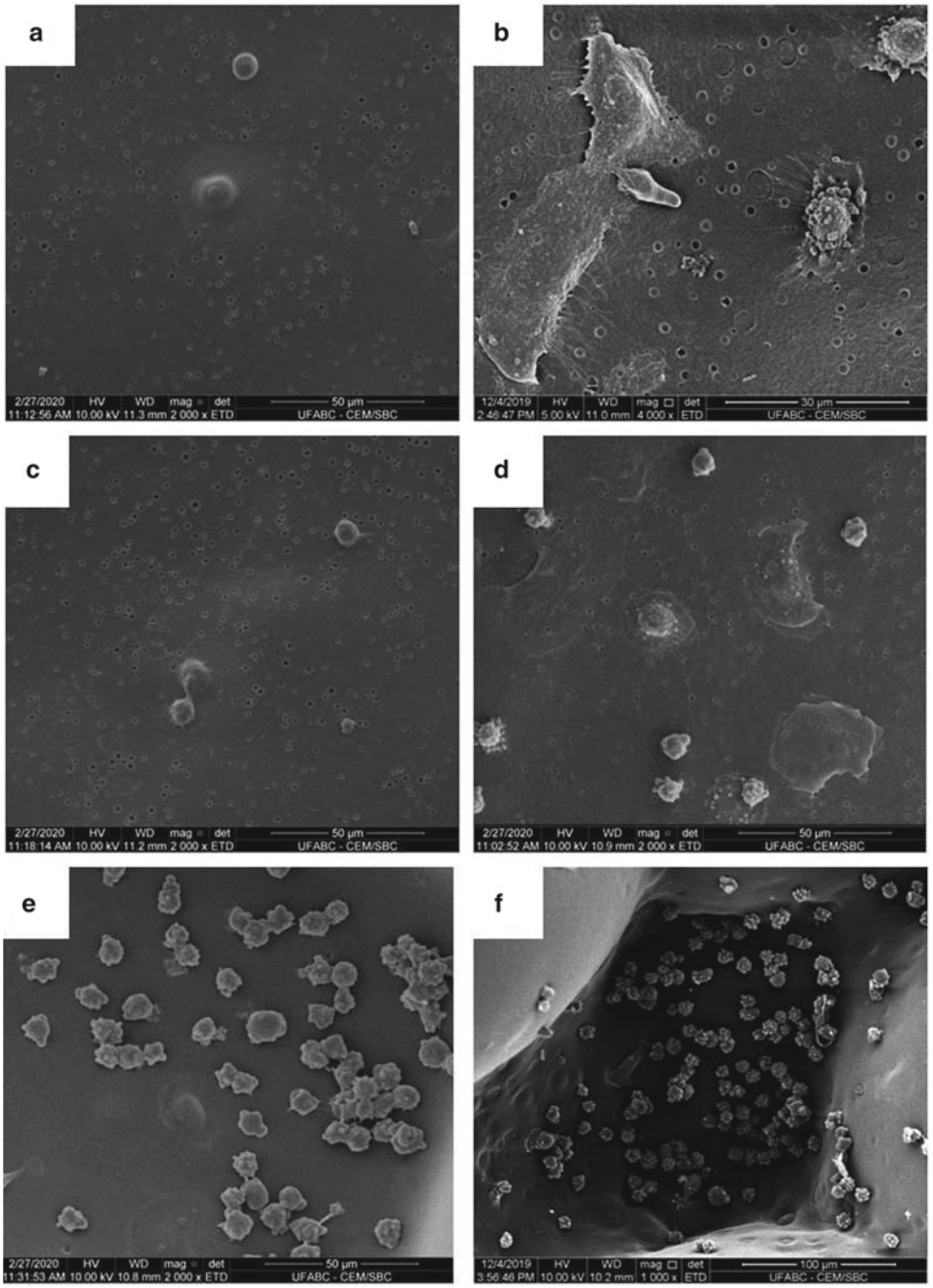

Fig. 5 Vero cells cultured on PLA biomaterials after 2 h, fixed with glutaraldehyde. **A**–**D**: dense samples; **E**, **F**: porous samples; **A**, **C**, **E**: dehydrated in ethanol; **B**, **D**, **F**: dehydrated at a critical point

Table 1 Image J measures on Figs. 4 and 5. Perimeter µm; area µm^2. SD: standard-deviation; E: ethanol; CP: critical point

Figure	N	Perimeter	Area	Mean perimeter	Mean area
4A-E	9	66,554	287,581	E: 53,808	E: 194,157
4D-CP	9	76,835	487,370	CP: 71,530	CP: 355,952
5E-E	5	41,061	100,732	Difference	Difference
5B-CP	5	66,224	224,533	24,78%	45,45%
SD		15,224			

reducing costs and possible risks from handling them, but critical point drying is recommended.

Acknowledgements We thank the UFABC for the research development structure and the Multiuser Centers (CEM-UAFBC), for the samples preparation and SEM analysis.

Conflict of Interest

The authors declare that they have no conflict of interest.

References

1. Williams DF (1987) Definition in biomaterials, consensus conference ESB
2. Langer R, Vacanti JP (1993) Tissue engineering. Science 260:920–926
3. Barbanti SH, Zavalia CAC (2005) Polímeros bioreabsorvíveis na engenharia de tecidos. Polímeros: Ciência e Tecnologia 15:13–21
4. Oliveira CS, Nascimento M, Junior EA et al (2010) Avanços e aplicações da bioengenharia tecidual. Ciências Médicas e Biológicas 9:28–36
5. Jahno, VD, Ligabue R, Einloft, S, Ribeiro, GBM et al (2006) Síntese e caracterização do poli(ácido l-láctico) e sua avaliação em culturas de osteoblastos humanos. Cong Bras Eng Ciênc Mat 7837–7847
6. Vert M, Li SM, Spenlehauer G, Guerin P (1992) Bioresorbability and biocompatibility of aliphatic polyesters. J Mater Sci Mater Med 3:432–446
7. Danisovic L, Varga I, Zamborsky R, Böhmer D (2012) The tissue engineering of articular cartilage: cells, scaffolds and stimulating factors. Exp Bio Med 237:10–17
8. Jafari M, Paknejad Z, Rad MR et al (2017) Polymeric scaffolds in tissue engineering: a literature review. J Biomed Mater Res B Appl Biomater 105:431–459
9. International Standarts Organization. ISO 10993-5 (2009b) Biological evaluation of medical devices—Part 5: tests for in vitro cytotoxicity, p 34
10. Dewez JL, Lhoest JB, Detrait E et al (1998) Adhesion of mammalian cells to polymer surfaces: from physical chemistry of surfaces to selective adhesion on defined patterns. Biomaterials 19:1441–1445
11. Wang X, Lou T, Zhao W et al (2016) The effect of fiber size and pore size on cell proliferation and infiltration in PLA scaffolds on bone tissue engineering. J Biomater Appl 30:1545–1551
12. Zeltinger J, Sherwood JK, Graham DA et al (2004) Effect of pore size and void fraction on cellular adhesion, proliferation, and matrix deposition. Tissue Eng 7:557–572
13. Lombello CB, Malmonge SM, Wada ML (2000) Morphology of fibroblastic cells cultured on poly (HEMA-co-AA) substrates. Cytobios 101:115–122
14. Santos Jr AR, Wada MLF (2007) Polímeros Biorreabsorvíveis como Substrato para Cultura de Células e Engenharia Tecidual. Polímeros: Ciênc Tecnol 17:308–317
15. Ammerman NC, Beier-Sexton M, Aad AF (2008) Growth and maintenance of Vero cell lines. Curr Prot Microb 11:4E:A.4E.1–A.4E.7
16. Nascimento MHM, Ferreira M, Malmonge SM, Lombello CB (2017) Evaluation of cell interaction with polymeric biomaterials based on hyaluronic acid and chitosan. J Mater Sci Mater Med 28 (5)
17. Zhu WJ (2018) Preparation and observation methods can produce misleading artefacts in human sperm ultrastructural morphology. Andrologia e13043. https://doi.org/10.1111/and.13043
18. Impe J, Smet C, Tiwari B et al (2018) State of the art of nonthermal and thermal processing for inactivation of micro-organisms. J Appl Microbiol 125:16–35
19. Nascimento, MHM, Lombello CB. (2016) Hidrogéis a base de ácido hialurônico e quitosana para engenharia de tecido cartilaginoso. Polímeros: Ciênc Tecnol 26:360–370
20. Ferraraz DC, Tatsui NH, Rodrigues LR, Lombello CB (2019) Platelet-rich plasma as supplement and scaffold for the culture of Vero cell line. Res Biomed Eng 35:1–9
21. Zhang W, Soffe R, Nahavandi S, Shukla R, Khoshmanesh K (2014) High resolution scanning electron microscopy of cells using dielectrophoresis. PLoS ONE 9(8):
22. Amaducci MRL (2007) Efeitos do campo eletromagnético em células e bactérias. Dissertação(mestrado), UNICAMP, Campinas, SP, p. 102
23. Wisse E, Braet F, Duimel H, Vreuls C et al (2010) Fixation methods for electron microscopy of human and other liver. World J Gastroenterol 16:2851–2866
24. Barth OM, Silva MAN, Barreto-Vieira DF (2016) Low impact to fixed cell processing aiming transmission electron microscopy. Mem Inst Oswaldo Cruz 111:411–413
25. Carr J, Anderson R, Favero M (1996) Comparison of chemical dehydration and critical point drying for the stabilization and visualization of aging biofilm present on interior surfaces of PVC distribution pipe. J App Bacteriol 80:225–232
26. Barbieri DM, Fernandes T, Capelo O et al (2016) Método rápido, de baixo custo e reprodutível para secagem de biofilme bacteriano analisado em MEV. II Cong Paran Microbiol, Londrina
27. Glauert AM (1975) Practical methods in electron microscopy. Vol III: fixation, dehydration and embedding of biological specimens. North-Holland Publishing Company, pp 1–207
28. Lombello CB. (2018) Capítulo 6: Microscopia eletrônica para biologia celular. In: Santos Jr AR, Lombello CB (eds) Biologia celular: uma abordagem prática do ensino. EduFABC
29. Heckman C, Kanagasundaram S, Cayer M, Paige J (2007) Preparation of cultured cells for scanning electron microscope. Center for Microscopy and Microanalysis. Protocol Exchange. https://doi.org/10.1038/nprot.2007.504
30. Bray D (2000) Critical point drying of biological specimens for scanning electron microscopy. In: Williams JR, Clifford AA (eds) Supercritical fluid methods and protocols. methods in biotechnology™, vol 13. Humana Press
31. Thevenot P, Tang L, HU W (2008) Curr Top Med Chem 8:270–280
32. Muscariello L, Rosso F, Marino G et al (2005) A critical overview of ESEM applications in the biological field. J Cell Physiol 205:328–334

Development of a Gelatin-Based Hydrogel to be Used as a Fibrous Scaffold in Myocardial Tissue Engineering

C. Parente and S. M. Malmonge

Abstract

Myocardial Tissue Engineering (MTE) is a set of techniques that uses biomaterials to reproduce the native extracellular matrix (ECM) of tissues, in this case, the myocardium. The present contribution relates the results of the study about the electrospinning of gelatin, a naturally occurring biopolymer, in view to obtain nanofibrous scaffolds for use in MTE. Gelatin solutions were prepared using gelatin type B and 2,2,2-Trifluoroethanol (TFE) as a solvent. The fibrous were created through electrospinning technique. The voltage, distance and concentration of the solutions were varied to improve the quality of the fibers. The crosslinking method was validated with the use of films, prepared by solvent evaporation technique, with 1-Ethyl-3-(3-dimethylaminopropyl) carbodiimide (EDC). The morphology of the fibers was investigated by scanning electron microscope (SEM) and the efficiency of the crosslinking processes were evaluated by swelling test and differential scanning calorimetry (DSC). The best fibers were formed (without the presence of drops or beads) by electrospinning a gelatin solution in the following parameters (10% (w/v), 10 kV and 20 cm) or (5% (w/v), 12 kV and 12 cm). The crosslinking process was done using EDC in the films of gelatin. It was possible to observe that different degrees of crosslinking guarantee different properties, such as water swelling as well as different thermal and mechanical properties.

Keywords

Myocardial tissue engineering • Gelatin • Hydrogel • Electrospinning • Scaffold

1 Introduction

Gelatin is a biomaterial derived from collagen, that can be used as a hydrogel scaffold, in nanofiber form, in Myocardial Tissue Engineering (MTE), because its characteristics mimic the biochemical and ultrastructural properties of the native extracellular matrix (ECM) of tissues, which is known to influence cell behavior and growth. Ischemic heart disease and stroke are the biggest numbers of deaths worldwide [1]. It is known that the heart does not have the ability to regenerate completely. Studies have shown that only 1% of cardiac cells are renewed per year, which is not enough for the heart to recover after a major ischemic trauma, such as a heart attack [2]. Cardiopathies usually leads to heart failure and the most common treatments available include revascularization surgery and heart transplantation, however there are restrictions, such as difficulty in finding compatible donors and contraindications, which are frequent in patients over the age of 65 years [3].

Alternative treatments include the use of circulatory assist devices and alternative procedures that regenerate the functions, or at least part of them, of the myocardium. The use of stem cells has brought to MTE a new goal to work with. Studies that analyze the effect of stem cells injected directly into the myocardium have been shown to be positive, even though it has become clear that most of these cells die due to the lack of a favorable environment and mechanical and electrical stimuli for their growth, thus not producing the effect of inducing the necessary revascularization and myogenesis, which would eventually promote complete muscle regeneration and its physical and morphological properties [4]. For the MTE to be efficient, the characteristics of the biomaterials used as scaffold must be considered. They must resemble those found in cardiac tissue, helping or staying neutral for regeneration to happen efficiently.

The mechanical properties of myocardial, stiffness and contraction, are responsible for the primary function of the heart, to pump blood through the circulatory system. When

C. Parente (✉) · S. M. Malmonge
Engenharia Biomédica, Universidade Federal do ABC, São Bernardo do Campo, Brazil

T. F. Bastos-Filho et al. (eds.), *XXVII Brazilian Congress on Biomedical Engineering*, IFMBE Proceedings 83, https://doi.org/10.1007/978-3-030-70601-2_25

the myocardium suffers an ischemic episode and consequently loss of muscle, there may be both a reduction in the capacity for contraction, which is associated with a decrease in cardiac performance, causing a reduced ejection fraction, and an increase in muscle stiffness, causing inadequate filling of the heart chambers [5]. Mechanical tests show that stiffness in the left ventricle ranges from 10 to 20 kPa during diastole and 200–500 kPa during systole. In addition, stiffness in the range of native cardiac tissue (10–20 kPa) tends to induce cardiomyocyte characteristics more similar to native cardiomyocytes [6].

Gelatin is a protein that has been completely denatured, breaking the triple helix of the type I collagen molecule into a single stripe. Gelatin has similar benefits to collagen in terms of biocompatibility and biodegradability and can be used to form nanofibrous scaffold [7]. Electrospinning is a technique used to form nanofibers which uses a high voltage power supply, a grounded metal collector and a syringe attached to a syringe pump. The biomaterial solution is loaded into the syringe and extruded in the form of nanofibers in the collector through the cone of Taylor. In case of gelatin, these nanofibers need to be crosslinked to avoid dissolution and to improve its mechanical properties [8].

This paper relates the results obtained in a study that aimed the development of a gelatin nanofibrous scaffold, using the electrospinning technique, that could be crosslinked, for a future use in MTE with the goal to allow cell proliferation and myocardial regeneration. The hypothesis being tested is that is possible to produce gelatin fibers by electrospinning and that crosslinking process would be able to increase the mechanical properties to approach the same characteristics of the myocardium. The gelatin was the material selected to prepare films through the solvent evaporation technique that were used on the mechanical tests furthermore. The fibers were Electrospun using Trifluoroethanol (TFE) as a solvent and the parameters (concentration, voltage and distance) were varied to improve the quality of the fibers that were then crosslinked with 1-Ethyl-3-(3-dimethylaminopropyl) carbodiimide (EDC). The morphology of the fibers was investigated by scanning electron microscope (SEM) and the efficiency of the crosslinking processes were evaluated by water swelling test and differential scanning calorimetry (DSC).

2 Materials and Methods

The materials used were gelatin type B (*Gelita do Brasil LTDA, Cotia, SP, Brazil)*, Ethanol (etOH) (*Synth, Labsynth Produtos para Laboratórios, LTDA, Diadema, SP, Brazil*), 1-Ethyl-3-(3-dimethylaminopropyl) carbodiimide (EDC) (*Sigma Aldrich, St. Louis, MO, USA*) and 2,2,2-Trifluoroethanol (TFE) (*Sigma Aldrich, St. Louis, MO, USA*).

2.1 Gelatin Films

Gelatin films were used to determine the crosslinking protocol. The gelatin films were prepared using the technique of solvent evaporation. Using TFE as a solvent, the solution were agitated for 30 min at room temperature, to allow complete dissolution of the raw material, in two different concentrations, 5 and 10% and let it to evaporate in petri dishes for 48 h [9].

2.2 Nanofibers Through Electrospinning

The technique used to produce nanofibers was the electrospinning, which used a high voltage power supply (Inergiae Conversores Estaticos LTDA, APIS 0330A Benchtop 30 kV–10 mA) attached to a syringe pump (World Precision Instruments (WPI) model AL-1000) with a 10 ml glass syringe and an aluminum static collector. The flow rate was kept constantly, 1 ml/h. The process parameters (potential field (kV) and needle to collector distance (cm)) were varied to optimize the stability of the electrostatic jet during electrospinning, all according to previous studies [10, 11]. The solutions prepared, in two different concentrations, 5 and 10%, were loaded into the syringe and then collected on the static metal collector.

2.3 Crosslinking

The films and nanofibers were crosslinked by soaking them 24 h in a solution 0.2 M of EDC in etOH, using enough solution to promote the crosslink in different molar ratio between active groups of gelatin and EDC (1:1; 1:0.5; 1:0.25 and 1:0.1). The excess of the crosslink agent was washed off by washing the samples with deionized water [11].

2.4 Characterization

Initially, samples of gelatin films were submitted to characterization techniques aiming to conclude about the efficiency of crosslinking gelatin hydrogel by immersion in EDC ethanolic solution. In this step, the films were evaluated for water swelling, thermal and mechanical behavior.

The samples of film were evaluated about its ability to absorb liquid (swelling) by emerging them in distilled water for 30 min and weighed every 5 min. Differential Scanning Calorimetry (DSC) was performed on a Q series, TA Instruments, applying an inert atmosphere, a flow rate of 50 m/min of N_2 with samples in aluminum crucible with lid (using one empty as reference). The samples were first stabilized at 10 °C, warmed up to 200 °C and then cooled until

−10 °C, warmed a second time up to 200 °C always in a speed of 10 °C/min. Additionally the films were mechanically evaluated according to the stress × strain test under tension, using a Tytron 250, MTS with a load cell of 250 N, a speed of strain of 1 mm/min and space between the gripers of 20 mm. From the stress × strain curves, it was possible to determine the module of elasticity (E), yield strength (σ_r) and strain at break (ε_r). All the analysis were performed in triplicate.

Finally, morphologicale valuation of electrospun gelatin fibers was performed in view to conclude about the fiber formation. The morphology was evaluated on a Quanta 250, FEI scanning electron microscope (SEM). Electrospun gelatin samples were sputtered with gold in a LEICA, model ACE 200 sputtering and fixed with the help of a carbon conductive tape. The samples were observed to check for the presence or absence of fibers and defects.

3 Results

Gelatin is like a polyelectrolytic polymer that has many functional groups. Its carboxyl and amine functional groups can be ionized by acidic or hydrolyzed agents to carry negative charges. In addition, the strong hydrogen bond that constitutes the behavior of gelatin results in a network of three-dimensional macromolecules that hinder the mobility of the polymer molecule chains. Because gelatin is a highly polar biopolymer, its solubilization is only possible in high polarity solvents such as fluoride alcohol TFE [10].

The films produced through the solvent evaporation technique were transparent, manageable, with no visible imperfections, probably signs of an amorphous structure as can be seen in Fig. 1.

Electrospinning of the TFE based gelatin solution produced fibers that can vary due to the change of parameters, according to Table 1.

Changing concentration, which is directly related to the viscosity, the more viscous the solution, the higher is the diameter of the jet leaving the needle, as well as the diameter of the fibers. The voltage applied to the needle and the distance between the collector determine the intensity of the formed electric field, which drives the jet in the Taylor cone. A higher electric field will conduct more fluid in the jet and cause greater electrostatic force in the nanofibers. If the electric field is too low, the jet is pushed only intermittently by the syringe. When the electric field is very high, the polymer solution can be pushed by the syringe in a disordered way, not forming fibers in the collector [12, 13].

With the solution 10% concentrated, 12 kV of voltage applied and 12 cm of distance, the fibers formed were randomly with defects related to the deposition of drops (which appears as dark marks on the SEM images—Fig. 2a). On the second condition, with the same concentration but 10 kV of voltage and the same distance, the fibers formed presented significant more defects than the first experiment, with the

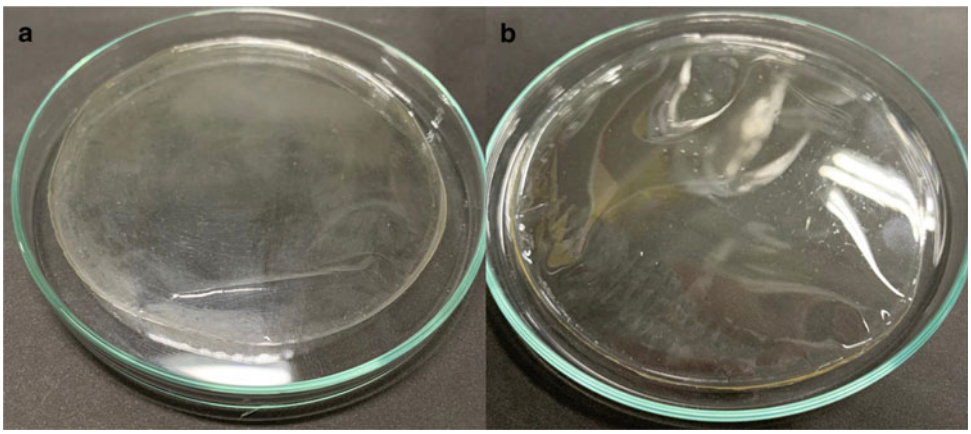

Fig. 1 Photos of the gelatin films produced through solvent evaporation technique. **a** Film of gelatin with the solution 5% w/v. **b** Film of gelatin with the solution 10% w/v

Table 1 Parameters varied during electrospinning: concentration (w/v), voltage (kV) and distance (cm)

Concentration (% w/v)	Voltage (kV)	Distance (cm)
5	15 12 10	12 12 12
10	12 10 10	12 12 20

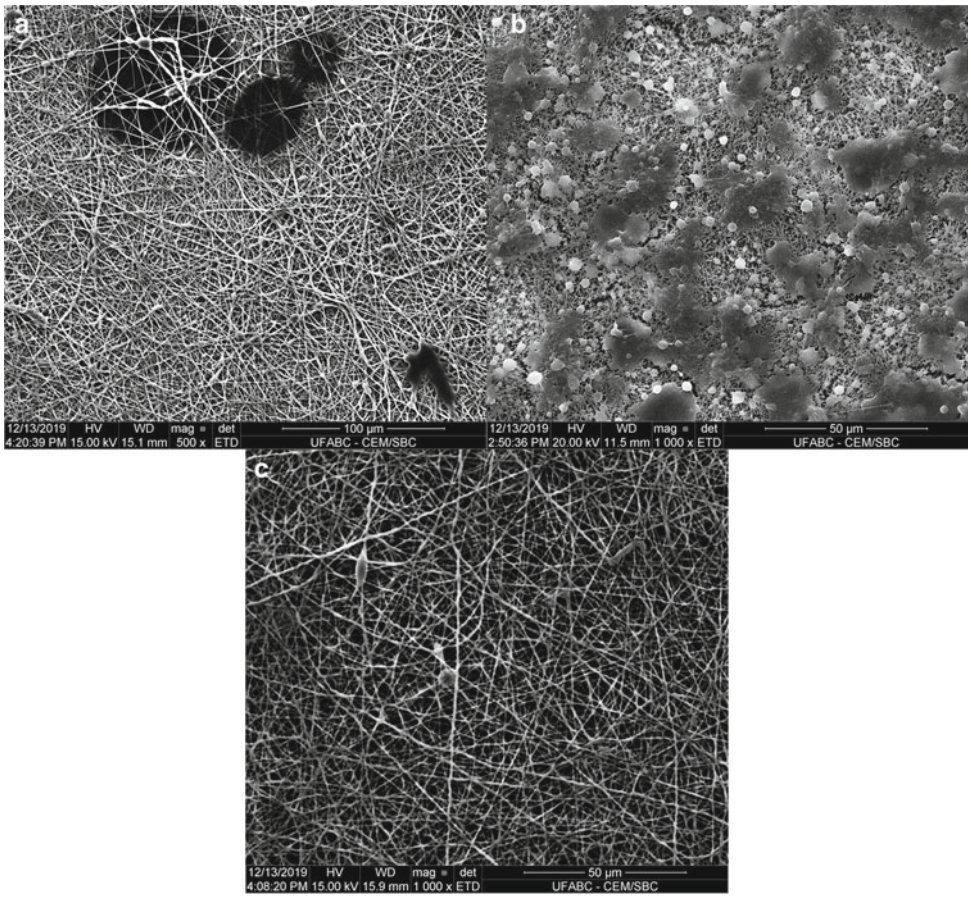

Fig. 2 Scanning electron microscopy micrographs of Electrospun nanofibers of the 10% solution of TFE gelatin based. **a** 12 kV, 12 cm, **b** 10 kV, 12 cm, **c** 10 kV, 20 cm

presence of spherical beads (Fig. 2b). The third condition differentiate from the second one by the distance, 20 cm, it is possible to see fibers, with spherical beads, as in the second experiment and without the drops of the first test (Fig. 2c).

With the solution 5% concentrated all the three conditions were able to form fibers (Fig. 3), although only the second test, 12 kV and 12 cm of distance (Fig. 3b) presented fibers without the abundance of spherical beads. The presence of fibers without beads it is important for the study because one of the goals of the Myocardial Tissue Engineering is the design and fabrication of a tissue-like material to mimic extracellular matrix (ECM) of the tissue that is to be engineered, thus, the scaffold needs to be fibrous to allow cell population and proliferation [14].

The test of swelling, responsible to show the ability of the material to absorb water, shows that the crosslink ratio changes its properties. The gelatin film when immersed in an alcoholic EDC solution, must permeate the gelatin chains to find and react with the −COOH groups. According to Fraga, 1985, the crosslinking reaction occurs preferably with the −COOH groups present in the segments accessible to EDC, which depends on the ability of diffusion of the crosslinker in the hydrogel. Crosslinking probably occurs preferentially in the −COOH groups of the flexible segments of gelatin, since during the formation of the film, the rigid segments acquire helical conformation [15]. It was possible to observe that as the crosslinking ratio increases, the ability to absorb water decreases, the non-crosslinked sample absorbed 90% of its weight in water, as the crosslinked ones were in the range of 70–80%.

Considering the application of the scaffold to be used in myocardial tissue engineering, the mechanical evaluation of the biomaterial is crucial, since the myocardium plays an important mechanical function that determines the cellular function of cardiomyocytes. Some of the properties most used is the left ventricular stiffness, which ranges from 10 to 20 kPa during diastole and 200–500 kPa during systole [16]. In addition, according to studies, the tensile strength of the scaffold must be taken into account since the pressure in the left ventricle, for example, can vary from 3 to 140 mmHg in each heartbeat [17].

A typical graphic and the results of the stress × strain test of the gelatin films under tension can be seen in Fig. 4 and Table 2. It is possible to observe that the mechanical behavior of the graphic is slightly nonlinear, also called as J-shaped, a typical behavior of a biological tissue, whereas synthetic elastomers tend to present linear patterns. The structural mechanism behind these two different elastic

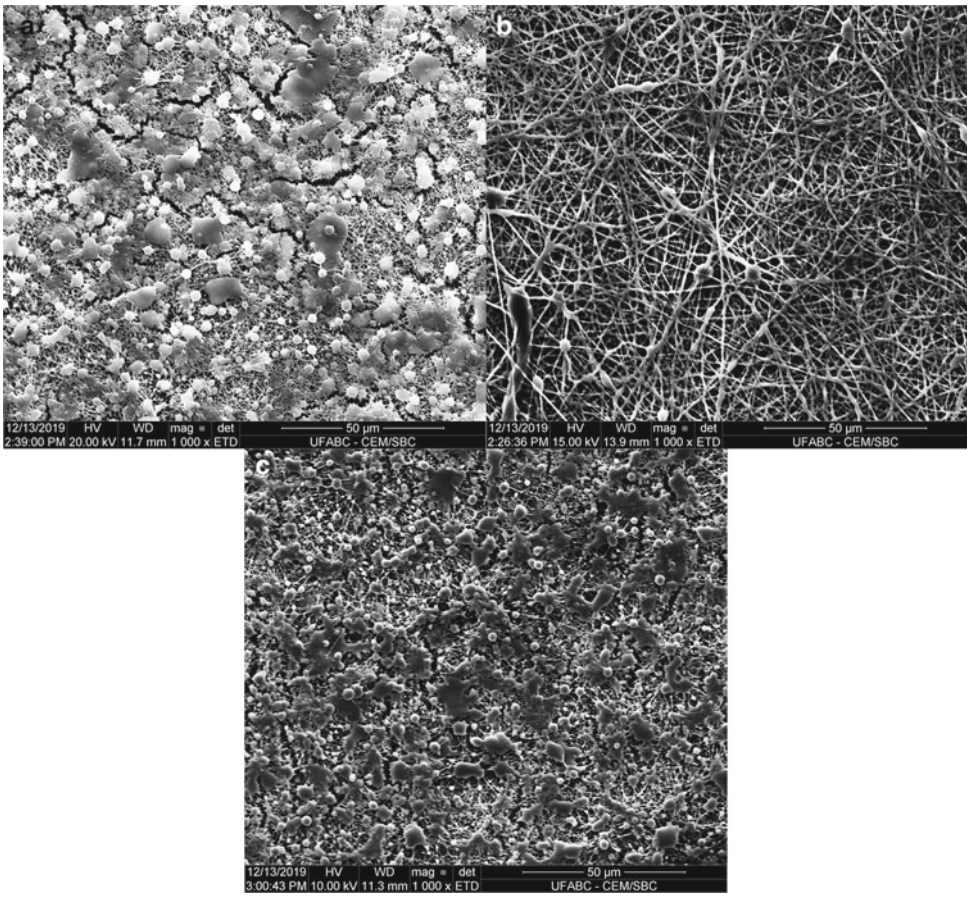

Fig. 3 Scanning electron microscopy micrographs of Electrospun nanofibers of the 5% solution of TFE gelatin based. **a** 15 kV, 12 cm, **b** 12 kV, 12 cm, **c** 10 kV, 12 cm

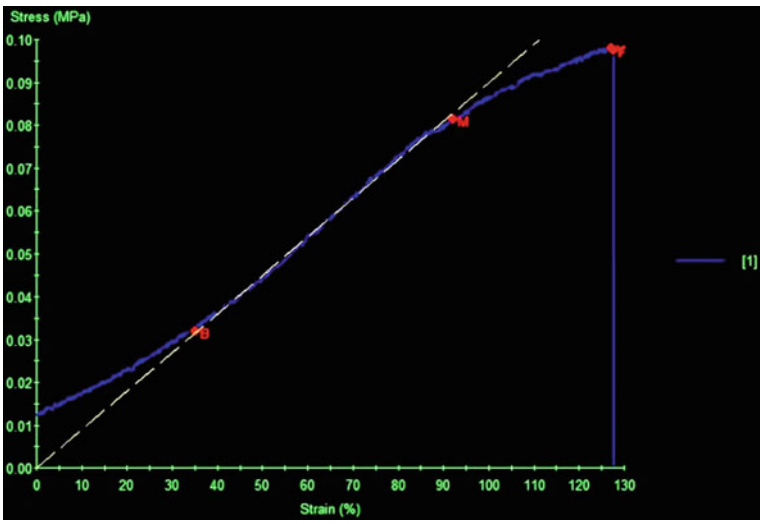

Fig. 4 Typical graphic of stress × strain test. Graphic related to one sample of a gelatin film produced by the solvent evaporation technique, 5% w/v

Table 2 Results of stress × strain test with gelatin films

Crosslink ratio	Module of elasticity (MPa)	Tensile strength (MPa)	Deformation at rupture (%)
1:0.25	0.027 ± 0.012	0.025 ± 0.070	80.25 ± 6.18
1:0.5	0.051 ± 0.021	0.040 ± 0.012	77.36 ± 12.49
1:1	0.126 ± 0.042	0.100 ± 0.083	11.28 ± 33.35

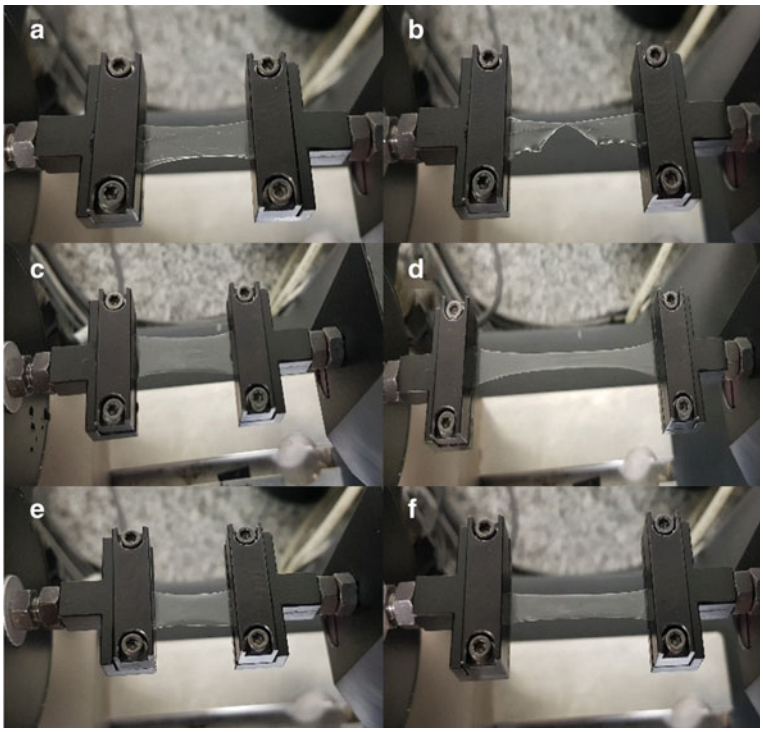

Fig. 5 Samples of gelatin films during stress × strain test at the beginning and at the end of the test. Crosslinking ratio 1:0.25 (**A** and **B**), 1:0.5 (**C** and **D**) and 1:1 (**E** and **F**)

behavior is that the polymer chains are randomly tangled in a synthetic elastomer, whereas protein nanofibres are aligned in the muscular tissue [14].

During the tests of this study, the samples of the non-crosslinked films could not be carried on due to lack of resistance for the sample to remain on the gripper. The results show that as the crosslinking ratio of the films is changed, it is observed that the increase in the molar ratio between reactive groups and EDC, promotes an increase in the elastic modulus, an increase in the tensile strength and a decrease in the deformation at rupture. The samples of the films crosslinked in a 1:025 showed approximately 80% of deformation whereas the films crosslinked in a ratio 1:1 showed approximately 11% of deformation only. The deformation of the films can be better observed on Fig. 5.

4 Discussion

Such results show that the hydrogel becomes more rigid and more resistant to tension due to the increase in the number of crosslinking links, which means, the higher the crosslinking density, the less flexibility and movement capacity of the biopolymer chains that are anchored by the crosslinks.

The mechanical tensile strength values are the same order of magnitude or only slightly lower than the values to which the cardiac muscle is subjected. The mechanical behavior shown by the films can be explained assuming that gelatin follows the model described by Fraga and Willians, that says the chemical structure of gelatin is formed by a composite block copolymer by amino acid sequence − (Glycine-AB) ×− (Glycine-Proline-Hydroxyproline) y− and that the blocks containing proline and hydroxyproline have rotation restrictions due to peptide bonds that promote rigidity to the structure [15].

The results obtained by differential scanning calorimetry (DSC) by using the thermograms referring the first heating of each film under study showed the occurrence of a first endothermic event around 90–100 °C. Some authors have attributed this endothermic peak to the destruction of the crystalline structure related to the triple helix of collagen and, in the case of gelatin, the destruction of the crystalline arrangement, or ordered helical structures that can occur due to the strong interactions between groups present in the chain. Some authors call this thermal event the temperature of denaturation, since it destroys the typical morphology of collagen chains [18].

On the thermogram resulting from the second heating, the presence of endothermic peaks was no longer observed. After the "melting" of the gelatin, which occurred during the first heating, the material was cooled relatively quickly (10 °C/min) and, therefore, the crystalline rearrangement did not occur (that is, the reconstitution of helical gelatin structures and their aggregation did not occur). The DSC analysis showed that the gelatin films resulting from the preparation and cross-linking protocols used in this study resulted in

materials with a semi-crystalline structure behavior, however, after melting and cooling at the employed speed, all the films behaved as structural material totally amorphous.

5 Conclusions

The present contribution reported the results about crosslinking process of gelatin films using 1-Ethyl-3-(3-dimethylaminopropyl) carbodiimide (EDC). It was concluded that the different degrees of crosslinking guarantee different properties, such as water absorption capacity (swelling) as well as different thermal and mechanical properties.

The mainly result showed in this study was the nanofibers created through electrospinning using a gelatin solution dissolved in 2,2,2-trifluoroethanol (TFE) with 5 and 10% of concentration of solute. It was concluded that the concentration as long with different parameters changed the characteristics of the fibers. The best fibers were formed (without the presence of drops or beads) with the conditions of 10%, 10 kV and 20 cm and concentration of 5%, 12 kV and 12 cm.

Acknowledgements The authors acknowledge recognition of "Central Experimental Multiusuário" from The Universidade Federal do ABC (CEM-UFABC) and the technicians of the biomaterial's laboratory, by the infra structure and technical support. The financial support received from "Conselho Nacional de Desenvolvimento Científico e Tecnológico—CNPQ—processo 402984/2016-1" and CAPES to the Post-Graduation program of Biomedical Engineering of UFABC.

Conflict of Interest The authors have declared that there is no conflict of inter-est related to this manuscript.

References

1. World Health Statistics 2017: monitoring health for the SDGs. At https://www.who.int/news-room/fact-sheets/detail/the-top-10-causes-of-death
2. Bergmann O, Bhardwaj R et al (2009) Evidence for cardiomyocyte renewal in humans. Science. https://doi.org/10.1126/science.1164680
3. Ayub-Ferreira SM, Souza Neto JD et al (2016) Diretriz de Assistência Circulatória Mecânica da Sociedade Brasileira de Cardiologia. Arq Bras Cardiol 107(2Suppl.2):1–33
4. Passier R, Mummery C et al (2008) Stem-cell-based therapy and lessons from the heart. Nature 453:322–329. https://doi.org/10.1038/nature07040
5. Stienen G (2015) Pathomechanisms in heart failure: the contractile connection. J Muscle Res Cell Motil 36:47–60. PubMed: 25376563
6. Chatterjee K, Massie B (2007) Systolic and diastolic heart failure: differences and similarities. J Card Fail 13:569–576. PubMed: 17826648
7. Stainsby G (2011) Gelatin gels. In: Advances in meat research, collagen as a food, vol 4, pp 209–222
8. Mei L, Wang Y et al (2016) Facile electrospinning of an efficient drug delivery system. Exp Opin Drug Deliv 13:741–753
9. Zheng-Ming H et al (2004) Electrospinning and mechanical characterization of gelatin nanofibers. Polymer 45(15):5361–5368
10. Dong B et al (2009) Electrospinning of collagen nanofiber scaffolds from Benign solvents. Macromolecular Rapid Commun 30(7):539–542
11. Barnes C, Pemble IV et al (2007) Cross-linking electrospun type II collagen tissue engineering scaffolds with carbodiimide in ethanol, vol 13(7). Tissue Engineering, Mary Ann Liebert Inc
12. Kong L, Ziegler GR (2013) Quantitative relationship between electrospinning parameters and starch fiber diameter. Carbohydr Polym
13. Sener A, Altay A et al (2011) Effect of voltage on morphology of electrospun nanofibers. In: 7th international conference on electrical engineering
14. Chen Q, Bocaccini A (2014) Myocardial tissue engineering. Woodhead Publishing Limited
15. Fraga A, Willians R (1985) Thermal properties of gelatin films. Polymer 26(1):113–118
16. Chen Q, Bismarck A et al (2008) Characterisation of a soft elastomer poly(glycerol sebacate) designed to match the mechanical properties of myocardial tissue. Biomaterials 29:47–57. PubMed: 17915309
17. Tyberg J, Taichman G et al (1986) The relationship between pericardial pressure and right atrial pressure: an intraoperative study. Circulation 73:428–432. PubMed: 3948353
18. Shehap A, Mahmoud H et al (2015) Preparation and thermal properties of Gelatin/TGS composite films. Middle East J Appl Sci 5(1):157–170

Experimental and Clinical Performance of Long-Term Cannulas for Mechanical Circulatory Assistance

H. T. T. Oyama, S. Bacht, M. Mazzetto, L. F. Caneo, M. B. Jatene, F. B. Jatene, and I. A. Cestari

Abstract

Mechanical circulatory assistance with left ventricle assist devices (VADs) can be used for hemodynamic stabilization in patients waiting for heart transplantation. In this application the VAD is connected to the heart with the use of special cannulas. The purpose of this work is to present in the performance of long-term cannulas designed for pediatric patients undergoing circulatory assistance. Pressure drop of cannulas with different sizes were tested using a mock loop of the pediatric arterial circulation. Considering a flow range of 0.52–1.25 L/min the pressure drops obtained was 9.43 to 22.1 mm Hg, respectively. Good clinical results were obtained with cannulas associated with a centrifugal pump or DAV for a period of approximately 4–64 days, with no thrombus formation on the tips of the cannulas or bleeding. The implantation of cannulas proved to be technically feasible and their removal was easy to perform in cases of ventricular recovery or transition to a long-term assistance device.

Keywords

Cannula • Biocompatible • Mechanical assistance • Centrifugal pump • VAD

1 Introduction

Heart transplantation is the therapy of choice for the treatment of terminal heart diseases. However, the lack of availability of donor organs limits this procedure and new techniques have been developed and improved to extend the life expectancy of patients waiting for heart transplantation [1].

The use of mechanical circulatory assist device is one alternative treatment for patients who develop cardiogenic shock refractory to drug therapy in order to convert a terminal condition into a stable clinical condition that allows a heart transplant to be performed, thus functioning as a bridge for transplantation. Mechanical assistance to the heart can be provided by pulsatile or continuous flow devices and the most used for this purpose are the intra-aortic balloon, centrifugal pumps and ventricle assist devices [2–4].

Our group is developing a pediatric pulsatile ventricular assist device (VAD) actuated by a pneumatic system device can be used to assist the left, right or both ventricles [5] and it is connected to the heart by special cannulas. Hemodynamic stabilization in patients who require cardiopulmonary support can also be performed with the use of extracorporeal centrifugal pumps which provide continuous flow [6]. The use of this type of pump is indicated when there is the expectation of heart recovery.

This work aims to present the development of biocompatible cannulas for long-term implants of centrifugal pumps or VADs used as circulatory support in pediatric patients as a bridge to decision or to heart transplantation.

2 Materials and Methods

2.1 The Cannulas

Cannulas are usually made by flexible tubes of different dimensions and hardness, straight or curved, open at both

H. T. T. Oyama (✉) · S. Bacht · M. Mazzetto · I. A. Cestari
Lab. de Bioengenharia, Instituto do Coração Hosp. das Clínicas, Fac. Medicina Univ, São Paulo, SP, Brazil
e-mail: helena.oyama@incor.usp.br

L. F. Caneo · M. B. Jatene · F. B. Jatene
Div. Cirurgia Cardiovascular, Instituto do Coração Hosp. das Clínicas, Fac. Medicina Univ, São Paulo, SP, Brazil

T. F. Bastos-Filho et al. (eds.), *XXVII Brazilian Congress on Biomedical Engineering*, IFMBE Proceedings 83, https://doi.org/10.1007/978-3-030-70601-2_26

ends and intended to be introduced into the body. Cannulas are used to connect an assist device to the heart. Different models of cannulas are available to suit specific surgical needs. For implants lasting longer than 30 days, cannulas must be fabricated with medical grade biocompatible materials, which can be used as permanent implants. The cannulas describe in this work were produced using silicone elastomer, ringed PTFE vascular grafts and inorganic patch of Polyethylene Glycol Terephthalate (Dacron® fabric) and whenever metals parts were necessary, titanium was used.

Cannulas of various configurations were developed considering VAD implantation in patients of different sizes. Molds in 316L stainless steel were developed for modeling and vulcanizing the silicone. Material processing was carried out under class 100 laminar flow) inside an ISO 8 classified room according to the NBR ISO 14644 standard.

When used to connect to the VAD the drainage cannula is inserted into the apex of the left ventricle to fill the pump. This cannula is termed apical or ventricular cannula has a chamfered titanium tip and is fixed through a direct suture with the ventricle, through a Dacron® fabric collar. The blood returns to the patient through an arterial cannula sutured in the ascending aorta or pulmonary artery, depending on whether assistance is performed in the left or right ventricle. The arterial cannula is manufactured with medical grade silicone a ringed PTFE vascular graft for suturing it directly to the aorta. Different cannulation techniques are used for unit or biventricular assistance and different cannulas are necessary for each application. Accordingly, there can be application with respect to the shape, length, and diameter of the cannulas.

2.2 "In Vitro" Testing

The experimental arrangement used the cannulas is shown in Fig. 1. Cannulas were connected to the inflow and outflow ports of a pediatric VAD mimicking the left ventricle on a hydraulic simulator of the pediatric circulation. The simulator was filled with a blood analog fluid (glycerin solution diluted in 0.9% NaCl saline solution) and instrumented with a flow transducer (Transonic, USA) in the aortic segment of the simulator and two pressure transducers (Edwards Life Science, USA) positioned in the cannula at the exit of the DAV (following the direction of flow) and at the afterload chamber. This arrangement allowed the measurement of the pressure difference between the two ports, which represents the pressure drop along the cannula. A differential transducer (Validyne Engineering Co, USA) was placed at the same points for direct differential pressure measurements. After conditioning (4 channel pressure conditioner, Bioengineering Division, Brazil) signals were recorded using the DataQ WinDaq DI-220 acquisition system, (DataQ Instruments, USA) on a computer.

Cannulas with an internal diameter of 6 and 8 mm and a length of 220 mm were evaluated under the same conditions to compare the results. During trials, VAD was activated at different rates at constant filling pressure (−10 mmHg) and the afterload was adjusted to the physiological infantile condition (about 90 mm Hg × 60 mm Hg).

2.3 "In Vivo Validation"

Long term cannula implantation was performed with support of cardiopulmonary bypass (CPB) through median sternotomy in a conventional manner. The aorta and right atrium were cannulated to start CPB in 6 patients. The average age

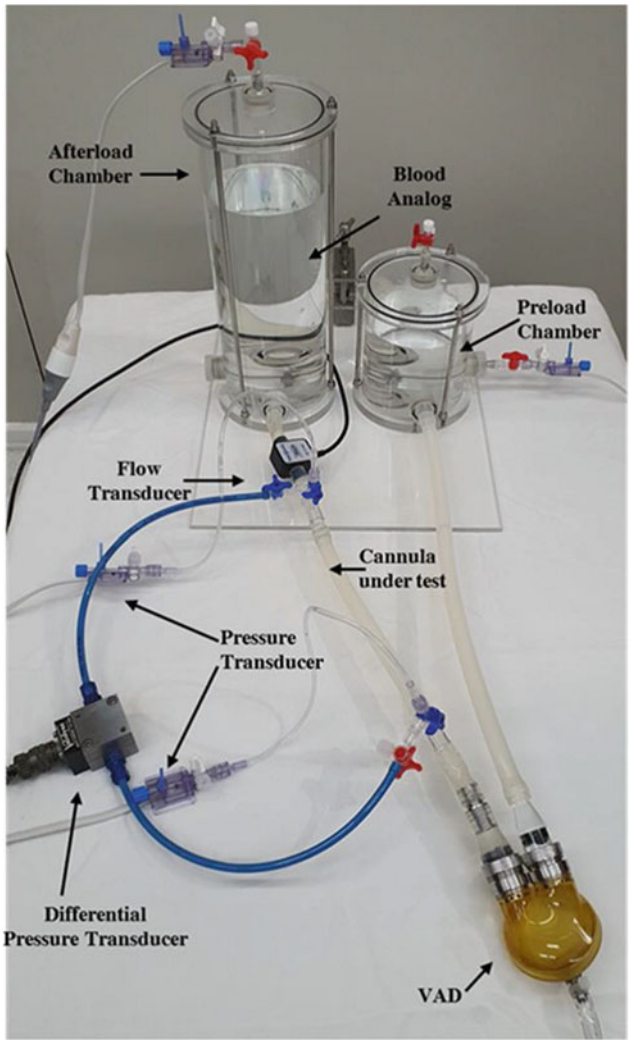

Fig. 1 Experimental set up simulating the use of the cannula connecting a VAD to the mock loop of the pediatric circulation

of these patients was 7.3 years. These patients were on a waiting list for transplantation with a diagnosis of Dilated Cardiomyopathy (DCM), Total Atrioventricular Septum Defect (total AVSD) or Restrictive Cardiomyopathy (RCM) and classified according to INTERMACS (Interagency Registry for Mechanically Assisted Circulatory Support) 1 or 2. The reason for the indication for MCS was Bridge to Transplantation (BTT) in 4; Bridge to Bridge (BTB) in 1 and initially as a Bridge for Recovery (BTR) and later considered for BTT (no recovery of function in the first 5 days). The study was approved by the HC-FMUSP ethics committee (SDC 4009/13/134).

3 Results

The dimension of the cannulas is present in Table 1.

"In vitro" tests—The pressure drop was determined by taking the difference between the pressure recorded at cannula inlet and at its outlet considering the direction of the flow. A differential pressure curve as a function of time was obtained. As this differential pressure curve is periodic and has negative values in part of the cycle, the value of the head loss was determined through the effective value (rms), which for a function over time is given by Eq. 1, where p(t) is a function of differential pressure over time and T is the period.

$$p(t)_{rms} = \lim_{T\to\infty}\left(\sqrt{\frac{1}{2T}\int_{-T}^{T}[p(t)]^2 dt}\right) \quad (1)$$

The effective value can be determined by the relationship of the average value ($p_{average}$) and the standard deviation σ according to Eq. 2:

$$p_{rms}^2 = p_{average}^2 + \sigma^2 \quad (2)$$

Figure 2 shows the results represent the pressure drop values along the cannulas under the different flow conditions. The error bars in the graphs indicate the standard deviation of the means.

As shown in the figure, the pressure drops of cannulas with 6 mm internal diameter are almost twice that of larger diameter cannulas.

"Clinical evaluation"—The implantations of apical or ventricular cannulas for use with the VAD or with the centrifugal pump were performed following a similar protocol. The tunnel for exteriorization was defined and made, so that the cannula is below the last costal arch. The tunnel

Table 1 Dimensions of the cannulas

Internal diameter	Apical cannula		Atrial cannula			Arterial cannula		
(mm)	Tip (titanium) (mm)	Total (mm)	Tip (mm)	Tip silicone angle	Total (mm)	graft PTFE Ø (mm)	Length graft (mm)	Total (mm)
6	27	220			240	6	10	180
8	29	220	25	45°	240	8, 10	15	195

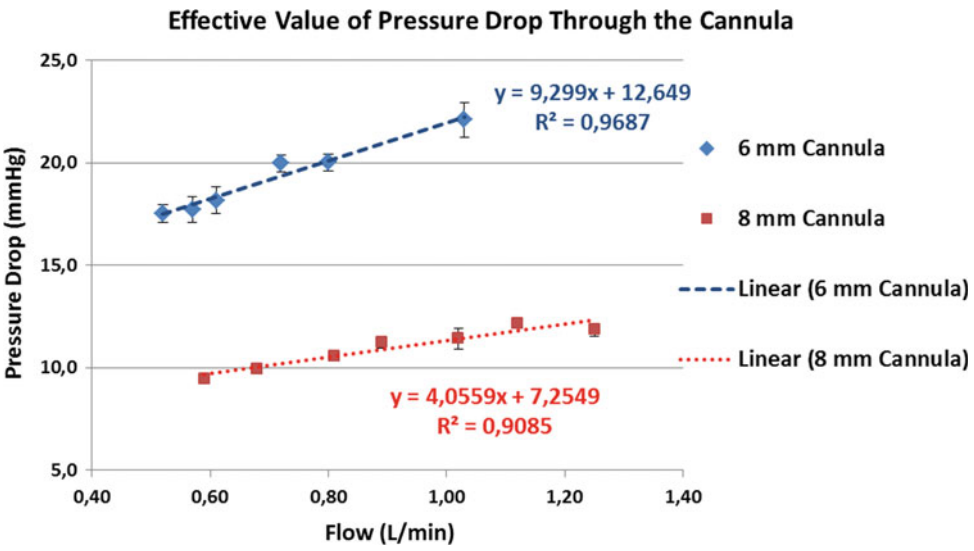

Fig. 2 Pressure drop as a function of flow for the two diameters evaluated

exit was made slightly smaller than the diameter of the cannula so that the part coated with Dacron® fabric very tight and allows a perfect fixation and subsequent growth of healing tissue which will promote great stability of the position of the cannula. A circular and transmural left ventricle (LV) fragment is removed in the diameter of the tip of the cannula to be implanted. The tip of the cannula was introduced into the LV and the stitches were tied as shown in Fig. 3. Hemostatic biological glue is applied at the end to promote better hemostasis. After fixing the distal part of the cannula, it is removed from the interior of the thoracic cavity and externalized through the tunnel initially performed. The heart is placed in its anatomical position so that it is comfortably positioned with the cannula well accommodated in a way that does not deform the left ventricle anatomy is not deformed by it.

The profile of the patients, diagnosis, type of indication, and time of assistance, as well as the evolution with the use of these devices are presented in Table 2.

4 Conclusions

The pressure drop values for the 6 mm diameter cannula ranged from 17 to 22 mm Hg and for the 8 mm cannula the from 9 to 12 mm Hg with increasing flows from 0.52 to 1.03 and from 0.59 to 1.25, respectively. It can be observed that there is a difference between the cannulas of different diameters with the cannula of smaller offering greater resistance in all conditions analyzed [7]. It is also noted how the flow changes the value of the pressure drop, which increases with the increase of this quantity [8].

The implantation of long-term cannulas proved to be technically feasible, allowing adequate decompression of the left ventricle and, due to the fact that the cannulas have a conical end, they can be used in pulse pumps and also in centrifugal pumps. No thrombus was observed at the tips of the cannulas or bleeding. The association of the long-term cannula with the centrifugal pump allowed adequate support for patients on the waiting list for heart transplantation and

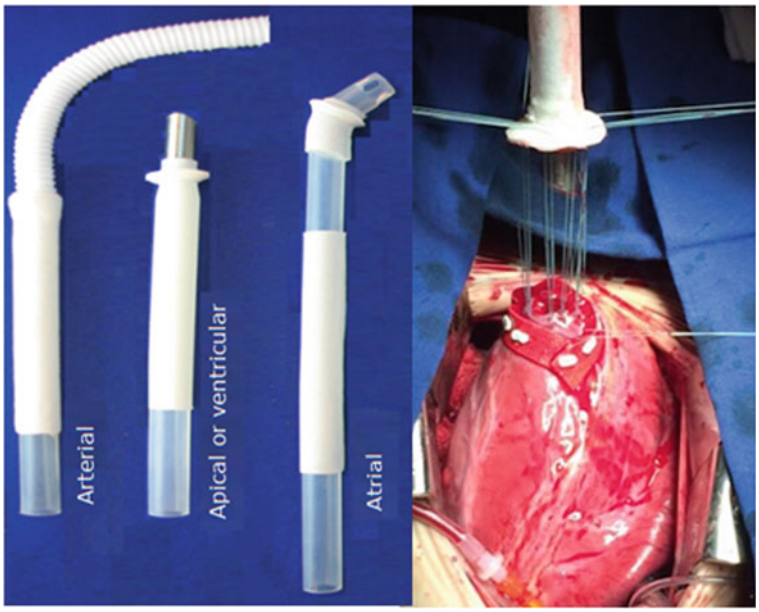

Fig. 3 **a** Cannulas model; **b** positioning and fixing the apical cannula at the LV tip

Table 2 Patients and evolution of assistance with centrifugal pump and long-term cannulas

P	Time	Diagnosis	Indication	Assistance time (h)	Type of assistance
1	9 years	DCM	BTT	41	LVAD
2	12 years	DMC	BTT	160	LVAD
3	5 years	Total AVSD	BTT	632	BiVAD
4	1 month	DMC	BTT	155	LVAD
5	13 years	RMC	BTT	840	BiVAD
6	5 years	RMC	BTT, BTB	1584	LAVD

LVAD: assistance of isolated left ventricle; BiVAD: assistance for both ventricles

enabled greater patient mobility in the bed due to the great stability in its fixation. The removal of the cannulas was easy to perform and, when necessary, the transition was simples

Acknowledgements We thank FINEP (1253/13), FAPESP (2012/5083-6) and CNPq (467270/2014-7) for the financial support.

Conflict of Interest The authors have declared that there is no conflict of inter-est related to this manuscript.

References

1. Bacal F, Marcondes-Braga FG, Rohde LEP, Xavier Júnior JL, de Souza Brito F, Moura LZ et al (2018) 3ª Diretriz Brasileira de Transplante Cardíaco. Arq Bras Cardiol 111(2):230–289
2. Ayub-Ferreira SM, Souza Neto JD, Almeida DR, Biselli B, Avila MS, Colafranceschi AS et al (2016) Diretriz de assistência circulatória mecânica da Sociedade Brasileira de Cardiologia. Arq Bras Cardiol 107(2Supl.2):1–33
3. Fiorelli AI, Oliveira JL Jr, Coelho GHB, Rocha DC (2008) Mechanical circulatory support: why and when. Rev Med 87(1):1–15
4. Simon MA, Watson J, Baldwin JT, Wagner WR, Borovetz HS (2008) Current and future considerations in the use of mechanical circulatory support devices. Annu Rev Biomed Eng 10:59–84
5. Cestari IA, Mazzetto M, Oyama HT, Bacht S, Jatene MB, Cestari IN, Jatene FB (2019) Design and hydrodynamic performance of a pediatric pulsatile pump. In: Costa-Felix R, Machado J, Alvarenga A (eds) XXVI Brazilian congress on biomedical engineering. IFMBE proceedings, vol 70/1. Springer, Singapore, pp 85–88
6. Maat APWM, Van Thiel RJ, Dalinghaus M, Bogers AJJC (2008) Connecting the Centrimag Levitronix pump to Berlin Heart Excor cannula; a new approach to bridge to bridge. J Heart Lung Transpl 27(1):113–115
7. McDonald CI et al (2015) Hydrodynamic evaluation of aortic cardiopulmonary bypass cannula using particle image velocimetry. Research Article Find in PubMed. https://doi.org/10.1177/0267659115586282
8. Caneo LF et al (2018) Functional performance of different venous limb options in simulated neonatal/pediatric cardiopulmonary bypass circuits. Braz J Cardiovasc Surg 33(3):224–232. https://doi.org/10.21470/1678-9741-2018-0074

Evaluation of *Lantana Trifolia* Total Extract in Cell Culture: Perspective for Tissue Engineering

C. F. L. Silva, L. R. Rezende, F. N. Ambrosio, J. Badanai, R. A. Lombello, and C. B. Lombello

Abstract

Phytotherapy can have several applications, such as anti-inflammatory, analgesic, antinociceptive, antimicrobial, antiviral and tissue regeneration. It is important to characterize the effects of these drugs to verify clinical safety, avoiding possible adverse reactions, like toxicity, digestive discomfort and headache. In this research, the effects of total aqueous and ethanolic extract of *Lantana trifolia* L was analyzed on Vero cell cultures, seeking to understand how the cellular response to different concentrations (25, 50, 75 and 100 µl/ml) of the extracts. There were carried out quantitative and qualitative, morphological evaluation, of the cultured cells in the presence of the extracts. The quantitative results showed cell viability dependent on the concentration of test extract. The cellular viability remained above 70%, therefore for all experimental conditions, resulting in non-cytotoxic effects, both for aqueous and ethanolic extracts. With the statistical analysis of the results obtained it was possible to conclude that there was no significant variation in cell viability, that is, although the extract is non-cytotoxic, it does not cause cell proliferation in the medium. The quantitative results are in accordance with the qualitative analyzes.

Keywords

Biocompatibility • Cell culture • Cell differentiation • Plant extract • *Lantana trifolia*

C. F. L. Silva · J. Badanai · C. B. Lombello (✉)
Center for Engineering, Modeling and Applied Social Sciences (CECS), Federal University of ABC (UFABC), Alameda da Universidade, s/n, São Bernardo do Campo, SP, Brazil
e-mail: christiane.lombello@ufabc.edu.br

L. R. Rezende · F. N. Ambrosio · R. A. Lombello
Center for Natural and Human Sciences (CCNH), Federal University of ABC (UFABC), São Bernardo do Campo, SP, Brazil

1 Introduction

Phytotherapy, medicines originated from plants, are widely used in the prevention and combat of diseases. Currently there are several herbal medicines in common and daily use, made in the form of teas and juices, such as chamomile, *Chamomilla recutita* L., which has an anxiolytic and sedative effect [1]. *Erythrina crista-galli*, which is known as cork, has been shown, in pharmacological studies, to present antinociceptive, anxiolytic, sedative, muscle relaxant and antibacterial activities, and *Erythrina velutina* extracts that has anxiolytic and sedative properties [2].

Although most herbal medicines do not have a well-known toxic profile, daily use has become common. Many people use herbal medicines indiscriminately, without worrying about adverse and harmful effects to the organism. Phytotherapic are used by self-medication or by medical prescription and most of them do not have a well-known toxic profile [3]. Despite the benefits of medicinal side effects can occur, such as abortion, hypotension, headache, dizziness, among others [1].

According to the WHO (World Health Organization) about 65–80% of the population, mainly in developing countries, use herbal medicines in primary health care [4]. Despite the fact that medicinal plants are already part of popular culture, in the last decades the interest in herbal medicine has increased considerably among users [5].

In this context, Brazil is a privileged country, due to the large variety of its flora, and the consequent variety of phytotherapy for disease prevention and treatment that directs scientific studies in different areas. The phytotherapy research has great potential for contribution in the economic field, due to the high demand for low-cost and reliable medicines, as well as in the scientific field, with contributions to the medical and pharmaceutical areas [6–8].

Among the great number of plant species of phytotherapic interest, with reported clinical applications, we can

T. F. Bastos-Filho et al. (eds.), *XXVII Brazilian Congress on Biomedical Engineering*, IFMBE Proceedings 83, https://doi.org/10.1007/978-3-030-70601-2_27

mention the family Verbenaceae, which includes the genus *Lantana* [9, 10], that is associated with antimicrobial and anti-inflammatory activity. There are also reposts of several effects on the organism for *Lantana* sp., among them we can mention toxicity related to respiratory and digestive disorders [10–12]. These data indicate that more careful analyzes should be carried out to indicate the safety of these phytotherapic.

One representative of the genus, *L. trifolia* L, presents few studies characterizing its phytotherapic potential. Reports of the use of tea from the leaves of this species for the treatment of gastric ulcers are accompanied by description sedative, anti-inflammatory and analgesic effects [10–14].

There are few studies in the scientific literature on the potential effects that *L trifolia* may have on different cells, indicating concentration related toxicity [14]. Thus, new data about this species may result in a great contribution to the scientific literature, guiding the next steps and application in a tissue regeneration or tissue engineering application [14, 15]. In this study both the aqueous and ethanolic extract of *L. trifolia* were considered non cytotoxic.

2 Objectives

The objective of this study was to evaluated Vero cells cultured in the presence of total aqueous and ethanolic extract of *L trifolia*, using morphological analyses and MTT (3-(4,5-dimethyl-2-thiazolyl)-2,5-diphenyl-2H-tetrazolium bromide) technique.

3 Materials and Methods

3.1 Preparation of Lantana Trifolia Total Extracts

The plant material was collected at São Bernardo do Campo/SP, at the UFABC Campus, and an exsiccate was deposited at the UFABC herbarium.

There were prepared total extract of *L trifolia* leaves [14], according to techniques previously described in the literature [16–20].

Briefly, the leaves were stored in an oven at 60 °C for 48 h, and then crushed. The extracts were obtained with 2.5 g of the materials in 12.5 ml of solution, being the experimental conditions: water at room temperature, and ethanol. After 24 h, in a closed system, the extracts obtained were filtered and frozen. The aqueous extracts were subjected to lyophilization, and the ethanolic extracts were subjected to the rotoevaporation procedure. The extracts were prepared in phosphate buffer solution (PBS), pH 7.4.

The extracts were sterilized by filtration through a syringe filter. The use concentrations for both aqueous and ethanolic extracts were: 25, 50, 75 and 100 µl/ml [14–17].

3.2 Vero Cell Culture

Vero cell lineage (CCIAL 057) was used [21]. The cells were cultured in HAM F10 medium, with 10% fetal bovine serum (FCS) and 10 µg/ml penicillin/streptomycin, and maintained at 37 °C with 5% CO_2.

For the extract assay, the cells were inoculated in a 96-well culture plate, the density of 2×10^4 cells/well, and maintained in the culture condition for 48 h, until the monolayer reached the confluency. After this period, the culture medium was replaced by extract solutions in the mentioned concentrations (25, 50, 75 and 100 µl/ml).

As control for the experiments, the ideal culture conditions were considered negative control and 0.25% phenol in the culture medium was used as positive control, considering the cytotoxicity analyzes of the extracts.

3.3 Qualitative Analyses: Cell Morphology

The cells under experimental conditions (presence of total extracts), and controls, were evaluated after 24 h in culture for the qualitative morphological analyzes, with an inverted microscopy, and phase contrast (Axiovert A1, Zeiss).

3.4 Cell Quantification: MTT Assay

Quantitative evaluation of cell cultures was performed using the MTT assay (3-(4,5-dimethyl-2-thiazolyl)-2,5-diphenyl-2H-tetrazolium bromide) [22]. The culture medium was removed and MTT solution was incubated for 4 h. After that period, the MTT solution was removed, and DMSO (dimethylsulfoxide) was added. The quantification of cells was performed by spectrophotometric reading at 540 nm (SpectraMax M5), considering the negative control as 100% cell viability. The results were expressed in relative percentage. The tests were performed in quadruplicate. Statistical analyses were used with the Bonferroni—ANOVA model.

4 Results and Discussions

Vero cells (Fig. 1) are epithelial cells of the kidney of the African green monkey (*Cercopithecus aethiops*), with typical monolayer growth in an elongated morphological pattern, fibroblast-like cells [23].

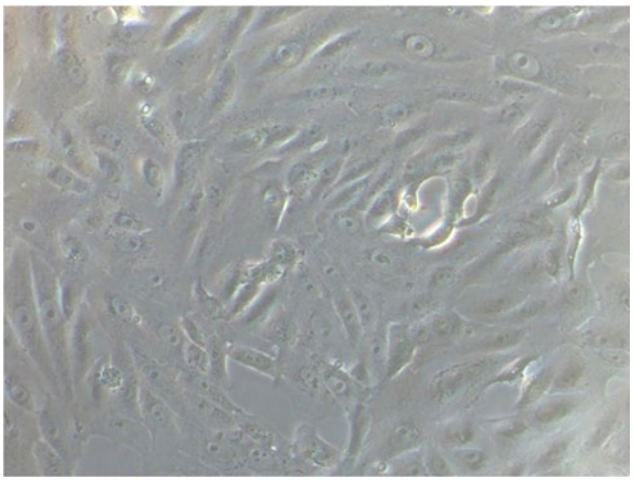

Fig. 1 Vero cells in culture, morphological control, before the application of the extracts. Observation: 400×

The analyzes were performed using aqueous and ethanolic extract of *Lantana trifolia*, with 25, 50, 75, and 100 µg/ml, and the positive and negative control. All extracts remained in culture for 24 h in order to assess cell morphology.

It is possible to observe the experimentation controls after the 24 h period (Fig. 2). The negative control shows the standard morphological pattern of Vero cells, monolayer culture, with no signs of cell death (Fig. 2a). In contrast, the positive control shows an opposite pattern, although a considerable quantity of cells are present, the morphology is altered, with loss of cell adhesion, monolayer discontinuity and cell vacuolization, configuring cytotoxicity.

In cell culture in the presence of aqueous extract, the cell response was similar to the pattern observed in the negative control, indicating no-cytotoxicity (Fig. 3a, b), but at concentrations of 50 and 100 µg/ml (Fig. 3c, d), it is possible to

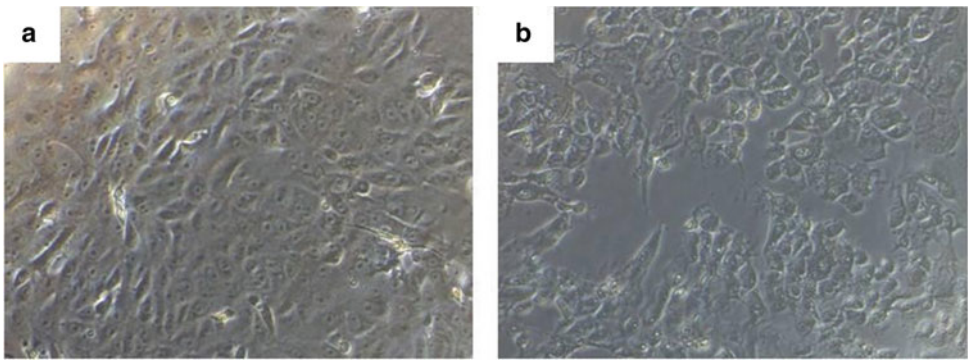

Fig. 2 Cytotoxicity controls, Vero cells. **a**. negative control; **b**. positive control. Observation: 400×

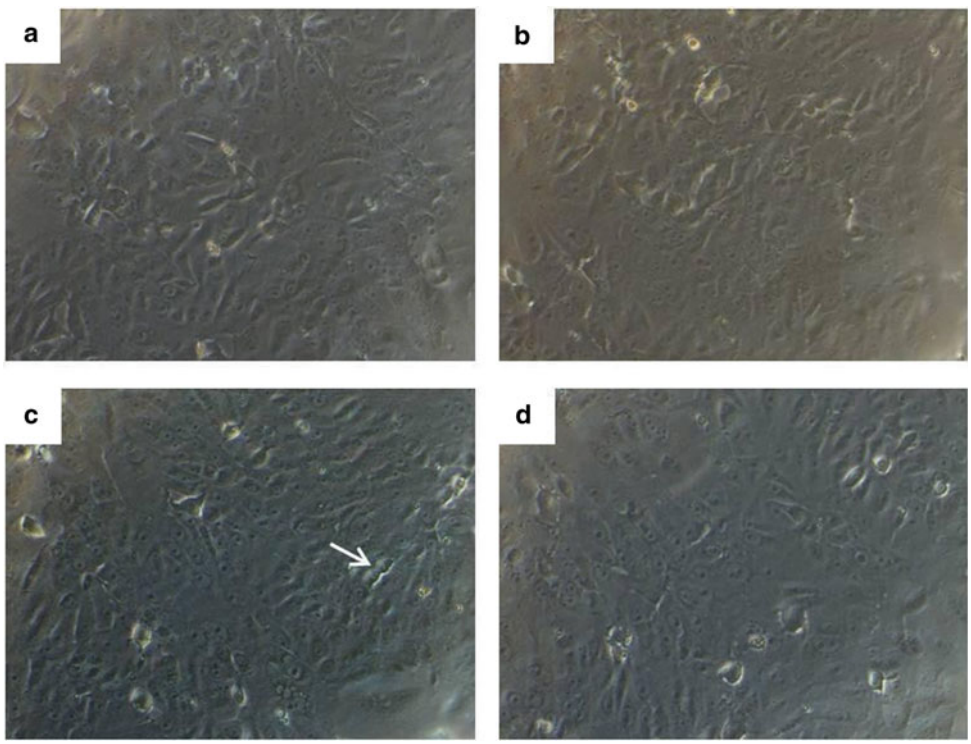

Fig. 3 Vero cells, cytotoxicity of aqueous *Lantana trifolia* extract in different concentrations: **a**. 25 µg/ml; **b**. 50 µg/ml; **c**. 75 µg/ml; **d**. 100 µg/ml. Observation: 400×

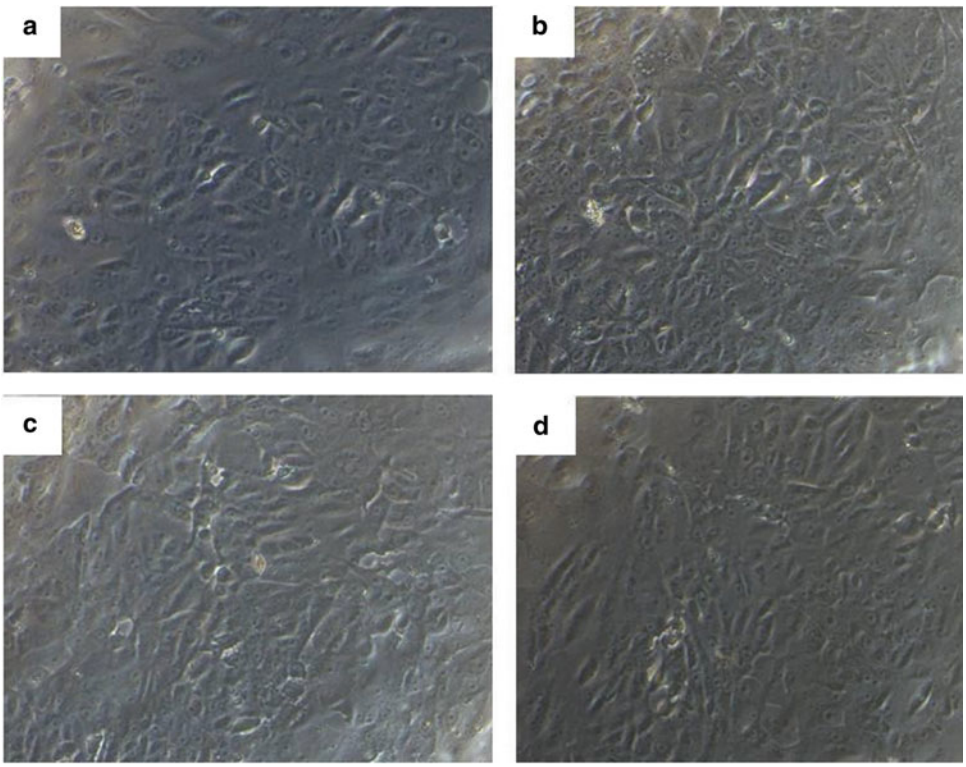

Fig. 4 Vero cells, cytotoxicity of ethanolic *Lantana trifolia* extract in different concentrations: **a**. 25 μg/ml; **b**. 50 μg/ml; **c**. 75 μg/ml; **d**. 100 μg/ml. Observation: 400×

observe some cell morphological alterations. However some cells in the process of division can be observed (Fig. 3c).

The cells cultured in the presence of ethanolic extract (Fig. 4) with the same concentrations (25, 50, 75, and 100 μg/ml), showed morphological results similar to the aqueous extract and to the negative control, for all concentrations tested.

Comparatively, quantitative (MTT) assays were carried out, and the results were in concordance with morphological analysis, showing non-cytotoxic results for aqueous (Fig. 5) or ethanolic (Fig. 6) extracts, and data are above 70% viability.

The statistical analysis showed no significant differences between the different extracts tested and the negative control, indicating that the aqueous and ethanolic extracts in all concentrations are non-cytotoxic, and also do not induce cell proliferation. Morphological and quantitative data are in accordance.

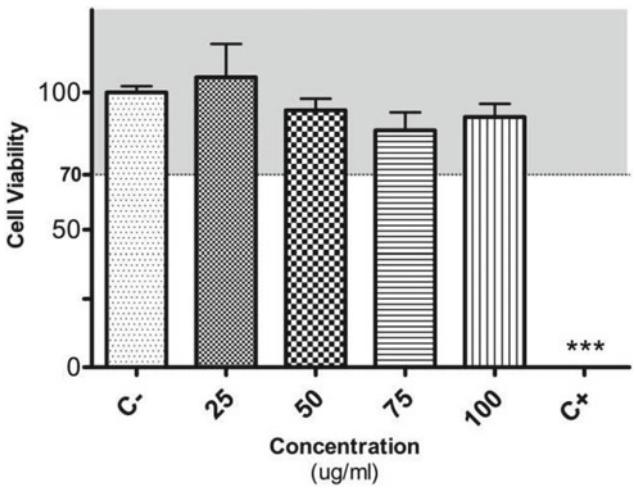

Fig. 5 Vero cells, cytotoxicity of aqueous extract of *Lantana trifolia* in different concentrations: **a**. 25 μg/ml; **b**. 50 μg/ml; **c**. 75 μg/ml; **d**. 100 μg/ml

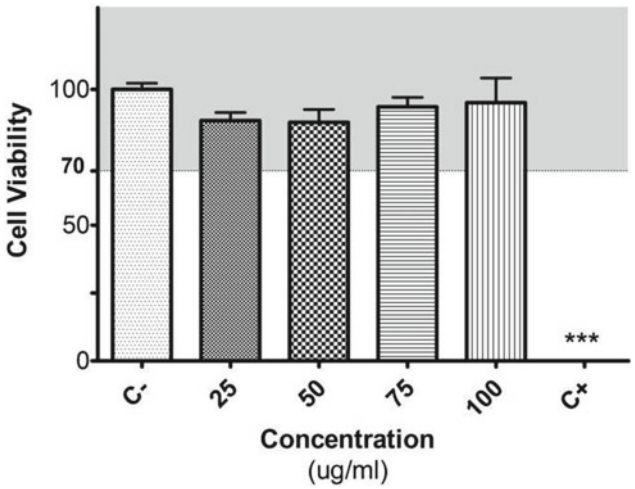

Fig. 6 Vero cells, cytotoxicity of ethanolic extract of *Lantana trifolia* in different concentrations: **a**. 25 μg/ml; **b**. 50 μg/ml; **c**. 75 μg/ml; **d**. 100 μg/ml

There are not many studies on *L. trifolia* in the scientific literature, but the non-cytotocicity of aqueous extracts is related, as well as ethanolic extracts may show signs of cell cytotoxicity, concentration dependent [14], for other *Lantana* species, *L. camara* and *L. montevidensis* [24–26]. The data presented are promising, and allow to expand the studies for the application of tissue engineering with total *L. trifolia* extracts for tissue engineering, associated with biomaterials or controlled delivery systems.

5 Conclusion

The total aqueous and ethanolic extract of *L. trifolia* showed no cytotoxicity on Vero cells.

Acknowledgements We thank the Federal University of ABC (UFABC) for the student financial support.

Conflict of Interest The authors declare that they have no conflict of interest.

References

1. Ceolin T, Reck RM, Barbieri RL et al (2009) Plantas medicinais utilizadas como calmantes por agricultores ecológicos da região sul do Rio Grande do Sul, Brasil. Rev Enfermag 3:1034–1041
2. Siqueira MS, Sousa RM, Tirloni CAS et al (2019) Implicações de extrato de *Erythrina crista-galli* como ansiolítico para *Carassius auratus*. Ciênc anim bras 20:e-5052
3. Silveira PF, Bandeira MAM, Arrais PSD (2008) Farmacovigilância e reações adversas às plantas medicinais e fitoterápicos: uma realidade. Rev Bras Farmacogn 18:618–626
4. Rahman SZ, Singhal KC (2002) Problems in pharmocovigilance of medicinal products of herbal origin and means to minimize them. Uppsalla Rep 17S:1–4
5. Rosa C, Camara SG, Beria JU (2011) Representações e intenção de uso da fitoterapia na atenção básica à saúde. Ciênc Saúde Coletiva 16:311–318
6. Eldin S, Dunford A (2001) Fitoterapia na atenção primária à saúde. Editora Manole, São Paulo
7. Badke MR, Budó MLD, Nat Alvim et al (2012) Saberes e práticas populares de cuidado em saúde com o uso de plantas medicinais. Contexto Enfermag 21:363–370
8. Hasenclever L, Paranhos J, Costa OR et al (2017) A indústria de fitoterápicos brasileira: desafios e oportunidades. Ciênc Saúde Coletiva [internet] 22:2559–2569
9. Lorenzi H, Matos FJA (2008) Plantas medicinais no Brasil: nativas e exóticas. Instituto Plantarum, Nova Odessa
10. Sousa EO, Costa JGM (2012) Genus *Lantana*: chemical aspects and biological activities. Rev Bras Farmacogn [online] 22:1115–1180
11. Mengitsu G (2015) Evaluation of the antidiarrhoeal activity of 80% methanol extract and solvent fractions of the leaves of *Lantana camara* Linn (Verbenaceae) in mice. Ethio Pharm J 31:107–121
12. Santos RL (2011) Análise sobre a fitoterapia como prática integrativa no sistema único de saúde. Rev Bras Plantas Med Botucatu 13:486–491
13. Silva TSC, Suffredini IB, Ricci EL et al (2015) Antinociceptive and anti-inflammatory effects of *Lantana camara* L. extract in mice. Rev Bras Plantas Med [internet] 17:224–229
14. Badanai JM, Rezende LR, Ambrsio FN et al (2019) Avaliação dos efeitos de extratos de *Lantana camara* e *Lantana trifolia* em culturas celulares. anais do 6º Workshop de Orgãos Artificiais. Biomateriais e Engenharia de Tecidos (OBI)
15. Haycock JW (2011) 3d cell culture: a review of current approaches and techniques. Method Mol Biol 695:1–15
16. Sousa EO (2011) Atividade antibacteriana e interferência de L*antana camara* L. e *Lantana montevidensis* (spreng.) briq. na resistência de aminoglicosídeos. Rev Bras Biociências 9:1–5
17. Lima MP (2008) Influência dos extratos de *Casearia sylvestris*; *Bauhinia microstachy*a; *Rauvolfia sellowii* e *Himatanthus lancifolius* sobre o comportamento de células HL-60, K-562, Daudi e REH. 2008. 104 Dissertação (Mestrado). Curso de Ciências Farmacêuticas, Ciências da Saúde, Universidade Federal do Paraná, Curitiba
18. Branco Neto MLC, Ribas Filho JM, Malafaia O et al (2006) Avaliação do extrato hidroalcoólico de aroeira (*Schinus terebinthifolius* Raddi) no processo de cicatrização de feridas em pele de ratos. Acta Cirúr Bras 21:17–22
19. Almeida MCO, Melo ACR, Pinheiro MLB (2011) Chemical constituents and leishmanicidal activity of *Gustavia elliptica* (Lecythidaceae). Quím Nova 34:1182–1187
20. Carlini EA, Duarte-Almeida JM, Tabach R (2012) Assessment of the toxicity of the Brazilian pepper trees *Schinus terebinthifolius* Raddi (aroeira-da-praia) and *Myracrodruon urundeuva* Allemão (aroeira-do-sertão). Phytoth Res 27:692–698
21. Ammerman NC (2008) Growth and maintenance of Vero cell lines. Curr Protocols Microbiol 11:a.4e.1–a.4e.7
22. Mosmann T (1983) Rapid colorimetric assay for cellular growth and survival: application to proliferation and cytotoxicity assays. J Immunol Meth 65:55–65
23. Lombello CB, Malmonge SM, Wada ML (2000) PolyHEMA and polyHEMA-poly(MMA-co-AA) as substrates for culturing Vero cells. J Mater Sci Mater Med 11:541–546
24. Santos HM Jr (2010) Evaluation of native and exotic Brazilian plants for anticancer activity. J Natural Medic 64:231–238
25. Silva CS, Gomes R, Ribeiro K et al (2017) Toxicidade e atividade antioxidante das folhas de Lantana montevidensis: contribuição para o seu potential farmacológico e seus componentes químicos. Reunião Regional da SBPC, Cariri/CE, pp 1–4
26. Figueira ACG (2019) Efeitos mutagênicos e citotóxicos do óleo essencial de Lantana camara usando teste do micronúcleo em medula óssea de camundongos. Rev Ciências Amb Saúde 46:24–32

Study on the Disinfection Stability of Bullfrog Skin

D. N. de Moraes, D. IKozusny-Andreani, C. R. Tim, L. Assis, A. P. Da Costa, and M. M. Amaral

Abstract

Currently, look for alternative healing membranes that can perform actions such as safe and secure physical barrier, allowing proper gas exchange, being clinically effective, easy to apply, manipulating and assisting in wound care. Face this need, demonstration or potential of bull skin for use as a healing membrane, being used in this work antibiotic for skin disinfection. O ozone (O_3) is known for its high antimicrobial effect without development of resistant tissue. The present work had standardized disinfection performance using ozone and the bull skin membrane lifetime test. Opened in February 2019 and after verified microbiological test-if there was no contamination. Through the preliminary results of the useful life test, the next steps of the study to evaluate dressings in animal model were determined.

Keywords

Ozone • *Rana catesbeian* • Shelf-life

1 Introduction

Skin grafting is a technique widely used in plastic and reparative surgery to treat extensive skin lesions. It is mainly indicated to treat surgery to repair chronic wounds, burns, abrasions or traumas, skin lesions after trauma or surgery and congenital deformities [1].

The acceleration of wounds healing provided by the biological occlusive curative methods has been studied. These biological curatives have antibacterial action, but it mainly stimulates the processes of granulation, contraction and epithelialization, forming a physical barrier against an invading bacteria and preventing the retention of exudate, affecting beneficial activities [2].

In Brazil, burn injuries are responsible for 57% of the young people deaths, between 0 and 19 years old. About 1 million burn cases occurs each year and about 2500 people die from these injuries. Materials with antibacterial and skin analog properties can be used as a biological occlusive dressing, being useful to accelerate the formation of granulation tissue, thus favoring the healing process [3].

In this scenario, new technologies are needed that can be used to replace the skin during healing. Several studies have focused on the development of biomaterials for this proposal, such as healing membranes with therapeutic functions [2]. Each solution must follow three criteria of tissue engineering, being: it must be safe for the patient; be clinically effective and easy to apply and handle [4].

Several materials of biological origin have been studied as possible skin substitutes (curative membranes or biological dressings), among them are the amniotic membrane of human and rabbits, pig, rabbit, human skin [5–7] and amphibian skin [8–10].

The use of Nile tilapia skin as biological dressing has been studied. It has morphological characteristics and resistance close to human skin [11].

In an article published by *Revista Brasileira de Queimaduras* in 2017, in animal studies, it was observed that the tilapia skin showed good adherence and it has potential for application as a biological dressing, helping in the healing process [12].

A possible alternative is to use *Rana catesbeiana* (bullfrog) skin. It is one of the most economically important commercial frog species in the world. The creation of frogs for meat consumption in Brazil is a growing market, generating a large volume of tailings residues that could be used in other processes [10].

The bullfrog (*Rana catesbeiana*) is an amphibian with great commercial relevance in ranching, with good

D. N. de Moraes (✉) · D. IKozusny-Andreani · C. R. Tim · L. Assis · A. P. Da Costa · M. M. Amaral
Instituto Cientifico e Tecnologico, Universidade Brasil, São Paulo, Brazil

T. F. Bastos-Filho et al. (eds.), *XXVII Brazilian Congress on Biomedical Engineering*, IFMBE Proceedings 83, https://doi.org/10.1007/978-3-030-70601-2_28

adaptation to breeding, simple handling and commercial value. Its skin is used in clothes, shoes, belts, bags, wallets, gloves, objects and ornaments production. It is a great source of collagen and oils being used in the cosmetics and dermo-medications industry. It also has promising potential for use as curative membrane in skin lesions [13, 14].

The bullfrog's skin corresponds to 11% of the entire animal. It has great potential for applications as a curative membrane, presenting a great diversity of toxins of its defense system [5]. In the cells lining the skin of this animal, it is possible to find several assets, such as aliphatic, aromatic and heterocyclic molecules, in addition to a diverse range of steroids, alkaloids, biological amines, guanines, proteins, peptides and the entire enzyme system involved in their biosynthesis [6].

In amphibians' skin, there is a large amount of mucus-secreting glands, which produce aqueous fluid that maintains skin moisture, which is essential for skin breathing and makes it slippery, being a defense against predators [6].

The use of bullfrog skin (*Rana catesbeiana*) a curative membrane could provide mechanical barrier protective to aggressive agents and external contamination, with effective gas exchange due to its cellular composition, high concentration of collagen, water and nutrients, biocompatibility, biological interaction with the substrate with the release of tissue biomodulators [10].

Skin replacement is an important step in the treatment of various etiologies. These products are intended to aid in the healing process and even the healing of skin lesions, depending on the substitute used. Currently, existing skin types have associated advantages and disadvantages. More studies and advances using synthetic and biological materials are still needed, and even more tests with the materials that exist on the market for improvements and adjustments in the way they are used [11].

An extremely important step in the preparation of curative membranes for xenografts (grafts from a different specie) is the sterilization for its use and conservation. It sterilization guarantee that there will be no contamination of the patient. Thus, different approaches for sterilization of the bullfrog skin and its effects on the skin healing process should be explored [6].

The use of sterilization techniques for *Rana catesbeiana* skins that maintain their properties are desirable so that they can be applied as curative membranes, guaranteeing safety and quality for future treatments. The use of sterilization techniques for *Rana catesbeiana* skins that maintain their properties are desirable for those that can be applied as curative membranes, safety and quality for future applications.

Ozone is known for its high antimicrobial power, it is an effective oxidizing agent to inactivate viruses, bacteria, fungi, protozoa. The main advantage of Ozone is that it does not create antibiotics resistance [5].

The present work aimed to study the disinfectant stability of Ozone, associated or not with other agents, in *Rana catesbeiana* skins for biological dressing applications.

2 Materials and Methods

2.1 Sample Preparation

The skin samples of Bullfrog (*Rana Catesbeiana*) were obtained at Ranário Ranakan, in Juquitiba-SP, and the microbiological evaluation and tests were carried out at the Microbiology Laboratory of Universidade Brasil, campus of Fernandópolis-SP.

Hundred animal skin (Fig. 1) were removed and frozen. Before starting the disinfection process, muscle residues were removed with the aid of a sterile scalpel and washed with distilled water is abundant.

250 standards samples of 1 cm × 1 cm were cut with a sterile scalpel. The skins sample were kept in the refrigerator (-8 °C) in a closed container until the time of the experiment.

2.2 Experimental Groups

The samples were divided into three groups:

$$\text{Group} : \text{Ozonized skin} + \text{Copaiba oil}$$

The copaiba oil used in clinical trials was purchased from *Mundo dos Oléos*. The oil used is from *Copaifera officinalis*. This oil came with a whole prospectus where it contains all the technical information about the physical-chemical analyzes in which the oils are submitted, together with all the organoleptic characteristics of it.

$$\text{Group} : \text{Ozonized skin} + \text{Melaleuca oil}$$

Tea tree oil used in clinical trials was purchased from the company *Mundo dos Oléos*. The oil used comes from Melaleuca alternifolia. This oil came with a whole prospectus where it contains all the technical information about the physical-chemical analyzes in which the oils are submitted, together with all the organoleptic characteristics of it.

$$\text{Group} : \text{Ozonized skin} + \text{chitosan}.$$

Chitosan samples used in clinical trials were prepared using chitin which was dispersed in 50% aqueous NaOH solution, containing 10% sodium dodecyl sulfate (SDS) and 1% sodium borohydride ($NaBH_4$). The produced N-deacetylation reaction was kept under constant stirring for 12 h. After that time the tests started.

Fig. 1 *Rana Catesbeiana* skin in the **A** rear perspective and **B** frontal perspective

2.3 Ozone Disinfection

The skin samples were processed in a container of 1000 mL filled with sterile deionized water. Ozone gas generated by Ozone Life (São Paulo, Brazil) equipment, connected to the medical oxygen cylinder, was dispersed in the water for 30 min, totaling an ozone dosage of 700 L/min^{-1}. After disinfection, the skin samples were transferred to a sterile plate to start the microbiological analysis procedure.

2.4 Stability Assessment and Microbiological Analysis

Every month, for 12 months, 5 samples from each group were submitted to a microbiological evaluation. A qualitative microbiological evaluation was carried out, with no intention of verifying the presence of bacteria in the motivated groups. It was recorded the presence or absence of contamination.

The experimental procedure was performed under laminar flow, following the biosafety standards. With a swab, the entire surface of the bullfrog's skin was rubbed to collect biological material for microbiological analysis.

The collected material was diluted in 10 mL of sterile saline solution (NaCl, 0.5%) and homogenized. 1000 µL of the homogenized solution were transferred to tubes containing 9 mL of sterile saline, obtaining dilutions 10^{-1}. Following the same process, serial dilutions (10^{-2}, 10^{-3} 10^{n}) were obtained.

The diluted solution was cultured, inoculating 100 µL of the dilutions in 100 mm Petri dishes containing TSA agarized media, and Sabouraud-dextrose (Oxoid®). The inoculum was seeded over the entire surface of the medium, using Drigalski loops, until the excess liquid was absorbed.

This procedure was repeated 3 times, the plates sown and incubated were kept in an oven for 24 h (1st reading) and 48 h (2nd reading).

3 Results and Discussion

Each studied group presented bacterial decontamination after the processed with ozone. Table 1 presents the observed presence of bacterial contamination in each of the studied groups.

The groups disinfected with ozone and stored in tea tree oil and in chitosan show bacterial growth in the first month after disinfection.

The group composed of ozonated skins and stored in copaiba oil does not show microbiological growth even after 12 months of storage. This result shows the importance of the stored method on the stability of the biological dressing.

Microbiological analysis shows the presence of only two bacterial species in the skins, Escherichia coli and Staphylococcus epidermidis. Differently from the study by FERREIRA et al. (2006), which analyzed the skin of amphibians on the farm where it verified the presence of *Mycobacterium marinum* [7].

Table 1 Presence bacterial contamination in each group

Month	Ozone + copaiba oil	Ozone + tea tree oil	Ozone+ chitosan
0	−	−	−
1	−	+	+
2	−	+	+
3	−	+	+
4	−	+	+
5	−	+	+
6	−	+	+
7	−	+	+
8	−	+	+
9	−	+	+
10	−	+	+
11	−	+	+
12	−	+	+

Legend: (−) no bacterial growth; (+) bacterial growth

According to previous published work, copaiba oil has several therapeutic properties such as being anti-inflammatory, healing, antiseptic, antibacterial [15]. In the present work, its association with ozone gas improved its antibacterial effect. Thus. copaiba oil proved to be an effective antibacterial agent when associated with ozone gas to keep *Rana catesbeiana* skin dressings inert.

4 Conclusions

In this work a previous stablished Ozone sterilization protocol was used the analysis of the stability and duration of the sterilization. This step is necessary to determine the time that the biological dressing could remain sterilized without contamination by microorganisms. Three different preservative systems were applied Copaiba oil, tea tree oil and chitosan.

The microbiological analysis shown that the disinfection process was able to promote disinfection of the bullfrog (*Rana catesbeiana*) skin, being an ozonation time/dose process.

After stability assessment, only the Copaiba oil was capable to maintain the disinfection after 1 month, remaining disinfected even after 12 months.

This storage process keeps the skins free from the presence of microorganisms, allowing its future application in skin grafts for animal model studies.

Acknowledgements D.N. de Moraes acknowledges CAPES for the financial support. This work was financially supported by CAPES and FAPESP (grant nº 2017/21851-0).

Conflict of Interest The authors declare that there has been no conflict of interest.

References

1. Andreassi, Bilenchi R, Biagioli M, D'Aniello C (2005) Classification and pathophysiology of skin grafts. Clin Dermatol 23:332–337. https://doi.org/10.1016/j.clindermatol.2004.07.024
2. Liptak JM (1997) An overview of the topical management of wounds. Aust Vet J 408–413
3. Haslam IS, Oubos EW, Mangoni ML, Yoshizato K, Vaudry H, Kloepper JE, Pattwell DM, Maderson PFA, Paus R (2014) From frog integument to human skin: dermatological perspectives from frog skin biology. Biol Rev
4. Horch R, Kopp J, Kneser U, Beier J, Bach A (2005) Tissue engineering of cultured skin substitutes. J Cell Mol Med
5. Balasubramani M, Tr Kumar, Babu M (2001) Skin substitutes: a review. Burns 27:534–44
6. Ovington L (2010) Dressing and skin substitute. In: McCulloch J, Kloth L (eds) Wound healing evidence-based management, 4th ed. FA Davis, Philadelphia, PA, pp 183–186
7. Chakrabarty K, Dawson R, Harris P, Layton C, Babu M, Gould L (1999) Development of autologous human dermal–epidermal composites based on sterilized human allodermis for clinical use. Br J Dermatol 141:811–823
8. Haslam IS, Roubos EW, Mangoni ML, Yoshizato K, Vaudry H, Kloepper JE, Pattwell DM, Maderson PFA, Paus R (2014) From frog integument to human skin: dermatological perspectives from frog skin biology. Biol Rev 89:618–655
9. Bazaz MR, Mashreghi M, Shahri NM, Mashrenghi M, Asoodeh A, Rassouli MB (2015) Evaluation of antimicrobial and healing activities of frog skin on Guinea Pigs Wounds. Jundishapur Microbiol 8(8):
10. Falcão SC, Lopes SI, Coelho ARB, El Almeida (2002) Pele de *Rana Catesbeiana* como curativo biológico oclusivo no tratamento

de feridas cutâneas produzidas em cães: Alterações macroscópicas e microscópicas resultantes da interação desses tecidos. Estudo-preliminar. Acta Cir Bras 17(3):151–159
11. Lopes MS, Ferreira JR, da Silva KB, de Oliveira Bacelar Simplício I, de Lima CJ, Fernandes AB (2015) Disinfection of corrugated tubing by ozone and ultrasound in mechanically ventilated tracheostomized patients. J Hosp Infect 90(4):304–9. https://doi.org/10.1016/j.jhin.2015.03.004
12. Lima EM Jr, Picollo NS, de Miranda MJB, Ribeiro, WLC, Alves APNN, Ferreira GE, Parente EA, Moraes-Filho MO (2017) Uso da pele de tilápia (*Oreochromisniloticus*), como curativo biológico oclusivo, no tratamento de queimaduras RevBras Queimaduras 16(1):10–17
13. Ferreira R, Fonseca SL, Afonso AM, Silva MG, Saad MH, Lilenbaum W (2006) A report of mycobacteriosis caused by Mycobacterium marinum in bullfrogs (Rana catesbeiana). Veterinary J 171:177–180
14. Limova M (2010) Active wound coverings: bioengineered skin and dermal substitutes. Surg Clin North Am 90(6):1237–1255
15. Ramos MFS (2006) Development of microcapsules containing the copaiba volatile fraction by spray-drying: stability study and pharmacological evaluation. 2006. 119f. Thesis, Doctorate in Pharmaceutical Sciences. Faculty of Pharmaceutical Sciences of Ribeirão Preto, University of São Paulo

Corrosion Analysis of a Marked Biomaterial

Eurico Felix Pieretti, Maurício David Martins das Neves, and Renato Altobelli Antunes

Abstract

Marking is one of the last steps of manufacturing an implantable biomaterial. The marks on its surface constitute a permanent set of information in order to provide identification and traceability of the biomedical device. These markings become stress concentrators and regions with probability for the occurrence of failures that can lead to fracture; besides damaging the passive layer, naturally formed on stainless steels surfaces, favoring the beginning of several forms of degradation. This work presents the effect of two metal implant marking techniques on the corrosion resistance of ISO 5832-1 austenitic stainless steel, one of the most used surgical biomaterials used in Brazil. Engraving was carried out with mechanical and laser beam marking techniques were prepared. The electrochemical behavior was characterized by cyclic potentiodynamic polarization curves and indicate that the laser marking technique is the one that most affects the passive layer of the material when compared to the mechanical engraving.

Keywords

Biomaterials • Engraving • Traceability • Laser • Corrosion

E. F. Pieretti (✉) · R. A. Antunes
Federal University of ABC/CECS, UFABC, Santo André, SP, Brazil
e-mail: efpieretti@usp.br

E. F. Pieretti · M. D. M. das Neves
Nuclear and Energy Research Institute/CCTM, IPEN-CNEN, São Paulo, SP, Brazil

1 Introduction

Biomaterials are used in prostheses or implantable medical devices in order to replace or assist certain parts of the human body so that they can properly perform their functions [1]. These materials must have a strict chemical composition and adequate surface finishing so that they are not rejected by the body during the lifespan period [2].

For hundreds of years, people have been looking for alternatives to relieve pain, reduce suffering and prolong life with greater quality. Reports on the use of synthetic materials have been found since the year 1550, with the use of gold thread for sutures [1]. Currently, advances in the biomedical engineering field have allowed the reconstruction of various parts of the human body using biomaterials.

Biomaterial is defined as a material, except drugs, of natural or synthetic origin, which can be used for a certain period of time, in order to treat, increase or replace any tissues, organs or functions of the human body in a biocompatible way, that is, without rejection [2]. Considering the biological response caused by biomaterials in body tissues, these can be classified into: bioinert, biotolerates, bioactive, resorbable [1, 3, 7].

Based on their chemical composition, they can be classified into: metallic, polymeric, ceramic or composites [1].

The biomaterial selection must take into account its physical, chemical and biomechanical properties. The main properties that must be taken into account are: mechanical strength, modulus of elasticity, flexion and torsion, fatigue resistance, corrosion susceptibility, roughness and permeability [3, 4]. Among these, metals are preferred biomaterials for orthopedic applications due to their higher mechanical properties [1–6].

Metals are widely used in orthopedic and neuromuscular stimulation areas. Orthopedic applications involve the use of biomaterial for the restoration or replacement of some part of the skeletal system. In neural stimulation, metallic biomaterials are used in an electronic system in order to provide

T. F. Bastos-Filho et al. (eds.), *XXVII Brazilian Congress on Biomedical Engineering*, IFMBE Proceedings 83, https://doi.org/10.1007/978-3-030-70601-2_29

electrical stimulation for tissues, which would otherwise be impossible due to the degree of tissue deterioration [4].

The development of biomaterials proves to be fundamentally important, in the sense that it provides an improvement in people's standard of living, represented by an increase in life expectancy, in general health and in the well-being of the population.

Many metals alloys have a thin oxide layer that provides corrosion protection. This is formed by a reaction of the metallic surface and the medium and is responsible for the passivation phenomenon. Failure in the passive film, often in a localized form, results in attack or localized corrosion that can occur as pits, crevices, under stress and associated with fatigue [7].

Although all metallic biomaterials currently used have well-characterized electrochemical properties, many manufacturing processes can alter the corrosion resistance of finished products [7, 8]. In addition, devices with complex shapes, with corners, edges, recesses, tips and other design irregularities, may have their resistance to localized corrosion affected [9–12]. Surface finishing steps, as well as surface marking, can cause increased susceptibility to localized corrosion due to surface changes [13–17].

Metallic implantable medical devices are subject to some markings in accordance with current standards; which aim to promote the traceability and after use identification. These markings become stress concentrators and places potentially subject to be the origin of failures that can lead to fracture; causing damage to passive layer and favoring the corrosion onset [7–17]. Degradation by corrosion or wear shortens an implantable medical device lifespan [17, 18].

This work aims to contribute to the knowledge dissemination in the areas of engineering and health. In this way, it is intended to present the effect of two different marking techniques, via laser beam or pantographic, on the resistance to pitting corrosion of metallic biomaterials specimens.

2 Materials and Methods

The starting material for this study was a cold-rolled ISO 5832-1 austenitic stainless steel sheet that was initially sanded in silicon carbide sieves up to 600 mesh and polished with diamond paste up to 3 μm, washed in acetone for 3 min on ultrasound, and rinsed in deionized water. Mechanical markings were performed using the pantographic process. The laser beam markings were performed using a Q-switched Nd: YAG laser equipment, pumped by nanosecond pulsed diode, with wavelength of 1064 nm, output power of 50 W, and power stability of 2%. The ratio marked length over total exposed area was the same for all marked specimens submitted to electrochemical characterization. It was engraved the numeral eight "8" with the same size on both methods.

Cyclic potentiodynamic technique was employed for electrochemical characterization, which, in addition to the pitting potential, makes it possible to determine the repassivation potential. The resulting density increases from the potential at which the polarization curve was lifted to a moment when a sudden increase occurs, a certain value is reached and the potential sweep direction is reversed. The repassivation potential corresponds to the potential where the downward curve crosses the axis of the electrode potentials.

The method is intentionally designed to achieve conditions that are sufficiently severe to cause the passive layer breakdown, which may not necessarily be found in vivo [19].

Cyclic potentiodynamic polarization tests were carried out in Gamry PCI4/300 potentiostat/galvanostat equipment. The electrolyte was a phosphate buffered saline solution (PBS), with a pH equal to 7.4, at 37 °C. The electrochemical arrangement was a glass flat cell with three electrodes, consisting of a working electrode with 1.0 cm^2 exposed area, a counter electrode (platinum wire with a 2.0 cm^2 geometric area) and an Ag/AgCl (3 M, KCl) reference electrode. At least ten tests were carried out for each condition, in order to ensure reproducibility.

Surface characterization was performed by scanning electron microscopy (SEM)—Philips XL30. The micrographs were obtained after the electrochemical tests, without the use of metallographic etching.

3 Results and Discussion

Cyclic potentiodynamic polarization curves for laser-marked and mechanically engraved ISO 5832-1 SS specimens are shown in Fig. 1. The as-polished material (without markings) was also tested for comparison. The curves represent the reproducible behavior obtained in the electrochemical test.

The marked specimens showed lower resistance to localized corrosion than the pristine specimens. This effect is due to the alteration, generated by the markings, in the surfaces finishing produced on this type of biomaterial. This result is accentuated in specimens with laser engravings [7, 8, 17].

The markings have produced discontinuities on the surfaces of the evaluated biomaterial. This fact explains the drop in corrosion resistance and can be identified by the pitting potentials shown in Fig. 1, which reached values in the order of 0.6 V for the laser beam marking conditions and 1.0 V for pantographic marking conditions.

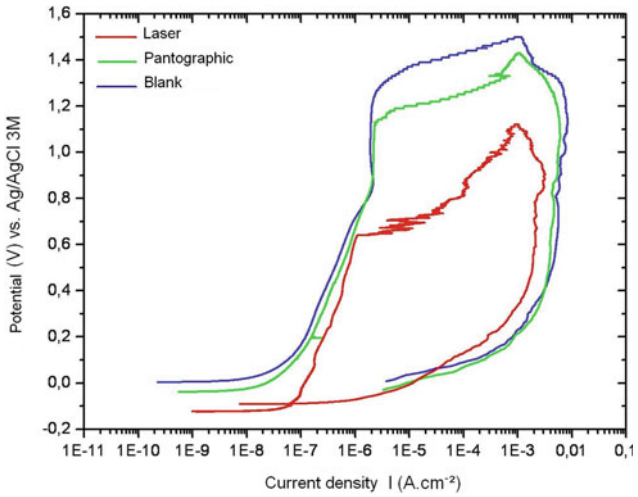

Fig. 1 Cyclic polarization curves for the ISO 5832-1 SS in three different surface finishing conditions

Knowledge of corrosion mechanisms is extremely important in the biomaterials field. Combined with biomechanical and biocompatibility tests, it enables safe use for biomedical purposes [20–25].

For comparison and better identification, all the presented images were captured in SEM - Philips XL30 equipment, using secondary electrons mode, with the same magnifications, namely: 50x and 200x magnitude for both types of marking. The specimens with laser marks are shown in Figs. 2, 3 and 4, and the samples with mechanical marks, in the images of Figs. 5, 6 and 7. All images were obtained after cyclic polarization tests.

Scanning electron microscopy (SEM) was used to characterize the corrosion morphology obtained after the corrosion test. Clearly, pits associated with marked regions can be observed on the evaluated surfaces. In some specimens treated by laser beam, crevice corrosion was also found,

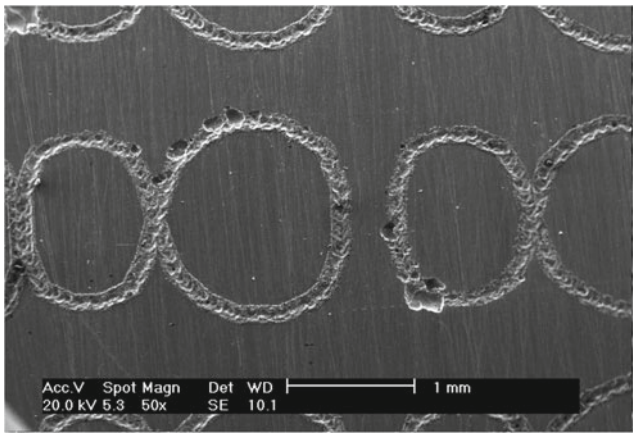

Fig. 2 SEM image of pits at the laser marked region biomaterial specimen, after electrochemical test

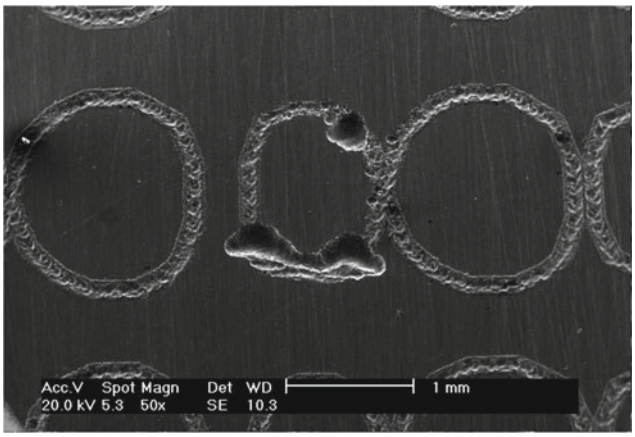

Fig. 3 SEM image for laser treated surface, after electrochemical test. Emergence of pits and crevices are shown

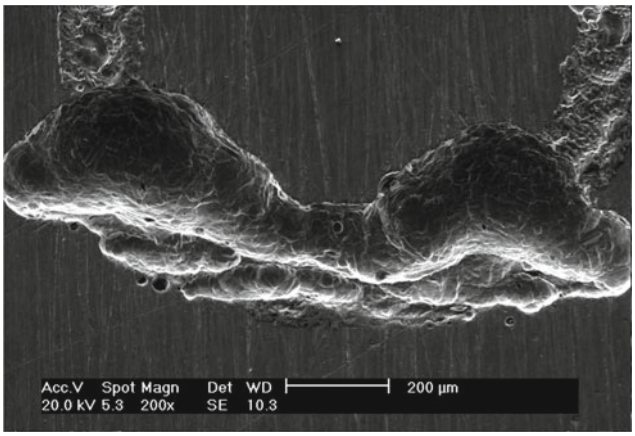

Fig. 4 Crevice magnification for Fig. 3 at the laser marking ring

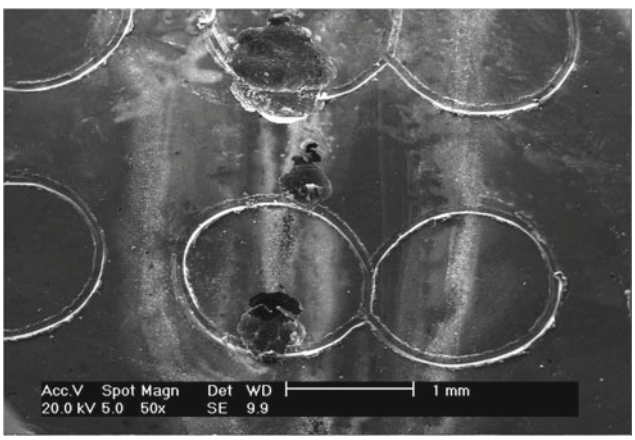

Fig. 5 SEM image of pantographic marked specimen, after electrochemical test, showing pits in the engravings

which is caused by differential aeration. The appearance of crevice corrosion mechanism in laser marked specimens can be explained by the topography changes generated by the

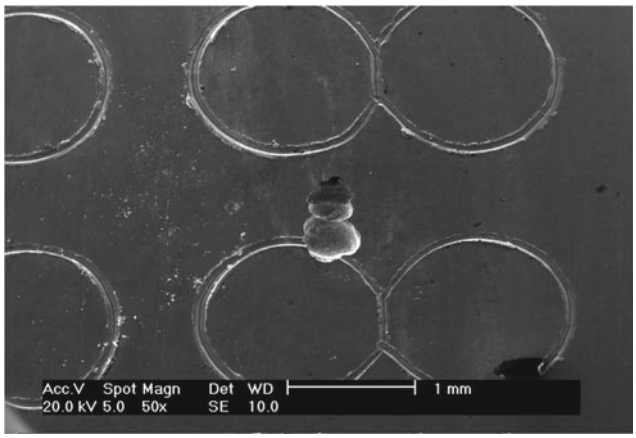

Fig. 6 Image obtained by scanning electron microscopy (SEM) for a biomaterial with pantographic markings, after electrochemical test, showing a pit located at the engraving

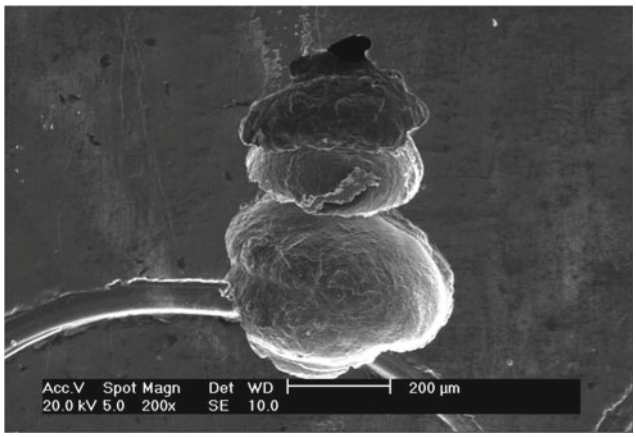

Fig. 7 Magnification of a corrosion pit found in the region of the pantographic marked ring

coherent laser beam, which produced protuberance and grooved regions on the surfaces [7, 17].

The differences in surface finish between the two marking conditions are apparent. In the case of pantographically marked specimens, the finish is smoother, as there was only the removal of material using a mechanical tool. In the case of laser-marked specimens, the resulting finish, in the engraving region, has a much rougher appearance, since localized fusion of the biomaterial's metallic surface occurs, followed by extremely fast solidification.

The markings consisted of numerical characters generated on ISO 5832-1 SS specimens. In Fig. 2, corrosion pits around laser markings are observed. Note the rough appearance produced by the laser pulses.

Figure 3 shows pitting and crevice corrosion on the laser marked biomaterial surface. The pits are identified as "holes" with more circular shapes, at the top of the central engraving shown in this figure; and the crevice, like a large and irregular crater, at the bottom of the same character in this figure. The crevice is more evident at higher magnification, as shown in Fig. 4. The difference in the relief imposed by the laser beam incidence induced this type of corrosion degradation. Inside this crevice, it is possible to notice the aggressiveness caused by the laser conditions, as the microstructure was revealed and some SS grains were pulled out.

The roughness produced by the laser beam pulses caused changes in the topography of the samples, forming regions of peaks, valleys, recesses, protuberances, and essentially anodic places with differential aeration [7, 16, 25].

Corrosion pits formed on the markings produced by the pantographic method are observed in Fig. 5. The less rough appearance generated by the pantograph in the marking is noted. In the mechanical process, material is removed in order to produce the desired image on the surface. In this technique, the pits are also formed in the places with markings, however not as many pits as in laser process were found.

In Fig. 5, pits of different sizes and rounded shapes are shown, associated with the marking rings; that is, despite the "smoother" appearance produced on the surfaces by the pantograph, the markings constitute discontinuities and become regions prone to initiation of localized corrosion attack.

In Fig. 6, an arising pit on a ring marked by mechanical technique is shown, as highlighted in the central region. In this micrograph, the association of the beginning of the pitting corrosion mechanism with the marking area is evident. The sudden change in the surface finish is a decisive factor for starting the corrosion process, which propagates autocatalytically. Figure 7 presents an enlargement of the pit shown in Fig. 6. The ring engraving constitutes a discontinuity in the surface finish for the biomaterials specimens. These two types of processing for identification cause topographic changes. In this sense, the roughness analysis produced by these techniques will be evaluated later and presented in future works.

In this study, it was evident that the two types of markings evaluated produced a deleterious effect on the localized corrosion resistance. The decrease in corrosion resistance was more accentuated by laser beam-treated specimens. This is due to the temperatures reached by the beam, which are sufficient to melt the surface and the rapid extraction of heat from them, explained by the duration of each pulse, which is in the order of nanoseconds.

The laser beam incidence sites, in addition, have greater roughness, become essentially anodic zones [7, 8, 16], which favors the onset of corrosion processes.

The need to present qualitative results and to evaluate aspects of identification of visual alterations on the biomaterials surfaces is important because it supports the results obtained through the electrochemical techniques with accelerated tests.

According to the ABNT NBR 15613-2: 2010 standard, the tests must be accelerated to obtain responses in a timely manner, which would otherwise be impractical by conventional techniques, since, by immersion it would imply a loss of negligible mass.

The fact that the result of the biomaterial is compared with itself enables a paired analysis. There is no point in comparing with other types of biomaterials with different natures, and the comparison with other metallic alloys should consider biocompatibility, biofunction, physical, chemical and metallurgical characteristics, properties, type of processing, performance, applications, cost and market availability.

4 Conclusions

The markings evaluated in this work represent discontinuities on the biomaterials surfaces. Electrochemical tests indicate that the pitting corrosion mechanism is accentuated in samples with laser marks, and less accentuated in samples with pantographic marks. Regions with crevice corrosion were observed in the laser marked specimens, explained by the differential aeration resulting from the topographic alteration generated by the laser beam.

Conflict of Interest The authors declare that they have no conflict of interest.

References

1. Lyman DJ, Seare WJ Jr (1974) Biomedical materials in surgery. Mater Sci 4:415–433
2. Williams DF (1976) Corrosion of implant materials. Mater Sci 6:237–266
3. Gibbons DF (1975) Biomedical materials. Bioph Bioeng 4:367–375
4. Hench LL (1975) Prosthetic implant materials. Mater Sci 5:279–300
5. Anderson JM (2001) Biological response to materials. Mater Res 31:81–110
6. Im GI (2020) Biomaterials in orthopaedics: the past and future with immune modulation. Biomat Res 24:1–4
7. Pieretti EF (2012) Efeito da marcação na resistência à corrosão de implantes ortopédicos produzidos em aço inoxidável ABNT NBR ISO 5832-1. Instituto de Pesquisas Energéticas e Nucleares-Universidade de São Paulo, São Paulo
8. Pieretti EF (2016) Biomecânica aplicada na avaliação de propriedades de implantes ortopédicos metálicos tratados por feixe laser. Instituto de Pesquisas Energéticas e Nucleares- Universidade de São Paulo, São Paulo
9. Hakiki NE, Belo MC, Simões AMP, Ferreira MGS (1998) Semiconducting properties of passive films formed on stainless steels. J Electrochem Soc 145:3821–3829
10. Pieretti EF, Neves MDM (2017) Laser marked and textured biomaterial evaluated by mott-schottky technique. Int J Electrochem Sci 12:9204–9211
11. Pieretti EF, Neves MDM (2016) Influence of laser marks on the electrochemical behaviour of the ASTM F139 stainless steel for biomedical application. Int J Electrochem Sci 11:3532–3543
12. Pieretti EF, Costa I, Marques RA, Leivas TP, Neves MDM (2014) Electrochemical study of a laser marked biomaterial in albumin solution. Int J Electrochem Sci 9:3828–3836
13. Pieretti EF, Palatnic RP, Leivas TP, Costa I, Neves MDM (2014) Evaluation of laser marked ASTM F 139 stainless steel in phosphate buffer solution with albumin. Int J Electrochem Sci 9:2435–2444
14. Pieretti EF, Pessine EJ, Correa OV, Rossi W, Neves MDM (2015) Effect of laser parameters on the corrosion resistance of the ASTM F139 stainless steel. Int J Electrochem Sci 10:1221–1232
15. Manhabosco SM, Santos AP, Marcolin ML, Pieretti EF, Neves MDM, Dick LFP (2016) Localized corrosion of laser marked M340 martensitic stainless steel for biomedical applications studied by the scanning vibrating electrode technique under polarization. Electrochim Acta 200:189–196
16. Pieretti EF, Manhabosco SM, Dick LFP, Hinder S, Costa I (2014) Localized corrosion evaluation of the ASTM F139 stainless steel marked by laser using scanning vibrating electrode technique, X-ray photoelectron spectroscopy and Mott-Schottky techniques. Electrochim Acta 124:150–155
17. Pieretti EF, Costa I (2013) Surface characterisation of ASTM F139 stainless steel marked by laser and mechanical techniques. Electrochim Acta 114:838–843
18. Pieretti EF, Antunes RA, Neves MDM (2019) Tribological evaluation of an optical fiber laser marked stainless steel for biomedical applications. In: IFMBE proceedings 70/1-Springer Nature, XXVI brazilian congress on biomedical engineering, Búzios-RJ, Brazil, 2018
19. ABNT NBR 15613-2: 2010, Implantes para cirurgia—Resistência à corrosão Parte 2: Determinação de suscetibilidade à corrosão de pequenos componentes—Medida de polarização potenciodinâmica cíclica
20. Marques RA, Rogero SO, Terada M, Pieretti EF, Costa I (2014) Localized corrosion resistance and citotoxicity evaluation of ferritic stainless steels for use in implantable dental devices with magnetic connections. Int J Electrochem Sci 9:1340–1354
21. Pieretti EF, Cozza RC, Neves MDM (2016) Biotribological behaviour evaluation of the ISO 5832-1 stainless steel for biomedical applications treated by optical fiber laser. In: 3rd International conference on biotribology delegate programme booklet, ICoBT, London, UK, 2016, pp 44
22. Pieretti EF, Baratela FJC, Higa OZ, Wilcken JTS, Cozza RC, Leivas TP, Neves MDM (2014) Biotribological behaviour and cytotoxicity evaluation of laser and mechanically marked biomaterial. In: 2nd International conference on biotribology, delegate programme booklet, ICoBT, Toronto, Canada, 2014
23. Pieretti EF, Marques RA, Wilcken JTS, Cozza RC, Neves MDM (2014) Dental tribology evaluation of ferritic stainless steels for magnetic implants. In: 2nd International conference on biotribology, delegate programme booklet, ICoBT, Toronto, Canada, 2014
24. Pieretti EF, Cozza RC, Leivas TP, Rossi W, Neves MDM (2014) Wear of femtosecond laser treated ASTM F 138 stainless steels for orthopaedic applications. In: 2nd International conference on biotribology, delegate programme booklet, ICoBT, Toronto, Canada, 2014
25. Dick LFP, Marcolin ML, Manhabosco SM, Santos AP, Pieretti EF, Neves MDM (2015) Localized corrosion of laser marked M340 martensitic steel for biomedical applications. In: EMCR Proceedings of 11th international symposium on electrochemical methods in corrosion research, Tróia, Portugal, 2015

Mechanical and Morphological Analysis of Electrospun Poly(ε-Caprolactone) and Reduced Graphene Oxide Scaffolds for Tissue Engineering

M. J. S. Maizato, H. T. T. Oyama, A. A. Y. Kakoi, and I. A. Cestari

Abstract

Electrospinning has been widely applied to obtain nanofiber based biomaterials to be used as scaffolds in tissue engineering. The aim of this work is to obtain and characterize membranes of a composite material obtained by electrospinning of Poly(ε-caprolactone) (PCL) combined with reduced graphene oxide (rGO) 0.05% (PCLrGO005) and 0.5% (PCLrGO05) concentrations. Besides rGO concentration, the influence of electrospinning parameters was investigated (PCLrGO005M). The mechanical behavior of the new materials was studied considering the mechanical tensile test according to the ASTM D638 standard. Surface qualitative analysis was done by measuring fiber diameter using scanning microscopy. Four different membranes were obtained by random electrospinning using two needles and 5 mL volume solution at 18 kV, 15 cm needle distance and 0.033 mL/min flow rate or modified parameters of 15 kV, 10 cm needle distance and 0.012 mL/min flow rate. The modulus of elasticity, maximum load, tensile stress and strain were obtained for all membranes and analyzed by ANOVA. The morphological surface analysis of the scaffolds showed that the nanomaterial scaffolds of PCL and rGO with good mechanical properties and uniform surface morphology can be obtained by careful adjustments of electrospinning process parameters.

Keywords

Electrospinning • Graphene oxide • Nanofiber • Poly (ε-caprolactone) • Mechanical properties

1 Introduction

Electrospinning is a technique for producing fibers with diameters on a nanometer scale (nanofibers). This technology is considered a powerful tool because it is simple, inexpensive and versatile and important for the manufacture of products or structures that depend on the high surface area [1, 2]. Electrospinning has been used successfully in several areas: biotechnology, pharmaceutical, environmental engineering, medicine and tissue engineering.

The electrospinning system consists of three main components: a high voltage source, a syringe with a capillary and a grounded collector (usually a metal plate or rotating mandrel). It is possible to use polymers as a solution when completely dissolved in specific solvents, forming a polymeric solution. The solution is introduced into the syringe, being submitted to an electric field, where an electric charge is induced on its surface and this field forms the Taylor Cone. When the electric field reaches a critical value, the electrical forces overcome the surface tension and a jet of solution is ejected from the Taylor cone towards the grounded collector. As it travels between the capillary tip and the collector, the solvent evaporates, and only the polymer is collected [3].

Electrospinning can be done with random or aligned deposition. When the deposition is aligned on a preferential axis, the membrane formed is considered anisotropic and when the deposition is random, the membrane formed is considered isotropic. In the present work PCL membranes were produced by electrospinning adding reduced Graphene as reinforcement material and using a random deposition technique for producing scaffolds for tissue engineering applications.

Poly(ε-caprolactone) (PCL) is a biodegradable plastic obtained from petroleum derivatives. It is a semi crystalline polymer with a melting point of 58–60 °C, low viscosity and easy processability at room temperature [4]; the short chain PCL is amorphous and correspondingly soft and gummy.

M. J. S. Maizato (✉) · H. T. T. Oyama · A. A. Y. Kakoi · I. A. Cestari
Laboratório de Bioengenharia do Instituto do Coração, Hospital das Clinicas HCFMUSP, Faculdade de Medicina, Universidade de Sao Paulo, Sao Paulo, Brazil
e-mail: marina.maizato@incor.usp.br

T. F. Bastos-Filho et al. (eds.), *XXVII Brazilian Congress on Biomedical Engineering*, IFMBE Proceedings 83, https://doi.org/10.1007/978-3-030-70601-2_30

PCL is highly soluble and combines well with other plastics, adhering well to a large number of surfaces. Compared to other biopolymers it is simpler to obtain and non-toxic. It has been approved by the Food and Drug Administration (FDA) for specific applications used in contact with the body, such as devices for drug delivery and suture threads [5].

Graphene is the name given to a flat monolayer of carbon atoms linked together, with hybridization in sp^2, forming a two-dimensional network, with a honeycomb structure, being the basis for other carbon-based nanomaterials [6, 7]. This material has received large interest due to its excellent physical-chemical, mechanical, thermal, electrical and optical properties. Graphene Oxide (GO) is a structure derived from graphene basically constituted by hydroxyl, epoxide and carboxylate groups connected to the graphene sheets, giving an amphiphilic character, with its edges predominantly hydrophilic and its basal plane predominantly hydrophobic, dispersing in water [8]. Chemically it is easily functionalized, but it has high electrical resistance. The chemical reduction of GO may be used as a means to improve its electrical conductivity [9] which is especially important when this material is used as a substrate in cardiac and neuronal tissue engineering applications.

Reduced Graphene Oxide (rGO), unlike GO, has in its structure much of the sp^2 conjugated carbon restored, which improves its electrical conductivity [9].

This work presents a preliminary study of the mechanical characteristics of nanomaterial membranes obtained with PCL and a combination of PCL and rGO in concentrations of 0.05 and 0.5%.

2 Materials and Methods

2.1 Electrospinning Solutions

PCL (CAPA®6406, Solvay, Brazil) and rGO (C2312 rGOB007/Pw1, Graphenea, Spain) were solubilized in Chloroform (Sigma Aldrich, Brazil) and N, N Dimethylformamide (Sigma Aldrich, Brazil) at 9:1 ratio.

Electrospinning solutions were prepared using solute and solvent concentration by weight. Electrospinning solution of PCL membrane was made with 15% of PCL. Composite membranes used 15% of PCL and two concentrations of rGO: 0.05% for composite (PCLrGO005) and (PCLrGO005M) and 0.5% rGO for (PCLrGO05).

2.2 Preparation of Membranes by Electrospinning

Membranes were prepared using a vertical electrospinning set up. For each membrane 5 mL volume spin solution was used at room temperature 23 °C, 55% of relative humidity, using two needles.

Two conditions were used for preparation of membranes: (i) electrospinning voltage of 18 kV with needle distance of 15 cm and 0.033 mL/min flow rate, to make membranes PCL, PCLrGO005 and PCLrGO05. (ii) 15 kV voltage, 10 cm needles distance and 0.012 mL/min flow rate for PCLrGO005M.

2.3 Mechanical Testing

Mechanical tensile tests were performed using standard test equipment (Instron 3365, USA) and its data analysis tool (Bluehill 3 software). Tests were carried out according to the ASTM D638 standard [10], at 10 mm/min speed, with 100 N load cell. Accordingly, 5 specimens were tested for each assay using the PCL membranes and composites obtained by random electrospinning which were considered isotropic materials.

Specimens were prepared for mechanical tensile tests to determine modulus of elasticity, maximum load, tensile at maximum load, tensile at break, strain at maximum load. A size V cutting knife [10] was used to prepare the specimens cut in random directions. Sample thickness was measured using a 0.01 mm accuracy thickness gauge (Starret, model 1015MA, Brazil.) Each assay was repeated three times.

2.4 Qualitative Morphological Evaluation

Scanning Electron Microscopy (SEM) images were obtained (Hitachi TM3000 MEV equipment, Japan), to compare surface homogeneity of the membranes. The characterization of the surface allows the adjustment of electrospinning parameters in order to obtain adequate mechanical and surface characteristics.

A patch of each membrane was selected and the diameters of 180 nanofibers were measured using a software ZEN 2.3 (blue edition, Carl Zeiss, Germany) to determine the average diameter of the fibers for each membrane.

2.5 Statistical Analysis

Statistical analysis was performed by ANOVA and statistical difference was considered for $p < 0.05$ (Sigma Plot, Systat Software Inc., USA).

3 Results and Discussion

Figure 1 shows typical stress vs. strain curves obtained for the nanomaterial membranes. Figure 2 presents the mechanical tensile test results considering the modulus of elasticity (E); maximum load (max load); tensile stress at maximum load (σ max), tensile stress at break (σ rup) and strain at maximum load (strain). Significant differences are indicated in the figure.

The strain at maximum load is shown in Fig. 2. As seen, strain is increased when adding rGO at 0.05% concentration but using higher concentration of rGO (0.5% rGO) resulted in decreased strain.

Figure 3 shows the micrographs of the electrospun membranes. The images allow qualitatively observation of the diameter of the nanofibers, the spatial distribution and the interstices.

Table 1 presents the diameters of the fibers quantified on the surface of the membranes. It is known that the diameter of the electrodeposited fibers affects the mechanical, electrical and optical properties and as such it is one of the most important parameters. The diameter can be influenced by the electrical conductivity of the solution, the strength of the electric field and the flow rate utilized. The use of high conductivity solutions may produce reduced diameters and, on the other hand, fibers of larger diameter can be produced using high electrical voltage that causes more fluid to be ejected during the electrospinning process. Electrical voltage also influences bead formation which can be minimized when the surface tension is balanced with the electrostatic repulsion forces added to the viscoelastic solution [11, 12].

We observed that a limitation of the method utilized is the difficulty of controlling membrane thickness and fiber diameter as it can be seen by the large standard deviations shown in (Fig. 2).

SEM surface morphology analysis show that electrospun membranes (PCLGO005M) obtained with 15 kV, 10 cm needles distance and 0.012 mL/min flow rate presented improved uniformity.

Milleret and cols [13], showed that in small caliber vascular grafts made with poly(lactic-co-glycolic acid) (PLGA)

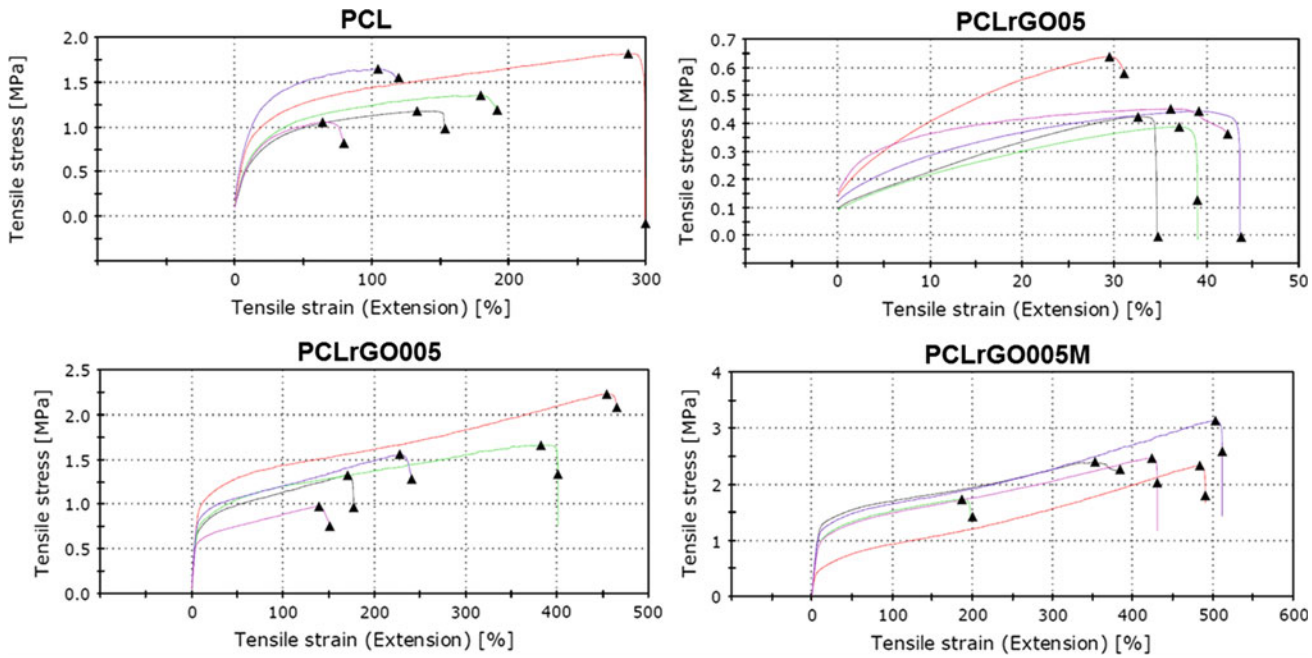

Fig. 1 Typical stress vs strain curves for the nanomaterial membranes studied Poly(ε-caprolactone) (PCL) and adding reduced graphene at 0.5% concentration oxide (rGO) (PCLrGO05) and 0.05% (PCLrGO005) and modified electrospinning parameters with 0.05% rGO (PCLrGO005M)

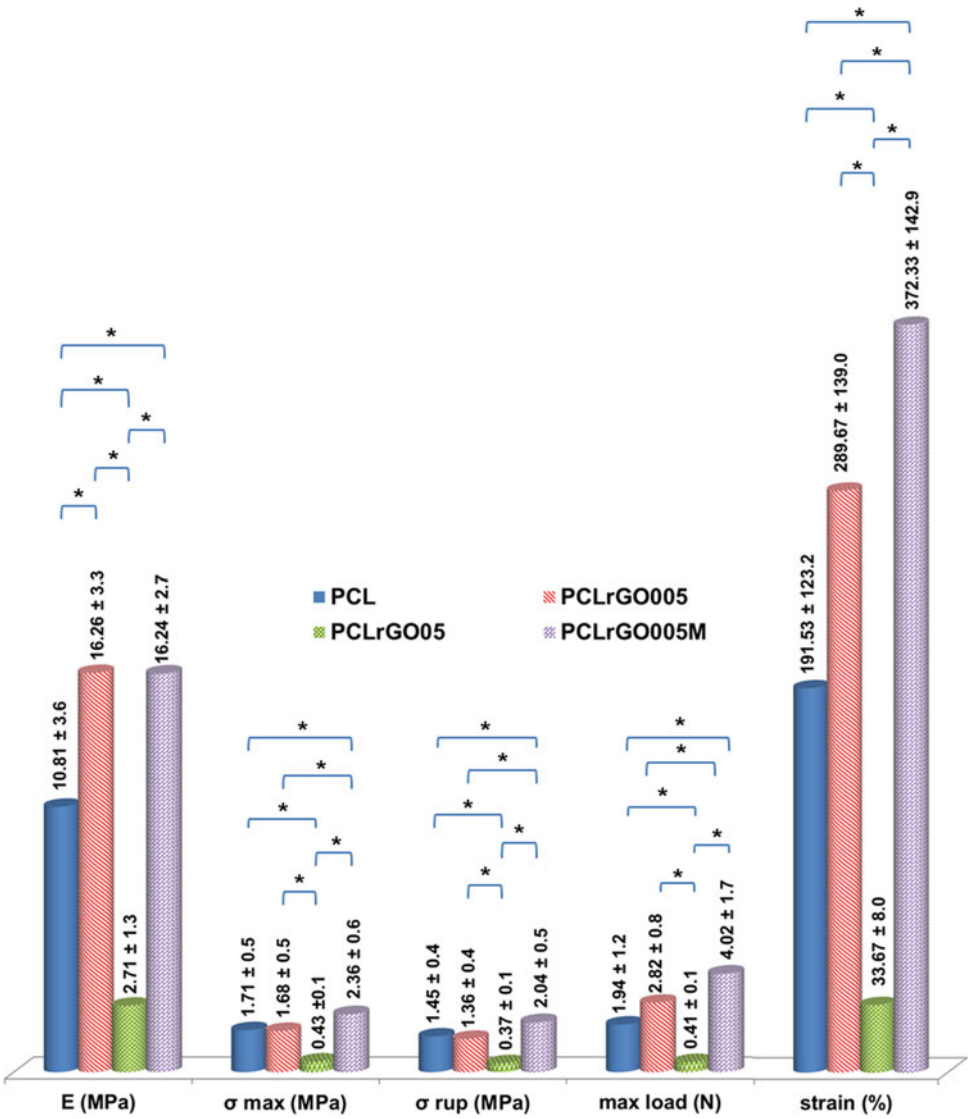

Fig. 2 Results of the tensile test shows the results of the mean and standard deviation of the modulus of elasticity (E); tensile stress at maximum load (σ max), tensile stress at break (σ rup), maximum load (max load) and strain at maximum load (strain) for nanomaterial membranes studied Poly(ε-caprolactone) (PCL) and adding 0.5% reduced graphene oxide (rGO) (PCLrGO05) or 0.05% (PCLrGO005) and for modified electrospinning parameters (PCLrGO005M). The significant differences in the statistical study are pointed in the figure

electrospun fibrous scaffolds fibers smaller than 1 μm induced less activation of coagulation and platelet adhesion, when compared to larger diameters. Also, it has been shown that surface topography can influence cell growth and alignment [14].

The result of the ANOVA statistical analysis for mechanical tensile test is presented in Fig. 2 and statistical differences ($p < 0.05$) are marked (*) for all membranes.

Statistical analysis of the fiber diameters on the surface of the membranes was performed using ANOVA. Fiber diameters were different for all membranes produced ($p < 0.05$).

4 Conclusions

Adjusting electrospinning parameters influence the characteristics of the fibers obtained. We found that reduced graphene oxide may be used to improve mechanical performance of PCL membranes in combination with adjustments in the electrospinning process. In our work a combination of voltage, distance from the needles from the plate and the flow rate may resulted in uniform scaffolds of PCL using reduced graphene oxide at 0.05% concentration (PCLrGO005M membranes).

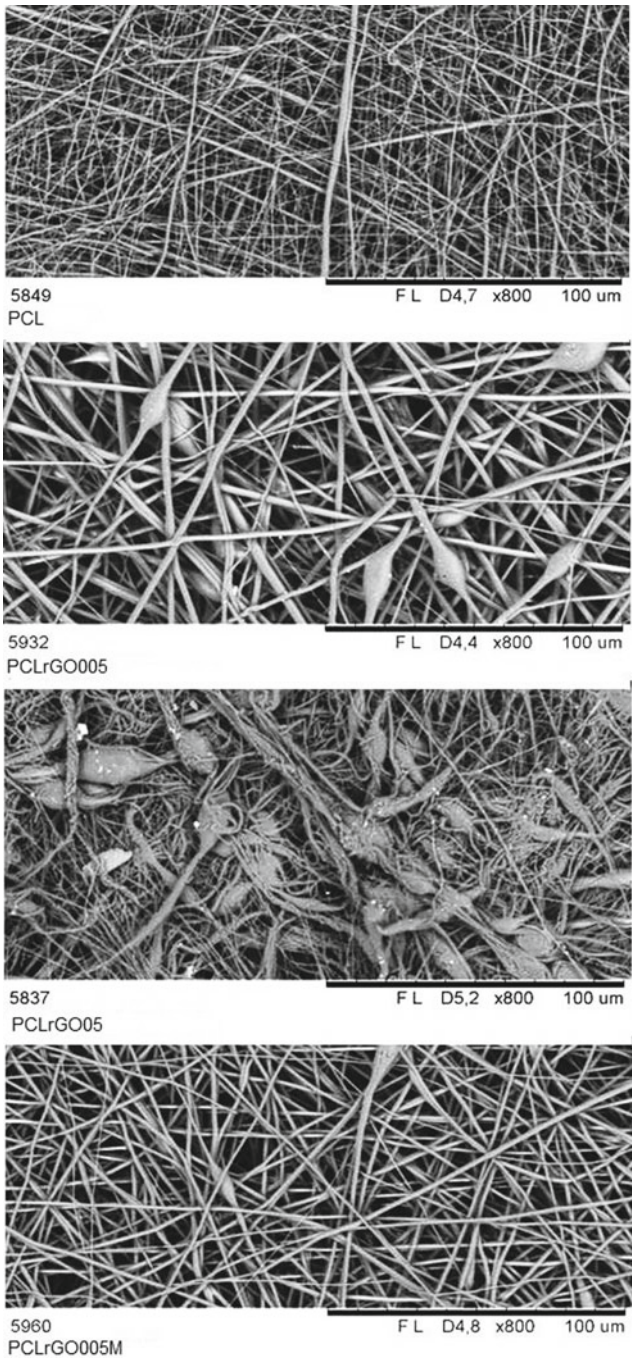

Fig. 3 Images of surfaces micrographs of electrospinning scaffolds prepared with PCL, PCLrGO005, PCLrGO05 and PCLrGO005M

Table 1 Fiber diameters (mean) and standard deviation (STD) obtained for the membranes studied

Material	Diameter (nm)	STD (nm)
PCL	656	300
PCLrGO005	1582	690
PCLrGO05	842	310
PCLrGO005M	1290	370

The addition of reduced graphene oxide to PCL combined with adequate electrospinning processing conditions resulted in scaffolds with good morphological and mechanical properties which are desired properties for tissue engineering scaffolds.

Acknowledgements The authors thank the National Council for Scientific and Research Development–CNPq (Grant 2017/20994-1 and FINEP (1253/13).

Conflict of Interest All authors declare no conflict of interest.

References

1. Liu H, Ding X, Zhou G, Li P, Wei X, Fan Y (2013) Review article: Electrospinning of nanofibers for tissue engineering applications. J Nanomaterials. https://doi.org/10.1155/2013/495708
2. Khorshidi S, Solouk A, Mirzadeh H, Mazinani S, Lagaron JM, Sharifi S, Ramakrishna S (2016) A review of key challenges of electrospun scaffolds for tissue-engineering applications. J Tissue Eng Regen Med 10:715–738
3. Bhardwaj N, Kundu SC (2010) Electrospinning: a fascinating fiber fabrication technique. Biotechnol Adv 28:325–347
4. Solvay chemicals material safety data sheet (2007)
5. Azimi B, Nourpanah P, Rabiee M, Arbab S (2014) Poly (ε-caprolactone) fiber: an overview. J Eng Fiber Fabrics V9(3): 74–90. http://wwwjeffjournal.org
6. Geim AK, Novoselov KS (2007) The rise of graphene. Nat Mater 6:183–191
7. Shih CJ, Paulus GLC, Wang QH et al (2012) Understanding surfactant/graphene interactions using a graphene field effect transistor: relating molecular structure to hysteresis and carrier mobility. Langmuir 28(22):8579–8586
8. Shah R, Kauser A, Muhammad B, Shah S. (2015) Progression from graphene and graphene oxide to high performance polymer-based nanocomposite: a review. Polym-Plast Technol Eng 54(2):173–183
9. Pei S, Cheng HM (2012) The reduction of graphene oxide. Carbon 50:3210–3228
10. ASTM D638 (2014) standard test method for tensile properties of plastics
11. Calíope PB (2009) Caracterização de nanofibras através de técnicas de processamento de imagens. Tese de doutorado depositado na Escola Politécnica da USP, 150p
12. Kwon K, Kiodai S, Matsuda T (2005) Electrospun nano to microfiber fabrics made of biodegradable copolyesters: structural characteristics, mechanical properties and cell adhesion potential. Biomaterial 27(18):3929–3939
13. Milleret V, Hefti T, Hall H, Vogel V, Eberli D (2012) Influence of the fiber diameter and surface roughness of electrospun vascular graft on blood activation. Acta Biomater 8:4349–4356
14. Cortella LRX, Cestari IA, Guenther D, Lasagni AF, Cestari IN (2017) Endothelial cell responses to castor oil-based polyurethane substrates functionalized by direct laser ablation. Biomed Mater 12

Experimental Apparatus for Evaluation of Calcium Fluctuations in Cardiomyocytes Derived from Human-Induced Pluripotent Stem Cells

M. C. Araña, R. D. Lahuerta, L. R. X. Cortella, M. Mazzetto, M. Soldera, A. F. Lasagni, I. N. Cestari, and I. A. Cestari

Abstract

In this work, we developed and tested an experimental apparatus to evaluate calcium fluctuations in cardiomyocytes derived from human-induced pluripotent stem cells (hiPSC-CM). The set-up is composed of a signal module for registration and analysis of the signals and a perfusion chamber. This chamber allows the maintenance of the cells, control of perfusion and temperature, and electric stimulation. The signal module consists of a CCD camera attached to a fluorescence microscope with the appropriate software and hardware for eliciting and recording fluorescent signals originating from hiPSC-CM intracellular Ca^{+2} concentration changes, under electrical stimulation. We employed this system for analysis of calcium fluctuation from hiPSC-CM cultivated on micro textured polyethylene terephthalate surfaces.

Keywords

Calcium fluctuations • hiPSC-CM • Experimental apparatus • Fluorescence • Surface microtopography

M. C. Araña · R. D. Lahuerta · L. R. X. Cortella · M. Mazzetto · I. N. Cestari (✉) · I. A. Cestari
Bioengineering Department, Heart Institute—HCFMUSP, São Paulo, Brazil
e-mail: icestari@incor.usp.br

M. C. Araña
Physics Department, UFSCar, São Carlos, Brazil

M. Soldera · A. F. Lasagni
Institute for Manufacturing Technology, Technische Universität Dresden, Dresden, Germany

M. Soldera
PROBIEN-CONICET, Dto. de Electrotecnia, Universidad Nacional Del Comahue, Neuquén, Argentina

A. F. Lasagni
Fraunhofer-Institut Für Werkstoff- und Strahltechnik IWS, Dresden, Germany

1 Introduction

According to the World Health Organization (WHO), cardiovascular diseases are the main cause of morbidity and mortality in the twenty-first century [1]. More than 300 thousand deaths related to cardiovascular diseases occur yearly in Brazil [2]. Cardiomyocytes are the most abundant cell type in the heart. These cells are responsible for cardiac contraction, acting as a pump, and generating systemic arterial pressure. They have high metabolic activity and are sensitive to hypoxia, making these cells susceptible to injury during an acute myocardial infarct. Adult cardiomyocytes are entirely differentiated cells and present low regenerating capacity, accomplishing limited tissue renovation in case of injuries, stimulating the search for cell replacement therapies [3].

Induced pluripotent stem cells (iPSCs) were reported for the first time in 2006 from mice experiments [3]. They are reprogrammed cells with features similar to embryonic stem cells, such as the capacity of self-renewal and differentiation into many cell types, including cardiac myocytes. hiPSCs were established in a similar way to mouse iPSCs by introduction of a set of transcription factors. The generation hiPSC-CM was first reported using embryoid bodies with media containing serum, but the efficiency was only 5–10% [3]. Since then, several groups have introduced technical improvements to increase generation efficiency. However, hiPSC-CM are phenotypically immature and resemble cardiac myocytes in the embryonic state. Immature cardiac myocytes show less-organized sarcomeric structures and calcium handling machinery. Consequently, multiple studies in tissue engineering have looked for ideal conditions for hiPSC-CM maturation, aiming at the substitution of affected tissues in case of injuries [4–6]. Some of these studies have reported the use of 2D and 3D supports, called scaffolds, which favor their growth and maintenance in conditions that mimic native tissues. Recent works have shown that topographies produced using micro-nano laser structuring techniques [7] may support cellular growth [8].

T. F. Bastos-Filho et al. (eds.), *XXVII Brazilian Congress on Biomedical Engineering*, IFMBE Proceedings 83, https://doi.org/10.1007/978-3-030-70601-2_31

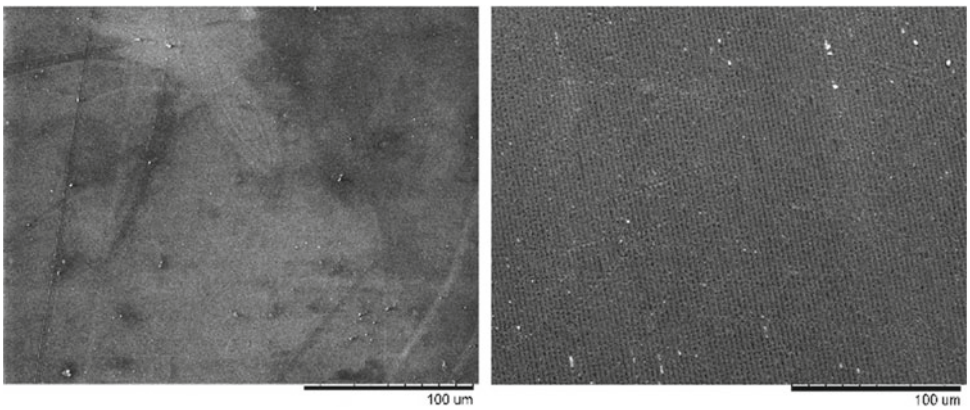

Fig. 1 Unmodified polyethylene terephthalate foil (left) and line-like patterns with a spatial period of 3.0 μm fabricated in PET foil by laser ablation and hot embossing (right)

One technique to investigate myocyte maturation is to characterize their calcium transients using fluorescent intracellular Ca^{2+} indicators (Ca_i^{2+}) such as the green-emitting fluorophore Fluo-4 AM [9, 10]. The objective of this work was to develop an experimental apparatus for recording and analyzing hiPSC-CM intracellular calcium fluctuation and test this experimental set-up to study hiPSC-CM response to surface topographies consisting on periodic line-like patterns fabricated with polyethylene terephthalate (PET) foils by laser ablation and hot embossing.

2 Materials and Methods

The experimental set-up is composed of a cell reservoir where we placed hiPSC-CM (PluriCell Biotech®, São Paulo, Brazil) after labeling with the fluorophore Fluo-4 AM (Life Technologies, USA) and a module for signal registration, processing, and analysis. The reservoir allows for the control of perfusion, temperature, and electric stimulation. The signal module is composed of a CCD camera attached to an inverted microscope equipped with an epifluorescence illuminator and appropriate filters. Fluorescent signals from Ca^{2+} fluctuations were detected by the camera and sent via a data script written in Python, which automatically generates a fluorescent intensity graph displaying the relative fluorescence of the sample as a function of time. The analysis of the obtained curves, such as rising and decay time, reveals intrinsic properties of the calcium fluctuations that may correlate to cell maturation.

2.1 PET and Micro-Textured PET

The Roll-to-Roll hot embossing (R2R) technique consists of a hot metal cylinder containing an external sleeve with microstructures fabricated using the direct laser interference patterning (DLIP) method. After pressing the sleeve against a running PET foil, the microstructures are transferred to the polymer. It was shown that this technique can efficiently produce line-like patterns with spatial periods from 1 to 5.5 μm [7] and that the resulting topographies can induce endothelial cell morphology [8]. Nickel sleeves with a thickness of 200 μm, 300 mm wide, and 300 mm diameter (Saechsische Walzengravur GmbH, Germany) were structured by DLIP using a solid-state ps-laser with 1064 nm laser wavelength (Edgewave PX200, Germany) and a pulse duration of 10 ps. Line-like structures with a spatial period of 3.0 μm (Fig. 1) were produced employing a pulse-to-pulse feed of 40 μm, a spot diameter of 190 μm, and a single pulse laser fluence of 0.56 J/cm^2. To obtain a hydrophobic surface on the nickel sleeve and avoid sticking of the polymeric foil [11], the sleeve was covered with a self-assembled monolayer (SAM) based on phosphonic acid derivatives (1H,1H,2H,2H-perfluoro-n-decylphosphonic acid and 1H,1H,2H,2H-perfluoro-noctylphosphonic acid dissolved in isopropanol with a molar concentration of 2 mmol/L). After the immersion during 1 h in this solution, the sleeve was rinsed with isopropanol and dried in an oven at 150 °C for 10 min.

2.2 hiPSC-CM Culture and Plating

hiPSCs were purchased from Pluricell Biotech (São Paulo, Brazil) and cultivated following the manufacturer's instructions. Cells were plated at 15th day of differentiation on a 24-well plate (Sarstedt®) previously coated with extracellular matrix (Geltrex®, Thermo Fisher) at a density of 1.37×10^5 cm^2 and cultured at 37 °C and 5% CO_2 with RPMI (Thermo Fisher) with plating medium supplement (PluriCardio® PMS). The culture medium was replaced by RPMI containing maintenance medium supplement (PluriCardio® MMS) every 24 h. At the 19th day of differentiation cells were harvested from 24-well plate with 0.35% trypsin/EDTA solution (Gibco) and seeded on sterilized control unmodified and micro-textured PET coated with extracellular matrix (Geltrex®, Thermo Fisher) at a density of 1.7×10^4 cm^2 inside a 96-well microplate (Sarstedt®).

Culture medium was replaced with RPMI containing MMS every 24 h. Experimental groups were defined as follows: (a) unmodified PET (control) and (b) PET-L3 (line-like pattern featuring spatial period of 3 μm). Cultures were used after 48 h of the final platting step.

2.3 Loading of Fluorescent Indicator

Cells were loaded with Fluo-4 AM (Life Technologies®, USA) following the manufacturer's protocol [12]. Briefly, the culture medium in the wells was gently aspirated and the loading solution containing Hank's balanced salt solution (HBSS), 5.0 μM Fluo-4 AM, 0.02% of non-ionic detergent Pluronic F127, 20 mM HEPES and 2.5 mM of Probenecid was added to each well. Plates were incubated for 45 min at 37 °C and 5% CO_2 before the loading solution was aspirated and replaced by the reading solution containing HBSS, 20 mM HEPES and 2.5 mM Probenecid. Before being passed to the cell maintenance reservoir, cells were incubated for 30 min at 37 °C and 5% CO_2 to allow the de-esterification of AM esters.

3 Results and Discussion

3.1 Cell Chamber

The experimental cell chamber developed (Fig. 2) was able to maintain the temperature at 36.5 ± 0.5 °C. Electrical stimulation was stable throughout the experiment and implemented using a modified C-Stim Chamber System (IonOptix®, USA). Platinum electrodes were connected to a MyoPacer Stimulator (IonOptix®, Milton, USA) allowing access to the most diverse pulse configurations, such as polarity, amplitude, duration and frequency. Also, the chamber provides perfusion with a laminar flow of up to 30 μL/s. Temperature control in the cell chamber was possible through a PET substrate coated with a conductive indium tin oxide (ITO) film (60 Ω/cm^2, Sigma-Aldrich, St. Louis, MO, USA). Two copper plates connected to a voltage source were attached with conductive glue to the ITO film, allowing the passage of electrical current in the substrate and consequently the release of heat by the Joule effect. Thus, by controlling the current flow through the ITO film with voltage source, it was possible to control the temperature of the solution in the chamber. The system was calibrated using a thermistor, making it possible to correlate the current and temperature of the solution. An opening was made in the conductive ITO film, in the size of PET discs in which the cells were plated, so that the ITO film would not filter the fluorescent light. A steel support was built in the dimensions of the well to prevent floating of the PET and PET-L3 disc.

3.2 Module for Registration and Analysis of the Signals

For data collection, the modified well containing Fluo4 AM labelled hiPSC-CM was placed under an inverted microscope (TM300, Nikon, Japan) equipped with a mercury arc lamp. Fluo-4 absorption/emission peaks are 494/506 nm, and signal visualization was possible using an appropriate filter set to isolate the green light coming from labelled cells. The fluorescent light signal was captured by a RTE/CCD-1300-Y/HS camera (Princeton Instruments, USA) attached to the microscope. The camera's temporal resolution may be adjusted by changing the exposure time and the number of pixels. For these experiments, 64 × 64 pixels with × 2 binning and an exposure time of 20 ms were used and resulted in a resolution of 50 frames per second (fps). For faster phenomena, such as voltage analysis, 100 fps may be employed using 16 × 16 pixels and × 4 binning.

The MicroMAX Controller (Princeton Instruments, USA) connected to the camera transmitted the signal to the

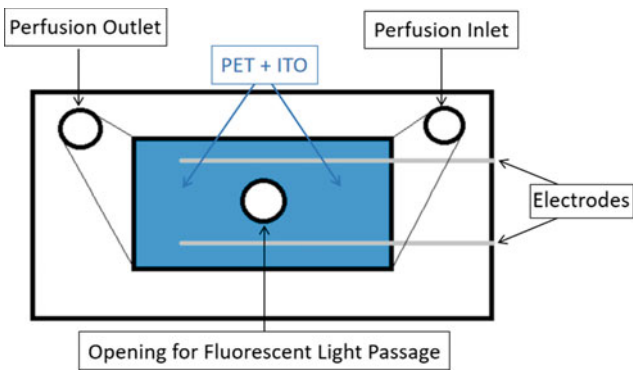

Fig. 2 Drawing of the cell chamber (not in scale)

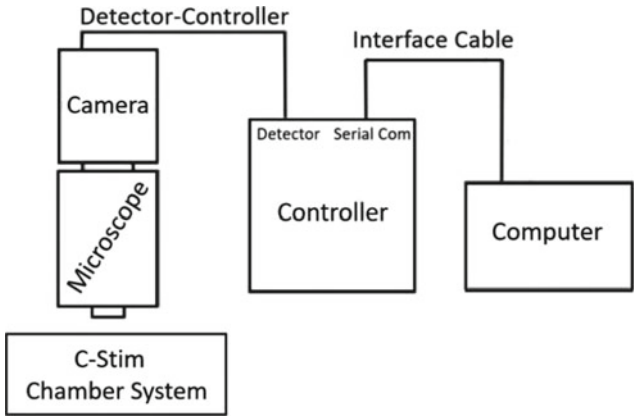

Fig. 3 Schematic representation of the experimental set-up

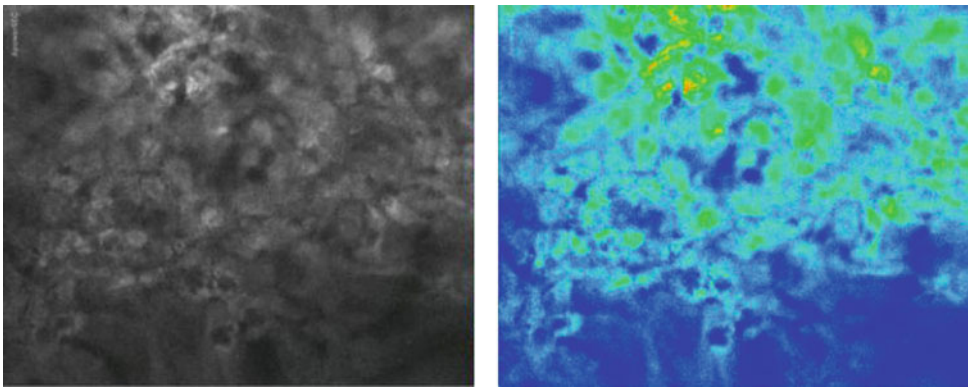

Fig. 4 Image collected with the CCD sensor in experiment with hiPSC-CM spontaneously contracting in unmodified PET (left) and visual map of the field made by WinView/32 software (right)

computer, which has the WinView/32 software (Princeton Instruments, USA), as shown in Fig. 3. WinView/32 is a software used for the post-processing of data obtained through the camera (CCD) and controller, capable of generating visual maps of light intensity (Fig. 4). For the analysis, information about the exposure times of the CCD sensor, compensation, and the average light intensity in each pixel are necessary to obtain a sequence of frames that will compose the video.

In order to automate and improve the post-processing of the obtained signals, a script was implemented in the Python 3.5 programming language [13] to read binary files (SPE 2.x format with experiment data) using scientific analysis libraries Numpy and Matplotlib [14, 15]. This implementation allows the combination with specific scientific computing libraries of filtering [16] and computer vision [17]. In this way, it was possible to map the luminous intensity levels in each pixel of each frame captured by the camera. This generates graphs of the luminous intensity variation in the time domain (Fig. 5) allowing the analysis of the free intracellular calcium dynamics in the cells. The graph is composed of 3 curves automatically generated by the script which aids in the data interpretation: the blue curve (Ca_i^{2+}) is the average light intensity in each of the frames, the dashed curves are the standard deviation curve plus the Ca_i^{2+} curve (UPP, in orange) and the standard deviation subtracted from the Ca_i^{2+} curve (LWR, in green).

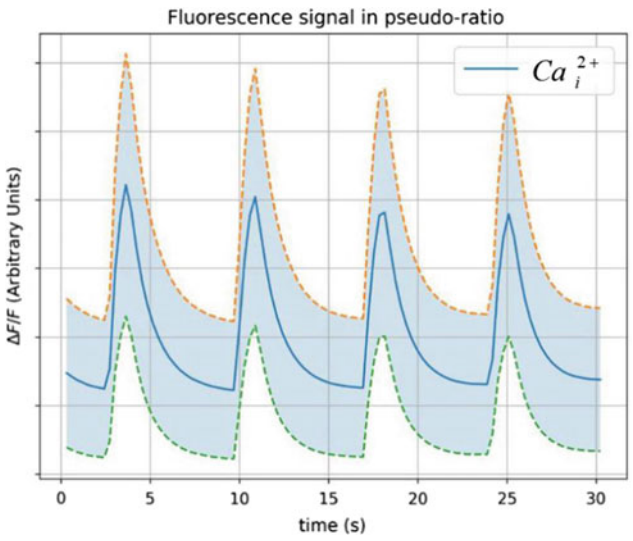

Fig. 5 Average levels of luminous intensity in each pixel of each frame captured at 50 frames per second in experiment with hiPSC-CM spontaneously contracting in PET-L3 as a function of time

4 Conclusions

The developed experimental apparatus allowed the recording of the intracellular calcium fluctuations of hiPSC-CM under electrical stimulation, temperature control and constant perfusion of the recording solution. Fluorescent signals were recorded with adequate time resolution, and post-processing with the implemented script automatically generated luminous intensity graph in the time domain. In this way, the reservoir for cell maintenance, together with the module for registration and analysis of the signals, are an efficient set-up for the study of Ca^{2+} fluorescent signals from hiPSC-CM which was used to study their response to surface microtopography.

Acknowledgements This work was supported by São Paulo Research Foundation (FAPESP, grant 2012/50283-6), the National Council for Scientific and Research Development (CNPq, grants 467270/2014-7 and 311191/2017-7) and the Brazilian Innovation Agency (FINEP, grant 1253). Funded by the European Regional Development Fund (ERDF) and co-financed under taxation on the basis of the budget adopted by the members of the Saxon State Parliament. M.S. acknowledges the Alexander von Humboldt Foundation.

References

1. WHO—The top 10 causes of death at https://www.who.int/news-room/fact-sheets/detail/the-top-10-causes-of-death
2. SBC at http://www.cardiometro.com.br/

3. Yoshida Y, Yamanaka S et al (2017) Induced pluripotent stem cells 10 years later: for cardiac applications. Circ Res 120:1958–1968. https://doi.org/10.1161/CIRCRESAHA.117.311080
4. Kofron CM, Mende U et al (2017) In vitro models of the cardiac microenvironment to study myocyte and non-myocyte crosstalk: bioinspired approaches beyond the polystyrene dish. J Physiol 12:3891–3905. https://doi.org/10.1113/JP273100
5. Chen Y, Zeng D et al (2015) Three-dimensional poly-(e-caprolactone) nanofibrous scaffolds directly promote the cardiomyocyte differentiation of murine-induced pluripotent stem cells through Wnt/B-catenin signaling. BMC Cell Biol 16:1–13. https://doi.org/10.1186/s12860-015-0067-3
6. Ghosh LD, Jain A et al (2018) Elucidating molecular events underlying topography mediated cardiomyogenesis of stem cells on 3D nanofibrous scaffolds. Mater Sci Eng C 88:104–114. https://doi.org/10.1016/J.msec.2018.03.012
7. Rank A, Lang V, Lasagni AF et al (2017) High-Speed roll-to-roll hot embossing of micrometer and sub micrometer structures using seamless direct laser interference patterning treated sleeves. Adv Eng Mater 19(11):1700201. https://doi.org/10.1002/adem.201700201
8. Cortella LRX et al (2017) Endothelial cell responses to castor oil-based polyurethane substrates functionalized by direct laser ablation. Biomed Mater 12(6): https://doi.org/10.1088/1748-605X/aa8353
9. Itzhaki I, Rapoport S et al (2011) Calcium handling in human induced pluripotent stem cell derived cardiomyocytes. PLoS ONE 6(4): https://doi.org/10.1371/journal.pone.0018037
10. Sharma A, Marceau C, Hamaguchi R et al (2014) Human induced pluripotent stem cell-derived cardiomyocytes as an in vitro model for coxsackievirus B3-induced myocarditis and antiviral drug screening platform. Circ Res 115(6):556–566. https://doi.org/10.1161/CIRCRESAHA.115.303810
11. Leitgeb M et al (2016) Multilength scale patterning of functional layers by roll-to-roll ultraviolet-light-assisted nanoimprint lithography. ACS Nano 10(5):4926–4941. https://doi.org/10.1021/acsnano.5b07411
12. FLUO-4 new calcuim assay kits (F36205, F36206) at https://tools.lifetechnologies.com/content/sfs/manuals/mp36205.pdf
13. Rossum GV, Drake F (2009) Python 3 reference manual. CreateSpace, Scotts Valley, CA
14. Van der Walt S, Colbert SC, Varoquaux G et al (2011) The NumPy array: a structure for efficient numerical computation. Comput Sci Eng 13:22–30. https://doi.org/10.1109/MCSE.2011.37
15. Hunter JD et al (2007) Matplotlib: a 2D graphics environment. Comput Sci Eng 9:90–95. https://doi.org/10.1109/MCSE.2007.55
16. Virtanen P, Gommers R, Oliphant TE et al (2020) SciPy 1.0: fundamental algorithms for scientific computing in python. Nat Methods 17:261–272. https://doi.org/10.1038/s41592-019-0686-2
17. Bradski G et al (2000) The OpenCV library. Dr Dobb's J Softw Tools 25:120–125

Cytotoxicity of Alumina and Calcium Hexaluminate: Test Conditions

R. Arbex, L. R. Rezende, F. N. Ambrosio, L. M. M. Costa, and C. B. Lombello

Abstract

Tissue Engineering involves the proposal for tissue repair using biomaterials: materials used in biomedical applications in order to regenerate tissues or restore their functions. To verify the viability of biomaterials, one must consider their biological performance, that is, their interaction with the organism, including properties related to biofunctionality and biocompatibility. Initial biocompatibility tests are carried out with cytotoxicity evaluation. However, although the test conditions for cytotoxicity tests are standardized, some studies present divergent data regarding the cytotoxicity of biomaterials. Sample preparation conditions and test conditions can directly affect the results. The objective of the present work is to evaluate different cytotoxicity conditions of alumina (Al_2O_3) and calcium hexaluminate (CA_6) samples as a function of the variables: sample washing conditions, sample size and total test time. The biomaterial samples were positioned on a Vero cell confluent monolayer. In order to verify cell morphology, it was used inverted microscopy with phase contrast. The results indicate that both alumina and washed alumina are viable and non-cytotoxic. The hexaluminate presented slight cytotoxicity, in different experimental conditions.

Keywords

Biomaterials • Cell culture techniques • Materials tests

1 Introduction

Tissue Engineering aims to restore the function of tissues impaired by disease or trauma, using different biomaterials, implantation of cells and biologically active molecules [1]. Its development led to the concept that cells, tissues, organs and systems could be regenerated, restructured and rehabilitated.

In this context, the concept of biomaterial is defined as "any substance or combination of substances, except drugs, of natural or synthetic origin, which can be used during any period of time, as part or as systems that treat, increase or replace any tissues, organs or body functions" [2]. Therefore, the development and application of biomaterials demands extreme care to achieve safety and efficacy of use.

To verify the viability of biomaterials, one must consider their biological performance, that is, their interaction with the organism, including properties related to biofunctionality and biocompatibility [3, 4].

Biofunctionality is evaluated according to the physical, chemical and biological properties performed by the biomaterial in a specific function and determined time, once in the organism [5, 6].

Biocompatibility is defined as the capacity of the biomaterial to induce an appropriate response in the host in a specific application [2, 4].

Alumina (Al_2O_3) biomaterials show biomechanical properties that allow its use in articulations, as prosthesis recovering, bone substitutes and dental implants [7]. This ceramic shows hardness, low friction coefficient, wear resistance and corrosion resistance that makes it suitable for the mentioned applications [8]. The cell adhesion to these biomaterials can be compared to hydroxyapatite [9, 10].

R. Arbex (✉) · C. B. Lombello
Center for Engineering, Modeling and Applied Social Sciences (CECS), Federal University of ABC (UFABC), São Bernardo do Campo, SP, Brazil
e-mail: raquel.arbex@aluno.ufabc.edu.br

L. R. Rezende · F. N. Ambrosio
Center for Natural and Human Sciences (CCNH), Federal University of ABC (UFABC), São Bernardo do Campo, SP, Brazil

L. M. M. Costa
Federal University of Alagoas (UFAL), Maceió, AL, Brazil

T. F. Bastos-Filho et al. (eds.), *XXVII Brazilian Congress on Biomedical Engineering*, IFMBE Proceedings 83, https://doi.org/10.1007/978-3-030-70601-2_32

The toxicity of alumina is dependent on biomaterial surface morphology and site of implantation, leading to specific body response. Alumina biocompatibility is still an area of research viewing medical device improvement [7]. Other biomaterials may be associated with alumina to improve some characteristics, including the biological response. Calcium hexaluminate (CA_6) is a new material that shows promising characteristics for biomedical use, but with few data on biological response [11, 12].

Determining biocompatibility is fundamental to evaluate the biological response to the biomaterial considering the homeostasis. Biocompatibility tests begin with the cytotoxicity assays, using *in vitro* cellular models, due to the methodology used and the objectivity of the results [13–16].

The objective of this study is to evaluate the different cytotoxicity conditions of samples of alumina and calcium hexaluminate materials. The conditions of washing the samples, size, and test time were evaluated, in order to establish the effect on previous preparation on cytotoxicity response.

2 Materials and Methods

2.1 Biomaterials

The biomaterials were made with samples of alumina (Al_2O_3) and calcium hexaluminate (CA_6). They were produced from different precursors, calcinated alumin (99,8% Al_2O_3, A1000SG, Almatis, USA), calcium carbonate (99% $CaCO_3$, Vetec, Brazil) and calcium hydroxide (98% Ca $(OH)_2$, Synth, Brazil) through sintering reactions at 1500 °C. Calcium hexaluminate used, in a first system, alumina and calcium carbonate ($CaCO_3$). In a second system, the precursors were alumina and calcium aluminate cement (CAC). Both alumina and calcium hexaluminate were submitted to sterilization by gamma radiation (45 kGy) for cell culture assays.

The biomaterials samples differential preparation included: previous washing (in PBS during 3 days, solution daily changed), and size (considering the standards recommendation, and it was also tested half and double sized samples). The third protocol variation referred to culture time: 24, 48 and 72 h.

2.2 FTIR

Fourier Transform Infrared Spectroscopy (FTIR) in absorbance mode was made on sterile and non-sterile samples of alumina and calcium hexaluminate, ranging from 700 to 1100 cm^{-1} (Frontier, PerkinElmer).

2.3 Surface Morphological Analysis

The biomaterials surface morphology analyses were made with scanning electron microscopy (SEM) (FEI, Quanta 250).

2.4 Vero Cell Culture

The Vero cell lineage (CCIAL 057), cited by cytotoxicity standards [9] was used in these experiments [16], cultured in HAM F10 medium, with 10% fetal bovine serum (FCS) and 10 μg/mL penicillin/streptomycin, at 37 °C with 5% CO_2.

As control for the experiments, the ideal culture conditions were considered negative control and 0.25% phenol in the culture medium was used as positive control, considering the cytotoxicity analyzes of the extracts.

2.5 Qualitative Analyses: Cell Morphology

The qualitative cytotoxicity was evaluated by morphological analysis, with an inverted microscopy, with phase contrast (Axiovert A1, Zeiss). The analisis were made after 24, 48 and 72 h.

The 72 h cultures, and size assay cultures, were fixed with 2.5% glutaraldehyde, in buffer (pH 7.4) for 30 min and stained with methylene blue for the morphological evaluation.

3 Results and Discussions

Alumina, or aluminum oxide (Al_2O_3), is an inert material. The most common crystalline form (α-Al_2O) is known as curundum. Alumina can be used as a ceramic biomaterial in prostheses and surgical devices mainly related to support or substitute bone structures [17, 18]. It also can be used for controlled release of hormones, vaccines and medications [19]. Other ceramic biomaterials are widely used in biomedical applications, but the development of new biomaterials, with adequate mechanical properties, resorption and biocompatibility, is an important area of research. In this context we can mention the calcium hexaluminate (CA_6) that can be used as a thermal insulator in the aerospace and steel industries. This ceramic is not largely explored for clinical uses, although it can be an alternative to fibrous ceramic materials [20]. The FTIR showed that the sterilization did not alter biomaterials structure (Fig. 1) and the peaks at the region of 600–800 cm^{-1} were preserved. These peaks are common for bonds between metal and oxygen atoms [21, 22].

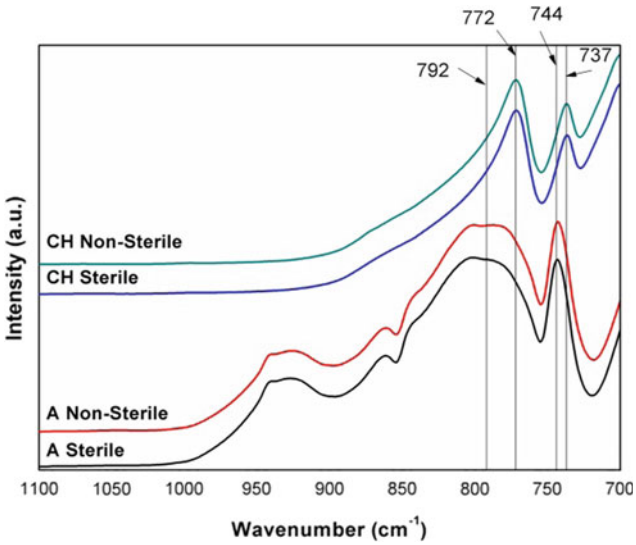

Fig. 1 FTIR analysis of (A) alumina and (CH) calcium hexaluminate sterile and non-sterile

The scanning electron microscopy (SEM) analysis showed that the sterilization method also did not alter biomaterials structure (Fig. 2).

The cytotoxic evaluation of calcium hexaluminate, in comparison with alumina biomaterial samples, was carried out in order to determine the safety of its clinical use, with cell Vero lineage (Fig. 3). The cytotoxicity analysis of the biomaterials is based on the morphological pattern comparison to the controls [13, 14].

It was observed that the cells cultivated for 24 h in the presence of alumina formed a confluent cell monolayer, and cells with typical, polygonal, morphology (Fig. 4). The washing procedure of the biomaterials did not result in a significant difference in cell morphology. The observations characterized the alumina as non-cytotoxic biomaterial (Fig. 4b, c). Calcium hexaluminate dissolved partially in the culture medium and interfered with cell monolayer formation (Fig. 4) that did not reach confluence, and cell morphology was altered in the presence of the biomaterial (Fig. 4e). The washing procedure minimized debris presence in culture, but cell morphology was altered (Fig. 4f).

The cytotoxicity results were maintained for 48 h assay (Fig. 5). The cells that came into contact with the alumina maintained the morphology, the cell monolayer showed greater confluence, that is, the cells continue to proliferate with no significant difference to the washed samples. The calcium hexaluminate appears to have continuously

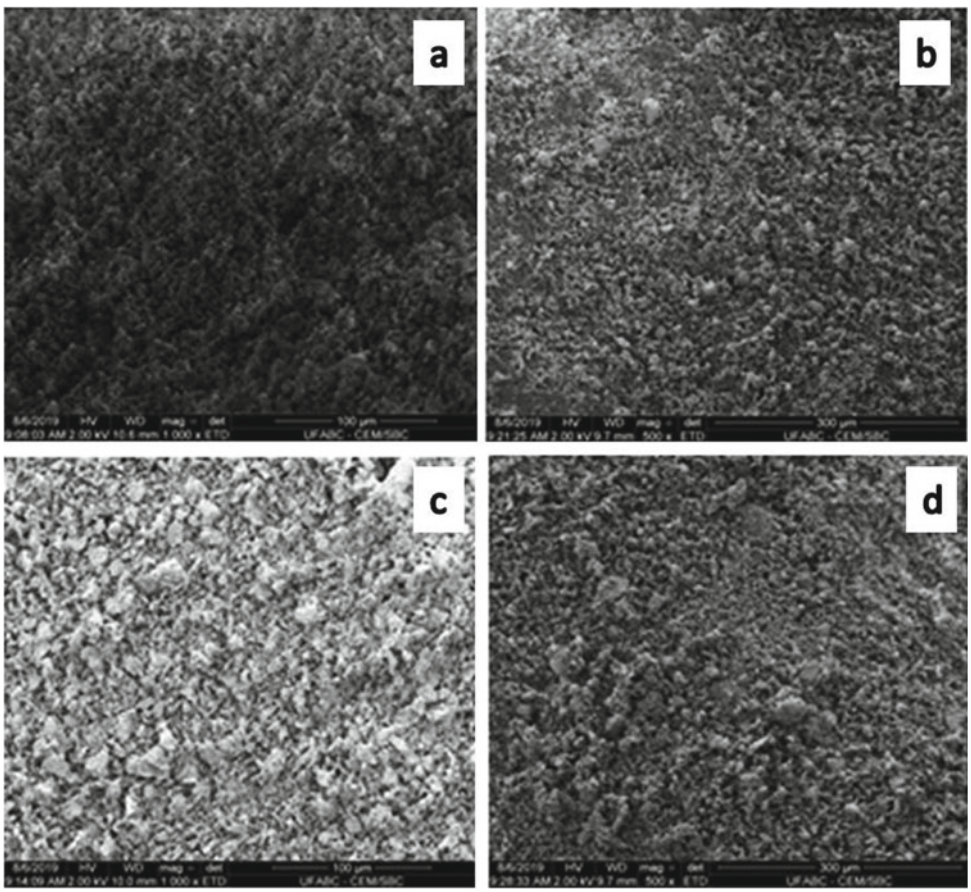

Fig. 2 SEM of alumina (**a**, **b**) and calcium hexaluminate (**c**, **d**), before (**a**, **c**) and after (**b**, **d**) sterilization

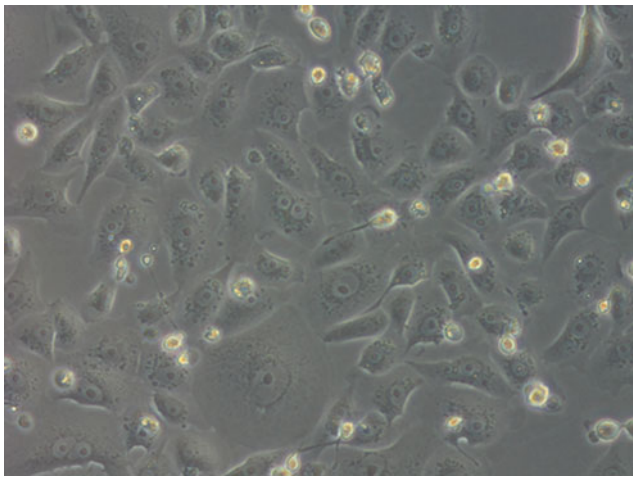

Fig. 3 Vero cell culture, normal morphology,confluent monolayer. Observation:400x

dissolved in culture medium, and few cells were observed. However, these few cells have characteristic morphology for the lineage, with a predominantly elongated cytoplasm. The calcium hemalumiate debris difficult cell monolayer formation, but within 48 h the remaining cell recovered the morphological aspect of non-citotoxicity.

After 72 h (Fig. 6), it can be observed that the cell monolayer on the negative control is completely confluent, indicative of cell proliferation, and the cells maintain the characteristic morphology for the lineage, however the presence of cells in suspension begins to show the inhibition by contact. The cells in contact with alumina organized a semi-confluent monolayer, and showed characteristic morphology for the lineage. But in contact with calcium hexaluminate there were observed very few cells, however recovering the characteristic morphology for the lineage.

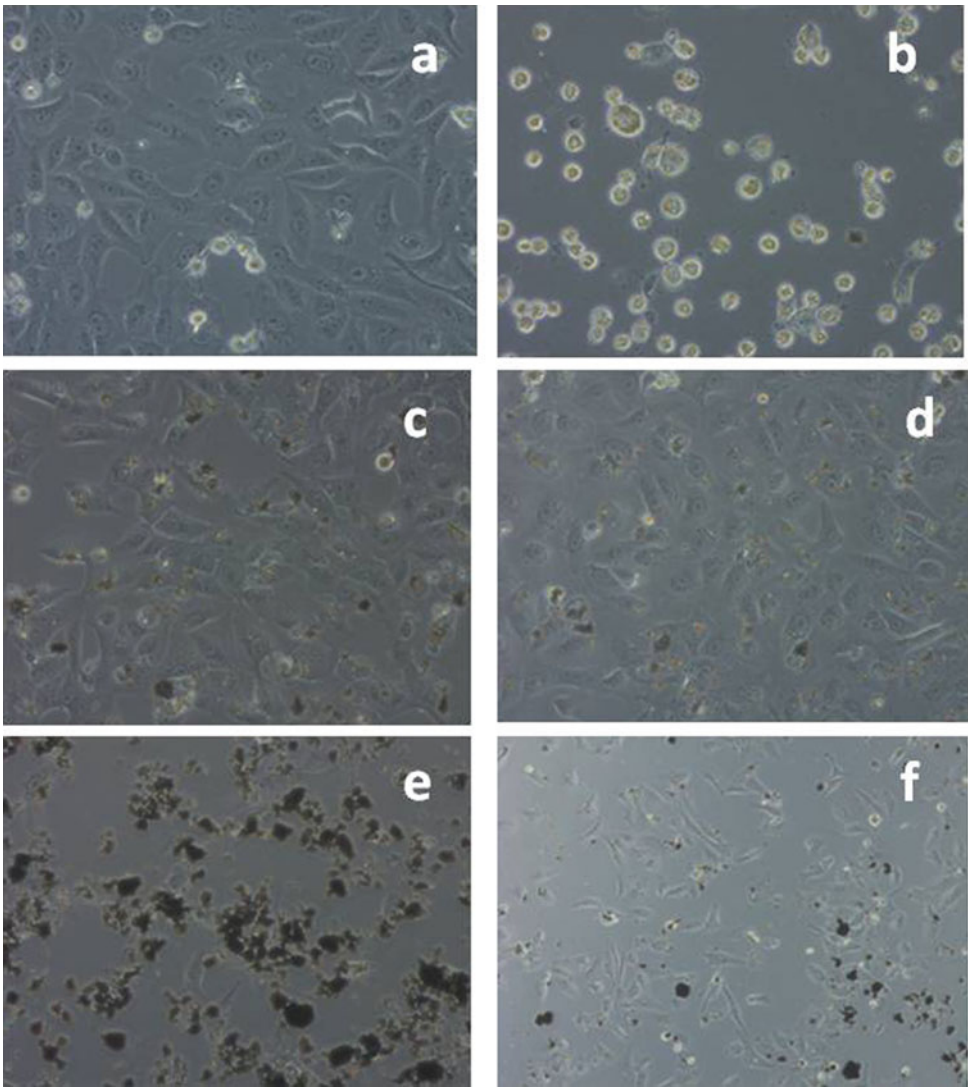

Fig. 4 Vero cell cytotoxicity assay, 24 h. **a** negative control; **b** positive control; **c** alumina; **d** washed alumina; **e** calcium hexaluminate; **f** washed calcium hexaluminate. Observation:200x

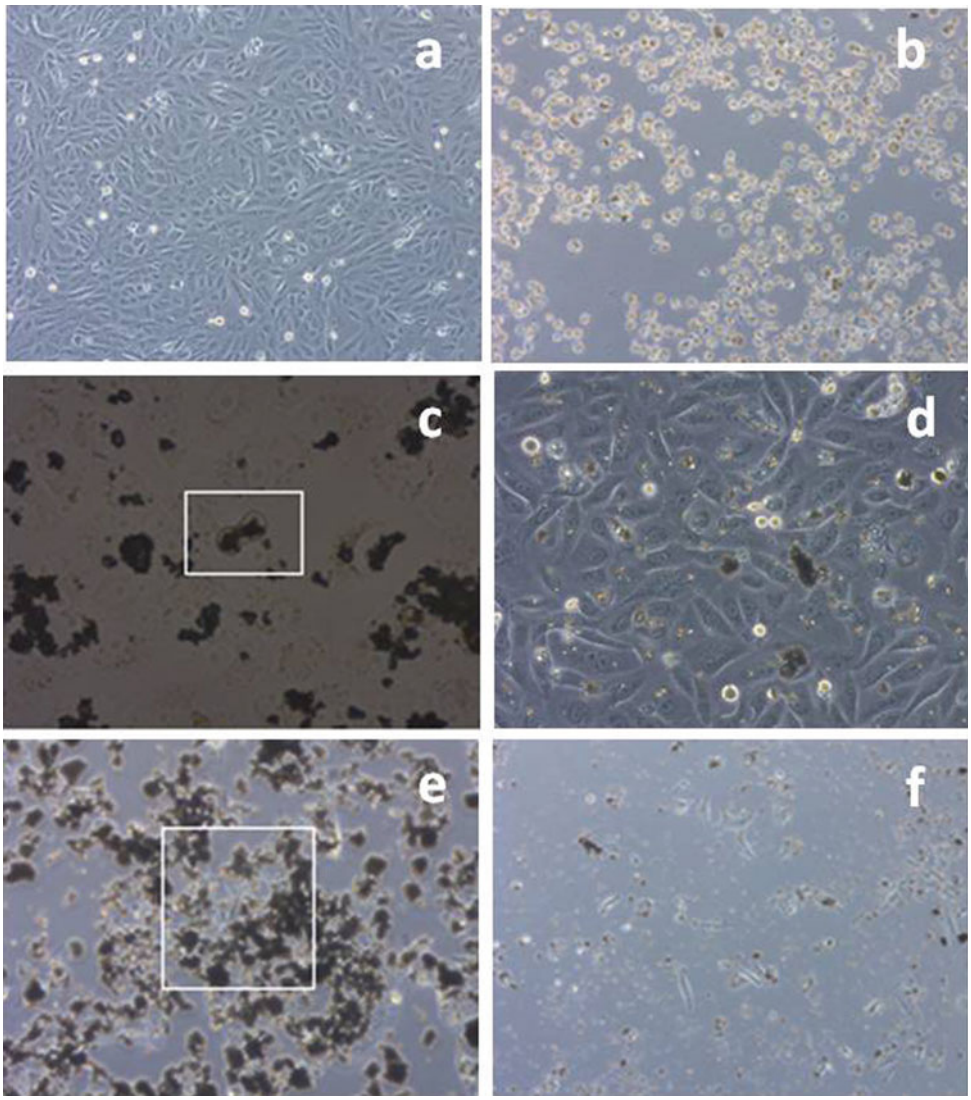

Fig. 5 Vero cell cytotoxicity assay, 48 h. **a** Negative control; **b** positive control; **c** alumina; **d** washed alumina; **e** calcium hexaluminate; **f** washed calcium hexaluminate. Observation:200x

The cell morphology is more evidenced with methylene blue staining (Fig. 7).

It was observed that both alumina and hexaluminate dissolved in culture medium, a condition that directly interfered with cell development. The washing of both materials decreased this dissolution, easing its presence and effect on the cells. Dissolution is evident even in the first 24 h of culture and remains throughout the test time.

Alumina, washed and not washed, proved to be non-cytotoxic. There was no significant morphological change in the cells in contact with these materials, and the confluence of the monolayer seems to be influenced by the presence of material dissolved in culture, and not directly by the influence of alumina on cell viability.

For hexaluminates, not washed and washed, the influence of samples dissolved in culture on cell organization is evident, with no monolayer being formed until the longest test time, 72 h. Some cells maintaining characteristic morphology are observed mainly in 72 h. However, only in the test with washed material. The observations indicate cytotoxicity of this material, in the conditions without and with washing, but with recovery of cell morphology in the longest culture times.

The variation in the size (Fig. 8) of the alumina samples did not interfere with cytotoxicity. The results with calcium hexaluminate are expressive. The cytotoxicity was directly related to sample size.

Regarding the experimentation time, the most expressive results were observed after 48 h, after this period, the high confluence of the monolayer can interfere in the analysis of the results, since the cells may begin to show inhibition by contact, as observed for the negative control.

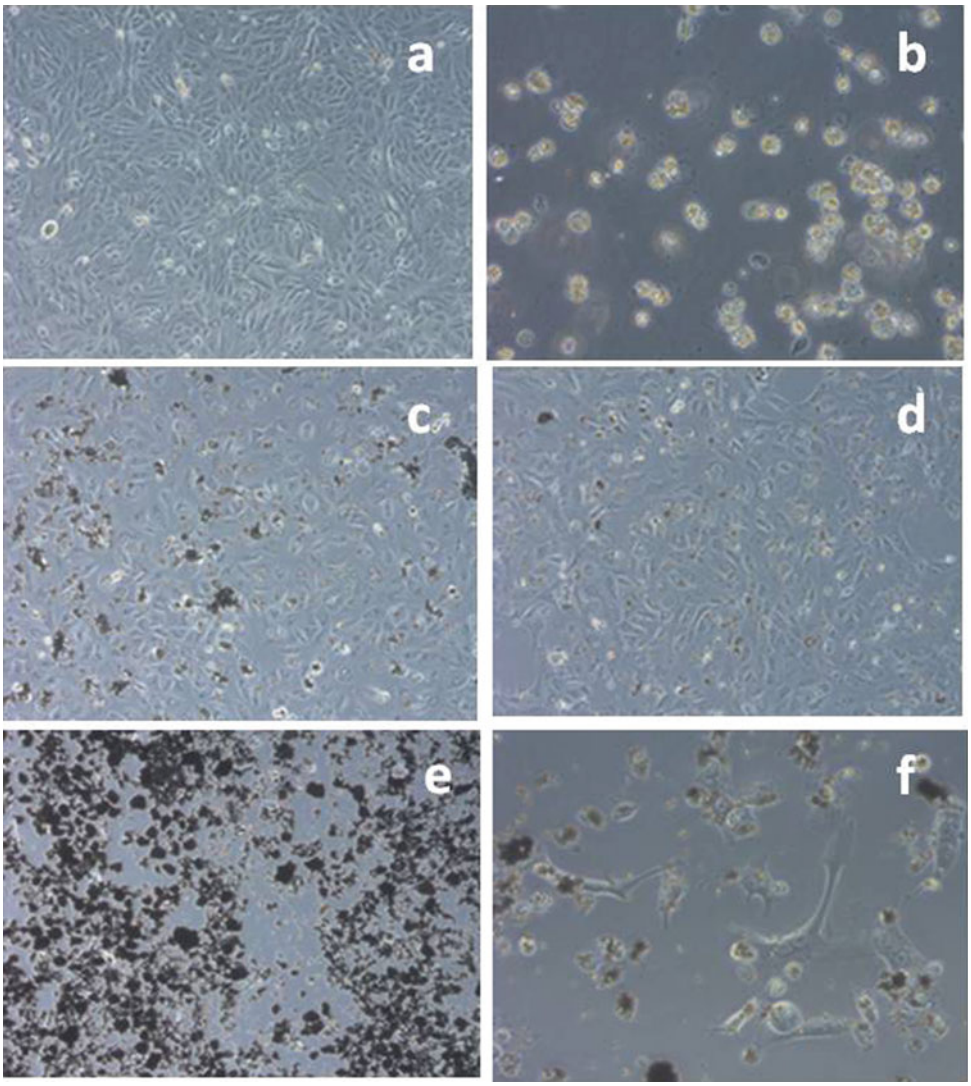

Fig. 6 Vero cell cytotoxicity assay, 72 h. a: negative control; b: positive control; c: alumina;d: washed alumina; e: calcium hexaluminate; f: washed calcium hexaluminate. Observation:200x

The size sample alteration, reduced in half and double size, of alumina biomaterials did not influence cell development. On the other hand, the larger calcium hexaluminate samples were cytotoxic, unlike the smaller samples, which, even showing cytotoxicity, allowed the development of some cells.

The analysis of experimental conditions for the evaluation of cytotoxicity is demonstrated in the literature, with an important impact on the results obtained [14, 23, 24]. In this study, the previous washing, analysis time and sample size were added to the existing scientific reports, once directly influencing the results.

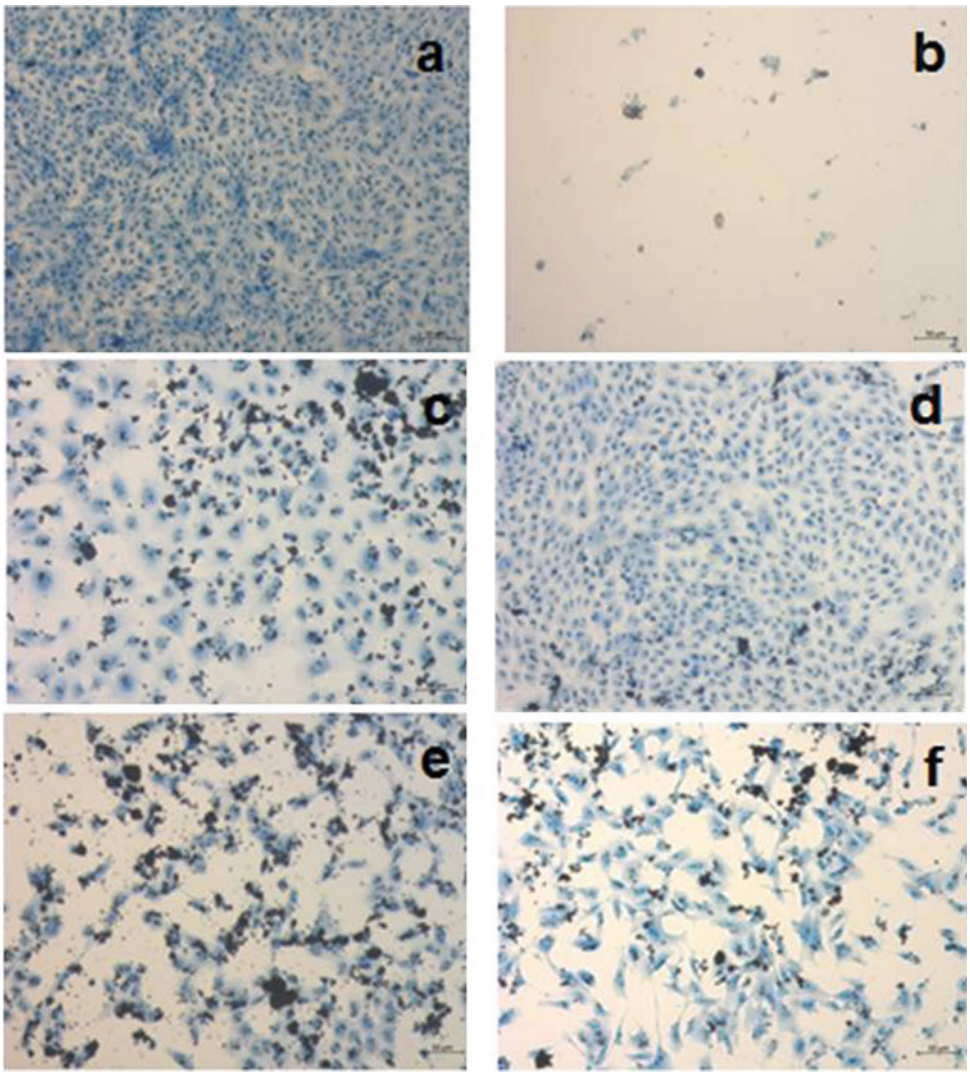

Fig. 7 Vero cell cytotoxicity assay, 72 h, methylene blue stainings. **a** Negative control; **b** positive control; **c** alumina;d: washed alumina; **e** calcium hexaluminate; **f** washed calcium hexaluminate. Observation:200x

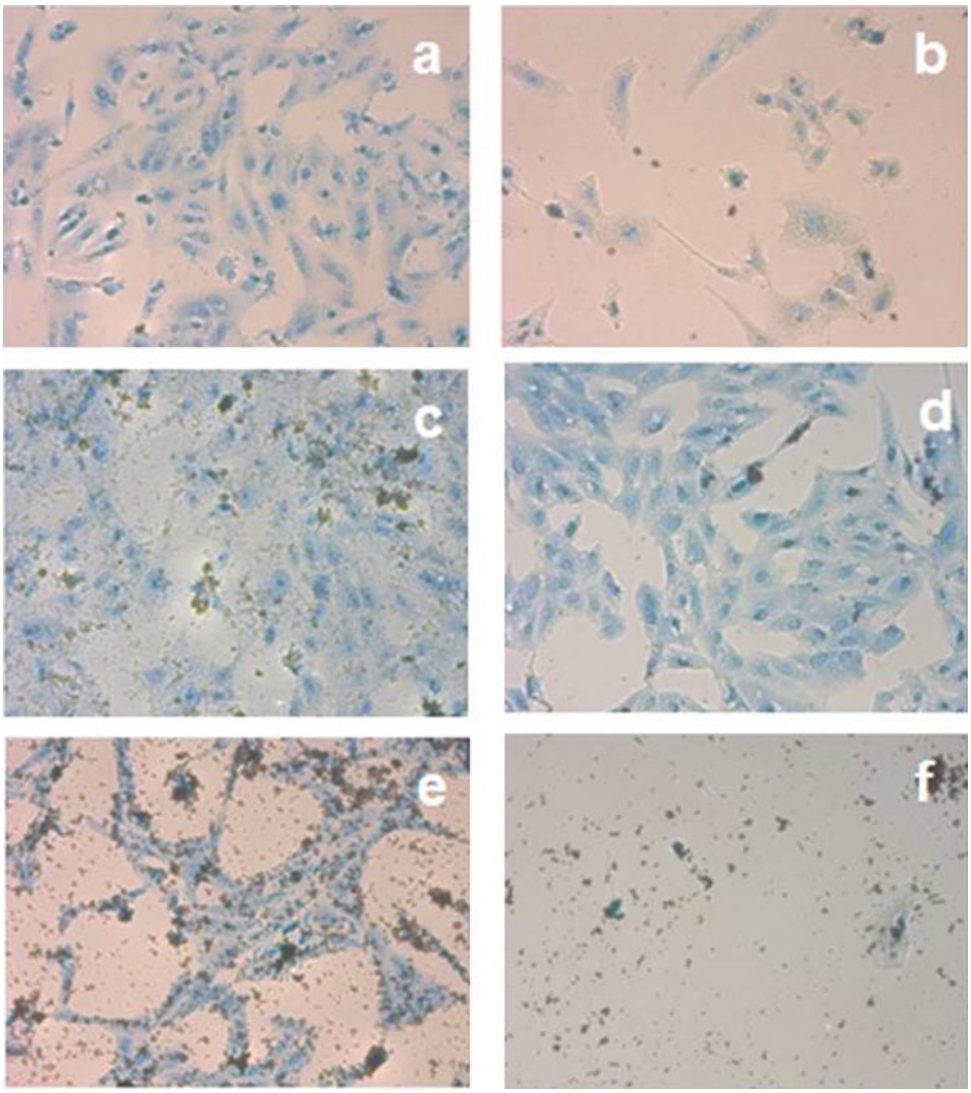

Fig. 8 Vero cell cytotoxicity assay, 24 h, methylene blue stainings. **a** negative control; **b** positive control; **c** alumina reduced size; **d** alumina double size sample; **e** calcium hexaluminate reduced size; **f** calcium hexaluminate double size sample. Observation:200x

4 Conclusions

The alumina was considered non-cytotoxic. Both the washing condition and the size of the samples did not interfere with the development of the cells. The calcium hexaluminate showed a slight cytotoxicity. The best results refer to the washed hexaluminate and half the dimension referenced by the standard. Unwashed biomaterial dissolved in the culture medium and impaired cell development, while biomaterial with double size referenced by the standard caused higher cytotoxicity. The longer culture period attenuated the cytotoxic effects on cell morphology.

Acknowledgements We thank the Federal University of ABC (UFABC) and UFABC's Multiuser Central Facilities (CEMs) for the infrastructure support.

Conflict of Interest The authors declare that they have no conflict of interest.

References

1. Langer R, Lanza R, Vacanti J (2007) Principles of tissue engineering. 3rd ed. Academic Press
2. Williams DF (1987) Definitions in biomaterials. In: Proceedings of a consensus conference of the european society for biomaterials, Chester, England, Mar 3–5. Elsevier, New York
3. Fleming JE, Cornell CN, Muschler GF (2000) Bone cells and matrices in orthopedic tissue engineering. Orthop Clin North Am 31:357–374
4. International Standards Organization ISO 10993-1 (2009) Biological evaluation of medical devices—Part 1: evaluation and tests. p 21

5. Vert M, Li SM, Spenlehauer G et al (1992) Bioresorbability and biocompatibility of aliphatic polyesters. J Mater Sci Mater Med 3:432–446
6. Oréfice RL, Pereira MM, Mansur HS (2006) Biomateriais: fundamentos & aplicações. In: Médica C, de Janeiro R
7. Rahmati M, Mozafari M (2019) Biocompatibility of alumina-based biomaterials-a review. J Cell Physiol 234:3321–3335
8. Cordingley R, Kohan L, Ben-Nissan B et al (2003) Alumina as an orthopaedic biomaterial-characteristics, properties, performance and applications. J Austral Ceram Soc Article ID:2160
9. Fischer H, Niedhart C, Kaltenborn N et al (2005) Bioactivation of inert alumina ceramics by hydroxylation. Biomaterials 26:6151–6157
10. Malik MA, Puleo DA, Bizios R et al (1992) Osteoblasts on hydroxyapatite, alumina and bone surfaces in vitro: morphology during the first 2 h of attachment. Biomaterials 13:123–128
11. Salomão R, Poiani AJB, Costa LMM (2019) Porous beads of in-situ calcium hexaluminate prepared by extrusion-dripping. Int Ceram Rev 68:40–49
12. Salomão R, Ferreira VL, Oliveira IR et al (2016) Mechanism of pore generation in calcium hexaluminate (CA_6) ceramics formed in situ from calcined alumina and calcium carbonate aggregates. J Europ Ceram Soc 36:4225–4235
13. Pizzoferrato P, Ciapetti G, Stea S et al (1994) Cell culture methods for testing biocompatibility. Clin Mater 15:173–180
14. Cruz AS, Figueiredo CA, Ikeda TI et al (1998) Comparação de métodos para testar a citotoxicidade "in vitro" de materiais biocompatíveis. Rev Saúde Pub 32:153–159
15. International Standards Organization. ISO 10993-5 (2009) Biological evaluation of medical devices—Part 5: tests for in vitro cytotoxicity. p 34
16. Wang MO, Etheridge JM, Thompson JA et al (2013) Evaluation of the in vitro cytotoxicity of cross-linked biomaterials. Biomacromol 14:1321–1329
17. Kobayashi S, Hara H, Okudera H et al (1987) Usefulness of ceramic implants in neurosurgery. Neurosurgery 21:751–755
18. Polack FM, Heimke G (1980) Ceramic keratoprosthesis. Ophthalmol 87:693–698
19. Dee KC, Puleo DA, Bizios R (2003) An introduction to tissue-biomaterial interactions. Wiley-Liss, New Jersey
20. Lima MPCVP, Leite VMC, Salomão R et al. (2016) Caracterização de hexaluminato de cálcio produzido a partir de alumina hidráulica. 60º Cong Bras Ceram, Águas de Lindóia/SP
21. Neiva LS, Borges CRPB, Brasileiro MI et al (2015) Materiais cerâmicos catalíticos à base de hexa-aluminato de metais alcalino terrosos (Ba e Ca): síntese e análise estrutural. Cerâmica 61:350–358
22. Wang HK, Yi CY, Tian L et al (2011) Ag-Cu bimetallic nanoparticles prepared by microemulsion method as catalyst for epoxidation of styrene. J Nanomaterials 2012:4–6
23. Masson AO, Lombello CB (2016) Ensaios de citotoxicidade in vitro: comparação dos métodos de contato direto e por extrato. 25º Cong Bras Eng Biom, Foz do Iguaçu/PR
24. Huck C, Barud HS, Basso FG et al (2017) Cytotoxicity of new calcium aluminate cement (EndoBinder) containing different radiopacifiers. Brazilian Dental J 28:57–64

Tendon Phantom Mechanical Properties Assessment by Supersonic Shear Imaging with Three-Dimensional Transducer

V. C. Martins, G. B. G. Rolando, L. L. De Matheo, W. C. A. Pereira, and L. F. Oliveira

Abstract

Phantom mimics biological tissues properties, i.e., acoustic and mechanical. Tendon connects muscle to bone and allows joint motion. To evaluate tendon mechanical properties, i.e. Young modulus, in vitro and in vivo studies were developed. In the 90s, Elastography emerged as a promise tool to tissue mechanical properties assessment, i.e., breast and liver. Recently, Supersonic Shear Imaging (SSI) technique was developed to calculate quantitative Elastic modulus (E) from transversal shear wave propagation velocity (C_S). The most recent 3D transducer can provide a tridimensional visualization of an organ (sagittal, transverse and coronal). The aim of this study is to assess transverse shear wave propagation velocity (C_S) on tendon phantom using SSI with 3D transducer. This tendon phantom was composed basically PVCP plastisol® and glycerin (15%). For image acquisition, the Aixplorer v.11 equipment (Supersonic Imagine, Aix-en-Provence, France) with 3D transducer (Super linear TM volumetric SLV 16–5, 5–16 MHz) were used. The 3D transducer was placed randomly at the phantom surface and three images were acquired. Each one presented the three orthogonal planes (sagittal, transverse and coronal) and the respective intersection points between two other planes. For each plane, a 5.0 mm ROI (Region of Interest) was positioned around the intersection point to measure C_S. The mean C_S values were 6.2 m/s (±0.3), 6.4 m/s (±0.4) and 6.3 m/s (±0.3) for sagittal, transverse and coronal planes, respectively. These results were different to the only study which evaluated an anisotropic phantom tendon with SSI. However, when compared to previous studies, the results were similar to human healthy patellar tendon. This is a whole homogeneous phantom and it was not possible to mimic the oriented fibers presented on the tendon. Future studies should be performed with anisotropic phantoms to standardize the validation of elastography techniques dedicated to healthy and pathological tissues.

Keywords

Supersonic shear imaging • Tendon • *Phantom* • Elastography

1 Introduction

Phantom is a material which mimics biological tissues, i.e., acoustic and mechanical properties [1]. Among the phantoms developed at the Ultrasound Laboratory (COPPE/UFRJ), bone, muscle, breast and recently tendon phantom can be highlighted [1, 2].

Tendon connects muscles to bone. Their main function is to transmit mechanical load between those structures to provide joint motion [3]. Tendon is composed basically by collagen, proteoglycans, glycoproteins, water and cell (fibrocytes) [4]. Collagen is the major component (type I, III, V, IX) and type I makes up 60% of the dry mass and approximately 95% of the total [5]. In addition to collagen, proteoglycans vary over different locations according to the mechanical load on tendon [3, 6].

Tendon structure is highly complex. A hierarchical organization contains fibrils, bundles and collagen fibers which are oriented in the same direction of mechanical loads which act on tendons. The specific fiber orientation allows tendon to resist high imposed loads [4, 6]. Although

V. C. Martins (✉) · G. B. G. Rolando · L. L. De Matheo · W. C. A. Pereira · L. F. Oliveira
Biomedical Engineering Program, Federal University of Rio de Janeiro, COPPE/UFRJ, Rio de Janeiro, RJ, Brazil

V. C. Martins
Physiotherapy School, Federal Institute of Rio de Janeiro, IFRJ, Rio de Janeiro, RJ, Brazil

L. F. Oliveira
Physical Education and Sports School, Federal University of Rio de Janeiro, EEFD/UFRJ, Rio de Janeiro, RJ, Brazil

T. F. Bastos-Filho et al. (eds.), *XXVII Brazilian Congress on Biomedical Engineering*, IFMBE Proceedings 83, https://doi.org/10.1007/978-3-030-70601-2_33

mechanical loads are beneficial to tendon homeostasis, too high or repetitive loads (overuse) can lead to tendinopathy. This pathological condition can alter tendon structure and mechanical properties, impairing function [7]. According to [8] age-related must alter tendon structure and mechanical properties reducing the load resistance capacity.

Historically, tendon mechanical properties were first evaluated by in vitro studies. A tendon specimen (ex vivo) was submitted to a known stress (load) over a time and its deformation (strain) was then measured. Thus, Young modulus were calculated from stress and strain ratio (Eq. 1) [9, 10].

Later, in vivo studies were developed to calculate tendon Young modulus [11, 12]. For patellar tendon, i.e., ultrasound was used to assess tendon cross-sectional area (A) and dynamometer was used to measure quadriceps femoral Torque (T). The force (F) exerted by quadriceps femoral was calculated by dividing the torque by the femur length (distance), and then stress is calculated by dividing the force (F) by area (A). Tendon initial length (L_O—tendon at rest) and final length (L) were both measured by ultrasound to calculate patellar tendon length variation (ΔL). Thus, strain is found by dividing length variation (ΔL) by length at rest (L_o). Equation 1 shows Young modulus calculated from Stress (F/A) Strain ($\Delta L/L_o$) [12].

$$\text{Young modulus} = \frac{\frac{F}{A}}{\frac{\Delta L}{Lo}} \tag{1}$$

where, F—force exerted from quadriceps femoral; A—patellar tendon cross-sectional area; ΔL—tendon length variation; L0—tendon length at rest (initial length).

Finally, for both methods (in vitro and in vivo), the *Stress x Strain* curve was plotted to evaluate tendon behavior. However, these methods had high uncertainty [13].

Ultrasound (US) has been a useful tool largely used in Medicine to evaluate tissue morphological and material characteristics, i.e. tendon, muscles, liver and breast. However, the US does not provide any information about tissue mechanical properties, i.e., rigid or elastic tendon [14, 15]. Elastography, a recent technique developed by [16], emerged as a promising non-invasively and real-time diagnostic tool to detect variations on tissue stiffness. Therefore, it is possible to identify a tissue pathological condition such as breast or liver cancer [17].

At the beginning, in the Quasi-Static Elastography technique (free-hand), stress was applied manually at the tissue through the transducer. So, besides being an operator-dependent technique, it can only provide a qualitative evaluation of a structure, i.e., hard or soft tissue [15]. Over the years, Elastography technique has been enhanced so that it is possible to obtain a quantitative parameter to assess mechanical property, i.e. Elastic modulus (E). So, Supersonic Shear Imaging (SSI) provides E given in kPa, calculated from transverse shear wave propagation velocity —"C_S" (Eq. 2). SSI technique works at two stages: Pushing Mode—An acoustic radiation force (ARF) is generated by the transducer on tissue with many focuses at different depths. The stress caused by ARF will cause a perturbation on the tissue and then, transverse and longitudinal waves will be generated. These waves will propagate longitudinally and transversely to the ARF application direction, respectively. Transverse shear wave propagation velocity (C_S) is proportional to tissue stiffness: C_S is faster when propagated in a rigid tissue [14, 18].

Imaging Mode: Ultrafast Imaging acquisition provides a full image plane scanning by a high temporal resolution per acquisition—about 5.000 or more images per second. Thus, SSI transducers can measure transverse shear wave propagation time over a given distance to obtain C_S (m/s). Elastic modulus (E) is then calculated by Eq. 2 [19].

$$E = 3\rho C_S^2 \tag{2}$$

where: E—Elastic Modulus (kPa), ρ—density of biological tissue (1.0 g/mm^3), C_S—transverse shear wave propagation velocity (m/s).

According to Eq. 2, Elastic modulus assumes that all biological tissues have the following characteristics: purely elastic, isotropic and density ρ = 1.0 g/mm^3. However, tendons are viscoelastic, anisotropic and its density is not exactly 1.0 g/mm^3 [20]. One way to minimize these errors is using C_S values which are measured directly from tissue.

Recently, the development of a 3D (three-dimensional) transducer has been providing a more complete structure evaluation in three orthogonal planes: (A) sagittal, (B) transverse and (C) coronal (Fig. 1) [17, 18].

In the current literature, studies with tendon phantom assessed by elastography are few and very limited. There are no studies with 3D elastography for tendon phantom evaluation. Thus, the aim of this study is to assess C_S in tendon phantom by SSI with 3D transducer.

2 Materials and Methods

2.1 Phantom Preparation

The phantom preparation process was carried out at the Ultrasound Laboratory (LUS-COPPE/UFRJ). PVCP, commercially called Plastisol®, consists of fine particles suspended in liquid plasticizer. When it is heated, the plasticizer permeates the PVC particles increasing the polymer chains. At approximately 180 °C, the melting of the PVC microcrystals formed the homogeneous matrix. The polymeric chains froze with cooling but remained plasticized. Thus, a

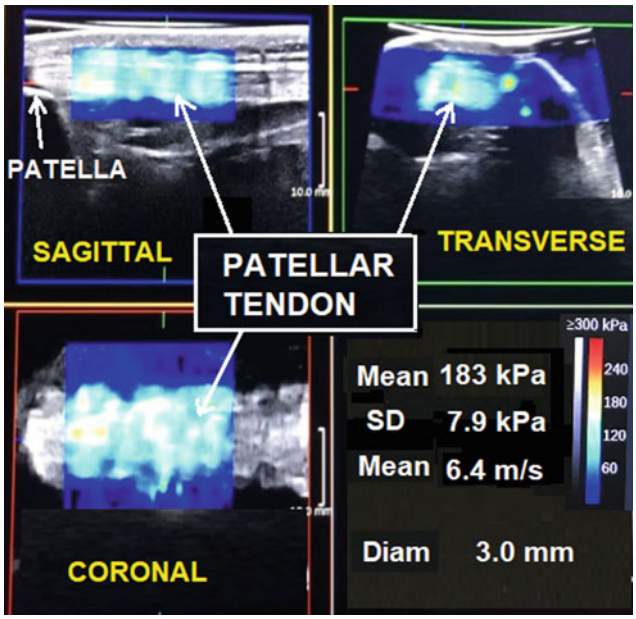

Fig. 1 Patellar tendon assessed by SSI technique with 3D transducer. The image shows the three orthogonal planes: Sagittal; Transverse and Coronal. Color map (elastogram) in each plane and the scale are shown (Elastic modulus - kPa) and the mean C_S (m/s) and Elastic Modulus (kPa) values

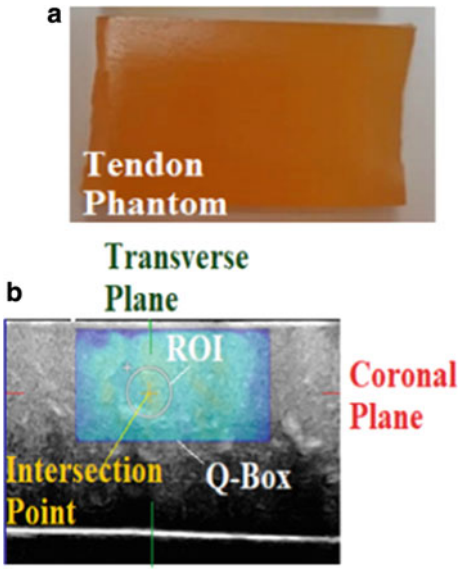

Fig. 2 **a** Tendon phantom; **b** SSI sagittal plane image showing Q-Box (color map). Inside the Q-Box, ROI was positioned around the intersection point between both complementary planes: transverse (green) and coronal (red)

solid and flexible material with high cohesion chains was formed [1, 21]. Attenuation coefficient of PVCP is 0.38 dB. cm^{-1}, which is lower than that found in the literature for tendons. However, it is possible to alter attenuation values by adding spreading components [1, 21].

The phantom preparation process follows a protocol developed by [21]. Spreaders were added to the liquid PVCP and mixed until the material became homogeneous. After this stage it remained for 60 min in a vacuum pump (Ind. Mec. Primer Ltda. Model 166, 104 N 1016) to remove possible air bubbles. The solution was then heated in the microwave (Blue Touch®, Electrolux) for 2 min (power = 100%) and for 4 times of 30 s each (power = 70%) until it reached 180 °C. After that, it was again taken to the vacuum pump for another 2 min. Finally, the solution (liquid) is poured into the container and remains there until it solidifies (Fig. 2). Glycerin 15% was added to the phantom because it improves attenuation coefficient [22].

2.2 Image Acquisition—SSI with 3D Transducer

Image acquisition was performed at the Movement Analysis and Exercise Physiology Laboratory (LAMFE-COPPE/UFRJ). The Aixplorer v.11 equipment (Supersonic Imagine, Aix-en-Provence, France) and 3D transducer (Super linear TM volumetric SLV 16–5, 5–16 MHz) were used. The 3D transducer was placed directly to the phantom surface with conductive gel between them. The entire phantom has homogeneous characteristics, so the transducer position (transverse or longitudinal) did not change the color map characteristics and C_S values (Fig. 2).

2.3 Image Processing

Three images of tendon phantom were acquired and each one displays C_S (m/s) and E (kPa) values for all three planes (Fig. 3). Each image (sagittal, transverse or coronal planes) shows the two other complementary planes and the intersection point (Figs. 2 and 3) between them. I.e., for a sagittal plane image, it is possible to identify transverse and coronal planes as well as respective intersection point. Then, a 5.0 mm Region of Interest (ROI) was positioned around the intersection point and the C_S values were accessed in a common region to the 3 planes.

Figure 3 shows tendon phantom and three orthogonal planes images as well as C_S and EM values in m/s and kPa, respectively.

2.4 Results

Table 1 shows C_S values (mean and std. dev.) obtained from three images for each plane.

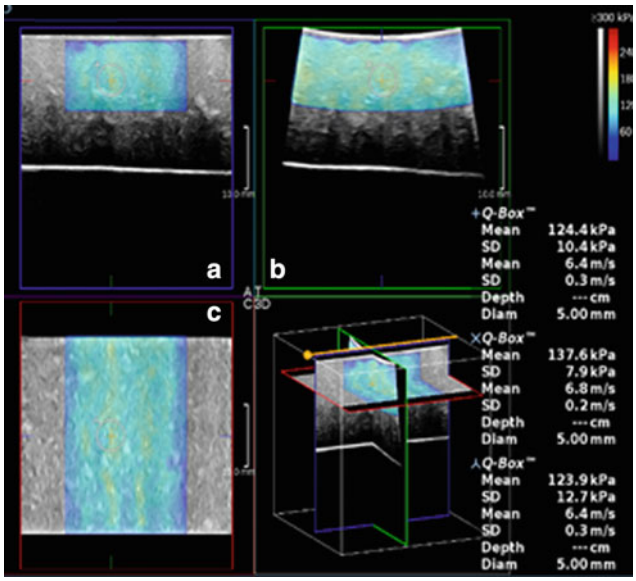

Fig. 3 Schematic representation of transducer placed at tendon phantom surface (on the top). Tendon phantom and image from three planes: **a** Sagittal; **b** Transverse and **c** Coronal. Each one contains the color map, the respective intersection point and the ROI positioned around it. The related scale in shown on top of right (kPa). On the right, it shows Cs (m/s) and Elastic Modulus (kPa) values

Table 1 C_S Values obtained (mean and std. dev.) from three images for each plane

Plane	Sagittal (A) C_S (m/s)	Transverse (B) C_S (m/s)	Coronal (C) C_S (m/s)
Image 1	5.9	6.0	6.0
Image 2	6.4	6.8	6.4
Image 3	6.4	6.4	6.5
Mean ± St. dev.	6.2 ± 0.3	6.4 ± 0.4	6.3 ± 0.3

3 Discussion

The aim of this study was to assess tendon phantom C_S by SSI with 3D transducer. Although there are no studies using 3D elastography to assess tendon phantoms, it is possible to compare the results with C_S values in previous studies which evaluated healthy patellar tendon in humans.

The following studies presented C_S values close to those found in this study. [18] performed SSI (3D transducer) on the patellar tendon of 18 healthy subjects and found C_S values = 6.2 m/s (sagittal plane) and 6.1 m/s (transverse plane). [10] assessed 11 subjects and found C_S values = 6.0 m/s, [23] obtained C_S = 6.6 m/s in 20 volunteers, [24] assessed 25 subjects and C_S values ranged from 5.8 to 6.3 m/s and [25] obtained values from 6.2 to 6.7 m/s in a study with 22 participants.

Phantoms can mimic biological tissues properties, i.e. acoustic, rheological and mechanical. However, studies with tendon phantoms are still limited as well as elastography with 3D transducer to tendon assessment [1, 2]. In the current literature, there is no study with 3D SSI transducers to evaluate tendon phantom.

Aristizabal et al. [26] developed a gelatin-based phantom composed with fishing line material with preferential orientation and the phantom exhibited anisotropy that resembles that observed in the pork muscle. Slane and Thelen [27] created a phantom from polyvinyl chloride-plastisol with randomly dispersed glass beads used as ultrasound scatter particles. The authors investigated the fidelity of a 2D elastography method for evaluating motion and strain of tendon-shaped phantoms and ex vivo tendon specimens subjected to axial loading. A phantom made with eleven pre-cut acrylic tubes filled with a gelatin mixture (10–15% gelatin, 2–6% psyllium hydrophilic mucilloid fiber) was evaluated by [28]. Three-dimensional ultrasound provided accurate measures of phantom volume and length and reliable in vivo measures of Achilles tendon volume, length and average cross-sectional area, with all intra-class correlations coefficients greater than 0.98. [2] evaluated the anisotropy behavior of transverse isotropic (TI) PVA hydrogel phantom using SSI with 2D transducer positioned at 0º and 90° to the fibers. Elastic anisotropy was observed since the shear wave speed was 3.2 m/s at 0° and 1.95 m/s at 90°. Therefore, the phantom mimics anisotropy of biological fibrous tissues at different scales such as cardiac, muscular or tendon. Although this is not a phantom which mimics only tendon, the C_S values found by [2] was lower than the results of this study.

The tendon phantom of this study is all homogeneous, so there were no variations on C_S values when the transducer position was changed from longitudinal to transverse to surface. Tendon fibers orientation gives it a high capacity to resist and transmit loads in the same direction [6], however, due tendon anisotropy, the behavior is different when loads are transversely applied to tendon fibers [15]. The development of anisotropic phantoms for elastography would help to standardize the validation of elastography techniques dedicated to fibrous tissues, i.e. tendon [2, 15].

In this study, the transducer was placed randomly at the phantom surface, and then, C_S values were measured from the ROI positioned only around the intersection point (Fig. 3). Even though it is a homogeneous phantom, there was no established criteria to define other specific points/regions to be evaluated in addition to this intersection point. In future studies, a more complete assessment of this phantom should be performed.

4 Conclusion

Tendon phantom of this study showed C_S values similar to patellar tendon of healthy subjects, however, these results are different from that found in an isotropic phantom.

Future studies should be performed with phantoms with parallel oriented fibers and made with different materials to mimic tendon anisotropy as well as mechanical properties of healthy and pathological tendon.

Acknowledgements To FAPERJ, CNPq, CAPES and FINEP for financial support.

Conflict of Interest The authors declare that they have no conflict of interest.

References

1. De Matheo LL, Geremia J, Gregorio MJ et al (2018) PVCP-based anthropomorphic breast phantoms containing structures similar to lactiferous ducts for ultrasound imaging: a comparison with human breasts. Ultrasonics 90:144–152
2. Chatelin S, Bernal M, Deffieux T et al (2014) Anisotropic polyvinyl alcohol hydrogel phantom for shear wave elastography in fibrous biological soft tissue: a multimodality characterization. Phys Med Biol 59:6923–6940
3. Scott A, Backman LJ, Speed C (2015) Tendinopathy: update on pathophysiology. J Orthop Sports Phys Therapy 45(11):833–841
4. Wang JHC (2009) Mechanobiology of tendon. J Biomechanics 39 (9):1563–1582
5. Chang A, Miller TT (2009) Imaging of tendons. sports. Health 1 (4):293–300
6. Wang JHC, Guo Q, Li B (2012) Tendon biomechanics and mechanobiology—a mini-review of basic concepts and recent advancements. J Hand Therapy 25(2):133–141
7. Malliaras P, Cook J, Purdam C et al (2015) Patellar tendinopathy: clinical diagnosis, load management, and advice for challenging case presentations. J Orthop Sports Phys Ther 45(11):887–898
8. Hsiao MY, Chen YC, Lin CY et al (2015) Reduced patellar tendon elasticity with aging: in vivo assessment by shear wave elastography. Ultrasound Med and Biol 41(11): 2899–2905
9. Crisco JJ, Dunn TC, McGovern RD (1998) Stress wave velocities in bovine patellar tendon. J Biomech Eng 120:321–326
10. Zhang ZJ, Fu SN (2013) Shear elastic modulus on patellar tendon captured from supersonic shear imaging: correlation with tangent traction modulus computed from material testing system and test-retest reliability. PlosOne 8(6):
11. Hansen P, Bojsen-Moller J, Aagaard P et al (2006) Mechanical properties of the human patellar tendon *in vivo*. Clin Biomech 21 (1):54–58
12. Yeh CH, Kuo PL, Genisson JL et al (2016) Shear-Wave measurements for evaluation of tendon diseases. IEEE Trans Ultrason Ferroelectr Freq Control 11:1906–1921
13. Helland C, Bojsen-Moller J, Rastaad T et al (2013) Mechanical properties of the patellar tendon in elite volleyball players with and without patellar tendinopathy. Brit J Sports Med 47:862–868
14. Gennisson JL, Deffieux T, Fink M et al (2013) Ultrasound elastography: principles and techniques. Diagn Interv Imaging 94:487–495
15. Lima KMME, Costa Junior JFS, Pereira WCA et al (2018) Assessment of the mechanical properties of the muscle-tendon unit by supersonic shear wave imaging elastography: a review. Ultrasonography 37(1):3–15
16. Ophir J, Céspedes I, Ponnekanti H et al (1991) Elastography: a quantitative method for imaging the elasticity of biological tissues. Ultrason Imaging 13:111–134
17. Li Yin BS, Lu R, Cao W et al (2018) Three-dimensional shear wave elastography of skeletal muscle: preliminary study. J Ultrasound Med 37(8):2053–2062
18. Martins VC, Oliveira VB, Brandão MCA et al (2018) Supersonic shear imaging 3-D transducer for two-dimensional evaluation of patellar tendon mechanical properties. In: IFMBE proceedings of XXVI Brazilian congress on biomedical eng, Armação Dos Búzios, Brazil, vol 70, no 1, pp 377–381
19. Bercoff J, Pernott M, Tanter M et al (2004) Monitoring thermally-induced lesions with supersonic shear imaging. Ultrason Imaging 26(2):71–84
20. Ryu JA, Jeong WK (2017) Current status of musculoskeletal application of shear wave elastography. Ultrasonography 36 (3):185–197
21. De Matheo LL, von Krüger MA, Pereira WCA (2016) Characterization of the acoustic properties of paraffin phantoms in gel carnauba wax for ultrasound. XXV Brazilian Congress of Biomedical Eng. Foz do Iguaçu, Brazil, pp 1027–1031
22. Cabrelli LC, Grillo FW, Sampaio DRT et al (2017) Acoustic and elastic properties of glycerol in oil-based gel phantoms. Ultrasound Med Biology 43(9):2086–2094
23. Zhang ZJ, Ng GYF, Lee WC et al (2014) Changes in morphological and elastic properties of patellar tendon in athletes with unilateral patellar tendinopathy and their relationships with pain and functional disability. PlosOne 9(10):
24. Zhang ZJ, Ng GYF, Fu SN et al (2015) Effects of habitual loading on patellar tendon mechanical and morphological properties in basketball and volleyball players. Europ JApp Physiol 115 (11):2263–2269
25. Mannarino P, Lima KMM, Fontenelle CRC et al (2017) Analysis of the correlation between knee extension torque and patellar tendon elastic property. Clinical Physiol Funct Imag 38(3):378–383
26. Aristizabal S, Amador C, Qiang B et al (2014) Shear wave vibrometry evaluation in transverse isotropic tissue mimicking phantoms and skeletal muscle. Phys Med Biol 59(24):7735–7752
27. Slane LC, Thelen DG (2014) The Use of 2D ultrasound elastography for measuring tendon motion and strain. J Biomech 47(3):750–754
28. Obst SJ, Newsham-West R, Barret R (2014) In vivo measurement of human achilles tendon morphology using free-hand 3-D ultrasound. Ultrasound Med Biol 40(1):62–70

Physiological Control of Pulsatile and Rotary Pediatric Ventricular Assist Devices

T. R. Melo, T. D. Cordeiro, I. A. Cestari, J. S. da Rocha Neto and A. M. N. Lima

Abstract

Several control strategies have been proposed to achieve physiological adaptation of ventricular assist devices (VADs). This paper presents physiological control systems for pediatric VADs that were developed in a scientific cooperation between Bioengineering Division of the Heart Institute, Hospital das Clínicas, Faculty of Medicine on the University of São Paulo (InCor–HCFMUSP) and the Electrical Engineering Department at the Federal University of Campina Grande (DEE - UFCG). The pumping principle and mathematical models of two types of pediatric VADs (pulsatile and rotary) are described. The control strategies for the physiological control systems are discussed, and the main achievements and challenges for implementing these control systems are presented.

Keywords

Ventricular assist device • Pediatric patient • Lumped parameter model • Physiological control system

1 Introduction

Ventricular assist devices (VADs) are mechanical circulatory support devices implanted to assist the left ventricle (LVAD), the right ventricle (RVAD), or both ventricles (BiVAD) [1]. VADs are used successfully in the treatment of end-stage heart failure (HF), and regardless of pumping principle, are classified as pulsatile VADs or rotary VADs.

Pulsatile VADs are volume-displacement pumps, in which a pulsatile stroke volume is generated from the displacement of a membrane or by using a dual pusher-plate sac-type mechanism driven by a pulsed driver. Among the advantages, this type of pump work with intermittent assistance (similarly to the human organism) and good results for the long-term. As for disadvantages, it can be cited the size and weight, potential infections, degradation of the membrane and formation of blood clots [2,3].

Rotary VADs, known as rotary blood pumps (RBPs), provide rotational energy from an electric console to continuously pump the blood to the patient's body. The RBPs can be axial pump or centrifugal pump, according to the impeller design. The characteristics of this type of pump used as VAD in clinical usage are the reduced size and weight, the durability, silent device (without friction), reduced hemolysis risk, and long life expectancy (10–15 years). The main disadvantages are infection risks, occurrence of arrhythmias and suction phenomenon [4,5].

VADs physiological control denotes a feedback control system that aims at reducing the number of human interventions for regulating the levels of the hemodynamic variables. Different types of VADs control systems are available to fulfill these physiological objectives. Petrou et al. [6] done an in vitro comparison of physiological controllers for LVADs proposed in literature. Wang et al. [7] proposed and verified physiological control algorithms for BiVAD support. Leao et al. [8] developed multi-objective physiological control for RBPs with in vitro evaluation.

There have been great advances in VADs treatment for pediatric patients with HF. Miniaturized rotary VADs are more adopted for pediatric patient with promising results. For infants and small children, paracorporeal pulsatile VADs is the main option for long-term support. Despite widely available of VADs in adults, pediatric VADs are very limited, and there are few studies in the literature that describe pediatric VAD physiological control systems [9–11]. In this context,

T. R. Melo (✉) · J. S. da Rocha Neto · A. M. N. Lima
Graduate Program in Electrical Engineering, Federal University of Campina Grande, Aprigio Veloso 882, 58429-900, Campina Grande, PB, Brazil
e-mail: thamiles.melo@ee.ufcg.edu.br

T. D. Cordeiro
Institute of Computing, Federal University of Alagoas, Maceió, AL, Brazil

I. A. Cestari
Bioengineering Division, Heart Institute, São Paulo, SP, Brazil

T. F. Bastos-Filho et al. (eds.), *XXVII Brazilian Congress on Biomedical Engineering*, IFMBE Proceedings 83, https://doi.org/10.1007/978-3-030-70601-2_34

the current work aims at discussing the design of physiological control systems for pediatric ventricular assist devices. These pediatric devices were designed and manufactured at InCor - HCFMUSP.

2 Ventricular Assist Devices

This section describes both the pediatric pulsatile VAD and pediatric rotary VAD used in this study.

2.1 pVAD

The pediatric VAD (pVAD InCor) is a pulsatile paracorporeal device pneumatically driven pump has a blood chamber with ejection volume of 15 ml, an air chamber, a membrane between these chambers, and valve prostheses on both the inlet and the outlet connectors of the blood chamber [12]. An image of this pVAD can be seen in Fig. 1a.

A pneumatic driver generates a pressure signal, $p_d(t)$, combining ejection and filling pressures, $p_e(t)$ and $p_f(t)$, respectively. The pressure $p_e(t)$ remains constant for a fixed period, known as VAD systolic period T_{sys}. This pressure is delivered to the air chamber and causes a membrane displacement which closes the inlet valve and open the outlet valve. After that, $p_d(t)$ is switched from $p_e(t)$ to $p_f(t)$, decreasing the air chamber pressure and allowing the filling of the blood chamber. Negative values can be used to $p_f(t)$ (vacuum) to improve blood volume suction in the blood chamber. A detailed description of the pVAD InCor lumped parameter model (Fig. 1b) can be found in Sousa et al. [13].

The pVAD drive can operate in three distinct modes: *full-to-empty mode*, where the pVAD ejection is activated with the filling of blood chamber; *asynchronous mode*, where the pVAD works at constant frequency apart native heartbeat; and *synchronized mode*, which works according to the patient's heartbeat in co-pulsation (pulsation in systole) or counter-pulsation (pulsation during diastole), based on ECG signal.

2.2 pRBP

The pediatric RBP (pRBP InCor) is a centrifugal rotary blood pump with a priming volume of 20 mL, to be used as a bedside pump for the patient. This device is composed by three subsystems: electrical, mechanical and hydraulic. The DC motor is the core of the electrical subsystem, in which the motor driver module provides the armature voltage. In the mechanical subsystem, there is a magnetic coupling between the pRBP and the DC motor shaft. In hydraulic system, the pump differential pressure and pump flow may be measured by central access inlet connector and peripheral access outlet connector

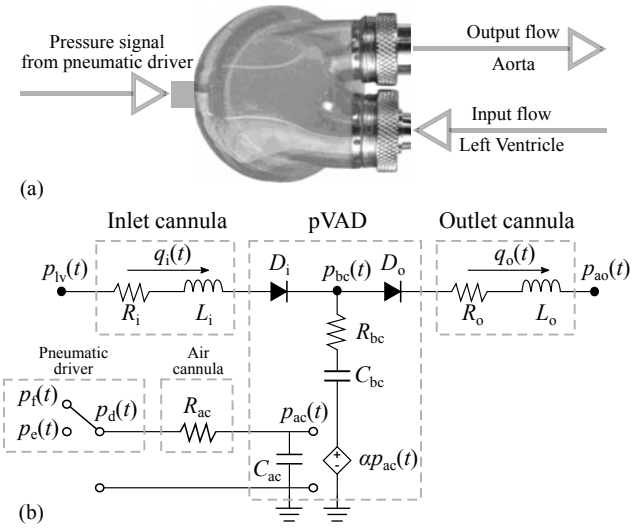

Fig. 1 **a** Image of the pulsatile pediatric ventricular assist device as if it was connected between the left ventricle and the aorta. **b** Representation of the pVAD 0D model. Legend: $p_{lv}(t)$ = left ventricular pressure; $p_{ao}(t)$ = aortic pressure; $p_{bc}(t)$ = blood chamber pressure; $p_{ac}(t)$ = air chamber pressure; $p_d(t)$ = pneumatic driver pressure; $p_e(t)$ = ejection pressure; $p_f(t)$ = filling pressure; $q_i(t)$ = input flow; $q_o(t)$ = output flow; D_i, D_o = inlet and outlet valves; R_i, L_i = resistance and inertance in inlet cannula; R_o, L_o = resistance and inertance in outlet cannula; R_{ac}, C_{ac} = resistance and compliance in air chamber; R_{bc}, C_{bc} = resistance and compliance in blood chamber

of the pump. An image of the pRBP under consideration can be seen in Fig. 2a.

The pRBP variables are the pump differential pressure, $\Delta p_{RBP}(t)$ (the pressure difference between the pump outlet, $p_{out}(t)$, and pump inlet, $p_{in}(t)$); the pump flow, $q_{RBP}(t)$; the motor armature voltage, $v_a(t)$; the motor armature current $i_a(t)$; and the rotational speed $\omega(t)$. A detailed description of the pRBP InCor lumped parameter model (Fig. 2b) can be found in Melo et al. [14].

The pRBP actuator can operate in two modes: *constant mode*, in which a fixed value of rotational speed is defined, generating a continuous flow in the pump; *variable mode*, in which the pump rotational speed modulation is incorporated in the control loop, operating in co-pulsation (increases the pump speed in the systolic period; consequently, increasing the pump flow in systole and the arterial pressure pulse amplitude) or counter-pulsation (increases the pump speed in the diastolic period; as a result, reducing the pump flow in diastole and the arterial pressure pulse amplitude).

3 Physiological Control Strategies

The operating modes of pulsatile and rotary VADs are usually chosen by the physicians (human-in-the-loop approach). They evaluate the patient's condition to define the most ade-